Transactions of the ASME®

Journal of Applied Mechanics

Published Quarterly by The American Society of Mechanical Engineers

VOLUME 67 • NUMBER 3 • SEPTEMBER 2000

Transactions of the ASME, Journal of Applied Mechanics (ISSN 0021-8936) is published quarterly (Mar., June, Sept., Dec.) The American Society of Mechanical Engineers, Three Park Avenue, New York, NY 10016. Periodicals postage paid at New York, NY and additional mailing office. POSTMASTER: Send address changes to Transactions of the ASME, Journal of Applied Mechanics, c/o THE AMERICAN SOCIETY OF MECHANICAL ENGINEERS, 22 Law Drive, Box 2300, Fairfield, NJ 07007-2300. **CHANGES OF ADDRESS** must be received at Society headquarters seven weeks before they are to be effective. Please send old label and new address. **STATEMENT from By-Laws.** The Society shall not be responsible for statements or opinions advanced in papers or . . . printed in its publications (B7.1, Para. 3).

TECHNICAL PAPERS

(**Contents continued on inside back cover**)

This journal is printed on acid-free paper, which exceeds the ANSI Z39.48-1992 specification for permanence of paper and library materials. ♾™
♻ 85% recycled content, including 10% post-consumer fibers.

Journal of Applied Mechanics Volume 67, Number 3 SEPTEMBER 2000

BRIEF NOTES

DISCUSSIONS

ANNOUNCEMENTS AND SPECIAL NOTES

An Energy-Based Model of Longitudinal Splitting in Unidirectional Fiber-Reinforced Composites

K. Oguni

G. Ravichandran
Mem. ASME

Graduate Aeronautical Laboratories,
California Institute of Technology,
Pasadena, CA 91125

Unidirectional fiber-reinforced composites are often observed to fail in a longitudinal splitting mode in the fiber direction under far-field compressive loading with weak lateral confinement. An energy-based model is developed based on the principle of minimum potential energy and the evaluation of effective properties to obtain an analytical approximation to the critical stress for longitudinal splitting. The analytic estimate for the compressive strength is used to illustrate its dependence on material properties, surface energy, fiber volume fraction, fiber diameter, and lateral confining pressure. The predictions of the model show good agreement with available experimental data.
[S0021-8936(00)02003-1]

1 Introduction

Fiber-reinforced composite materials are used in the form of laminates in numerous structural applications by taking advantage of their directional properties. Such applications are often limited by the compressive strength of the composite materials that are used. Failure modes in composite laminates are complex and are not always easily understood (e.g., [1,2]). On the other hand, unidirectional fiber-reinforced composites serve as excellent model materials for investigating the associated strength and failure issues. Unidirectional fiber-reinforced composites also have much lower compressive strength than their tensile strength for loading in the fiber direction. Therefore, the prediction of the compressive strength is a critical issue in designing composite materials and composite structures. Commonly observed failure modes in unidirectional composites under compression in the fiber direction include (i) longitudinal or axial splitting due to transverse cracking, (ii) fiber kinking (initiation and propagation of kink bands or microbuckles), and (iii) longitudinal splitting followed by fiber kinking (see for e.g., [2,3]). These failure modes are also observed under axial compression in the presence of lateral confinement. However, the mechanisms, which govern these failure modes in composites, are not completely understood. The effect of lateral confinement on compressive strength is an outstanding issue because of its relevance in developing and validating existing phenomenological failure models for composites (e.g., [4,5]). Also, in composite laminates, even under uniaxial compression, the stress state is multiaxial, and hence there is a need for models that can reliably predict their strength under multiaxial stress states. For the kinking mode of failure, a wide range of experimental, analytical, computational efforts have been undertaken (e.g., [2,3,6–9]). On the other hand, relatively little is known about longitudinal splitting due to transverse cracking. A number of researchers have observed an increase in the compressive strength with increasing lateral confinement (e.g., [10–12]). Further, from a materials design point of view, it is desirable to have models that can predict the strength of the composites in terms of the properties of fiber, matrix, and their interface. Motivated by these experimental observations and the current lack of satisfactory models for longitudinal (axial) splitting in composites (with an exception in the work by [9]), a new energy-based approach for predicting compressive strength of unidirectional fiber reinforced composites has been developed and is presented here.

One way to investigate the longitudinal splitting under compression is to compute the energy release rate and track the evolution of dominant microcracks in the composites. However, the stress field and the evolution law for a crack embedded in a highly heterogeneous material such as fiber-reinforced composites is extremely complicated and hence a satisfactory analytic approach appears not to be plausible in this case. In this paper, an energetic approach similar to the one that has been used for studying axial splitting in isotropic brittle solids such as ceramics ([13]) is employed to gain insights into longitudinal splitting phenomena in fiber-reinforced composites. By combining the principle of minimum potential energy and the effective properties of the composite, an energy-based criterion for longitudinal splitting of unidirectional fiber-reinforced composite is established. Hashin [14] has used a similar approach in determining the energy release rate for fracture in laminated composites.

Due to the heterogeneity and anisotropy of the fiber-reinforced composite, excessive elastic energy is stored in the composite under compression. Longitudinal splitting can be regarded as a process in which the excessive elastic energy is released through the formation of new surfaces. Therefore, when the reduction of the stored elastic energy by splitting compensates the surface energy, the specimen splits. This energy-based failure criterion combined with the effective properties of the composite based on the elastic properties of the matrix and the fiber provides an analytical expression for the critical stress (compressive strength) for longitudinal splitting. This expression illustrates the effect of material properties, surface energy, fiber volume fraction, fiber diameter, and lateral confining pressure on the critical axial compressive stress for longitudinal splitting. The model predictions are compared with available experimental results in the literature ([10,11,15]) and show good agreement. The predictions break down for large confining pressures due to failure mode transition to kinking which is not accounted for in the present model.

Contributed by the Applied Mechanics Division of THE AMERICAN SOCIETY OF MECHANICAL ENGINEERS for publication in the ASME JOURNAL OF APPLIED MECHANICS. Manuscript received by the ASME Applied Mechanics Division, June 9, 1999; final revision, Dec. 7, 1999. Associate Technical Editor: K. T. Ramesh. Discussion on the paper should be addressed to the Technical Editor, Professor Lewis T. Wheeler, Department of Mechanical Engineering, University of Houston, Houston, TX 77204-4792, and will be accepted until four months after final publication of the paper itself in the ASME JOURNAL OF APPLIED MECHANICS.

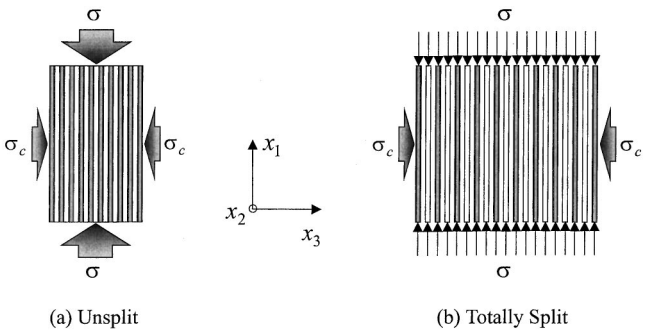

Fig. 1 Schematics of unsplit and longitudinally split configurations of a unidirectional fiber composite

2 Energy-Based Model for Longitudinal Splitting

2.1 Problem Formulation. Consider a cylindrical specimen of an ideal[1] unidirectional fiber-reinforced composite under lateral confining stress, σ_c, and axial compressive stress, σ, shown schematically in Fig. 1(*a*). Under this setting, compare two configurations shown in Fig. 1: (*a*) one is unsplit, and (*b*) the other is totally split in the fiber direction. Let the total potential energy density of unsplit and split specimen be Π_u and Π_s, respectively. Comparison between Π_u and Π_s provides the critical axial stress for splitting under given lateral confining stress, σ_c. The criterion for longitudinal splitting is the minimization of the total potential energy density of the specimen. In other words, when Π_u exceeds Π_s, the specimen splits ([13]).

The total potential energy is computed in terms of the effective material properties as a function of the properties of fiber and matrix using the concept of representative volume element (RVE). Instead of considering the entire problem, an auxiliary problem is set up focusing on an element (RVE) which consists of a fiber surrounded by the matrix according to the volume fraction under the same strain or stress boundary condition as that of the original problem. If the specimen is macroscopically homogeneous, the average strain and stress over the RVE are the same as that of the entire specimen. In the problem under consideration, because of the random in-plane distribution of the fibers, the RVE reduces to a circular cylinder which consists of a single straight fiber of the specimen length surrounded with matrix according to the fiber volume fraction. The issues related to establishing RVEs in fiber-reinforced composites are well established (e.g., [16–18]).

2.2 Energy Criterion for Longitudinal Splitting

2.2.1 Total Potential Energy of Unsplit Specimen. The total potential energy density of the unsplit specimen, Π_u, is the same as the elastic energy density. Hence, under stress (traction) boundary condition, Π_u is given as follows:

$$\Pi_u=\frac{1}{V}\int_V\left\{\frac{1}{2}\boldsymbol{\varepsilon}(x):\mathbf{C}(x):\boldsymbol{\varepsilon}(x)-\boldsymbol{\sigma}(x):\boldsymbol{\varepsilon}(x)\right\}dx$$

$$=\frac{1}{V}\int_V\left\{-\frac{1}{2}\boldsymbol{\sigma}(x):\mathbf{S}(x):\boldsymbol{\sigma}(x)\right\}dx=-\frac{1}{2}\overline{\boldsymbol{\sigma}}:\mathbf{S}_*:\overline{\boldsymbol{\sigma}} \tag{2.1}$$

where V is the volume of the RVE, $\mathbf{C}(x)$ and $\mathbf{S}(x)$ are the fourth-order elasticity and compliance tensors at point $\boldsymbol{x}$, respectively, $\boldsymbol{\varepsilon}(x)$ is the strain field, $\boldsymbol{\sigma}(x)$ is the stress field, and $\overline{\boldsymbol{\sigma}}$ is the volumetric average stress tensor over V which corresponds to the prescribed stress on the boundary of the specimen. $\mathbf{S}_*$ is the effective compliance tensor of the unsplit specimen.

[1]The fibers of the same diameter are aligned and homogeneously distributed in the plane (x_2-x_3) perpendicular (transverse) to the fiber direction (x_1).

Because of the unidirectional reinforcement of the fibers, the specimen is transversely isotropic. Besides, the cartesian coordinates, x_1, x_2, and x_3 directions are also the principal directions. Therefore, to evaluate Π_u, we need only four independent effective moduli, namely, the longitudinal Young's modulus, E_1^*, Poisson ratio, ν_{21}^*, the plane strain bulk modulus, K_{23}^* and the shear modulus, G_{23}^*. Using the cylindrical RVE introduced before, effective elastic moduli of the unidirectional composite for random in-plane distribution of fibers, $E_1^*, \nu_{21}^*, K_{23}^*$, and the upper and lower bounds for G_{23}^* have been obtained by Hashin and Rosen [16]. Since the lower bound corresponds to the macro-stress prescribed problem, the lower bound for G_{23}^* is used here. The expressions for the moduli tensor and related elasticity constants are shown in the Appendix in terms of the elastic constants of the fiber and the matrix as well as their volume fractions.

The average stress-strain relation for the RVE is given as follows:[2]

$$\begin{aligned}\overline{\sigma}_{11}&=C_{11}^*\overline{\varepsilon}_{11}+C_{12}^*\overline{\varepsilon}_{22}+C_{12}^*\overline{\varepsilon}_{33}\\ \overline{\sigma}_{22}&=C_{12}^*\overline{\varepsilon}_{11}+C_{22}^*\overline{\varepsilon}_{22}+C_{23}^*\overline{\varepsilon}_{33}\\ \overline{\sigma}_{33}&=C_{12}^*\overline{\varepsilon}_{11}+C_{23}^*\overline{\varepsilon}_{22}+C_{22}^*\overline{\varepsilon}_{33}\end{aligned} \tag{2.2}$$

The prescribed stress boundary conditions are

$$\overline{\sigma}_{11}=-\sigma \quad \overline{\sigma}_{22}=\overline{\sigma}_{33}=-\sigma_c \quad \overline{\sigma}_{12}=\overline{\sigma}_{13}=\overline{\sigma}_{23}=0 \tag{2.3}$$

where σ and σ_c are the magnitudes of the axial stress and the lateral confinement. Compressive stress components are assumed to be negative. The total potential energy density for the unsplit specimen, Π_u, is a quadratic form of the compressive stress, σ,

$$\begin{aligned}\Pi_u&=-\frac{1}{2}\begin{bmatrix}-\sigma\\-\sigma_c\\-\sigma_c\end{bmatrix}^T\begin{bmatrix}C_{11}^* & C_{12}^* & C_{12}^*\\ C_{12}^* & C_{22}^* & C_{23}^*\\ C_{12}^* & C_{23}^* & C_{22}^*\end{bmatrix}^{-1}\begin{bmatrix}-\sigma\\-\sigma_c\\-\sigma_c\end{bmatrix}\\ &=\frac{(C_{22}^*+C_{23}^*)\sigma^2-4C_{12}^*\sigma_c\sigma+2C_{11}^*\sigma_c^2}{4C_{12}^{*2}-2C_{11}^*(C_{22}^*+C_{23}^*)}\\ &=-\frac{1}{2}\left\{\frac{\sigma^2}{E_1^*}+\frac{4\nu_{21}^*\sigma_c\sigma}{E_1^*}+\left(\frac{1}{K_{23}^*}+\frac{4\nu_{21}^{*2}}{E_1^*}\right)\sigma_c^2\right\}.\end{aligned} \tag{2.4}$$

2.2.2 Total Potential Energy of Split Specimen. Under the same boundary condition as that of the unsplit specimen (2.3) and assuming that *each* RVE splits at the boundary of the matrix and the fiber, i.e., the split is caused by an interfacial crack (delamination), the split RVE can be regarded as two columns, consisting of either the fiber or the matrix. Such a simplifying assumption enables gaining insights into the strength of composites. The elastic energy density of the RVE after splitting, E_s, is given by

$$E_s=\frac{1}{V}\int_V\left\{-\frac{1}{2}\boldsymbol{\sigma}(x):\mathbf{S}(x):\boldsymbol{\sigma}(x)\right\}dx$$

$$=-\frac{1}{2}\overline{\boldsymbol{\sigma}}:\mathbf{S}^*:\overline{\boldsymbol{\sigma}}=-\frac{1}{2}\overline{\boldsymbol{\sigma}}:(v_f\mathbf{S}_f+v_m\mathbf{S}_m):\overline{\boldsymbol{\sigma}} \tag{2.5}$$

where $\mathbf{S}^*$ is the effective compliance tensor of the split specimen, v_f, v_m are volume fractions of fiber and matrix, respectively. The matrix volume fraction v_m is assumed throughout to be $(1-v_f)$.

The fiber and the matrix are assumed to be isotropic and the compliance tensor of fiber and matrix, $\mathbf{S}_f, \mathbf{S}_m$ can be expressed in terms of their respective Young's moduli (E_f, E_m) and Poisson's ratios (ν_f, ν_m). Therefore, the elastic energy density for the split specimen, E_s, is given as a quadratic form of the axial compressive stress, σ

[2]Expressions for $C_{11}^*, C_{12}^*, C_{22}^*, C_{23}^*$ are shown in the Appendix.

$$E_s = -\frac{1}{2}\overline{\boldsymbol{\sigma}}:(v_f \mathbf{S}_f + v_m \mathbf{S}_m):\overline{\boldsymbol{\sigma}}$$

$$= -\frac{1}{2}\left[\frac{v_f}{E_f}\{\sigma^2 - 4\nu_f\sigma\sigma_c + 2(1-\nu_f)\sigma_c^2\} + \frac{(1-v_f)}{E_m} \times\{\sigma^2 - 4\nu_m\sigma\sigma_c + 2(1-\nu_m)\sigma_c^2\}\right]. \quad (2.6)$$

The surface energy per unit volume, Γ, of the RVE due to splitting can be obtained by introducing a surface energy per unit area, γ

$$\Gamma = \frac{2\gamma A}{V} = \frac{2\gamma(2\pi a h)}{\pi R^2 h} = \frac{4\gamma v_f}{a} \quad (2.7)$$

where A is the lateral surface area of a fiber in the RVE, a is the radius of the fiber, and R is the radius of the RVE. Note that Γ (2.7) is independent of the height of the RVE, h, the height of the specimen. The surface energy γ can be interpreted as the energy release rate ($G_c = 2\gamma$) for interfacial crack initiation along the fiber-matrix interface or delamination ([19]) and the failure is assumed to proceed catastrophically following initiation ([20]). The relationship between the energy release rate G, and the local stress intensity factors K_{I} and K_{II} and the phase angle can be found in Liu et al. [19].

In the present analysis, the surface energy per unit area, γ, is assumed to be a constant (i.e., γ is independent of σ and σ_c). In reality, as confining pressure σ_c increases, the resistance to longitudinal (axial) splitting or delamination failure increases considerably and hence, the fracture energy, G_c or γ. Even though this appears to be consistent with what one might expect, nothing is known at present concerning the effect of pressure on fracture toughness of composite materials.

The total potential energy density of the split specimen, Π_s, is the sum of the elastic energy density, E_s and the surface energy density, Γ,

$$\Pi_s = E_s + \Gamma. \quad (2.8)$$

2.3 Criterion for Longitudinal Splitting. From the principle of minimum potential energy, the criterion for axial splitting can be expressed as

$$\Pi_u - \Pi_s < 0 \Rightarrow \text{unsplit} \quad (2.9a)$$

$$\Pi_u - \Pi_s = 0 \Rightarrow \text{neutral} \quad (2.9b)$$

$$\Pi_u - \Pi_s > 0 \Rightarrow \text{split}. \quad (2.9c)$$

Assuming that Γ is independent of stress state, the equipotential line $\Pi_u - E_s = \Gamma$, i.e., $\Pi_u - \Pi_s = 0$ provides the stress state for the neutral condition (2.9*b*). Examining the quadratic form $\Pi_u - E_s$, it can be shown that $\Pi_u - E_s$ is a monotonically increasing function of σ for $\sigma_c = constant$ provided $\sigma > \sigma_c$. Therefore, the critical condition is given by the equality

$$\Pi_u - \Pi_s = 0. \quad (2.10)$$

The criterion for longitudinal splitting (2.10) could be interpreted in terms of the surface energy of the newly created surfaces ($G_c = 2\gamma$) which cause the reduction in the elastic energy of the intact (unsplit) material.

3 Results

3.1 Compressive Strength. Substituting for Π_u and Π_s from (2.4) to (2.8), the critical stress for longitudinal splitting can be obtained by solving (2.10). Since the form of the total potential energy is a quadratic of σ, there are two roots σ_1 and σ_2:

$$\sigma_{1,2} = \frac{p_2\sigma_c \pm \sqrt{p_2^2\sigma_c^2 - p_1(p_3\sigma_c^2 - \Gamma)}}{p_1} \quad (3.1)$$

where p_1, p_2, and p_3 are expressed in terms of the elastic constants of the materials

$$p_1 = \frac{1}{2}\left(\frac{v_f}{E_f} + \frac{v_m}{E_m} - \frac{1}{E_1^*}\right), \quad p_2 = \frac{v_f\nu_f}{E_f} + \frac{v_m\nu_m}{E_m} - \frac{\nu_{21}^*}{E_1^*},$$

$$p_3 = \frac{v_f(1-\nu_f)}{E_f} + \frac{v_m(1-\nu_m)}{E_m} - \frac{1}{2}\left(\frac{1}{K_{23}^*} + \frac{4\nu_{21}^{*2}}{E_1^*}\right).$$

For a given confining pressure σ_c and surface energy density γ, $\sigma_1 \geqslant \sigma_2$, hence, σ_1 is taken as the critical stress σ^*. Letting $\sigma_c = 0$ in (3.1), the critical stress without confinement, i.e., the unconfined longitudinal compressive strength for the composite can be obtained:

$$\sigma^*|_{\sigma_c=0} = 2\left(\frac{2\gamma v_f}{a}\right)^{1/2}\left(\frac{v_f}{E_f} + \frac{v_m}{E_m} - \frac{1}{E_1^*}\right)^{-1/2}. \quad (3.2)$$

Equation (3.2) shows that unconfined strength is proportional to the square root of surface energy and inversely proportional to the square root of fiber diameter. This result indicates that for a given volume fraction, all other things remaining unchanged, composites with larger fiber diameter are more susceptible to axial splitting than smaller diameter fibers. Since $E_f \gg E_m$ in usual fiber-reinforced composites, $v_m/E_m \gg v_f/E_f$ and $E_1^* \cong v_f E_f$ hold. Based on these evaluations, (3.2) can be simplified as follows:

$$\sigma^*|_{\sigma_c=0} = 2\left(\frac{2\gamma v_f}{a}\right)^{1/2}\left(\frac{1-v_f}{E_m} - \frac{1}{v_f E_f}\right)^{-1/2}. \quad (3.3)$$

Examining the quadratic form of the energy surface, $\Phi(\sigma, \sigma_c) = \Pi_u - \Pi_s$ for a constant surface energy density γ, and assuming that the longitudinal (fiber direction) compliance is smaller than the lateral (transverse) compliance in the composite (typical for most fiber reinforced composites) the following inequality holds:

$$\frac{d\sigma^*}{d\sigma_c} \leqslant 1 \quad (3.4)$$

subject to the constraints

$$\sigma > \sigma_c \quad (3.5a)$$

and

$$d\Phi = \frac{\partial\Phi}{\partial\sigma}d\sigma + \frac{\partial\Phi}{\partial\sigma_c}d\sigma_c = 0. \quad (3.5b)$$

The first constraint (3.5*a*) corresponds to axial compression and the second constraint (3.5*b*) corresponds to the equi-potential line. From (3.4), one can conclude that if the splitting failure is governed by the principle of minimum total potential energy and the surface energy density γ is a constant, the slope of the relationship between compressive strength and confining pressure, i.e., σ^* versus σ_c, cannot exceed unity. Even if the surface energy density γ is an increasing function of confining pressure σ_c, the inequality (3.4) holds at least for small σ_c. The effect of lateral confinement and material properties on the compressive strength of composites can be investigated by using (3.1).

3.2 Model Predictions. Examining the functional form shown in (3.1) and (3.2), important parameters for longitudinal splitting can be identified as γ/a, v_f, and σ_c. To investigate the dependence of compressive strength on each of these parameters and compare the effect of each parameter, parametric studies have been performed. In the present parametric study, two different types of commonly used fiber-reinforced composite are investigated to illustrate the dependence of compressive strength on material properties. These materials are a unidirectional E-glass/vinylester composite (indicated as ''G/VE'' in the figures) and a unidirectional carbon/epoxy composite (indicated as ''C/ER'' in the figures). Experimental data and material properties for these materials are available in the literature ([11,15]). The relevant

Table 1 Material properties of fiber and matrix and geometry of fiber

	Fiber				Matrix		Interface
	E_f (GPa)	ν_f[(d)]	v_f	a (μm)	E_m (GPa)	ν_m	γ[(d)] (J/m^2)
E-Glass/Vinylester	72.4[(a)]	0.2	0.1−0.6[(a)]	12.1[(a)]	3.69[(a)]	0.38[(d)]	110,210
Carbon/Epoxy	260[(b)]	0.2	0.36[(b)]	3.4[(b)]	1.63[(b)]	0.34[(b)]	140
Carbon/Epoxy	234[(c)]	0.2	0.6[(c)]	3.4[(d)]	4.28[(c)]	0.34[(d)]	140

[(a)]Waas et al. [15];
[(b)]Weaver and Williams [10];
[(c)]Parry and Wronski [11];
[(d)]assumed

material properties including those of the fiber and the matrix as well as the radius of the fibers for these composites are shown in Table 1. Surface energy density γ's shown in Table 1 are obtained by calibration to the corresponding experimental data for unconfined compressive strength.

Figure 2 shows the compressive strength of two types of composite for different γ/a and σ_c (0 and 100 MPa) with fixed fiber volume fraction $v_f=60$ percent. One can observe a strong dependence of compressive strength on γ/a (proportional to $\sqrt{\gamma/a}$) and relatively weak dependence on σ_c. Also, the compressive strength seems to be almost insensitive to the choice of the material for a given value of γ/a. Small values of γ/a correspond to low interfacial energy (weak interface) and/or large diameter fibers, whereas large values of γ/a correspond to large interfacial energy (tough interface) and/or small diameter fibers. The unconfined compressive strengths of E-glass/vinylester composite and carbon/epoxy composite with $v_f=60$ percent are 667 MPa [15] and 1.5 GPa ([11]), respectively. Based on these experimental observations, if the v_f is identical, the carbon/epoxy composite appears to be stronger than the E-glass/vinylester composite. However, the strong dependence on γ/a plays a significant role here. Suppose γ is of the same order for both composites, fiber radii a for E-glass/vinylester composite and carbon/epoxy composite are 12.1 μm and 3.4 μm, respectively (see Table 1). This results in γ/a for the carbon/epoxy composite to be approximately four times as that of the E-glass/vinylester composite.

Figure 3 shows unconfined compressive strength (i.e., $\sigma_c=0$) as a function of γ/a and v_f. For a given γ/a, effect of v_f on compressive strength is much stronger than that of the material properties. This observation together with the insensitivity of the strength to the choice of the material observed in Fig. 2 has the following implication. The compressive strength of the unidirectional fiber-reinforced composite is relatively insensitive to the magnitude of the material properties of each constituent, i.e., fiber and matrix. Instead, the degree of anisotropy introduced by combining the materials with different material properties is an important factor in the determination of compressive strength. Longitudinal splitting can be considered to be the process in which excessive stored elastic energy due to the heterogeneity and anisotropy can be released through the formation of new surfaces. The importance of anisotropy has been evidenced in this parametric study.

Compressive strength for different v_f and σ_c with fixed γ/a is shown in Fig. 4. Based on experimental observations, $\gamma/a=1.32\times10^7$ J/m^3 and $\gamma/a=4.17\times10^7$ J/m^3 are used for E-glass/vinylester and carbon/epoxy, respectively, as the best fitting values for the model prediction of their unconfined compressive strength ([11,15]). It is again seen that if the same values for γ/a were used, the compressive strength for both materials are close to each other as expected from previously shown parametric studies (Figs. 2 and 3). In this case, the difference between the results for two different levels of confinement $\sigma_c=0$ MPa $\sigma_c=100$ MPa is small and nearly constant for all values of v_f shown here. This shows that the effect of σ_c on compressive strength is much weaker than that of v_f and is relatively insensitive for a given v_f.

3.3 Comparison With Experiments. To verify the validity of the energy-based model for longitudinal splitting, the compressive strengths predicted by the present model are compared with the experimental results obtained for E-glass/vinylester and carbon/epoxy composites. Uniaxial compression tests on unidirectional fiber-reinforced E-glass/vinylester composite with different fiber volume fraction ranging from 0 percent to 60 percent were performed by Waas et al. [15]. For carbon/epoxy composites, compression tests on unidirectional fiber-reinforced composites under superposed hydrostatic confinement have been performed

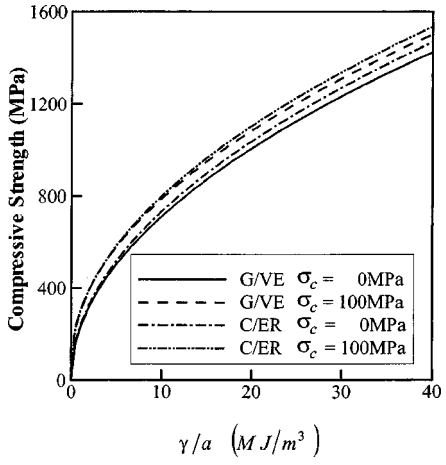

Fig. 2 Effect of surface energy and lateral confinement on compressive strength (G/VE stands for E-Glass/vinylester and C/ER stands for carbon/epoxy)

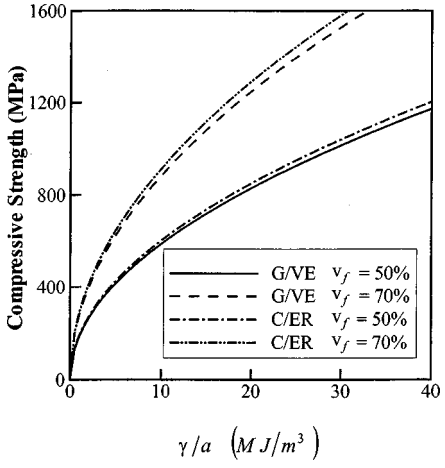

Fig. 3 Effect of surface energy and fiber volume fraction on unconfined compressive strength ($\sigma_c=0$) (G/VE stands for E-Glass/vinylester and C/ER stands for carbon/epoxy)

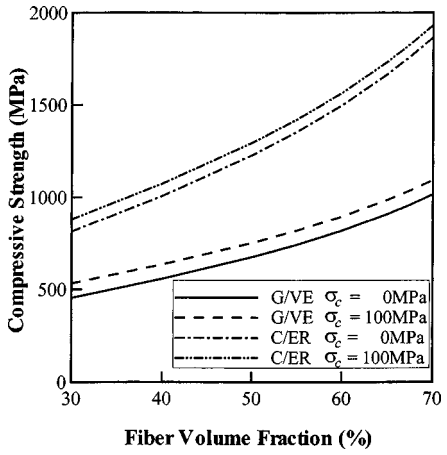

Fig. 4 Effect of fiber volume fraction and lateral confinement on compressive strength (G/VE stands for E-Glass/vinylester and C/ER stands for carbon/epoxy)

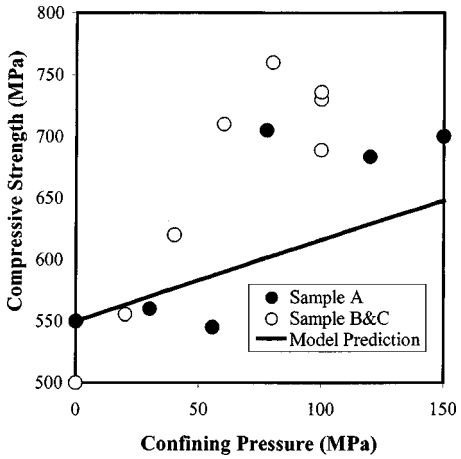

Fig. 6 Comparison between experimental results ([10]) and model prediction for carbon/epoxy composite, v_f=36 percent

by Weaver and Williams [10] and Parry and Wronski [11]. The input parameters for the model prediction including material properties, fiber radius, and surface energy of the material used in their experiments have been shown in Table 1.

Comparison between the model prediction and experimental results by Waas et al. [15] provides the measure of the validity of the present model with respect to changing v_f. Experimental results for the unconfined compressive strength from Waas et al. [15] are shown in Fig. 5. Examining the trend in compressive strength, one can observe a dip between $v_f=30$ percent and $v_f=40$ percent. Based on this observation, analysis is performed for two groups of data sets. One is for low v_f, i.e., $v_f \leqslant 30$ percent, the other is for high v_f, i.e., $v_f \geqslant 40$ percent. Only the difference in these analyses is the input parameter for the surface energy γ. The values of the surface energy which enable the model predictions to show good agreement with experimental results are $\gamma=210$ J/m^2 for the low v_f data set and $\gamma=110$ J/m^2 for the high v_f data set. In the present model, γ has been assumed to be the surface energy associated with delamination between the fiber and the matrix. The surface energy associated with the creation of new surfaces in the matrix has been neglected. In the case of high v_f, surface energy associated with matrix failure is negligible since the average distance between fibers is small and the area of the surface created by matrix failure is much smaller than the one created by interface (fiber-matrix) debonding. On the other hand, as the fiber volume fraction decreases, the average distance between fibers increases and the surface energy associated with matrix failure becomes no longer negligible, which results in the increase of total surface energy. Also, the nonlinearity of the matrix for vinylester ([15]) which is important at low volume fractions of the fiber has been neglected in the present analysis. The increase in surface energy associated with matrix failure is consistent with the requirement for larger surface energy γ for lower v_f. Further work towards quantification of fracture energies as a function of volume fraction in fiber reinforced composites is needed. The model predictions for the matrix-dominated region and the fiber-interface dominated region can be regarded, respectively, as upper and lower bound for compressive strength of the composite.

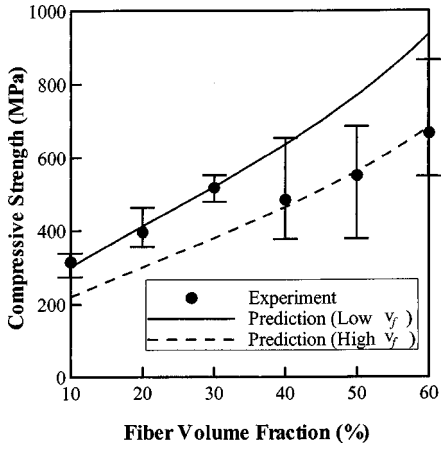

Fig. 5 Comparison between experimental results ([15]) and model predictions for E-Glass/vinylester composite

The experimental result shows considerable scatter for $v_f \geqslant 40$ percent. In general, the interfacial toughness is highly dependent on local conditions such as size/orientation of initial imperfection, mode mixity, and bonding (interface strength and toughness). As a result, the interface properties vary more than the material properties of each constituent of composite, i.e., fiber and matrix. The fracture energy of fiber-reinforced composites (G_c) depends strongly on the local mode mixity ([19]). Therefore, for the case of low v_f, the scatter in compressive strength is relatively small since the matrix plays a signifiant role in determining the surface energy associated with splitting. On the other hand, since the surface energy associated with fiber/matrix debonding is dominant for high v_f, the local interfacial conditions play a significant role in determining the compressive strength. This results in a large scatter of the compressive strength for composites with high v_f as seen from the experimental results in Fig. 5.

Comparison between the model prediction and experimental results by Weaver and Williams [10] (WW) and Parry and Wronski [11] (PW) provides a measure of the validity of the present model with respect to the confining pressure, σ_c. To the best knowledge of the authors, WW and PW are the most widely accepted reliable experimental data regarding compressive failure of unidirectional fiber-reinforced composites under superposed hydrostatic confinement including detailed discussion on failure modes. Although some specimen geometry dependence of failure mode is reported in PW and short specimens used in WW show end effect, their experiments are convincing enough to regard longitudinal splitting as the dominant failure mode under weak lateral confinement. The critical stress σ^* is plotted against the confining pressure σ_c in Fig. 6 (WW for $0 \leqslant \sigma_c \leqslant 150$ MPa) and in Fig. 7 (PW for $0 \leqslant \sigma_c \leqslant 300$ MPa). In the experiments by PW, for higher confining pressure ($\sigma_c > 150$ MPa), the slope of σ_c versus σ^* graph is steeper than those for lower confining pressure as seen in Fig. 7.

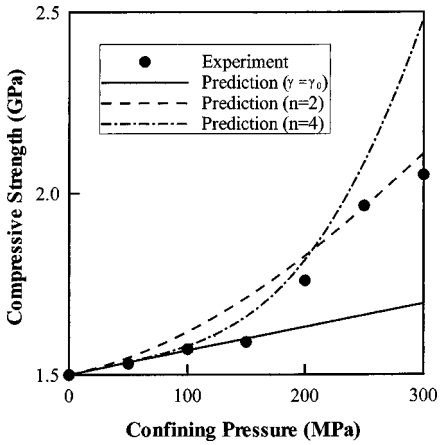

Fig. 7 Comparison between experimental results ([11]) and model predictions with the effect of increasing surface energy for carbon/epoxy composite, $vf=60$ percent

This increase of the slope is also observed in the experiments by WW. Besides, both observed failure mode transition from longitudinal splitting to kink banding around $\sigma_c = 150$ MPa. Therefore, the comparisons are restricted to low levels of confinement, i.e., $0 \leqslant \sigma_c \leqslant 150$ MPa. Surface energy per unit area, γ, used here is assumed to be the same for both the cases and is shown in Table 1. The model predictions show significant agreement with the experimental results, especially with those obtained by PW (Fig. 7). The theoretical predictions agree with the experimental results given by WW (Fig. 6) for confining pressures $0 \leqslant \sigma_c \leqslant 50$ MPa. However, in the range of $50 \leqslant \sigma_c \leqslant 150$ MPa, the agreement is not good. The experimental results show considerable scatter for confining pressures $50 \leqslant \sigma_c \leqslant 150$ MPa although the samples A, B, and C are made of the same material. It is believed that due to low fiber volume fraction (36 percent), a host of failure modes might have occurred under the confining pressure $50 \leqslant \sigma_c \leqslant 150$ MPa in the experiments by WW, and this could explain the scatter in experimental results. Also, $v_f = 36$ percent happens to be in the range of transition zone from matrix-dominated region to interface dominated region for longitudinal (axial) splitting of E-glass/vinylester composite discussed above. Although the material is different, the geometrical interpretation about the increase of the area of the matrix failure still holds in this case. Therefore, the large scatter in compressive strength might be a result of the characteristic of the transition zone between low and high volume fraction of fibers.

In the present model, the only adjustable parameter is surface energy per unit area, γ, which is not readily available for the composites considered here from experimental measurements. However, the values γ used in the model predictions appear to be consistent with data available for similar composite materials ([21]) by assuming $G_c = 2\gamma$.

4 Conclusions and Discussion

An energy-based model has been developed for predicting the compressive strength of unidirectional fiber-reinforced composites which fail by longitudinal (axial) splitting. The following conclusions are based on the analytic results (3.1) and (3.2):

(i) The critical stress for longitudinal splitting is proportional to $\sqrt{\gamma/a}$ and this parameter is the most dominant term in the determination of the compressive strength of fiber-reinforced composites. According to the present model, composites with larger fracture energy and small fiber diameters would result in higher strength.

(ii) The degree of the anisotropy plays a significant role and the effect of fiber volume fraction appears only in this context in influencing the compressive strength.

(iii) The effect of confining pressure on compressive strength is relatively weak.

The model prediction has been compared with the experimental results and showed good agreement. This agreement supports the validity of the present method for the analysis of longitudinal splitting (delamination failure) in unidirectional fiber-reinforced composites.

The assumption of a constant γ would predict longitudinal splitting at all levels of confinement and with markedly lower strength than experimentally observed ones at high confining pressures. Beyond certain confining pressure, longitudinal splitting is completely suppressed and the failure mode translates to kink banding ([10–12]). In order to illustrate the effect of increasing fracture surface energy γ with increasing pressure, γ is assumed to depend on σ_c as follows:

$$\gamma = \gamma_0 \left\{ 1 + \alpha_n \left(\frac{\sigma_c}{\sigma_0^*} \right)^n \right\} \tag{4.1}$$

where γ_0 is surface energy for $\sigma_c = 0$, σ_0^* is the unconfined compressive strength, n is the confining pressure hardening exponent, and α_n is a positive dimensionless parameter corresponding to the exponent n. For $n \neq 0$ in (4.1), γ increases as σ_c increases and this results in nonlinear dependence of model prediction of compressive strength on σ_c. In this case, the inequality (3.4) for the slope of σ^* versus σ_c being less than unity holds at least for small σ_c. The dependence of γ on σ_c (4.1) can be viewed to reflect the increase in the energy release rate G_c as the local mode-mixity for interface cracking changes from mostly mode I to mode II ([19]) with increasing confinement.

The model predictions of compressive strength for the carbon/epoxy composite used by Parry and Wronski [11] for the cases $n=2$ and $n=4$ in (4.1) are shown in Fig. 7. Input parameters for the model predictions are $\gamma_0 = 140$ J/m^2, $\sigma_0^* = 1.5$ GPa, $\alpha_2 = 15.58$, and $\alpha_4 = 823.6$. Comparison between the cases of $n=2$ and $n=4$ shows that as the exponent n increases, the curvature of the failure envelope can be increased and as a result, the model prediction for longitudinal splitting stays close to experimental result in wider range of confinement than the prediction based on smaller n and exceeds the experimental value at high confining pressures where formation of kink bands, instead of longitudinal splitting, is observed in experiments. This observation implies that if γ increases as a function of σ_c and its dependence on σ_c is strong, i.e., exponent n is large, longitudinal or axial splitting can be observed up to certain levels of confinement and is suppressed at high levels of confinement where other failure modes such as kink band formation should be considered.

Acknowledgment

This work was supported by the Office of Naval Research (Dr. Y. D. S. Rajapakse, Scientific Officer) through a grant to the California Institute of Technology.

Appendix

Following Hashin and Rosen [16], the expression for the effective moduli of the unidirectional fiber composite (x_1-fiber direction) E_1^*, ν_{21}^*, K_{23}^*, and G_{23}^* are given below:

$$E_1^* = (v_f E_f + v_m E_m) \frac{E_m(D_1 - D_3 F_1) + E_f(D_2 - D_4 F_2)}{E_m(D_1 - D_3) + E_f(D_2 - D_4)},$$

$$\nu_{21}^* = \frac{v_f E_f L_1 + v_m E_m L_2 \nu_m}{v_f E_f L_3 + v_m E_m L_2}$$

$$K_{23}^* = K_m \frac{K_f(1 + 2\nu_m v_f) + 2K_m \nu_m v_m}{K_f v_m + K_m(v_f + 2\nu_m)};$$

$$G_{23}^{*}=G_m\Big/\left[1+\frac{2(1-\nu_m)}{1-2\nu_m}v_fA_4\right]\quad\text{(lower bound)}$$

where $D_1=1-\nu_f$, $D_2=(1+v_f)/v_m+\nu_m$, $D_3=2\nu_f^2$, $D_4=2\nu_m^2v_f/v_m$,

$$F_1=\frac{\nu_mv_fE_f+\nu_fv_mE_m}{\nu_fv_fE_f+\nu_mv_mE_m},\quad F_2=\frac{\nu_f}{\nu_m}F_1,$$

$$L_1=2\nu_f(1-\nu_m^2)v_f+\nu_m(1+\nu_m)v_m,\quad L_2=v_f(1-\nu_f-2\nu_f^2),$$

$$L_3=2(1-\nu_m^2)v_f+(1+\nu_m)v_m,$$

$$\begin{aligned}A_4=&2(G_f-G_m)(2\nu_m-1)[G_m(4\nu_f-3)(v_f^3-1)\\&-G_f\{(4\nu_m-3)\nu_f^3-1\}]/[G_m^2(4\nu_f-3)(v_f-1)^4\\&-2G_fG_m\{-5+6\nu_m-4\nu_f+6v_f^2-4\nu_mv_f^3+(3-2\nu_m)\nu_f^4\\&+2\nu_f(3-4\nu_m+4v_m-6v_f^2+4\nu_mv_f^3-v_f^4)\}\\&+G_f^2\{3+4v_f-6v_f^2+4v_f^3(3-6\nu_m+4\nu_m^2)\\&+(3-4\nu_m)v_f^4-\nu_m\}]\end{aligned}$$

E_f, ν_f, v_f and E_m, ν_m, v_m are the Young's moduli, Poisson's ratios, and the volume fractions of the fiber and the matrix, respectively.

The elastic moduli $C_{11}^{*},C_{12}^{*},C_{22}^{*},C_{23}^{*}$ are expressed using E_1^{*}, ν_{21}^{*}, K_{23}^{*}, and G_{23}^{*} given above;

$$C_{11}^{*}=E_1^{*}+4\nu_{21}^{*2}K_{23}^{*}$$

$$C_{12}^{*}=2\nu_{21}^{*}K_{23}^{*}$$

$$C_{22}^{*}=K_{23}^{*}+G_{23}^{*}$$

$$C_{23}^{*}=K_{23}^{*}-G_{23}^{*}.$$

References

[1] Shuart, M. J., 1989, ''Failure of Compression-Loaded Multidirectional Composite Laminates,'' AIAA J., **27**, pp. 1274–1279.

[2] Waas, A. M., and Schultheisz, C. R., 1996, ''Compressive Failure of Composites, Part II: Experimental Studies,'' Prog. Aerosp. Sci., **32**, pp. 43–78.

[3] Fleck, N. A., 1997, ''Compressive Failure of Fiber Reinforced Composites,'' Adv. Appl. Mech., **33**, pp. 43–117.

[4] Tsai, S. W., and Wu, E. M., 1971, ''A General Theory of Strength for Anisotropic Materials,'' J. Compos. Mater., **5**, pp. 58–80.

[5] Christensen, R. M., 1997, ''Stress Based Yield/Failure Criteria for Fiber Composites,'' Int. J. Solids Struct., **34**, pp. 529–543.

[6] Budiansky, B., and Fleck, N. A., 1993, ''Compressive Failure of Composites,'' J. Mech. Phys. Solids, **41**, pp. 183–211.

[7] Kyriakides, S., Arseculeratne, R., Perry, E. J., and Liechti, K. M., 1995, ''On the Compressive Failure of Fiber Reinforced Composites,'' Int. J. Solids Struct., **32**, pp. 689–738.

[8] Schultheisz, C. R., and Waas, A. M., 1996, ''Compressive Failure of Composites, Part I: Testing and Micromechanical Theories,'' Prog. Aerosp. Sci., **32**, pp. 1–42.

[9] Lee, S. H., and Waas, A. M., 1999, ''Compressive Response and Failure of Fiber Reinforced Unidirectional Composites,'' Int. J. Fract., **100**, pp. 275–306.

[10] Weaver, C. W., and Williams, J. G., 1975, ''Deformation of a Carbon-Epoxy Composite Under Hydrostatic Pressure,'' J. Mater. Sci., **10**, pp. 1323–1333.

[11] Parry, T. V., and Wronski, A. S., 1982, ''Kinking and Compressive Failure in Uniaxially Aligned Carbon Fibre Composite Tested Under Superposed Hydrostatic Pressure,'' J. Mater. Sci., **17**, pp. 893–900.

[12] Sigley, R. H., Wronski, A. S., and Parry, T. V., 1992, ''Axial Compressive Failure of Glass-Fibre Polyester Composites Under Superposed Hydrostatic Pressure: Influence of Fibre Bundle Size,'' Compos. Sci. Technol., **43**, pp. 171–183.

[13] Bhattacharya, K., Ortiz, M., and Ravichandran, G., 1998, ''Energy-Based Model of Compressive Splitting in Heterogeneous Brittle Solids,'' J. Mech. Phys. Solids, **46**, pp. 2171–2181.

[14] Hashin, Z., 1996, ''Finite Thermoelastic Fracture Criterion With Application to Laminate Cracking Analysis,'' J. Mech. Phys. Solids, **44**, pp. 1129–1145.

[15] Waas, A. M., Takeda, N., Yuan, J., and Lee, S. H., 1997, ''Static and Dynamic Compressive Behavior of Glass Fiber Reinforced Unidirectional Composites,'' *Proceedings of the American Society for Composites, Twelfth Technical Conference*, Dearborn, MI, Technomic, Lancaster, PA, pp. 552–561.

[16] Hashin, Z., and Rosen, B. W., 1964, ''The Elastic Moduli of Fiber-Reinforced Materials,'' ASME J. Appl. Mech., **31**, pp. 223–232.

[17] Hill, R., 1964, ''Theory of Mechanical Properties of Fibre-Strengthened Materials: I. Elastic Behavior,'' J. Mech. Phys. Solids, **12**, pp. 199–212.

[18] Nemat-Nasser, S., and Hori, M., 1993, *Micromechanics: Overall Properties of Heterogeneous Materials*, Elsevier, New York.

[19] Liu, C., Huang, Y., Lovato, M. L., and Stout, M. G., 1997, ''Measurement of the Fracture Toughness of a Fiber-Reinforced Composite Using the Brazilian Disk Geometry,'' Int. J. Fract., **87**, pp. 241–263.

[20] Lambros, J., and Rosakis, A. J., 1997, ''Dynamic Crack Initiation and Growth in Thick Unidirectional Graphite/Epoxy Plates,'' Compos. Sci. Technol., **57**, pp. 55–65.

[21] Daniel, I. M., and Isahi, O., 1994, *Engineering Mechanics of Composite Materials*, Oxford University Press, Oxford, UK.

H. Lee
Assoc. Mem. ASME
Research Fellow in Aeronautics,
California Institute of Technology,
Pasadena, CA 91125

S. Krishnaswamy[1]
Associate Professor,
Mem. ASME
Department of Mechanical Engineering,
Northwestern University,
Evanston, IL 60208-3030
e-mail: s-krishnaswamy@nwu.edu

Quasi-Static Propagation of Subinterfacial Cracks

The problem of quasi-static crack propagation in a three-point bend specimen containing an initial crack that is parallel to and offset from a bimaterial interface is considered. An approximate dislocation-based fracture model is used to identify conditions under which such cracks are attracted to or repelled by the interface. Possible configurations (material/geometry) where such subinterfacial cracks experience pure mode I conditions are determined. Experimental results are presented showing quasi-static crack propagation of subinterfacial cracks for three regimes: (attractive) into the interface; (repulsive) away from the interface; as well as (equilibrium) parallel to the interface.
[S0021-8936(00)01903-6]

1 Introduction

Interfacial and subinterfacial cracks in bimaterial systems are of interest due to their relevance to fracture and failure of composite structures and microelectronic devices. There are several theoretical studies on interfacial cracks ([1–11]) and subinterfacial cracks ([12–15]), which have dealt with such issues as the nature of the crack-tip singularity and possible crack-face contact. Crack propagation in bimaterial systems occurs always (for interfacial cracks) or mostly always (for subinterfacial cracks) under mixed-mode conditions. Mixed-mode crack propagation even in homogeneous linear elastic media is still not completely understood ([16]), even though the theoretical basis for mixed-mode crack-tip stress states is well laid out in terms of classical linear elastic fracture mechanics. It appears that at large mode-mixities the standard fracture propagation criteria based on maximum energy release rate, maximum tangential stress, or the minimum strain energy density all deviate from each other and also from experimental data (see, for example, [17–19,16,20]. Post-mortem examination of the surfaces of mixed-mode fracture in essentially brittle materials has indicated that at large mode-mixity, the crack surface is rougher than at small mode-mixity, suggesting a change in crack propagation mechanisms and in the fracture process zone ([16,21]).

The situation is much more complex for interface and subinterface cracks because the mode-mixity here arises not only from geometric conditions but also from material mismatch. Extensive studies on interfacial crack propagation dealing with fracture toughness issues, dynamics, and material nonlinearity have been undertaken over the past decade ([22–33]).

The focus of this paper is much narrower than the issues studied by the researchers cited above, and it concerns the propagation of *subinterfacial* cracks that are off but close to an interface between two dissimilar linear elastic materials. The theoretical basis for this is rather straightforward as these subinterfacial cracks are entirely in one material, and therefore their propagation should be governed by the concepts of classical linear elastic fracture mechanics for *homogeneous* bodies, at least as long as the crack does not run into the interface. The effect of the second material can only be to alter the stress state, and hence the mode-mixity, at the vicinity of the subinterfacial crack. Early studies by Erdogan [15] have outlined the analysis methodology that we shall adopt here.

The basic question that we shall attempt to answer in this work is this: For a three-point bend bimaterial PMMA/Al6061 specimen containing a subinterfacial crack of initial length ''*a*'' that is parallel to the interface but offset by a distance ''*d*'' are there specific locations ''*d*/*a*'' at which the subinterface crack will experience pure mode I conditions? If so, such a crack can be expected to grow parallel to the interface at least incrementally. We shall call such positions ''equilibrium positions'' for the subinterfacial crack. This is essentially the same question as the one raised by Hutchinson, Mear and Rice [34] with later extensions by Yang and Kim [35]. The answers that were provided by the Hutchinson, Mear, and Rice [34] analysis are applicable to the center crack geometry, and by an argument of far-field dominance of an *interfacial* crack-tip field, to other situations where such dominance is obtained. This latter condition implies that the ratio ''*d*/*a*'' should be sufficiently small and the planar extent of the specimen should be sufficiently large so that one can assume that there are distances at which the subinterfacial crack can be thought of as being essentially on the interface.

Unfortunately, for the configurations pertinent to this study the prevalence of a far-field interfacial crack-tip field cannot be assumed. In this work, we therefore attempt to answer the above question both theoretically using dislocation-based fracture models and finite element numerical simulations, as well as experimentally using optical interferometry.

In Section 2, details of a simple analytical model are discussed for the three-point bend subinterfacial crack geometry following the lines of Erdogan [15]. Relevant details of a full-field optical measurement technique (Polariscope/Shearing Interferometer: PSI) that is used in this study are described in Section 3. Quasi-static subinterfacial crack propagation experiments are described in Section 4. Three-point bend specimens made of PMMA/A16061 bimaterial systems were loaded to initiate and propagate subinterfacial cracks. The experiments indicate the conditions under which a subinterfacial crack is attracted to or repelled by the interface, and also demonstrate that, under certain circumstances, if the crack happened to be initially located at the right position, it may even grow in its own plane parallel to the interface. The experimental results are compared with crack trajectories predicted by finite element simulations, and with the results of the dislocation-based fracture analysis.

2 Analysis of Subinterfacial Cracks in a Three-Point Bend Bimaterial Specimen

Consider the three-point bend PMMA/A16061 bimaterial specimen shown in Fig. 1(*a*). The subinterfacial crack is in material ''1'' (PMMA). A state of plane stress is assumed to prevail. Our

[1]To whom correspondence should be addressed.

Contributed by the Applied Mechanics Division of THE AMERICAN SOCIETY OF MECHANICAL ENGINEERS for publication in the ASME JOURNAL OF APPLIED MECHANICS. Manuscript received by the ASME Applied Mechanics Division, May 18, 1999; final revision, Jan. 11, 2000. Associate Technical Editor: K. T. Ramesh. Discussion on the paper should be addressed to the Technical Editor, Professor Lewis T. Wheeler, Department of Mechanical Engineering, University of Houston, Houston, TX 77204-4792, and will be accepted until four months after final publication of the paper itself in the ASME JOURNAL OF APPLIED MECHANICS.

goal is this: determine any possible ''equilibrium'' position ''*d*'' (distance between interface and crack) of the subinterfacial crack of length ''*a*'' in a given three-point bimaterial specimen (of relevant in-plane dimension ''*w*'' assuming that all other dimensions are much greater than *w*) which leads to a pure mode I stress state. The ''characteristic distances'' at which any such equilibrium position is obtained will be denoted nondimensionally by d^*/a.

Unlike the center crack specimen which is readily analyzed but is virtually impossible to experimentally test, the three-point bend specimen is very easy to test but much harder to analyze. Therefore an approximate method of analysis is described here, the validity of which is verified experimentally. The solution to the actual problem (Fig. 1(*a*)) can be obtained by superposition of the following two subproblems: (a) a beam in three-point bending but containing no crack (Fig. 1(*b*); and (b) a plate with no far-field

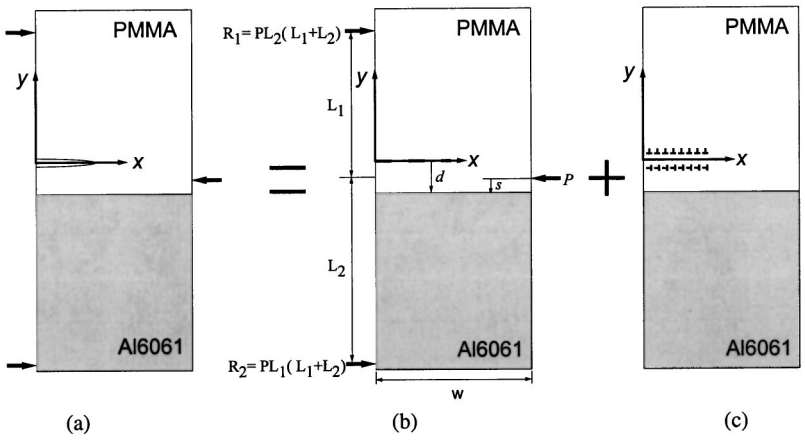

Fig. 1 Three-point bend PMMA/Al 6061 specimen: (*a*) actual specimen=(*b*) beam without crack and only applied load+(*c*) plate without applied load and only dislocations to cause crack

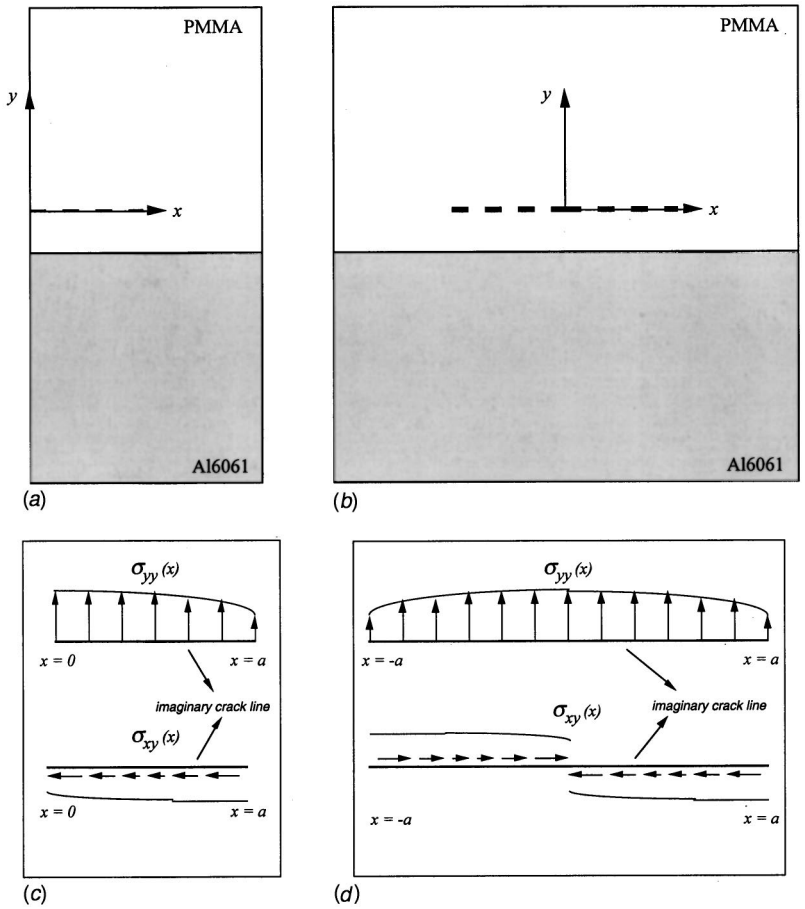

Fig. 2 Modification of edge crack problem to center crack problem: (*a*) edge crack model, (*b*) center crack model, (*c*) traction stresses of edge crack, (*d*) traction stresses of center crack

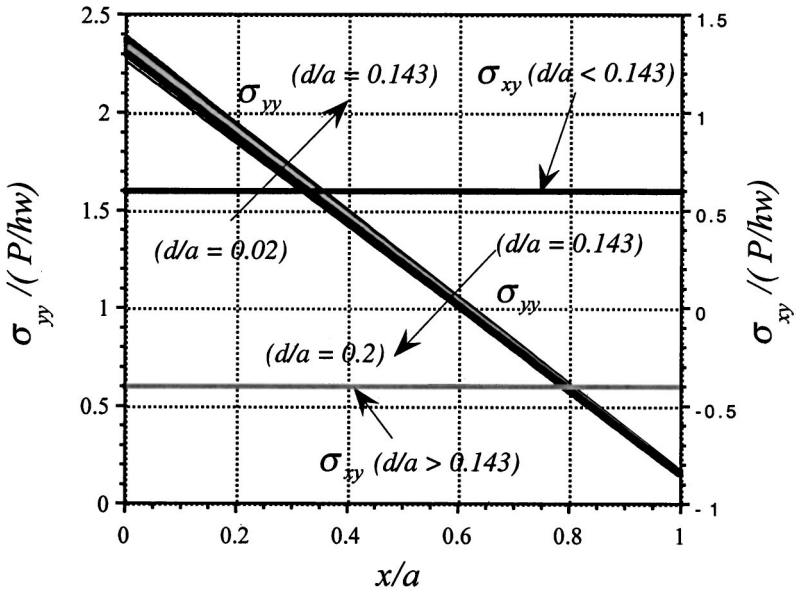

Fig. 3 The traction stresses at imaginary crack line locations from Bernoulli-Euler beam bending analysis

loading and containing dislocation distributions to create the crack by nulling out the appropriate crack-line traction stresses (Fig. 1(*c*)). The first subproblem is easily analyzed using Bernoulli-Euler beam theory. The second subproblem, however, is a bit more complicated because it needs to be built up from the solution for a single edge dislocation off the interface between two bimaterial *quarter*-spaces ([36]). Such a solution is very hard to obtain primarily because of the difficulty associated with obtaining a traction-free edge plane. In any event, the traction-free conditions on the other free boundaries will never be exactly met in a finite geometry. Because of these limitations, the approach that will be taken here is to obtain the dislocation distributions necessary to create a *center* crack in an infinite geometry, but using the crack line traction stresses obtained from subproblem (a) appropriately extended (''mirrored'') for a center crack as shown in Fig. 2. The rationale for this is that the stress field for an edge dislocation falls as $1/r$ with distance r, and therefore the crack-tip behavior is therefore primarily going to be dictated by the dislocation distributions near the vicinity of the tip. That the ''mirrored'' center crack specimen will always have traction stresses along the midline $x=0$ (which is the edge of the real specimen) due to the dislocations that straddle the midline means that our approximate analysis will be in error in some significant ways. Whether our approximate solution is acceptable or not will be determined experimentally (Section 4).

2.1 Subproblem (a): Beam Analysis. From a Bernoulli-Euler analysis of beam bending (Fig. 1(*b*)), the traction stresses on the expected crack-line are given by

$$\sigma_{yy}(x,d)=\frac{PL_1}{L_1+L_2}\left\{\frac{12}{hw^3}\right\}[L_2-s+d]\left[\frac{w}{2}-x\right];\ \text{for}\ s>d$$
$$=\frac{PL_2}{L_1+L_2}\left\{\frac{12}{hw^3}\right\}[L_1+s-d]\left[\frac{w}{2}-x\right];\ \text{for}\ s<d; \tag{1}$$

$$\sigma_{xy}(x,d)=-\frac{PL_2}{L_1+L_2}\frac{1}{hw};\ \text{for}\ s>d$$
$$=+\frac{PL_1}{L_1+L_2}\frac{1}{hw};\ \text{for}\ s<d; \tag{2}$$

where the plate thickness is h. Figure 3 shows the traction stresses on the expected crack-line for the case when $L_1=0.15$ m, $L_2=0.1$ m, $w=0.15$ m, $s=0.01$ m and crack length $a=0.07$ m. These parameters correspond to specimen III discussed in Section 4. Note that the Bernoulli-Euler beam theory is expected to predict the normal stress distribution very well, but is not expected to produce an accurate measure of the shear stress distribution. While, second-order corrections (such as the Timoshenko theory) may be used to get a better estimate of the shear stress distribution, this is not essential for our purposes as the results of this analysis will prove to be adequate.

2.2 Subproblem (b): Dislocation Distribution. We can now use the traction stresses obtained from subproblem (a) in subproblem (b) to null out the tractions along the subinterfacial crack line. Using this approach, the problem of the subinterface crack results in a system of Cauchy-type singular integral equations for the dislocation distribution densities ([15])

$$\int_{-a}^{a}\frac{2B_y(x')}{x-x'}dx'+\int_{-a}^{a}B_y(x')K_{11}(x,x';d)dx'$$
$$+\int_{-a}^{a}B_x(x')K_{12}(x,x';d)dx'=-\frac{\sigma_{yy}(x',d)}{D} \tag{3}$$

$$\int_{-a}^{a}\frac{2B_x(x')}{x\text{-}x'}dx'+\int_{-a}^{a}B_y(x')K_{21}(x,x';d)dx'$$
$$+\int_{-a}^{a}B_x(x')K_{22}(x,x';d)dx'=-\frac{\sigma_{xy}(x',d)}{D} \tag{4}$$

where $B_x(x')$ and $B_y(x')$ are glide and climb edge dislocation density functions along the crack line $x'=-a$ to a; $\sigma_{yy}(x',d)$ and $\sigma_{xy}(x',d)$ are the traction stresses from subproblem (a) along the crack line; and D and the kernel functions $K_{ij}(x,x';d)$ are given in the Appendix. In order to have uniqueness of solution, the dislocation density functions $B_x(x')$ and $B_y(x')$ must satisfy

$$\int_{-a}^{a}B_y(x')dx'=0 \tag{5}$$

$$\int_{-a}^{a}B_x(x')dx'=0 \tag{6}$$

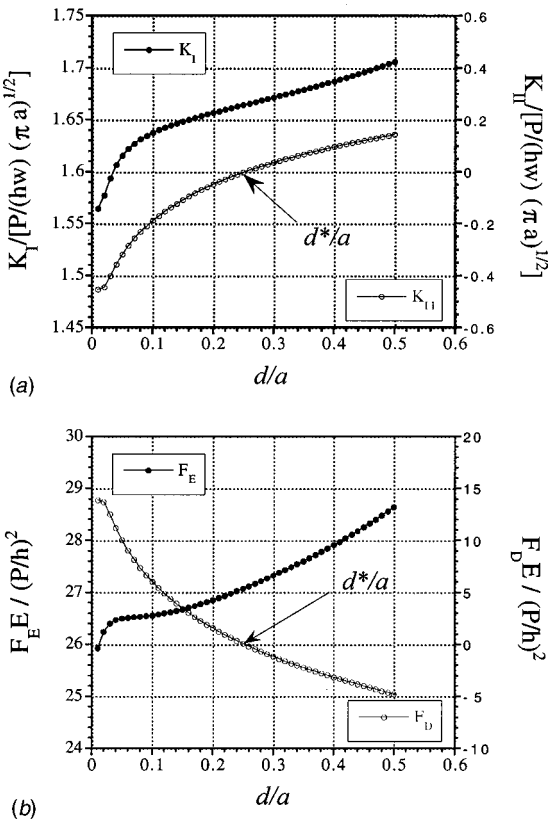

Fig. 4 Stress intensity factor and crack extension and deflection forces for the PMMA/Al 6061 bimaterial specimen III as predicted by the model

which assure crack closure at the tip ([37]). The above set of Cauchy-type singular Eqs. (3)–(6) is solved using the numerical method developed by Erdogan and Gupta [37] and the details of this are spelt out in Lee [38].

Once the dislocation distributions are obtained, the stress intensity factors can be calculated directly from ([39])

$$K_I = -\frac{2\mu_1}{\sqrt{1+\kappa_1}}\sqrt{\pi a}\left[\sqrt{a^2-x^2}.B_y(x)\right]_{x\to a} \tag{7}$$

$$K_{II} = \frac{2\mu_1}{\sqrt{1+\kappa_1}}\sqrt{\pi a}\left[\sqrt{a^2-x^2}.B_x(x)\right]_{x\to a} \tag{8}$$

where μ_1 is the shear modulus of material ''1'' and the material parameter κ_1 involves Poisson's ratio and is defined in the Appendix.

A dislocation in the presence of a stress-field experiences a force on it and it can be shown ([39]) that the forces on the dislocations (that form the crack) due to the applied far-field load are directly related to the *J*-integral, which can in turn be related to the stress intensity factor through

$$F_E = J_x = \oint_\Gamma \left(W dy - T_i \frac{\partial u_i}{\partial x} ds \right) = \frac{1+\kappa_1}{8\mu_1}(K_I^2 + K_{II}^2) \tag{9}$$

$$F_D = J_y = -\oint_\Gamma \left(W dx + T_i \frac{\partial u_i}{\partial y} ds \right) = -\frac{1+\kappa_1}{4\mu_1} K_I K_{II}. \tag{10}$$

Here F_E is called the crack extension force and F_D is called the crack deflection force and the positive signs of F_E and F_D are taken such that the forces on the right crack are along the positive *x* and *y*-directions respectively. Also in the above: *W* is the strain energy density, T_i are the tractions, and u_i are the displacements and the integral is over any loop Γ enclosing the right crack-tip. It is seen from the above that when $K_{II}=0$, the crack deflection force F_D is zero, and the crack can be expected to grow in its own plane in pure mode I. However, when $K_{II}>0$, the deflection force F_D is negative (i.e., directed along the negative *y*-direction in Fig. 2), and the crack can be said to be *attracted* to the interface. Contrarily, when $K_{II}<0$, the deflection force F_D is positive (ie directed along the positive *y*-direction), and the crack is *repelled* by the interface. Note that K_I is always assumed to be positive in order for the crack to grow.

The results of the above analysis are given below for one particular case when: $L_1=0.15$ m, $L_2=0.1$ m, $w=0.15$ m, $s=0.01$ m and crack length $a=0.07$ m for PMMA/A16061 specimen III (discussed in Section 4). The stress intensity factors and the corresponding crack deflection forces are shown in Fig. 4(*a*,*b*), respectively, for various crack positions ''d/a.'' It appears that the characteristic distance d^*/a is around 0.25 where K_{II} and hence the deflection force F_D vanish for this configuration. In this case, if the subinterfacial crack happens to be farther away than the equilibrium position, i.e., $(d/a)>(d^*/a)$, we see that the crack deflection force $F_D<0$, and so such a crack-tip will be attracted to the interface. Conversely, if $(d/a)<(d^*/a)$, the crack deflection force $F_D>0$, and so the crack-tip will be repelled by the interface.

3 Shearing Interferometery

Shearing interferometric techniques are useful in mapping stress-field distributions in optically isotropic materials (such as polymethylmethacrylate—PMMA) or opaque materials (such as aluminum) where photoelasticity is inapplicable. See Tippur, Krishnaswamy, and Rosakis [40] for details of a shearing technique called Coherent Gradient Sensor (CGS); and Lee and Krishnaswamy [41] for a combined Polariscope-Shearing Interferometer (PSI). The optical layout and the schematic of the shearing interferometric mode of the latter PSI device are shown in Figs. 5(*a*,*b*). A 5 mW HeNe laser is used as the coherent light source. A quarter waveplate is used to circularly polarize the beam. A set of micro-objective lenses, spatial filter, and beam collimator, are used to obtain a clean and collimated plane wave. The beam then passes through the transparent PMMA specimen under test. The transmitted beam is then sheared by a specially designed prism as shown in Fig. 5(*b*). The specially cut prism is made of birefringent calcite and generates two orthogonally polarized parallel and laterally shifted copies of the input beam. These two beams are made to interfere by use of an analyzer. The resulting interference pattern produces fringes related to the gradients of the stress-induced phase shift in the transmitted beam. For optically isotropic materials such as PMMA, the stress-induced phase retardation is independent of polarization, and the total phase retardation Φ_{sp} at any point due to transmission through the specimen is related to the stresses at that point through ([40])

$$\Phi_{sp}(x,y) = \frac{2\pi hc}{\lambda}\{\sigma_1+\sigma_2\} \tag{11}$$

where *h* is specimen thickness, λ is wavelength of the laser beam, *c* is a stress optic constant of the optically isotropic PMMA material, and σ_1 and σ_2 are in-plane principal stresses.

As discussed in Lee and Krishnaswamy [41], the interference pattern produces bright fringes in regions where

$$\frac{ch}{\lambda}\cdot\Delta X\cdot\frac{\partial(\sigma_1+\sigma_2)}{\partial X} = m. \tag{12}$$

Here *m* is an integer representing the fringe order, and the spatial shearing amount ΔX (induced by the prism) is along the global *X*-direction as shown in Fig. 6. (Note that for convenience the origins of the coordinate system are shifted in relation to the one used in the analysis Section 2).

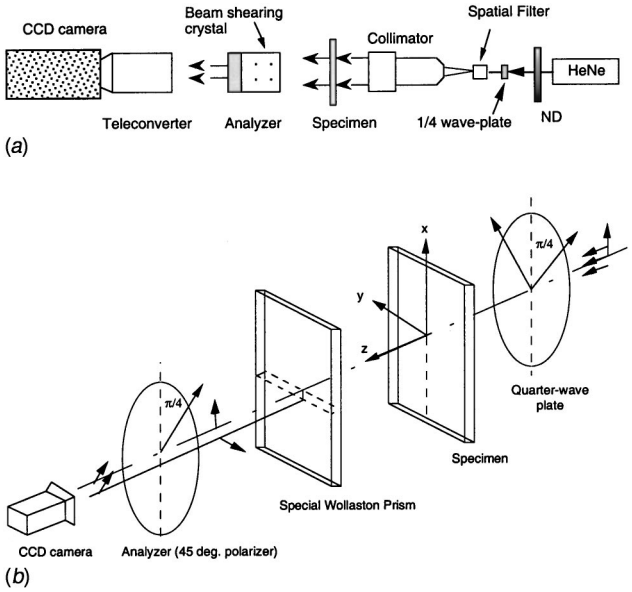

Fig. 5 (*a*) Optical layout of the shearing interferometric system, (*b*) schematic of the shearing interferometer

Subinterfacial crack-tip stress states can be expected to be asymptotically the same as that for a crack which is entirely in an isotropic homogeneous medium, at least as long as the crack does not run into the interface. Since in general the propagating crack path can be along an arbitrary direction, it is convenient to define a local (variable) coordinate system (x,y) which is instantaneously aligned with the curved crack path (Fig. 6). The local coordinate system is rotated with respect to the global system by the crack kink angle φ. The in-plane stresses near the subinterfacial crack-tip are then asymptotically given by

$$\sigma_{ij}(r,\theta^*)=\sum_{n=0}^{\infty}\frac{r^{(n-1)/2}}{\sqrt{2\pi}}\{\mathrm{Re}(k_n)\tilde{\sigma}^{I}_{ijn}(\theta^*)+\mathrm{Im}(k_n)\tilde{\sigma}^{II}_{ijn}(\theta^*)\} \tag{13}$$

where θ^* is the polar angle measured with respect to the local x-axis; r is the radial coordinate with respect to the instantaneous crack tip; k_n are complex amplitudes of which $k_0=\mathbf{K}=K_{\mathrm{I}}+iK_{\mathrm{II}}$ is the complex stress intensity factor where K_{I} and K_{II} represent mode I and mode II components, respectively; and $\hat{\sigma}^{\mathrm{I}}_{ijn}(\theta)$ and $\hat{\sigma}^{\mathrm{II}}_{ijn}(\theta)$ are dimensionless functions that are completely known (listed in full in Lee [38]). Experimentally, however, the fringes are related to the global X-gradients of the sum of these stresses, since the shearing prism is fixed so as to provide shearing along the initial crack line parallel to the interface. It is therefore convenient to cast Eq. (13) in terms of the global coordinates; that is, as functions of (r,θ) where $\theta=\theta^*+\varphi$. One then obtains the fringe relations by a direct use of chain differentiation:

$$ch\sum_{n=0}^{\infty}(n-1)\frac{r^{(n-3)/2}}{\sqrt{2\pi}}\left\{\begin{array}{l}\mathrm{Re}(k_n)\cos\left(\dfrac{n-3}{2}\theta-\dfrac{n-1}{2}\varphi\right)\\ +\mathrm{Im}(k_n)\sin\left(\dfrac{n-3}{2}\theta-\dfrac{n-1}{2}\varphi\right)\end{array}\right\}=\frac{m\lambda}{\Delta X}. \tag{14}$$

Extraction of the stress intensity factor (and the other higher order terms k_n) from an experimental fringe pattern proceeds as follows. The crack origin, and the kink angle φ are identified, and the fringe locations (r,θ) of various fringe orders m are digitized. The experimental data are then used in an over-deterministic least-squares scheme ([42]) using Eq. (14) to obtain the k_n's. Details of the data analysis procedure including examples illustrating the accuracy of the experimental procedure are given in Lee and Krishnaswamy [41].

4 Experimental Results of Quasi-Static Propagation

We shall now present selected results of subinterfacial crack propagation in several PMMA/A16061 bimaterial three-point bending specimens. The relevant material properties of PMMA and A16061 are given in Table 1. To avoid the use of a third adhesive material to bond the two halves together and to make a strong interface, methylmethacrylate monomer was used. A sharp crack parallel to and offset from the bimaterial interface was initiated by gently driving a razor blade inserted at the end of an edge notch. The residual stresses along the bimaterial interface due to heat generated in the curing process were optically observed to be negligible. Qualitatively, we do not expect residual stresses to play a significant role in these experiments. Three different loading conditions were used to generate different initial mode-mixities for the subinterfacial cracks. A pneumatically driven loading machine was used to increase the applied load P in order to initiate and cause to propagate the initial subinterfacial crack. The loading rate was about 1 N/sec. A video recorder operated at 1000 frame/sec was used to image the crack propagation and to obtain shearing interferometric data as described in Section 3. In all the experiments reported here, the crack propagation speed was less than 1 mm/sec in the region of interest. Therefore inertial effects were deemed negligible.

The analysis for extracting the stress intensity factor $\mathbf{K}$ from the experimental results is based on a linear elastic assumption of the underlying stress fields. The size of the plastic zone as the crack initiated and propagated was estimated to be much smaller than the other relevant geometric scales a, d. Numerical simulations of the experiments were therefore done assuming quasi-static, linear elastic conditions. The finite element crack propagation program FRANC2D ([43]) was used because it has built-in fracture criteria and automatic remeshing as the crack propagates.

4.1 PMMA/A16061 Bimaterial Specimen I. Specimen I had the following geometric parameters: $L_1=150$ mm, $L_2=150$ mm, $w=150$ mm, $s=10$ mm, $d=10$ mm, plate thickness $h=9$ mm, and initial crack length $a=30$ mm. This configuration

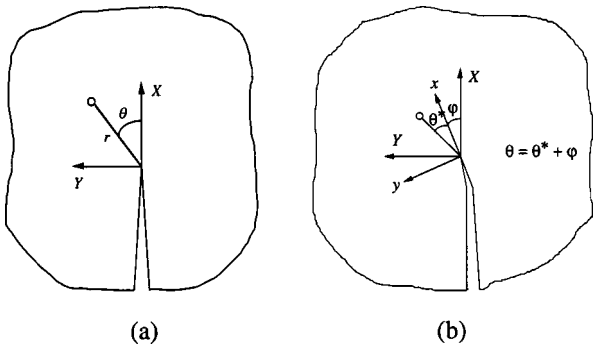

Fig. 6 Global and local coordinate systems for a propagating crack

Table 1 Material properties

Material Properties	Young's Modulus E (GPa)	Poisson's Ratio ν	Stress-Optic Constant c
PMMA	3.24	0.35	$0.923*10^{-10}$ m^2/N
Al6061	69	0.3	-

is symmetric with respect to the specimen but not material geometry. As the applied load P was increased, the subinterfacial crack initiated and began to propagate initially outward from the bimaterial interface, subsequently finding a path that is almost parallel to the interface. Figure 7(*a*) shows a photograph of the fractured specimen indicating the crack trajectory. Superposed on this is the numerically simulated crack path obtained using the maximum tangential stress criterion for crack growth in a finite element simulation of this specimen. We note two things: (i) even though the load configuration for bimaterial specimen I is symmetric with respect to the specimen geometry, the crack propagates along a curved path due to mode-mixity arising from the material mismatch and (ii) the maximum tangential stress criterion used in the numerical simulation captures the crack propagation path for this case extremely well.

Figure 7(*b*) shows a sequence of shearing interferometric images as the crack initiates and then propagates. Analyzing these fringe patterns as set out in Section 3, the magnitude of the stress intensity factor $|\mathbf{K}|=\sqrt{K_{\mathrm{I}}^2+K_{\mathrm{II}}^2}$ is observed to increase during the initial crack propagation phase for up to about 4 mm of growth (Fig. 7(*c*)). The fracture toughness value for this subinterfacial crack propagation case appears to be around $1.1\sim1.2\ \mathrm{M\cdot Pa}\sqrt{m}$ which is close to the measured value for the fracture toughness of *homogeneous* PMMA as one would expect. The phase angle of **K** defined as $\phi=\tan^{-1}(K_{\mathrm{II}}/K_{\mathrm{I}})$ starts around -15 deg due to the large mode-mixity arising from the material mismatch. This large negative phase angle (negative K_{II}) leads to a positive (''repulsive'') crack deflection force F_D, resulting in the crack initially propagating outward from the interface. The fact that K_{II} (or equivalently the phase angle of the stress intensity factor **K**) rapidly decreases and is minimal after about 5 mm of propagation demonstrates that the subinterfacial crack seeks to propagate along a path that leads to zero mode II, at least for trajectories that are sufficiently far from the bimaterial interface. This is consistent with behavior expected of cracks in homogeneous elastic materials.

4.2 PMMA/Al6061 Bimaterial Specimen II. Specimen II had the following geometric parameters: $L_1=50$ mm, $L_2=150$ mm, $w=150$ mm, $s=10$ mm, $d=10$ mm, plate thickness $h=9.5$ mm, and initial crack length $a=30$ mm. In this case, the crack first propagates inward, contacts the interface, and subsequently grows along the interface (Fig. 8(*a*)). Superposed on the experimental data is the path predicted by a finite element simulation using the maximum tangential stress criterion as before. The numerical path is also observed to initially turn towards the interface, but the actual crack trajectory itself does not match very well with that observed in the experiment. Further mesh refinement does not improve the simulation, and the reason for the discrepancy therefore lies elsewhere.

The shearing interferometric fringes for this case are shown in Fig. 8(*b*). Analyzing these to extract the stress intensity factors as before, we find that the mode II component of **K** starts out very large (Fig. 8(*c*))(the initial phase angle is around $+30$ deg at initial propagation) and does not disappear as the crack runs into the interface. The effect of this positive K_{II} (negative F_D) is to cause the crack to be attracted in to the interface. While the overall behavior is as expected, the actual divergence of the experimental path from that predicted numerically can be explained from some of the interferometric fringe patterns in Fig. 8(*b*) that are shown zoomed in Fig. 8(*d*). These fringe patterns clearly indicate that in this case where the mode-mixity *remains* large during propagation, the crack surfaces contact each other over macroscopically significant distances behind the crack front. The simulations, however, do not capture crack contact. One of the major effects of crack flank contact should be an apparent increase in the fracture toughness attributable to an increase in energy dissipation due to friction between the crack flank surfaces. This is reflected in Fig. 8(*c*), where the magnitude of the stress intensity factor **K** is much higher than that required for propagation in homogeneous PMMA

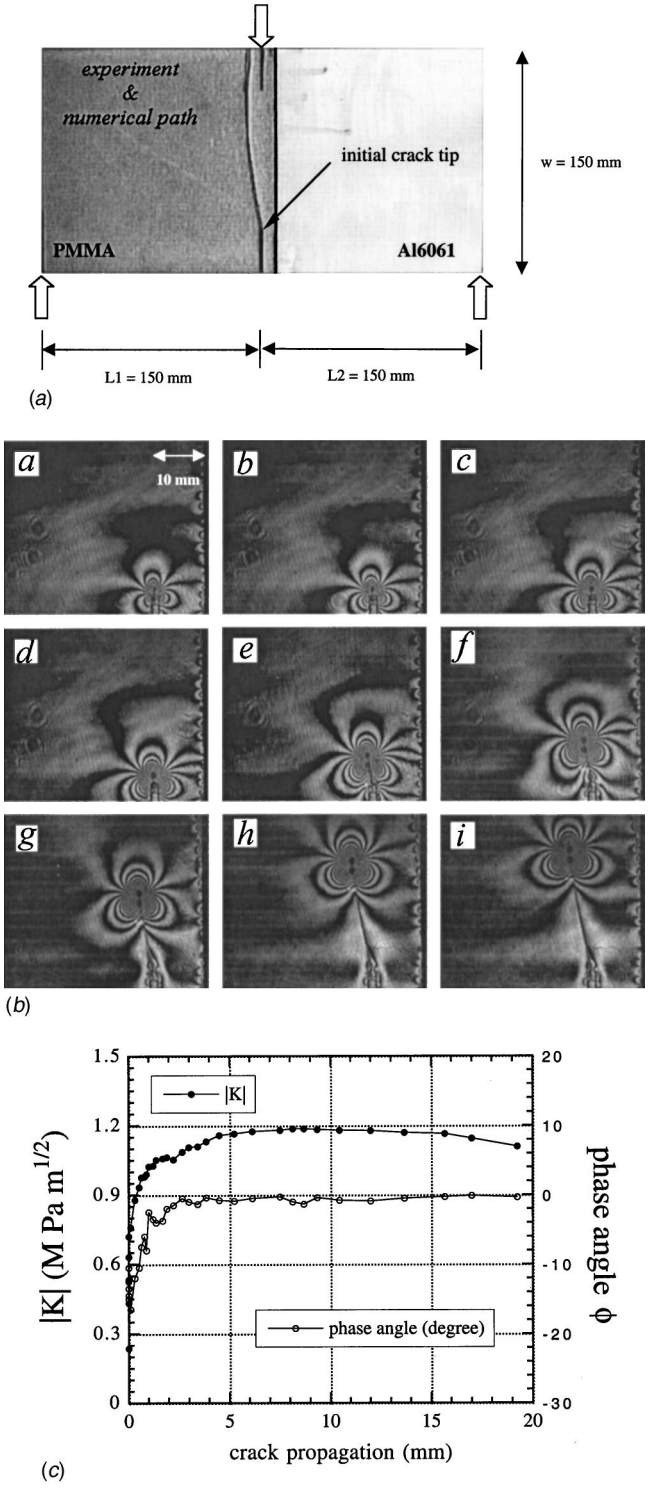

Fig. 7 (*a*) Comparison of crack propagation trajectories in PMMA/Al 6061 bimaterial specimen I, numerical simulation superposed on the experimental results; (*b*) shearing interferometric fringes for PMMA/Al 6061 bimaterial specimen I; (*c*) measured stress intensity factor and phase angle versus crack propagation distance of PMMA/Al 6061 bimaterial specimen I

under predominantly mode I conditions. A post-mortem examination of the crack surfaces showed that these were much rougher in this case (specimen II) than when the mode-mixity was smaller (specimen I). It is also interesting to note that the crack surface contact is dramatically changed when the crack hits the interface

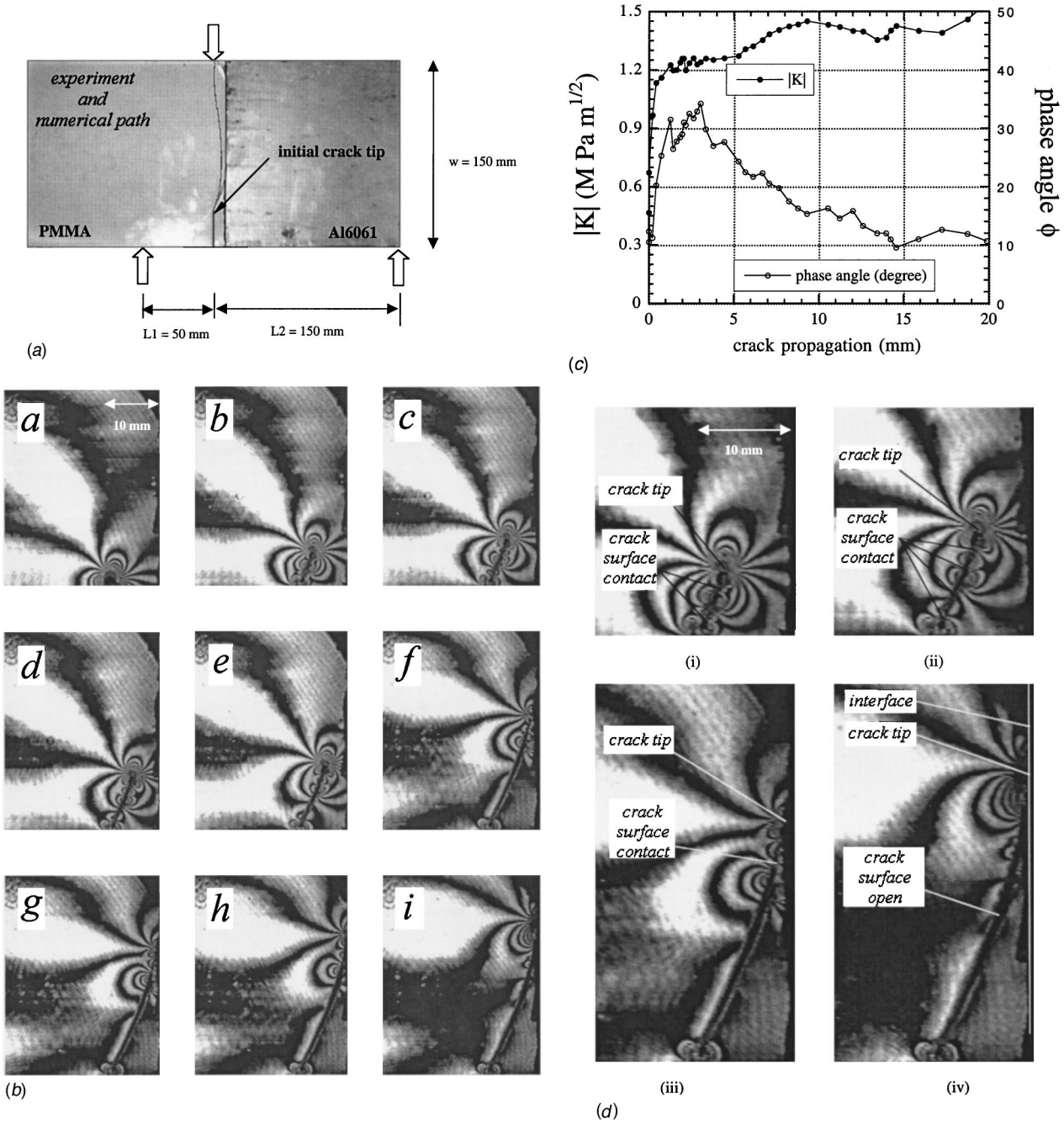

Fig. 8 (*a*) **Comparison of crack propagation trajectories in PMMA/Al 6061 bimaterial specimen II; numerical simulation superposed on the experimental results.** (*b*) **Shearing interferometric fringes for PMMA/Al s6061 bimaterial specimen II.** (*c*) **Measured stress intensity factor and phase angle versus crack propagation distance of PMMA/Al 6061 bimaterial specimen II.** (*d*) **Crack surface contacts in PMMA/Al 6061 bimaterial specimen II. (i), (ii), (iii), and (iv) are zoomed images of Figs. 8(*b*), (*d*), (*g*), and (*i*), respectively.**

(see Fig. 8(*d*) (iii) and (iv)). At this point, the subinterfacial crack surfaces actually open out and appear to be no longer in contact. However, the near-tip *interfacial* crack is still expected to have some contact region, but this is beyond the field of view of this experimental setup.

It must be confessed that the interpretation of the experimental data in terms of the asymptotic crack-tip field for a *homogeneous* material becomes increasingly untenable as the crack approaches and eventually hits the interface. The results of this particular experiment and their interpretation as set out above should therefore be viewed at best qualitatively.

4.3 PMMA/Al6061 Bimaterial Specimen III. Bimaterial specimen III had the following geometric parameters: $a = 70$ mm, $d = 16$ mm, $s = 10$ mm, $L_1 = 100$ mm, $L_2 = 150$ mm, $h = 9$ mm. The numerically predicted crack growth path using the maximum tangential stress criterion is straight for this case, and this compares well with what was observed experimentally as shown in Fig. 9(*a*). Figure 9(*b*) shows a sequence of the interferometric fringe patterns as the crack propagating parallel to the bimaterial interface. The mode-mixity is observed to be minimal right from the crack initiation point (Fig. 9(*c*). The fracture toughness $|\mathbf{K}|$ converges to the value for homogeneous PMMA (about

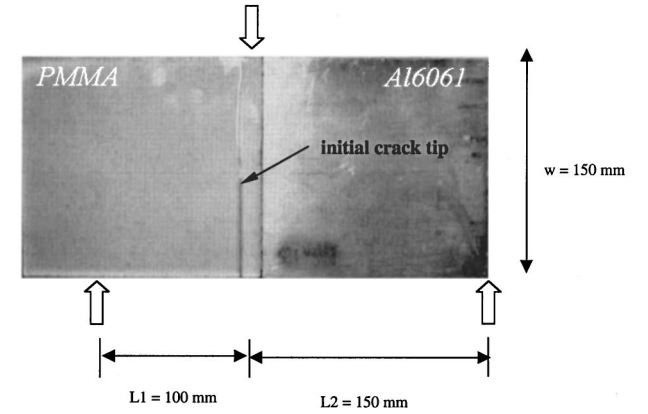

(*a*)

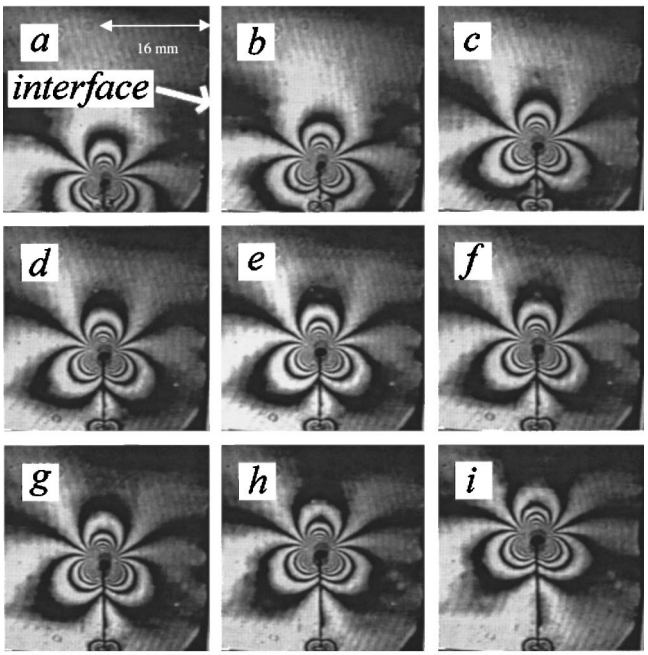

(*b*)

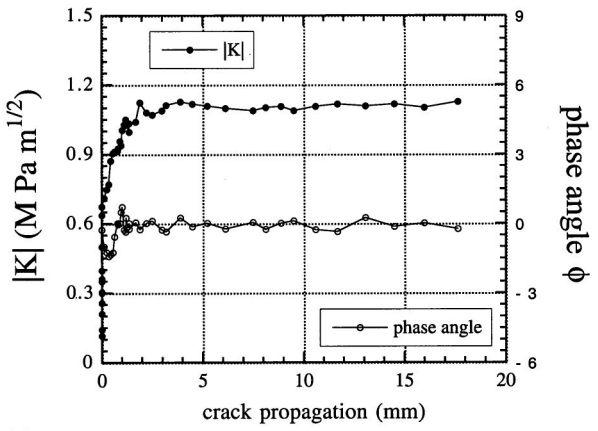

(*c*)

Fig. 9 (*a*) **Comparison of crack propagation trajectories in PMMA/Al 6061 bimaterial specimen III; numerical simulation superposed on the experimental results.** (*b*) **shearing interferometric fringes for PMMA/Al 6061 bimaterial specimen III.** (*c*) **Measured stress intensity factor and phase angle versus crack propagation distance for bimaterial PMMA/Al 6061 specimen III.**

1.1 $M\cdot Pa\sqrt{m}$). Despite the fact that this is a bimaterial specimen with the crack in close proximity to the interface, the phase angle of **K** for the whole propagation regime shown remains essentially around 0 deg. Due to this essentially zero mode-mixity from the initial state, the crack propagates almost in a straight line parallel to the interface. The characteristic ''equilibrium'' distance for this specific PMMA/A16061 bimaterial combination and loading condition of specimen III was calculated analytically as described in Section 2 to be $d^*/a=0.25$. Note that this agrees reasonably well with the experimentally measured value of $d^*/a=0.23$, thereby validating to a certain extent the analytical model.

5 Discussions and Conclusion

Based on the experimental data and the analyses presented in the previous sections, we can draw the following conclusions:

1 When the initial mode-mixity leads to a negative K_{II} (a positive crack deflection force F_D), as in specimen 1, then the interface repels the crack-tip. Crack propagation therefore occurs in such a manner that the crack moves further away from the interface. In the process, the mode-mixity diminishes further, and the crack eventually finds a path of $K_{II}=0$. In this case, conventional fracture criteria (for cracks in a homogeneous material) predict the subinterfacial crack path quite well.

2 When the initial mode-mixity leads to a positive K_{II} (leading to a negative F_D), as in specimen 2, the interface attracts the crack-tip causing it to grow closer to the crack. While this prediction from the analysis is seen to hold, the numerical simulations for crack trajectories using the maximum tangential stress criterion appear to predict the actual crack path poorly. Indeed, part of this is due to the fact that the crack flanks contact at these large mode-mixities, a factor not taken into account in the conventional criterion. Analyses that allow for contact and include energy dissipation mechanisms involving frictional contact may be necessary to get a better handle on the crack behavior in this case.

3 It is possible to find *macroscopically significant* equilibrium positions for certain material/loading combinations for which a subinterfacial crack experiences zero mode-mixity. Note that by macroscopically significant, we mean that d^*/a is neither too small that a far-field interfacial crack-tip field can be expected to prevail (interfacial limit), nor too large that the bimaterial interface is too remote to be ''seen'' by the crack (homogeneous limit). It was shown that a subinterfacial crack could actually grow parallel to the interface (and in reasonable proximity to it) for some significant distance of propagation. An approximate and simple dislocation/beam theory fracture model was shown to provide a reasonably good estimate of the equilibrium position.

The results of this work are of course specific to the situations studied. The larger utility of this work is in terms of what the results suggest:

(a) It is possible to obtain reasonable estimates of equilibrium positions, and crack attractive and crack repulsive zones for a subinterfacial crack using simple beam models in a dislocation-based fracture analysis.

(b) Propagation of cracks initially located in crack repulsive zones can be quite well described by conventional criteria such as the maximum tangential stress criterion that are used in available fracture codes such as FRANC2D.

(c) Propagation of subinterfacial cracks initially located in crack attractive zones, are likely to be less successfully modeled by conventional criteria as the crack-tip gets pulled closer to the interface.

Acknowledgment

Support of this work through NSF is gratefully acknowledged. The finite element simulations were done using FRANC2D developed by Dr. Ingraffea of Cornell University.

Appendix

The various terms that appear in Eqs. (3), (4) can be shown to be ([15,38])

$$K_{11}(x,x';d)=\frac{(\lambda+\delta)(x-x')}{(x-x')^2+4d^2}-\frac{8\delta d^2((x-x')^3-12(x-x')d^2)}{((x-x')^2+4d^2)^3}+\frac{16d^2\delta(x-x')}{((x-x')^2+4d^2)^2}$$

$$K_{12}(x,x';d)=-\frac{2(\lambda-\delta)d}{(x-x')^2+4d^2}+\frac{8\delta d^2(6(x-x')^2d-8d^3)}{((x-x')^2+4d^2)^3}$$

$$K_{21}(x,x';d)=\frac{2(\lambda-\delta)d}{(x-x')^2+4d^2}-\frac{8\delta d^2(6(x-x')^2d-8d^3)}{((x-x')^2+4d^2)^3}$$

$$K_{22}(x,x';d)=\frac{(\lambda+\delta)(x-x')}{(x-x')^2+4d^2}-\frac{8\delta d^2((x-x')^3-12(x-x')d^2)}{((x-x')^2+4d^2)^3}\times\frac{16d^2\delta(x-x')}{((x-x')^2+4d^2)^2}.$$

The material combination parameters are

$$D=\frac{\mu_1}{\pi(\kappa_1+1)};\quad \lambda=\frac{\alpha+\beta}{\beta-1},\quad \text{and}\quad \delta=\frac{\beta-\alpha}{\beta+1},$$

where α and β are Dundurs parameters defined by

$$\alpha=\frac{\mu_1(\kappa_2+1)-\mu_2(\kappa_1+1)}{\mu_2(\kappa_1+1)+\mu_1(\kappa_2+1)},$$

and

$$\beta=\frac{\mu_1(\kappa_2-1)-\mu_2(\kappa_1-1)}{\mu_2(\kappa_1+1)+\mu_1(\kappa_2+1)}$$

and $\kappa_i=3-4\nu_i$ for plane strain, $\kappa_i=3-\nu_i/1+\nu_i$ for plane stress: and μ_i,ν_i are the shear modulus and Poisson's ratio of material $i=(1,2)$, respectively.

References

[1] Williams, M. L., 1959, ''The Stresses Around a Fault or Crack in Dissimilar Media,'' Bull. Seismol. Soc. Am., **49**, pp. 199–204.

[2] Sih, G. C., and Rice, J. R., 1964, ''The Bending of Plates of Dissimilar Materials With Cracks,'' ASME J. Appl. Mech., **31**, pp. 477–482.

[3] Rice, J. R., and Sih, G. C., 1965, ''Plane Problems of Cracks in Dissimilar Media,'' ASME J. Appl. Mech., **32**, pp. 418–423.

[4] England, A. H., 1965, ''A Crack Between Dissimilar Media,'' ASME J. Appl. Mech., **32**, pp. 400–402.

[5] Erdogan, F., 1965, ''Stress Distribution in Bonded Dissimilar Materials With Cracks,'' ASME J. Appl. Mech., **32**, pp. 403–410.

[6] Comninou, M., 1977, ''The Interface Crack,'' ASME J. Appl. Mech., **44**, pp. 631–636.

[7] Comninou, M., and Dundurs, J., 1980, ''On the Behavior of Interface Cracks,'' Res. Mech., **1**, pp. 249–264.

[8] Knowles, J. K., and Sternberg, E., 1983, ''Large Deformation Near a Tip of an Interface Crack Between Two Neo-Hookean Sheets,'' J. Elast., **13**, pp. 257–293.

[9] Rice, J. R., 1988, ''Elastic Fracture Mechanics Concepts for Interfacial Cracks,'' ASME J. Appl. Mech., **55**, pp. 98–103.

[10] Shih, C. F., and Asaro, R., 1990, ''Elastic-Plastic and Asymptotic Fields of Interface Cracks,'' Int. J. Fract., **42**, pp. 101–116.

[11] Deng, X., 1994, ''An Asymptotic Analysis of Stationary and Moving Cracks With Frictional Contact Along Bimaterial Interfaces and in Homogeneous Solids,'' Int. J. Solids Struct., **31**, pp. 2407–2429.

[12] Dundurs, J., and Mura, T., 1964, ''Interaction Between an Edge Dislocation and a Circular Inclusion,'' J. Mech. Phys. Solids, **12**, pp. 177–189.

[13] Dundurs, J., and Sendeckyi, G. P., 1965, ''Behavior of an Edge Dislocation Near a Bimetallic Interface,'' ASME J. Appl. Mech., **36**, pp. 3353–3354.

[14] Dundurs, J., 1969, ''Discussion of Edge-Bonded Dissimilar Orthogonal Elastic Wedges Under Normal and Shear Loading,'' ASME J. Appl. Mech., **36**, pp. 650–652.

[15] Erdogan, F., 1971, ''Bonded Dissimilar Materials Containing Cracks Parallel to the Interface,'' Eng. Fract. Mech., **3**, pp. 231–240.

[16] Bhattacharjee, D., and Knott, J. F., 1995, ''Effect of Mixed Mode I and II Loading on the Fracture Surface of Polymethyl Methacrylate (PMMA),'' Int. J. Fract., **72**, pp. 359–381.

[17] Gdoutos, E. E., and Zacharopoulos, D. A., 1987, ''Mixed-Mode Crack Growth in Plates Under Three-Point Bending,'' Exp. Mech., **27**, pp. 366–369.

[18] Mahajan, R. V., and Ravi-Chandar, K., 1989, ''An Experimental Investigation of Mixed-Mode Fracture,'' Int. J. Fract., **41**, pp. 235–252.

[19] Suresh, S., Shih, C. F., Morrone, A., and O'Dowd, N. P., 1990, ''Mixed-Mode Fracture Toughness of Ceramic Materials,'' J. Am. Ceram. Soc., **73**, pp. 1257–1267.

[20] Galvez, J., Elices, M., Guinea, G. V., and Planas, J., 1996, ''Crack Trajectories Under Mixed Mode and Non-Proportional Loading,'' Int. J. Fract., **81**, pp. 171–193.

[21] Evans, A. G., and Hutchinson, J. W., 1989, ''Effects of Non-Planarity on the Mixed Mode Fracture Resistance of Bimaterial Interfaces,'' Acta Metall., **37**, pp. 909–916.

[22] Suo, Z., and Hutchinson, J. W., 1989, ''Steady-State Cracking in Brittle Substrates Beneath Adherent Films,'' Int. J. Solids Struct., **25**, pp. 1337–1353.

[23] Cao, H. C., and Evans, A. G., 1989, ''An Experimental Study of the Fracture Resistance of Bimaterial Interfaces,'' Mech. Mater. **7**, pp. 295–304.

[24] Charalambides, P. G., Lund, J., Evans, A. G., and McMeeking, R. M., 1989, ''A Test Specimen for Determining the Fracture Resistance of a Bimaterial Interface,'' J. Appl. Mech. **56**, pp. 77–82.

[25] Wang, J.-S., and Suo, Z., 1990, ''Experimental Determination of Interfacial Toughness Curves Using Brazil-Nut-Sandwiches,'' Acta Metall. Mater., **38**, No. 7, pp. 1279–1290.

[26] Shih, C. F., Asaro, R., and O'Dowd, N. P., 1991, ''Elastic-Plastic Analysis Cracks on Bimaterial Interfaces; Part III: Large-Scale Yielding,'' ASME J. Appl. Mech., **58**, pp. 450–463.

[27] Tippur, H. V., and Rosakis, A. J., 1991, ''Quasi-Static and Dynamic Crack Growth Along Bimaterial Interfaces: A Note on Crack-Tip Field Measurements Using Coherent Gradient Sensing,'' Exp. Mech., **31**, pp. 243–251.

[28] Liechti, K. M., and Chai, Y.-S., 1991, ''Biaxial Loading Experiments for Determining Interfacial Fracture Toughness,'' ASME J. Appl. Mech., **58**, pp. 680–687.

[29] O'Dowd, N. P., Shih, C. F., and Stout, M. G., 1992, ''Test Geometries for Measuring Interfacial Fracture Toughness,'' Int. J. Solids Struct., **29**, No. 5, pp. 571–589.

[30] Mason, J. J., Lambros, J., and Rosakis, A. J., 1992, ''The Use of a Coherent Gradient Sensor in Dynamic Mixed-Mode Fracture Mechanics Experiments,'' J. Mech. Phys. Solids, **40**, pp. 641–661.

[31] Foltyn, P. A., and Ravi-Chandar, K., 1993, ''Initiation of an Interface Crack Under Mixed-Mode Loading,'' ASME J. Appl. Mech., **60**, pp. 227–229.

[32] Tvergaard, V., and Hutchinson, J. W., 1993, ''The Influence of Plasticity on Mixed Mode Interface Toughness,'' J. Mech. Phys. Solids, **41**, pp. 1119–1135.

[33] Xu, L., and Tippur, H. V., 1995, ''Fracture Parameters for Interfacial Cracks: An Experimental-Finite Element Study of Crack Tip Fields and Crack Initiation Toughness,'' Int. J. Fract., **71**, pp. 345–363.

[34] Hutchinson, J. W., Mear, M., and Rice, J. R., 1987, ''Crack Paralleling an Interface Between Dissimilar Materials,'' ASME J. Appl. Mech., **54**, pp. 828–832.

[35] Yang, M., and Kim, K., 1992, ''The Behavior of Subinterface Cracks With Crack-Face Contact,'' Eng. Fract. Mech., **44**, pp. 155–165.

[36] Kelly, P., Hills, D. A., and Nowell, D., 1994, ''The Complete Stress Field due to a Dislocation Anywhere in Two Bonded Quarter-Planes,'' ASME J. Appl. Mech., **61**, pp. 992–993.

[37] Erdogan, F., and Gupta, G. D., 1972, ''On the Numerical Solution of Singular Integral Equations,'' Q. Appl. Math., **30**, pp. 525–534.

[38] Lee, H, 1998, ''Quasi-Static Subinterfacial Crack Propagation,'' Ph.D. dissertation, Northwestern University, Evanston, IL.

[39] Weertman, J., 1996, *Dislocation Based Fracture Mechanics*, World Scientific, Singapore.

[40] Tippur, H. V., Krishnaswamy, S., and Rosakis, A. J., 1991, ''A Coherent Gradient Sensor for Crack Tip Deformation Measurement: Analysis and Experimental Measurements,'' Int. J. Fract., **48**, pp. 193–204.

[41] Lee, H., and Krishnaswamy, S., 1996, ''A Compact Polariscope/Shearing-Interferometer for Mapping Stress Fields in Bimaterial Systems,'' Exp. Mech., **36**, pp. 404–411.

[42] Sanford, R. J., 1989, ''Determining Fracture Parameters With Full-Field Optical Methods,'' Exp. Mech., **29**, pp. 241–247.

[43] Wawryzynek, P., and Ingraffea, A., 1995, *A Two-Dimensional Crack-Propagation Simulator*, Version 2.7, Cornell University Press, Ithaca, NY.

Theory of Anisotropic Thin-Walled Beams

V. V. Volovoi
Post Doctoral Fellow

D. H. Hodges
Professor

School of Aerospace Engineering,
Georgia Institute of Technology,
Atlanta, GA 30332-0150

Asymptotically correct, linear theory is presented for thin-walled prismatic beams made of generally anisotropic materials. Consistent use of small parameters that are intrinsic to the problem permits a natural description of all thin-walled beams within a common framework, regardless of whether cross-sectional geometry is open, closed, or strip-like. Four ''classical'' one-dimensional variables associated with extension, twist, and bending in two orthogonal directions are employed. Analytical formulas are obtained for the resulting 4×4 cross-sectional stiffness matrix (which, in general, is fully populated and includes all elastic couplings) as well as for the strain field. Prior to this work no analytical theories for beams with closed cross sections were able to consistently include shell bending strain measures. Corrections stemming from those measures are shown to be important for certain cases. Contrary to widespread belief, it is demonstrated that for such ''classical'' theories, a cross section is not rigid in its own plane. Vlasov's correction is shown to be unimportant for closed sections, while for open cross sections asymptotically correct formulas for this effect are provided. The latter result is an extension to a general contour of a result for I-beams previously published by the authors.
[S0021-8936(00)03003-8]

1 Introduction

The following discussion is restricted to the theory of prismatic beams where the three-dimensional constitutive law and strain-displacement relationships can be considered linear. Any beam theory is associated with introduction of variables which depend only on the coordinate along the beam axis. For a general type of deformation at least four such one-dimensional variables have to be introduced: extensional, torsional, and two bending variables (corresponding to deformation along two orthogonal directions). The corresponding one-dimensional governing equations are uncoupled for isotropic beams with doubly symmetric cross sections and are given by Euler-Bernoulli theory for extension and bending and St. Venant theory for torsion. If one wishes to extend this theory to composite beams, the governing equations become coupled due to the appearance of off-diagonal terms in the cross-sectional stiffness matrix. This 4×4 stiffness matrix C_{ab} characterizes elastic properties of the beam. Then, the strain energy per unit length is expressed in terms of the four one-dimensional strain measures as

$$2F_{\text{classical}}=\alpha_a C_{ab}\alpha_b \quad \text{where} \quad \alpha^T=\{U_1',U_2'',U_3'',\theta'\}. \tag{1}$$

For thin-walled beams this problem was first posed in Reissner and Tsai [1]. However, the approach employed therein led to a complicated set of equations, especially in the case of closed cross sections. The solution of those equations was presented only for a special type of three-dimensional constitutive equations.

The introduction of the variational-asymptotic method in context of anisotropic beams Berdichevsky [2] allowed the treatment of this problem from a different perspective: beam theory can obtain three-dimensional elasticity without making any *ad hoc* assumptions using the small parameter $\frac{a}{l}\ll1$, where a is a characteristic dimension of the cross section and l is a the wavelength of deformation along the beam reference line. For a general (but not thin-walled) cross section the problem is reduced to a system of two-dimensional equations on a cross section. A development of a numerical solution of this problem is presented in Cesnik and Hodges [3].

Applying the variational-asymptotic procedure to thin-walled cross sections where another small parameter exists, namely $\frac{h}{a}\ll1$ (where h is a wall thickness), allows one to start with shell theory rather than three-dimensional elasticity. Rather than having to solve a two-dimensional problem over the cross-sectional plane, one instead solves a one-dimensional problem over the length of the thin walls. This dimensional reduction can be also conducted in another way: the asymptotic procedure with respect to $\frac{h}{a}$ can be applied directly to the two-dimensional cross-sectional problem that results when starting with three-dimensional elasticity. Both approaches lead to the same final results, but the latter procedure is more computationally involved.

The former procedure was used in Berdichevsky et al. [4] to obtain analytical solutions for closed sections. The resulting convenient cross-sectional stiffness formulas published in that paper are presently widely used in engineering community. Although shell bending strain measures were neglected in that paper, these for most practical purposes do not affect final stiffness results. However, as shown below, for certain material properties the deviation of their results from the asymptotically correct results might be significant.

Concerning the application of the variational-asymptotic method to beams with open cross sections, an I-beam was viewed as an assembly of strips in Volovoi et al. [5]. Asymptotically correct formulas were obtained therein which account for Vlasov's correction. Those results are generalized here for beams with arbitrary open contours.

2 Present Approach

Beams are considered thin walled if $h\ll a,R$ where R is a characteristic radius of curvature of the midsurface. No assumptions are made about the relative orders of a and R, and shell theory is employed. A curvilinear system of coordinates is introduced (see Fig. 1), with s and ξ being contour and through-the-thickness coordinates, respectively; $\mathbf{r}=x_i\mathbf{x}_i$ is a position vector of the shell midsurface, vectors are denoted with bold letters. The notation to be used is

Contributed by the Applied Mechanics Division of THE AMERICAN SOCIETY OF MECHANICAL ENGINEERS for publication in the ASME JOURNAL OF APPLIED MECHANICS. Manuscript received by the ASME Applied Mechanics Division, Sept. 18, 1998; final revision, Mar. 7, 2000. Associate Technical Editor: W. K. Liu. Discussion on the paper should be addressed to the Technical Editor, Professor Lewis T. Wheeler, Department of Mechanical Engineering, University of Houston, Houston, TX 77204-4792, and will be accepted until four months after final publication of the paper itself in the ASME JOURNAL OF APPLIED MECHANICS.

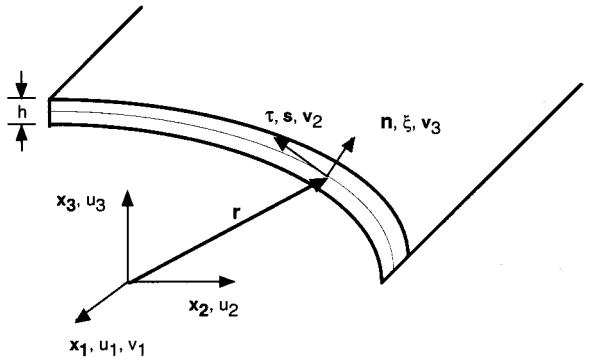

Fig. 1 Configuration and coordinate system

$$(\dot{\ }) \equiv \frac{d(\ )}{ds} \qquad (\ )' \equiv \frac{d(\ )}{dx_1}$$

$$\begin{aligned} \boldsymbol{\tau} &= \dot{\mathbf{r}} = \dot{x}_2 \mathbf{x}_2 + \dot{x}_3 \mathbf{x}_3 \\ \mathbf{n} &= \boldsymbol{\tau} \times x_1 = \dot{x}_3 \mathbf{x}_2 - \dot{x}_2 \mathbf{x}_3 \\ r_\tau &= \boldsymbol{\tau} \cdot r = \dot{x}_2 x_2 + x_3 \dot{x}_3 \\ r_n &= \mathbf{n} \cdot \mathbf{r} = x_2 \dot{x}_3 - x_3 \dot{x}_2 \\ R &= \dot{x}_2 / \ddot{x}_3 = -\dot{x}_3 / \ddot{x}_2 . \end{aligned} \tag{2}$$

Curvilinear displacements v_i are expressed in terms of Cartesian displacements u_i as

$$\begin{aligned} v_1 &= u_1 \\ v_2 &= u_2 \dot{x}_2 + u_3 \dot{x}_3 \\ v_3 &= u_2 \dot{x}_3 - u_3 \dot{x}_2 \end{aligned} \tag{3}$$

Shell strain measures are taken from the works of Koiter [6] and Sanders [7], which for cylindrical shells yields

$$\begin{aligned} &\gamma_{11} = v_{1,1} \quad \rho_{11} = v_{3,11} \\ &2\gamma_{12} = v_{1,2} + v_{2,1} \quad \rho_{12} = v_{3,12} + \frac{1}{4R}(v_{1,2} - 3v_{2,1}) \\ &\gamma_{22} = v_{2,2} + \frac{v_3}{R} \quad \rho_{22} = v_{3,22} - \left(\frac{v_2}{R}\right)_{,2} . \end{aligned} \tag{4}$$

Here $\gamma_{\alpha\beta}$ and $\rho_{\alpha\beta}$ are the extensional (membrane) and bending strain measures, respectively. Then, the strain energy density of the shell has the form

$$2\mathrm{E}_{\mathrm{shell}} = hE_e^{\alpha\beta\gamma\delta}\gamma_{\alpha\beta}\gamma_{\gamma\delta} + h^3 E_b^{\alpha\beta\gamma\delta}\rho_{\alpha\beta}\rho_{\gamma\delta} + 2h^2 E_{eb}^{\alpha\beta\gamma\delta}\gamma_{\alpha\beta}\rho_{\gamma\delta} \tag{5}$$

where Greek indices vary from 1 to 2; $E_e^{\alpha\beta\gamma\delta}$ and $E_b^{\alpha\beta\gamma\delta}$ are two-dimensional material constants corresponding to membrane and bending deformation, respectively, and $E_{eb}^{\alpha\beta\gamma\delta}$ corresponds to coupling between these two types of deformation. These two-dimensional material constants are obtained from the reduced three-dimensional material constants $D^{\alpha\beta\gamma\delta}$ by use of the relations

$$\{E_e^{\alpha\beta\gamma\delta}, E_{eb}^{\alpha\beta\gamma\delta}, E_b^{\alpha\beta\gamma\delta}\} = \frac{1}{h}\int_{-h/2}^{h/2} D^{\alpha\beta\gamma\delta}\left\{1, \frac{\xi}{h}, \left(\frac{\xi}{h}\right)^2\right\} d\xi. \tag{6}$$

These constants are, in turn, obtained from the regular three-dimensional constants as

$$D^{\alpha\beta\gamma\delta} = E^{\alpha\beta\gamma\delta} - \frac{E^{\alpha\beta 33}E^{\gamma\delta 33}}{E^{3333}} - H_{\mu\lambda}G^{\alpha\beta\mu}G^{\gamma\delta\lambda}$$

$$\text{where } H^{-1}_{\mu\lambda} = E^{\mu 3\lambda 3} - \frac{E^{\mu 333}E^{\lambda 333}}{E^{3333}}$$

$$G^{\alpha\beta\mu} = E^{\alpha\beta\mu 3} - \frac{E^{\alpha\beta 33}E^{\mu 333}}{E^{3333}}. \tag{7}$$

For the following derivation it is convenient to rewrite Eq. (5) as

$$2\mathrm{E}_{\mathrm{shell}} = \psi_1 Q_{ij}\psi_j + 2\phi_i S_{ij}\psi_j + \phi_i P_{ij}\phi_j \tag{8}$$

where $\psi^T \equiv \{\gamma_{11}, h\rho_{11}, h\rho_{12}\}$, and $\phi^T \equiv \{\gamma_{12}, \gamma_{22}, h\rho_{22}\}$; $i,j = 1 \ldots 3$ and 3×3 matrices Q_{ij}, S_{ij}, and P_{ij} are corresponding combinations of $E_e^{\alpha\beta\gamma\delta}$, $E_{eb}^{\alpha\beta\gamma\delta}$, and $E_b^{\alpha\beta\gamma\delta}$.

In the derivation below it is the axial coordinate x_1 that is distinct from the other two, so it is now convenient for Greek indices to vary from 2 to 3. The variational-asymptotic method Berdichevsky [2,8] is used in what follows. While we avoid a detailed discussion of this method, sufficient information is provided here to facilitate understanding of the derivation. We are using the term ''asymptotically correct'' concerning an approximate solution to denote its agreement with the expansion of the exact solution to a specified order in terms of a specific small parameter. It is clear that any theory which is not asymptotically correct will certainly fail to achieve the accuracy of one which is.

Setting up the Problem. Since only statics is considered, only the strain energy and work of external forces are present in the total functional. External forces are considered slowly varying so that our minimization is not affected by those forces. This leads to minimization of the strain energy density given in Eq. (5) with the strains given by Eqs. (4). Next, this functional is represented in terms of a series with respect to small parameters. A recursive procedure is invoked when perturbation of the previous approximation is used to obtain the following approximation. From this point of view ''classical'' approximation corresponds to the first (main) nonvanishing terms in that series.

In our case there are two small parameters: $\frac{a}{l}$ and $\frac{h}{a}$. These parameters are considered independent: for a given order of terms with respect to $\frac{a}{l}$ we sort out the terms with respect to $\frac{h}{a}$ as well. The small parameter $\frac{a}{l}$ enters the problem from the observation that $X_{,1} \approx \frac{X}{l}$ and $X_{,2} \approx \frac{X}{a}$ for any quantity X.

''Zeroth'' Approximation. This is a starting point of the recursive procedure. All terms that contain the small parameter $\frac{a}{l}$ in the functional are set to zero. The resulting functional is degenerate and the general solution for its kernel (null space) is found. This defines one-dimensional variables. In our case setting all terms in Eqs. (4) containing derivatives with respect to a ''slow'' axial variable leads to an expression for nonzero strains of ''zeroth'' functional given by

$$\begin{aligned} &2\gamma_{12} = v_{1,2} \quad \rho_{12} = \frac{1}{4R}v_{1,2} \\ &\gamma_{22} = v_{2,2} + \frac{v_3}{R} \quad \rho_{22} = v_{3,22} - \left(\frac{v_2}{R}\right)_{,2} . \end{aligned} \tag{9}$$

Since Eq. (5) is a positive-definite quadratic form of strains, for a displacement field to belong to the kernel of ''zeroth'' functional, all strains in Eq. (9) must vanish. It can be directly checked that the general solution of this problem has the form

$$\begin{aligned} v_1 &= U_1 \quad v_2 = U_\alpha \dot{x}_\alpha + \theta r_n \\ v_3 &= U_2 \dot{x}_3 - U_3 \dot{x}_2 - \theta r_\tau \end{aligned} \tag{10}$$

where U_i and $\theta \equiv v_2/R - v_{3,2}$ are arbitrary functions of x_1. It is easy to see (using Eqs. (3)) that these one-dimensional variables correspond to motion of a cross section as a rigid body: $U_i(x_1)$ translation of a cross section in the x_i-direction, and $\theta(x_1)$ is the rotation of a cross section about x_1.

Asymptotic Recursion. Perturbation of the displacement field which was obtained at the previous step is now introduced, namely,

$$v_1 = U_1 + \hat{w}_1$$
$$v_2 = U_2\dot{x}_2 + U_3\dot{x}_3 + \theta r_n + \hat{w}_2 \tag{11}$$
$$v_3 = U_2\dot{x}_3 - U_3\dot{x}_2 - \theta r_\tau + \hat{w}_3 .$$

Substituting this displacement field, Eq. (11), into the strains, Eqs. (4), and, in turn, substituting the strains into Eq. (5), one obtains an energy functional. Only the leading terms with respect to small parameters are retained at this step, and a minimization with respect to $\hat{\omega}_i$ is conducted. As a result of this procedure the perturbations $\hat{\omega}_i$ are found as functions of one-dimensional variables and their derivatives.

In the most general case, deformations due to all four one-dimensional strain measures are of the same order (denoted by ϵ, a nondimensional constant of the order of the maximum strain in the beam). If this were not the case, any smaller deformations could be simply neglected in the main approximation. The one-dimensional strain measures are given in Eq. (1). The only problem is to determine appropriate dimensional constants that need to multiply these measures to provide a term of the order ϵ (this does not affect U_1' which is already nondimensional). As shown below, this constant must be either a or h, depending on the geometry of the contour. One can calculate the appropriate order using the expression for the one-dimensional energy for the isotropic case, since all material properties are assumed to be of the same magnitude, so the order of the one-dimensional strain measures is not affected. However, these orders will naturally fall out of our derivation. Let us emphasize that the order of perturbations is not assumed but determined during the minimization. In fact, it is easily estimated prior to the minimization by reckoning that leading quadratic and linear terms in the functional with respect to the unknown perturbation are of the same order.

2.1 Phantom Step. There are some terms in the strains which are larger in magnitude than the corresponding strain component itself. Those terms are balanced by equally large terms, so that their combination is of a smaller order. We call such terms ''phantom'' ones. Since at each step of asymptotic procedure only the leading terms are considered, it means that those ''phantom'' terms are minimized to zero. This procedure is often referred to, somewhat cruelly, as ''killing'' excessively large terms in the energy. Substituting the displacement field of Eqs. (11) into Eqs. (4), one obtains

$$\underset{\epsilon}{\gamma_{11}} = \underset{\epsilon}{U_1'} + \underset{\epsilon}{\hat{w}_{1,1}}$$
$$2\underset{(a/l)^{-1}\epsilon}{\gamma_{12}} = \underset{(a/l)^{-1}\epsilon}{\dot{x}_2 U_2'} + \underset{(a/l)^{-1}\epsilon}{\dot{x}_3 U_3'} + \underset{\epsilon}{r_n\theta'} + \underset{(a/l)^{-1}\epsilon}{\hat{w}_{1,2}} + \underset{(a/l)\epsilon}{\hat{w}_{2,1}}$$
$$\underset{\epsilon}{\gamma_{22}} = \underset{\epsilon}{\hat{w}_{2,2}} + \underset{\epsilon}{\frac{\hat{w}_3}{R}}$$
$$\underset{\epsilon}{h\rho_{11}} = h[\underset{\epsilon}{\dot{x}_3 U_2''} - \underset{\epsilon}{\dot{x}_2 U_3''} - \underset{(a/l)\epsilon}{\theta'' r_\tau} + \underset{(a/l)^2\epsilon}{\hat{w}_{3,11}}]$$
$$\underset{(a/l)^{-1}\epsilon}{h\rho_{12}} = h\left[\underset{\epsilon}{\frac{1}{4R}}\{\underset{(a/l)^{-1}\epsilon}{\dot{x}_\alpha U_\alpha'} + \underset{\epsilon}{\theta' r_n} - \underset{(a/l)^{-1}\epsilon}{\hat{w}_{1,2}}\} - \underset{\epsilon}{\theta'} + \underset{(a/l)\epsilon}{\hat{w}_{3,12}} - \underset{(a/l)\epsilon}{\frac{3}{4R}(\hat{w}_{2,1})}\right]$$
$$\underset{\epsilon}{h\rho_{22}} = h\left(\underset{\epsilon}{\hat{w}_{3,2}} - \underset{\epsilon}{\frac{\hat{w}_2}{R}}\right)_2 . \tag{12}$$

At this step, terms with $\rho_{\alpha\beta}$ do not enter the minimization procedure. The reason for this is that, for each term in $\rho_{\alpha\beta}$, there is a similar term in $\gamma_{\alpha\beta}$, but multiplied by $\frac{a}{h}$. So retaining only the leading terms with respect to $\frac{h}{a}$ allows us to discard terms from $\rho_{\alpha\beta}$. The most obvious ''phantom'' terms of order $(\frac{a}{l})^{-1}$ are present in γ_{12} which defines the orders for the warping, written underneath the individual terms in Eqs. (12), and the solution for $\hat{\omega}_{1,2}$

$$\hat{w}_{1,2} = -U_\alpha'\dot{x}_\alpha . \tag{13}$$

There might be, however, some other ''phantom'' terms which are of order $(\frac{a}{l})^0$, but still ''too large'' due to the presence of another small parameter $\frac{h}{a}$. In other words they are of order $\epsilon(\frac{h}{a})^{-1}$. The presence of one of this type of terms is related to a fundamental difference between open and closed cross sections. A constraint of single-valuedness has to be satisfied around the closed contours of closed sections for certain variables; these constraints do not apply for open cross sections. In particular, this applies to the single-valuedness of $\hat{\omega}_1$. For open cross sections $r_n\theta'$ in γ_{12} is a ''phantom'' since this term is killed by adding term $-r_n\theta'$ to the right-hand side in Eq. (13). In this case the largest nonzero terms in the functional that are proportional to θ' will come from the ρ_{12} and $\theta' \approx \frac{\epsilon}{h}$. Integration with respect to circumferential coordinate of Eq. (13) yields

$$\hat{w}_1 = -U_\alpha' x_\alpha - \theta' \int_{s_0}^{s} r_n ds \tag{14}$$

where the coefficient for θ' is called the ''sectorial coordinate'' and is given by $\eta(s) \equiv \int_{s_0}^{s} r_n ds$. The sectorial coordinate is, in fact, a solution of a classical St. Venant torsional problem in the shell approximation. To avoid redefining U_1, embedded in s_0 constant of integration should be chosen such that $\int \hat{\omega}_1 ds = 0$. It is obviously convenient to choose the origin of the Cartesian coordinates in the geometric center of the cross section, so that $\int x_2 ds = \int x_3 ds = 0$.

On the other hand, for a closed cross section, $r_n\theta'$ in γ_{12} is not a ''phantom''! The requirement of single-valuedness for $\hat{\omega}_1$ prevents the possibility of displacement field as in Eq. (14); only the last term creates a problem, since $\oint r_n\theta' ds$ is not zero. As a result, terms proportional to $r_n\theta'$ do enter the functional, which implies that $a\theta' \approx \epsilon$. Then the terms with θ' in ρ_{12} will be of order $\epsilon(\frac{h}{a})$ and can be neglected. Therefore, for the closed sections the equivalent of the last term in Eq. (14) belongs to the next step of approximation.

There is another ''phantom'' term that is also of the form $\epsilon(\frac{h}{a})^{-1}$. If $a \approx R$ then

$$\gamma_{22}(\hat{w}_2, \hat{w}_3) \approx \left(\frac{h}{a}\right)^{-1} h\rho_{22}(\hat{w}_2, \hat{w}_3). \tag{15}$$

Thus, minimization of the main terms in the functional simply renders

$$\gamma_{22} = \hat{w}_{2,2} + \frac{\hat{w}_3}{R} = 0. \tag{16}$$

However, each individual term in Eq. (16) is not zero, but rather of order $\epsilon(\frac{h}{a})^{-1}$ and is undetermined at this step. The second equation for these unknowns stems from ρ_{22} and due to Eq. (15) will be provided in the next approximation. If a and R are not of the same order, then orders of γ_{22} and ρ_{22} for a given displacement field are uncoupled, and no ''phantom'' terms are present. In particular this is the case when no curvature is present (i.e., $R = \infty$). However, formulas for classical stiffnesses will have the same form in both cases, as shown below.

2.2 Classical Approximation. At this step terms of order ϵ^2 in the functional are recovered. Displacement field obtained at the previous step is perturbed again. Denoting these perturbations as w_i, one can write

$$\begin{aligned} v_1 &= U_1 - x_\alpha U'_\alpha - \underline{\theta' \eta} + w_1 \\ v_2 &= U_\alpha \dot{x}_\alpha + \theta r_n + \hat{w}_2 + w_2 \\ v_3 &= U_2 \dot{x}_3 - U_3 \dot{x}_2 - \theta r_\tau + \hat{w}_3 + w_3 . \end{aligned} \tag{17}$$

This is the most general form of the perturbed displacement field. As described above, the underlined term is present only for open cross sections, while $\hat{w}_\alpha$ are present only if $a \approx R$. The latter terms are still unknown, but connected by Eq. (16). Substitution of Eqs. (17) into Eqs. (4) leads to the following expressions for strains:

$$\gamma_{11} = \underset{\epsilon}{U'_1} - \underset{\epsilon}{x_\alpha U''_\alpha} - \underset{(a/l)\epsilon a/h}{\underline{\theta'' \eta}} + \underset{(a/l)\epsilon}{w_{1,1}}$$

$$2\gamma_{12} = \underset{\epsilon}{\underline{\underline{r_n \theta'}}} + \underset{\epsilon}{w_{1,2}} + \underset{(a/l)\epsilon a/h}{\hat{w}_{2,1}}$$

$$\gamma_{22} = \underset{\epsilon}{w_{2,2}} + \frac{w_3}{R}$$

$$h\rho_{11} = h[\underset{\epsilon}{x_3 U''_2} - \underset{\epsilon}{x_2 U''_3} - \underset{(a/l)\epsilon}{\theta'' r_\tau} + \underset{(a/l)^2\epsilon}{\hat{w}_{3,11}} + w_{3,11}]$$

$$h\rho_{12} = h\left[\underset{\epsilon}{-\theta'} + \underset{\epsilon}{\frac{\theta' r_n + w_{1,2}}{4R}} + \underset{(a/l)\epsilon}{\hat{w}_{3,12}} + w_{3,12} - \underset{(a/l)^2\epsilon}{\frac{3(\hat{w}_{2,1} + w_{2,1})}{4R}} \right]$$

$$h\rho_{22} = h\left[\underset{\epsilon}{\left(\hat{w}_{3,2} - \frac{\hat{w}_2}{R} \right)_2} + \underset{\epsilon}{\left(w_{3,2} - \frac{w_2}{R} \right)_2} \right]. \tag{18}$$

Note that the still unknown $\hat{w}_\alpha$ are present along with w_α—they are distinct, so that $\frac{h}{a}\hat{w}_\alpha \approx w_\alpha$. This allows one to neglect the latter with respect to former in $\rho_{\alpha\beta}$. Of course, when terms due to $\hat{w}_\alpha$ vanish, terms due to w_α have to be retained—this is the case for γ_{22} (or for $\rho_{\alpha\beta}$ when $\hat{w}_\alpha$ themselves vanish—see the previous step). Underlined terms exist only for open sections while double-underlined term only for closed cross sections. Let us keep in Eqs. (18) only terms of order ϵ, denote them with bars and sort the result into two arrays: those containing the one-dimensional strain measures ($\overline{\psi}^T \equiv \{\overline{\gamma}_{11}, h\overline{\rho}_{11}, \overline{\rho}_{12}\}$) and those with only unknown quantities which will be found in the process of minimization ($\overline{\phi}^T \equiv \{\overline{\gamma}_{12}, \overline{\gamma}_{22}, h\overline{\rho}_{22}\}$). This provides the motivation for writing strain the energy density in the form Eq. (8) and resembles the semi-inversion procedure that was used in Reissner and Tsai [1]. Depending on the geometry of the cross section, the following distinct cases can be identified.

2.3 Strips and Open Cross Sections. Ironically, strips represent the only case where all three components of $\overline{\psi}$ are needed. If we align the larger dimension of the strip along with x_2 then $x_3 = 0$ and U_3 drops from the $\overline{\gamma}_{11}$, therefore the largest term with U_3 comes from $\overline{\rho}_{11}$. The double-underlined term in Eqs. (18) is absent (no constraint of single-valuedness), so the largest terms with θ comes from $\underline{\overline{\rho}}_{12}$. The resulting orders follow as $aU''_2 \approx hU''_3 \approx h\theta' \approx \epsilon$, so $\overline{\psi}^T = \{U'_1 - x_2 U''_2, hU''_3, -h\theta'\}$, or in matrix form $\overline{\psi} = T_{\text{strip}}(s)\alpha$, where T_{strip} is a 3×4 matrix.

For open cross sections U_3 does not drop out from the $\overline{\gamma}_{11}$ so $\overline{\rho}_{11}$ can be neglected and $aU''_3 \approx \epsilon$. Thus, the known strains depend on the one-dimensional strain measures as $\overline{\psi}^T = \{U'_1 - x_2 U''_2 - x_3 U''_3, 0, -h\theta'\}$, or in matrix form, $\overline{\psi} = T_{\text{open}}(s)\alpha$.

There is no constraint on $\overline{\phi}$, so minimization is straightforward, yielding

$$\overline{\phi}_i = -P^{-1}_{ij} S_{jk} \overline{\psi}_k . \tag{19}$$

Substituting the result into Eqs. (8), we obtain the final expression for the classical strain energy, given by

$$C = \int T^T (Q - SP^{-1}S) T ds \tag{20}$$

where T is either T_{strip} or T_{open}, depending on the cross section in question.

2.4 Closed Cross Sections. As described above, $\overline{\gamma}_{12}$ contains nonzero terms of order θ' neglected so that $\overline{\psi}^T = \{U'_1 - x_2 U''_2 - x_3 U''_3, 0, 0\}$. Here the 3×4 matrix T, which connects $\overline{\psi}$ and α, effectively becomes a column matrix $T = \{1, -x_2, -x_3, 0\}$; the $\overline{\phi}_i$ are not arbitrary and proper constraints have to be imposed if the minimization is conducted in terms of these unknowns. For n-celled sections there are $4 \times n$ such constraints—four constraints per each cell. Single-cell formulas are derived below, but the procedure is equally applicable for multiple cells as well.

Let us consider most general case when $R \approx a$ (the other cases are analogous with obvious simplifications and lead to the same constraints). We denote $\Xi \equiv h\hat{w}_{3,2} - h\hat{w}_2/R$, so that $\Xi_{,2} = \phi_3$. Clearly $\oint \phi_3 ds \equiv \oint \Xi_{,2} ds = 0$. Three other constraints stem from the requirement of single-valuedness of displacements in Cartesian coordinates, such that $\oint u_{i,2} ds = 0$. Note the analogy between the imposed constraints and the introduction of one-dimensional variables Eqs. (10). First, $0 = \oint u_{1,2} ds = \oint \hat{w}_{1,2} ds$, so that $\oint \overline{\phi}_1 ds = \theta' \oint r_n ds$. The other two constraints are a bit less straightforward. Using Eqs. (3) the following relations can be written for $\hat{w}_\alpha$:

$$\begin{aligned} &\oint [\hat{w}_{2,2}\dot{x}_2 + \hat{w}_2 \ddot{x}_2 + \hat{w}_{3,2}\dot{x}_3 + \hat{w}_3 \ddot{x}_3] ds = 0 \\ &\oint [\hat{w}_{2,2}\dot{x}_3 + \hat{w}_2 \ddot{x}_3 - \hat{w}_{3,2}\dot{x}_2 - \hat{w}_3 \ddot{x}_2] ds = 0. \end{aligned} \tag{21}$$

Taking advantage of Eqs. (2) this can be rewritten as

$$\begin{aligned} &\oint \left[\dot{x}_2 \left(\hat{w}_{2,2} + \frac{\hat{w}_3}{R} \right) + \dot{x}_3 \left(\hat{w}_{3,2} - \frac{\hat{w}_2}{R} \right) \right] ds = 0 \\ &\oint \left[\dot{x}_3 \left(\hat{w}_{2,2} + \frac{\hat{w}_3}{R} \right) + \dot{x}_2 \left(\hat{w}_{3,2} - \frac{\hat{w}_2}{R} \right) \right] ds = 0. \end{aligned} \tag{22}$$

Recalling Eq. (16), one finds that

$$\oint \dot{x}_\alpha \Xi ds = 0 \quad \text{or} \quad \oint x_\alpha \phi_3 ds = 0.$$

Therefore, for a single-cell cross section functional to be minimized has the form

$$\begin{aligned} 2\Lambda = \oint [&\overline{\psi}_1^2 Q_{11} + 2\overline{\phi}_i S_{i1} \overline{\psi}_1 + \overline{\phi}_i P_{ij} \overline{\phi}_j + 2\lambda_1 (\overline{\phi}_1 + \theta' r_n) \\ &+ 2\overline{\phi}_3 (\lambda_\alpha x_\alpha + \lambda_4)] ds \end{aligned} \tag{23}$$

where λ_a are Lagrange multipliers; here and below $a = 1, \ldots, 4$. For multiple-cell cross sections, such a set of four Lagrange multipliers has to be introduced for each cell, while minimization should be conducted over the whole cross section.

Then the solution is given by

$$\overline{\phi}_i = -c_i \overline{\psi}_1 - P^{-1}_{ij} t_j \quad \text{where} \quad c_i \equiv P^{-1}_{ij} S_{j1} . \tag{24}$$

Here $t^T = \{\lambda_1, 0, (\lambda_\alpha x_\alpha + \lambda_4)\} \equiv \hat{T}(s)\lambda$. We can rewrite Eqs. (24) explicitly in terms of α and λ, yielding

$$\overline{\phi}_i = -c_i T_a \alpha_a - P^{-1}_{ij} \hat{T}_{ja} \lambda_a . \tag{25}$$

Substituting Eqs. (25) into expressions for constraints, we obtain

$$-\alpha_a \oint [c_1 T_a - E_a] ds = \lambda_a \oint [P_{1j}^{-1} \hat{T}_{ja}] ds$$
$$-\alpha_a \oint [\{1, x_\alpha\} c_3 T_a] ds$$
$$= \lambda_a \oint [\{1, x_\alpha\} P_{3j}^{-1} \hat{T}_{ja}] ds \quad (26)$$

here $E=\{0,0,0,r_n\}$. These are four linear equations for λ in terms of the one-dimensional strain measures: $F\lambda = J\alpha$, $\lambda = F^{-1}J\alpha$. Substituting the result into Eqs. (24) we obtain the solution for $\bar{\phi}$ as

$$\bar{\phi} = -(cT + P^{-1}\hat{T}F^{-1}J)\alpha \equiv Y(s)\alpha. \quad (27)$$

Finally, substituting Eq. (27) into Eq. (23) yields the stiffness matrix:

$$C = \oint T^T Q T - Y^T P Y + LE \quad (28)$$

where $L_a = F_{1b}^{-1} J_{ba}$ (LE corresponds to the term $\lambda_1 \theta' r_n$).

From the present point of view, the derivation in Berdichevsky et al. [4] is equivalent to setting $\bar{\phi}_3$ to zero. It can be shown using Eqs. (24) and (26) that this assumption is appropriate for so-called circumferentially uniform sections (CUS) (i.e., when material constants can be taken outside the integral and satisfying three constraints on $\bar{\phi}_3$ renders it zero). However, there are some cases that the influence of this term does make a difference. To demonstrate this let us consider a box-beam with geometry and material properties taken from Smith and Chopra [9]. Two following configurations are considered:

outer dimensions: height $b=0.53$ in.
width $a=0.953$ in.
wall thickness: $h=0.03$ in.
material properties: $E_l = 20.6\times10^6$ psi
$E_t = 1.42\times10^6$ psi
$G_{lt} = 8.7\times10^5$ psi
$G_{tn} = 6.96\times10^5$ psi
$\nu_{lt} = \nu_{tn} = 0.42$

antisymmetric: right and upper wall layup: $(\Theta)_3/(-\Theta)_3$
antisymmetric: left and lower wall layup: $(-\Theta)_3/(\Theta)_3$
symmetric: right and left wall layup: $(\Theta)_3/(-\Theta)_3$
symmetric: upper and lower wall layup: $(-\Theta)_3/(\Theta)_3$. (29)

Both antisymmetric and symmetric layups exhibit essentially no elastic coupling, and the one-dimensional stiffness matrices are diagonal.

The torsional rigidity can be significantly overestimated if $\bar{\phi}_3$ is disregarded. This can be observed by comparing the results of Berdichevsky et al. [4] with the present ones and with the numerical results obtained from VABS Cesnik and Hodges [3]. The results of Berdichevsky et al. [4] are far too stiff in torsion relative to VABS results while the present theory exhibits excellent agreement with VABS. Indeed, for $h=0.03$ the difference is less than three percent (see Figs. 2 and 3). With decreasing thickness (leaving the other dimensions the same) analytical results converge to the numerical results. In fact by $h=0.006$ in the analytical, results exceed the precision of 1000 six-noded finite elements in VABS. One should recall here that finite elements with large aspect ratios are notoriously fickle. We also note that the difference between

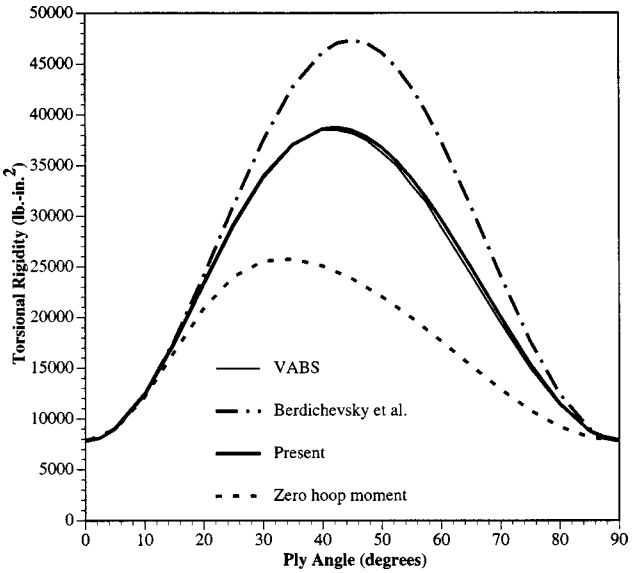

Fig. 2 Torsional rigidity, antisymmetric layup $h=0.03$ in

the results of Berdichevsky et al. [4] and those of the present asymptotically correct theory is practically independent of thickness, as can be seen Fig. 4.

It has to be emphasized that while the cases where the theory from Berdichevsky et al. [4] breaks down are quite rare, it might actually create a false sense of security: For the considered symmetric case torsional rigidity is overpredicted by a factor of two! On the other hand, another quite obvious approximation would be to set the hoop bending moment to zero. This can be interpreted as a thin-walled equivalent of the so-called ''uniaxial stress'' assumption (when all stresses in the cross-sectional plane are set to zero) that is quite common in beam theories, e.g., Rand [10] and Kim and White [11]. As can be observed from Figs. 2 and 3, this assumption leads to an underprediction of their torsional rigidity. It has to be added that for the specific cases considered in Berdichevsky et al. [4], the differences between our results and theirs are negligible. Thus, for the sake of brevity, the excellent correlations published therein with experimental and numerical data need not be repeated here.

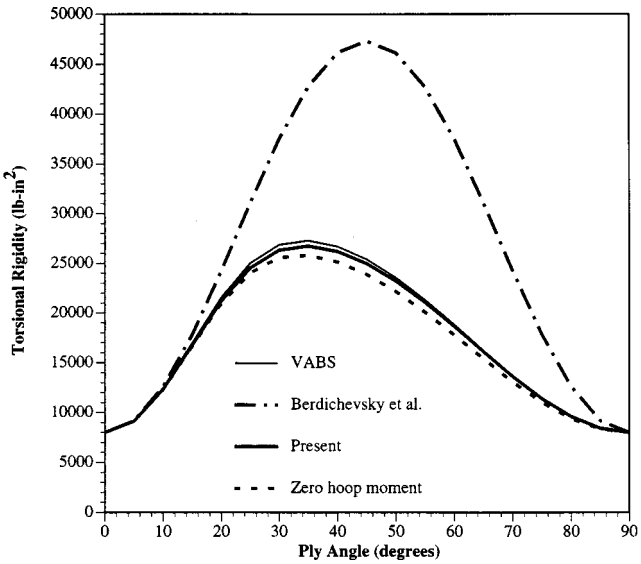

Fig. 3 Torsional rigidity, symmetric layup $h=0.03$ in

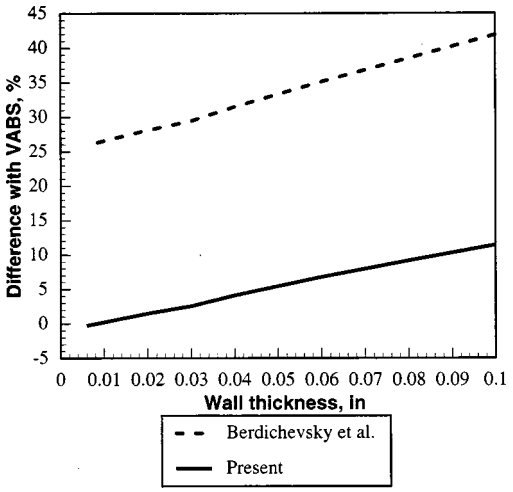

Fig. 4 Difference in torsional rigidity, $\Theta = 60$ deg

The general conclusion can be drawn that, while for most layups either ''no bending shell strain measures'' or ''no hoop moment'' might work quite satisfactorily, only the present theory can insure correct results for all the cases.

Strain Field. Let us emphasize that for all types of cross sections—even in ''classical'' approximation—the cross section is *not* rigid in its own plane! The in-plane strains are not zero but are given by Eqs. (19) and (27). By the same token, unless one deals with isotropy or similarly restricted case, the shear strain γ_{12} is nonzero and essential to the analysis, even without resorting to Timoshenko-like theories. On the other hand, within the precision of this approximation, γ_{11}, ρ_{11}, and ρ_{12} have very simple expressions, since they are given by appropriate components of $\overline{\psi}$.

Recovering Displacements. When there is no curvature $\overline{\phi}^T = \{w_{1,2}, w_{2,2}, hw_{3,22}\}$, so once $\overline{\phi}$ is obtained this relationship can be integrated. In order to preserve the definition of one-dimensional variables one has to eliminate rigid-body motions from this warping (i.e., $\int w_i ds = \int (w_2 x_3 - w_3 x_2) ds = 0$), this allows one to define w_i uniquely which then should be substituted into Eqs. (17) to obtain the full displacement field. However, when $R \approx a$ only $\hat{w}_i$, and w_1 can be obtained, whereas knowing $\overline{\phi}_2$ is not sufficient to recover w_2 and w_3 individually. Thus, the full displacement field cannot be recovered in this case. The latter situation is similar to the one described in Berdichevsky and Misyura [12].

2.5 Second-Order Terms. The next step of the asymptotic procedure allows us to obtain terms in the strain energy up to $\epsilon^2(\frac{a}{l})^2$. While generally this is a cumbersome procedure, it turns out that sometimes these terms are very significant—and easily calculated. This can be clearly seen from Eqs. (18). There are two terms present in γ_{11} and γ_{12} which are of order $\epsilon(\frac{a}{l})(\frac{a}{h})$. While we neglected those terms in the ''classical'' approximation, they clearly can be quite large. We perturb the ''classical'' displacement field in a manner similar to the previous step in which w_i was introduced into the displacement field. This led to the presence of the unknown $\overline{\phi}$ in the strain field. Here we introduce $\tilde{w}_i$, which in turn leads to $\tilde{\phi}$ in the strain. Let us note that due to the Euler-Lagrange equations for w_i, the leading cross terms between w_i and $\tilde{w}_i$ vanish in the functional. The term from γ_{11} exists for open cross sections only; it is zero for strips, since $\eta = 0$. No constraints are imposed on $\tilde{\phi}$, so the problem is similar to the unconstrained problem for closed sections in which $\tilde{\phi}_i = c_i \theta'' \eta$. This leads to the one-dimensional strain energy per unit length

$$2F_{\text{Vlasov}} = \alpha_a C_{ab} \alpha_b + 2M_a \alpha_a \theta'' + \Gamma \theta''^2 \tag{30}$$

where C_{ab} is given by Eq. (20) for open cross sections and

$$M_a = \int \eta s_{1i} T_{ia} ds$$
$$\Gamma = \int \eta^2 (Q_{11}^2 - c_i P_{i1}) ds. \tag{31}$$

Note that M_a does not have a contribution from $\tilde{w}_i$, since terms of order ϵ are correctly obtained using only classical warping. This generalizes the formulas provided in Volovoi et al. [5] where I-beams were treated as an assembly of strips rather than as a contour, and the results were extensively correlated with three-dimensional simulations. For isotropy the formulas obtained reduce to Vlasov theory.

Finally, let us consider the term $\hat{w}_{2,1}$ from γ_{12}, which is of order $\epsilon(\frac{a}{l})(\frac{a}{h})$ if $R \approx a$. If the cross section is open, there is no constraint on $\tilde{w}$, so by choosing $\tilde{w}_{1,2} = \tilde{\phi}_1 - \hat{w}_{2,1}$ (here $\tilde{\phi}_1$ refers to the solution for Vlasov correction), this term can be killed. Theoretically, for closed sections this is not true if $\oint \hat{w}_{2,1} ds$ is not zero. Value of this integral depends on the constraints imposed on classical warping. Using constraints that are chosen so that warping does not affect the definition of one-dimensional variables, it can be shown that for a closed contour of a constant curvature $\oint \hat{w}_{2,1} ds = 0$. For a general geometry this is not so, but constraints can be adjusted appropriately. Therefore, this term is not expected to play a significant role.

3 Conclusions

Using small parameters $\frac{a}{h}$ and $\frac{h}{a}$, which are inherent to thin-walled beams, and without appeal to any *ad hoc* geometric assumptions whatsoever, asymptotically correct theories are derived for thin-walled anisotropic beams. These theories include closed-form expressions for cross-sectional stiffness constants as well as recovering relations for strain (and displacement when possible).

It is noted that the term ''asymptotical correctness'' concerning an approximate solution denotes its agreement to a specified order in a small parameter with an asymptotic expansion of the exact solution in that parameter. Asymptotical correctness is the most important characteristic of any approximate solution.

The resulting Vlasov-like theory for beams with open cross sections is a generalization of the previously published theory for I-beams in Volovoi et al. [5]. However, unlike any existing theory for closed sections, the effects of shell-bending strain measures are included herein and their importance is demonstrated. It is shown that the Vlasov effect for strips and beams with closed cross section is negligible.

Unlike most treatments of thin-walled beams in the literature, the present results are simultaneously obtained for open and closed-section anisotropic beams, including strip-beams. The significant differences entailed by these different geometries are shown to be naturally resolved within the same asymptotic framework. Now that an asymptotically correct theory is in place for thin-walled beams, one can undertake critical assessment of previously published theories of thin-walled beams.

References

[1] Reissner, E., and Tsai, W. T., 1972, ''Pure Bending, Stretching, and Twisting of Anisotropic Cylindrical Shells,'' J. Appl. Mech., **39**, pp. 148–154.
[2] Berdichevsky, V. L., 1982, ''On the Energy of an Elastic Rod,'' J. of Appl. Math. Mech., **45**, pp. 518–529.
[3] Cesnik, C. E. S., and Hodges, D. H., 1997, ''VABS: A New Concept for Composite Rotor Blade Cross-Sectional Modeling,'' J. Am. Helicopter Soc., **42**, No. 1, pp. 27–38.
[4] Berdichevsky, V. L., Armanios, E. A., and Badir, A. M., 1992, ''Theory of Anisotropic Thin-Walled Closed-Section Beams,'' Composites Eng., **2**, Nos. 5–7, pp. 411–432.
[5] Volovoi, V. V., Hodges, D. H., Berdichevsky, V. L., and Sutyrin, V., 1998,

''Asymptotic Theory for Static Behavior of Elastic Anisotropic I-Beams,'' Int. J. Solids Struct., **36**, No. 7, pp. 1017–1043.
[6] Koiter, W. T., 1959, ''A Consistent First Approximation in the General Theory of Thin Elastic Shells,'' *Proceedings of the IUTAM Symposium: Symposium on the Theory of Thin Elastic Shells*, North-Holland, Amsterdam, pp. 12–33.
[7] Sanders, J. L., 1959, ''An Improved First Order Approximation Theory for Thin Shells,'' Technical Report 24, NASA.
[8] Berdichevsky, V. L., 1983, *Variational Principles of Continuum Mechanics*, Nauka, Moscow.
[9] Smith, E. C., and Chopra, I., 1991, ''Formulation and Evaluation of an Analytical Model for Composite Box-Beams,'' J. Am. Helicopter Soc., **36**, No. 3, pp. 23–35.
[10] Rand, O., 1997, ''Generalization of Analytical Solutions for Solid and Thin-Walled Composite Beams,'' *Proceedings of the American Helicopter Society 53rd Annual Forum*, Viriginia Beach, VA, American Helicopter Society, New York, pp. 159–173.
[11] Kim, C., and White, S. R., 1997, ''Thick-Walled Composite Beam Theory Including 3-D Elastic Effects and Torsional Warping,'' Int. J. Solids Struct., **34**, Nos. 31–32, pp. 4237–4259.
[12] Berdichevsky, V. L., and Misyura, V., 1992, ''Effect of Accuracy Loss in Classical Shell Theory,'' J. Appl. Mech., **59**, pp. S217–S223.

On Torsion of Closed Thin-Wall Members With Arbitrary Stress-Strain Laws: A General Criterion for Cross Sections Exhibiting No Warping

A. Chiskis

R. Parnes

Department of Solid Mechanics,
Materials and Structures,
Faculty of Engineering,
Tel-Aviv University,
Ramat Aviv 69978, Israel

Warping due to torsion of closed thin-wall elastic members having constant thickness is investigated under the assumption of small strain but with arbitrary isotropic shear stress-strain laws. Based on a derived general criterion, it is shown that there exists a class of cross-sections which undergo no warping. For cases where warping exists, an example of simplified calculations, using the derived expressions, is presented for warping of a thin-wall rectangle. [S0021-8936(00)03503-0]

1 Introduction

The problem of torsion has attracted attention for some time and has been considered under different aspects (Day [1], Podio-Guidugli [2], and Ericksen [3]) both for linear or nonlinear behavior (see Truesdell [4]). Thin-walled constructions may be of interest, as indicated below, not only for technical applications in traditional engineering but also in such a new field as nanotechnology, where the absence of warping may be of special interests for molecular thin-wall structures.[1]

In the present paper warping in thin-wall constructions of constant thickness is considered. We restrict here the problem to members undergoing small strains but governed by arbitrary isotropic shear stress-strain ($\tau-\gamma$) relations. For experimental consideration of physical nonlinearity in real materials, see Bell [7].

While it is known that the absence of warping is possible only for circular cross sections (or circular rings), under the thin-wall approximation the situation changes dramatically. It is shown that thin-wall constructions possessing the property of no warping may be convex as well as nonconvex.

Finally for the case where a member does not satisfy the established criterion, based on the derived expressions, a simple example of calculations of warping of a thin-wall rectangle is also presented.

2 General Relations

We consider below the standard Saint-Venant representation for a prismatic member undergoing torsion about the z-axis such that all cross sections lie initially in the x-y plane. Letting $\boldsymbol{\gamma}$ and $\boldsymbol{\tau}$,

$$\boldsymbol{\gamma}=\gamma_x\mathbf{i}+\gamma_y\mathbf{j}, \quad \boldsymbol{\tau}=\tau_x\mathbf{i}+\tau_y\mathbf{j}, \tag{1}$$

be vector fields independent of z,

$$\boldsymbol{\gamma}=\boldsymbol{\gamma}(x,y) \quad \boldsymbol{\tau}=\boldsymbol{\tau}(x,y),$$

(where $\boldsymbol{\gamma}$ and $\boldsymbol{\tau}$ represent angle changes and stress components) the strain and stress tensors, $\boldsymbol{\epsilon}$ and $\mathbf{T}$, are given by

$$2\boldsymbol{\epsilon}=\begin{pmatrix} 0 & 0 & \gamma_x \\ 0 & 0 & \gamma_y \\ \gamma_x & \gamma_y & 0 \end{pmatrix} \quad \mathbf{T}=\begin{pmatrix} 0 & 0 & \tau_x \\ 0 & 0 & \tau_y \\ \tau_x & \tau_y & 0 \end{pmatrix}. \tag{2}$$

Using dyadic notation, we may represent (2) conveniently in the following form:

$$2\boldsymbol{\epsilon}=\boldsymbol{\gamma}\otimes\mathbf{k}+\mathbf{k}\otimes\boldsymbol{\gamma}, \quad \mathbf{T}=\boldsymbol{\tau}\otimes\mathbf{k}+\mathbf{k}\otimes\boldsymbol{\tau}. \tag{3}$$

Here $\mathbf{k}$ is the unit vector corresponding to the axis of rotation. From (1) and (3) it follows that

$$\boldsymbol{\gamma}=2\boldsymbol{\epsilon}\cdot\mathbf{k}. \tag{4}$$

We note that the equilibrium equation $\boldsymbol{\nabla}\cdot\mathbf{T}=0$ is then reduced to one scalar equation

$$\tilde{\boldsymbol{\nabla}}\cdot\boldsymbol{\tau}=0, \quad (\tilde{\boldsymbol{\nabla}}=\partial_x\mathbf{i}+\partial_y\mathbf{j}). \tag{5a}$$

i.e.,

$$\frac{\partial\tau_x}{\partial x}+\frac{\partial\tau_y}{\partial y}=0. \tag{5b}$$

Representing the displacement vector $\mathbf{u}$ as the out-of-plane *warping* w, (independent of z) and the in-plane displacement $\tilde{\mathbf{u}}$ due to rotation (which depends on z through the angle of rotation, Θz, where Θ is the unit angle of twist),

$$\mathbf{u}=w\mathbf{k}+\tilde{\mathbf{u}}, \quad \tilde{\mathbf{u}}=\Theta z\mathbf{k}\times\boldsymbol{\rho}, \quad w=w(x,y), \tag{6}$$

where $\boldsymbol{\rho}\equiv x\mathbf{i}+y\mathbf{j}$ is the in-plane position vector measured from the axis of rotation. Using the definition of the small strain tensor $2\boldsymbol{\epsilon}=\boldsymbol{\nabla}\otimes\mathbf{u}+\mathbf{u}\otimes\boldsymbol{\nabla}$, it follows from (4) and (6) that

$$\boldsymbol{\gamma}=\tilde{\boldsymbol{\nabla}}w+\partial_z\tilde{\mathbf{u}}=\tilde{\boldsymbol{\nabla}}w+\Theta\mathbf{k}\times\boldsymbol{\rho}, \tag{7a}$$

from which

$$\tilde{\boldsymbol{\nabla}}w=\boldsymbol{\gamma}-\Theta\mathbf{k}\times\boldsymbol{\rho}, \tag{7b}$$

or, in coordinate form,

[1] While a classical mechanics approach was recently used by Yakobson, Brakec, and Bernholc [5] and Falvo et al., [6] in investigating the buckling stability and corrugation of carbon nanotubes due to bending, no such study of torsion appears in the literature.

Contributed by the Applied Mechanics Division of THE AMERICAN SOCIETY OF MECHANICAL ENGINEERS for publication in the ASME JOURNAL OF APPLIED MECHANICS. Manuscript received by the ASME Applied Mechanics Division, Apr. 13, 1999; final revision, May 5, 2000. Associate Technical Editor: J. T. Jenkins. Discussion on the paper should be addressed to the Technical Editor, Professor Lewis T. Wheeler, Department of Mechanical Engineering, University of Houston, Houston, TX 77204-4792, and will be accepted until four months after final publication of the paper itself in the ASME JOURNAL OF APPLIED MECHANICS.

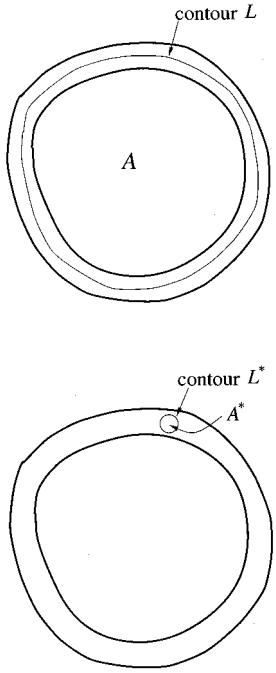

Fig. 1

$$\frac{\partial w}{\partial x} = \gamma_x + \Theta y\,, \qquad \frac{\partial w}{\partial y} = \gamma_y - \Theta x\,. \tag{7c}$$

The structure of Eq. (7*b*) bears two consequences:

Consequence i (''Global compatibility''). We consider the arbitrary contour L as shown in Fig. 1(*a*). Applying the compatibility condition $\oint_L \nabla w \cdot d\mathbf{L} = 0$, substituting (7*b*) and using Green's theorem, we obtain

$$\oint_L \boldsymbol{\gamma} \cdot d\mathbf{L} = 2\Theta \mathbf{A}, \tag{8a}$$

where A is the area within the contour.

Consequence ii (''Local compatibility''). Choosing a different contour, L^*, surrounding an arbitrary area A^* in the vicinity of a cross section point (see Fig. 1(*b*)) and applying Stoke's theorem to (8*a*), we obtain $\oint_{A^*} \nabla \times \boldsymbol{\gamma} \cdot \mathbf{k} dA = 2\Theta A^*$, which is equivalent to (8*a*) for the chosen contour. Since A^* and L^* are arbitrary, we may contract the contour L^* to a point, from which we obtain

$$\mathbf{k} \cdot (\nabla \times \boldsymbol{\gamma}) = 2\Theta. \tag{8b}$$

Note that one may formally obtain this relation by taking the rotor of (7*b*).

In what follows below, we consider isotropic elastic materials either having physical-nonlinear behavior

$$\boldsymbol{\tau} = f(|\boldsymbol{\gamma}|)\,\boldsymbol{\gamma}, \tag{9a}$$

or linear behavior

$$\boldsymbol{\tau} = G\boldsymbol{\gamma}. \tag{9b}$$

It will be seen below that the determination of warping is independent of *any specific* constitutive relation.

3 The Closed Contour Thin-Wall Approximation

We consider below a closed thin-wall construction whose cross-section consists of closed curvilinear segments in the x-y plane. One may thus imagine a thin ring of arbitrary shape. Several examples of interesting geometrical shapes will be discussed further.

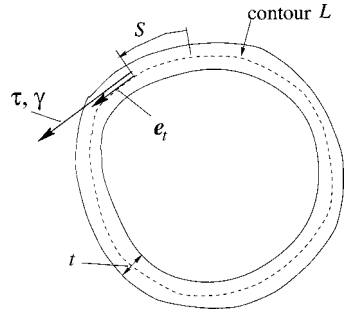

Fig. 2

The contour is then determined by the middle-curve of the cross section; the position of a given point on this curve is defined by the arc-length coordinate, S and the cross section thickness by $t = t(S)$.

The usual approximation for *closed* thin-wall structures is[2] (see Fig. 2):

$$\boldsymbol{\tau} = \tau(S)\mathbf{e}_t\,, \quad |\mathbf{e}_t| = 1, \tag{10}$$

where $\mathbf{e}_t$ is the unit tangent vector to the contour curve lying in the x-y plane. Equation (10) obviously satisfies the boundary conditions $\mathbf{Tn} = 0$, where $\mathbf{n}$ is the normal to the contour, i.e., the absence of the traction on the lateral surfaces of the cylinder. Physically, τ is the average shear stress through the thin-wall cross section. The equilibrium equation is then reduced to conservation of the shear flux q along a section of the cross section:

$$q = \tau t = \text{const.}$$

(For multicell cross section shapes, the constant fluxes are different for any given segment.)

Due to constitutive Eq. (9), the shear vector $\boldsymbol{\gamma}$ has a representation similar to (10) (see Fig. 2)

$$\boldsymbol{\gamma} = \gamma(S)\mathbf{e}_t\,, \tag{11}$$

where the scalar constitutive relation relating τ and γ is

$$\tau = f(\gamma)\gamma \equiv F(\gamma). \tag{12}$$

Neglecting the thickness of the contour segment, we rewrite relation (7*b*) in the form

$$\frac{dw}{dS} = \mathbf{e}_t \cdot \nabla w = \mathbf{e}_t \cdot \boldsymbol{\gamma} - \Theta \mathbf{e}_t \cdot (\mathbf{k} \times \boldsymbol{\rho}). \tag{13}$$

When the contour line consists of straight segments another representation is simpler. We first note that $\mathbf{e}_t \cdot (\mathbf{k} \times \boldsymbol{\rho}) = \mathbf{k} \cdot (\boldsymbol{\rho} \times \mathbf{e}_t) = \rho_\perp$, where $\rho_\perp$ is the distance from the axis of rotation to a straight segment (or its prolongation) (see Fig. 3). Therefore, we have

$$\frac{dw}{dS} = \gamma - \Theta \rho_\perp\,. \tag{14}$$

The relation (14) is crucial for further consideration of the warping, w.

We observe in passing that since, under the thin-wall approximation, w is assumed to be a function only of the arc length, i.e.,

[2]The present paper by no means is devoted to derivation of this well-known approximation which is discussed in any standard reference (see, e.g., Timoshenko and Goodier [8]). Obviously, from the three-dimensional elasticity point of view, the approximation corresponds to the main term in the asymptotic expansion. However, for molecular structures with widths of several atomic/molecular spaces, one assumes this as a rational approximation relating shear force and angle of shear of the corresponding molecular lattice/structure.

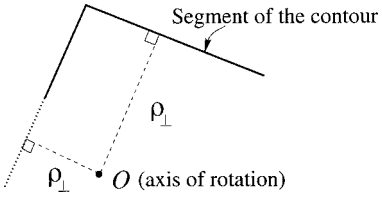

Fig. 3

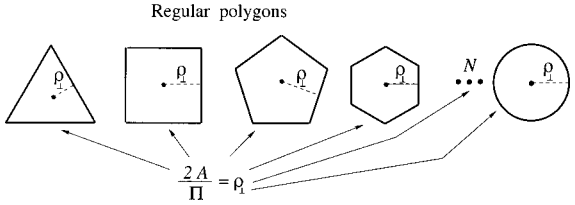

Fig. 4

$w = w(S)$, the local compatibility condition becomes irrelevant. Therefore only the global compatibility condition is required to remove any ambiguity in w.

4 Constant Thickness Doubly Connected (Single-Cell) Section

For a wall of constant thickness, ($t(S) = \text{const}$) τ is constant, and therefore, γ is necessarily a constant, which can be easily determined from the ''global compatibility,'' relation (8*a*), for *the closed contour*. Thus, using

$$\oint \boldsymbol{\gamma} \cdot d\mathbf{L} = \gamma \oint \mathbf{e}_t \cdot d\mathbf{L} = \gamma\Pi,$$

(where Π is the perimeter of the contour), we obtain

$$\gamma = \frac{2\Theta A}{\Pi}. \tag{15}$$

We emphasize here that no specific τ-γ relation was used in deriving (15).

We then rewrite (14) as

$$\frac{dw}{dS} = \Theta\left(\frac{2A}{\Pi} - \rho_\perp\right). \tag{16}$$

We observe that since axial displacement in the torsion problem is determined up to an arbitrary translation along the axis z, without restriction of generality, we may assume $w = 0$ at some point at the contour. (It is convenient to choose this point by considerations of symmetry if such symmetry exists.) We note that a relation corresponding to (16) is known for thin-wall *linear* elastic multicell structures (see, for example, Murray [9]). However, as we have shown here, this relation is equally valid for physically nonlinear elastic members undergoing small strains.

4.1 Shapes of Contours With No Warping. We now investigate the geometrical shapes of contours for which $w \equiv 0$. Since at some point of the contour $w = 0$, then $w \equiv 0$ if and only if $dw/dS \equiv 0$. Thus, from (16) we have

$$\rho_\perp = \text{const} = \frac{2A}{\Pi}. \tag{17}$$

Note that any curve may be approximated as the limit case of a polygon. Therefore, without restriction of generality, we may restrict our attention to considerations of polygons which satisfy relation (17).

We note that relation (17) demands that the distance from any side of such a polygon to the point representing the axis of rotation be the same for *all* sides of the polygon.

We first consider *convex* polygons, both regular and irregular polygons.

(*i*) It is clear that the class of *regular polygons* possesses the property $\rho_\perp = \text{const}$ (Fig. 4); by means of simple triangulation, we find $\rho_\perp = 2A/\Pi$ is always true for any such polygon.

(*ii*) We now generalize to the class of irregular convex polygons which are symmetric with respect to the x and y-axes. Examples of such polygons are shown in Fig. 5. (It follows that the center of twist coincides with the origin of the axes, O.) Upon drawing an inscribed circle of radius R with center at O touching *all* sides of the polygon, condition $\rho_\perp = \text{cosnst}$ is satisfied automatically since $\rho_\perp = R$. To show that $R = 2A/\Pi$ we triangulate the area by N triangles (N being the number of sides of the polygon); the area of *k-th* triangle is $A_k = \frac{1}{2} a_k R$, where a_k is the length of its side. We then have

$$A = \sum_1^N A_k = \frac{R}{2} \sum_1^N a_k = \frac{R\Pi}{2}. \tag{18}$$

Clearly, a circle corresponds to a regular polygon with $N \to \infty$.

As an example of a *nonconvex* polygon we consider below the contour of a six-pointed (David) star.

It is obvious that $\rho_\perp^{(D)}$ for the contour of this star is the same as that for the ''inscribed'' hexagon $\rho_\perp^{(h)}$ (Fig. 6). It is easy to see (by considering triangles), that the area A_D of the contour of the star is twice the area A_h of the inscribed hexagon; moreover, the perimeter Π_D of the star is twice the perimeter Π_h of the hexagon. Since $\rho_\perp^{(D)} = \rho_\perp^{(h)} \equiv \rho_\perp$ and, since for the hexagon $2A_h/\Pi_h = \rho_\perp^{(h)}$,

$$\rho_\perp^{(D)} = \frac{2 \times 2A_h}{2\Pi_h} = \frac{2A_D}{\Pi_D}.$$

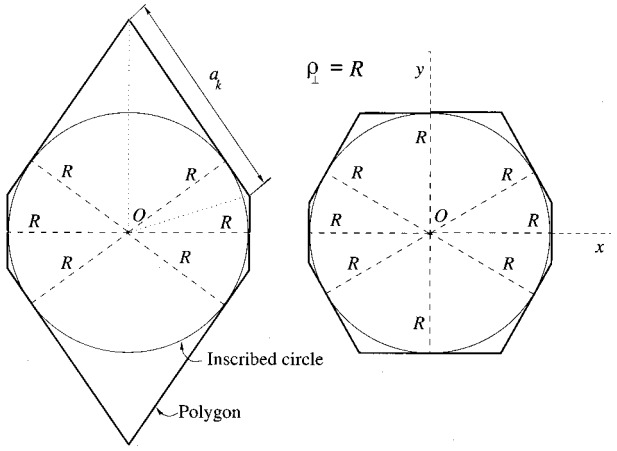

Fig. 5

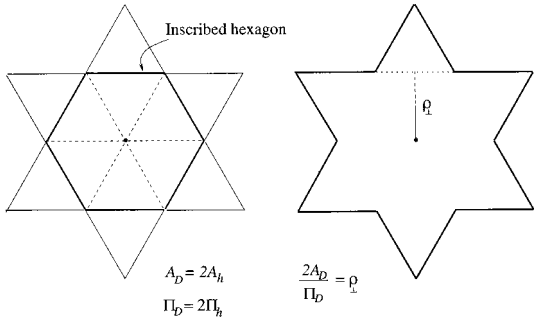

Fig. 6

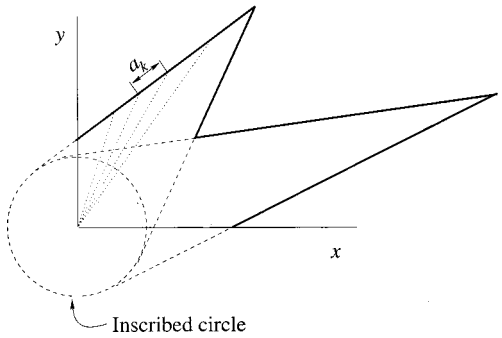

Fig. 7

It follows that a closed thin-wall member whose cross-section is in the shape of a six-pointed star will not warp under torsion.

4.2 Generalization of the Results. Based on the criterion of (17), we may generalize the results. We first recall that the criterion for no warping requires that the distance $\rho_\perp$ from the center of rotation to the sides (or their prolongation) of the section be constant. This criterion may be reformulated as follows:

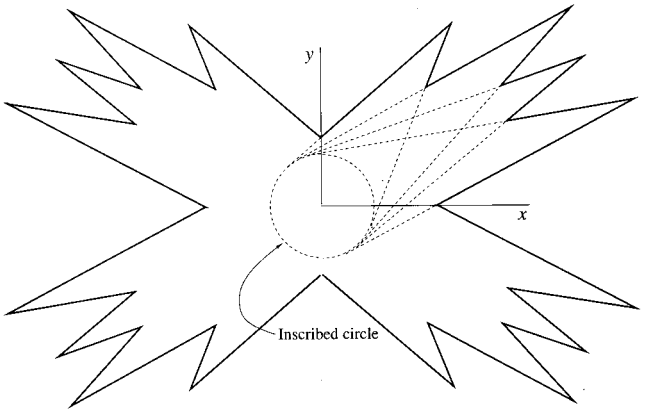

(a)

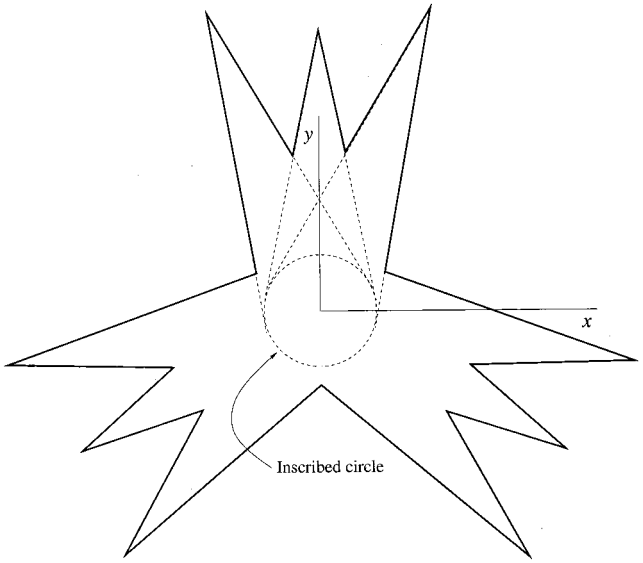

(b)

Fig. 8

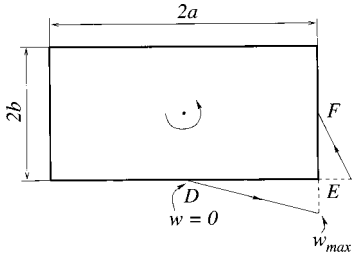

Fig. 9

A closed thin-wall section of constant thickness will not warp under torsion provided there exists an inscribed circle (whose center coincides with the center of rotation of the section) which is tangent to all sides (or their prolongation) of the section.

To show that the constant$=2A/\Pi$, consider, for example, Fig. 7, where one quadrant of the section is shown. Then, by ''Kepler triangulation,'' it is clear that relation (18) holds where here a_k is as shown in the figure.

Thus, there exists also an infinite number of star-like (nonconvex) sections possessing the required symmetry which do not warp under torsion; some of these are shown in Fig. 8.

Such sections may have technological applications, for example, as cooling or heating elements since they possess relatively large surface areas for a given volume.

4.3 An Example of Simplified Calculations of Warping. As an example of the simplified calculations using the above derived relations for a section undergoing warping, we consider a rectangle with sides $2a$ and $2b$, $a>b$, (Fig. 9). Then, $A=4ab$, $\Pi=4(a+b)$, $\rho_\perp^{(a)}=b$ and $\rho_\perp^{(b)}=a$, where $\rho_\perp^{(a)}$ and $\rho_\perp^{(b)}$ denote $\rho_\perp$ to the sides with length $2a$ and $2b$, respectively.

We then write relation (16) as

$$\frac{dw^{(a)}}{dS}=\Theta\left(\frac{2\times 4ab}{4(a+b)}-b\right)=\Theta\,\frac{b(a-b)}{a+b},$$
$$\frac{dw^{(b)}}{dS}=\Theta\left(\frac{2\times 4ab}{4(a+b)}-a\right)=-\Theta\,\frac{a(a-b)}{a+b}. \tag{19}$$

Note here, that although constants $dw^{(a)}/dS\neq dw^{(b)}/dS$, therefore dw/dS is a piece-wise linear function of the arc length (see Fig. 7). These constants satisfy the following relation:

$$a\,\frac{dw^{(a)}}{dS}=-b\,\frac{dw^{(b)}}{dS}. \tag{20}$$

Now, due to the symmetry of the contour, $w=0$ at the middle point D of the side having length $2a$. Assuming $\Theta>0$ and letting S be positive in the counterclockwise direction, since $dw^{(a)}/dS>0$, the warping, w, increases starting from this point up to the

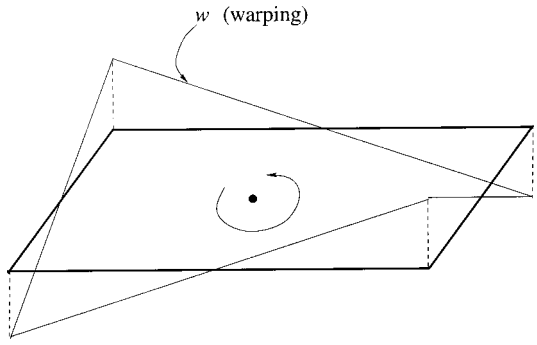

Fig. 10

corner E; at the corner the derivative changes the sign and w decreases (since $dw^{(b)}/dS<0$); due to (20) it then becomes zero exactly at the middle point F of the side with the length $2b$. The maximal value of w is clearly

$$w_{\max}=a\,\frac{dw^{(a)}}{dS}=\Theta\,\frac{ab(a-b)}{a+b}. \tag{21}$$

A three-dimensional view of w is shown in Fig. 10.

It is emphasized that the above results is known for a linear elastic single cell according to engineering theory (see, for example, Murry [9]) but, being purely kinematic in nature, is independent of any particular stress-strain relations.

Acknowledgment

The authors have pleasure to acknowledge discussions with Prof. Boris Tsirelson of the School of Mathematics, Tel-Aviv University, who pointed out a geometric generalization of the criterion.

References

[1] Day, W. A., 1981, ''Generalized Torsion: The Solution of a Problem of Truesdell's,'' Arch. Ration. Mech. Anal., **76**, pp. 283–288.
[2] Podio-Guidugli, P., 1983, ''St. Venant Formulae for Generalized St. Venant Problems,'' Arch. Ration. Mech. Anal., **81**, pp. 13–20.
[3] Ericksen, J. L., 1979, ''On St.-Venant's Problem for Thin-Walled Tubes,'' Arch. Ration. Mech. Anal., **70**, pp. 7–12.
[4] Truesdell, C., 1972, *A First Course in Rational Continuum Mechanics*, The Johns Hopkins University Press, Baltimore, MD.
[5] Yakobson, B. I., Brabec, C. J., and Bernholc, J., 1996, ''Nanomechanics of Carbon Tubes: Instabilities Beyond Linear Response,'' Phys. Rev. Lett., **76**, pp. 2511–2514.
[6] Falvo, M. R., Clary, G. J., Taylor, R. M., Chi, V., Brooks, F. P., Washburn, S., and Superfine, R., 1997, ''Bending and Buckling of Carbon Nanotubes Under Large Strain,'' Nature (London), **389**, pp. 582–584.
[7] Bell, F. J., 1973, *Mechanics of Solids, I.* (Handbuch der Physik, Vol. VIa/1), C. Truesdell ed., Springer, Berlin.
[8] Timoshenko, S. P., and Goodier, J. N., 1970, *Theory of Elasticity*, 3rd Ed., McGraw-Hill, New York.
[9] Murray, N. W., 1984, *Introduction to the Theory of Thin-Walled Structures*, Clarendon Press, Oxford, UK.

E. M. Ortt[1]
Assoc. Mem. ASME

D. J. Doss[1]
Assoc. Mem. ASME

E. Legall

N. T. Wright
Mem. ASME

J. D. Humphrey[2]
Mem. ASME

Department of Mechanical Engineering,
University of Maryland,
Baltimore, MD 21250

A Device for Evaluating the Multiaxial Finite Strain Thermomechanical Behavior of Elastomers and Soft Tissues

Described here is the design and development of a computer-controlled device capable of measuring the finite strain thermomechanical behavior of a general class of polymeric materials including elastomers and biological soft tissues. The utility of this device for thermoelastic and thermophysical investigations is demonstrated by the measurement of the in-plane stress-stretch response and in-plane and out-of-plane components of thermal diffusivity of neoprene rubber undergoing finite deformations. [S0021-8936(00)01603-2]

Introduction

The thermomechanical behavior of elastomeric, and specifically rubber-like, materials has generated considerable interest in the mechanics community for close to two centuries. With the advent of laser, ultrasound, and microwave-based medical devices, a similar interest has recently arisen in the thermomechanical behavior of soft tissues ([1]). A general thermomechanical analysis of these material behaviors requires, of course, both multiaxial thermoelastic and thermophysical data. Likewise, formulation of nonlinear constitutive relations necessitates appropriate theoretical frameworks to design and interpret the requisite experiments ([2]). For example, theory reveals that a complete description of reversible finite strain thermomechanical behavior requires identification of two independent constitutive functions ([3]), the Helmholtz potential

$$\psi = \hat{\psi}(\mathbf{C}, T), \tag{1}$$

and the referential heat flux vector

$$\mathbf{q}_0 = \hat{\mathbf{q}}_0(\mathbf{C}, T, \nabla_0 T), \tag{2}$$

where $\mathbf{C}\,(=\mathbf{F}^T\cdot\mathbf{F})$ is the right Cauchy-Green deformation tensor, $\mathbf{F}\,(=\partial\mathbf{x}/\partial\mathbf{X})$ the deformation gradient tensor, T the temperature, $\nabla_0 T\,(=\partial T/\partial\mathbf{X})$ the referential temperature gradient, and $\mathbf{x}$ and $\mathbf{X}$ the position of a material particle in the current and reference configurations, respectively. Stress-strain-temperature relations result from derivatives of $\hat{\psi}$ with respect to $\mathbf{C}$. Although a number of functional forms for $\hat{\psi}$ have been suggested ([4–7]), a widely accepted form remains elusive due, in large part, to the continuing lack of multiaxial thermoelastic data. That is, most investigators have focused on describing the available uniaxial data ([8–11]) and hence the peculiar one-dimensional Gough-Joule and thermoelastic inversion effects. Recently, however, Ogden [7] proposed a method for finding $\hat{\psi}$ as a function of biaxial stretches and temperature, whereas Humphrey and Rajagopal [12] showed that in-plane biaxial tests allow measurement of thermoelastic response functions (e.g., $\partial\hat{\psi}/\partial I_C$ where $I_C=\mathrm{tr}\,\mathbf{C}$) similar to the isothermal results of Rivlin and Saunders [13]. Both cases require measuring biaxial stress and stretch at multiple temperatures.

Alternatively, there has been little attention to the possible finite strain dependence of the heat flux. Rather, most reports assume Fourier conduction $\mathbf{q}(\mathbf{x},T)=-k(T)\nabla T$ where $\mathbf{q}(\mathbf{x},T)$ is the spatial heat flux, $\nabla T\,(=\partial T/\partial\mathbf{x})$ the spatial gradient of temperature, and $k(T)$ the scalar (i.e., isotropic) spatial thermal conductivity ([14]). For finite strains, referring the conductivity tensor to the reference configuration simplifies material symmetry considerations, and thereby facilitates the formulation of general constitutive relations. Thus, note that $\mathbf{q}=(1/J)\mathbf{F}\cdot\mathbf{q}_o$, where $J=\det\mathbf{F}$. Moreover, a generalized Fourier conduction has the form

$$\mathbf{q}(\mathbf{x},T)=\frac{1}{J}\mathbf{F}\cdot(-\mathbf{K}(\mathbf{C},T)\cdot\nabla_0 T(\mathbf{X},T)) \tag{3}$$

where $\mathbf{K}(\mathbf{C},T)$ is the referential thermal conductivity tensor. Of the tractable finite strain tests (e.g., combined extension and torsion of a cylinder, membrane inflation, etc.), the in-plane biaxial extension of a thin rectangular sheet ([13,15]) is also convenient for thermophysical testing. Not only is the resulting strain field homogeneous in the central region and the state of stress planar, thin specimens facilitate isothermal testing and measurement of thermal diffusivity. For example, Doss and Wright [16] recently demonstrated that the transient flash diffusivity method ([17]) may be extended to measure the diagonal components of the spatial thermal diffusivity tensor $\boldsymbol{\alpha}$ of thin sheets of stiff polyvinyl chloride (PVC). Specifically, the flash diffusivity method yields $\boldsymbol{\alpha}$ via the spatial energy equation which, in the absence of stress power and volumetric heat addition, is

$$\frac{dT(\mathbf{x},T)}{dt}=\boldsymbol{\alpha}(\mathbf{C},T):\nabla(\nabla T(\mathbf{x},t)) \tag{4}$$

where t is time. For materials in mechanical equilibrium, the convective terms within the material are negligible, of course, and the total derivative on the left-hand side of Eq. (4) reduces to a partial derivative with respect to time. Appendix A contains an outline of the one-dimensional solution of Eq. (4) that Parker et al. [17] employed in the initial description of the flash method. Here, Eq. (4) is solved using a finite difference formulation as part of a Marquardt parameter estimation algorithm for both the traditional (one-dimensional) flash method (measuring the out-of-plane component α_{33} only) and the extended flash method (measuring the three diagonal components of $\boldsymbol{\alpha}$). This allows for more accurate representation of the boundary conditions. Appendix A also outlines this model. Regardless, note that finite strain constitutive relations are more easily formulated in terms of the referential

[1]Current address: Black & Decker, Inc., 701 E. Joppa Road, Towson, MD 21286.
[2]To whom correspondence should be addressed. Biomedical Engineering Program, Texas A&M University, 233 Zachry Engineering Center, College Station, TX 77843-3120. E-mail: jdh@acs.tamu.edu

Contributed by the Applied Mechanics Division of THE AMERICAN SOCIETY OF MECHANICAL ENGINEERS for publication in the ASME JOURNAL OF APPLIED MECHANICS. Manuscript received by the ASME Applied Mechanics Division, Apr. 21, 1999; final revision, Dec. 13, 1999. Associate Technical Editor: K. T. Ramesh. Discussion on the paper should be addressed to the Technical Editor, Professor Lewis T. Wheeler, Department of Mechanical Engineering, University of Houston, Houston, TX 77204-4792, and will be accepted until four months after final publication of the paper itself in the ASME JOURNAL OF APPLIED MECHANICS.

thermal diffusivity $\boldsymbol{\alpha}_0$. Fortunately, one can infer $\boldsymbol{\alpha}_0$ from the measurable $\boldsymbol{\alpha}$ via $\boldsymbol{\alpha}=(1/J)\mathbf{F}\cdot\boldsymbol{\alpha}_0\cdot\mathbf{F}^T$ where $\boldsymbol{\alpha}_0(\mathbf{C},T)=\mathbf{K}(\mathbf{C},T)/(\rho_0 c_F(\mathbf{C},T))$; here ρ_0 is the referential mass density and c_F the specific heat at constant deformation.

There is, therefore, a clear need for a multiaxial thermomechanical test system that can exploit the available theoretical results. This paper describes the design and construction of a new device capable of both in-plane biaxial thermoelastic testing and measurement of the orthogonal components of $\boldsymbol{\alpha}$. Illustrative data are presented for neoprene subject to equibiaxial stretch ratios $\lambda \equiv \lambda_1=\lambda_2$ ($\lambda_i=l_i/L_i$, no sum on i, with l_i and L_i being current and reference lengths, respectively) with $\lambda\in[1,1.5]$, at temperature levels of 21 and 41°C.

Experimental System

Figure 1 is a schema of the overall optical-thermomechanical system. The system consists of five subsystems, one each for (a) biaxial loading, (b) in-plane strain measurement, (c) environmental control, (d) flash illumination, and (e) point-wise temperature measurement.

Biaxial Loading System. The load frame is machined from one piece of mild steel to outer dimensions of 45.7×45.7 cm with a 2.54 cm square cross section. The outer and inner surfaces are ground to ensure that opposing sides are flat and parallel. The frame is mounted on an optical table using a standard 2.54-cm diameter, 15.2-cm long support rod at each corner. A pair of horizontal through-holes (1.27-cm diameter and 4.45 cm apart) are centered on each side of the frame (Fig. 2(*a*)) such that the axes of any pair of holes are collinear with those of the opposing pair and perpendicular to the other two pairs. Each of the eight holes is fitted with a 1.91-cm-long linear recirculating ball bearing specifically designed for linear travel of shafts with minimal transverse play.

Nearly uniformly distributed in-plane biaxial forces are applied to the square specimen through four load carriages (Fig. 2(*b*)). Each edge of the specimen is attached to a single carriage using Kevlar thread (or silk suture for biological tissues). The load carriages consist of two parallel 0.635-cm-diameter solid, hardened stainless steel rods. Each rod is supported in one of the aforementioned through-holes by one of the linear bearings in the load frame and a neoprene O-ring sandwiched between two Rulon bearings, which form a watertight seal for the environmental chamber. Proper alignment of this chamber within the load frame ensures free and smooth translation of the load carriages. The outside end of each pair of rods is attached to a cross bar that separates the shafts and facilitates the application of axial forces. The inside end of each load carriage consists of three separate aluminum pieces: a cross bar that connects the two rods, a coupling bar, and a T-bar that has a series of equally spaced holes (0.75 cm apart) that serve as rigging points for the specimen loading threads. Two of the load carriages, one on each axis, have watertight and temperature compensated ($T\in[-29,93]$°C) load cells mounted between the cross bar and coupling bar.

The last component of the loading subsystem is the mechanism for inducing axial load. Each of the four carriage assemblies is independently loaded via a 1-mm lead ball-screw driven by a stepper motor. A ball-nut attached to the outer cross bar of each load carriage converts the rotation of the ball-screw into linear displacement of the carriage assembly. The stepper motors are individually controlled by a four-axis indexer card in the Pentium personal computer (PC). Such a drive system allows implementation of fully automated stretching protocols.

Strain Measurement. In-plane finite strains are measured optically by tracking the position histories of four small, contrasting markers that are affixed to the bottom surface of the specimen (Fig. 2(*b*)). This approach has been described previously ([18]), and is sufficient because of the homogeneity of the strain field in the central region, as confirmed via pilot experiments as well as by finite element analysis. For example, finite element analysis (ABAQUS), assuming a Mooney-Rivlin material response, revealed that the strain field is essentially homogeneous and extensional (< 5 percent shear) in the central sixteenth of the planar area of a square elastomeric specimen ([19]) that is loaded by five equidistant point loads at each edge. A CCD video camera, frame-grabber board in the PC, and custom software track the position of each of the four markers at the 30 Hz frame rate. The software algorithm, based on Downs et al. [20], uses a correlation method to locate the markers first in a ''coarse'' and then in a ''fine'' search region. The marker positions serve as input to a bilinear isoparametric interpolation algorithm that provides the components of **F** in the central region at each configuration (see Appendix B). The components of **F** provide information for feedback control (described below) of the thermoelastic tests at thermal equilibrium. In thermophysical tests, the components of **F** are reg-

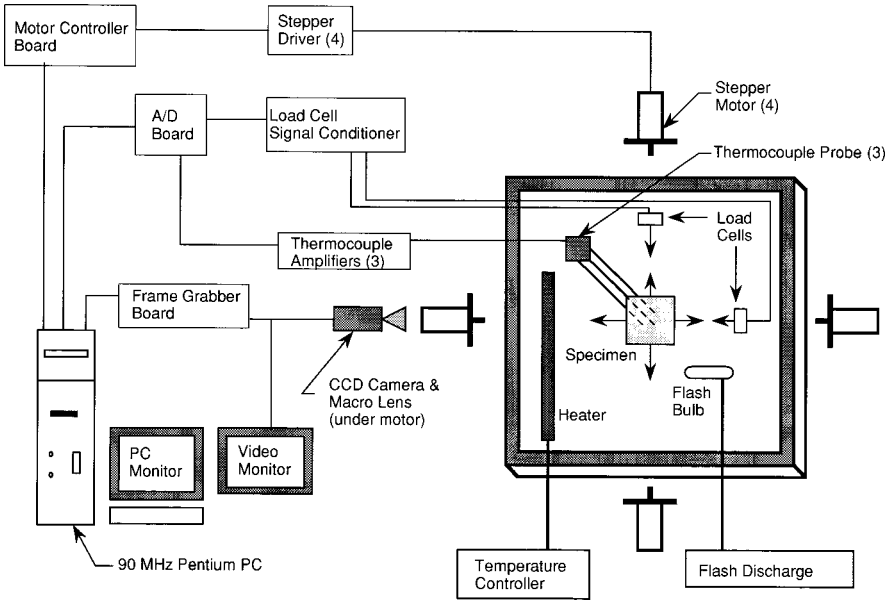

Fig. 1 A schematic drawing of the overall experimental system

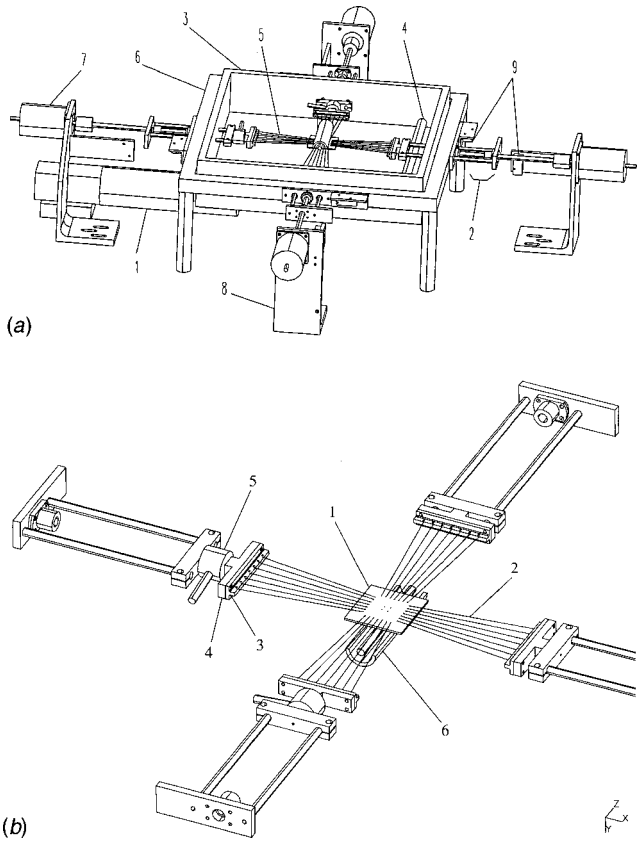

Fig. 2 Biaxial extension device. Panel (a) is an oblique view of the device where (1) camera, (2) load carriage, (3) environmental chamber, (4) heater, (5) Kevlar threads, (6) load frame, (7) motors, (8) motor supports, and (9) limit switches; in-plane directions defined as 1 and 2. Panel (b) is a schema of (1) the specimen with centrally placed tracking markers, (2) Kevlar threads, (3) T-bar, (4) coupling bar, (5) load cell, and (6) flashbulb and reflector, as seen from below.

istered prior to the flash illumination (i.e., at mechanical equilibrium), which only slightly perturbs the strain field.

Environmental Chamber. The environmental chamber allows testing of the sample in air or liquid at nearly constant temperatures (± 1°C). The chamber is constructed from a 1.27-cm-thick polycarbonate sheet and sealed with silicone adhesive to prevent leakage of the solution. With outside dimensions $40.0 \times 40.0 \times 7.62$ cm, the polycarbonate shell fits inside of the load frame (Fig. 2(*a*)). Though not shown for clarity, top and bottom plates are screwed onto the polycarbonate shell and silicone rubber gaskets form seals between the plates and shell.

The top plate of the chamber has a central port that allows the flash lamp (described below) to be placed in close proximity to the specimen, thereby ensuring that enough energy is absorbed by the sample to obtain a desirable temperature rise on its bottom surface. The separation between the lamp and an approximately 2-mm-thick specimen may be adjusted between 1.0 and 3.0 cm. In addition, the top plate allows access by the thermocouple probe for measurement of the temperature field on the bottom face of the sample. The bottom plate has a central $96 \times 96 \times 1.5$ mm glass window that allows the camera to view the aforementioned markers for strain measurement. Additionally, the bottom plate has drains to remove liquid from the chamber.

The chamber can be maintained between room temperature and 90°C by a 750 W, 1.27-cm-diameter, 30.5-cm-long submersible heater that is mounted in the chamber (Fig. 2(*a*)) and modulated by a thermostatic controller.

Temperature Measurement and Flash System. The principle of the flash technique for measuring thermal diffusivity is described elsewhere ([21–23,17,24]). Briefly, a flash system consists of a radiant energy source (e.g., a flash lamp or pulsed laser) capable of delivering a short burst that heats one face of the specimen, and a probe to measure the associated temperature history on the opposite face. Here, a linear xenon flashtube, mounted in an aluminum reflector, illuminates the top face of the specimen. When the in-plane components of $\boldsymbol{\alpha}$ are to be measured, a 50×50 mm aperture plate with a central 20×20 mm opening is mounted between the source and the specimen; the aperture is removed for measurement of α_{33} alone. Three 0.25-mm-diameter E-type thermocouple probes are mounted in an aluminum bar and form the apexes of a right isosceles triangle having two 15-mm sides, and when aligned with the aperture, they measure the temperature at the center of the projection of the lighted area and at two points outside this projection along the two in-plane axes. For measurements of α_{33} alone, only the central thermocouple output need be used. A small amount of high thermal conductivity silicone paste is used to insure good contact between the thermocouple probe and the specimen surface. The fixture is attached, through the port in the top plate of the environmental chamber, to a micrometer head that can raise or lower the thermocouples as required. A second CCD camera and mirror (not shown) monitors the contact between the specimen and the thermocouples.

Data Acquisition and Control. Eight independent channels of information are recorded simultaneously using an analog-to-digital (A/D) conversion board in the PC. The A/D board has high-gain amplification and a cold junction compensation circuit, specifically designed for acquisition of thermocouple data, recorded on one of the eight channels. The E-type thermocouples occupy three channels, whereas two T-type thermocouples, one at the glass window covering the flashbulb to mark the flash event on the data file and another above the specimen to record the ambient temperature, occupy two channels. The two load cells are connected to a signal conditioner, the output of which occupies the last two channels.

The strategy to control the biaxial finite deformation involves actuating the two opposing motors in one stretching direction at a constant velocity and varying the velocity of the two motors in the orthogonal direction so that the measured stretch in that direction is within a small error ϵ of the desired stretch. Hence, let λ_d be the desired stretch (either λ_1 or λ_2), λ_a be the measured stretch, and δ the difference between λ_a and λ_d. If $|\delta| \leq \epsilon$, then the velocities of the two motors on that axis are set to zero. If $|\delta| > \epsilon$, however, then the motor velocities must be adjusted to bring λ_a back to within ϵ of λ_d. The velocities ω of the controlled motors are adjusted proportionally to δ using $\omega = G\delta$, where G is a suitably valued parameter determined by trial and error during preliminary tests until the control of the specimen is acceptable. If G is too small, the stepper motors move continuously in the same direction, indicating that ω is too low and possibly not keeping the stretches within ϵ. Conversely, if G is too large, the motors oscillate, indicating an overshoot of λ_d, thus requiring the motors to reverse. A suitable value of G between these two extremes should thus be selected. Note that if $\delta > 0$, then $\lambda_a > \lambda_d$ and the direction of rotation of the motors must be such that λ_a is decreased; if $\delta < 0$ then the specimen must be stretched more. Once the controlling velocity is determined, its value is sent to the motor controller card. The control cycle is repeated throughout the experiment at 30 Hz by calculating the new stretch ratios, determining the controlling velocity, and sending the new velocity to the motor controller card.

Specimen Preparation. Thermoelastic tests were performed on specimens measuring 50-mm square cut from 1.6-mm-thick precast sheets of high-grade neoprene rubber with a Shore A hardness value of 35–45 (McMaster Carr). Outside of the biaxial device, each edge of the specimen was sewn to a T-bar using a

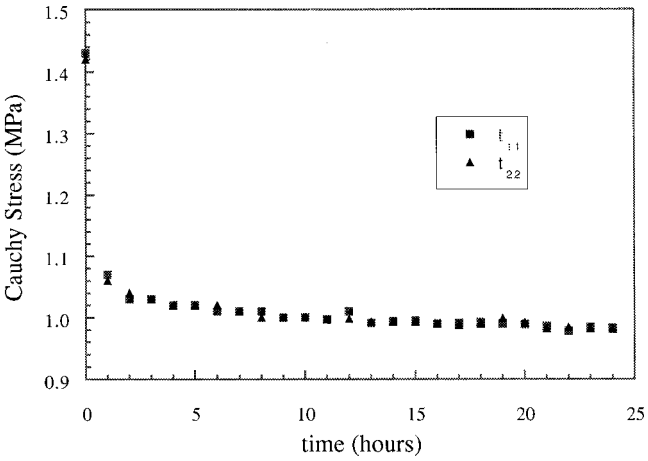

Fig. 3 Stress relaxation curve of a neoprene rubber specimen during preconditioning

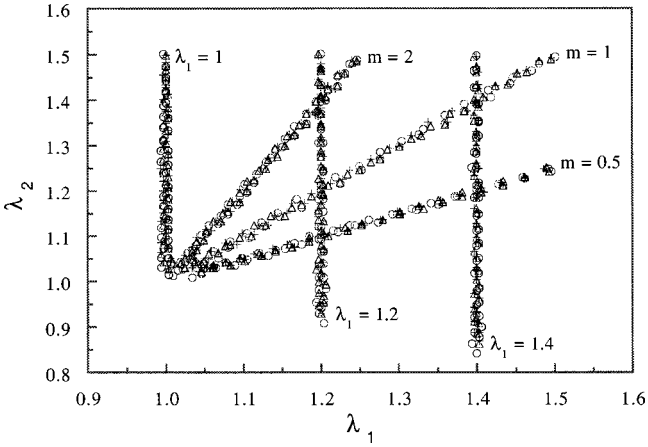

Fig. 4 Illustrative in-plane stretches λ_1 and λ_2 for computer controlled equibiaxial, proportional, and constant λ_1 stretching protocols. Data are for three cycles each (cycle 1: +, 2: △, 3: ○), thus showing reproducibility and robust control.

0.254-mm-diameter sewing needle and 0.2-mm-diameter Kevlar thread. Six holes spaced about 3.75 mm apart and 10 mm from the edge of the specimen were used on each edge. Four white 200-μm spots of titanium white acrylic paint were placed in the central 5×5 mm square (i.e., 1/100th of the planar area) of the specimen on the bottom face of the black specimen. The T-bars were then attached to the coupling bars (Fig. 2(*b*)). Prior to thermoelastic testing, each specimen was systematically preconditioned, thermally and mechanically: each neoprene sample was held at an in-plane equibiaxial stretch ratio of $\lambda=1.45$ at 41°C for 24 hours. The reduced range of temperatures examined in these first measurements on neoprene, as compared with the 90°C capability of the chamber, are the result of the reduced tear resistance of neoprene at elevated temperatures. Figure 3 shows the stress relaxation response of a typical specimen during preconditioning. The relaxation response was 86 percent complete after two hours and more than 95 percent complete after 12 hours. Immediately following the 24 hours of such preconditioning, the sample was unloaded and subjected to thermoelastic testing. Preconditioning for the thermophysical tests was similar. New specimens were preconditioned at an equibiaxial stretch of $\lambda=1.52$ at 25°C for 16 hours.

Illustrative Results

Stress-Strain Response. Figure 4 illustrates the ability of the system to execute well the prescribed protocols in (a) constant λ_1 tests, with $\lambda_1=1$, 1.2, 1.4, and (b) proportional stretch tests where $(\lambda_2-1)/(\lambda_1-1)=m$, with $m=2$, 1, 0.5; equibiaxial stretch is a special case with $m=1$. Each of the tests consisted of three cycles at a frequency of about 0.017 Hz. The repeatability over the three cycles for each type of test illustrates the robust control and the effect of preconditioning. Recall that the automated control of the motors was based on the video strain measurement of the in-plane stretches, thus permitting corrections at 30 Hz.

For homogeneous principal extensions $\mathbf{F}=\mathrm{diag}[\lambda_1,\lambda_2,\lambda_3]$ and $J=\det\mathbf{F}=\lambda_1\lambda_2\lambda_3=\rho_0/\rho$ (where ρ_0 and ρ are the reference and current mass densities, respectively), hence λ_3 can be determined at each temperature, given $\rho=\rho(T)$. Data obtained from Anter Laboratories (Pittsburgh, PA) on neoprene samples tested at $T\in[20,60]$°C suggest that, to first order,

$$\rho(T)=\rho_0[1+\beta(T-T_0)]^{-1} \tag{5}$$

where $\rho_0=1.317\ \mathrm{g/cm^3}$, $\beta=3.915\times10^{-4}(°\mathrm{C})^{-1}$, and $T_0=20$°C is the reference temperature at which ρ_0 is measured. Figure 5 shows illustrative in-plane Cauchy stress as a function of modified stretch ratio $\lambda_1^*(=J^{-1/3}\lambda_1)$ for one sample at three temperature levels ($T=25,33.2,41.2$°C). The stretches are calculated in the central region of the specimen with respect to the stress-free reference configuration at the reference temperature. The characteristic nonlinear behavior is well known and has been well documented in the past ([8,25,26,11]). Similar measurements on specific materials of interest will add greatly to the existing thermoelastic database that is needed to evaluate current constitutive thermoelastic models ([5,12,7]) as well as to develop new constitutive descriptors of other such materials.

Thermal Diffusivity. Two types of tests illustrate the ability of the device to measure thermal diffusivity of specimens subjected to finite in-plane deformation: measurements of (a) α_{33} for three specimen thicknesses and multiple equibiaxial stretches and (b) the diagonal components of $\boldsymbol{\alpha}$ as a function of finite equibiaxial deformation at room temperature.

First, α_{33} was measured for three neoprene specimens of nominal thicknesses of 1.6, 2.4, and 3.2 mm. Following preconditioning and then registration of the unloaded reference configuration (i.e., recording the marker positions) at $T_0\approx21$°C (i.e., ambient room temperature), the top surface of each specimen was subjected to a series of five pulses from the flash lamp, each separated by ten minutes to allow the specimen to regain thermal equilibrium. Figure 6 shows a typical bottom surface temperature response following the flash. For a bottom surface temperature T_b,

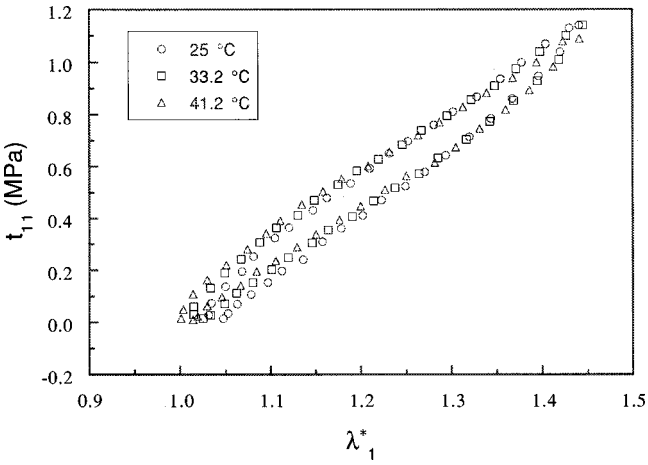

Fig. 5 Typical Cauchy stress-stretch curves for neoprene at three temperatures for equibiaxial stretch tests

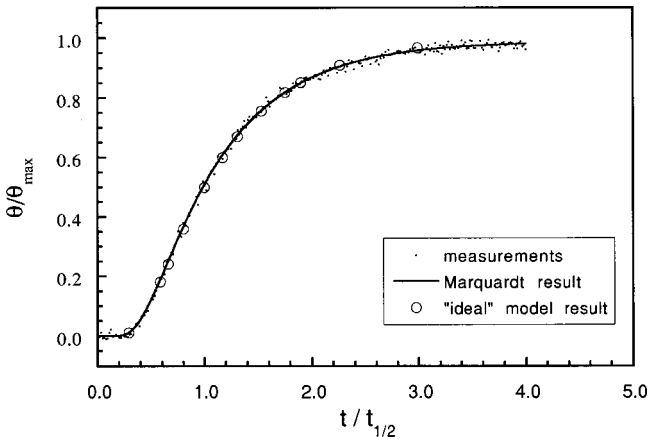

Fig. 6 Bottom surface temperature history for a one-dimensional flash test showing the close agreement between the measurements, the temperature history calculated as part of the data reduction, and that calculated assuming the boundary conditions originally used by Parker et al. [17] and the value of α_{33} determined by the Marquardt data reduction. $\tau_{1/2} \approx 4$ s.

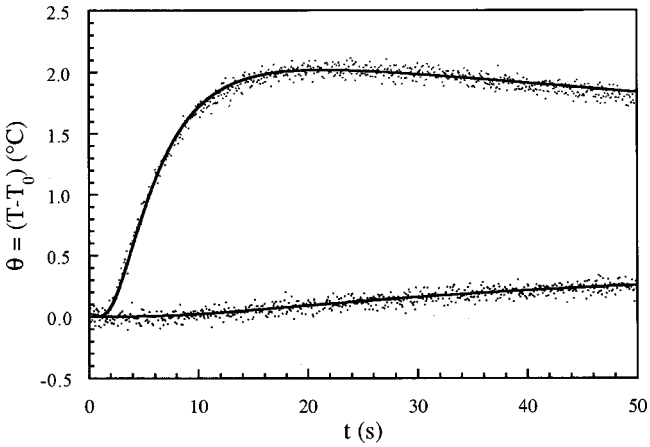

Fig. 7 Temperature history of the central and one of the lateral thermocouples for equibiaxial in-plane stretch of $\lambda = 1.03$. Solid line is model result.

the temperature excess $\theta = T_b - T_0$ has been scaled by the maximum temperature excess measured on the bottom surface $\theta_{\max}$ (typically about 3°C). Time has been scaled by $t_{1/2}$ (typically about 4 s), which is the time at which the bottom surface reaches $\theta_{\max}/2$. After the five pulses, the specimen was extended equibiaxially to the next desired stretch, its marker positions recorded in this equilibrium configuration following stress relaxation, and the flash procedure repeated. Once all data were collected at room temperature, another series of stretch and flash data were collected at 40°C. After increasing the temperature level, the sample was allowed to reach thermal equilibrium prior to inducing mechanical stretch.

Since the transient temperature rise on the bottom surface due to each flash was about 3°C and of similar magnitude on the top face, after a brief initial transient (10 ms), data were collected at nearly mechanical and thermal equilibrium. Here, the bottom surface temperature history was measured directly and α_{33} was calculated using the Marquardt parameter estimation algorithm coupled with a finite difference solution of Eq. (4) outlined in Appendix A. Figure 6 shows close agreement between the measurements, the temperature history calculated as part of the data reduction, and that calculated assuming the boundary conditions originally used by Parker et al. [17] and the value of α_{33} determined by the Marquardt data reduction. The mean values of α_{33} found in these one-dimensional measurements are 0.119 mm^2/s at 21°C and 0.117 mm^2/s at 40°C. These values are within five percent of those measured by Anter Labs and match well the trend with temperature, though this decrease is within the scatter of the measurements and thus, not statistically significant.

A second set of tests measured the diagonal components of $\boldsymbol{\alpha}$ for three specimens with a nominal thickness of 2.4 mm. Again, following preconditioning, each specimen was tested at two equibiaxial stretch states of approximately $\lambda = 1.03$ and 1.52. A minimum of five flash tests were performed at each of the two deformation states. Figure 7 shows the measured bottom-surface temperature history of a typical test along with the best-fit results based on the three-dimensional finite difference model. Again, there is close agreement between the data and the model. Because of the difference in the temperature response rate and levels for the central and lateral thermocouples, the variables have been left in dimensional form.

At the smaller deformation ($\lambda = 1.03$), α_{33} is found to be 0.116 mm^2/s, which is within 2.4 percent of the value measured with the one-dimensional test and within the standard deviation of both tests. The in-plane values are found to be 0.151 and 0.153 mm^2/s, which are about 31 percent higher than α_{33}. As was suggested by the results of Doss and Wright [16] for PVC, this is likely the result of extrusion processes during the manufacturing of the neoprene sheets. Indeed, Choy et al. [27] found an increased diffusivity in the draw direction and decreased diffusivity in the direction normal to the draw of highly drawn polyethylene using a one-dimensional flash method. At the larger deformation ($\lambda = 1.52$), the mean value of α_{33} is found to be 0.112 mm^2/s, about 5.9 percent lower than the undeformed value. In contrast, the in-plane values increase to 0.165 and 0.159 mm^2/s. It should be noted that the specimen appeared to be partially translucent to the flash energy at the stretched state. This leads to error in the indicated value of α_{33} because the boundary value problem used to determine α_{33} from the temperature history is no longer strickly valid. If such error is small, it reveals itself by the indicated value of α_{33} changing as the fraction of the temperature history used in data reduction increases. Taylor [24] showed that in such circumstances the value of α_{33} may be found by extrapolating the indicated values of α_{33} calculated using different fractions of the temperature history to the one indicated at zero fraction of the temperature history. This method of correction was employed at the high stretch states. The values of α_{11} and α_{22} remained independent of the fraction of the temperature history used in data reduction because they are strongly dependent on the temperature histories of the thermocouples that are outside the projection of the aperture opening.

Conclusions

The ability to measure the multiaxial mechanical response of elastomers, and similarly planar soft tissues, promises more complete data for the formulation of constitutive models for finite strain thermomechanics. The active control of the finite deformation, via the real-time video feedback to the motor controllers, allows measurement of the material response to a wide variety of deformations that theory reveals would be useful. The equibiaxial, proportional, and constant stretch tests discussed here have illustrated this capability. Reprogramming the motor control algorithm would allow constant invariant (cf. [12]) and other tests to be easily performed, as well. Data from such multiaxial tests are not readily available in the literature.

Formulating models of general thermoelastic response requires that the temperature field within the material also be modeled. To this end, this device incorporates an extension of the flash thermal diffusivity technique that allows measurement of the in-plane components of diffusivity as well as the more commonly measured out-of-plane component. Data presented illustrate that neo-

prene rubber at low stretches may still have anisotropic thermal diffusivity and that these values may change with stretch, even over the moderate range of equibiaxial stretches examined. Such coupling may be more marked for other materials, particularly, elastomeric composites and soft tissues.

Acknowledgments

Support from the Army Research Office through grant DAAH04-95-2-2 (to JDH and NTW) as part of a Center of Excellence Award for Materials (A. S. Khan, Director) and from the Whitaker Foundation (to NTW) through a Biomedical Engineering Research Grant made this work possible. The authors would also like to thank Dr. M. G. da Silva who designed the first generation, manually controlled device.

Appendix A

Analysis of the Temperature History. In the flash method as originally developed, the top face of a planar specimen is uniformly illuminated by an impulse ([17]). The temperature field is then described by a simplified Eq. (4) as

$$\frac{\partial T}{\partial t}=\alpha_{33}\frac{\partial^2 T}{\partial x_3^2} \tag{A1}$$

where $x_3\in[0,d]$, d is the current thickness, and the subscript 3 indicates the out-of-plane direction. Neglecting convective losses, a good assumption in the short time of most one-dimensional measurements, the solution of Eq. (*A*1) for the temperature rise at the rear surface of the specimen that has experienced such a uniform impulse is ([28])

$$T(d,t)=\frac{Q}{\rho c_F d}\left[1+\sum_{n=1}^{\infty}(-1)^n\exp\left(-\frac{n^2\pi^2}{d^2}\alpha_{33}t\right)\right] \tag{A2}$$

where Q is the area-density of energy associated with a pulse of radiant energy that is assumed to be instantaneously and uniformly absorbed in a thin layer at the top face of the specimen. Noticing that the bottom face temperature history contains the parameter $\gamma=(\pi^2\alpha_{33}t/d^2)$, this solution provides a simple expression for determining α_{33} from a single point on the temperature history curve defined by Eq. (*A*2). Choosing $t_{1/2}$ as the time at which the temperature reaches one-half its maximum value $T_{\max}=Q/\rho c_F d$ yields $\gamma=1.38$. The result is

$$\alpha_{33}=\frac{1.38d^2}{\pi^2 t_{1/2}}. \tag{A3}$$

An alternative analysis, that is also employed here, is to use a Marquardt algorithm ([29]) to estimate α_{33} by minimizing the difference between a measured temperature history and results of a finite difference solution of Eq. (*A*1). The advantage of this approach is that the assumed boundary conditions may be relaxed to include possible convective losses and a finite light pulse.

Moreover, an analytical solution is not practical for determining the components of $\boldsymbol{\alpha}$ in the three-dimensional tests. Instead, the Marquardt algorithm is used again, now in conjunction with a finite difference solution of Eq. (4) written for the principal directions of the specimen. The in-plane edges of the specimen are assumed to be adiabatic because the temperature history needed to determine the components of $\boldsymbol{\alpha}$ is shorter than the time required for a significant temperature rise at these edges. A convective boundary is specified on the top face, except under the aperture opening, where a spatially uniform, time-varying heat flux is specified during the flash and followed by a convective boundary condition afterwards. The bottom boundary assumes conduction into the air underneath the specimen. Conduction in the air layer underneath the specimen plays a significant role in the temperature history at the transverse thermocouple locations of specimens of moderate thermal diffusivity (such as the range of 0.11 to 0.16 mm^2/s measured here). Recall that the aperture opening is 10 mm on a side and the distance between the central and transverse thermocouples in 15 mm, but $d\approx 3$ mm. Furthermore, the thermal diffusivity of air at room temperature is 22.5 mm^2/s as compared with the neoprene with 0.12 mm^2/s. Thus, once the air has been heated by the central region of the bottom face of the specimen, it provides an alternative path for energy transport. Since the temperature rise of the transverse thermocouples in the three-dimensional tests run here is on the order of 0.3°C, even a small addition of energy from the air can cause significant error in the determination of in-plane thermal diffusivity. The Rayleigh number is small enough to indicate the absence of buoyancy-driven flows in the air underneath the specimen ([30]). This was confirmed by measurements of the temperature response of the air and comparison with finite difference modeling. Calculated specimen temperature histories were unchanged for included air layers thicker than 13 mm.

The Marquardt algorithm and finite difference model estimate five parameters: the three components of thermal diffusivity (α_{11}, α_{22}, and α_{33}), the scaled heat flux to the specimen as defined by $q''_{\max}/\rho C$, and a convective heat loss term defined as $2hdt/\rho C dx$, where dx is the node spacing and dt the time-step. Further details are available in Doss and Wright [16].

Appendix B

Strain Measurement. Assuming a homogeneous deformation in the central region, the in-plane components of **F** can be found via ([18])

$$F_{11}=1+\frac{\partial u_1}{\partial X_1}\quad F_{12}=\frac{\partial u_1}{\partial X_2} \tag{B1}$$

$$F_{21}=\frac{\partial u_2}{\partial X_1}\quad F_{22}=1+\frac{\partial u_2}{\partial X_2} \tag{B2}$$

where u_i and X_i are the components of the displacement ($=x_i-X_i$) and original position vectors, respectively. The displacement gradients $\partial u_i/\partial X_i$ can be found via a bilinear isoparametric interpolation of any four markers that define a quadrilateral. For example, let

$$X_i=\sum_{j=1}^{n} f^j(\zeta,\eta)X_i^j \tag{B3}$$

$$u_i=\sum_{j=1}^{n} f^j(\zeta,\eta)u_i^j \tag{B4}$$

where n $(=4)$ denotes the number of markers and

$$f^j(\zeta,\eta)=\frac{1}{4}(1+\zeta\zeta^j)(1+\eta\eta^j) \tag{B5}$$

is a standard bilinear interpolation. In the case of equibiaxial extension (with no rotations), $F_{11}=\lambda$, $F_{22}=\lambda$ and $F_{12}=F_{21}=0$.

References

[1] Wright, N. T., Chen, S., and Humphrey, J. D., 1998, ''Time-Temperature Equivalence Applied to Heat-Induced Changes of Cells and Proteins,'' ASME J. Biomech. Eng., **120**, pp. 22–26.

[2] Truesdell, C., and Noll, W., 1965, ''The Nonlinear Field Theories of Mechanics,'' *Handbuch der Physik*, Vol. III/3, S. Flugge, ed., Springer-Verlag, Berlin.

[3] Bowen, R. M., 1989, *Introduction to Continuum Mechanics for Engineers*, Plenum Press, New York.

[4] Chadwick, P., and Creasy, C. F. M., 1984, ''Modified Entropic Elasticity of Rubber-Like Materials,'' J. Mech. Phys. Solids, **32**, No. 5, pp. 337–357.

[5] Haslach, Jr., H. W., and Zheng, N., 1995, ''Thermoelastic Generalization of Isothermal Elastic Constitutive Models for Rubber-like Materials,'' Rubber Chem. Technol., **69**, pp. 313–324.

[6] Mormon, Jr., K. N., 1995, ''A Thermomechanical Model for Amorphous Polymers in the Glassy, Transition and Rubbery Regions,'' *Recent Research in Thermo-mechanics of Polymers in the Rubbery-Glassy Range*, M. Negahban, ed., pp. 89–114, ASME, New York, pp. 89–114.

[7] Ogden, R. W., 1992, ''On the Thermoelastic Modeling of Rubber-Like Solids,'' J. Thermal Stress, **15**, pp. 533–557.
[8] Allen, G., Bianchi, U., and Price, C., 1963, ''Thermodynamics of Elasticity of Natural Rubber,'' Trans. Faraday Soc., **59**, pp. 2493–2502.
[9] Allen, G., Kirkham, M. J., Padget, J., and Price, C., 1971, ''Thermodynamics of Rubber Elasticity at Constant Volume,'' Trans. Faraday Soc., **67**, pp. 1278–1292.
[10] Anthony, R. L., Caston, R. H., and Guth, E., 1942, ''Equations of State for Natural and Synthetic Rubber-Like Materials I. Unaccelerated Natural Rubber,'' J. Phys. Chem., **46**, pp. 826–840.
[11] Shen, M. C., McQuarrie, D. A., and Jackson, J. L., 1967, ''Thermoelastic Behavior of Natural Rubber,'' J. Appl. Phys., **38**, No. 2, pp. 791–797.
[12] Humphrey, J., and Rajagopal, K. R., 1998, ''Finite Thermoelasticity of Constrained Elastomers Subject to Biaxial loading,'' J. Elast., **49**, pp. 189–200.
[13] Rivlin, R. S., and Saunders, D. W., 1951, ''Large Elastic Deformations of Isotropic Materials VII. Experiments on the Deformation of Rubber,'' Philos. Trans. R. Soc. London, Ser. A, **243**, pp. 252–288.
[14] Dashora, P., 1994, ''A Study of Variation of Thermal Conductivity of Elastomers With Temperature,'' Phys. Scr., **49**, pp. 611–614.
[15] Treloar, L. R. G., 1975, *The Physics of Rubber Elasticity*, 3rd Ed., Clarendon, Oxford, UK.
[16] Doss, D. J., and Wright, N. T., 2000, ''Simultaneous Measurement of the Orthogonal Components of Thermal Diffusivity in PVC Sheet,'' ASME J. Heat Transfer, **122** in press.
[17] Parker, W. J., Jenkins, R. J., Butler, C. P., and Abbott, G. L., 1961, ''Flash Method of Determining Thermal Diffusivity, Heat Capacity and Thermal Conductivity,'' J. Appl. Phys., **32**, No. 9, pp. 1679–1684.
[18] Humphrey, J. D., Vawter, D. L., and Vito, R. P., 1987, ''Quantification of Strains in Biaxially Tested Soft-Tissues,'' J. Biomech., **20**, No. 1, pp. 59–65.
[19] Wright, N. T., da Silva, M. G., Doss, D. J., and Humphrey, J., 1995, ''Measuring Thermal Properties of Elastomers Subject to Finite Strain,'' *Thermal Conductivity 23*, K. E. Wilkes et al., eds., Technomic, Lancaster, PA, pp. 639–646.
[20] Downs, J., Halperin, H. R., Humphrey, J. D., and Yin, F. C. P., 1990, ''An Improved Video-based Computer Tracking System for Soft-Biomaterials Testing,'' IEEE Trans. Biomed. Eng., **37**, pp. 903–907.
[21] Agari, Y., Ueda, A., and Nagai, S., 1994, ''Measurement of Thermal Diffusivity and Specific Heat Capacity of Polymers by Laser Flash Method,'' J. Polym. Sci., Part B: Polym. Phys., **33**, pp. 33–42.
[22] Lachi, M., and Degiovanni, A., 1991, ''Determination des Diffusivites Thermiques des Materiaux Anisotropes par Methode Flash Bidirectionelle,'' J. Phys. III, No. 12, pp. 2027–2046.
[23] Mallet, D., Lachi, M., and Degiovanni, A., 1990, ''Simultaneous Measurements of Axial and Radial Thermal Diffusivities of an Anisotropic Solid in Thin Plate: Application to Multi-Layered Materials,'' *Thermal Conductivity 21*, C. J. Cremers and H. A. Fine, eds., Plenum Press, New York, pp. 91–107.
[24] Taylor, R. E., 1975, ''Critical Evaluation of Flash Method for Measuring Thermal Diffusivity,'' Rev. Int. Hautes Temp. Refract., **12**, pp. 141–145.
[25] Kawabata, S., and Kawai, H., 1977, ''Strain Energy Function of Rubber Vulcanizates From Biaxial Extension,'' Adv. Polym. Sci., Vol. 24, H. J. Cantow et al., Springer-Verlag, New York, pp. 89–124,
[26] Obata, Y., Kawabata, S., and Kawai, H., 1970, ''Mechanical Properties of Natural Rubber Vulcanizates in Finite Deformation,'' J. Polym. Sci., Part A: Gen. Pap., **8**, pp. 903–919.
[27] Choy, C. L., Luk, W. H., and Chen, F. C., 1978, ''Thermal Conductivity of Highly Oriented Polyethylene,'' Polymer, **19**, pp. 155–162.
[28] Carslaw, H. S. and Jaeger, J. C., 1959, *Conduction of Heat in Solids*, 2nd Ed., Clarendon Press, Oxford, UK.
[29] Press, W. H., Teukolsky, S. A., Vetterling, W. T., and Flannery, B. P., 1992, *Numerical Recipes in C*, Cambridge University Press, Cambridge, UK.
[30] Gebhart, B., Jaluria, Y., Mahajan, R. L., and Sammukia, B., 1988, *Buoyancy-Induced Flows and Transport*, Hemisphere, New York.

Anti-Optimization Versus Probability in an Applied Mechanics Problem: Vector Uncertainty

M. Zingales
Research Assistant

I. Elishakoff
Professor

Department of Mechanical Engineering,
Florida Atlantic University,
777 Glades Road,
Boca Raton, FL 33431-0991

In this study probabilistic and nonprobabilistic anti-optimization approaches are contrasted to evaluate their relative advantages and disadvantages while solving a mechanical problem in presence of vector uncertainty. The different cases that are analyzed in probabilistic setting that deal with either uniform or generic probability density functions for the uncertain variables varying in a rectangular domain. This case has been compared with interval analysis, a particular case of anti-optimization. The presence of a convex, smooth boundary of the uncertain domain has been also considered for comparing results obtained with these two alternative methods. It is shown that in case of vector uncertainty the anti-optimization method yields the same solution for the design problem as is provided by means of more complex probabilistic considerations.
[S0021-8936(00)03103-2]

1 Introduction

Consider first the simplest problem involving a single random variable. Let the simply supported column be not straight but be bent into an initial, unloaded shape. Unlike the straight column, the bending will occur immediately upon application of the axial load P, regardless of its magnitude, due to its offset from the slightly curved centerline of the bar. The total deflection of the column at any point is the sum of its initial deviation from the straight line and the additional deflection due to the applied load P. If the initial displacement is represented as $a_0 L \sin(\pi x/L)$ where a_0 is the amplitude, L=length, then the total displacement $\delta = aL$ in the middle cross section is connected to the load P as follows:

$$a = \frac{a_0}{1 - P/P_{cl}}; \quad P_{cl} = \frac{\pi^2 EI}{L^2}$$

where P_{cl} is the Euler load. Let a_0 have a uniform density $1/(\mu_2 - \mu_1)$ in the range $[\mu_1, \mu_2]$. Reliability is given by the probability that the total displacement is not greater than a preselected value α, $R = \text{Prob}(a \leqslant \alpha)$.

Reliability becomes

$$R = \begin{cases} 0, & \alpha(1 - P/P_{cl}) < \mu_1 \\ \dfrac{\alpha(1 - P/P_{cl})}{\mu_2 - \mu_1}, & \mu_1 < \alpha(1 - P/P_{cl}) < \mu_2 \\ 1, & \alpha(1 - P/P_{cl}) > \mu_2 . \end{cases}$$

We want to design the column with required reliability r, i.e., $R \geqslant r$. We find the design value of P/P_{cl} from the equality

$$\frac{\alpha(1 - P/P_{cl})}{\mu_2 - \mu_1} = r$$

leading to the design value

$$\frac{P}{P_{cl}} = 1 - \frac{\mu_1 + r(\mu_2 - \mu_1)}{\alpha}.$$

When $r \to 1$, P/P_{cl} tends to the value $1 - \mu_2/\alpha$. This value can be obtained *without* probabilistic arguments. Indeed, since μ_2 is the maximum value of a_0, it is immediately seen that the performance will be guaranteed if

$$\alpha(1 - P/P_{cl}) \geqslant \mu_2 .$$

This immediately results in the minimum admissible value of P/P_{cl} that coincides with simple yet more elaborate probabilistic analysis. This simple idea is being generalized in this study for more realistic case of bounded variation of two variables.

In a two-dimensional case uncertain vector is identified with two coordinates. These may vary in a rectangular region, which enables one to the use of the interval analysis in a vector setting. If is intuitively understood that the smallest length interval shall be chosen to characterize the one-dimensional uncertainty; for the two-dimensional case one should seek for a rectangle of minimum area, since then the further evolution of the system will be more closely bracketed. Yet, this may not be a best representation of the available data whose scatter must be modeled. Indeed, in some cases, enclosing the data by regions other than rectangle may result in even a smaller area, enclosing all available data. The possibility arises, for example, of enclosing the data by the minimum area ellipse, whose area may turn out to be smaller than that of the minimum area rectangle. Along these thoughts, in addition to interval analysis ([1–3]) the ellipsoidal modeling was developed ([4–6]) for uncertainty analysis. Interestingly, these two lines of thoughts (on intervals and ellipsoids) intersected in extremely few works, and essentially have been developed in parallel, and mostly without knowledge about the developments in other fields.

It appears that the ellipsoidal framework has some advantages over the interval analysis in the sense that it deals with a smooth, convex boundary of the enclosed data with associated straightforward analytical or numerical treatment. Yet the ellipsoidal data may suggest that the components are functionally dependent. This tacit assumption may be unjustified in some circumstances. Hence the independent data may be better justified as enclosed by a rectangular region. Interval and ellipsoidal modeling are particular cases of the convex modeling ([7,8]). In fact, convex description of uncertainty is richer than the ellipsoidal one: In addition to the

Contributed by the Applied Mechanics Division of THE AMERICAN SOCIETY OF MECHANICAL ENGINEERS for publication in the ASME JOURNAL OF APPLIED MECHANICS. Manuscript received by the ASME Applied Mechanics Division, Oct. 23, 1998; final revision, Feb. 29, 2000. Associate Technical Editor: W. K. Liu. Discussion on the paper should be addressed to the Technical Editor, Professor Lewis T. Wheeler, Department of Mechanical Engineering, University of Houston, Houston, TX 77204-4792, and will be accepted until four months after final publication of the paper itself in the ASME JOURNAL OF APPLIED MECHANICS.

ellipsoids per se, it includes sets with functions with envelope bounds, or those with bounded integral squares, or those with bounded integral squares of its derivatives and so on.

The case when the uncertain variables do not belong to a convex set may dealt with the methods of nonlinear programming ([9]). All these analyses share the main ideas of *anti-optimization*, namely, of the desire to determine least favorable responses, in order to guarantee the successful performance despite the presence of uncertainty.

In this paper the two-dimensional uncertain imperfections are considered in the context of the column impact problem. The probabilistic modeling of uncertainties of various kinds in the dynamic buckling setting were dealt with by Goncharenko [10], Budiansky and Hutchinson [11], Lindberg [12], Ariaratnam [13], Kil'dibekov [14], Amazigo and Frank [15], Amazigo [16], Lockhart and Amazigo [17], Maymon and Libai [18], Elishakoff [19], Bogdanovich [20,21] and others.

Convex modeling of the dynamic buckling problems was facilitated by Ben-Haim and Elishakoff [22], Elishakoff and Ben-Haim [23], Lindberg [24,25] and Ben-Haim [26]. These two avenues of thoughts on the uncertainty modeling, namely, the probabilistic and anti-optimization ones, have not been compared in either of the above studies. This will be the principal objective of the present paper. The direct comparison of designs yielded by two alternative approaches sheds light on the possible compatibility or incompatibility of these two alternative approaches.

2 Deterministic Analysis

The differential equation for the uniform column under axial impact load

$$P(t)=P\langle t\rangle^0 \tag{1}$$

reads

$$EI\frac{\partial^4 w}{\partial x^4}+P(t)\frac{\partial^2 w}{\partial x^2}+mA\frac{\partial^2 w}{\partial t^2}=-P(t)\frac{\partial^2 w_0}{\partial x^2} \tag{2}$$

with E=modulus of elasticity, I=moment of inertia, m=mass density, A=cross-sectional area, $P(t)$=axial load, $w_0(x)$=initial imperfection, constituting a small deviation of the initial shape of the unstressed column, and $w(x)$=additional transverse deflection of the column's axis, so that

$$w_T(x,t)=w_0(x)+w(x,t) \tag{3}$$

represents a total displacement. In Eq. (1) $\langle t\rangle^0$ is a singularity function, namely, a unit step function

$$\langle t\rangle^0=\begin{cases}0, & t<0\\ 1, & t\geqslant 0.\end{cases} \tag{4}$$

In Eq. (2) following notation are adopted: x=axial coordinate, t=time, $P(t)$=axial load, m=material density, and A=cross-sectional area.

The attendant boundary conditions for the column that is simply supported at its both ends read

$$w(x,t)=0 \quad \text{at } x=0 \quad \text{and} \quad x=L \tag{5}$$

$$\frac{\partial^2 w}{\partial x^2}=0 \quad \text{at } x=0 \quad \text{and} \quad x=L \tag{6}$$

where L is the column's length. The initial conditions are

$$w(x,t)=0, \quad \frac{\partial w(x,t)}{\partial t}=0 \quad \text{at } t=0. \tag{7}$$

Let the initial imperfections be given as a sum of two sinusoidal terms as follows:

$$w_0(x)=f_1(x)+f_2(x)=h_1\sin\left(\frac{\pi x}{L}\right)+h_2\sin\left(\frac{a\pi x}{L}\right), \tag{8}$$

h_1 and h_2 being the amplitudes of $f_j(x)$, $(j=1,2)$, respectively. In Eq. (1) the integer $a>1$ represents the wave number in the variation of $f_2(x)$. Following Elishakoff [19], we will use the nondimensional quantities

$$\xi=\frac{x}{L}, \quad \lambda=\omega_1 t, \quad u=\frac{w}{\Delta}, \quad \gamma=\frac{P}{P_{cl}}, \quad u_0=\frac{w_0}{\Delta} \tag{9}$$

where ξ=nondimensional axial coordinate, λ=nondimensional time, $u_0(\xi)$=nondimensional initial displacement, $u(\xi,t)$=nondimensional additional displacement, and α=nondimensional axial load. In Eq. (9)

$$\omega_1=\left(\frac{\pi}{L}\right)^2\sqrt{\frac{EI}{mA}}, \quad \Delta=\sqrt{\frac{I}{A}}, \quad P_{cl}=\frac{\pi^2 EI}{L^2} \tag{10}$$

where ω_1=fundamental natural frequency of the ideal column, i.e., of a column with neither initial imperfections nor axial load, Δ=radius of inertia, P_{cl}=classic, and Euler's buckling load (Fig. 1). The nondimensional amplitudes of initial imperfections are

$$g_1=h_1/\Delta, \quad g_2=h_2/\Delta. \tag{11}$$

The additional displacement is sought as a superposition,

$$u(\xi,\lambda)=u_1(\xi,\lambda)+u_2(\xi,\lambda), \tag{12}$$

where the functions $u_1(\xi,\lambda)$ and $u_2(\xi,\lambda)$ are solutions of the following equations, respectively:

$$\frac{\partial^4 u_j}{\partial\xi^4}+\pi^2\gamma\frac{\partial^2 u_j}{\partial\xi^2}+\pi^4\frac{\partial^2 u_j}{\partial\lambda^2}=-\pi^2\gamma\frac{d^2 u_0^{(j)}}{d\xi^2} \quad (j=1,2) \tag{13}$$

with the initial imperfections expressed as

$$u_0^{(1)}(\xi)=g_1\sin(\pi\xi), \quad u_0^{(2)}(\xi)=g_2\sin(a\pi\xi). \tag{14}$$

The functions $u_j(\xi,\lambda)$ are represented in the separable forms as the initial imperfections in Eq. (14), namely,

$$u_1(\xi,\lambda)=e_1(\lambda)\sin(\pi\xi), \quad u_2(\xi,\lambda)=e_2(\lambda)\sin(a\pi\xi) \tag{15}$$

where $e_1(\lambda)$ and $e_2(\lambda)$ are time-dependent functions. Substitution of Eqs. (14)–(15) in Eq. (13) yields ordinary differential equations with respect to functions $e_1(\lambda)$ and $e_2(\lambda)$:

$$\frac{d^2 e_1(\lambda)}{d\lambda^2}+(1-\gamma)e_1(\lambda)=\gamma g_1 \tag{16}$$

$$\frac{d^2 e_2(\lambda)}{d\lambda^2}+a^2(a^2-\gamma)e_2(\lambda)=\gamma a^2 g_2. \tag{17}$$

Satisfying the initial conditions $e_j(0)=0$ and $\dot{e}_j(0)=0$ $(j=1,2)$ yields

$$e_1(\lambda)=\begin{cases}\dfrac{\gamma g_1}{\gamma-1}(\cosh(r\lambda)-1), & \gamma>1\\ g_1\lambda^2/2, & \gamma=1\\ \dfrac{\gamma g_1}{1-\gamma}(1-\cos(r\lambda)), & \gamma<1\end{cases} \tag{18}$$

where

$$r=\sqrt{|\gamma-1|}. \tag{19}$$

For $e_2(\lambda)$ we have

$$e_2(\lambda)=\begin{cases}\dfrac{\gamma g_2}{\gamma-a^2}(\cosh(aq\lambda)-1), & \gamma>a^2\\ \dfrac{1}{2}\gamma a^2 g_2\lambda^2, & \gamma=a^2\\ \dfrac{\gamma g_2}{a^2-\gamma}(1-\cos(aq\lambda)), & \gamma<a^2\end{cases} \tag{20}$$

with

$$q=\sqrt{|\gamma-a^2|}. \tag{21}$$

The nondimensional modal displacements $z_i(\xi,\lambda)$, $(i=1,2)$ are introduced:

$$\begin{aligned} z_1(\xi,\lambda)&=u_0^{(1)}(\xi)+u_1(\xi,\lambda)=[g_1+e_1(\lambda)]\sin(\pi\xi)\\ z_2(\xi,\lambda)&=u_0^{(2)}(\xi)+u_2(\xi,\lambda)=[g_2+e_2(\lambda)]\sin(a\pi\xi). \end{aligned} \tag{22}$$

With the aid of Eqs. (15)–(16) we form a total displacement $w_T(x,t)$ or its nondimensional counterpart $z(\xi,\lambda)$

$$z(\xi,\lambda)=w_T(x,t)/\Delta=z_1(\xi,\lambda)+z_2(\xi,\lambda) \tag{23}$$

with, defining $w_T^{(j)}(x,t)$ the nondimensional displacement $w_T^{(j)}(x,t)=w_0^{(j)}(x)+w_j(x,t)$ $j=1,2$ we have

$$\begin{aligned} z_1(\xi,\lambda)&=w_T^1(x,t)/\Delta=v_1(\lambda)\sin(\pi\xi)\\ z_2(\xi,\lambda)&=w_T^2(x,t)/\Delta=v_2(\lambda)\sin(a\pi\xi). \end{aligned} \tag{24}$$

The functions $v_j(\lambda)$, $(j=1,2)$ of the nondimensional time λ alone, read

$$v_1(\lambda)=\frac{\gamma g_1}{\gamma-1}\left\{\cosh(r\lambda)-\frac{1}{\gamma}\right\}=g_1a_1^{(1)}(\lambda),\quad \gamma>1 \tag{25a}$$

$$v_1(\lambda)=g_1(\lambda^2+2)/2=g_1a_1^{(2)}(\lambda),\quad \gamma=1 \tag{25b}$$

$$v_1(\lambda)=\frac{\gamma g_1}{1-\gamma}\left\{\frac{1}{\gamma}-\cos(r\lambda)\right\}=g_1a_1^{(3)}(\lambda),\quad \gamma<1 \tag{25c}$$

$$v_2(\lambda)=\frac{\gamma g_2}{\gamma-a^2}\left\{\cosh(aq\lambda)-\frac{a^2}{\gamma}\right\}=g_2a_2^{(1)}(\lambda),\quad \gamma>a^2 \tag{25d}$$

$$v_2(\lambda)=g_2(\gamma a^2\lambda^2+2)/2=g_2a_2^{(2)}(\lambda),\quad \gamma=a^2 \tag{25e}$$

$$v_2(\lambda)=\frac{\gamma g_2}{a^2-\gamma}\left\{\frac{a^2}{\gamma}-\cos(aq\lambda)\right\}=g_2a_2^{(3)}(\lambda),\quad \gamma<a^2. \tag{25f}$$

Since there exist different analytical expressions for $v_j(\lambda)$ depending on the value of γ, the total displacement possesses various analytical representations. In particular, five different cases occur as follows:

$$z(\xi,\lambda)=a_1^{(3)}(\lambda)g_1\sin(\pi\xi)+a_2^{(3)}(\lambda)g_2\sin(a\pi\xi),\quad \gamma<1 \tag{26a}$$

$$z(\xi,\lambda)=a_1^{(2)}(\lambda)g_1\sin(\pi\xi)+a_2^{(3)}(\lambda)g_2\sin(a\pi\xi),\quad \gamma=1 \tag{26b}$$

$$z(\xi,\lambda)=a_1^{(1)}(\lambda)g_1\sin(\pi\xi)+a_2^{(3)}(\lambda)g_2\sin(a\pi\xi),\quad 1<\gamma<a^2 \tag{26c}$$

$$z(\xi,\lambda)=a_1^{(1)}(\lambda)g_1\sin(\pi\xi)+a_2^{(2)}(\lambda)g_2\sin(a\pi\xi),\quad \gamma=a^2 \tag{26d}$$

$$z(\xi,\lambda)=a_1^{(1)}(\lambda)g_1\sin(\pi\xi)+a_2^{(1)}(\lambda)g_2\sin(a\pi\xi),\quad \gamma>a^2. \tag{26e}$$

Note that although there are five different cases, each of the parameters a_1 or a_2 have three separate expressions. If the initial imperfection amplitudes g_1 and g_2 are given deterministically, the design is performed in the manner of the total displacement not to exceed the threshold value c. Hereinafter the cross section of the column is assumed to be of the circular shape.

The main thrust of this study is an investigation of the effect of uncertainty in initial imperfections on the resulting design values of the cross-sectional radius. If g_1 and g_2 constitute uncertain variables, the output $z(\xi,\lambda)$ will likewise represent the uncertain function. Properties of the function $z(\xi,\lambda)$ depend on the information provided about the uncertain variables g_j. We will investigate several alternative avenues of describing this vector uncertainty, either probabilistically or without recourse to the stochasticity concept.

3 Probabilistic Analysis

Let the amplitudes of the initial imperfections g_1 and g_2 constitute a random vector with specified joint probability density function $f_{G_1G_2}(g_1,g_2)$. Capital letters denote the random variables whereas the lower case notation is reserved for the set of possible values that are taken by the random variables. We are interested in finding the reliability of the system, namely, the probability that the total displacement will remain in a safe region, in accordance with the Hoff's criterion.

The reliability is defined as the probability that $\max_\xi Z(\xi,\lambda)$ remains in a safe region. For simplicity we fix $a=5$. Hence

$$Y\equiv\max_\xi Z(\xi,\lambda)=\max Z(1/2,\lambda)=V_1(\lambda)+V_2(\lambda). \tag{27}$$

Functions $V_1(\lambda)$ and $V_2(\lambda)$ are multiplicative random processes depending upon the nondimensional parameter λ

$$V_1(\lambda)=G_1a_1^{(i)}(\lambda),\quad (i=1,2,3) \tag{28}$$

$$V_2(\lambda)=G_2a_2^{(j)}(\lambda),\quad (j=1,2,3). \tag{29}$$

Now,

$$R(\lambda)=\text{Prob}(-d\leqslant Y=V_1(\lambda)+V_2(\lambda)\leqslant c). \tag{30}$$

In view of Eq. (27), the reliability in Eq. (30) becomes

$$R(\lambda)=\text{Prob}(Y\leqslant c)-\text{Prob}(Y\leqslant -d). \tag{31}$$

Equation (31) can be rewritten as follows:

$$R(\lambda)=F_{Y,\lambda}(c;\lambda)-F_{Y,\lambda}(-d;\lambda) \tag{32}$$

where $F_{Y,\lambda}$ is the probability distribution functions of random process Y, and

$$Y(\lambda)=G_1a_1^{(i)}(\lambda)+G_2a_2^{(j)}(\lambda), \tag{33}$$

indicating that it represents a linear combination of two random variables with deterministic real-valued positive functions of nondimensional time λ as coefficients. The evaluation of the reliability, as stated in Eq. (31), needs the particularization of the joint probability density function of the random variables G_1 and G_2. We will consider the cases in which G_1 and G_2 are either statistically independent or dependent.

4 Initial Imperfections With Uniform Probability Density Over a Rectangular Domain

Let the initial imperfections be independent random variables with a uniform probability density function in a rectangular domain (Figs. 1 and 2):

$$\begin{aligned} f_{G_1G_2}(g_1,g_2)=&\frac{1}{\alpha_2-\alpha_1}\frac{1}{\beta_2-\beta_1}\{\langle g_1-\alpha_1\rangle^0-\langle g_1-\alpha_2\rangle^0\}\\ &\times\{\langle g_2-\beta_1\rangle^0-\langle g_2-\beta_2\rangle^0\} \end{aligned} \tag{34}$$

where the $\langle\cdot\rangle^0$ indicates the singularity function. The variations of G_1 and G_2 are confined to the intervals, $G_1\in[\alpha_1,\alpha_2]$ and $G_2\in[\beta_1,\beta_2]$, respectively (Fig. 2). Moreover, we assume, for the sake of simplicity, that $\alpha_j>0$, $\beta_j>0$ $(j=1,2)$. Marginal probability densities read

$$\begin{aligned} f_{G_1}(g_1)&=\frac{1}{\alpha_2-\alpha_1}\{\langle g_1-\alpha_1\rangle^0-\langle g_1-\alpha_2\rangle^0\}\\ f_{G_2}(g_2)&=\frac{1}{\beta_2-\beta_1}\{\langle g_2-\beta_1\rangle^0-\langle g_2-\beta_2\rangle^0\}. \end{aligned} \tag{35}$$

with

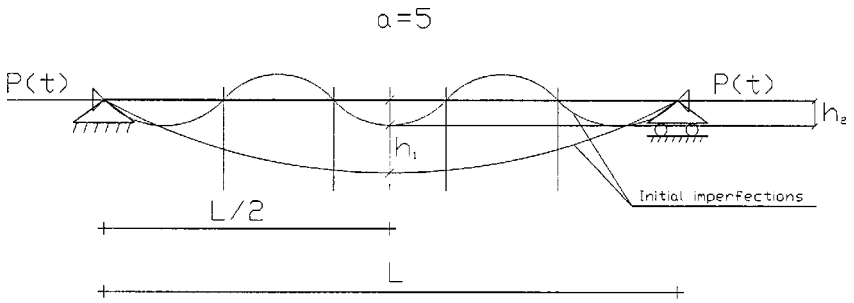

Fig. 1 Description of the structural model

$$f_{G_1G_2}(g_1,g_2)=f_{G_1}(g_1)f_{G_2}(g_2). \tag{36}$$

In order to perform the reliability analysis of the column it is necessary to find the probability distribution function $F_{Y,\lambda}(y,\lambda)$ of the random variable $Y(\lambda)$ in Eq. (31). With the second term in this latter equation vanishing identically we obtain

$$F_{Y,\lambda}(z,\lambda)=\int_{-\infty}^{\infty}\int_{-\infty}^{(z-a_2^{(j)}(\lambda)g_2)/a_1(\lambda)} f_{G_1G_2}(t_1,t_2)dt_1dt_2. \tag{37}$$

By substituting Eq. (35) in Eq. (37) and performing integration, the reliability function is obtained as

$$\begin{aligned}R(\lambda)=&\frac{1}{\alpha_2-\alpha_1}\frac{1}{\beta_2-\beta_1}\left[\frac{1}{a_2^{(j)}a_1^{(j)}}\langle c-a_1^{(j)}\alpha_1-a_2^{(j)}\beta_1\rangle^2\right]\\&-\frac{1}{\alpha_2-\alpha_1}\frac{1}{\beta_2-\beta_1}\left[\frac{1}{a_2^{(j)}a_1^{(j)}}\langle c-a_1^{(j)}\alpha_1-a_2^{(j)}\beta_2\rangle^2\right]\\&-\frac{1}{\alpha_2-\alpha_1}\frac{1}{\beta_2-\beta_1}\left[\frac{1}{a_2^{(j)}a_1^{(j)}}\langle c-a_1^{(j)}\alpha_2-a_2^{(j)}\beta_1\rangle^2\right]\\&+\frac{1}{\alpha_2-\alpha_1}\frac{1}{\beta_2-\beta_1}\left[-\frac{1}{a_2^{(j)}a_1^{(j)}}\langle c-a_1^{(j)}\alpha_2-a_2^{(j)}\beta_2\rangle^2\right]\end{aligned} \tag{38}$$

where

$$\langle x\rangle^2=\begin{cases}x^2/2, & x\geqslant 0\\ 0, & x<0.\end{cases} \tag{39}$$

Equation (38) suggests several useful conclusions regarding the characterization of the reliability. At the initial time instance $t=0$ (or $\lambda=0$), we have $a_1^{(j)}(0)=a_2^{(j)}(0)=1$ for $j=1,2,3$. We conclude that if the failure boundary c is set at the $\alpha_1+\beta_1$ or lower, then the reliability vanishes. This implies that if the failure boundary satisfies the inequality

$$c\leqslant\alpha_1+\beta_1, \tag{40}$$

no possibility of design associated with nonvanishing reliability exists for the column subjected to nonzero values of the applied load P. Figs. 3–6 portray some interesting aspects which may be deduced by investigation of the various terms in Eq. (38). We first observe that each one of the four terms represents the area of the region created by the straight line

$$c=a_1^{(j)}g_1+a_2^{(j)}g_2 \tag{41}$$

and an appropriate boundary of the rectangular domain of the initial imperfection amplitudes g_1 and g_2. Let us consider various straight lines passing through either of the four corners of the boundary, and parallel to the line given in Eq. (41). The plane (g_1,g_2) is subdivided into five regions denoted Γ_j, $(j=1,\ldots,5)$ (Fig. 3). The broken line in Fig. 3 represents the line in Eq. (41). Four solid lines are parallel to it, and pass through either corner A, B, C, or D. In case the line in Eq. (41) belongs to region Γ_2 (Fig. 3), the coordinates of the intersection points A^* and B^* with the edges AD and AB, respectively, are given by

$$A^*\equiv\left(\frac{c-a_2^{(j)}\beta_1}{a_1^{(j)}},\beta_1\right);\quad B^*\equiv\left(\alpha_1,\frac{c-a_1^{(j)}\alpha_1}{a_2^{(j)}}\right). \tag{42}$$

The distances $\overline{AA}^*$ and $\overline{AB}^*$ are

$$\overline{AA}^*=(c-a_2^{(j)}\beta_1)/a_1^{(j)}-\alpha_1;\quad \overline{AB}^*=(c-a_1^{(j)}\alpha_1)/a_2^{(j)}-\beta_1. \tag{43}$$

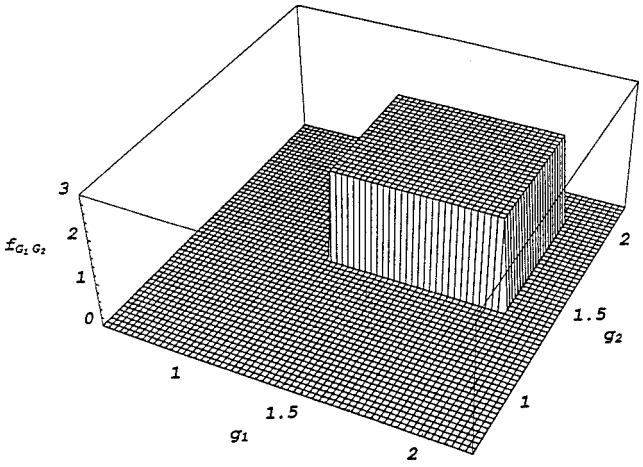

Fig. 2 Uniform probability density function over a rectangular domain

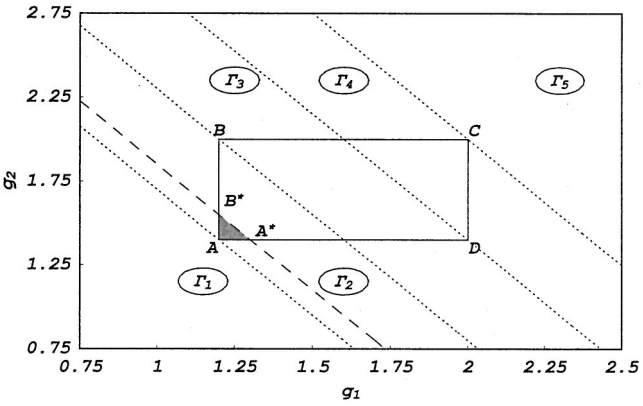

Fig. 3 Geometrical representation of the first term in reliability expression (Eq. (44))

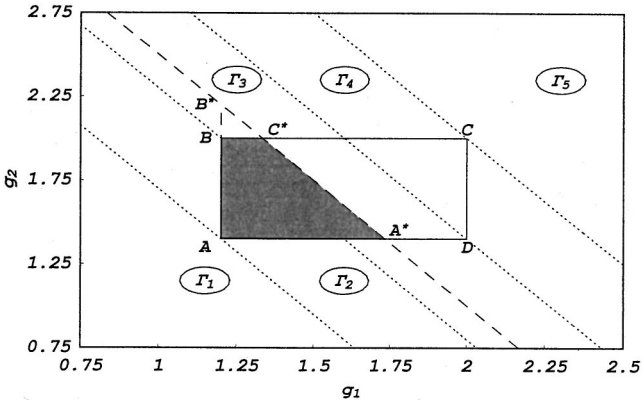

Fig. 4 Geometrical representation of the second term in reliability expression, (Eq. (47))

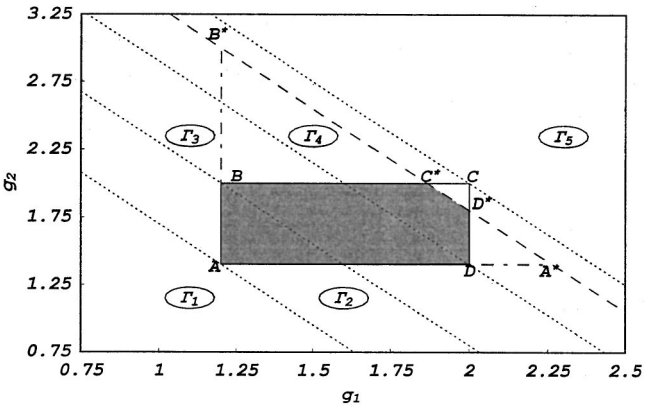

Fig. 5 Geometrical representation of the third term in reliability expression (Eq. (50))

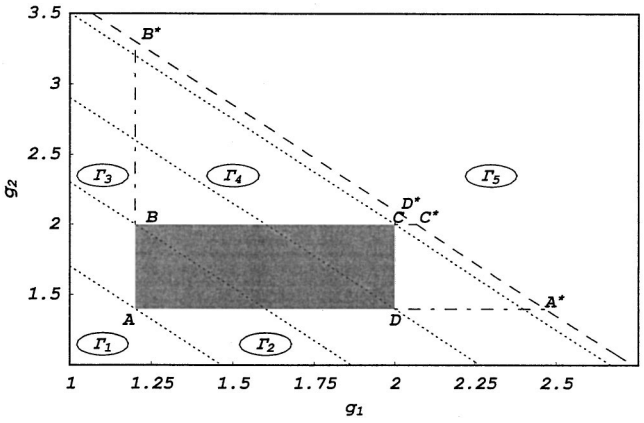

Fig. 6 Geometrical representation of the fourth term in reliability expression (Eq. (52))

The area $S_{AB^*A^*}$ under the triangle AB^*A^* is denoted as a hatched region (Fig. 3). It equals

$$S_{AB^*A^*}=(\overline{AB}^*)(\overline{AA}^*)/2=(c-a_1^{(j)}\alpha_1-a_2^{(j)}\beta_1)^2/2a_1^{(j)}a_2^{(j)}. \tag{44}$$

The reliability of the system is determined by multiplying the area in Eq. (44) by the constant value of the probability density function $(\alpha_2-\alpha_1)^{-1}(\beta_2-\beta_1)^{-1}$. In this case only the first term in the bracketed expression in Eq. (38) is nonvanishing. By inspection of Eq. (38) the coincidence between this latter term and the area $S_{AB^*A^*}$ is recognized.

Figure 4 deals with the case in which the straight line in Eq. (41) belongs to the region Γ_3. The shaded area ABC^*A^*, multiplied by the above constant value of the probability density function, represents the reliability of the system. This area is obtained as a difference between the area of the triangle AB^*A^* and the area of the triangle BB^*C^*. The coordinates of the intersection point C^* are

$$C^*\equiv\left(\frac{c-a_2^{(j)}\beta_2}{a_1^{(j)}},\beta_2\right) \tag{45}$$

whereas the expression of the coordinates of B^* coincides with Eq. (42). The side lengths for the triangle AB^*A^* are then given by Eq. (43) and the ones of the triangle BB^*C^* read

$$\overline{BB}^*=(c-a_1^{(j)}\alpha_1)/a_2^{(j)}-\beta_2;\quad \overline{BC}^*=(c-a_2^{(j)}\beta_2)/a_1^{(j)}-\alpha_2. \tag{46}$$

The area $S_{BB^*C^*}$ equals

$$S_{BEC^*}=(\overline{BB}^*)(\overline{BC}^*)/2=(c-a_1^{(j)}\alpha_1-a_2^{(j)}\beta_2)^2/2a_1^{(j)}a_2^{(j)} \tag{47}$$

and is recognized as the second term in Eq. (38). Note that the area of the triangle AB^*A^* coincides with the first term of the same equation.

Analogously, the geometrical meanings of the third and the fourth terms involved in Eq. (38) may be deduced by examining Fig. 5 and Fig. 6, respectively. In fact, Fig. 5 deals with the case that the broken line belongs to region Γ_4. In this case the reliability is given by the area ABC^*D^*D and it is obtained as the algebraic sum:

$$S_{BC^*D^*DA}=S_{AB^*A^*}-S_{BEC^*}-S_{DD^*A^*}. \tag{48}$$

The first two terms of this expression have been already identified. In order to obtain the last area in Eq. (48) we determine the coordinates of point D^*,

$$D^*\equiv\left(\alpha_2,\frac{c-a_1^{(j)}\alpha_2}{a_2^{(j)}}\right). \tag{49}$$

Note that the coordinates of the point A^* are given in Eq. (42). The area of the triangle DD^*A^* is so obtained as

$$S_{DD^*A^*}=(\overline{DD}^*)(\overline{DA}^*)/2=(c-a_1^{(i)}\alpha_2-a_2^{(j)}\beta_1)^2/2a_1^{(j)}a_2^{(j)}. \tag{50}$$

It coincides with the third term in Eq. (38). To determine the geometric interpretation of the fourth term in Eq. (38) let us consider the case when the broken line belongs to the region Γ_5 (Fig. 6). The reliability is given as the product of the area of the rectangle $ABCD$ and the density $(\alpha_2-\alpha_1)^{-1}(\beta_2-\beta_1)^{-1}$. The area itself equals $(\alpha_2-\alpha_1)(\beta_2-\beta_1)$. Hence the reliability is unity as expected. On the other hand, in order to identify the fourth term in Eq. (29) we represent the area $ABCD$ as the following algebraic sum:

$$S_{ABCD}=S_{AB^*A^*}-S_{BB^*C^*}-S_{DD^*A^*}+S_{CC^*D^*}. \tag{51}$$

The first three terms in Eq. (51) are given by their respective counterparts in Eq. (29). The fourth term in Eq. (51) may be easily obtained by inspection of Eq. (45) and Eq. (49). The area of the triangle CC^*D^* reads

$$S_{CC^*D^*}=(\overline{CC}^*)(\overline{CD}^*)/2=(c-a_1^{(j)}\alpha_2-a_2^{(j)}\beta_2)/2a_1^{(j)}a_2^{(j)}. \tag{52}$$

It represents the fourth term in Eq. (38). As is seen each term in the reliability expression has an appropriate geometrical meaning. Naturally, if the broken line lies in the region Γ_1 then one imme-

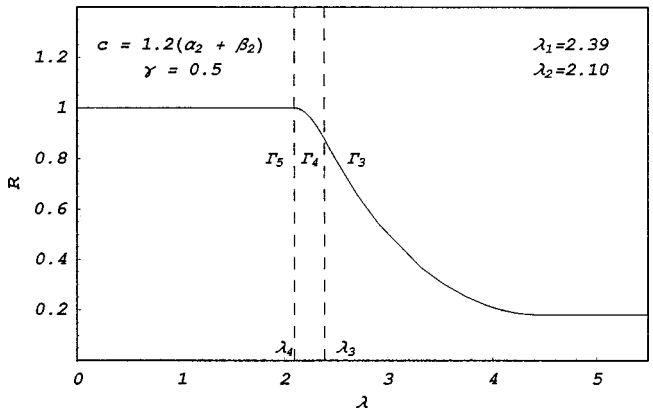

Fig. 7 Reliability versus nondimensional time, initial imperfections with uniform probability density ($D=[1.2,2]\times[1.4,2]$), Eqs. (26*a*) and (38)

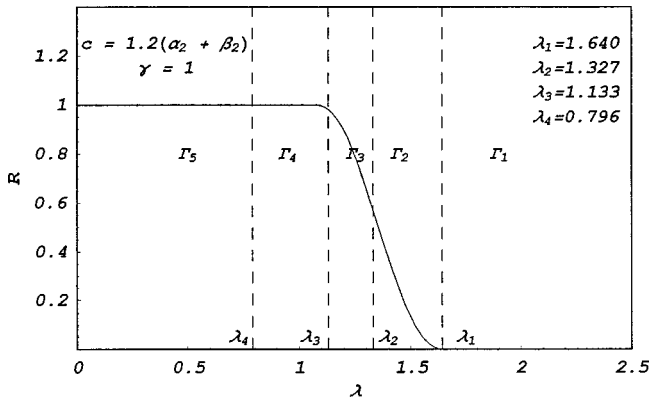

Fig. 8 Reliability versus nondimensional time, initial imperfections with uniform probability density function ($D=[1.2,2]\times[1.4,2]$), Eqs. (26*b*) and (38)

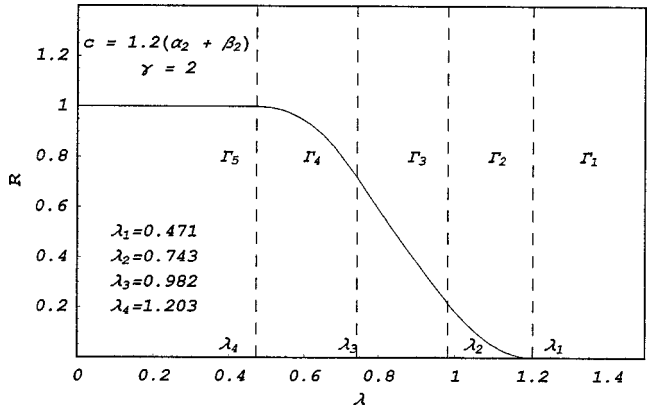

Fig. 9 Reliability versus nondimensional time, initial imperfections with uniform probability density ($D=[1.2,2]\times[1.4,2]$), Eqs. (26*c*) and (38)

diately deduces that the reliability vanishes. Likewise, if the broken line passes through the region Γ_5, the corresponding reliability is unity.

The results of sample calculations are portrayed in Figs. 7–11. The cases correspond to the five independent expressions for the coefficients $a_1^{(j)}$ and $a_2^{(j)}$, $(j=1,3)$ in Eq. (25). It is seen from Eq. (26) that these cases correspond, respectively, to $\gamma<1$, $\gamma=1$, $1<\gamma<25$, $\gamma=25$, $\gamma>25$. For a specified value of the failure boundary c and the different values of the ratio P/P_{cl}, the reliability functions are depicted as functions of a nondimensional time λ. For case $\gamma<1$ (Fig. 7) buckling occurrence is not a certain event: The structure may or may not buckle depending upon the system's parameters. Remarkably, the reliability does not necessarily tend to zero with the increase of time λ. Instead, it gains a minimum value given by

$$R(\lambda)=R(\pi/r) \quad \text{for } \lambda\geqslant\pi/r, \tag{53}$$

depending on the value c that delimits stable and unstable states. When the nondimensional time reaches the value π/r the displacement of the middle cross section of the system will achieve its maximum value, corresponding to the least possible reliability. In these circumstances, the value $R(\pi/r)$ represents the guaranteed minimum reliability that the column may possess.

The main objective of this study is to design the system, i.e., to obtain the radius of the circular cross section ρ_d of the column such as to maintain a prescribed reliability r_c up to a preselected time instant $\bar{t}$, for a specified value of the failure boundary c.

It is advantageous, however, to view the failure boundary c as a function of the remaining parameters $c(\rho_d,t,E,L,m)$, yielding for various combinations of its arguments, the failure boundary corresponding to satisfactory performance with the specified reliability r_c. Thus, specifying the mechanical and the geometrical characteristics of the column and the external load allows one to

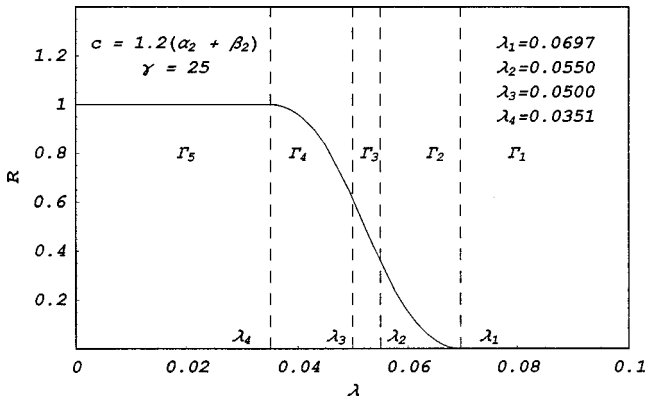

Fig. 10 Reliability versus nondimensional time, initial imperfections with uniform probability density ($D=[1.2,2]\times[1.4,2]$), Eqs. (26*d*) and (38)

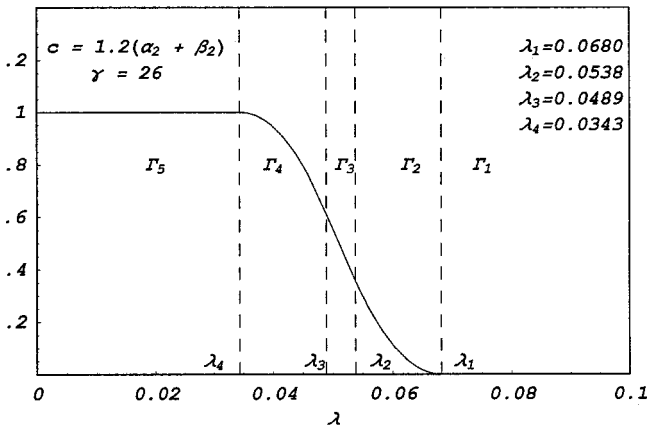

Fig. 11 Reliability versus nondimensional time, initial imperfections with uniform probability density ($D=[1.2,2]\times[1.4,2]$), Eqs. (26*e*) and (38)

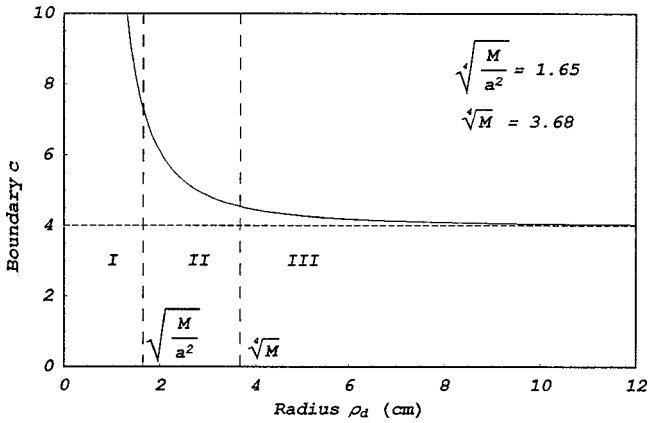

Fig. 12 Design curve $c=c(\rho_d)$, $\bar{t}=0.2$ uniform probability density function and unity reliability requirement ($P=3000$ Kg, $D=[1.2,2]\times[1.4,2]$), Eq. (38)

obtain design curves $c=c(\rho_d,\bar{t})$ shown in Figs. 12–14. The value of the cross-sectional radius ρ_d necessary for a successful performance is obtained by means of these curves, specifying the value of the failure boundary c. Note that the ratio between the external load P and the classic Euler's load P_{cl}, defined as γ depends upon the cross-sectional radius ρ,

$$\gamma=\frac{P}{P_{cl}}=\frac{PL^2}{\pi^2EI}=\frac{M}{\rho^4},\quad M=\frac{4PL^2}{\pi^3E}. \tag{54}$$

It is immediately observed, in view of Eq. (29), that when

$$\lim_{\rho\to\rho_d} a_1^{(i)}(\rho,\bar{t})\alpha_2+a_2^{(j)}(\rho,\bar{t})\beta_2=c \tag{55}$$

the reliability tends to unity from below.

Figure 12 depicts the failure boundary c versus the radius ρ_d for the prescribed time $\bar{t}=0.5$ seconds, and unity reliability. As may be observed the dependence $c=c(\rho_d)$ has an asymptote at $c=4$, when $\alpha_2=2$ and $\beta_2=2$, this numerical result can be derived from analytical considerations. In fact, when ρ_d tends to infinity

$$\lim_{\rho_d\to\infty} a_j^{(3)}(\rho_d,\bar{t})=1,\quad \text{for } (j=1,2), \tag{56}$$

and Eq. (55) takes the following form:

$$c=\alpha_2+\beta_2. \tag{57}$$

Since in Fig. 12 $\alpha_2+\beta_2=4$, the asymptote when $\rho_d\to\infty$ is represented by $c=4$. This result is straightforward: An infinite value of the cross section's radius ρ_d yields an infinite frequency of vibration of the column. In these circumstances the system will remain in the same position, represented by its initial imperfection alone.

Figure 13 portrays a design surface $c=c(c,\bar{t})$ allowing one to obtain for a specified time $\bar{t}$ and failure boundary c, the required radius ρ_d of the cross-sectional area, so that the reliability is r_c. In Fig. 13 r_c is taken to be unity. Figure 14 depicts design curves for various codified reliabilities $r_c=0.8$, $r_c=0.9$, and $r_c=1.0$. Figures show that smaller values of design cross-sectional radius are needed when less stringent required reliabilities are imposed for a specified failure boundary, as it should be.

Let us examine the dependence $c=c(\rho_d)$ in Figs. 12 and 14. Each figure is composed by three different subregions. Values of the cross section's radius $\rho_d\leqslant\rho_{dc}^{(2)}=\sqrt[4]{M/a^2}$ (Region I) lead to a load ratio $\gamma\geqslant a^2$. Therefore, the functions $a_1^{(j)}(\rho_d,t)$ and $a_2^{(j)}(\rho_d,t)$ in the expression of the failure boundary c are represented by Eq. (25a) and Eq. (25b). In this case the displacement function $\max_\xi Z(\rho_d,t)$ is a monotonically increasing function with time t. Large failure boundary c, combined with small values of the time interval t where the successful probabilistic performance is required are necessary for high prescribed reliabilities r_c.

In case $\rho_{dc}^{(2)}<\rho_d\leqslant\rho_{dc}^{(1)}=\sqrt{M}$ the load ratio γ belongs to the open interval $[1,a^2)$. The expression of the failure boundary c contains two functions: A trigonometric function for $a_2^{(3)}(\rho_d,t)$ and an expression, $a_1^{(1)}(\rho_d,t)$, that is monotonically increasing. In this case too, large values of the failure boundary c along with small performance times would guarantee the high reliability requirement. To get more insights at the dependence upon the time t we express the argument of the cosine function in Eq. (25f), in view of Eq. (54),

$$\varepsilon_1=\frac{\sqrt{a^2\rho_d^4-M}}{\rho_d}\left(\frac{\pi}{L}\right)^2\sqrt{\frac{E}{m}}\bar{t}, \tag{58}$$

allowing one to get a better look at the influence of the preselected time $\bar{t}$. In fact, the function $a_2^{(3)}(\rho_d,\bar{t})$ in Eq. (25f) attains its maximum for values of ρ_d and t making Eq. (58) to equal π, reliability reaches its minimum level. For values of parameters

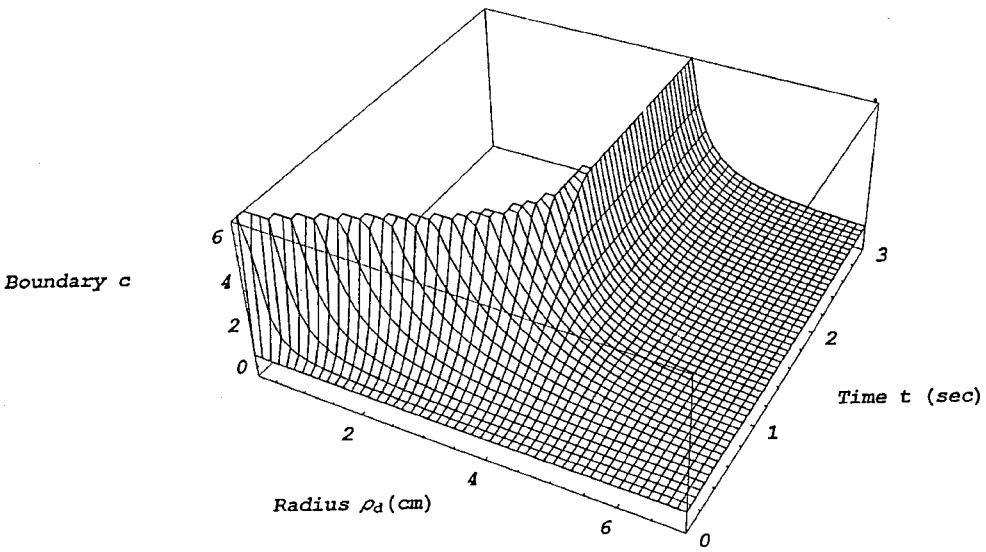

Fig. 13 Design surface $c=c(\rho_d,t)$ uniform probability density function and unity reliability requirement ($P=3000$ Kg, $D=[1.2,2]\times[1.4,2]$), Eq. (38)

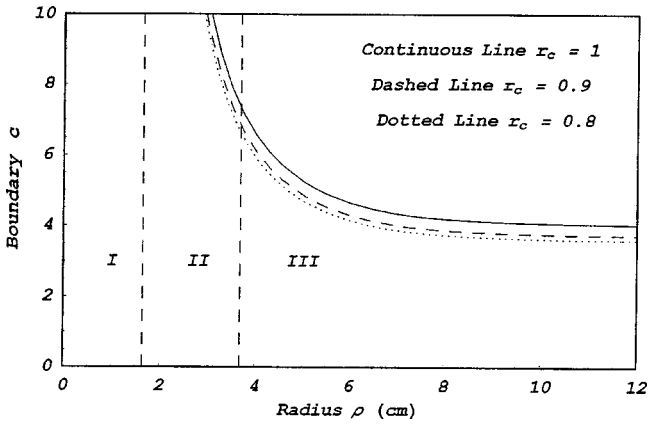

Fig. 14 Comparison of design curve; uniform probability density function and different codified reliabilities, $\bar{t}=0.5$ ($P=3000$ Kg, $D=[1.2,2]\times[1.4,2]$), Eq. (38)

leading to expression in Eq. (58) to be larger than π the previously achieved minimum reliability is valid. Values of $\rho_d \geqslant \rho_{dc}^{(1)} = \sqrt[4]{M}$ lead to a load ratio $\gamma<1$; hence the expression of the failure boundary $c(\rho_d,t)$ involves Eq. (25*a*) for $a_1^{(j)}(\rho_d,\bar{t})$. Interestingly, if the argument of the trigonometric function in the expression of $a_1^{(3)}(\rho_d,t)$, bearing in mind Eq. (54)

$$\varepsilon_2=\frac{\sqrt{\rho_d^4-M}}{\rho_d}\left(\frac{\pi}{L}\right)^2\sqrt{\frac{E}{m}}\bar{t} \tag{59}$$

is larger than π, for a specified time $\bar{t}$ and ρ_d the reliability achieved for $\varepsilon_2=\pi$ is retained. Hence the cosine function in the expression of $a_1^{(3)}(\rho_d,t)$ must be replaced by -1.

The function $a_1^{(3)}(\rho_d,\bar{t})$ becomes in this case

$$a_1^{(3)}(\rho_d,\bar{t})=-\frac{1+\rho_d^4/M}{1-\rho_d^4/M}. \tag{60}$$

As may be observed (Fig. 14), different values of the required reliability r_c lead to appropriate asymptotic values. In fact, let us design the system for high reliability requirement (Region Γ_4, Fig. 5). The expression of the failure boundary as a function of reliability, with the aid of Eq. (28) is given by

$$c=\alpha_2 a_1^{(j)}+\beta_2 a_2^{(j)}-\sqrt{2a_1^{(j)}a_2^{(j)}(1-r_c)(\alpha_2-\alpha_1)(\beta_2-\beta_1)}. \tag{61}$$

Evaluation of the limit value of Eq. (53) for infinite value of the cross section's radius ρ_d results in

$$\lim_{\rho_d\to\infty} c=\alpha_2+\beta_2-\sqrt{2(1-r_c)(\alpha_2-\alpha_1)(\beta_2-\beta_1)}. \tag{62}$$

Equation (62) allows obtaining the asymptotic value of the failure boundary function $c(\rho_d,\bar{t})$ by specifying the reliability value.

The results of this section clearly demonstrate that for high values of required reliability the design radii ρ_d of the cross-sectional area are extremely close.

The following question begs to be asked: Do the design values of the cross section radius ρ_d depend upon the particular form of the probability density function $f_{G_1G_2}(g_1,g_2)$? One can anticipate, generally speaking, that the designs depend on the probabilistic inputs. Yet, as it will be elucidated, the design in extremely high reliability regions is practically independent upon the input probabilistic information.

5 Initial Imperfections With General Distribution in a Rectangular Domain

Let the initial imperfections possess a general probability density function in a rectangular domain,

$$f_{G_1G_2}(g_1,g_2)=Af^*_{G_1G_2}(g_1,g_2)\{\langle g_1-\alpha_1\rangle^0-\langle g_1-\alpha_2\rangle^0\}\times\{\langle g_2-\beta_1\rangle^0-\langle g_2-\beta_2\rangle^0\} \tag{63}$$

located in the first quadrant of the plane (g_1,g_2). A represents a normalization coefficient depending upon the specific expression of the probability density function $f^*_{G_1G_2}(g_1,g_2)$ that extends over the entire plane.

The reliability expression, with $z=c$ substituted into Eqs. (37) and taking into account Eq. (63) reads

$$\begin{aligned}R(\lambda)&=\int_{-\infty}^{\infty}dt_2\int_{-\infty}^{(c-a_2^{(j)}t_2)/a_1^{(i)}}Af^*_{G_1G_2}(t_1,t_2)[\langle t_1-\alpha_1\rangle^0\\&\quad-\langle t_1-\alpha_2\rangle^0][\langle t_2-\beta_1\rangle^0-\langle t_2-\beta_2\rangle^0]dt_1\\&=\int_{-\infty}^{\infty}[\langle t_2-\beta_1\rangle^0-\langle t_2-\beta_2\rangle^0]dt_2\\&\quad\times\int_{-\infty}^{(c-a_2^{(j)}t_2)/a_1^{(i)}}Af^*_{G_1G_2}(t_1,t_2)[\langle t_1-\alpha_1\rangle^0-\langle t_1\\&\quad-\alpha_2\rangle^0]dt_1.\end{aligned} \tag{64}$$

Denoting the inner integral in Eq. (64) $I(t_2)$ Eq. (64) can be rewritten as

$$\begin{aligned}R(\lambda)&=\int_{-\infty}^{+\infty}I(t_2)[\langle t_2-\beta_1\rangle^0-\langle t_2-\beta_2\rangle^0]dt_2\\&=\int_{\beta_1}^{\beta_2}I(t_2)dt_2\\&=\int_{\beta_1}^{\beta_2}dt_2\int_{-\infty}^{(c-a_1^{(i)}t_2)/a_2^{(j)}}Af^*_{G_1G_2}(t_1,t_2)\\&\quad\times[\langle t_1-\alpha_1\rangle^0-\langle t_1-\alpha_2\rangle^0]dt_1.\end{aligned} \tag{65}$$

In a high reliability range c lies in the region Γ_4 (Fig. 5), in the vicinity of a critical value c^* where

$$c^*=a_1^{(i)}\alpha_2+a_2^{(j)}\beta_2 \quad \text{with} \quad (i,j=1,2,3). \tag{66}$$

The highest reliability requirement will be obtained when the line in Eq. (41) tends to pass through the point B. This corresponds to value $c=c^*$ substituted in Eq. (41). Thus we calculate the limit

$$\begin{aligned}\lim_{c\to c^*}R(\lambda)&=\lim_{c\to c^*}\int_{\beta_1}^{\beta_2}dt_2\int_{-\infty}^{(c-a_2^{(j)}t_2)/a_1^{(i)}}Af^*_{G_1G_2}(t_1,t_2)\\&\quad\times[\langle t_1-\alpha_1\rangle^0-\langle t_1-\alpha_2\rangle^0]dt_1\\&=\int_{\beta_1}^{\beta_2}dt_2\int_{-\infty}^{\alpha_2+(a_2^{(j)}/a_1^{(j)})(\beta_2-t_2)}Af^*_{G_1G_2}(t_1,t_2)\\&\quad\times[\langle t_1-\alpha_1\rangle^0-\langle t_1-\alpha_2\rangle^0]dt_1\\&=\int_{\beta_1}^{\beta_2}dt_2\int_{-\infty}^{\alpha_2}Af^*_{G_1G_2}(t_1,t_2)\\&\quad\times[\langle t_1-\alpha_1\rangle^0-\langle t_1-\alpha_2\rangle^0]dt_1\\&\quad+\int_{\beta_1}^{\beta_2}dt_2\int_{\alpha_2}^{\alpha_2+(a_2^{(j)}/a_1^{(j)})(\beta_2-t_2)}Af^*_{G_1G_2}(t_1,t_2)\\&\quad\times[\langle t_1-\alpha_1\rangle^0-\langle t_1-\alpha_2\rangle^0]dt_1.\end{aligned} \tag{67}$$

The inner integral vanishes because integration is carried out in the interval $[\alpha_2, \alpha_2 + a_2^{(j)}/(\beta_2 - t_2)a_1^{(i)}]$. However, since $\beta_1 \leqslant t_2 \leqslant \beta_2$, the upper limit of integration is greater than α_2. But in the interval beyond α_2 the integrand in the square parenthesis vanishes.

Reliability is then given only by the first term in Eq. (67) yielding

$$\lim_{c \to c^*} R(\lambda) = \int_{\beta_2}^{\beta_2} dt_2 \int_{\alpha_1}^{\alpha_2} A f^*_{G_1 G_2}(t_1, t_2) dt_1 = 1 \tag{68}$$

representing the integral of the probability density function in its entire domain. In this case of unitary reliability the design value of the cross section's radius ρ_d is found from Eq. (66).

6 Initial Imperfection With Uniform Probability Density Function: Circular Domain

This section deals with a different shape of the variable domain. The magnitudes of the initial imperfections G_1, G_2 are modeled as random variables belonging to a circular domain on the plane (g_1, g_2). The joint probability density function is assumed uniform as

$$f_{G_1 G_2}(g_1, g_2) = \begin{cases} \dfrac{1}{\pi K^2}, & \text{for } (g_1 - g_{10})^2 + (g_2 - g_{20})^2 \leqslant K^2 \\ 0, & \text{elsewhere} \end{cases} \tag{69}$$

with g_{10} the abscissa of the center of the circle, g_{20} the ordinate, and K the radius. As may be seen in Fig. 15 we assume, without loss of generality, the circle to be placed in the first quadrant of the plane (g_1, g_2), for $(i, j = 1,2,3)$ the straight line

$$y = a_1^{(i)}(\overline{\lambda}) g_1 + a_2^{(j)}(\overline{\lambda}) g_2 \tag{70}$$

is also drawn in a generic position depending on the values of the function $a_1^{(i)}(\lambda)$ and $a_2^{(j)}(\lambda)$.

According to Eq. (32), in order to find the reliability, it is necessary to integrate the probability density function below the straight line in Eq. (69), or over the hatched area in Fig. 15,

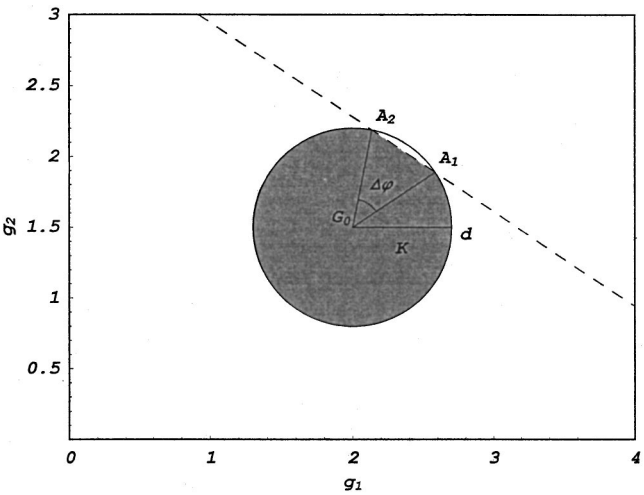

Fig. 15 Domain of integration of the probability density function ($g_{10}=2$, $g_{20}=1.5$, $K=1.0$), Eq. (73)

$$R(\lambda) = \int\int_D f_{G_1 G_2}(t_1, t_2) dt_1 dt_2$$

$$= \int_{-\infty}^{\infty} \int_{-\infty}^{(c - a_2^{(j)} t_2)/a_1^{(i)}} \frac{1}{\pi K^2} dt_1 dt_2 . \tag{71}$$

Double integral in the latter equation will be calculated with the aid of a polar coordinate system whose origin is on the circle's center:

$$\begin{aligned} g_1 &= g_{10} + \delta \cos(\varphi) \\ g_2 &= g_{20} + \delta \sin(\varphi) \end{aligned} \tag{72}$$

with δ polar distance and φ polar angle. In this coordinate system reliability becomes

$$R(\lambda) = 1 - \int\int_{D_c} \frac{1}{\pi K^2} \rho d\rho d\varphi \tag{73}$$

where D_c is the nonhatched area in Fig. 15. Equation (70) yields

$$R(\lambda) = 1 - \frac{1}{2\pi}[\Delta\varphi - \sin(\Delta\varphi)] \tag{74}$$

with $\Delta\varphi = \varphi_2 - \varphi_1$ the angular difference of the phase angles φ_1 and φ_2 between the polar axis δ and the polar directions $\mathbf{G_0 A_1}$ and $\mathbf{G_0 A_2}$, respectively. Polar phase angles φ_1 and φ_2 may be obtained by solving the following system:

$$a_1^{(i)} \cos(\varphi) + a_2^{(j)} \sin(\varphi) = \frac{1}{\delta}(c - a_1^{(i)} g_{10} - a_2^{(j)} g_{20}) \tag{75a}$$

$$\delta^2[\sin^2(\varphi) + \cos^2(\varphi)] = K^2 \tag{75b}$$

where the first equation represents a straight line in the polar coordinate system, the latter one is instead the equation of a circle.

System in Eqs. (75*a*),(75*b*) has the solution

$$\varphi_1 = \cos^{-1}\left(\frac{f a_1^{(i)} + a_2^{(j)} \sqrt{[a_2^{(j)}]^2 + [a_1^{(i)}]^2 - f^2}}{[a_1^{(i)}]^2 + [a_2^{(j)}]^2} \right) \tag{76a}$$

$$\varphi_2 = \cos^{-1}\left(\frac{f a_1^{(j)} - a_2^{(j)} \sqrt{[a_2^{(j)}]^2 + [a_1^{(i)}]^2 - f^2}}{[a_1^{(i)}]^2 + [a_2^{(j)}]^2} \right) \tag{76b}$$

with

$$f = \frac{1}{K}(c - a_1^{(i)} g_{10} - a_2^{(j)} g_{20}). \tag{77}$$

In case of $R(\lambda)$, tending to unity from below, we get from Eq. (74)

$$\Delta\varphi \to 0 \quad \text{or} \quad \varphi_1 \to \varphi_2 . \tag{78}$$

Hence the square root terms under the radical in Eqs. (76*a*),(76*b*) tend to

$$a_2^{(j)^2} + a_1^{(i)^2} - f^2 \to 0^+ . \tag{79}$$

Thus

$$f \to \sqrt{[a_1^{(i)}]^2 + [a_2^{(j)}]^2}^- . \tag{80}$$

The geometrical meaning of the condition stated in Eq. (80) can be shown expressing the system in Eqs. (74*a*),(74*b*) back in Cartesian coordinates. Thus, bearing in mind Eq. (80) and Eq. (72), we write Eq. (74) in the form

$$g_2 = \frac{a_1^{(i)} g_{10} + a_2^{(j)} g_{20} - a_1^{(i)} g_1 + K\sqrt{[a_1^{(i)}]^2 + [a_2^{(j)}]^2}}{a_1^{(i)}} \tag{81a}$$

$$(g_1 - g_{10})^2 + (g_2 - g_{20})^2 = K^2 . \tag{81b}$$

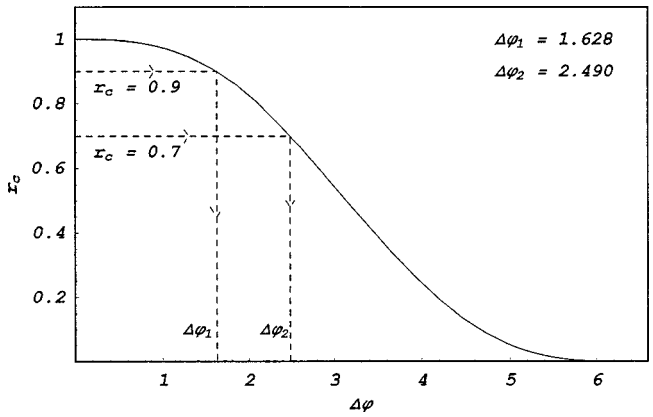

Fig. 16 Reliability versus phase angle difference, Eq. (74)

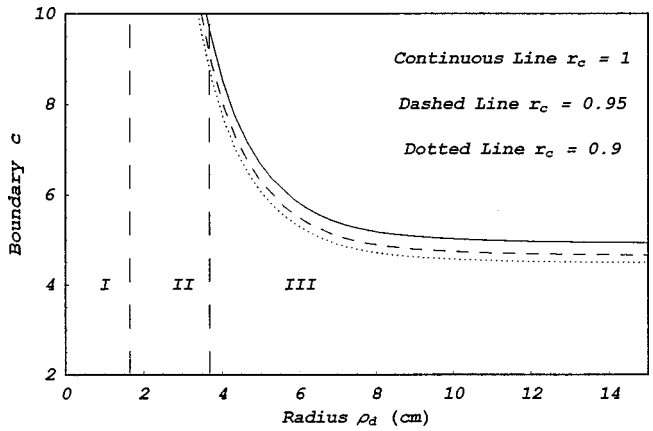

Fig. 17 Comparison of design curves for uniform probability density function over a circular domain and different required reliabilities $\bar{t}=0.5$, $P=3000$ Kg ($g_{10}=2$, $g_{20}=1.5$, $K=1.0$), Eq. (86)

Substituting Eq. (81*a*) into Eq. (81*b*) we get a second degree algebraic equation for the unknown g_1,

$$q_0 g_1^2 - 2g q_1 + q_2 = 0, \tag{82}$$

with coefficients

$$q_0 = \left(1 + \left[\frac{a_1^{(i)}}{a_2^{(j)}}\right]^2\right)$$

$$q_1 = {}_1\left(g_{10} + \frac{2[a_1^{(i)}]^2 g_{10}}{[a_2^{(j)}]^2} + \frac{2a_1^{(i)} K\sqrt{[a_1^{(i)}]^2+[a_2^{(j)}]^2}}{[a_2^{(j)}]^2}\right) \tag{83}$$

$$q_3 = g_{10}^2 + \left[\frac{a_1^{(i)}}{a_2^{(j)}}\right]^2 g_{10}^2 + \left[\frac{a_1^{(i)}}{a_2^{(j)}}\right]^2 K^2 + \frac{2a_1^{(i)}\sqrt{[a_1^{(i)}]^2+[a_2^{(j)}]^2}\, g_{10} K}{[a_2^{(j)}]^2}$$

whose discriminant $q_1^2 - 4q_0 q_1$ is identically zero. Two coinciding solutions of this latter Eq. (82) read

$$g_1^{(1)} = g_1^{(2)} = g_{10} + \frac{a_1^{(i)} K}{\sqrt{[a_1^{(i)}]^2+[a_2^{(j)}]^2}} \tag{84}$$

this implies that the straight line in Eq. (81*a*) and the circle in Eq. (81*b*) share one common point. Thus we conclude that the straight line in Eq. (81) is a tangent to the circular domain of the initial imperfections. Equation (80) can then be interpreted as the condition that the straight line in Eq. (75*a*) is tangent to the circle in Eq. (75*b*) (Fig. 15).

In order to design the system with a prescribed required reliability r_c we must solve Eq. (74) for the angular phase difference $\Delta\varphi$, with r_c substituted for R. Figure 16 depicts the curve $R = R(\Delta\varphi)$, allowing one to obtain the phase difference $\Delta\varphi$ given the value of the design reliability r_c. For example, for $r_c = 0.9$, $\Delta\varphi = 1.628$.

Having found $\Delta\varphi$ that corresponds to r_c, we proceed to design the system. In order to obtain the design curves $c = c(\rho_d)$ for specified time and preselected reliability r_c, one subtracts Eq. (76*a*) from Eq. (76*b*), leading to

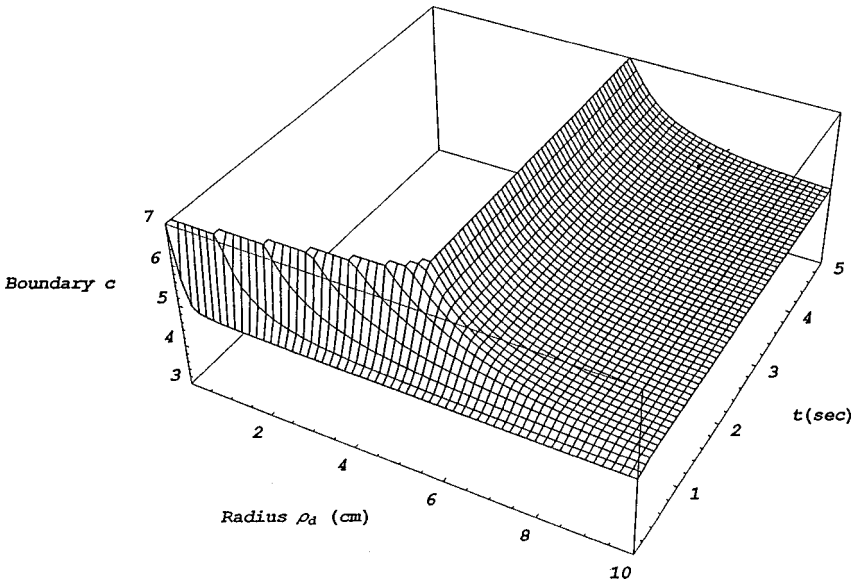

Fig. 18 Design surface $c = c(\rho_d, t)$, uniform probability density function over circular domain and required unity reliability ($P=3000$ Kg, $g_{10}=2$, $g_{20}=1.5$, $K=1.0$), Eq. (86)

$$\Delta\varphi=\varphi_2-\varphi_1$$
$$=\cos^{-1}\left(\frac{fa_1^{(i)}-a_2^{(j)}\sqrt{[a_2^{(j)}]^2+[a_1^{(i)}]^2-f^2}}{[a_2^{(j)}]^2+[a_1^{(i)}]^2}\right)$$
$$-\cos^{-1}\left(\frac{fa_1^{(i)}+a_2^{(j)}\sqrt{[a_2^{(j)}]^2+[a_1^{(i)}]^2-f^2}}{[a_2^{(j)}]^2+[a_1^{(i)}]^2}\right). \quad (85)$$

Once $\Delta\varphi$ is determined from Fig. 16 one can conclude the value of f from Eq. (85). The solution of Eq. (85) for f, in conjunction with Eq. (77) allows one to obtain the required expression for the design curve $c=c(\rho_d)$ which reads

$$c(\rho_d)=a_1^{(i)}(\rho_d)g_{10}+a_2^{(j)}(\rho_d)g_{20}$$
$$+\frac{K}{\sqrt{2}}\sqrt{([a_1^{(i)}(\rho_d)]^2+[a_2^{(j)}(\rho_d)]^2)[1+\cos(\Delta\varphi)]} \quad (86)$$

and is portrayed in Fig. 17 for specified time $\bar{t}=0.5$ and different values of r_c. Figure 18 represents the design surface for unity reliability as a function $c=c(\rho_d,t)$ allowing one to find the cross-sectional radius ρ_d for specified exploitation time t and the failure boundary c.

7 Initial Imperfections as Interval Variables: Interval Analysis

Let the initial imperfection amplitude be represented by a vector interval variable:

$$g_1=[\alpha_1,\alpha_2]$$
$$g_2=[\beta_1,\beta_2] \quad (87)$$

so that the displacement function of the middle cross section of the column is an interval variable as well,

$$z=[\zeta_1,\zeta_2]=[\alpha_1,\alpha_2]a_1^{(i)}(\lambda)+[\beta_1,\beta_2]a_2^{(j)}(\lambda) \quad (i,j=1,2,3), \quad (88)$$

with ζ_1 being the lower bound and ζ_2 the upper one. Since g_1 and g_2 are positive, so are the additional displacements. Hence in the safety requirement condition $-d\leqslant z\leqslant c$ only the condition $z\leqslant c$ is operative. System's design via the anti-optimization technique identifies the worst possible reachable condition for the uppermost bound ζ_2 of the interval variable z. If $\zeta_2\leqslant c$, the system will remain in the safe domain, otherwise it will fail. Expressing the argument of the functions $a_1^{(j)}(\lambda)$ and $a_2^{(j)}(\lambda)$ in terms of the cross-sectional radius ρ_d and the preselected time $\bar{t}$ by means of Eq. (41) we obtain the formal design relation

$$\zeta_2=\alpha_2 a_1^{(j)}(\rho_d,\bar{t})+\beta_2 a_2^{(j)}(\rho_d,\bar{t})=c \quad (j=1,2,3). \quad (89)$$

Comparing Eq. (89) and Eq. (55) we conclude that the former matches the design condition in case of unity reliability requirement given in Eq. (55). If the uncertainty region coincides with the domain represented in Fig. 2, then the design surface $c(\rho_d,t)$ represented by Eq. (89) coincides with Fig. 14. Thus, the anti-optimization method and the probabilistic one with highest reliability requirement leads to the same design values for the cross-sectional radius ρ_d.

8 Initial Imperfections as Convex Variables: Circular Domain

Let us consider the case when the information about the uncertain imperfection magnitude is given as

$$(g_1-g_{10})^2+(g_2-g_{20})^2\leqslant K^2 \quad (90)$$

where g_{10} is the abscissa and g_{20} is the ordinate of the center of the circle and K its radius (Fig. 19). The displacement of the middle cross section reads

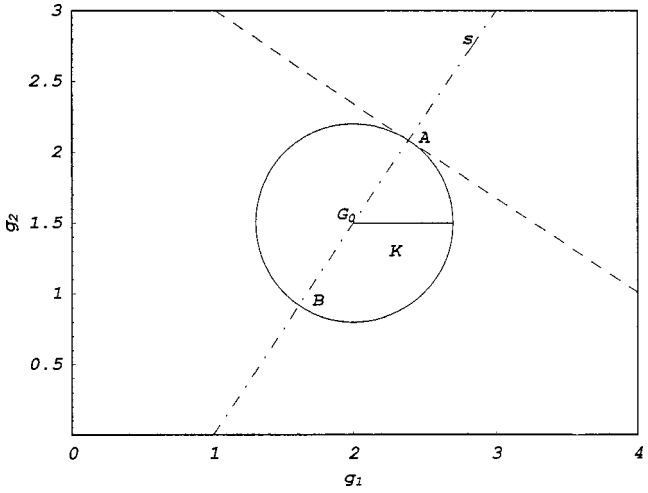

Fig. 19 Initial imperfections amplitudes modeled by convex variables: anti-optimization design ($g_{10}=2$, $g_{20}=1.5$, $K=1.0$), Eq. (100)

$$z=g_1a_1^{(j)}(\lambda)+g_2a_2^{(j)}(\lambda), \quad (j=1,2,3) \quad (91)$$

where g_1,g_2 are uncertain variables belonging to the set stated by Eq. (90). The set (90) in this expression is convex, hence the appropriate analysis was referred to as *convex modeling* by Ben-Haim and Elishakoff [7].

The Hamiltonian function for this problem is given as

$$H=a_1^{(j)}g_1+a_2^{(j)}g_2+h[(g_1-g_{10})^2+(g_2-g_{20})^2-K^2] \quad (92)$$

and h is the Lagrange multiplier associated with the condition in Eq. (82). Necessary conditions for extrema read

$$\frac{\partial H}{\partial g_1}=a_1^{(j)}+2h(g_1-g_{10})=0 \quad (93a)$$

$$\frac{\partial H}{\partial g_2}=a_2^{(j)}+2h(g_2-g_{20})=0 \quad (93b)$$

$$\frac{\partial H}{\partial h}=(g_1-g_{10})^2+(g_2-g_{20})^2-K^2=0. \quad (93c)$$

The solutions of Eqs. (93*a*), (93*b*), and (93*c*), denoted by $\bar{g}_1$ and $\bar{g}_2$ corresponding to minimum z, read

$$\bar{g}_1=g_{10}+\frac{Ka_1^{(i)}}{\sqrt{a_1^{(i)^2}+a_2^{(j)^2}}} \quad (94)$$

$$\bar{g}_2=g_{20}+\frac{Ka_2^{(j)}}{\sqrt{a_1^{(i)^2}+a_2^{(j)^2}}}. \quad (95)$$

It is remarkable that Eq. (94) coincides with Eq. (84) which represents the abscissa of the touching points between the circular domain of the random variables in Eq. (69) and the straight line in Eq. (70). Let us investigate the geometrical meaning given by the Eqs. (93*a*), (93*b*), and (93*c*) and the results in Eqs. (94) and (95). Eliminating parameter h from Eq. (93*a*) and Eq. (93*b*) leads to

$$g_2=\frac{a_2^{(j)}}{a_1^{(i)}}g_1+\frac{1}{a_1^{(i)}}(a_1^{(i)}g_{20}-a_2^{(j)}g_{10}). \quad (96)$$

This expression represents a straight line with slope $a_2^{(j)}/a_1^{(i)}$ passing through the center of the circle. This line is identified as in Fig. 19 with label s. Equation (96) must be solved in conjunction with Eq. (93*c*). Thus the solution of the anti-optimization problem is found as the intersection point of the straight line s and the

circle represented by Eq. (93*c*). There are two intersection points (Fig. 19) denoted *A* and *B* corresponding, respectively, to maximum and minimum of the displacement function. In order to deal with the anti-optimization technique, one must look for the maximum of the displacement function, namely the point *A* in Fig. 19; Eqs. (94) and (95) refer to point *A*.

The design problem can be stated differently. Let us consider the expression

$$g_2 = -\frac{a_1^{(i)}}{a_2^{(j)}} g_1 + (a_1^{(i)} g_{10} + a_2^{(j)} g_{20} + K\sqrt{[a_1^{(i)}]^2 + [a_2^{(j)}]^2}) \quad (97)$$

representing a line orthogonal to *s* and tangent to the circle in point *A*. One may obtain the solution of the system in Eq. (93) by solving the system

$$g_1 a_1^{(j)} + g_2 a_2^{(j)} - T = 0 \quad (98a)$$

$$(g_1 - g_{10})^2 + (g_2 - g_{20})^2 = K^2 \quad (98b)$$

where the line in Eq. (98*a*) is perpendicular to line Eq. (97). The parameter T is a free parameter that must be chosen so that the straight line in Eq. (98*a*) constitutes a tangent to the circle in Eq. (98*b*). It may be deduced by inspection of Eq. (94) that the parameter T coincides with the failure boundary value c.

The value of T is obtainable by solving Eqs. (89*a*),(89*b*),

$$T = c = a_1^{(i)}(\rho_d, t) g_{10} + a_2^{(j)}(\rho_d, t) g_{20} + K\sqrt{[a_1^{(i)}(\rho_d, t)]^2 + [a_2^{(j)}(\rho_d, t)]^2}. \quad (99)$$

Rewriting Eq. (86) in Cartesian coordinates for unity required reliability r_c as

$$c = a_1^{(i)}(\rho_d, t) g_{10} + a_2^{(j)}(\rho_d, t) g_{20} + K\sqrt{[a_1^{(i)}(\rho_d, t)]^2 + [a_2^{(j)}(\rho_d, t)]^2}. \quad (100)$$

One immediately recognizes that with the different models of uncertainty treated in Section 6 and in the present one lead to the same analytical expression of the failure boundary surface. Then, with initial imperfection amplitude given in the same region of variation, these different approaches result into the same design surface.

9 Critical Remarks

As it is shown in this study, the two-dimensional interval analysis provides a design which is a limiting case of the probabilistic design when the required reliability tends to unity from below. Likewise, convex modeling yields a design to which the probabilistic calculations tend when the variation of uncertain variables is limited to the circular domain. The natural question arises: Can the nonprobabilistic method be preferred to the probabilistic approach? In general, should the simpler method be preferred to the more complex one?

It appears instructive to reproduce here three relevant quotations:

1 ''The aim of science is to seek the simplest explanations of complex functions. We are apt to fall into the error of thinking that the facts are simple because simplicity is the goal of our quest. The guiding motto in the life of every natural philosopher should be, 'Seek simplicity and distrust it.' '' (Alfred North Whitehead).

2 ''Everything should be made as simple as possible, but not one bit simpler.'' (Albert Einstein)

3 ''Never use a long word where a short one will do. If it is possible to cut a word, always cut it out.'' (George Orwell).

If one follows these recommendations one concludes that the interval analysis is the simplest yet tenable method of describing uncertainty. It leads to the same answers as the theory of probability, but without a ''long word,'' in the above terminology; it also appears that the uncertainty modeling cannot be made ''one bit simpler,'' to borrow Einstein's words, than the interval analysis. Yet in accordance with Whitehead we do not discourage the ''distrust.'' Indeed, the following challenging questions appears to be in order: Can the interval or ellipsoidal analyses describe first-excursion failure, fatigue problems, wind loads, earthquake engineering, and a long list of other issues dealt with some degree of success, recognized at least by some researchers, by the theory of probability and random processes? These inspiring questions remain yet to be answered. Yet, results reported in this study appear to be encouraging. They provide a direct bridge between the seemingly opposite techniques. Establishment of identity of designs furnished by the probabilistic and nonprobabilistic analyses shows that all the analytical roads lead to the same results for the problem in question.

Acknowledgments

This study has been supported by the N.A.S.A. Langley Research Center (I. E.) and the Italian Ministry of Science and Technological Research (M. Z.). This financial support is gratefully appreciated.

References

[1] Moore, R., 1979, *Methods and Applications of Interval Analysis*, S.I.A.M., Philadelphia.
[2] Alefeld, G., and Herzberger, J., 1983, *Introduction to Interval Computations*, Academic Press, New York.
[3] Neumaier, A., 1990, *Interval Methods for System of Equations*, Cambridge University Press, New York.
[4] Schweppe, F. C., 1973, *Uncertain Dynamic Systems*, Prentice-Hall, Englewood Cliffs, NJ.
[5] Chernousko, F. L., 1994, *State Estimation for Dynamic System*, CRC Press, Boca Raton.
[6] Kurzhanski, A. B., and Valyi, I., 1992, ''Ellipsoidal Techinques for Dynamic Systems: Control Synthesis for Uncertain Systems,'' Dyn. Control, **2**, pp. 87–111.
[7] Ben-Haim, Y., and Elishakoff, I., 1990, *Convex Models of Uncertainty in Applied Mechanics*, Elsevier, Amsterdam.
[8] Ben-Haim, Y., 1996, *Robust Reliability of the Mechanical Sciences*, Springer-Verlag, Berlin.
[9] Li, Y. W., Elishakoff, I., Starnes, Jr., J. H., and Shinozuka, M., 1996, ''Prediction of Natural Frequencies and Buckling Load Variability due to Uncertainty in Material Properties by Convex Modeling,'' Fields Inst. Commun., **9**, pp. 139–154.
[10] Goncharenko, V. M., 1962, ''Application of Markov Processes in Statistical Theory of Shell's Stability,'' Ukr. Mat. Zh., **14**, No. 2, pp. 198–202 (in Russian).
[11] Budiansky, B., and Hutchinson, J. W., 1964, ''Dynamic Buckling of Imperfection-Sensitive Structures,'' *Proceedings XI International Congress of Applied Mechanics*, H. Goertler, ed., Munich.
[12] Lindberg, H. E., 1965, ''Impact Buckling of Thin Bar,'' ASME J. Appl. Mech., **32**, pp. 312–322.
[13] Ariaratman, S. T., 1967, ''Stability of Column Under Random Loading,'' *Dynamic Stability of Structures*, G. Hermann, ed., Pergamon Press, New York.
[14] Kil'dibekov, I. G., 1971, ''Nonlinear Vibrations of Circular Cylindrical Shells Under Axial Loading and Acoustic Pressure,'' *Problemi Nadezhnosti v Stroitel'noi Mekhanike* (*Problems of Reliability in Structural Mechanics*) V. V. Bolotin and A. Chyras, eds., Vilnius, pp. 58–63.
[15] Amazigo, J. C., and Frank, D., 1973, ''Dynamic Buckling of an Imperfect Column on Non-Linear Foundation,'' Q. J. Mech. Appl. Math., **31**, pp. 1–9.
[16] Amazigo, J. C., 1974, ''Dynamic Buckling of Structures with Random Imperfections,'' *Stochastic Problem in Mechanics*, H. H. E. Leipholz, ed., University of Waterloo Press, Waterloo, Ontario, pp. 243–254.
[17] Lockhart, D., and Amazigo, J. C., 1975, ''Dynamic Buckling of Externally Pressurized Imperfect Cylindrical Shells,'' ASME J. Appl. Mech., **42**, pp. 316–320.
[18] Maymon, G., and Libai, A., 1977, ''Dynamics and Failure of Cylindrical Shells Subjected to Axial Impact,'' AIAA J., **15**, pp. 1621–1630.
[19] Elishakoff, I., 1978, ''Impact Buckling of Thin Bar Via Monte Carlo Method,'' ASME J. Appl. Mech., **45**, pp. 586–590.
[20] Bogdanovich, A. E., 1987, *Nonlinear Problems of Dynamics of Cylindrical Composite Shells*, ''Zinatne'' Publishers, Riga (in Russian).
[21] Bogdanovich, A. E., 1980, ''Review of Research on Stability of Cylindrical Shells due to Axial Dynamic Compression'' (*Elektrodinamika i Mekhanika Raspredelennikh System*) *Electrodynamics and Mechanics of Continua*, Riga, pp. 68–105 (in Russian).
[22] Ben-Haim, Y., and Elishakoff, I., 1989, ''Dynamics and Failure of Thin Bar

With Unknown but Bounded Imperfections,'' *Recent Advances in Impact Dynamics of Engineering Structures*, D. Hui and N. Jones, eds., ASME, New York, pp. 89–96.
[23] Elishakoff, I., and Ben-Haim, Y., 1990, ''Dynamics of Thin Cylindrical Shell Under Impact With Limited Deterministic Informations on Its Initial Imperfections,'' Struct. Safety, **8**, pp. 103–112.
[24] Lindberg, H. E., 1992, ''An Evaluation of Convex Modeling for Multimode Dynamic Buckling,'' ASME J. Appl. Mech., **59**, pp. 929–936.
[25] Lindberg, H. E., 1992, ''Convex Models for Uncertain Imperfection Control in Multimode Dynamic Buckling,'' ASME J. Appl. Mech., **59**, pp. 937–975.
[26] Ben-Haim, Y., 1993, ''Convex Models of Uncertainty in Radial Pulse Buckling of Shells,'' ASME J. Appl. Mech., **60**, pp. 683–688.

Nonlinear Dynamic Behaviors of a Complex Rotor-Bearing System

T. Zheng
Department of Mechanics
and Engineering Science,
Fudan University,
Shanghai 200433, P.R. China

N. Hasebe
Department of Civil Engineering,
Nagoya Institute of Technology,
Gokiso-Cho, Showa-Ku,
Nagoya 466, Japan

This paper deals with the long-term dynamic behaviors of a complex rotor-bearing system with multi-degrees-of-freedom and nonclosed form of the bearing forces. Since nonanalytical bearing forces can be available, to increase the numerical accuracy and decrease the CPU time, a new method is presented to calculate the Jacobians of the bearing forces and bearing forces themselves. The algorithm is concise and the computing efforts spent on the Jacobians are very small compared to spend on the bearing forces themselves. In terms of the feature that the nonlinear bearing forces act on the system individually, a new reduction method and corresponding integration technique is proposed to increase the numerical stability and decrease the computing time for the system analysis. The numerical schemes of this study are applied to a rotor system with multi-rigid disks and two elliptical bearing supports. The numerical results reveal very rich and complex nonlinear behavior of the system. [S0021-8936(00)00802-3]

1 Introduction

It is a common knowledge that general rotor systems display nonlinear behavior due to the hydrodynamic effects that come from bearing clearances, squeeze film dampers, seals and other sources. A jump phenomenon, which typically occurs in a nonlinear system, was first observed by Yamamoto [1]. The subharmonic responses in a simple rotor-bearing system was detected experimentally by Bently [2]. Analytical results also reveal the nonlinear behavior of the rotor-bearing systems. Assuming small nonlinearity for the bearing clearance, Childs [3] studied the occurrence of subharmonic motions of the rotor using the perturbation method. Choi and Noah [4] analyzed the coherence of super and subharmonics in a rotor-bearing model using a harmonic balance method along with a discrete Fourier transform procedure, which was originally used by Yamauchi [5]. Ehrich [6] showed the presence of high-order subharmonic responses in high-speed rotors with bearing clearance by numerical integrations. Apart from super and subharmonic responses, aperiodic whirling motions in a high-pressure oxygen turbopump of the space shuttle main engine were also reported by Childs [7] as well as Kim and Noah [8].

In rotordynamics, due to the complexity of the nonlinear analysis, the nonlinear models of the system are frequently treated as simple ones, such as a symmetrical rigid rotor (see, for example, [9–11]) or the Jeffcott rotor (see, for example, [4,12,13,6,8]). In these models the system only has two degrees-of-freedom and the nonlinear forces of the bearings keep the closed forms. However, in practice, the rotor is more complex and the nonlinear forces cannot get the closed forms unless a short (or long) bearing model is assumed. There are several publications ([14–16]) dealing with the order reduction methods of the system. These works study the periodic solutions of a high order of unbalanced rotor systems and try to save the computing time.

In this paper, a rotor system with many degrees-of-freedom and a nonclosed form of bearing forces is involved. Since the bearing forces acted on the rotor individually, a new reduction method, dealing with long-term behaviors of the system, is proposed to reduce the degrees-of-freedom of the system. By means of this method the nonlinear terms of the reduced system still have the local feature and then a corresponding modified Newmark method is proposed to integrate the responses of the reduced system. The iterations that are needed at each step of integrations execute only on small parts of the system equations related to the nonlinear terms. Therefore, compared to the Runge-Kutta method, this method not only is unconditionally stable but also saves the computing time significantly.

In the nonlinear analysis of a dynamic system, the Jacobians of the nonlinear forces are necessary to be used. However, for the real bearings, nonclosed form of bearing forces can be available; therefore, a great deal of computing effort is needed to calculate the Jacobians. Based on the theory of variational inequalities and the finite element method, a new method is presented to calculate the Jacobians of the bearing forces and the bearing forces themselves. The algorithm is concise and the computing efforts spent on the Jacobians are very small compared to those spent on the bearing forces themselves.

Finally, a flexible rotor with eight rigid disks and two elliptical bearing supports is analyzed. The periodic solutions and long-term behaviors of the system are investigated numerically, which reveal many interesting phenomena of a nonlinear system.

2 System Equations of Motion

A typical rotor-bearing system is composed of rigid disks, flexible shafts, and bearings. Using the finite element method ([17]), system equations of motion can be written as

$$M\ddot{z}+G\dot{z}+Kz=g(t)+f(z,\dot{z},\mu) \tag{1}$$

where M, G, $K\in R^{n\times n}$ and $g\in R^n$ are the mass matrix, gyroscope matrix, stiffness matrix, and unbalance force vector, respectively. For a rotor with r nodal points, the displacement vector is of the form

$$z=[x_1,y_1,\theta_{x_1},\theta_{y_1},x_2,y_2,\theta_{x_2},\theta_{y_2}\cdots,x_r,y_r,\theta_{x_r},\theta_{y_r}]^T$$

where x_i, y_i and θ_{x_i}, θ_{y_i} $(i=1,2,\ldots,r)$ are the lateral translations and rotation angles of the ith nodal point along the horizontal and vertical direction, respectively ([17]). Since the bearing supports are located individually, the nonlinear force vector is of the form

Contributed by the Applied Mechanics Division of THE AMERICAN SOCIETY OF MECHANICAL ENGINEERS for publication in the ASME JOURNAL OF APPLIED MECHANICS. Manuscript received by the ASME Applied Mechanics Division, April 28, 1998; final revision, November 26, 1999. Associate Technical Editor: W. K. Liu. Discussion on the paper should be addressed to the Technical Editor, Professor Lewis T. Wheeler, Department of Mechanical Engineering, University of Houston, Houston, TX 77204-4792, and will be accepted until four months after final publication of the paper itself in the ASME JOURNAL OF APPLIED MECHANICS.

$$f(z,\dot{z})=\begin{Bmatrix} 0 \\ \vdots \\ f_{x_i}(x_i,y_i,\dot{x}_i,\dot{y}_i) \\ f_{y_i}(x_i,y_i,\dot{x}_i,\dot{y}_i) \\ 0 \\ \vdots \\ f_{x_j}(x_j,y_j,\dot{x}_j,\dot{y}_j) \\ f_{y_j}(x_j,y_j,\dot{x}_j,\dot{y}_j) \\ 0 \\ \vdots \end{Bmatrix} \tag{2}$$

where f_{x_i} and f_{y_i} are the horizontal and vertical oil film forces of the bearing acted on the ith nodal point of the rotor. When the order of the vector components is rearranged (need not do in practice), to simplify notations, Eq. (1) can be partitioned as

$$\begin{bmatrix} M_a & M_{ab} \\ M_{ab}^T & M_b \end{bmatrix}\begin{Bmatrix} \ddot{z}_a \\ \ddot{z}_b \end{Bmatrix}+\begin{bmatrix} G_a & G_{ab} \\ -G_{ab}^T & G_b \end{bmatrix}\begin{Bmatrix} \dot{z}_a \\ \dot{z}_b \end{Bmatrix}+\begin{bmatrix} K_a & K_{ab} \\ K_{ab}^T & K_b \end{bmatrix}\begin{Bmatrix} z_a \\ z_b \end{Bmatrix} =\begin{Bmatrix} g_a \\ g_b \end{Bmatrix}+\begin{Bmatrix} f_a(z_a,\dot{z}_a) \\ 0 \end{Bmatrix}. \tag{3}$$

If the system has s bearings then z_a, $f_a(z_a,\dot{z}_a)\in R^{n_a}$ $(n_a=2s)$ are of the form

$$z_a=[x_1,y_1,\cdots,x_s,y_s]^T \tag{4}$$

$$f_a(z_a,\dot{z}_a)=\begin{Bmatrix} f_{x_1}(x_1,y_1,\dot{x}_1,\dot{y}_1) \\ f_{y_1}(x_1,y_1,\dot{x}_1,\dot{y}_1) \\ \vdots \\ f_{x_s}(x_s,y_s,\dot{x}_s,\dot{y}_s) \\ f_{y_s}(x_s,y_s,\dot{x}_s,\dot{y}_s) \end{Bmatrix}. \tag{5}$$

Generally only a few bearings are involved in the system, thus Eq. (3) is typically a high-order dynamic system with local nonlinear effects. Since much computing time is needed for a high-order nonlinear system, it is natural to reduce the degrees-of-freedom of the system if the decrease in accuracy of the system responses is small. Nelson et al. [18], Mclean and Hahn [14], Shiau and Jean [15], and Ntaraj and Nelson [16] have dealt with the order reduction techniques to study the periodic responses of the unbalanced rotor with the nonlinear bearing supports. Here a concise and more efficient reduction method for the rotor with the nonanalytical bearing supports is presented.

As shown in Eq. (3), only components of $z_a\in R^{n_a}$ are directly subjected of the nonlinear forces, therefore truncated modal transformation can be used to reduce the degrees-of-freedom of $z_b\in R^{n_b}$ $(n_b=n-n_a)$. In order to get the basis vectors of the transformation, first, the following two eigenproblems are solved:

$$\begin{aligned} K\tilde{\Phi}_A&=M\tilde{\Phi}_A\tilde{\Lambda}_A \\ K_b\Phi_b&=M_b\Phi_b\Lambda_b. \end{aligned} \tag{6}$$

The $n\times n_a$ matrix $\tilde{\Phi}_A$ and $n_b\times n_t$ matrix Φ_b are the two eigenmode matrices with

$$\tilde{\Phi}_A^TM\tilde{\Phi}_A=I,\ \ \tilde{\Phi}_A^TK\tilde{\Phi}_A=\tilde{\Lambda}_A,\ \ \Phi_b^TM_b\Phi_b=I,\ \ \Phi_b^TK_b\Phi_b=\Lambda_b.$$

The $n_a\times n_a$ matrices $\tilde{\Lambda}_A$ and $n_t\times n_t$ Λ_b are the two diagonal eigenvalue matrices.

Expanding Φ_b into $\Phi_B=\begin{bmatrix}0\\ \Phi_b\end{bmatrix}$ one can identify

$$\Phi_B^TM\Phi_B=\Phi_b^TM_b\Phi_b=I.$$

However, Φ_B is not orthogonal to $\tilde{\Phi}_A$, therefore a new vector set Φ_A should be established so that following orthogonal conditions are held:

$$\Phi_B^TM\Phi_A=0\ \text{ and }\ \Phi_A^TM\Phi_A=I.$$

This orthogonal process can be achieved by means of Gram-Schmidt method, namely

$$\tilde{\Phi}_A-\Phi_BE=\Phi_AR$$

where $E=\Phi_B^TM\tilde{\Phi}_A$ and R is an upper triangular matrix. In this way, we obtain the new vector set Φ_A, and then the transformation can be written as

$$\begin{Bmatrix} z_a \\ z_b \end{Bmatrix}=[\Phi_A,\Phi_B]\begin{Bmatrix} u_a \\ u_c \end{Bmatrix}=\begin{bmatrix} \Phi_a & 0 \\ \Phi_{ab} & \Phi_b \end{bmatrix}\begin{Bmatrix} u_a \\ u_c \end{Bmatrix} \tag{7}$$

where $u_a\in R^{n_a}$ and $u_c\in R^{n_t}$. Substitution of Eq. (7) into Eq. (3) and then the left multiplication of $[\Phi_A,\Phi_B]^T$ gives the reduced equations

$$\begin{Bmatrix} \ddot{u}_a(t) \\ \ddot{u}_c(t) \end{Bmatrix}+\begin{bmatrix} \Delta_a & \Theta \\ -\Theta^T & \Delta_b \end{bmatrix}\begin{Bmatrix} \dot{u}_a(t) \\ \dot{u}_c(t) \end{Bmatrix}+\begin{bmatrix} \Lambda_a & \Xi \\ \Xi^T & \Lambda_b \end{bmatrix}\begin{Bmatrix} u_a(t) \\ u_c(t) \end{Bmatrix} =\begin{Bmatrix} q_a(t) \\ q_c(t) \end{Bmatrix}+\begin{Bmatrix} f_a^*(u_a,\dot{u}_a) \\ 0 \end{Bmatrix} \tag{8}$$

where

$$\Delta_a=\Phi_A^TG\Phi_A,\ \ \Delta_b=\Phi_b^TG_b\Phi_b,\ \ \Theta=\Phi_A^TG\Phi_B,$$

$$\Lambda_a=\Phi_A^TK\Phi_A,\ \ \Xi=\Phi_A^TK\Phi_B,$$

$$f_a^*(u_a,\dot{u}_a)=\Phi_a^Tf_a(\Phi_au_a,\Phi_a\dot{u}_a),\ \ q_a=\Phi_A^Tg,\ \ q_c=\Phi_b^Tg_b.$$

Thus, the number of the equations of the system has been reduced from $n(=n_a+n_b)$ to $m(=n_a+n_c)$. It is evident that the nonlinear effects definitely remain while the reduced system still has the form of local nonlinearities, which has an important advantage during the integration procedures.

3 Nonlinear Forces and Jacobians of Journal Bearings

In nonlinear rotordynamics, a short (or long) bearing model is commonly used so that closed form of the bearing forces can be achieved. For the bearings used in practice, however, nonclosed form of the bearing forces can be available and then numerical calculations have to be done. The relax method and finite element method are commonly used to calculate oil film forces of the journal bearing. Nevertheless, since the Jacobians of the bearing forces are also required in the nonlinear analysis, many more calculations have to be involved. There are two methods to calculate the Jacobians (which appeared as the dynamic coefficients). One is the infinitesimal perturbation method ([19–21]) which solves partial derivatives of the Reynolds equation with respect to the journal displacements and velocities. The other is the finite perturbation method ([22,21]), which calculates the Jacobians from finite force differences with respect to the journal displacements and velocities. It is evident that the finite perturbation method is not suitable for the nonlinear system due to its poor accuracy. In this paper an efficient method is presented which calculates the Jacobians of the bearing forces simultaneously with the bearing forces themselves. When the subscripts indicating bearing numbers are ignored, to simplify the notations, the nonlinear forces of one bearing in Eq. (5) can be written as

$$\begin{cases} f_x=f_x(x,y,\dot{x},\dot{y}) \\ f_y=f_y(x,y,\dot{x},\dot{y}) \end{cases}. \tag{9}$$

These forces can be calculated by integrations of oil film pressure on the whole oil fields of the bearing (see, for example, [21]). That is

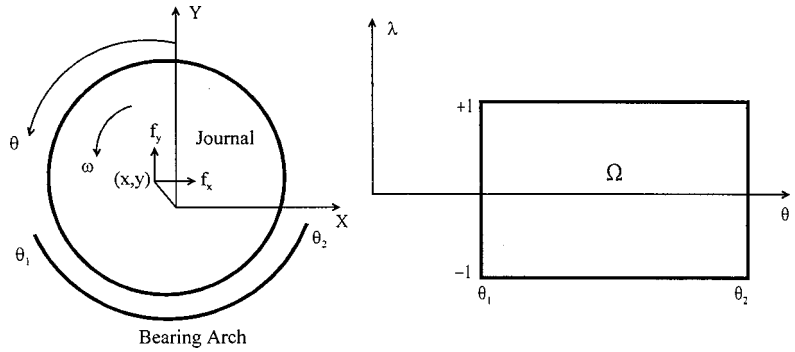

Fig. 1 Sketch showing one bearing arch of a journal bearing

$$f_x(x,y,\dot{x},\dot{y}) = \int\int_\Omega p(x,y,\dot{x},\dot{y}) \cdot \sin\theta d\Omega$$
$$f_y(x,y,\dot{x},\dot{y}) = -\int\int_\Omega p(x,y,\dot{x},\dot{y}) \cdot \cos\theta d\Omega \tag{10}$$

where the pressure function p is governed by the Reynolds equation for laminar flow, Ω is the oil field of the whole bearing, and θ is the angle from the vertical direction to the film location (see Fig. 1). For the bearing used in practice, cavitation of the oil film leads to a Reynolds boundary condition in the Reynolds equation. It was deduced ([23]) that the Reynolds equation with the Reynolds boundary condition is equivalent to following variational inequality: Find $p \in K$ such that

$$a(p,q) \geqslant b(q); \qquad \forall q \in K \tag{11}$$

where

$$a(p,q) = \int\int_\Omega h^3 \left(\frac{\partial p}{\partial \theta}\frac{\partial q}{\partial \theta} + \beta^2 \frac{\partial p}{\partial \lambda}\frac{\partial q}{\partial \lambda} \right) d\Omega \tag{12}$$

is the symmetric and elliptic bilinear form on $H_0^1(\Omega) \times H_0^1(\Omega)$.

$$b(q) = \int\int_\Omega (b \cdot q) d\Omega \tag{13}$$

is the linear functional on dual space of $H_0^1(\Omega)$.

$$K = \{p \in H_0^1(\Omega) | p \geqslant 0 \ \text{ in } \ \Omega\} \tag{14}$$

is the subset of the convex cone of $H_0^1(\Omega)$, which is a Sobolev space.

In the above equations, β is the length-to-diameter ratio of the bearing, the oil film thickens h and variable b can be written as in the dimensionless form

$$h = 1 + x\cos\theta - y\sin\theta$$
$$b = 3(x\cos\theta + y\sin\theta) + 6(\dot{x}\sin\theta + \dot{y}\cos\theta). \tag{15}$$

By means of the finite element method, the function p can be expressed as

$$p = \sum_{i=1}^{n} \tilde{p}_i \psi_i = \tilde{p}^T \psi \ \ (\tilde{p} = [\tilde{p}_1, \tilde{p}_2, \cdots \tilde{p}_n]^T, \psi = [\psi_1, \psi_2, \cdots \psi_n]^T) \tag{16}$$

where $\tilde{p}_i$ and ψ_i $(i = 1,2,\ldots,n)$ are the pressures of the nodal points and global interpolating functions of the finite element, respectively. Substituting Eq. (16) into inequality (11), one obtains the discrete inequality: Find $\tilde{p} \geqslant 0$ such that

$$\tilde{q}^T A \tilde{p} \geqslant \tilde{q}^T B \qquad \forall \tilde{q} \geqslant 0 \tag{17}$$

where $A = [a_{ij}] \in R^{n \times n}$, $B = \{b_i\} \in R^n$. The components of the matrix A and vector B can be calculated by Eqs. (12) and (13), namely

$$a_{ij} = a(\psi_i, \psi_j), \qquad b_i = b(\psi_i).$$

The discrete inequality (17) is equivalent to a linear complementary problem ([23]): find non-negative vectors $\tilde{p}, \tilde{q} \geqslant 0$ such that

$$A\tilde{p} - B = \tilde{q} \ \text{ and } \ \tilde{q}^T \tilde{p} = 0. \tag{18}$$

Using complementary iterations ([24]), Eqs. (18) can be written as

$$\begin{bmatrix} A_{pp} & A_{pq} \\ A_{qp} & A_{qq} \end{bmatrix} \begin{Bmatrix} \tilde{p}_+ \\ 0 \end{Bmatrix} - \begin{Bmatrix} B_p \\ B_q \end{Bmatrix} = \begin{Bmatrix} 0 \\ \tilde{q}_+ \end{Bmatrix} \tag{19}$$

where $\tilde{p}_+, \tilde{q}_+ > 0$. From Eqs. (12), (13), and (15), it can be concluded that A is the function of x, y and B is the function of x, y, $\dot{x}$, $\dot{y}$. Therefore Eq. (19) can be written as

$$\hat{A}(x,y)\tilde{p} = \hat{B}(x,y,\dot{x},\dot{y}) \tag{20}$$

where

$$\hat{A}(x,y) = \begin{bmatrix} A_{pp}(x,y) & 0 \\ 0 & I \end{bmatrix}; \qquad \hat{B}(x,y,\dot{x},\dot{y}) = \begin{Bmatrix} B_p(x,y,\dot{x},\dot{y}) \\ 0 \end{Bmatrix}.$$

After $\tilde{p}$ is solved and substituting Eq. (16) into (10), one obtains

$$f_x(x,y,\dot{x},\dot{y}) = \sum_{i=1}^{n} \tilde{p}_i \cdot s_i = s^T \tilde{p} \qquad (s = [s_1, s_2, \cdots, s_n]^T)$$
$$f_y(x,y,\dot{x},\dot{y}) = \sum_{i=1}^{n} \tilde{p}_i \cdot r_i = r^T \tilde{p} \qquad (r = [r_1, r_2, \cdots, r_n]^T) \tag{21}$$

where

$$s_i = \int\int_\Omega \psi_i \cdot \sin\theta d\Omega, \qquad r_i = -\int\int_\Omega \psi_i \cdot \cos\theta d\Omega. \tag{22}$$

According to Eqs. (21), the Jacobians of f_x and f_y with respect to journal displacements (x, y) and velocities $(\dot{x},\dot{y})$ are

$$\begin{bmatrix} \frac{\partial f_x}{\partial x} & \frac{\partial f_x}{\partial y} \\ \frac{\partial f_y}{\partial x} & \frac{\partial f_y}{\partial y} \end{bmatrix} = \begin{bmatrix} s^T\tilde{p}_x, & s^T\tilde{p}_y \\ r^T\tilde{p}_x, & r^T\tilde{p}_y \end{bmatrix};$$
$$\begin{bmatrix} \frac{\partial f_x}{\partial \dot{x}} & \frac{\partial f_x}{\partial \dot{y}} \\ \frac{\partial f_y}{\partial \dot{x}} & \frac{\partial f_y}{\partial \dot{y}} \end{bmatrix} = \begin{bmatrix} s^T\tilde{p}_{\dot{x}}, & s^T\tilde{p}_{\dot{y}} \\ r^T\tilde{p}_{\dot{x}}, & r^T\tilde{p}_{\dot{y}} \end{bmatrix} \tag{23}$$

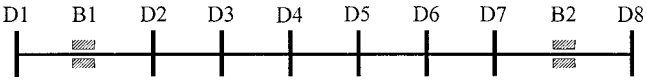

Fig. 2 Sketch of the rotor-bearing system for calculation

Table 1 Mass and Inertia of Disk D1–D8

Disk No.	D1	D2	D3	D4	D5	D6	D7	D8
Mass(kg)	22	30	34	36	38	40	42	22
Inertia(kg·m^2)	0.12	0.62	0.74	0.82	0.98	1.12	1.3	0.12

where $\tilde{p}_x=\partial\tilde{p}/\partial x$, $\tilde{p}_y=\partial\tilde{p}/\partial y$, $\tilde{p}_{\dot{x}}=\partial\tilde{p}/\partial\dot{x}$ and $\tilde{p}_{\dot{y}}=\partial\tilde{p}/\partial\dot{y}$ have to be solved first. Taking partial derivatives of Eq. (20) with respect to x, y, $\dot{x}$, $\dot{y}$ gives the following perturbed equations:

$$\hat{A}[\tilde{p}_x,\tilde{p}_y,\tilde{p}_{\dot{x}},\tilde{p}_{\dot{y}}]=[-\hat{A}_x\tilde{p}+\hat{B}_x,-\hat{A}_y\tilde{p}+\hat{B}_y,\hat{B}_{\dot{x}},\hat{B}_{\dot{y}}] \quad (24)$$

where $\hat{A}_x=\partial\hat{A}/\partial x$, $\hat{A}_y=\partial\hat{A}/\partial y$, $\hat{B}_x=\partial\hat{B}/\partial x$, $\hat{B}_y=\partial\hat{B}/\partial y$, $\hat{B}_{\dot{x}}=\partial\hat{B}/\partial\dot{x}$ and $\hat{B}_{\dot{y}}=\partial\hat{B}/\partial\dot{y}$, the components of which can be obtained by derivation of Eqs. (12) and (13), namely

$$\frac{\partial a_{ij}}{\partial x}=\frac{\partial a(\psi_i,\psi_j)}{\partial x}=3\int\int_\Omega h^2\cos\theta\left(\frac{\partial\psi_i}{\partial\theta}\frac{\partial\psi_j}{\partial\theta}+\beta^2\frac{\partial\psi_j}{\partial\lambda}\frac{\partial\psi_j}{\partial\lambda}\right)d\Omega$$

$$\frac{\partial a_{ij}}{\partial y}=\frac{\partial a(\psi_i,\psi_j)}{\partial y}$$

$$=-3\int\int_\Omega h^2\sin\theta\left(\frac{\partial\psi_i}{\partial\theta}\frac{\partial\psi_j}{\partial\theta}+\beta^2\frac{\partial\psi_i}{\partial\lambda}\frac{\partial\psi_j}{\partial\lambda}\right)d\Omega \quad (25)$$

$$\frac{\partial b_i}{\partial x}=3\int\int_\Omega\psi_i\cos\theta d\Omega,\qquad \frac{\partial b_i}{\partial y}=3\int\int_\Omega\psi_i\sin\theta d\Omega$$

$$\frac{\partial b_i}{\partial\dot{x}}=6\int\int_\Omega\psi_i\sin\theta d\Omega,\qquad \frac{\partial b_i}{\partial\dot{y}}=6\int\int_\Omega\psi_i\cos\theta d\Omega. \quad (26)$$

It is evident that Eqs. (26) need not be recomputed because they resemble Eqs. (22).

The computing works of above algorithm are mainly spent on finding the matrix $\hat{A}$ and vector $\tilde{p}$ by the complementary iterations. Since the perturbed Eq. (24) has the same coefficient matrix $\hat{A}$ as the original Eq. (20), it is evident that few calculation works join when perturbed Eqs. (24) are solved. Therefore, the computing time spent on the Jacobians is much less than those spent on the oil film forces themselves.

4 Integration of the Reduced System

In nonlinear analysis, the responses of the system are commonly integrated by the Runge-Kutta method. However, due to nonanalytical function of the bearing forces being involved, an unconditionally stable algorithm is needed. Otherwise the algorithm will be interrupted because the journal may go out of the bearing at a certain step of the integration procedures. In accordance with the local nonlinearities of Eqs. (8), the Newmark method (see, for example, [25]) is adopted in the following modified form. From time t to $t+\Delta t$, the integration equations can be written as

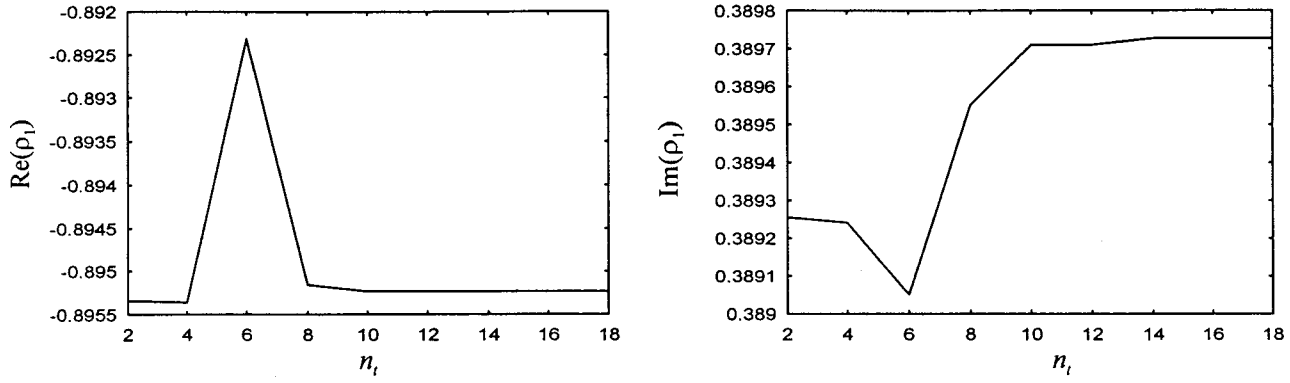

Fig. 3 Leading Floquet multiplier versus n_t for ω 494 rad/s

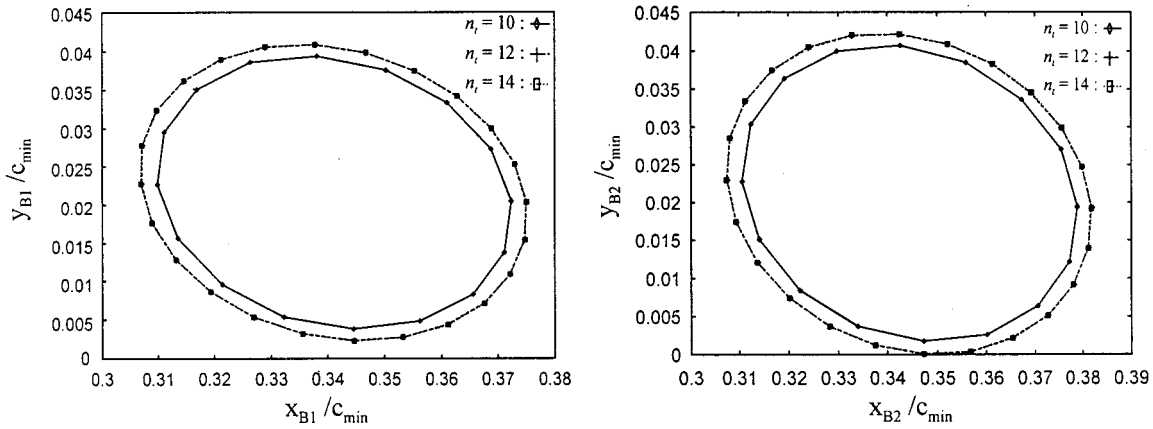

Fig. 4 Journal orbits of two bearing stations calculated by a different reduced model for $\omega=494$ rad/s

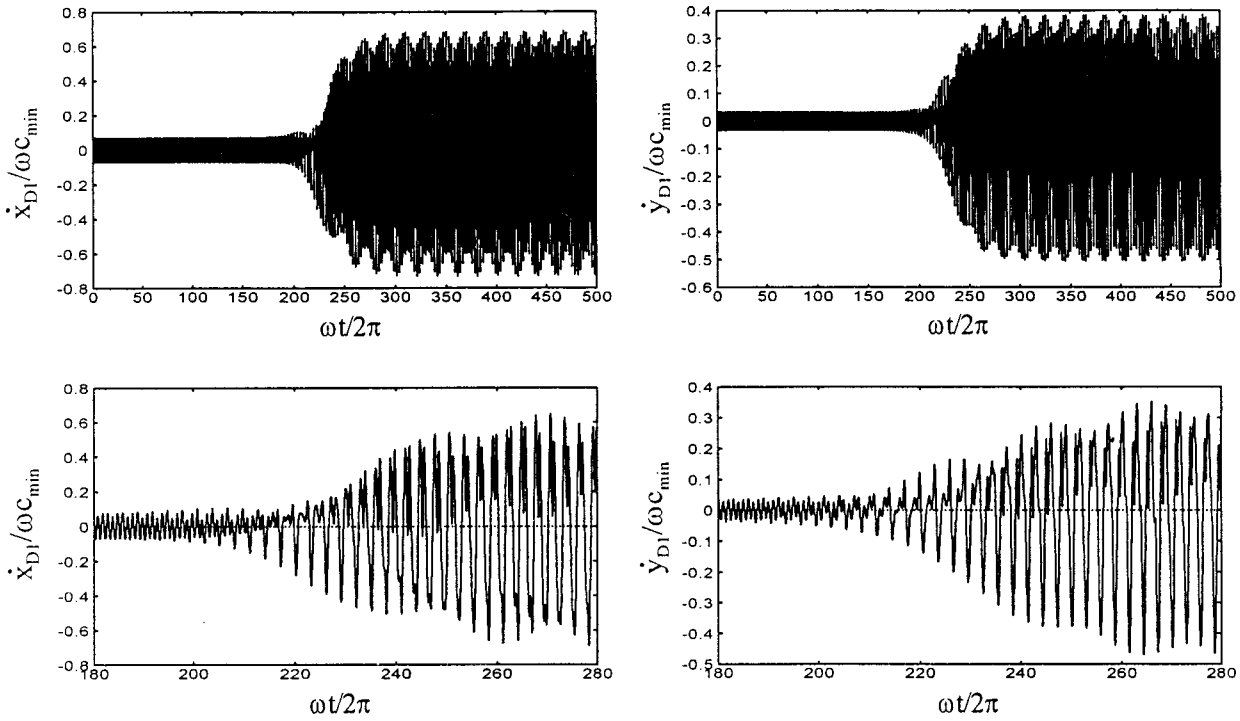

Fig. 5 A jump phenomenon—showing time series of velocities of station D1 for $\omega = 6720$ rad/s

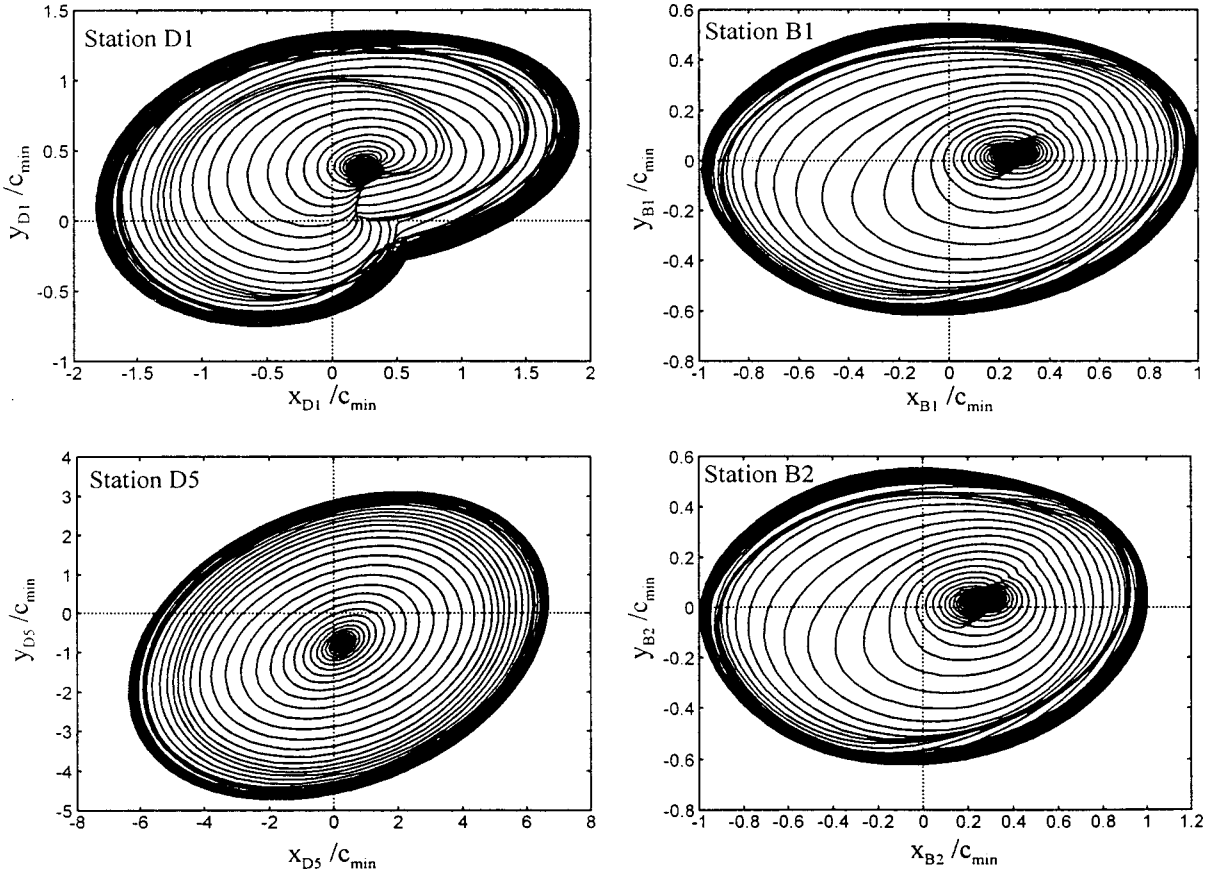

Fig. 6 A jump phenomenon—showing journal orbits of station D1, B1, D5, and B2 for $\omega = 6720$ rad/s

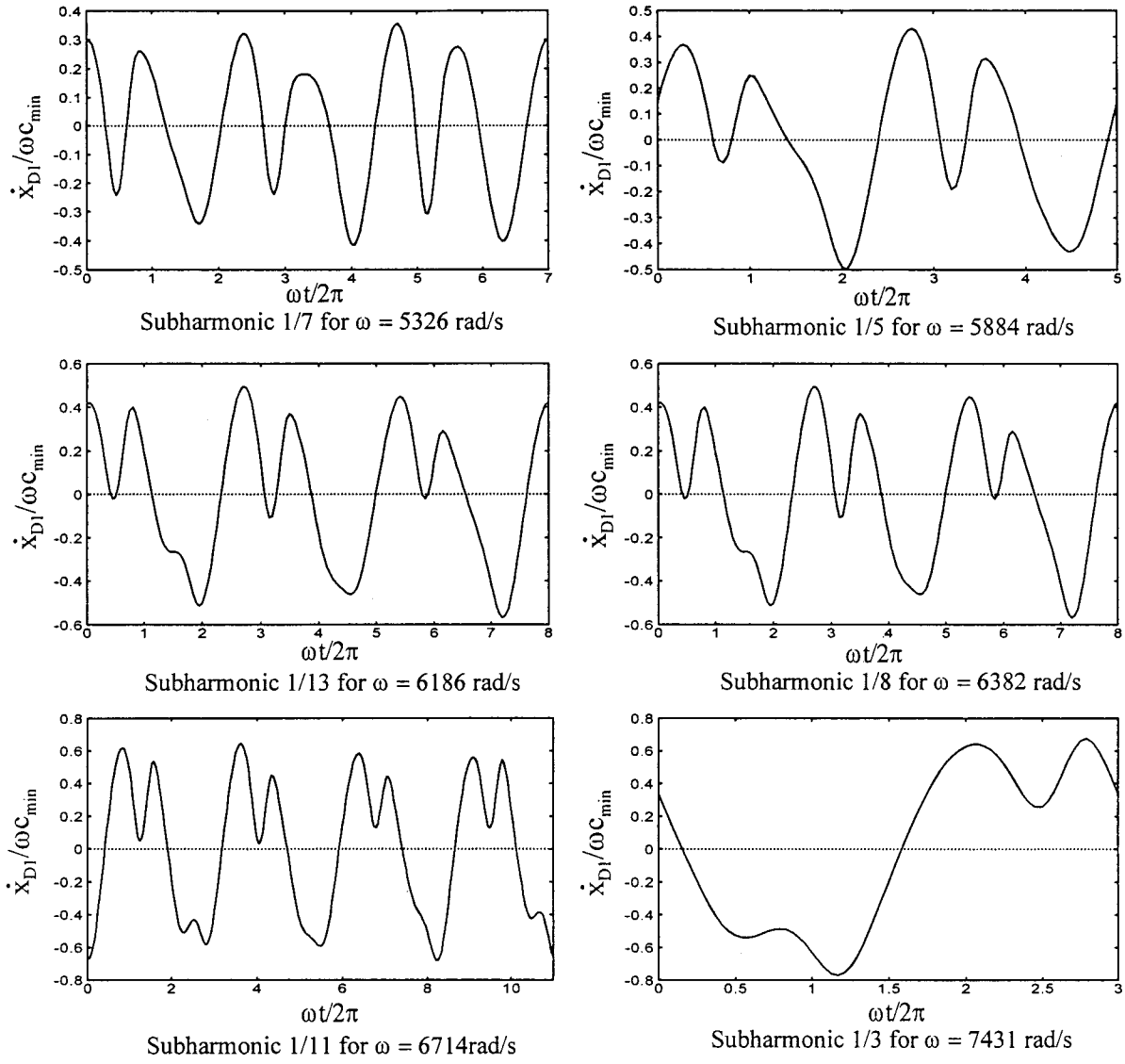

Fig. 7 Wave lines of horizontal velocity of station D1 for several subharmonic motions

$$\begin{bmatrix} \tilde{\Lambda}_a & \tilde{\Xi} \\ \tilde{\Xi}^* & \tilde{\Lambda}_b \end{bmatrix} \begin{Bmatrix} u_a^{t+\Delta t} \\ u_c^{t+\Delta t} \end{Bmatrix} = \begin{Bmatrix} \tilde{q}_a^t \\ \tilde{q}_c^t \end{Bmatrix} + \begin{Bmatrix} \tilde{f}_a(u_a^{t+\Delta t}) \\ 0 \end{Bmatrix} \tag{27}$$

where

$$\begin{bmatrix} \tilde{\Lambda}_a & \tilde{\Xi} \\ \tilde{\Xi}^* & \tilde{\Lambda}_b \end{bmatrix} = \begin{bmatrix} \Lambda_a + \frac{1}{\alpha\Delta t^2} I + \frac{1}{\alpha\Delta t}\Delta_a & \Xi + \frac{1}{\alpha\Delta t}\Theta \\ \Xi^T - \frac{1}{\alpha\Delta t}\Theta^T & \Lambda_b + \frac{1}{\alpha\Delta t^2} I + \frac{1}{\alpha\Delta t}\Delta_b \end{bmatrix},$$

$$\begin{Bmatrix} \tilde{q}_a^t \\ \tilde{q}_c^t \end{Bmatrix} = \begin{Bmatrix} q_a^t - \ddot{\tilde{u}}_a^t - \Delta_a \dot{\tilde{u}}_a^t - \Theta \ddot{u}_c^t \\ q_c^t - \ddot{\tilde{u}}_c^t - \Delta_b \dot{\tilde{u}}_c^t + \Theta^T \ddot{u}_a^t \end{Bmatrix} \tag{28}$$

$$\tilde{f}_a(u_a^{t+\Delta t}) = f_a^*(u_a^{t+\Delta t}, b u_a^{t+\Delta t} + \dot{\tilde{u}}_a^t)$$

and where $0.5 < \delta \leqslant 1$, $\alpha \geqslant 0.25(0.5+\delta)^2$ are the control parameters to get a stable algorithm (this study chooses $\alpha = 0.5$, $\delta = 1$) and

$$\begin{cases} \ddot{\tilde{u}}_k^t = -\dfrac{1}{\alpha\Delta t^2} u_k^t - \dfrac{1}{\alpha\Delta t}\dot{u}_k^t - \left(\dfrac{1}{2\alpha} - 1\right)\ddot{u}_k^t \\ \dot{\tilde{u}}_k^t = -\dfrac{\delta}{\alpha\Delta t} u_k^t - \left(\dfrac{\delta}{\alpha} - 1\right)\dot{u}_k^t - \left(1 - \dfrac{\delta}{2\alpha}\right)\Delta t \ddot{u}_k^t \end{cases} \quad (k = a, c). \tag{29}$$

Equations (27) are the nonlinear algebraic equations, so iterations are required. Since the nonlinear terms in Eqs. (27) are only related to $u_a^{t+\Delta t}$, the iterating efficiency can be improved greatly. In fact, the following n_a order of equations can be turned from Eqs. (27),

$$\hat{\Lambda}_a u_a^{t+\Delta t} = \hat{q}_a^t + \tilde{f}_a(u_a^{t+\Delta t}), \tag{30}$$

where $\hat{\Lambda}_a = \tilde{\Lambda}_a - \tilde{\Xi}\tilde{\Lambda}_b^{-1}\tilde{\Xi}^*$, $\hat{q}_a^t = \tilde{q}_a^t - \tilde{\Xi}\tilde{\Lambda}_b^{-1}\tilde{q}_c^t$. The Newton-Raphson method gives the following iterating procedures:

$$\begin{aligned} u_{a,k+1}^{t+\Delta t} &= u_{a,k}^{t+\Delta t} - [D_{u_a}\tilde{f}_a(u_{a,k}^{t+\Delta t}) - \hat{\Lambda}_a]^{-1} \\ &\quad \times (\hat{q}_a^t + \tilde{f}_a(u_{a,k}^{t+\Delta t}) - \hat{\Lambda}_a u_{a,k}^{t+\Delta t}) \\ u_{a,0}^{t+\Delta t} &= u_a^t, \qquad (k = 1,2,\cdots) \end{aligned} \tag{31}$$

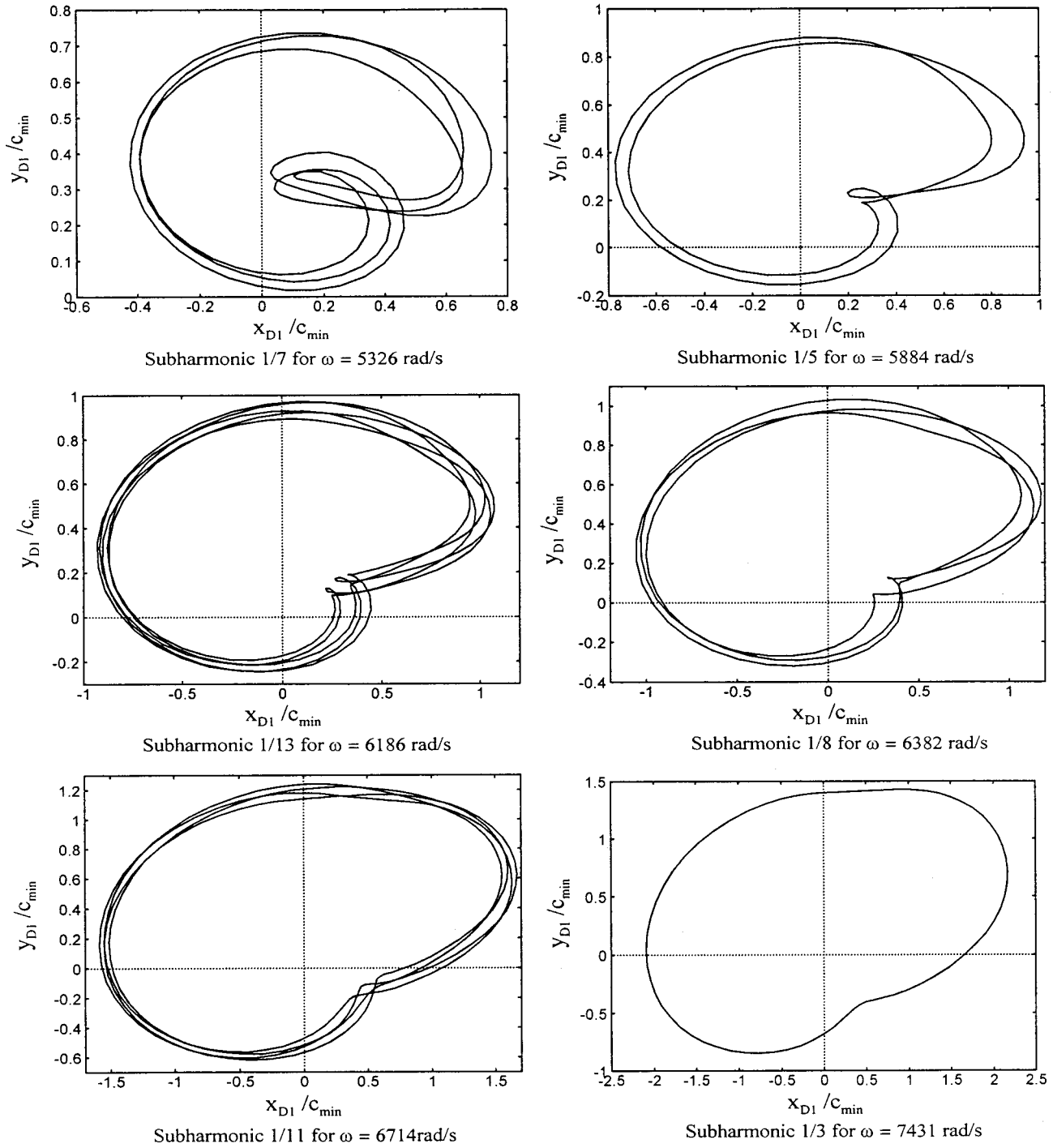

Fig. 8 Orbits of station D1 for several subharmonic motions

where

$$D_{u_a}\tilde{f}_a(u_a)=\Phi_a^T\left(\frac{\partial f_a(z_a,\dot{z}_a)}{\partial z_a}+b\,\frac{\partial f_a(z_a,\dot{z}_a)}{\partial \dot{z}_a}\right)\Phi_a\,. \tag{32}$$

Once $u_a^{t+\Delta t}$ is obtained, $u_c^{t+\Delta t}$ can be easily calculated by the following linear equations:

$$\tilde{\Lambda}_b u_c^{t+\Delta t}=\tilde{q}_c^t-\tilde{\Xi}*u_a^{t+\Delta t}. \tag{33}$$

When the gyroscope matrix is ignored, $\tilde{\Lambda}_b$ is diagonal, and then computing works can be greatly saved.

By means of the above technique the nonlinear iterations only need to be executed on the n_a dimensional scale. So not only the quantity of the calculations for each iteration step is saved but also the iteration steps for the convergence are decreased greatly. In contrast with the Runge-Kutta method, this method is much more stable and efficient for the present system.

For unbalance responses of the rotor system (1), the external force vector is of the form

$$g(t)=w+g_c\cos\omega t+g_s\sin\omega t \tag{34}$$

where w is a constant vector (mostly generated by gravity or gear forces), g_c, g_s are the unbalance force vectors, and ω is the rotating speed of rotor. So Eq. (8) is a periodic system with period $T=2\pi/\omega$. The periodic responses of the system can be computed

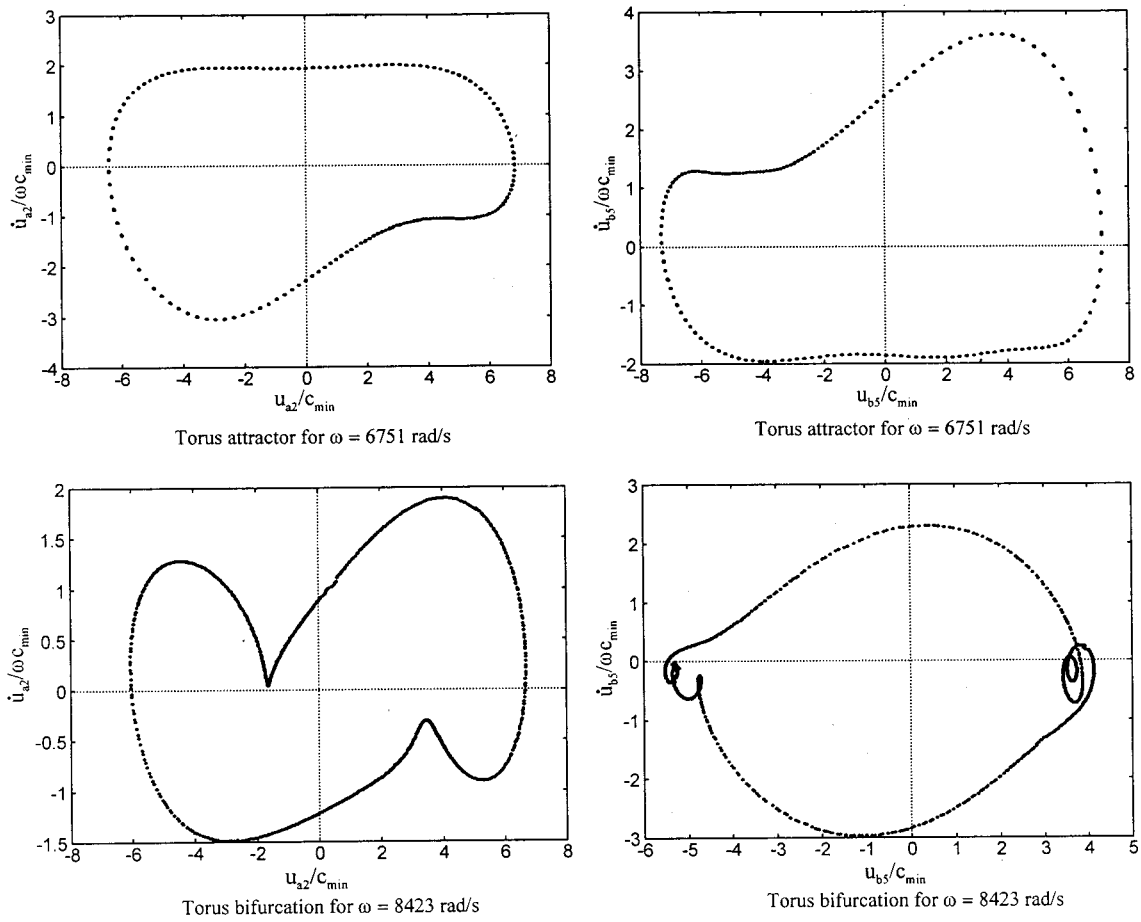

Fig. 9 Torus and torus bifurcation—second and ninth-order of modal phase plains of Poincaré map

by the shooting method and the stability of the responses can be determined by their characteristic multipliers, the so-called Floquet multipliers ([26]).

5 Numerical Examples and Results

The unbalance response of a rotor with eight rigid disks (noted D1–D8) and two bearings (noted B1 and B2) was analyzed numerically (see Fig. 2). The shaft (diameter 0.2 m, length 3.6 m, mass density 7850 kg/m^3, Young's modulus 2.06×10^{11} N/m^2, and shear modulus 8.24×10^{10} N/m^2) is equally separated by disks and bearings and each interval is divided into four finite elements. So the finite element model of the system has 37 nodes and two of them are supported by nonlinear bearings. Two elliptical bearings (pad arch: 160 deg, length-to-diameter ratio: 0.6, clearance to radius ratio: 0.003, elliptical ratio: 0.4, and oil viscosity: 0.022 N·sec/m^2) are used at B1 and B2 stations. The mass properties of eight disks are listed in Table 1. Three unbalance values (having total mass of rotor, 1-μm eccentricity, and the same rotating phase angle) are located at the D1, D5, and D8 stations. The calculated results are shown in the dimensionless form. The related unit of time, displacement, and velocity are $2\pi/\omega$, $c_{\min}$, and $\omega c_{\min}$ where ω is rotating speed of rotor and $c_{\min}$ is the top clearance of the elliptical bearing.

It is evident that the accuracy of the calculated results depends on how many eigenmodes are taken in the reduced model. In our case, the system has 148 degrees-of-freedom and four of them are directly affected by nonlinear forces ($n=148, n_a=4$). So the degrees-of-freedom of the reduced system depends on n_t, the number of the second set of eigenmodes (see Section 2, the degrees-of-freedom of the reduced system are $m=n_a+n_t$). Taking the rotating speed as $\omega=494$ rad/s, the periodic solutions of the unbalanced system were calculated for several values of n_t. Figure 3 shows leading Flouqet multiplier (noted ρ_1) against n_t. Figure 4 shows journal orbits at two bearing stations for some different n_t. It is seen from these two figures that the accuracy of the results increases as more eigenmodes are taken in the reduced model and reaches high precision when $n_t=12$, since the results of $n_t=12$ and 14 are almost identical. This is because higher order modes are nearly unexcited by the unbalance forces. Therefore, in the following calculations, the 16 degree-of-freedom reduced system is accepted and the modal displacements are arranged in the order $u_{a1}, u_{a2}, u_{a3}, u_{a4}, u_{b1}, \ldots, u_{b12}$.

It should be pointed out that by the present method the computing process is carried out smoothly, no matter how many steps are taken in one period although the nonclosed form of the bearing forces are used. However, if the Runge-Kutta method is used, the integration process will be interrupted unless many more steps (depend on forcing frequency and the highest natural frequency of the reduced system) are taken in one period.

The unbalance responses of the system loses stability as rotating speed increases to 5171 rad/s when two complex conjugate Floquet multipliers leave the unit circle transversely. So a quasi-periodic bifurcation appears ([27]). Beyond the bifurcation point unbalance responses become unstable. A jump phenomenon, which typically occurs in a nonlinear system, is detected for $\omega=6720$ rad/s. In Fig. 5, the time series of the velocities at station D1 appears to suddenly jump from a low level of unstable periodic response to a high level of stable quasi-periodic response. Figure 6 shows the jump figures of the journal orbits at stations D1, B1, D5, and B2, respectively.

Apart from the jump phenomena, the system shows a various

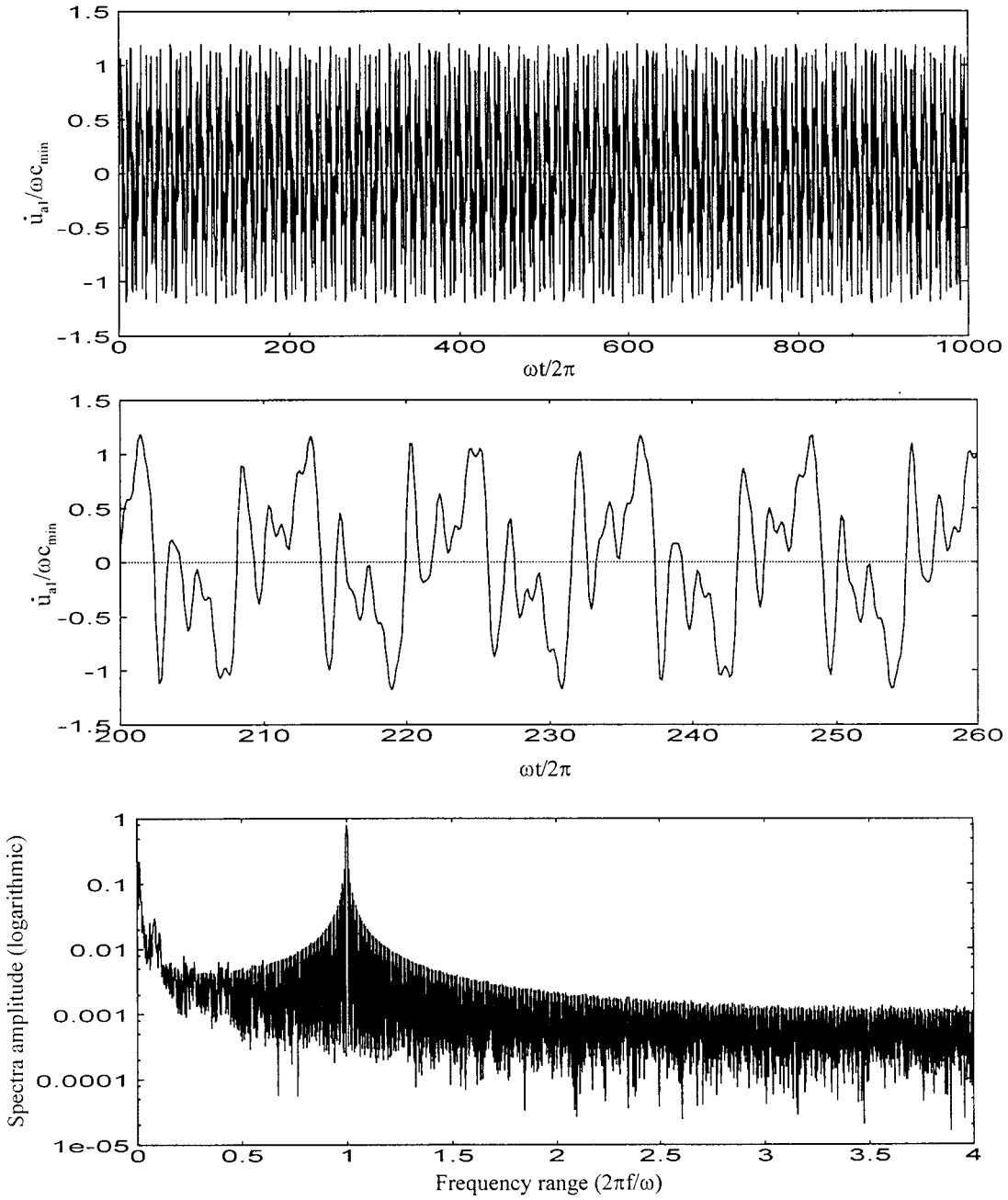

Fig. 10 Time series and corresponding FFT spectrum of first order of modal velocity for a chaotic state ($\omega = 12623$ rad/s)

order of subharmonic responses as well as quasi-periodic responses. Figures 7 and 8 give the horizontal velocity responses and orbits of one nodal point (station D1) for the subharmonic (1/7, 1/5, 1/13, 1/8, 1/11, and 1/3) motions. This phenomenon of subharmonic motions, in which the ratio of the forced frequency and the response frequency becomes rational, is called phase locking or mode locking ([27]). In fact, in the frequency range 5174–11340 rad/s a large number of closed branches of subharmonic motions (locked states), occurring in very tiny frequency intervals, can be found. Comparing to subharmonic motions, quasi-periodic responses are more frequently encountered in that frequency range. The quasi-periodic solution for $\omega = 6751$ rad/s appears a torus attractor in Poincaré section, and as ω increases to 8423 rad/s, a torus bifurcation happens ([28]). Figure 9 shows projections of Poincaré maps onto the two typical modal phase plains of these torus and torus bifurcation figures.

Finally, as rotating speed reaches to $\omega = 12623$ rad/s, a chaotic motion appears (Lyapunov exponents: $\lambda_1 = +1.36$, $\lambda_2 = 0, \lambda_3, \ldots < 0$; [26]). This chaotic state is illustrated by the time series of the first order of modal velocity and corresponding FFT spectrum (see Fig. 10). Logarithmic plot for FFT spectrum is used to highlight components with low power levels—an impotent feature of chaotic spectra. The time series is obviously irregular. The FFT spectrum is broadband, and contains substantial power at low frequencies. A sharp component at $\omega/2\pi$ is also present. Though a broad spectrum does not guarantee sensitivity to initial conditions, it is, in practice, a reliable indicator of chaos ([29]). Figure 11 shows trajectory of four typical modal phase plains, which present very beautiful patterns—a typical characteristic of a strange attractor.

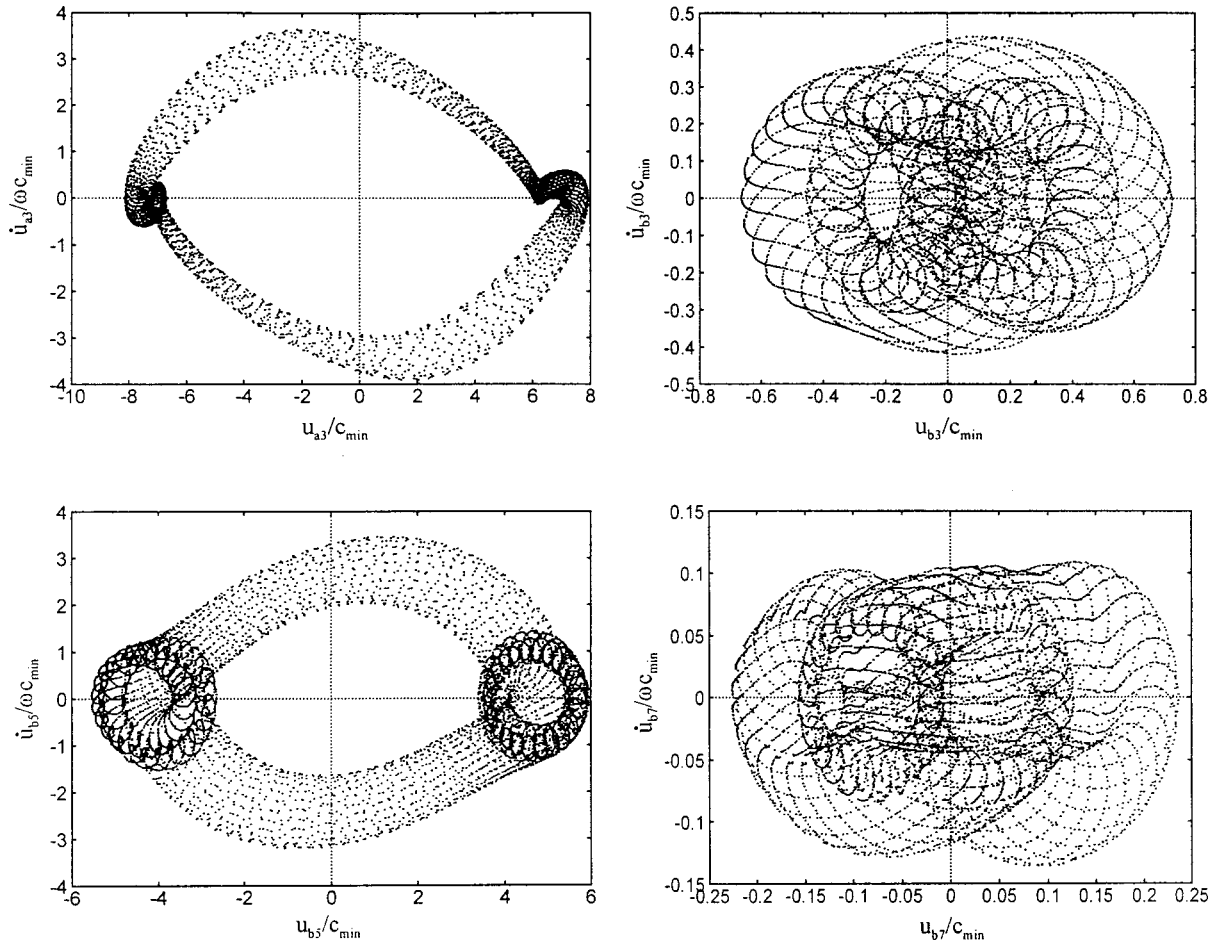

Fig. 11 Chaotic motion—trajectory of four typical order of phase plains for $\omega = 12623$ rad/s

6 Conclusion

By a hybrid of two sets of eigenmodes of a rotor-bearing system a new modal reduction technique was presented. The advantages of the reduction model are that not only the degrees-of-freedom of the system are greatly reduced but also the nonlinear terms in the reduced modal system remain the local features. A modified Newmark method, which is more suitable for the present system than the Runge-Kutta method, is developed to integrate the responses of the system. The new method is unconditionally stable and the nonlinear iterations only need to be executed on the equations related to the nonlinear forces. Since the number of the nonlinear forces are very small compared to the number of system equations, the new method saves significant computing time.

Since, for a rotor used in practice, the bearing forces cannot get the closed form, the nonlinear forces and Jacobians of them have to be calculated numerically. These calculations will take a great deal of computing time and cause accuracy problems. Based on the theory of variational inequalities and the finite element method, a new method is presented to calculate the Jacobians of the bearing forces and bearing forces themselves simultaneously. The algorithm is concise and the computing efforts spent on Jacobians are very small compared to those spent on the bearing forces themselves.

The numerical schemes of this study are applied to a large-order flexible rotor system with eight rigid disks and two elliptical bearings supports. The rotor is divided 36 finite elements, and then a discrete system with 148 degree-of-freedom and four nonlinear bearing forces is obtained. The numerical results show that a 16 degree-of-freedom reduced model gives satisfactory accuracy while the computing efforts are cut down greatly. A quasi-periodic bifurcation was found for a group of bearing parameters. After the bifurcation point a jump phenomenon was detected and the system appears a large number of closed branches of subharmonic motions (mode locking cases) occurring in very tiny frequency (rotating speed) intervals. As the rotating speed increases, the system undergoes torus, mode locking, torus bifurcation states, and finally goes to chaos.

Acknowledgment

This work was partly supported by the Chinese National Key Basic Research Special Fund (No. G1998020316).

References

[1] Yamamoto, T. T., 1954, ''On critical Speeds of a Shaft,'' Mem. Fac. Eng., Nagoya Univ. (Japan), **6**, No. 2.
[2] Bently, D., 1974, ''Forced Subrotative Speed Dynamic Action of Rotating Machinery,'' ASME Paper No. 74-PET-16, Petroleum Mechanical Engineering Conference, Dallas. Texas.
[3] Childs, D. W., 1982, ''Fractional-Frequency Rotor Motion due to Nonsymmetric Clearance Effects,'' ASME J. Eng. Gas Turbines Power, **104**, pp. 533–541.
[4] Choi, S. K., and Noah, S. T., 1992, ''Response and Stability Analysis of Piecewise-Linear Oscillators Under Multi-forcing Frequencies,'' Nonlinear Dyn., **3**, pp. 105–121.
[5] Yamauchi, S., 1983, ''The Nonlinear Vibration of Flexible Rotors, 1st Report, Development of a New Technique,'' JSME, **49**, pp. 1862–1868.
[6] Ehrich, F. F., 1988, ''High Order Subharmonic Response of High Speed Rotors in Bearing Clearance,'' ASME J. Vibr. Acoust., **110**, pp. 9–16.
[7] Childs, D. W., 1984, ''Rotordynamic Characteristics of HPOPT (High Pressure Oxygen Turbopump) of the SSME (Space Shuttle Main Engine),'' Turbomachinery Laboratories Report (Texas A&M Univ.), FDI-84.
[8] Kim, Y. B., and Noah, S. T., 1990, ''Bifurcation Analysis for a Modified Jaffcott Rotor With Bearing Clearance,'' Nonlinear Dyn., **1**, pp. 221–241.

[9] Brancati, R., Rocca, E., Rosso, M., and Rosso, R., 1995, ''Journal Orbits and Their Stability for Rigid Unbalanced Rotors,'' ASME J. Tribol., **117**, pp. 709–716.
[10] Della Pietra, L., De Rosa, E., and Rossi, C., 1991, ''Static and Dynamic Behavior of a Rigid Rotor on Journal Bearings,'' Meccanica, **26**, pp. 229–245.
[11] Lund, J. W., and Nielson, H. B., 1980, ''Instability Threshold of an Unbalanced Rigid Rotor in Short Journal Bearings,'' *Second International Conference on Vibration in Rotating Machinery*, Cambridge, UK.
[12] Choi, S. K., and Noah, S. T., 1994, ''Mode-Locking and Chaos in a Jeffcott Rotor With Bearing Clearance,'' ASME J. Appl. Mech., **61**, pp. 131–138.
[13] Day, W. B., 1987, ''Asymptotic Expansions in Nonlinear Rotordynamics,'' Q. Appl. Mech., **44**, pp. 779–792.
[14] Mclean, L. J., and Hahn, E. J., 1983, ''Unbalance Behavior of Squeeze Film Damped Multi-Mass Flexible Rotor Bearing System,'' ASME J. Lubr. Technol., **105**, pp. 22–28.
[15] Shiau, T. N., and Jean, A. N., 1990, ''Prediction of Steady State Response of Flexible Rotor System With Nonlinear Supports: A New Technique,'' ASME J. Vibr. Acoust., **112**, pp. 501–507.
[16] Nataraj, C., and Nelson, H. D., 1989, ''Periodic Solutions in Rotor Dynamic System With Nonlinear Supports: A General Approach,'' ASME J. Vibr. Acoust., **111**, pp. 187–193.
[17] Nelson, H. D., 1980, ''A Finite Rotating Shaft Element Using Timoshenko Beam Theory,'' ASME J. Mech. Des., **102**, pp. 793–803.
[18] Nelson, H. D., Mechan, W. L., Fleming, D. P., and Kascak, A. F., 1983, ''Nonlinear Analysis of Rotor Bearing System Using Component Mode Synthesis,'' ASME paper No. 83-GT-303.
[19] Lund, J. W., and Thomson, K. K., 1978, ''A Calculation Method and Data for the Dynamic Coefficients of Oil-Lubricated Journal Bearings,'' *Topics in Fluid Journal Bearing and Rotor Bearing Syst.*, ASME, New York, pp. 1–28.
[20] Klit, P., and Lund, J. W., 1986, ''Calculation of the Dynamic Coefficients of a Journal Bearing, Using a Variational Approach,'' ASME J. Tribol., **108**, pp. 421–425.
[21] Someya, T., 1989, *Journal Bearing Data Book*, Springer-Verlag, Berlin.
[22] Choy, F. K., Braun, M. J., and Hu, Y., 1991, ''Nonlinear Effects in a Plain Journal Bearing: Part 1—Analytical Study; Part 2—Results,'' ASME J. Tribol., **113**, pp. 555–570.
[23] Kinderlenhrer, D., and Stanpacchia, G., 1980, *An Introduction to Variational Inequalities and Their Applications*, Academic Press, New York.
[24] Zheng, T., Li, L., and Xu, Q., 1995, ''An Iterative Method for the Discrete Problems of a Class of Elliptical Variational Inequalities,'' Chin. J. Appl. Math. Mech., **16**, pp. 351–358 (English edition).
[25] Bathe, K., and Wilson, E., 1976, *Numerical Methods in Finite Element Analysis*, Prentice-Hall, Englewood Cliffs, NJ.
[26] Parker, T. S., and Chua, L. O. 1989, *Practical Numerical Algorithms for Chaotic System*, Springer-Verlag, New York.
[27] Seydel, R., 1988, *From Equilibrium to Chaos, Practical Bifurcation and Stability Analysis*, Elsevier, New York.
[28] Tufilaro, N. B., Abbortt, T., and Jeremiah, R., 1992, *An Experimental Approach to Nonlinear Dynamics and Chaos*, Addison-Wesley, Reading, MA.
[29] Baker, G. L., and Gollub, J. P., 1990, *Chaotic Dynamics: An Introduction*, Cambridge University Press, Cambridge, UK.

T. Farquhar[1]
Assistant Professor,
Department of Mechanical Engineering,
University of Maryland,
Baltimore, MD 21250
e-mail: farquhar@umbc.edu
Mem. ASME

J. Z. Wood
Northrop Grumman Corporation,
Baltimore, MD

J. van Beem
International Center for Maize and Wheat
Improvement,
Mexico

The Kinematics of Wheat Struck by a Wind Gust

A nonlinear model of the kinematics of a wheat stalk struck by a wind gust is developed. Individual stalks were excited from each of many directions and observed by videophotography. The underdamped flexural response involved anisotropic circling motion that can be reproduced by a nonlinear system of ODEs. In the model, the horizontal path traveled by the grain mass is described in principal coordinates X_I and X_{II}. The four required constants are stiffnesses $k_I < k_{II}$ in these directions, linear viscous damping ζ, and coupling strength β related to a torque imposed by wind drag. This stem torque can cause nonlinear coupling if both X_I and X_{II} are excited and if $k_I \neq k_{II}$, such that damping can vary by 30 percent over each cycle. The directionality of the single stalk may promote interplant collision, which could have important integrated effects on crop behavior at larger size scales. [S0021-8936(00)02303-5]

Introduction

Wind and gravity are the dominant forces acting on most terrestrial plant species ([1,2]). Structural failures that permanently displace a cereal crop from the vertical are called *lodging* ([3–6]). Lodging can inhibit crop development, promote fungal infection, and complicate harvesting ([7]). Modern cereal crops grown with high fertilizer inputs are often more susceptible to lodging than older varieties grown by traditional methods ([8–10]). Steady improvement of lodging resistance is an important priority in wheat breeding science ([11]). Lodging reduces grain yield 10 to 30 percent worldwide ([12]). Even the lower estimate is a significant fraction of total human caloric intake, and lodging is a major limiting factor on global food production.

Lodging is typically precipitated by wind combined with rain or irrigation ([7]). The particular structural failure may involve buckling or splitting of the lower stem ([13]), or rotation of the root relative to the soil ([14,15]). In either case, the driving force is the drag exerted on the grain mass at the top of the slender stem ([16]). Wind tunnel study has shown that velocity profiles near the surface of a model canopy are similar to a plane mixing layer ([17,18]). The turbulent flow is dominated by intermittent horizontal eddies and mean velocity drops rapidly closer to the ground ([19]). The top of each stalk is subjected to successive impulse loads from varying directions.

Wheat is a member of the monocot or grass family ([20]). A maturing plant consists of one or more tillers (stalks) growing from a single root (Fig. 1). The hollow culm (stem) is nodally segmented and supports an inflorescence called the spike. This grain bearing organ is typically covered with needle-like structures called awns. Each of the several leaves has a tubular base that ensheathes and supports the stem. The spike increases in size and mass as the tiller matures. This increases wind drag, and presumably, increases lodging tendency ([16]). There are observable differences in the lodging resistance of different varieties of wheat ([14,21]). In addition, environmental factors affect the lodging resistance of each variety to varying degrees ([15,22]). In practice, wheats with short stiff stems are often more resistant to stem buckling ([8–11]) while wheats with compliant stems may be less susceptible to root lodging in weak or water-saturated soils. Wheat scientists must balance the competing constraints imposed by stem rigidity and flexibility in order to select the best varieties for a given growing environment.

The ultimate goal of this research is to use applied mechanics to quantify the interaction between the atmospheric boundary layer and wheat. Surface winds can induce large-scale plant motions called *honami* ([23]). Similar phenomena can be induced by tidal currents passing over submerged aquatic vegetation ([24]). In both cases, the synchronous aeroelastic (or hydrodynamic) canopy behaviors ([25]) involve coherent phase-separated vibration of many plant stalks ([17]). The physics of these wave-like motions, and their possible relationship to lodging, are not fully understood. We can begin to address this issue by examining the kinematics of wheat at a smaller size scale. The objective of this study was to develop a model of a single stalk struck by a gust from an arbitrary angle.

Methods

Standard horticulture was used to grow two varieties of wheat using seed obtained from the International Center for Maize and Wheat Improvement, in Mexico. All plants were grown in a climate-controlled glasshouse at the USDA-ARS Research Center in Beltsville, MD. Both varieties are suitable for irrigated environments although *Baviacora* is more resistant to lodging than *Bacanora* ([21]). Planting density was equivalent to 400 seeds per square meter. The growing medium was a 4:1 clay soil and sand mixture. Natural light was supplemented with artificial lighting and cooling to obtain 14-hour photoperiod and 22°C nighttime temperature.

The free-vibration response of selected tillers was observed using videophotography. All tests were conducted on maturing plants at the timepoint called dough development or Growth Stage 83-85 ([26]). A straight stalk was chosen from each of ten pots per variety. All leaves were clipped close to the stem, and white tracking markers were painted on the nodes and spike. The other tillers in the same pot were cut at the ground level. The pot was draped with black cloth to minimize background clutter.

The tiller was subjected to a series of impulse tests. The test apparatus consisted of a high-pressure air source (scuba tank), a pressure regulator, a computer-controlled valve, and a special pneumatic gun (Fig. 2). The gun discharged a horizontal pulse or gust from a 2-mm-diameter nozzle. Flow visualization using water droplets showed the flow expanding within a 12-deg conical envelope as it traveled towards the tiller. The gun was aimed at the spike from a standoff distance of 0.50 m to ensure that the tiller did not hit the gun on its return swing. A Macintosh PM

[1]To whom correspondence should be addressed.

Contributed by the Applied Mechanics Division of THE AMERICAN SOCIETY OF MECHANICAL ENGINEERS for publication in the ASME JOURNAL OF APPLIED MECHANICS. Manuscript received by the ASME Applied Mechanics Division, July 30, 1999; final revision, Feb. 4, 2000. Associate Technical Editor: N. C. Perkins. Discussion on the paper should be addressed to the Technical Editor, Professor Lewis T. Wheeler, Department of Mechanical Engineering, University of Houston, Houston, TX 77204-4792, and will be accepted until four months after final publication of the paper itself in the ASME JOURNAL OF APPLIED MECHANICS.

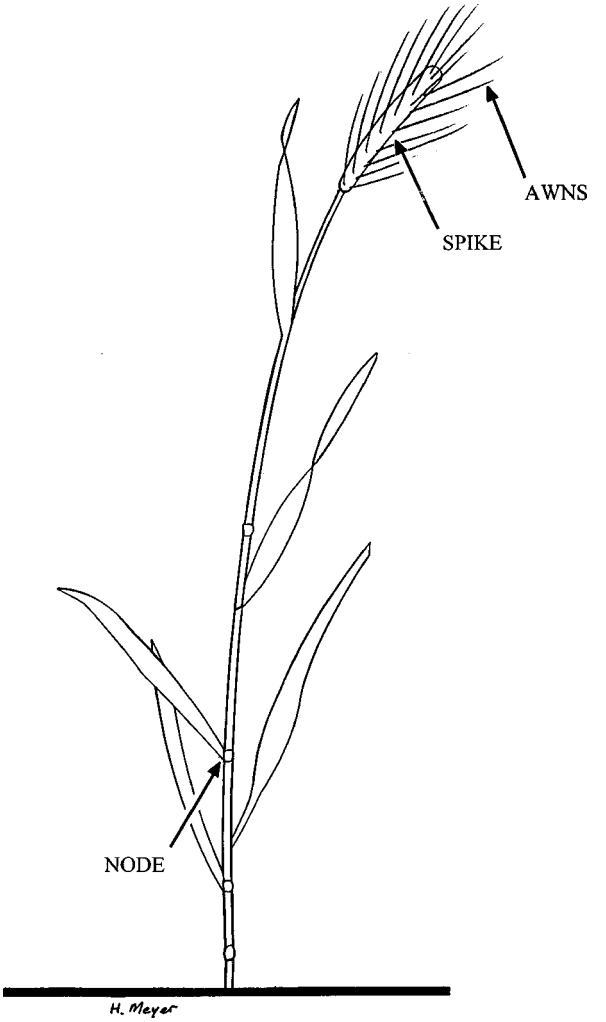

Fig. 1 Key structures of a single wheat stalk

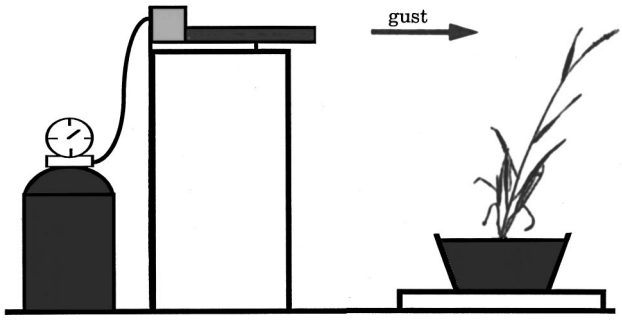

Fig. 2 Camera view of synthetic gust test apparatus

7100 computer with National Instruments data acquisition boards used LabView software to regulate the number, duration, and spacing of the gusts. In practice, four identical 0.250-second gusts were delivered at 25-second intervals for each angle. Each gust produced an underdamped flexural oscillation that was similar to the response observed in the field on a breezy day (i.e., 5–10 m/s winds). By convention, the x-axis was aligned with the gust, the y-axis was at right angles to the x-axis in the horizontal plane, and the z-axis was vertical.

The kinematic response was monitored by a tripod-mounted S-VHS video camera (Sony #SSC-S20). Referring to Fig. 2, the camera viewed the potted plant beneath a plane mirror inclined at 45 deg (the mirror is not shown). The setup allowed the camera to record the underdamped plant vibration in sideview ($x-z$) or in the topview ($x-y$) reflected by the overhead mirror. Each tiller was brightly illuminated by 500-W Fresnell lens stage lamps. A pinhole iris was used to maximize depth of field. The 480×640 pixel image was tightly framed using an electric zoom lens (Rainbow #M-II with #A-III controller). The video capture rate was 60 frames per second. The shutter speed was 0.001 second.

Tiller orientation relative to the gust was varied by rotating the pot. Tests were performed at each of 24 orientations at 15-deg increments relative to an arbitrary reference marked on the pot. In practice, the projected motion seen in the horizontal image plane captured the essential features of the underdamped transient.

Pilot study showed that the path in duplicate tests was reproducible within one or two pixels, so only one typical test was analyzed at each angle. A digital copy of the first five seconds of motion was made using a Sony Time-lapse VCR player (#SVT-S3100). The A/D conversion was performed using the built-in digitizer on a Macintosh PM 8600 computer. A digital clip for each angle was saved as a TIFF stack of 300 fields (60 MB per stack). The first field in each stack showed the tiller just before gust impact. NIH Image software was used to measure the $x-y$ coordinates of the spike marker. The pixel coordinates were found using semi-manual techniques because a skilled human operator (JZW) was more effective than pattern recognition algorithms, with regards to compensating for varying marker illumination, shadowing, and reflectivity. Pixel size was calibrated using a steel rule placed in the field of view. Spatial resolution was in the range of 1.1 to 1.7 mm per pixel.

Forward differencing of the video-based position data was used to calculate velocity and acceleration at each time-step. Simulation of the model response relied on numerical techniques outlined later in context. Various methods are available for assessing the significance of differences between experimental sample means ([27]). In general, the probability p that any given difference Δ is meaningful increases as the number of observations n increases. It is common practice in hypothesis testing to report the probability that a difference is significant, or alternately, to report that the difference is not significant (abbreviated N.S. in Table 1) because it did not attain a pre-selected probability level. In the present study, significance was set at $p<0.001$ and the comparisons of means were performed using confidence intervals based on the Student t test statistic ([28]).

Table 1 Average (standard deviation) of physical properties for two varieties

Variety	# tillers	m (g)	L (m)	x (m)	v (m/s)	a (m/s^2)	ω_x (Hz)
Bacanora	10	2.54 (.28)	.391 (.043)	.233 (.043)	1.98 (.09)	21.8 (2.9)	0.68
Baviacora	10	2.70 (.33)	.641 (.058)	.582 (.086)	1.84 (.07)	25.0 (3.4)	1.25
	p value =	N.S.	p<0.001	p<0.001	N.S.	N.S.	p<0.001

N.S. indicates not significant (see text).

Results—Experimental

In the sideview, each gust excited an underdamped oscillation that lasted 10 to 20 seconds. The peak velocity $\hat{v}$ and the peak acceleration $\hat{a}$ were not significantly different between the two varieties (Table 1). In contrast, the tiller length L, the peak displacement $\hat{x}$, and the frequency of oscillation along the gust axis $\overline{\omega_x}$ were significantly different. These and other differences between the two varieties were accentuated in slow motion. *Baviacora* exhibited a lopsided flopping motion with the spike oscillating at a higher frequency than the stem, while *Bacanora* exhibited a faster motion with the spike and stem oscillating as a unit. Figure 3 shows the first quarter cycle of motion for a typical tiller of each variety. Each set of interconnected black dots shows seven tracking markers at 1/30 second intervals. The leftmost set show the neutral position prior to gust impact, the rightmost set shows the maximum deflection after the gust, and the asterisk indicates the timepoint at which the gust ended. The space between successive markers is a measure of velocity. One can perceive higher frequency mode shapes superimposed on the fundamental mode but these did not persist past the first half-cycle. Hence, the response signal over most of the experimental record was dominated by low-frequency behavior.

The flexural response showed a clear dependence on gust orientation for some but not all tillers tested (i.e., 12/20=60 percent). For example, Fig. 4 shows the $x-y$ pathlines traveled by the spike of a tiller identified as *Baviacora-2*. Each pathline is a two-point fit to the unsmoothed position data. The record length is five seconds, the spatial resolution is 1 mm per pixel, and repeatability is 1 to 2 pixels. The gust always traveled from left to right since gust alignment relative to the tiller was changed by rotating the plant.

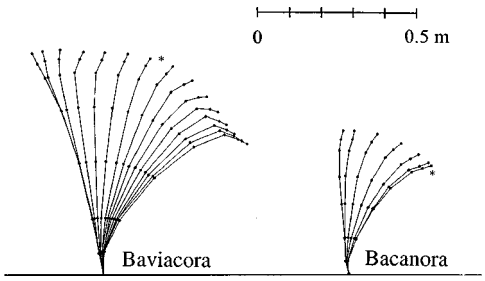

Fig. 3 First quarter cycle of motion for two varieties (sideview)

The indicated angle θ was measured relative to an arbitrary pot reference. Note various patterns of symmetry. For example, the 90-deg path mirrors the 150-deg path with respect to the horizontal axis. The intricacy of the global path arises from the presence of several vibration modes excited to varying degrees according to gust alignment.

Linearization is the key to rational analysis of many physical problems but linear theory cannot adequately explain the kinematic behavior typified by Fig. 4. In contrast, the ensuing development shows that simple nonlinear theory can provide very useful insights.

Results—Modeling

The salient feature of the free response was the anisotropic circling exhibited by some but not all tillers. We therefore seek to develop a model that can explain both the origin and the variability of this directional behavior. The shape of the pathlines in Fig. 4 is strongly angle-dependent. This kinematic anisotropy was quantified using a special deviation metric

$$\kappa=\sum_{i=1}^{\tau}\frac{|y_i|}{|x_i|+\rho}, \tag{1}$$

which was based on the raw integer valued pixel coordinates x_i and y_i at time-point t_i. The summation spanned the first $\tau=300$ time-points after gust impact. It is conceptually useful to consider κ to have SI units of m/m. The resolution factor $\rho=1$ avoided zero denominator errors if $x_i=0$.

For each variety, 4/10=40 percent of the tillers exhibited $\hat{\kappa}<1.0$ for all angles. In these cases, the spike behaved like a one-degree-of-freedom oscillator aligned with the gust. Let us view these tillers as a degenerate case of a more general situation. Specifically, for each variety, 6/10=60 percent of the tillers exhibited wide variations in $\hat{\kappa}$, which varied between zero and some value greater than 2.5 as the pot was rotated relative to the gust. For example, Fig. 5 shows κ as a function of gust angle θ for the tiller designated *Baviacora-2*.

The spike motion recorded in the topview had three degree-of-freedom (two translations, one rotation). Let us assume that the motion seen in the image plane was the sum of at most three isochronous vibrations, implying that the periodicity and decay of each were independent of amplitude ([29]). In this way, the infinite degree-of-freedom response of the physical tiller can be idealized as that of a finite degree-of-freedom harmonic oscillator.

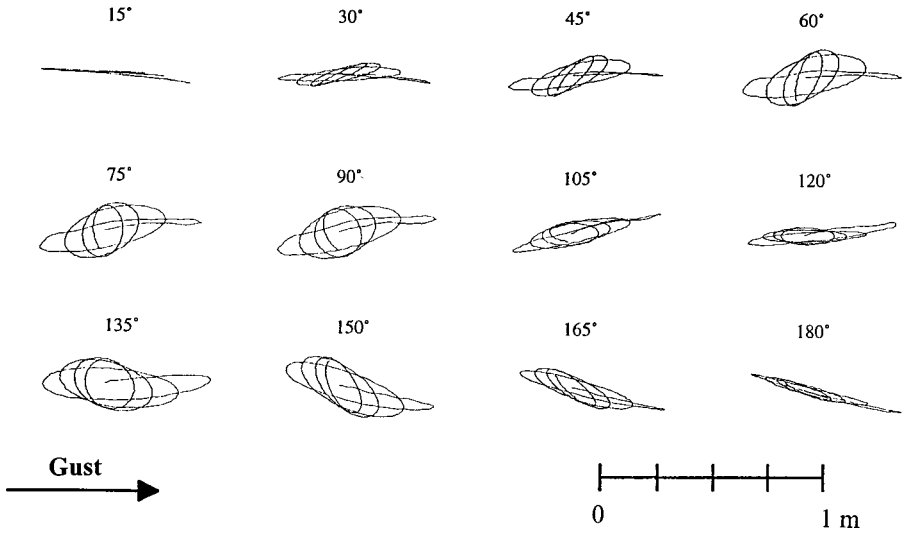

Fig. 4 Experimental pathlines for *Baviacora-2* (topview). The angle θ is measured relative to an arbitrary reference.

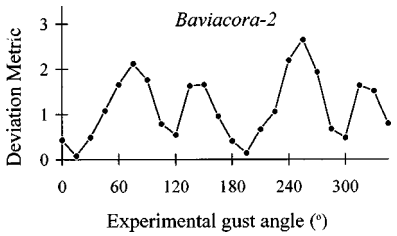

Fig. 5 Special deviation metric as a function of gust angle for *Baviacora-2*

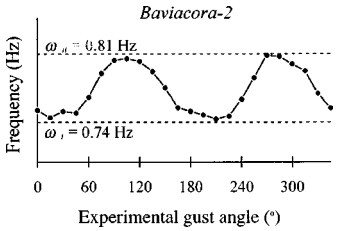

Fig. 7 Frequency of vibration along the gust axis as a function of gust angle for *Baviacora-2*

For an initial linear model, let us fix the rotational degree-of-freedom and assume that the $x-y$ motion of the spike is that of a mass m constrained by two orthogonal spring-and-dashpot units (Fig. 6). This lumped parameter model has two explicit degree-of-freedom X_I and X_{II} with associated stiffness $k_I < k_{II}$ and viscous damping C_I and C_{II} for $i=I$ or II. The physical gust of known duration was then idealized as an impulse $F(t)$ acting at $t=t_1$. This timepoint would occur just after the real pulse ended, implying about 0.250 seconds between the first frame of the video data and the model start time t_1. For each gust orientation i, the impulse must form some some as yet undetermined angle ϕ_I with the compliant degree-of-freedom X_I. Note that ϕ has an intrinsic relationship to the tiller function, and must therefore be distinguished from the angle θ measured relative to an arbitrary laboratory reference.

If δ is the Dirac delta and $F_o=1$, the impulse $F(t)=F_o\delta(t_1)$ can be resolved into components $F_I=\cos\phi$ and $F_{II}=\sin\phi$. If the two degrees-of-freedom are decoupled and the system is lightly damped, the equation of equilibrium is

$$\ddot{X}_i+2\zeta_i\omega_i\dot{X}_i+\omega_i^2X_i=\delta(t_1)\frac{F_i}{m}, \tag{2}$$

where $i=I$ or II, the damping factors $\zeta_I=C_I/(2\omega_I m)$ and $\zeta_{II}=C_{II}/(2\omega_{II}m)$, and the resonant frequencies $\omega_I\cong(k_I/m)^{0.5}$ and $\omega_{II}\cong(k_{II}/m)^{0.5}$. Note that the extrema of κ occur when the gust is aligned with either X_I or X_{II}.

One can set $F_o=1$ and $m=1$ after recognizing that the predicted model path is geometrically similar for all F and m. Equation (2) can be solved for $i=I$ and II using Laplace transform methods with initial conditions $X_i(t_1)=0$ and $\dot{X}_i(t_1)=0$. The particular solution has the form

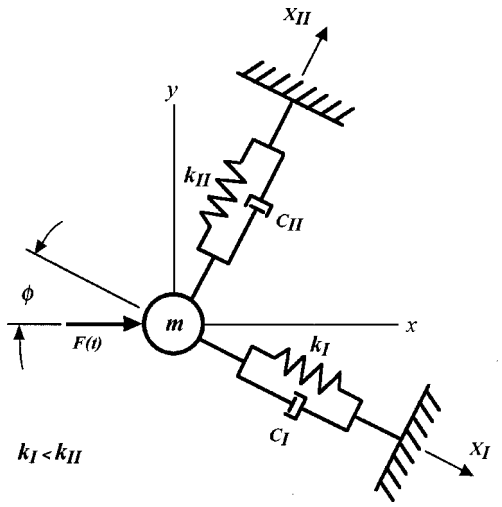

Fig. 6 Diagrammatic representation of a two-degree-of-freedom model.

$$X_i=\frac{F_i}{B_i}\exp(-A_it)\sin(B_it) \tag{3}$$

where $A_i=\zeta_i\omega_i$ and $B_i=\omega_i(1-\zeta_i^2)^{0.5}$ for $i=I$ and II.

The required constants were obtained for each tiller as follows. The frequency of vibration along the x-axis was observed to settle to a different value for each angle. The average value at angle θ_i (for $i=1$ to 24) was defined as

$$\omega_x(\theta_i)=\frac{2\pi(q-3)/4}{(\tau-p)/60}=\frac{30\pi(q-3)}{\tau-p} \tag{4}$$

where p was the time-point at which the spike reached its maximum upwind position (at 3/4 cycles), τ was the last time-point in the five-second record, and q was the noninteger number of quarter cycles in the digital clip. Figure 7 shows ω_x as a function of angle θ for *Baviacora-2*. The extrema of the discrete function were assumed to be very close to the resonant frequencies ω_I and ω_{II}, since the minimum ω_I should occur when ϕ is 0 or π radian, and the maximum ω_{II} should occur when ϕ is $\pi/2$ or $3\pi/2$ radians. For other angles, at least two vibration modes may be excited, with each contributing to the perceived x motion.

It had been tacitly assumed that two damping factors ζ_I and ζ_{II} were required to describe the linear viscous damping of motion along the two principal directions. Experimental estimates of these parameters were obtained using the logarithmic decrement ratio approach ([30]) for the four orientations aligned with one of the principal directions. The assumption of isochronicity required that each degree-of-freedom had constant stiffness, so the value of the log decrement ratio $\delta=2\pi\zeta$ was based on the average of the downwind log decrements

$$\hat{\delta}^{(i)}=\ln\frac{\hat{x}^{(i)}}{\hat{x}^{(i+1)}}, \quad i=(2,3,\ldots,s-1) \tag{5}$$

and the upwind log decrements

$$\check{\delta}^{(j)}=\ln\frac{\check{x}^{(j)}}{\check{x}^{(j+1)}}, \quad j=(1,2,\ldots,r-1) \tag{6}$$

where $\hat{x}^{(i)}$ is the maximum downwind displacement on cycle i and $\check{x}^{(j)}$ is the maximum upwind displacement on cycle j. The limits s and r denote the last complete downwind or upwind half-cycles. While the values of δ_I and δ_{II} could be different, they were essentially identical (within three percent) for each tiller considered. This motivated the additional constraint $\zeta_I=\zeta_{II}$ where ζ_I was a constant. In turn, this implied $C_{II}=(\omega_{II}/\omega_I)C_I$, which reduced the number of independent parameters in the model by one. Rao [30] has shown that the damping factor of an harmonic oscillator can be interpreted as the ratio of energy lost per cycle to the total energy in a vibrating system. Hence, it may be conceptually useful to consider ζ to have SI units of J/J.

The path of the linear model had to evolve at the correct frequencies ω_I and ω_{II}, but it could still drift away from reality when the physical system did not exhibit linear damping. The experimental record was short, so large discrepancies were only detected under certain conditions. In particular, the damping of

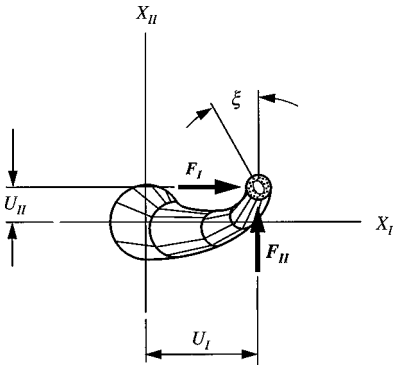

Fig. 8 Foreshortened topview of stem as viewed from the spike

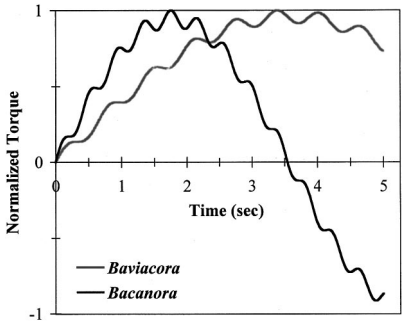

Fig. 9 Undamped stem torque as a function of time for two varieties (normalized by maximum value over interval)

the compliant axis X_I was lower and damping of the stiffer axis X_{II} was higher in some cases, but only when the gust formed an oblique angle with both principle axes.

This observation revealed the limitation of the linear theory. Fortuitously, the canonical form of the model can be modified to address this concern. Let us now view the recorded $x-y$ motion as that of a system in which dissipation can arise either from (1) linear viscous damping due to stem flexion, or from (2) nonlinear damping due to stem torque imposed by spike drag. To illustrate the physics, Fig. 8 shows a foreshortened view of a stem with four internodes obtained by looking down from the spike. The stem is rooted at the origin and the spike is attached at the shaded cross section. The flexural deflections are $U_I > U_{II}$, and spike drag F_D exerts force components F_I and F_{II} on the moving stem. This exerts a net torque that induces a twist angle ξ. Let us assume that the linear damping is proportional to viscous force F_L, and that the nonlinear damping is proportional to the stem torque. Hence, the variation in the magnitude and line of action of F_D is responsible for the model nonlinearity.

The drag on a rigid body exhibits quadratic dependence on airspeed but a flexible aeroelastic structure ([25]) can reduce its frontal area as relative velocity $\dot{X}$ increases. This is the situation for a green wheat spike ([16]), for which

$$F_D \cong -C_D \dot{X} \tag{7}$$

where the drag factor C_D is an empirical constant. Moreover, spike drag is not in general aligned with the velocity vector and can therefore subject the stem to torsional as well as flexural acceleration.

The time dependence of the torque can be appreciated by setting $\zeta=0$ (indicated below by a tilde). If the tiller in Fig. 8 is moving back to the neutral position shortly after the initial pulse, Eq. (7) indicates that drag components F_I and F_{II} are more or less proportional to velocity components varying with $\omega_I \cos \tilde{\omega}_I t$ and $\omega_{II} \cos \tilde{\omega}_{II} t$, and acting at moment arms varying more or less with $\sin \tilde{\omega}_{II} t$ and $\sin \tilde{\omega}_I t$, respectively. (Recall that the undamped model frequencies $\tilde{\omega}_I$ and $\tilde{\omega}_{II}$ are the resonant frequencies of the lightly damped physical system.) If we assume that the drag factor C_D is isotropic (i.e., a scalar), the stem torque is

$$T = -C_D(\dot{X}_{II} X_I - \dot{X}_I X_{II}) \tag{8}$$

where a positive value acts counterclockwise. In Fig. 8, T is positive and tends to swing the spike towards the stiff X_{II}-axis. At later times, the upper limit on T is the undamped torque $\tilde{T}$, which is

$$\tilde{T} = \tilde{\beta}[\tilde{\omega}_{II} \cos(\tilde{\omega}_{II} t) \sin(\tilde{\omega}_I t) - \tilde{\omega}_I \cos(\tilde{\omega}_I t) \sin(\tilde{\omega}_{II} t)] \tag{9}$$

where $\tilde{\beta} = -\sin 2\phi \, C_D/2$ must be zero if the gust is aligned with one of the principal axes. If $b = \omega_I + \omega_{II}$ and $a = \omega_{II} - \omega_I > 0$, it can be shown that

$$\tilde{T} = \frac{\tilde{\beta}}{2}[b \sin at - a \sin bt]. \tag{10}$$

For example, a tiller oscillating at $\omega_I = 0.9$ Hz and $\omega_{II} = 1.0$ Hz is subjected to a small torque varying at 1.9 Hz and a larger torque varying at 0.1 Hz. Figure 9 shows the undamped torque over the first five seconds based on the average ω_I and ω_{II} of both varieties. In general, the imposed torque is a nonperiodic function of time.

The nonlinear model preserved the basic structure of the linear model but related the torque to two nonlinear products involving both translational degrees-of-freedom. This allowed the time-varying effect of stem torque on the translational response to be recognized without explicitly adding the third degree-of-freedom ξ. With this conceptual advance, the damping parameters in Fig. 6 must vary in a specific nonperiodic manner, which is described by Eq. (8) within a single scaling factor. For unit impulse $F_o = 1$ and unit spike mass $m = 1$, the coupled equations of equilibrium are

$$\ddot{X}_I + (2\zeta\omega_I - \beta X_{II})\dot{X}_I + k_I X_I = \delta(t_1)\cos\phi, \tag{11}$$

and

$$\ddot{X}_{II} + (2\zeta\omega_{II} + \beta X_I)\dot{X}_{II} + k_{II} X_{II} = \delta(t_1)\sin\phi, \tag{12}$$

where $k_i = \omega_i^2$ for $i = I$ or II. The coupling strength β provides a measure of dissipation due to stem torque, and has SI units of radians per second per meter (Table 2). In general, the nonlinear damping can only be large when flexural anisotropy and deflection are both large. The nonlinear term in Eq. (11) carries a negative sign and tends to reduce the decay of X_I motion. In contrast, the nonlinear term in Eq. (12) carries a positive sign and tends to increase the decay of X_{II} motion.

Table 2 Average of model parameters required to fit kinematic response for two varieties

Variety	# tillers	κ (m/m)	k_I (N/m)	k_{II} (N/m)	ζ (J/J)	β (rad/sec/m)	Unique constants
Bacanora	4	0.73	0.142	0.142	0.09	0	k_i, ζ
	6	3.54	0.110	0.138	0.05	0.024	k_I, k_{II}, ζ
Baviacora	4	0.47	0.041	0.041	0.08	0	k_I, ζ
	6	2.71	0.058	0.070	0.06	0.141	k_I, k_{II}, ζ, β

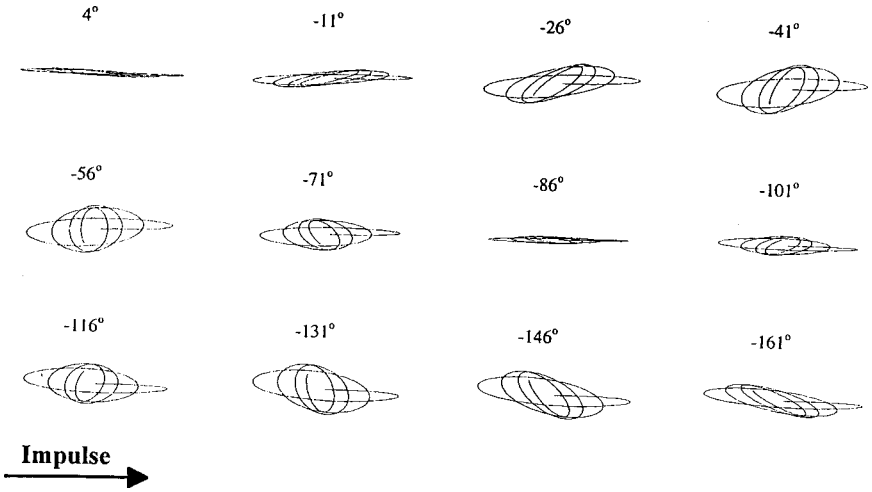

Fig. 10 Simulated model pathlines for *Baviacora-2* (compare to Fig. 4). The angle ϕ is measured relative to an intrinsic reference.

Equations (11) and (12) comprise a system of coupled nonlinear ODE's with four constants k_I, k_{II}, ζ, and β. Approximate solutions for the interval zero to five seconds can be found numerically by exploiting initial similarity to the linear system. A first trial solution of Eq. (11) for X_I at $t_2 = t_1 + \Delta t$ was obtained by setting X_{II} equal to the value that satisfied linear Eq. (2) for $i = II$. Equation (12) was then solved for X_{II} by setting X_I to the value just obtained. Newton-Raphson refinement was continued until X_I and X_{II} changed by less than 0.01 percent on successive interations. The solution was then marched forward using a similar procedure but starting with the X_i from the previous step. The time-step Δt was progressively increased from 0.005 to 0.02 seconds. This algorithm was effective because the damped solution was smooth. No more than ten iterations per step were required. Since the offset between model angle ϕ and experimental angle θ was unknown *a priori*, simulations were performed at 1-deg increments to allow accurate indexing of model and experimental pathlines.

The parameters k_I, k_{II}, and ζ were determined from the experimental record as described above. In the linear model, the coupling strength β was equal to zero. In the nonlinear model, β had a recognizable physical meaning but also served as an adjustable model parameter. The best match between model and experiment was obtained by optimizing the fit when the gust formed a 45-deg angle with both principal directions (i.e., when the nonlinearity was strongest). At these four orientations, the last cycle of the model path was defined backwards from the end of the digital clip. The optimal β was chosen using a least-squares criterion that minimized the angular mismatch between the long axes of the last model and experimental cycles.

Figure 10 shows the predicted pathlines for comparison to the experimental data shown earlier in Fig. 4. The quality of fit is typical of all tillers. In Table 2, the tillers are grouped by variety and by deviation metric. The average values of the model parameters are given for each of the four groups, which represent all 20 tillers studied. For either variety, the kinematic response could be allocated to one of two groups. In the first category, $\hat{\kappa}_{\max}$ was small, the flexural response was isotropic, and the damping was linear viscous. For these cases, only two unique model constants were required. In the second category, $\hat{\kappa}_{\max}$ was large, the flexural response was anisotropic, and the damping exhibited varying degrees of nonlinearity. In this case, three or four of the model constants were unique and nonzero.

There were consistent differences between the two varieties. For the variety called *Bacanora*, the flexural response was stiff, and the coupling strength β was always close to zero. For the variety called *Baviacora*, the response was flexible, and β was only close to zero when $\hat{\kappa}_{\max} < 1$. For the other *Baviacora* tillers, the coupling strength was large, the deviation metric varied with angle, and nonlinear damping had a detectable influence on the evolving path. In the next section, we show that the nonlinear theory provides a unifying description of the observed behavior while providing a plausible explanation for the considerable diversity between plants.

Discussion

A wheat tiller is a flexible living structure subjected to dynamic wind loads. We found that its behavior was unexpectedly rich in mechanical complexity. A horizontal gust caused lateral deflection of the cantilevered stem. The ensuing transient was highly repeatable but sometimes involved a strongly anisotropic response. Niklas and Moon [31] have also reported that garlic stalks can exhibit qualitatively similar circling motions. Previous studies of wheat have deemphasized this flexural directionality ([22,32]). Hence, the real novelty of the present study lies in its quantitative treatment of the kinematic anisotropy of a wheat stalk.

The free-vibration response to a gust was dominated by the low-frequency modes. The low ripple and high repeatability of the response signal made it reasonable to neglect forced-vibration response due to random excitation. Serial tests showed that the resonant frequencies were slightly lower if the leaves were not removed or if the soil was watered, but these observations did not detract from the generality of the conceptual model.

Comparison of Fig. 10 and Fig. 4 shows that the nonlinear model can reproduce the essential nature of the physical response. The nonlinear model has two explicit flexural modes coupled by an implicit torsional mode. The third mode allows drag to dissipate additional energy and the associated torque redirects the vertical plane of vibration towards the most compliant axis. Interestingly, the torsional stresses would be largest in the lower stem, whose properties have been correlated with lodging resistance ([21]).

Each of the four model constants has tangible physical meaning. For example, an isotropic response implies that $k_I \cong k_{II}$ and a stiff response implies that $\beta \cong 0$. However, more than half of the *Baviacora* tillers exhibited compliant anisotropic behavior, which requires the use of all four constants.

The degree of kinematic anisotropy could only be assessed by observing the physical response to a gust from several angles. While some stem internodes had slightly elliptical cross-sections and all spikes had an irregular flexible geometry, no single mea-

sure of structural anisotropy was able to explain the orientations of X_I and X_{II} inferred from the functional anisotropy. For this reason, the responses of two plants with similar appearance were often unexpectedly different. The model suggests that this kinematic variability between plants could be due to the subtle quantitative interplay between torsional and flexural vibration modes. Functional diversity within a plant population could have important implications for crop behavior at larger size scales. In particular, variations in the orientation and anisotropy of the circling response to a gust may increase the frequency of interplant collision. These impacts could substantially increase loadsharing and energy dissipation within a dense canopy. Kinematic anisotropy at the scale of the single tiller may be inseparably related to crop lodging resistance. Further quantitative study of this relationship should be instructive.

Acknowledgments

The authors wish to thank Dr. Nichole O'Neill at the United States Department of Agriculture (USDA-ARS) for supervising the plant management. We also wish to thank the anonymous reviewers for their very helpful comments.

References

[1] Niklas, K. J., 1992, *Plant Biomechanics: An Engineering Approach to Plant Form and Function*, The University of Chicago Press, Chicago, IL.
[2] Speck, T., Spatz, H. C., and Vogellehner, D., 1990, ''Contributions to the Biomechanics of Plants: I. Stabilities of Plant Stems With Strengthening Elements of Different Cross-Sections Against Weight and Wind Forces,'' Bot. Acta, **103**, pp. 111–122.
[3] Baker, C. J., 1995, ''The Development of a Theoretical Model for the Windthrow of Plants,'' J. Theor. Biol., **175**, pp. 355–372.
[4] Crook, M. J., and Ennos, A. R., 1993, ''The Mechanics of Root Lodging in Winter Wheat, Triticum aestivum L,'' J. Exp. Bot., **44**, pp. 1219–1224.
[5] Spatz, H.-Ch., and Speck, T., 1994, ''Local Buckling and Other Modes of Failure in Hollow Plant Stems,'' Biometrics, **2**, pp. 149–173.
[6] Travis, A. J., Murison, S. D., Hirst, D. J., Walker, K. C., and Chesson, A., 1996, ''Comparison of the Anatomy and Degradability of Straw From Varieties of Wheat and Barley That Differ in Susceptibility to Lodging,'' J. Agric. Sci., **127**, pp. 1–10.
[7] Fischer, R. A., and Stapper, M., 1987, ''Lodging Effects on High-Yielding Crops of Irrigated Semidwarf Wheat,'' Field Crops Res., **17**, pp. 245–258.
[8] Allan, R. E., 1986, ''Agronomic Comparisons Among Wheat Lines Nearly Isogenic for Three Reduced-Height Genes,'' Crop Sci., **26**, pp. 707–710.
[9] Busch, R. H., and Rauch, T. L., 1993, ''Agronomic Performance of Tall Versus Short Semidwarf Lines of Spring Wheat,'' Crop Sci., **33**, pp. 941–943.
[10] McClung, A. M., Cantrell, R. G., Quick, J. S., and Gregory, R. S., 1986, ''Influence of the Rht1 Semidwarf Gene on Yield, Yield Components, and Grain Protein in Durum Wheat,'' Crop Sci., **26**, pp. 1095–1099.
[11] Gent, M. P. N., and Kiyomoto, R. K., 1998, ''Physiological and Agronomic Consequences of Rht Genes In Wheat,'' J. Crop Production, **1**, pp. 27–46.
[12] CIMMYT, 1996, ''CIMMYT 1995/1996 World Wheat Facts and Trends,'' Technical Report, International Center for Maize and Wheat Improvement.
[13] Schulgasser, K., and Witztum, A., 1992, ''On the Strength, Stiffness and Stability of Tubular Plant Stems and Leaves,'' J. Theor. Biol., **155**, pp. 497–515.
[14] Crook, M. J., and Ennos, A. R., 1994, ''Stem and Root Characteristics Associated With Lodging Resistance in Four Winter Wheat Cultivars,'' J. Agric. Sci., **123**, pp. 167–174.
[15] Easson, D. L., White, E. M., and Pickles, S. J., 1993, ''The Effect of Weather, Seed Rate and Cultivar on Lodging and Yield in Winter Wheat,'' J. Agric. Sci., **121**, pp. 145–156.
[16] Farquhar, T., Meyer, H., and van Beem, J., 2000, ''Effect of Aeroelasticity on the Aerodynamics of Wheat,'' Mater. Sci. Eng., C, in press.
[17] Finnigan, J. J., and Mulhearn, P. J., 1978, ''Modeling Waving Crops in a Wind Tunnel,'' Boundary-Layer Meteorol., **14**, pp. 253–277.
[18] Brunet, Y., Finnigan, J. J., and Raupach, M. R., 1994, ''A Wind Tunnel Study of Air Flow in Waving Wheat: Single-Point Velocity Statistics,'' Boundary-Layer Meteorol., **70**, pp. 95–132.
[19] Shaw, R. H., Brunet, Y., Finnigan, J. J., and Raupach, M. R., 1995, ''A Wind Tunnel Study of Air Flow in Waving Wheat: Two-Point Velocity Statistics,'' Boundary-Layer Meteorol., **76**, pp. 394–376.
[20] Lersten, N. R., 1987, *Wheat and Wheat Improvement*, American Society of Agronomy, Madison, WI, Crop Science Society of America, Madison, WI, and Soil Science Society of America, Madison, WI, Chapter 2.
[21] van Beem, J., Farquhar, T., Meyer, H., Reynolds, M. P., Singh, R., and van Ginkel, M., 1998, ''Influence of the Rht Dwarfing Genes on Stem Morphology and Biochemistry, and Biomechanics and Associated Lodging Effects in Wheat,'' *Proceedings of the 9th International Wheat Genetics Symposium*, Vol. 2, Aug. 2–7, Saskatoon, Saskatchewan, Canada, pp. 366–368.
[22] Crook, M. J., and Ennos, A. R., 1995, ''The Effect of Nitrogen and Growth Regulators on Stem and Root Characteristics Associated With Lodging in Two Cultivars of Winter Wheat,'' J. Exp. Bot., **46**, No. 289, pp. 931–938.
[23] Inoue, E., 1955, ''Studies of the Phenomena of Waving Plants (Honami) Caused by Wind. Part 1. Mechanism and Characteristics of Waving Plants Phenomena,'' J. Agric. Met. (Japan), **11**, pp. 18–22.
[24] Ackerman, J. D., and Okubo, A., 1993, ''Reduced Mixing in a Marine Macrophyte Canopy,'' Funct. Ecol., **7**, pp. 305–309.
[25] Fung, Y. C., 1969, *An Introduction to the Theory of Aeroelasticity*, Dover, New York.
[26] Zadoks, J. C., Chang, T. T., and Konzak, C. F., 1974, ''A Decimal Code for the Growth Stages of Cereals,'' Weed Res., **14**, pp. 415–421.
[27] Saville, D. J., 1990, ''Multiple Comparison Procedures: The Practical Solution,'' Am. Stat., **44**, pp. 174–180.
[28] Kuehl, R. O., 1994, *Statistical Principles of Research Design and Analysis*, Duxbury Press, Pacific Grove, CA.
[29] Ehrich, F., and Abramson, H. N., 1995, *Shock and Vibration Handbook*, McGraw-Hill, New York, Chapter 4.
[30] Rao, S. S., 1995, *Mechanical Vibrations*, Addison-Wesley, Reading, MA.
[31] Niklas, K. J., and Moon, F. C., 1988, ''Flexural Stiffness & Modulus of Elasticity of Flower Stalks From Allium Sativum as Measured by Multiple Resonance Frequency Spectra,'' Am. J. Bot., **75**, pp. 1517–1525.
[32] Zebrowski, J., 1999, ''Dynamic Behavior of Inflorescence-Bearing Triticale and Triticum Stems,'' Planta, **207**, pp. 410–417.

Dynamic Singular Moments in a Perfectly Conducting Mindlin Plate With a Through Crack Under a Magnetic Field

Y. Shindo
Professor,
Department of Materials Processing,
Graduate School of Engineering,
Tohoku University,
Aoba-yama 02, Sendai 980-8579, Japan

I. Ohnishi
Toyota Motor Corporation,
1 Toyota-Cho,
Toyota 471-8572, Japan

S. Toyama
Toyo Engineering Corporation,
2-8-1 Akanehama,
Narashino 275-0024, Japan

Following Mindlin's theory of plate bending of magnetoelasticity, we consider the scattering of time-harmonic flexural waves by a through crack in a perfectly conducting plate under a uniform magnetic field normal to the crack surface. An incident wave giving rise to moments symmetric about the crack plane is applied. It is assumed that the plate has the electric and magnetic permeabilities of the free space. By the use of Fourier transforms we reduce the problem to solving a pair of dual integral equations. The solution of the dual integral equations is then expressed in terms of a Fredholm integral equation of the second kind. The dynamic moment intensity factor versus frequency is computed and the influence of the magnetic field on the normalized values is displayed graphically. It is found that the existence of the magnetic field produces lower singular moments near the crack tip. [S0021-8936(00)02603-9]

Introduction

If an electrically conducting material is used in a strong magnetic field, we must consider the effect of induced currents. The dynamic behavior of an electrically conducting elastic plate is sufficiently affected by the presence of a strong magnetic field ([1–3]). Design and development of superconducting structures require basic research on electromagnetic fracture mechanics. The stress intensity factor approach of linear elastic fracture mechanics has proved to be very successful in predicting the unstable fracture of brittle solids ([4,5]). When cracked conducting materials are subjected to strong magnetic fields, the same approach is expected to apply. Shindo et al. [6,7] have considered the scattering of time-harmonic flexural waves by a through crack in a conducting classical plate under a uniform magnetic field normal to the crack surface for two special cases, perfect conductivity and quasi-static electromagnetic field. For general references on magnetoelasticity, we refer to the monographs of Moon [8], Maugin [9], and Parton and Kudryavtsev [10].

In this investigation, the scattering of time-harmonic flexural waves by a through crack in a perfectly conducting Mindlin plate under a uniform magnetic field is analyzed to show the effect of induced current. At low temperatures many materials become superconducting, that is, perfectly conducting. Although the solutions of the present paper are concerned, in principle, with the infinite electric conductivity, they can be used to obtain an approximate appraisal of the influence of finite electric conductivity at low temperatures (see Appendix A). A frequently encountered crack shape is the surface crack. The solution of the through crack problem may be useful in studying the surface crack problem by the application of the plate theory-line spring method ([11]). The results for the case with a partial crack can be estimated by the formulation of the conducting plate containing a through crack under arbitrary membrane and bending loads and the solution of the corresponding plane-strain problem for the conducting medium with an edge crack. Mindlin's theory of plate bending ([12]) for magnetoelastic interactions in perfectly conducting bodies ([13]) is applied. The theory includes the effects of rotatory inertia and shear. The plate is engulfed by a uniform magnetic field directed normal to the crack and subjected to incident waves that generate vibratory motion in the transverse direction of the plate. Fourier transforms are used to reduce the magnetoelastic crack problem to a pair of dual integral equations which can be further reduced to a Fredholm integral equation of the second kind ([6]) that is amenable to numerical calculations. Dynamic moment intensity factors are determined for different wave frequencies and amplitudes of the magnetic field.

Contributed by the Applied Mechanics Division of THE AMERICAN SOCIETY OF MECHANICAL ENGINEERS for publication in the ASME JOURNAL OF APPLIED MECHANICS. Manuscript received by the ASME Applied Mechanics Division, June 10, 1997; final revision, Nov. 22, 1998. Associate Technical Editor: M. Taya. Discussion on the paper should be addressed to the Technical Editor, Professor Lewis T. Wheeler, Department of Mechanical Engineering, University of Houston, Houston, TX 77204-4792, and will be accepted until four months after final publication of the paper itself in the ASME JOURNAL OF APPLIED MECHANICS.

Magnetoelastic Thin Plate Bending

We consider an electrically conducting elastic plate of thickness $2h$. The coordinate axes x and y are in the middle plane of the plate and the z-axis is perpendicular to this plane. It is assumed that the plate has the electric and magnetic permeabilities $\varepsilon=\varepsilon_0=8.85\times10^{-12}$ F/m, $\kappa=\kappa_0=1.26\times10^{-6}$ H/m, respectively, with ε_0 and κ_0 being the free-space permeabilities. The conducting plate is permeated by a static uniform magnetic field $\mathbf{H}_0$. We consider small perturbations characterized by the displacement vector $\mathbf{u}$ produced in the plate. The magnetic and electric fields may be expressed in the form

$$\left.\begin{aligned}\mathbf{H}&=\mathbf{H}_0+\mathbf{h}\\ \mathbf{E}&=\mathbf{0}+\mathbf{e}\end{aligned}\right\} \tag{1}$$

where $\mathbf{H}$ and $\mathbf{E}$ are the magnetic and electric field intensity vectors, and $\mathbf{h}$ and $\mathbf{e}$ are the fluctuating fields and are assumed to be of the same order of magnitude as the particle displacement $\mathbf{u}$.

Neglecting displacement currents compared to the conduction currents, we have the following linearized field equations ([1]):

$$\text{curl}\ \mathbf{e}=-\kappa_0\mathbf{h}_{,t} \tag{2}$$

$$\text{curl}\ \mathbf{h}=\mathbf{j} \tag{3}$$

$$\text{div}\ \mathbf{h}=0 \tag{4}$$

$$\epsilon_o\ \text{div}\ \mathbf{e}=\rho_e \tag{5}$$

$$\sigma_{xx,x}+\sigma_{yx,y}+\sigma_{zx,z}+(\mathbf{j}\times\mathbf{B}_0)_x=\rho u_{x,tt} \tag{6}$$

$$\sigma_{xy,x}+\sigma_{yy,y}+\sigma_{zy,z}+(\mathbf{j}\times\mathbf{B}_0)_y=\rho u_{y,tt} \tag{7}$$

$$\sigma_{xz,x}+\sigma_{yz,y}+\sigma_{zz,z}+(\mathbf{j}\times\mathbf{B}_0)_z=\rho u_{z,tt} \tag{8}$$

where a comma denotes partial differentiation with respect to the coordinate or the time t, $\mathbf{j}$ is the current density, ρ_e is the free electric charge density, $\mathbf{B}_0=\kappa_0\mathbf{H}_0$ is the magnetic induction, ρ is the mass density, $(\sigma_{xx},\sigma_{yy},\sigma_{zz},\sigma_{xy}=\sigma_{yx},\sigma_{yz}=\sigma_{zy},\sigma_{zx}=\sigma_{xz})$ are the elastic stress components, and (u_x,u_y,u_z) are the components of $\mathbf{u}$. In a moving conductor the current is determined by Ohm's law as

$$\mathbf{j}=\sigma(\mathbf{e}+\mathbf{u}_{,t}\times\mathbf{B}_0) \tag{9}$$

where σ is the electric conductivity. The mechanical constitutive equations are taken to be the usual Hooke's law

$$\left.\begin{aligned}
\sigma_{xx}&=\lambda(u_{x,x}+u_{y,y}+u_{z,z})+2\mu u_{x,x}\\
\sigma_{yy}&=\lambda(u_{x,x}+u_{y,y}+u_{z,z})+2\mu u_{y,y}\\
\sigma_{zz}&=\lambda(u_{x,x}+u_{y,y}+u_{z,z})+2\mu u_{z,z}\\
\sigma_{xy}&=\mu(u_{x,y}+u_{y,x})\\
\sigma_{yz}&=\mu(u_{y,z}+u_{z,y})\\
\sigma_{xz}&=\mu(u_{z,x}+u_{x,z})
\end{aligned}\right\} \tag{10}$$

where λ, μ are the Lamé constants.

Outside the plate the external fields are solutions of

$$\text{curl } \mathbf{e}^e=-\kappa_0\mathbf{h}^e_{,t} \tag{11}$$

$$\text{curl } \mathbf{h}^e=0 \tag{12}$$

$$\text{div } \mathbf{h}^e=0 \tag{13}$$

$$\text{div } \mathbf{e}^e=0 \tag{14}$$

where the superscript e denotes the external value of the quantity so labeled.

If we let $\sigma\to\infty$, we get from Eq. (9)

$$\mathbf{e}+\kappa_0\mathbf{u}_{,t}\times\mathbf{H}_0=0. \tag{15}$$

The linearized boundary conditions are also obtained as

$$\left.\begin{aligned}
e^e_x(x,y,\pm h,t)-e_x(x,y,\pm h,t)&=0\\
e^e_y(x,y,\pm h,t)-e_y(x,y,\pm h,t)&=0
\end{aligned}\right\} \tag{16}$$

$$\left.\begin{aligned}
h^e_x(x,y,\pm h,t)-h_x(x,y,\pm h,t)&=j^s_y\\
h^e_y(x,y,\pm h,t)-h_y(x,y,\pm h,t)&=-j^s_x
\end{aligned}\right\} \tag{17}$$

$$\varepsilon_0\{e^e_z(x,y,\pm h,t)-e_z(x,y,\pm h,t)\}=\rho^s_e \tag{18}$$

$$h^e_z(x,y,\pm h,t)-h_z(x,y,\pm h,t)=0 \tag{19}$$

$$j_z(x,y,\pm h,t)=0 \tag{20}$$

$$\left.\begin{aligned}
\sigma^{Me}_{zz}(x,y,\pm h,t)-\{\sigma_{zz}(x,y,\pm h,t)+\sigma^M_{zz}(x,y,\pm h,t)\}&=0\\
\sigma^{Me}_{zy}(x,y,\pm h,t)-\{\sigma_{zy}(x,y,\pm h,t)+\sigma^M_{zy}(x,y,\pm h,t)\}&=0\\
\sigma^{Me}_{zx}(x,y,\pm h,t)-\{\sigma_{zx}(x,y,\pm h,t)+\sigma^M_{zx}(x,y,\pm h,t)\}&=0
\end{aligned}\right\} \tag{21}$$

where (B_{0x},B_{0y},B_{0z}), (e_x,e_y,e_z), and (h_x,h_y,h_z) are the components of $\mathbf{B}_0$, $\mathbf{e}$, and $\mathbf{h}$, respectively, j_z is the z-component of $\mathbf{j}$, j^s_x and j^s_y are the components of the surface current density $\mathbf{j}^s$, and ρ^s_e is the surface charge density. The Maxwell stress components are

$$\left.\begin{aligned}
\sigma^M_{zz}&=\kappa_0H_{0z}h_z-\kappa_0H_{0x}h_x-\kappa_0H_{0y}h_y\\
\sigma^M_{zy}&=\kappa_0H_{0y}h_z+\kappa_0H_{0z}h_y\\
\sigma^M_{zx}&=\kappa_0H_{0x}h_z+\kappa_0H_{0z}h_x
\end{aligned}\right\} \tag{22}$$

where (H_{0x},H_{0y},H_{0z}) are the components of $\mathbf{H}_0$.

We assume that the plate is permeated by a static uniform magnetic field of magnetic induction $B_0=\kappa_0H_0$ in the y-direction. By using Mindlin's theory of plate bending ([12]), the rectangular displacement components u_x, u_y, and u_z may assume the forms

$$u_x=z\Psi_x(x,y,t),\quad u_y=z\Psi_y(x,y,t),\quad u_z=\Psi_z(x,y,t) \tag{23}$$

in which Ψ_z represents the normal displacement of the plate, and Ψ_x and Ψ_y denote the rotations of the normals about the x and y-axes.

From Eqs. (2), (15), and (23), we obtain the magnetic field intensity components as

$$\left.\begin{aligned}
h_x&=H_0u_{x,y}=zH_0\Psi_{x,y}\\
h_y&=-H_0(u_{z,z}+u_{x,x})=-\frac{H_0}{1-\nu}z\{(1-2\nu)\Psi_{x,x}-\nu\Psi_{y,y}\}\\
h_z&=H_0u_{z,y}=H_0\Psi_{z,y}
\end{aligned}\right\} \tag{24}$$

where ν is the Poisson's ratio. From Eqs. (3) and (24), we also have

$$\left.\begin{aligned}
j_x&=h_{z,y}-h_{y,z}=H_0\left[\Psi_{z,yy}+\frac{1}{1-\nu}\{(1-2\nu)\Psi_{x,x}-\nu\Psi_{y,y}\}\right]\\
j_y&=h_{x,z}-h_{z,x}=H_0(\Psi_{x,y}-\Psi_{z,xy})\\
j_z&=h_{y,x}-h_{x,y}=-zH_0\left[\Psi_{x,yy}+\frac{1}{1-\nu}\{(1-2\nu)\Psi_{x,xx}-\nu\Psi_{y,xy}\}\right]
\end{aligned}\right\}. \tag{25}$$

The Lorentz body force components per unit volume are given by

$$\left.\begin{aligned}
(\mathbf{j}\times\mathbf{B}_0)_x&=-\kappa_0H_0j_z=z\kappa_0H_0^2\left[\Psi_{x,yy}+\frac{1}{1-\nu}\{(1-2\nu)\Psi_{x,xx}-\nu\Psi_{y,xy}\}\right]\\
(\mathbf{j}\times\mathbf{B}_0)_y&=0\\
(\mathbf{j}\times\mathbf{B}_0)_z&=\kappa_0H_0j_x=\kappa_0H_0^2\left[\Psi_{z,yy}+\frac{1}{1-\nu}\{(1-2\nu)\Psi_{x,x}-\nu\Psi_{y,y}\}\right]
\end{aligned}\right\}. \tag{26}$$

The bending and twisting moments per unit length $(M_{xx},M_{yy},M_{xy}=M_{yx})$ and the vertical shear forces per unit length (Q_x,Q_y) can be expressed in terms of Ψ_x, Ψ_y, and Ψ_z as

$$\left.\begin{aligned} M_{xx} &= \int_{-h}^{h} z\sigma_{xx}dz = D(\Psi_{x,x}+\nu\Psi_{y,y}) \\ M_{yy} &= \int_{-h}^{h} z\sigma_{yy}dz = D(\Psi_{y,y}+\nu\Psi_{x,x}) \\ M_{xy} &= M_{yx} = \int_{-h}^{h} z\sigma_{xy}dz = \frac{(1-\nu)}{2}D(\Psi_{y,x}+\Psi_{x,y}) \end{aligned}\right\} \quad (27)$$

$$\left.\begin{aligned} Q_x &= \int_{-h}^{h}\sigma_{xz}dz = \frac{\pi^2}{6}\mu h(\Psi_{z,x}+\Psi_x) \\ Q_y &= \int_{-h}^{h}\sigma_{yz}dz = \frac{\pi^2}{6}\mu h(\Psi_{z,y}+\Psi_y) \end{aligned}\right\} \quad (28)$$

where $D=4\mu h^3/3(1-\nu)$ is the flexural rigidity of the plate and μ is the shear modulus of elasticity. Now if we multiply Eqs. (6) and (7) by $z\,dz$ and integrate from $-h$ to h, we shall obtain the results

$$M_{xx,x}+M_{xy,y}-Q_x=\frac{2}{3}\rho h^3\Psi_{x,tt}-m_{xx} \quad (29)$$

$$M_{xy,x}+M_{yy,y}-Q_y=\frac{2}{3}\rho h^3\Psi_{y,tt}-m_{yy}\,. \quad (30)$$

The moments m_{xx} and m_{yy} are derived as

$$\left.\begin{aligned} m_{xx} &= h\{\sigma_{zx}(x,y,h,t)-\sigma_{zx}(x,y,-h,t)\}+\int_{-h}^{h} z(\mathbf{j}\times\mathbf{B}_0)_x dz \\ m_{yy} &= h\{\sigma_{zy}(x,y,h,t)-\sigma_{zy}(x,y,-h,t)\}+\int_{-h}^{h} z(\mathbf{j}\times\mathbf{B}_0)_y dz \end{aligned}\right\}. \quad (31)$$

If Eq. (8) is multiplied by dz and integrated from $-h$ to h, we obtain

$$Q_{x,x}+Q_{y,y}=2h\rho\Psi_{z,tt}-q. \quad (32)$$

The load q applied to the plate is derived as

$$q=\sigma_{zz}(x,y,h,t)-\sigma_{zz}(x,y,-h,t)+\int_{-h}^{h}(\mathbf{j}\times\mathbf{B}_0)_z dz. \quad (33)$$

Substituting Eqs. (27) and (28) into Eqs. (29), (30), and (31), we have the equations of motion for a Mindlin plate under the influence of magnetic field

$$\frac{S}{2}[(1-\nu)(\Psi_{x,xx}+\Psi_{x,yy})+(1+\nu)\Phi_{,x}]-\Psi_x-\Psi_{z,x} = \frac{4h^2\rho}{\pi^2\mu}\Psi_{x,tt}-\frac{6}{\pi^2\mu h}m_{xx} \quad (34)$$

$$\frac{S}{2}[(1-\nu)(\Psi_{y,xx}+\Psi_{y,yy})+(1+\nu)\Phi_{,y}]-\Psi_y-\Psi_{z,y} = \frac{4h^2\rho}{\pi^2\mu}\Psi_{y,tt}-\frac{6}{\pi^2\mu h}m_{yy} \quad (35)$$

$$\Psi_{z,xx}+\Psi_{z,yy}+\Phi=\frac{4h^2\rho}{\pi^2\mu}\frac{1}{R}\Psi_{z,tt}-\frac{6}{\pi^2\mu h}q \quad (36)$$

in which

$$\Phi=\Psi_{x,x}+\Psi_{y,y}\,. \quad (37)$$

The rotatory inertia and transverse shear effects are associated with R and S as given by

$$R=\frac{h^2}{3},\quad S=\frac{6D}{\pi^2\mu h}. \quad (38)$$

Problem Statement and Method of Solution

Consider a perfectly conducting Mindlin plate having a through crack of length $2a$ as shown in Fig. 1. The crack is located on the line $y=0, |x|<a$ and the cracked plate is permeated by the magnetic field ($H_{0y}=H_0, H_{0x}=H_{0z}=0$) of magnetic induction $B_0=\kappa_0 H_0$ normal to the crack surface. Incident waves giving rise to moments symmetric about the crack plane $y=0$ are applied:

$$\left.\begin{aligned} \Psi_x^i &= 0 \\ \Psi_y^i &= \Psi_{y0}\exp\{-i(ky+\omega t)\} \\ \Psi_z^i &= \Psi_{z0}\exp\{-i(ky+\omega t)\} \end{aligned}\right\} \quad (39)$$

where the superscript i stands for the incident component, (Ψ_{y0},Ψ_{z0}) are the amplitudes of the input waves, k is the wave number, and ω is the circular frequency. Substituting Eq. (39) into Eqs. (24), we obtain

$$\left.\begin{aligned} h_x^i &= 0 \\ h_y^i &= -ik\frac{\nu}{1-\nu}H_0 z\Psi_{y0}\exp\{-i(ky+\omega t)\} \\ h_z^i &= -ikH_0\Psi_{z0}\exp\{-i(ky+\omega t)\} \end{aligned}\right\}. \quad (40)$$

The field Eqs. (12) and (13) in the vacuum can be written as

$$\left.\begin{aligned} h_{z,y}^e-h_{y,z}^e &= 0 \\ h_{x,z}^e-h_{z,x}^e &= 0 \\ h_{y,x}^e-h_{x,y}^e &= 0 \end{aligned}\right\} \quad (41)$$

$$h_{x,x}^e+h_{y,y}^e+h_{z,z}^e=0. \quad (42)$$

Outside the plate the external fields are solutions of Eqs. (41) and (42). Solutions of these equations which vanish at $z=\pm\infty$ and have the wave factor $\exp\{-i(ky+\omega t)\}$ are

$$\left.\begin{aligned} h_x^{ei} &= 0 \\ h_y^{ei} &= iA_1\exp(-kz)\exp\{-i(ky+\omega t)\} \quad (z\geq h) \\ &= -iA_2\exp(kz)\exp\{-i(ky+\omega t)\} \quad (z\leq -h) \\ h_z^{ei} &= A_1\exp(-kz)\exp\{-i(ky+\omega t)\} \quad (z\geq h) \\ &= A_2\exp(kz)\exp\{-i(ky+\omega t)\} \quad (z\leq -h) \end{aligned}\right\} \quad (43)$$

where A_1 and A_2 are undetermined constants.

Boundary condition (19) leads to the determination of A_1 and A_2 as

$$A_1=A_2=-ikH_0\Psi_{z0}\exp(kh). \quad (44)$$

From Eqs. (21), the stress boundary conditions on the plate surfaces are

$$\sigma_{zz}=\kappa_0 H_0(h_y-h_y^e),\quad \sigma_{zx}=\sigma_{zy}=0,\quad (z=\pm h). \quad (45)$$

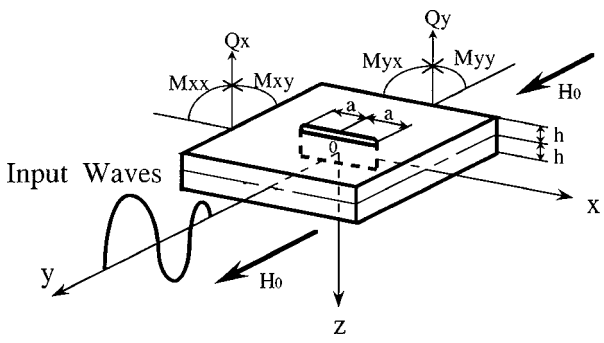

Fig. 1 A through crack in a perfectly conducting Mindlin plate and flexural waves

Making use of Eqs. (40), (43), (44), and (45) renders the stress components $\sigma^i_{zz}(x,y,\pm h,t)$ and $\sigma^i_{zy}(x,y,\pm h,t)$

$$\left.\begin{aligned}\sigma^i_{zz}(x,y,\pm h,t)&=-\kappa_0 H_0 h^{ei}_y(x,y,\pm h,t)+\kappa_0 H_0 h^i_y(x,y,\pm h,t)\\&=\left(\mp\kappa_0 H_0^2 k\Psi_{z0}\mp\kappa_0 H_0^2\frac{\nu}{1-\nu}kh\Psi_{y0}\right)\exp\{-i(ky+\omega t)\}\\ \sigma^i_{zy}(x,y,\pm h,t)&=\sigma^i_{zx}(x,y,\pm h,t)=0\end{aligned}\right\}. \tag{46}$$

From Eqs. (31) and (33), we obtain

$$\left.\begin{aligned}&m^i_{xx}=0,\quad m^i_{yy}=0\\&q^i=-2\kappa_0 H_0^2 k(1+kh)\Psi_{z0}\exp\{-i(ky+\omega t)\}\end{aligned}\right\}. \tag{47}$$

Substituting Eqs. (39) and (47) into Eqs. (35) and (36) yields

$$\frac{4}{3}(kh)^3\left(\frac{\omega}{c_2 k}\right)^4-\left\{\left(\frac{8}{3}\frac{1}{1-\nu}+\frac{1}{9}\pi^2\right)(kh)^3+\frac{\pi^2}{3}(kh)+\frac{4}{3}(kh)^2(1+kh)h_c\right\}\left(\frac{\omega}{c_2 k}\right)^2+\frac{8}{3}\frac{1}{1-\nu}(kh)^2(1+kh)h_c+\frac{2\pi^2}{9}\frac{1}{1-\nu}(kh)^3+\frac{\pi^2}{3}(1+kh)h_c=0 \tag{48}$$

$$i\frac{\pi^2}{6}\Psi_{y0}=\left\{\frac{\pi^2}{6}(kh)+2(1+kh)h_c-2(kh)\left(\frac{\omega}{c_2 k}\right)^2\right\}\Psi_{z0} \tag{49}$$

in which $c_2=(\mu/\rho)^{1/2}$ is the shear wave velocity and

$$h_c=\kappa_0 H_0^2/\mu. \tag{50}$$

The effect of the magnetic field ($H_{0y}=H_0$, $H_{0x}=H_{0z}=0$) on the flexural waves is discussed in Appendix A. The dependency of the flexural waves on kh for three directions of the magnetic field ($H_{0x}=H_0$, $H_{0y}=H_{0z}=0$; $H_{0y}=H_0$, $H_{0x}=H_{0z}=0$; $H_{0z}=H_0$, $H_{0x}=H_{0y}=0$) is also discussed in Appendix B.

The complete solution of the waves as diffracted by the crack is obtained by adding the incident and scattered waves, i.e.,

$$\left.\begin{aligned}\Psi_x(x,y,t)&=\Psi^i_x(x,y,t)+\Psi^s_x(x,y,t)\\ \Psi_y(x,y,t)&=\Psi^i_y(x,y,t)+\Psi^s_y(x,y,t)\\ \Psi_z(x,y,t)&=\Psi^i_z(x,y,t)+\Psi^s_z(x,y,t)\end{aligned}\right\} \tag{51}$$

where the superscript s stands for the scattered component. Likewise, the plate displacements, moments and shears can also be found by superposing the incident and scattered parts and the results are obvious. Only one quarter of the plate needs to be considered because of symmetry. For a traction-free crack, the quantities M_{yy}, M_{xy}, Q_y must each vanish for $x<a$ and $y=0$. The boundary conditions for the scattered field become

$$M^s_{xy}=0\quad(y=0,0\leqslant x<\infty) \tag{52}$$

$$Q^s_y=0\quad(y=0,0\leqslant x<\infty) \tag{53}$$

$$\left.\begin{aligned}&M^s_{yy}=-M^i_{yy}=-ikD\Psi_{y0}\exp(-i\omega t)\quad&(y=0,0\leqslant x<a)\\&\Psi^s_y=0&(y=0,a\leqslant x<\infty)\end{aligned}\right\}. \tag{54}$$

In what follows, the exponential time factor $\exp(-iwt)$ will be omitted as it always appears with the quantity $ikD\Psi_{y0}$ as indicated in Eq. (54).

We assume that the solutions Ψ_x, Ψ_y, and Ψ_z are of the forms

$$\left.\begin{aligned}\Psi_x(x,y)&=\frac{2}{\pi}\sum_{j=1}^{2}\int_0^\infty A_j(\alpha)\exp\{-\gamma_j(\alpha)y\}\sin(\alpha x)d\alpha\\ \Psi_y(x,y)&=\frac{2}{\pi}\sum_{j=1}^{2}\int_0^\infty B_j(\alpha)\exp\{-\gamma_j(\alpha)y\}\cos(\alpha x)d\alpha\\ \Psi_z(x,y)&=\frac{2}{\pi}\sum_{j=1}^{2}\int_0^\infty C_j(\alpha)\exp\{-\gamma_j(\alpha)y\}\cos(\alpha x)d\alpha\end{aligned}\right\} \tag{55}$$

where $A_j(\alpha)$, $B_j(\alpha)$, $C_j(\alpha)$, and $\gamma_j(\alpha)$ $(j=1,2)$ are the unknown functions to be determined later. It can be shown that the solutions (h^e_x,h^e_y,h^e_z) satisfying Eqs. (41) and (42) are given by

$$\left.\begin{aligned}h^e_x&=\frac{2}{\pi}\sum_{j=1}^{2}\int_0^\infty\frac{\alpha}{\{\alpha^2-\gamma_j^2(\alpha)\}^{1/2}}a_{1j}(\alpha)\exp\{-\gamma_j(\alpha)y\}\exp[-\{\alpha^2-\gamma_j^2(\alpha)\}^{1/2}z]\sin(\alpha x)d\alpha\\&\quad(z\geqslant h)\\&=-\frac{2}{\pi}\sum_{j=1}^{2}\int_0^\infty\frac{\alpha}{\{\alpha^2-\gamma_j^2(\alpha)\}^{1/2}}a_{2j}(\alpha)\exp\{-\gamma_j(\alpha)y\}\exp[\{\alpha^2-\gamma_j^2(\alpha)\}^{1/2}z]\sin(\alpha x)d\alpha\\&\quad(z\leqslant -h)\end{aligned}\right\} \tag{56}$$

$$\left.\begin{aligned}h^e_y&=\frac{2}{\pi}\sum_{j=1}^{2}\int_0^\infty\frac{\gamma_j(\alpha)}{\{\alpha^2-\gamma_j^2(\alpha)\}^{1/2}}a_{1j}(\alpha)\exp\{-\gamma_j(\alpha)y\}\exp[-\{\alpha^2-\gamma_j^2(\alpha)\}^{1/2}z]\cos(\alpha x)d\alpha\\&\quad(z\geqslant h)\\&=-\frac{2}{\pi}\sum_{j=1}^{2}\int_0^\infty\frac{\gamma_j(\alpha)}{\{\alpha^2-\gamma_j^2(\alpha)\}^{1/2}}a_{2j}(\alpha)\exp\{-\gamma_j(\alpha)y\}\exp[\{\alpha^2-\gamma_j^2(\alpha)\}^{1/2}z]\cos(\alpha x)d\alpha\\&\quad(z\leqslant -h)\end{aligned}\right\} \tag{57}$$

$$h_z^e=\frac{2}{\pi}\sum_{j=1}^{2}\int_0^\infty a_{1j}(\alpha)\exp\{-\gamma_j(\alpha)y\}\exp[-\{\alpha^2-\gamma_j^2(\alpha)\}^{1/2}z]\cos(\alpha x)d\alpha \quad (z\geqslant h)$$
$$=\frac{2}{\pi}\sum_{j=1}^{2}\int_0^\infty a_{2j}(\alpha)\exp\{-\gamma_j(\alpha)y\}\exp[\{\alpha^2-\gamma_j^2(\alpha)\}^{1/2}z]\cos(\alpha x)d\alpha \quad (z\leqslant -h) \tag{58}$$

where the unknowns $a_{1j}(\alpha)$ and $a_{2j}(\alpha)$ $(j=1,2)$ are to be evaluated from the boundary conditions (19) at $|z|=h$.

Boundary conditions (19) lead to the determination of $a_{1j}(\alpha)$ and $a_{2j}(\alpha)$ as

$$a_{1j}(\alpha)=a_{2j}(\alpha)=-H_0\gamma_j(\alpha)C_j(\alpha)\times\exp[\{\alpha^2-\gamma^2(\alpha)\}^{1/2}h] \quad (j=1,2). \tag{59}$$

Making use of Eqs. (56), (57), and (59) renders the x, y-magnetic intensity components $h_x^e(x,y,\pm h,t)$ and $h_y^e(x,y,\pm h,t)$

$$\left.\begin{aligned}h_x^e(x,y,\pm h,t)&=\mp\frac{2}{\pi}\sum_{j=1}^{2}\int_0^\infty\frac{H_0\alpha\gamma_j(\alpha)}{\{\alpha^2-\gamma_j^2(\alpha)\}^{1/2}}C_j(\alpha)\times\exp\{-\gamma_j(\alpha)y\}\sin(\alpha x)d\alpha\\ h_y^e(x,y,\pm h,t)&=\mp\frac{2}{\pi}\sum_{j=1}^{2}\int_0^\infty\frac{H_0\gamma_j^2(\alpha)}{\{\alpha^2-\gamma_j^2(\alpha)\}^{1/2}}C_j(\alpha)\times\exp\{-\gamma_j(\alpha)y\}\cos(\alpha x)d\alpha\end{aligned}\right\}. \tag{60}$$

From boundary conditions (45), we have

$$\left.\begin{aligned}\sigma_{zz}(x,y,\pm h,t)&=-\kappa_0H_0h_y^e(x,y,\pm h,t)+\kappa_0H_0h_y(x,y,\pm h,t)\\&=\pm\kappa_0H_0^2\left[\frac{2}{\pi}\sum_{j=1}^{2}\int_0^\infty\frac{\gamma_j^2(\alpha)}{\{\alpha^2-\gamma_j^2(\alpha)\}^{1/2}}C_j(\alpha)\times\exp\{-\gamma_j(\alpha)y\}\cos(\alpha x)d\alpha-\frac{h}{1-\nu}\{(1-2\nu)\Psi_{x,x}-\nu\Psi_{y,y}\}\right]\\ \sigma_{zy}(x,y,\pm h,t)&=\sigma_{zx}(x,y,\pm h,t)=0\end{aligned}\right\}. \tag{61}$$

From Eq. (33), we obtain

$$q=2\kappa_0H_0^2\left[h\Psi_{z,yy}+\frac{2}{\pi}\sum_{j=1}^{2}\int_0^\infty\frac{\gamma_j^2(\alpha)}{\{\alpha^2-\gamma_j^2(\alpha)\}^{1/2}}C_j(\alpha)\times\exp\{-\gamma_j(\alpha)y\}\cos(\alpha x)d\alpha\right]. \tag{62}$$

Substituting Eqs. (55) and (62) into Eqs. (34)–(36), in which we neglect the moments m_{xx}, m_{yy}, yields

$$a_0(\alpha)\gamma_j^4(\alpha)+b_0(\alpha)\gamma_j^2(\alpha)+c_0(\alpha)=0 \tag{63}$$

$$\left.\begin{aligned}\{\alpha^2-\gamma_j^2(\alpha)\}A_j(\alpha)&=\alpha G_j(\alpha)C_j(\alpha) \quad (j=1,2)\\ \{\alpha^2-\gamma_j^2(\alpha)\}B_j(\alpha)&=\gamma_j(\alpha)G_j(\alpha)C_j(\alpha) \quad (j=1,2)\end{aligned}\right\} \tag{64}$$

in which

$$\left.\begin{aligned}a_0(\alpha)&=1+\frac{12\kappa_0H_0^2}{\pi^2\mu h}\frac{1}{\{\alpha^2-\gamma_j^2(\alpha)\}^{1/2}}\\ b_0(\alpha)&=-2\alpha^2+\left(\frac{\omega}{\omega_0}\right)^2\left(\frac{1}{S}+\frac{1}{R}\right)+\frac{1}{S}\frac{12h_c}{\pi^2h}\frac{\left\{\left(\frac{\omega}{\omega_0}\right)^2-1\right\}}{\{\alpha^2-\gamma_j^2(\alpha)\}^{1/2}}-\frac{12h_c}{\pi^2h}\frac{\alpha^2}{\{\alpha^2-\gamma_j^2(\alpha)\}^{1/2}}\\ c_0(\alpha)&=\alpha^4-\left(\frac{\omega}{\omega_0}\right)^2\left(\frac{1}{S}+\frac{1}{R}\right)\alpha^2+\frac{1}{RS}\left(\frac{\omega}{\omega_0}\right)^2\left\{\left(\frac{\omega}{\omega_0}\right)^2-1\right\}\end{aligned}\right\} \tag{65}$$

$$G_j(\alpha)=\alpha^2-\gamma_j^2(\alpha)-\left(\frac{\omega}{\omega_0}\right)^2\frac{1}{R}-\frac{12h_c}{\pi^2h}\gamma_j(\alpha)\{i+h\gamma_j(\alpha)\} \quad (j=1,2) \tag{66}$$

and $\omega_0=\pi c_2/2h$ is the cutoff frequency.

The boundary conditions (52) and (53) render

$$\sum_{j=1}^{2}R_j(\alpha)C_j(\alpha)=0 \tag{67}$$

$$\sum_{j=1}^{2}\{P_j(\alpha)-\gamma_j(\alpha)\}C_j(\alpha)=0 \tag{68}$$

in which

$$R_j(\alpha)=-N_j(\alpha)\gamma_j(\alpha)-\alpha P_j(\alpha) \quad (j=1,2). \tag{69}$$

The unknown $C(\alpha)$ is related to $C_j(\alpha)(j=1,2)$ as follows:

$$C(\alpha)=\sum_{j=1}^{2}P_j(\alpha)C_j(\alpha). \tag{70}$$

Application of the boundary conditions (54) gives rise to a pair of dual integral equations:

$$\left\{\begin{aligned}&\int_0^\infty\alpha f(\alpha)C(\alpha)\cos(\alpha x)d\alpha=\frac{\pi}{2}\frac{M_{iy}}{D} \quad (0\leqslant x<a)\\ &\int_0^\infty C(\alpha)\cos(\alpha x)d\alpha=0 \quad (a\leqslant x<\infty)\end{aligned}\right. \tag{71}$$

in which M_{iy} and $f(\alpha)$ are known as

$$M_{iy}=-ikD\Psi_{y0} \tag{72}$$

$$f(\alpha)=\frac{1}{\alpha U(\alpha)}\left\{V_1(\alpha)-V_2(\alpha)\frac{S_1(\alpha)}{S_2(\alpha)}\right\} \tag{73}$$

$$U(\alpha)=P_1(\alpha)-P_2(\alpha)\frac{S_1(\alpha)}{S_2(\alpha)} \tag{74}$$

$$S_j(\alpha)=P_j(\alpha)-\gamma_j(\alpha) \quad (j=1,2) \tag{75}$$

$$V_j(\alpha)=-P_j(\alpha)\gamma_j(\alpha)+\nu\alpha N_j(\alpha) \quad (j=1,2). \tag{76}$$

Table 1 Material properties of aluminum

Material	Density ρ (kg/m^3)	Electrical Conductivity σ (mho/m)	Shear Modulus μ (N/m^2)
Aluminum	2700	3.54×10^7	2.37×10^{10}

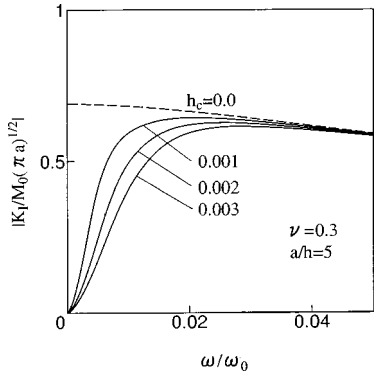

Fig. 2 Dynamic bending moment intensity factor $|K_I/M_0(\pi a)^{1/2}|$ versus ω/ω_0 ($a/h=5$)

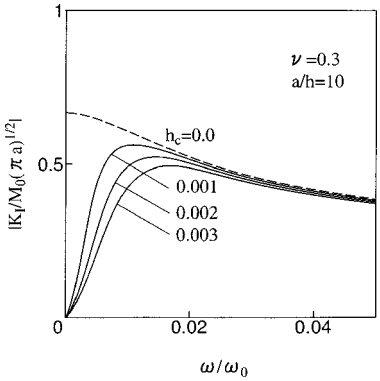

Fig. 3 Dynamic bending moment intensity factor $|K_I/M_0(\pi a)^{1/2}|$ versus ω/ω_0 ($a/h=10$)

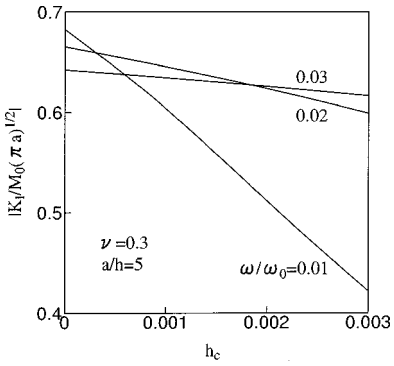

Fig. 4 Dynamic bending moment intensity factor $|K_I/M_0(\pi a)^{1/2}|$ versus h_c ($a/h=5$)

The second of Eqs. (71) would be satisfied if $C(\alpha)$ is taken as

$$C(\alpha)=\frac{\pi}{2}\frac{M_{iy}}{DF}a^2\int_0^1 \xi^{1/2}\Phi_1(\xi)J_0(a\alpha\xi)d\xi \tag{77}$$

where $J_0()$ being the first kind Bessel function of order zero, and

$$F=\lim_{\alpha\to\infty} f(\alpha). \tag{78}$$

Inserting Eq. (77) into the first of Eqs. (71) yields a Fredholm integral equation of the second kind:

$$\Phi_1(\xi)+\int_0^1 K_1(\xi,\eta)\Phi_1(\eta)d\eta=\xi^{1/2} \tag{79}$$

where the kernel $K_1(\xi,\eta)$ is given by

$$K_1(\xi,\eta)=(\xi\eta)^{1/2}\int_0^\infty \alpha\left[\frac{1}{F}f(\alpha/a)-1\right]J_0(\alpha\xi)J_0(\alpha\eta)d\alpha. \tag{80}$$

The moment intensity factor is defined by

$$K_I=\lim_{x\to a^+}\{2\pi(x-a)\}^{1/2}M_{yy}(x,0,t)=ikD\Psi_{y0}(\pi a)^{1/2}\Phi_1(1)$$
$$=M_0M_2(\pi a)^{1/2}\Phi_1(1) \tag{81}$$

in which

$$\left.\begin{aligned} M_0&=ik_1D\Psi_{y0}\\ M_2&=k/k_1\\ k_1^2&=\frac{1}{2}\left(\frac{\omega}{\omega_0}\right)^2\left\{\frac{1}{S}+\frac{1}{R}+\left[\left(\frac{1}{S}-\frac{1}{R}\right)^2+\frac{4}{RS}\left(\frac{\omega_0}{\omega}\right)^2\right]^{1/2}\right\}\end{aligned}\right\}. \tag{82}$$

Keep in mind that the factor $\exp(-i\omega t)$ has been suppressed.

Discussion of Results

The elastodynamic plate solution ([14]) is recovered when the magnetic field tends to zero. In the limit as $\omega\to0$, the corresponding static solution of $K_I=M_0(\pi a)^{1/2}$ is obtained. The considered conductor is aluminum. The material properties are given in Table 1. Computed are the numerical values of $\Phi_1(1)$ in Eq. (79) for $\nu=0.3$. The ratio $M_2=k/k_1$ in Eq. (81) is known from ω in Eq. (48) which can be further reduced to

$$a_1\left(\frac{k}{k_1}\right)^4+b_1\left(\frac{k}{k_1}\right)^3+c_1\left(\frac{k}{k_1}\right)^2+d_1\left(\frac{k}{k_1}\right)+e_1=0 \tag{83}$$

in which

$$\left.\begin{aligned} a_1&=\frac{2\pi^2}{9}\frac{h^4}{1-\nu}+\frac{8}{3}\frac{1}{1-\nu}h_ch^4\\ b_1&=\frac{8}{3}\frac{1}{(1-\nu)k_1}h_ch^3\\ c_1&=\frac{\pi^2}{3k_1^2}h_ch^2-\left(\frac{8}{3}\frac{1}{1-\nu}+\frac{\pi^2}{9}+\frac{4}{3}h_c\right)\frac{h^4}{k_1^2}\left(\frac{\omega}{c_2}\right)^2\\ d_1&=\frac{\pi^2}{3k_1^3}h_ch-\frac{4}{3k_1^3}h_ch^3\left(\frac{\omega}{c_2}\right)^2\\ e_1&=-\frac{\pi^2}{3k_1^4}h^2\left(\frac{\omega}{c_2}\right)^2+\frac{4}{3k_1^4}h^4\left(\frac{\omega}{c_2}\right)^4\end{aligned}\right\}. \tag{84}$$

The normalized magnetic field of $h_c=0.0$, 0.001, 0.002, and 0.003 corresponds, respectively, to magnetic induction $B_0=\kappa_0H_0=0.0$, 5.46, 7.73, and 9.46T.

A plot of the normalized moment intensity factor $|K_I/M_0(\pi a)^{1/2}|$ is given in Fig. 2 for the ratio $a/h=5$ and four different values of h_c. The dashed curve obtained for the case of $h_c=0.0$ coincides with the purely elastic case. The quantity $|K_I/M_0(\pi a)^{1/2}|$ for $h_c=0.0$ decays as the frequency increases. As the three curves for $h_c\neq0.0$ possess lower amplitude than that for $h_c=0.0$, the magnetic field is seen to decrease the local moment with increasing h_c. Such an effect dies out at high frequency. Figure 3 shows the result for the ratio $a/h=10$. The same gross effect is observed. The same data for $|K_I/M_0(\pi a)^{1/2}|$ is plotted

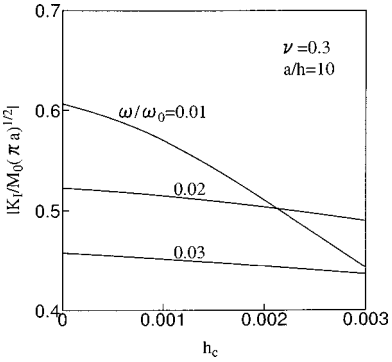

Fig. 5 Dynamic bending moment intensity factor $|K_I/M_0(\pi a)^{1/2}|$ versus h_c ($a/h=10$)

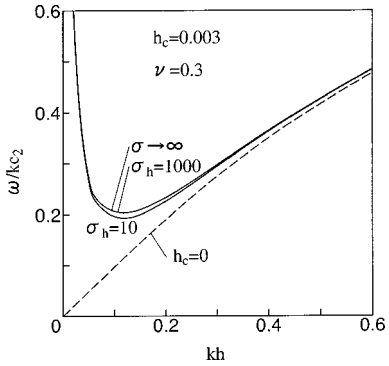

Fig. 6 Phase velocity ω/kc_2 versus wave number kh

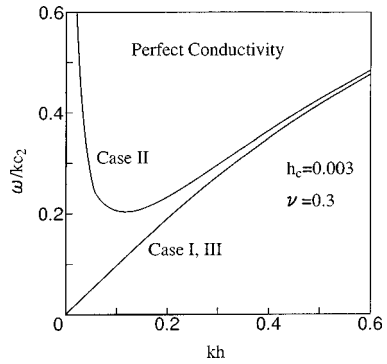

Fig. 7 Phase velocity ω/kc_2 versus wave number kh (perfect conductivity)

against h_c in Figs. 4 and 5. Note that $|K_I/M_0(\pi a)^{1/2}|$ approaches unity as $\omega/\omega_0 \to 0$ at $h_c=0.0$ and tends to decrease with increasing h_c.

In conclusion, the amplification of the moment intensity factor of a through crack in a Mindlin plate subjected to a steady-state magnetic field normal to the crack and an incident flexural wave is evaluated in this work. A perfectly conducting material is assumed for the plate. Significant decrease in the local moment intensity factor occurs at wave frequency $\omega/\omega_0 < 0.02$ and the magnetic field effect dies out gradually as the frequency is increased. All results are based on linear magnetoelasticity assuming a coupling between the induced current and deformation.

Appendix A

Here, the effect of the magnetic field of $H_{0y}=H_0$, $H_{0x}=H_{0z}=0$ on the flexural waves is studied. The frequency equation for a conducting Mindlin plate with finite electric conductivity is obtained as

$$\begin{aligned}
&\frac{4}{3}\sigma_h(kh)^3\left(\frac{\omega}{kc_2}\right)^5+i\frac{4}{3}(kh)^3(1+kh)\left(\frac{\omega}{kc_2}\right)^4\\
&-\left\{\left(\frac{8}{3}\frac{1}{1-\nu}+\frac{1}{9}\pi^2\right)\sigma_h(kh)^3+\frac{\pi^2}{3}\sigma_h(kh)\right.\\
&\left.+\frac{4}{3}(kh)^2(1+kh)h_c\sigma_h\right\}\left(\frac{\omega}{kc_2}\right)^3\\
&-i\left\{\left(\frac{8}{3}\frac{1}{1-\nu}+\frac{1}{9}\pi^2\right)(kh)^3+\frac{\pi^2}{3}(kh)\right\}(1+kh)\left(\frac{\omega}{kc_2}\right)^2\\
&+\left\{\frac{8}{3}\frac{1}{1-\nu}(kh)^2(1+kh)h_c\sigma_h+\frac{2\pi^2}{9}\frac{1}{1-\nu}\sigma_h(kh)^3\right.\\
&\left.+\frac{\pi^2}{3}(1+kh)h_c\sigma_h\right\}\left(\frac{\omega}{kc_2}\right)+i\frac{2\pi^2}{9}\frac{1}{1-\nu}(kh)^3(1+kh)=0
\end{aligned} \tag{A1}$$

where

$$\sigma_h=c_2h\sigma\kappa_0. \tag{A2}$$

Figure 6 shows the variation of the phase velocity ω/kc_2 with the wave number kh for $h_c=0.003(B_0=9.46\,\mathrm{T})$, $\nu=0.3$, $\sigma_h=10{,}1000$. The dashed curve refers to the case of $h_c=0.0$. The effect of the magnetic field on ω/kc_2 is observed at low wave number. The curve obtained for the case of a perfect conductivity, i.e., $\sigma\to\infty$, coincides with the case of $\sigma_h=1000$. The results show validity of the assumption that electrical conductivity is zero at cryogenic temperature.

Appendix B

The dependency of the flexural wave on kh for three magnetic fields of $H_{0x}=H_0$, $H_{0y}=H_{0z}=0$ (Case I), $H_{0y}=H_0$, $H_{0x}=H_{0z}=0$ (Case II), $H_{0z}=H_0$, $H_{0x}=H_{0y}=0$ (Case III) is studied. A perfect conductivity is assumed for the Mindlin plate.

(a) Case I ($H_{0x}=H_0$, $H_{0y}=H_{0z}=0$). From Eqs. (2), (15), (23), and (39), we obtain the magnetic field intensity components as

$$\left.\begin{aligned}
h_x^i&=-H_0(u_{y,y}^i+u_{z,z}^i)=-zH_0\frac{1}{1-\nu}\Psi_{y,y}^i\\
h_y^i&=H_0u_{y,x}^i=0\\
h_z^i&=H_0u_{z,x}^i=0
\end{aligned}\right\}. \tag{B1}$$

From Eqs. (3) and (*B*1), we also have

$$\left.\begin{aligned}
j_x^i&=h_{z,y}^i-h_{y,z}^i=0\\
j_y^i&=h_{x,z}^i-h_{z,x}^i=-H_0\frac{1}{1-\nu}\Psi_{y,y}^i\\
j_z^i&=h_{y,x}^i-h_{x,y}^i=zH_0\frac{1}{1-\nu}\Psi_{y,yy}^i
\end{aligned}\right\}. \tag{B2}$$

The Lorentz body force components per unit volume are given by

$$\left.\begin{aligned}
(\mathbf{j}\times\mathbf{B}_0)_x^i&=0\\
(\mathbf{j}\times\mathbf{B}_0)_y^i&=\kappa_0H_0j_z^i=z\kappa_0H_0^2\frac{1}{1-\nu}\Psi_{y,yy}^i\\
(\mathbf{j}\times\mathbf{B}_0)_z^i&=-\kappa_0H_0j_y^i=\kappa_0H_0^2\frac{1}{1-\nu}\Psi_{y,y}^i
\end{aligned}\right\}. \tag{B3}$$

From Eqs. (21), (43), and (*B1*), the stress boundary conditions on the plate surfaces are

$$\left.\begin{aligned}\sigma^i_{zz}&=\kappa_0 H_0(h^i_x-h^{ei}_x)\\&=-\kappa_0 H_0^2\frac{1}{1-\nu}z\Psi^i_{y,y}\\\sigma^i_{zy}&=0\end{aligned}\right\}\quad(z=\pm h). \tag{B4}$$

Making use of Eqs. (31) and (33) renders the moments m^i_{xx}, m^i_{yy} and the load q^i

$$\left.\begin{aligned}m^i_{xx}&=0\\m^i_{yy}&=\frac{2}{3}\kappa_0 H_0^2\frac{1}{1-\nu}h^3\Psi^i_{y,yy}\\q^i&=0\end{aligned}\right\}. \tag{B5}$$

Substituting Eqs. (39) and (*B5*) into Eqs. (35) and (36) yields

$$\frac{4}{3}(kh)^2\left(\frac{\omega}{kc_2}\right)^4-\left\{\left(\frac{8}{3}\frac{1}{1-\nu}+\frac{1}{9}\pi^2+\frac{4}{3}\frac{1}{1-\nu}h_c\right)(kh)^2+\frac{\pi^2}{3}\right\}\times\left(\frac{\omega}{kc_2}\right)^2+\left\{\frac{2\pi^2}{9}\frac{1}{1-\nu}+\frac{\pi^2}{8}\frac{1}{1-\nu}h_c\right\}(kh)^2=0, \tag{B6}$$

$$i\frac{\pi^2}{6}\Psi_{y0}=-\left\{\frac{\pi^2}{6}-2\left(\frac{\omega}{kc_2}\right)^2\right\}k\Psi_{z0}. \tag{B7}$$

(b) Case II ($H_{0y}=H_0$, $H_{0x}=H_{0z}=0$). From Eq. (48), we also have the frequency equation for Case II ($H_{0y}=H_0$, $H_{0x}=H_{0z}=0$) as

$$\frac{4}{3}(kh)^3\left(\frac{\omega}{c_2k}\right)^4-\left\{\left(\frac{8}{3}\frac{1}{1-\nu}+\frac{1}{9}\pi^2\right)(kh)^3+\frac{\pi^2}{3}(kh)+\frac{4}{3}(kh)^2(1+kh)h_c\right\}\left(\frac{\omega}{c_2k}\right)^2+\frac{8}{3}\frac{1}{1-\nu}(kh)^2(1+kh)h_c+\frac{2\pi^2}{9}\frac{1}{1-\nu}(kh)^3+\frac{\pi^2}{3}(1+kh)h_c=0. \tag{B8}$$

(c) Case III ($H_{0z}=H_0$, $H_{0x}=H_{0y}=0$). From Eqs. (2), (15), (23), and (39), we obtain the magnetic field intensity components as

$$\left.\begin{aligned}h^i_x&=H_0u^i_{x,z}=H_0\Psi^i_x\\h^i_y&=H_0u^i_{y,z}=H_0\Psi^i_y\\h^i_z&=-H_0(u^i_{x,x}+u^i_{y,y})=-zH_0\Psi^i_{y,y}\end{aligned}\right\}. \tag{B9}$$

From Eqs. (3) and (*B9*), we also have

$$\left.\begin{aligned}j^i_x&=h^i_{z,y}-h^i_{y,z}=-zH_0\Psi^i_{y,yy}\\j^i_y&=h^i_{x,z}-h^i_{z,x}=0\\j^i_z&=h^i_{y,x}-h^i_{x,y}=0\end{aligned}\right\}. \tag{B10}$$

The Lorentz body force components per unit volume are given by

$$\left.\begin{aligned}(\mathbf{j}\times\mathbf{B}_0)^i_x&=\kappa_0H_0j^i_y=0\\(\mathbf{j}\times\mathbf{B}_0)^i_y&=-\kappa_0H_0j^i_x=z\kappa_0H_0^2\Psi^i_{y,yy}\\(\mathbf{j}\times\mathbf{B}_0)^i_z&=0\end{aligned}\right\}. \tag{B11}$$

From Eqs. (19), (*B9*), (39), and (43), the constants A_1 and A_2 are determined as

$$A_1=A_2=\pm ikH_0h\Psi_{y0}\exp(kh). \tag{B12}$$

From boundary condition (21), we have

$$\left.\begin{aligned}\sigma^i_{zz}&=0\\\sigma^i_{zy}&=\kappa_0H_0(h^{ei}_y-h^i_y)=-\kappa_0H_0^2(kh+1)\Psi^i_{y0}\end{aligned}\right\}. \tag{B13}$$

From Eqs. (31) and (33), we obtain

$$\left.\begin{aligned}m^i_{xx}&=0\\m^i_{yy}&=-2\kappa_0H_0^2kh^2\Psi^i_{y,y}+\frac{2}{3}\kappa_0H_0^2h^3\Psi^i_{y,yy}\\q^i&=0\end{aligned}\right\}. \tag{B14}$$

Substituting Eqs. (39) and (*B14*) into Eqs. (35) and (36) yields

$$\frac{4}{3}(kh)^2\left(\frac{\omega}{kc_2}\right)^4-\left\{\left(\frac{8}{3}\frac{1}{1-\nu}+\frac{1}{9}\pi^2\right)(kh)^2+4kh\left(1+\frac{1}{3}kh\right)h_c+\frac{\pi^2}{3}\right\}\left(\frac{\omega}{kc_2}\right)^2+\frac{2\pi^2}{9}\frac{1}{1-\nu}(kh)^2+\frac{\pi^2}{3}kh\left(1+\frac{1}{3}kh\right)h_c=0 \tag{B15}$$

$$i\frac{\pi^2}{6}\Psi_{y0}=-\left\{\frac{\pi^2}{6}-2\left(\frac{\omega}{kc_2}\right)^2\right\}k\Psi_{z0}. \tag{B16}$$

Figure 7 shows the variation of the phase velocity ω/kc_2 with the wave number kh for $h_c=0.003$($B_0=9.46$ T) and $\nu=0.3$. The curves obtained for the *x*, *z*-direction magnetic fields (Cases I, III) almost coincide with the purely elastic case. The effect of the *y*-direction magnetic field (Case II) on flexural waves is more pronounced than those of *x*, *z*-direction magnetic fields (Case I, III).

References

[1] Dunkin, J. W., and Eringen, A. C., 1963, ''On the Propagation of Waves in an Electromagnetic Elastic Solid,'' Int. J. Eng. Sci., **1**, pp. 461–495.

[2] Ambartsumian, S. A., Bagdasarian, G. E., and Belubekian, M. V., 1971, ''On the Three-Dimensional Problem of Magnetoelastic Plate Vibrations,'' J. Appl. Math. Mech., **35**, pp. 184–195.

[3] Ambartsumian, S. A., Bagdasarian, G. E., and Belubekian, M. V., 1975, ''On the Equations of Magnetoelastic Thin Plate,'' J. Appl. Math. Mech., **39**, pp. 922–926.

[4] Murakami, Y. ed., 1987, *Stress Intensity Factors Handbook*, Vols. 1 and 2, Pergamon Press, Oxford, UK.

[5] Murakami, Y. ed., 1993, *Stress Intensity Factors Handbook*, Vols. 3, Pergamon Press, Oxford, UK.

[6] Shindo, Y., Ohnishi, I., and Suzuki, S., 1993, ''Dynamic Singular Moments in a Perfectly Conducting Plate With a Through Crack Under a Magnetic Field,'' *Mechanics of Electromagnetic Materials and Structures*, J. S. Lee, G. A. Maugin, and Y. Shindo, eds., ASME, New York, pp. 87–97.

[7] Shindo, Y., Ohnishi, I., and Tohyama, S., 1997, ''Flexural Wave Scattering at a Through Crack in a Conducting Plate Under a Uniform Magnetic Field,'' ASME J. Appl. Mech., **64**, pp. 828–834.

[8] Moon, F. C., 1984, *Magneto-Solid Mechanics*, John Wiley and Sons, New York.

[9] Maugin, G. A., 1988, *Continuum Mechanics of Electromagnetic Solids*, North-Holland, Amsterdam.

[10] Parton, V. Z., and Kudryavtsev, B. A., 1988, *Electromagnetoelasticity*, Gordon and Beach, New York.

[11] Joseph, P. F., and Erdogan, F., 1989, ''Surface Crack Problems in Plates,'' Int. J. Fract., **41**, pp. 105–131.

[12] Mindlin, R. D., 1951, ''Influence of Rotatory Inertia and Shear on Flexural Motions of Isotropic, Elastic Plates,'' ASME J. Appl. Mech., **18**, pp. 31–38.

[13] Kaliski, S., 1962, ''Magnetoelastic Vibration of Perfectry Conducting Plates and Bars Assuming the Principle of Plane Sections,'' Proc. Vib. Probl., **3**, pp. 225–234.

[14] Sih, G. C., and Chen, E. P., 1977, ''Dynamic Analysis of Cracked Plates in Bending and Extension,'' *Plates and Shells With Cracks* (Mechanics of Fracture 3), G. C. Sih, ed., Noordhoff, Leyden, pp. 231–272.

C. K. Chao
Professor

C. J. Tan
Graduate Student

Department of Mechanical Engineering,
National Taiwan University of Science
and Technology,
43, Keelung Road, Section 4,
Taipei, Taiwan 106, R.O.C.

On the General Solutions for Annular Problems With a Point Heat Source

A general analytical solution for the annular problem with a point heat source is provided in this paper. Based upon the method of analytical continuation and the technique of Fourier series expansions, the series solutions of the temperature and stress functions are expressed in complex explicit form. Single-valuedness of complex functions in the doubly connected region has been examined for both the stress-free and displacement-free boundary conditions. The dilatation stress in the annulus due to the application of a point heat source is discussed and shown in graphic form. [S0021-8936(00)02803-8]

1 Introduction

The boundary value problems for an annular region have received considerable attention from many researchers since those problems have applications to many different engineering structures such as pressure vessels, test specimens, and rollers. The solution for the stresses in a pressure vessel under uniform internal and external pressures was first included in the book published by Lamè [1]. By determining the Airy's stress function and using the Fourier series expansions, Michell [2] found a general solution and gave a conclusion that the stresses in the annulus are independent of the elastic constants provided that the resultant forces over the inner and outer boundaries are zero. Bowie and Freese [3] solved the annular problem containing a radial crack by using the modified mapping collocation technique. Using a particular form of the Airy's stress function, the annular problem with a dislocation was solved by Delale and Erdogan [4]. By treating the dislocation solution as the Green's function, the integral equation for a crack on the annulus was established and the crack-opening displacement and stress intensity factors were obtained ([4]). Worden and Keer [5] derived the Green's function for a point load or a dislocation in an annular region using analytic continuation across the boundaries of the annulus. In their solution, the potentials describing an equilibrated point load and a dislocation were found in the form of the Plemelj formulas plus an infinite series. The convergence of the infinite series is dependent on the wall ratio and their method is only appropriate for analyzing thick-walled annuli. For problems considering thin-walled members, Cheng and Finnie [6] obtained the stress intensity factors for radial cracks in circular cylinders and other simply closed cylindrical bodies. All the aforementioned studies consider only for isothermal cases. Very few solutions of the thermal stresses for the annular problem are found in the literature. The exact analytical solution is only found for the problem that the given temperature distributions are prescribed on the boundaries (see [7]).

One of the most difficult parts in solving the annular problem with doubly connected regions is that the single-valued condition of the displacements and the stresses must be satisfied. The problem will become more complicated if singularities or point heat sources reside in the annulus. In this work we first determine the temperature distributions of the annular problem subject to a point heat source and then solve for the thermal stresses. In the derivation of the thermal field the strength of a point heat source must be properly chosen such that the condition of energy balance between a point heat source and the given prescribed temperature distributions along the inner and outer boundaries is satisfied. Having the solution of the temperature field, the thermal stresses in the annular region is determined by the method based on analytic continuation theorem in conjunction with Laurent series expansions. The undetermined coefficients appearing in the series solution are solved using the Fourier series expansions. Both the stress-free and displacement-free conditions are considered either on the inner boundary or on the outer boundary. In the present analysis we exclude the case of the displacement-free condition considered on the inner and outer boundaries of the annulus. However, the method is easily extended to solve the displacement-free boundary for which the resultant force over an annular region is not zero which must be determined after the solution is obtained. The solution derived in the present problem with a point heat source can be used as a Green's function which allows us to derive the solution for the problem with distributed sources that is frequently encountered in practical applications.

2 Formulation of the Annular Problem

2.1 Basic Equations. For two-dimensional thermoelastic problems the resultant force and displacements can be expressed in terms of two stress potentials $\phi(z), \psi(z)$ and a single temperature potential $g'(z)$ as ([8])

$$-Y+iX=\phi(z)+z\overline{\phi'(z)}+\overline{\psi(z)} \tag{1}$$

$$2\mu(u+iv)=\kappa\phi(z)-z\overline{\phi'(z)}-\overline{\psi(z)}+2\mu\beta\int g'(z)dz \tag{2}$$

where $-Y+iX$ is the resultant force over an arc of the boundary measured from some fixed point, u and v are the displacements in the x-y plane, $\kappa=3-4\nu$, $\beta=(1+\nu)\alpha$ for plane strain and $\kappa=3-\nu/1+\nu$, $\beta=\alpha$ for plane stress with α being thermal expansion coefficient and ν the Poisson's ratio, μ is the shear modulus, z is the complex coordinate: $z=x+iy$, and the bars denote complex conjugation. The components of stress in polar coordinate system are

$$\sigma_{rr}+\sigma_{\theta\theta}=2[\phi'(z)+\overline{\phi'(z)}] \tag{3}$$

$$\sigma_{rr}+i\tau_{r\theta}=\phi'(z)+\overline{\phi'(z)}-\left[\overline{z\phi''(z)}+\frac{\overline{z}}{z}\overline{\psi'(z)}\right]. \tag{4}$$

2.2 Determination of Steady-State Temperature Distributions. Consider a circular annulus with inner radius a and outer radius b which is subjected to a point heat source with the strength

Contributed by the Applied Mechanics Division of THE AMERICAN SOCIETY OF MECHANICAL ENGINEERS for publication in the ASME JOURNAL OF APPLIED MECHANICS. Manuscript received by the ASME Applied Mechanics Division, July 28, 1998; final revision, Jan. 29, 1999. Associate Technical Editor: J. R. Barber. Discussion on the paper should be addressed to the Technical Editor, Professor Lewis T. Wheeler, Department of Mechanical Engineering, University of Houston, Houston, TX 77204-4792, and will be accepted until four months after final publication of the paper itself in the ASME JOURNAL OF APPLIED MECHANICS.

q_0 located at the point $z=z_0=r_0e^{i\theta_0}$ (see Fig. 1). For steady-state heat conduction problem the temperature potential $g'(z)$ can be written as

$$g'(z)=Q_0\ln(z-z_0)+\sum_{n=-\infty}^{\infty}\lambda_n z^n \tag{5}$$

where $Q_0=-q_0/2\pi k$ with k being heat conductivity and λ_n are the unknown coefficients which will be determined as the thermal boundary condition is imposed. In the present analysis, the temperatures at the inner and outer boundaries of the annulus are denoted by $T_1(\theta)$ and $T_2(\theta)$, respectively, i.e.,

$$T=\frac{1}{2}[g'(t)+\overline{g'(t)}]=T_1(\theta)$$

$$=\sum_{m=0}^{\infty}(A_m\cos m\theta+B_m\sin m\theta)\quad \text{on}\quad t=ae^{i\theta} \tag{6}$$

$$T=\frac{1}{2}[g'(t)+\overline{g'(t)}]=T_2(\theta)$$

$$=\sum_{m=0}^{\infty}(A'_m\cos m\theta+B'_m\sin m\theta)\quad \text{on}\quad t=be^{i\theta}. \tag{7}$$

On substituting (5) into (6) and (7) and applying the techniques of Fourier series we find

$$\lambda_0=A_0-\frac{Q_0}{4\pi}\int_0^{2\pi}\ln[a^2+r_0^2-2ar_0\cos(\theta-\theta_0)]d\theta \tag{8}$$

$$\lambda_n=\frac{1}{2\pi(b^{2n}-a^{2n})}\int_0^{2\pi}\{2(b^nT_2-a^nT_1)$$
$$-Q_0[b^n\ln(b^2+r_0^2-2br_0\cos(\theta-\theta_0))$$
$$-a^n\ln(a^2+r_0^2-2ar_0\cos(\theta-\theta_0))]\}e^{-in\theta}d\theta\quad(n\neq0) \tag{9}$$

and for consistency we require

$$A'_0=A_0-\frac{Q_0}{4\pi}\int_0^{2\pi}[\ln(a^2+r_0^2-2ar_0\cos(\theta-\theta_0))$$
$$-\ln(b^2+r_0^2-2br_0\cos(\theta-\theta_0))]d\theta. \tag{10}$$

It should be emphasized that the strength of a point heat source must be chosen to satisfy (10) such that the condition of energy balance between a point source and the temperatures prescribed at the inner and outer boundaries of the annulus is ensured within the context of steady state heat conduction theory ([9]). Mathematically, the difference between A'_0 and A_0 in (10), which accounts for the net heat flow from outside to inside the annulus, must be equal to the integral term which accounts for the heat generation due to the presence of a point heat source. For the problem with the absence of a point heat source, the temperature potential in (5) is replaced by

$$g'(z)=\lambda^*\ln z+\sum_{n=-\infty}^{\infty}\lambda_n z^n \tag{11}$$

where the unknown coefficients λ^* and λ_n can be obtained from (8)–(10) by putting $Q_0=\lambda^*$ and $r_0=0$ as

$$\lambda^*=\frac{A'_0-A_0}{\ln b-\ln a},\quad \lambda_0=\frac{A_0\ln b-A'_0\ln a}{\ln b-\ln a} \tag{12}$$

and

$$\lambda_n=\frac{(b^nA'_n-a^nA_n)-i(b^nB'_n-a^nB_n)}{b^{2n}-a^{2n}}\quad(n\neq0) \tag{13}$$

$$\lambda_{-n}=\frac{(b^{-n}A'_n-a^{-n}A_n)-i(b^{-n}B'_n-a^{-n}B_n)}{b^{-2n}-a^{-2n}}\quad(n\neq0). \tag{14}$$

Upon integration of (5) and (11), the temperature functions become

$$g(z)=Q_0[(z-z_0)(\ln(z-z_0)-1)]+\lambda_{-1}\ln z+g^*(z) \tag{15}$$

and

$$g(z)=\lambda^*z(\ln z-1)+\lambda_{-1}\ln z+g^*(z), \tag{16}$$

respectively, where

$$g^*(z)=\sum_{\substack{n=-\infty\\ n\neq-1}}^{\infty}\frac{\lambda_n}{n+1}z^{n+1} \tag{17}$$

is analytic and single-valued everywhere in the annulus.

3 Thermal Stresses in the Annulus

For the annular problem with a point heat source the stress functions can be written as ([10])

$$\phi(z)=Az\ln z+B\ln z+\phi^*(z) \tag{18}$$

$$\psi(z)=C\ln z+\psi^*(z) \tag{19}$$

where A is real constant and B, C are complex constants which are related by the following equations ([10]):

$$(\kappa+1)Az+\kappa B+\overline{C}=\frac{-2\mu\beta}{2\pi i}[g(z)]_c \tag{20}$$

$$B-\overline{C}=\frac{[-Y+iX]_c}{2\pi i} \tag{21}$$

where $[f(z)]_c=f(r,\theta+2\pi)-f(r,\theta)$ which denotes the jump of the function $f(z)$ when enclosing the contour c within the annulus.

Note that the singularity of the term $z\ln z$ appearing in (18) results from the logarithmic singularity of the temperature function induced by a point heat source. The two holomorphic functions $\phi^*(z),\psi^*(z)$ in (18) and (19), respectively, can be expressed in a series form as

$$\phi^*(z)=\sum_{n=-\infty}^{\infty}L_nz^n,\quad \psi^*(z)=\sum_{n=-\infty}^{\infty}M_nz^n \tag{22}$$

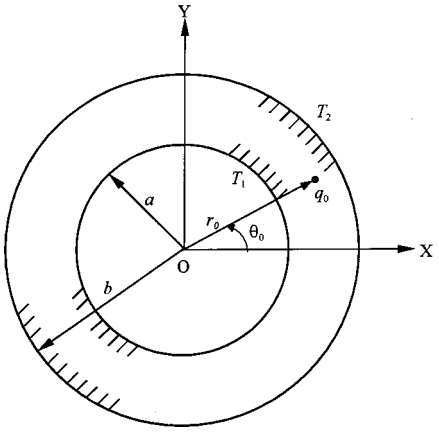

Fig. 1 Problem configuration for the annulus

where the constant coefficients L_n and M_n may be determined as the stress or displacement boundary condition is imposed. The boundary condition on the inner and outer boundaries of the annulus can be expressed, respectively, as

$$\gamma_1\phi(t)+t\overline{\phi'(t)}+\overline{\psi(t)}+\delta_1 g(t)=f_1(t) \quad \text{on } t=ae^{i\theta} \tag{23}$$

$$\gamma_2\phi(t)+t\overline{\phi'(t)}+\overline{\psi(t)}+\delta_2 g(t)=f_2(t) \quad \text{on } t=be^{i\theta} \tag{24}$$

where $\gamma_1=\gamma_2=1$, $\delta_1=\delta_2=0$, $f_1(t)=f_2(t)=R(t)$ for the stress boundary value problem with $R(t)$ being a known resultant force on the inner and outer boundaries of the annulus while $\gamma_1=\gamma_2=-\kappa$, $\delta_1=\delta_2=-2\mu\beta$, $f_1(t)=f_2(t)=-2\mu\beta D(t)$ for the displacement boundary value problem with $D(t)$ being a single-valued displacement function. Since the case of the displacement-free condition on both the inner and outer boundaries of the annulus is excluded from our analysis, the resultant force over the entire system becomes zero and the unknown coefficients *A*, *B*, and *C* appearing in (18) and (19) can be obtained by substituting (15) and (16) into (20) and (21) as

$$A=\frac{-2\mu\beta Q_0}{1+\kappa}, \quad B=\overline{C}=\frac{-2\mu B(\lambda_{-1}-Q_0 z_0)}{1+\kappa}, \quad \text{for } |z_0|<z<b \tag{25}$$

$$A=\frac{-2\mu\beta R_0}{1+\kappa}, \quad B=\overline{C}=\frac{-2\mu\beta\lambda_{-1}}{1+\kappa}, \quad \text{for } a<z<|z_0| \tag{26}$$

where $Q_0=-q_0/2\pi k$, $R_0=0$ for the problem with a point heat source and $Q_0=R_0=\lambda^*$, $z_0=0$ for the problem with the absence of a point heat source. Substitution of (15), (16), (18), and (19) into (23) and (24) results in

$$\gamma_1\phi^*(t)+t\overline{\phi^{*\prime}(t)}+\overline{\psi^*(t)}+\delta_1 g^*(t)=F_1(t) \quad \text{on } t=ae^{i\theta} \tag{27}$$

$$\gamma_2\phi^*(t)+t\overline{\phi^{*\prime}(t)}+\overline{\psi^*(t)}+\delta_2 g^*(t)=F_2(t) \quad \text{on } t=be^{i\theta} \tag{28}$$

where

$$\begin{aligned}F_1(t)=f_1(t)&+\gamma_1\left(\frac{2\mu\beta R_0}{1+\kappa}t\ln t+\frac{2\mu\beta\lambda_{-1}}{1+\kappa}\ln t\right)\\&+\frac{2\mu\beta R_0}{1+\kappa}t(1+\ln\overline{t})+\frac{2\mu\beta\overline{\lambda_{-1}}}{1+\kappa}\frac{t}{\overline{t}}+\frac{2\mu\beta\lambda_{-1}}{1+\kappa}\ln\overline{t}\\&-\delta_1 Q_0((t-z_0)\ln(t-z_0))-\delta_1\lambda_{-1}\ln t+\delta_1 Q_0(t-z_0)\end{aligned} \tag{29}$$

and

$$\begin{aligned}F_2(t)=f_2(t)&+\gamma_2\left(\frac{2\mu\beta Q_0}{1+\kappa}t\ln t+\frac{2\mu\beta(\lambda_{-1}-Q_0 z_0)}{1+\kappa}\ln t\right)\\&+t\frac{2\mu\beta Q_0}{1+\kappa}(1+\ln\overline{t})+\frac{2\mu\beta(\overline{\lambda_{-1}}-Q_0\overline{z_0})}{1+\kappa}\frac{t}{\overline{t}}\\&+\frac{2\mu\beta(\lambda_{-1}-Q_0 z_0)}{1+\kappa}\ln\overline{t}-\delta_2 Q_0((t-z_0)\ln(t-z_0))\\&-\delta_2\lambda_{-1}\ln t+\delta_2 Q_0(t-z_0).\end{aligned} \tag{30}$$

3.1 Single-Valuedness of Complex Functions. Before solving the boundary value problem (27) and (28), we must examine whether $F_1(t)$ and $F_2(t)$ are single-valued functions on the inner boundary or on the outer boundary. In the following discussions, c_1 pertains to the inner boundary while c_2 pertains to the outer boundary.

(1) Stress-Free Boundary Condition ($\gamma_1=\gamma_2=1, \delta_1=\delta_2=0$)

$$\begin{aligned}[F_1(t)]_{c_1}=[f_1(t)]_{c_1}&+\frac{2\mu\beta R_0}{1+\kappa}[t\ln t]_{c_1}+\frac{2\mu\beta\lambda_{-1}}{1+\kappa}[\ln t]_{c_1}\\&+\frac{2\mu\beta R_0}{1+\kappa}[t(1+\ln\overline{t})]_{c_1}+\frac{2\mu\beta\overline{\lambda_{-1}}}{1+\kappa}\left[\frac{t}{\overline{t}}\right]_{c_1}\\&+\frac{2\mu\beta\lambda_{-1}}{1+\kappa}[\ln\overline{t}]_{c_1} \quad \text{on } t=ae^{i\theta}\end{aligned} \tag{31}$$

where $f_1(t)$ represents the resultant force on the inner boundary c_1 which is a single-valued function and $[f_1(t)]_{c_1}=0$. Since c_1 is the internal boundary of the doubly connected region and is described in a clockwise manner, $[\ln t]_{c_1}=-2\pi i$, $[\ln\overline{t}]_{c_1}=2\pi i$ and knowing that $[t/\overline{t}]_{c_1}=0$, so $F_1(t)$ is a single-valued function on c_1

$$\begin{aligned}[F_2(t)]_{c_2}=[f_2(t)]_{c_2}&+\frac{2\mu\beta Q_0}{1+\kappa}[t\ln t]_{c_2}\\&+\frac{2\mu\beta(\lambda_{-1}-Q_0 z_0)}{1+\kappa}[\ln t]_{c_2}+\frac{2\mu\beta Q_0}{1+\kappa}[t(1+\ln\overline{t})]_{c_2}\\&+\frac{2\mu\beta(\overline{\lambda_{-1}}-Q_0\overline{z_0})}{1+\kappa}\left[\frac{t}{\overline{t}}\right]_{c_2}\\&+\frac{2\mu\beta(\lambda_{-1}-Q_0 z_0)}{1+\kappa}[\ln\overline{t}]_{c_2} \quad \text{on } t=be^{i\theta}\end{aligned} \tag{32}$$

where $f_2(t)$ is a known function and single-valued on c_2. Since c_2 is the outer boundary of the doubly connected region which is described in counterclockwise sense, $[\ln t]_{c_2}=2\pi i$, $[\ln\overline{t}]_{c_2}=-2\pi i$ and knowing that $[t/\overline{t}]_{c_2}=0$, so we have $[F_2(t)]_{c_2}=0$.

(2) Displacement-Free Boundary Condition ($\gamma_1=\gamma_2=-\kappa$, $\delta_1=\delta_2=-2\mu\beta$)

$$\begin{aligned}[F_1(t)]_{c_1}=[f_1(t)]_{c_1}&-\kappa\left(\frac{2\mu\beta R_0}{1+\kappa}[t\ln t]_{c_1}+\frac{2\mu\beta\lambda_{-1}}{1+\kappa}[\ln t]_{c_1}\right)\\&+\frac{2\mu\beta R_0}{1+\kappa}[t(1+\ln\overline{t})]_{c_1}+\frac{2\mu\beta\overline{\lambda_{-1}}}{1+\kappa}\left[\frac{t}{\overline{t}}\right]_{c_1}\\&+\frac{2\mu\beta\lambda_{-1}}{1+\kappa}[\ln\overline{t}]_{c_1}+2\mu\beta Q_0[(t-z_0)\ln(t-z_0)]_{c_1}\\&-2\mu\beta Q_0[(t-z_0)]_{c_1}+2\mu\beta\lambda_{-1}[\ln t]_{c_1} \quad \text{on } t=ae^{i\theta}\end{aligned} \tag{33}$$

where $f_1(t)$ represents the given displacement function which is single-valued on c_1. As c_1 is described in a clockwise sense and knowing that z_0 is located outside the contour c_1 and $R_0=0$ for a point heat source considered, we obtain $[\ln(t-z_0)]_{c_1}=0$, $[\ln t]_{c_1}=-2\pi i$, and $[\ln\overline{t}]_{c_1}=2\pi i$, so we have $[F_1(t)]_{c_1}=0$. As the problem with the absence of a point heat source, we obtain $R_0=Q_0$, $z_0=0$ and knowing that $[t\ln t]_{c_1}=-2\pi it$, $[t\ln\overline{t}]_{c_1}=2\pi it$, so we also have $[F_1(t)]_{c_1}=0$.

$$[F_2(t)]_{c_2}=[f_2(t)]_{c_2}-\kappa\left(\frac{2\mu\beta Q_0}{1+\kappa}[t\ln t]_{c_2}+\frac{2\mu\beta(\lambda_{-1}-Q_0z_0)}{1+\kappa}[\ln t]_{c_2}\right)+\frac{2\mu\beta Q_0}{1+\kappa}[t(1+\ln\bar{t})]_{c_2}+\frac{2\mu\beta(\overline{\lambda_{-1}}-Q_0z_0)}{1+\kappa}\left[\frac{t}{\bar{t}}\right]_{c_2}$$

$$+\frac{2\mu\beta(\lambda_{-1}-Q_0z_0)}{1+\kappa}[\ln\bar{t}]_{c_2}+2\mu\beta(Q_0[(t-z_0)\ln(t-z_0)]_{c_2}-Q_0[(t-z_0)]_{c_2}+\lambda_{-1}[\ln t]_{c_2})\quad\text{on } t=be^{i\theta} \tag{34}$$

where $f_2(t)$ is a known function and is a single-valued function on c_2. As c_2 is described in a counterclockwise sense and knowing that z_0 is located inside the contour c_2, we obtain $[\ln(t-z_0)]_{c_2}=2\pi i$,$[\ln t]_{c_2}=2\pi i$,$[\ln\bar{t}]_{c_2}=-2\pi i$, so we have $[F_2(t)]_{c_2}=0$. For the problem with the absence of a point heat source we obtain $z_0=0$ and knowing that $[t\ln t]_{c_2}=2\pi it$, $[t\ln\bar{t}]_{c_2}=-2\pi it$; so we also have $[F_2(t)]_{c_2}=0$.

On comparing (31)–(34) it is clear that both the stress and displacement boundary value problems may be solved by examining the Eqs. (27) and (28) for which $\phi^*(z)$, $\psi^*(z)$ are single-valued holomorphic functions and the single-valued functions $F_1(t)$ and $F_2(t)$ are interpreted according to (31)–(34).

3.2 Compatibility Identity. Consider the annular region $a<|z|<b$ by S and the annuli $a^2b^{-1}<|z|<a$, $b<|z|<b^2a^{-1}$ by S^- and S^+, respectively (see Fig. 2). If we use the continuation across each boundary, $\phi^*(z)$ can be extended from S into the annuli S^-,S^+ by the definitions ([11])

$$\phi^*(z)=-\frac{1}{\gamma_1}\left\{z\overline{\phi^{*\prime}\left(\frac{a^2}{\bar{z}}\right)}+\overline{\psi^*\left(\frac{a^2}{\bar{z}}\right)}+\delta_1g^*(z)\right\}\quad\text{for } z\in S^- \tag{35}$$

$$\phi^*(z)=-\frac{1}{\gamma_2}\left\{z\overline{\phi^{*\prime}\left(\frac{b^2}{\bar{z}}\right)}+\overline{\psi^*\left(\frac{b^2}{\bar{z}}\right)}+\delta_2g^*(z)\right\}\quad\text{for } z\in S^+. \tag{36}$$

$\phi^*(z)$ is thus holomorphic in the three regions S^-, S, S^+. Notice that $g^*(z)$ is also holomorphic and single-valued in S^- and S^+ because there is no singularity or point heat source located in the region S^- and S^+. If we invert these continuations we find

$$\psi^*(z)=-\gamma_1\overline{\phi^*\left(\frac{a^2}{\bar{z}}\right)}-\frac{a^2}{z}\phi^{*\prime}(z)-\delta_1\overline{g^*\left(\frac{a^2}{\bar{z}}\right)}\quad\text{for } z\in S \tag{37}$$

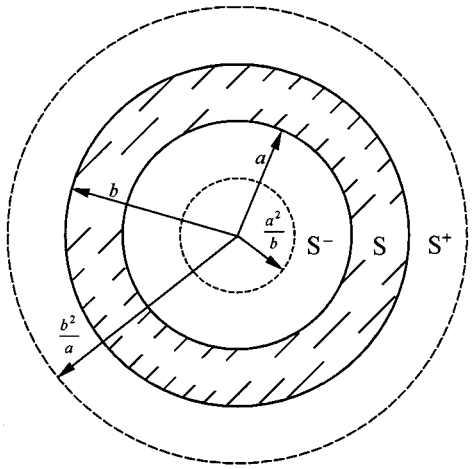

Fig. 2 Analytic regions of the annulus

$$\psi^*(z)=-\gamma_2\overline{\phi^*\left(\frac{b^2}{\bar{z}}\right)}-\frac{b^2}{z}\phi^{*\prime}(z)-\delta_2\overline{g^*\left(\frac{b^2}{\bar{z}}\right)}\quad\text{for } z\in S \tag{38}$$

and hence $\phi^*(z)$ must satisfy the compatibility identity

$$\gamma_2\overline{\phi^*\left(\frac{b^2}{\bar{z}}\right)}-\gamma_1\overline{\phi^*\left(\frac{a^2}{\bar{z}}\right)}+\frac{b^2-a^2}{z}\phi^{*\prime}(z)+\delta_2\overline{g^*\left(\frac{b^2}{\bar{z}}\right)}-\delta_1\overline{g^*\left(\frac{a^2}{\bar{z}}\right)}=0\quad\text{for } z\in S. \tag{39}$$

On substituting (35) and (36) into the boundary conditions (27) and (28) we obtain the following Hilbert problems:

$$\phi^*(t)-\phi^{*-}(t)=\frac{1}{\gamma_1}[F_1(t)-\delta_1(g^*(t)-g^{*-}(t))]\quad\text{on } t=ae^{i\theta} \tag{40}$$

$$\phi^*(t)-\phi^{*+}(t)=\frac{1}{\gamma_2}[F_2(t)-\delta_2(g^*(t)-g^{*+}(t))]\quad\text{on } t=be^{i\theta} \tag{41}$$

where $\phi^{*+}(z)$ and $\phi^{*-}(z)$ (or $g^{*+}(z)$ and $g^*(z)$) denote the limits on $|z|=b$ and $|z|=a$ of $\phi^*(z)$ (or $g^*(z)$) in S^+ and S^-, respectively. Since $\phi^*(z)$ and $g^*(z)$ are holomorphic and single-valued in S^-, S, and S^+, they may be represented by the Laurent series

$$\phi^*(z)=\begin{cases}=\sum_{n=-\infty}^{\infty}L_n^-z^n & (z\in S^-)\\ =\sum_{n=-\infty}^{\infty}L_nz^n & (z\in S)\\ =\sum_{n=-\infty}^{\infty}L_n^+z^n & (z\in S^+)\end{cases} \tag{42}$$

$$g^*(z)=\begin{cases}=\sum_{\substack{n=-\infty\\ n\neq-1}}^{\infty}\frac{\lambda_n^-}{n+1}z^{n+1} & (z\in S^-)\\ =\sum_{\substack{n=-\infty\\ n\neq-1}}^{\infty}\frac{\lambda_n}{n+1}z^{n+1} & (z\in S)\\ =\sum_{\substack{n=-\infty\\ n\neq-1}}^{\infty}\frac{\lambda_n^+}{n+1}z^{n+1} & (z\in S^+).\end{cases} \tag{43}$$

Hence the boundary conditions (40) and (41) take the form

$$a^n(L_n-L_n^-)=\frac{1}{2\pi\gamma_1}\int_0^{2\pi}F_1(ae^{i\theta})e^{-in\theta}d\theta-\frac{\delta_1}{\gamma_1}\frac{a^n(\lambda_{n-1}-\lambda_{n-1}^-)}{n}\quad(n\neq0) \tag{44}$$

$$b^n(L_n-L_n^+)=\frac{1}{2\pi\gamma_2}\int_0^{2\pi}F_2(be^{i\theta})e^{-in\theta}d\theta - \frac{\delta_2}{\gamma_2}\frac{b^n(\lambda_{n-1}-\lambda_{n-1}^+)}{n} \quad (n\neq 0) \tag{45}$$

and substituting in the compatibility identity (39) we obtain

$$\gamma_2 b^{2n}L_n^+-\gamma_1 a^{2n}L_n^-+(b^2-a^2)(2-n)\overline{L_{2-n}} + \delta_2 b^{2n}\frac{\lambda_{n-1}^+}{n}-\delta_1 a^{2n}\frac{\lambda_{n-1}^-}{n}=0 \quad (n\neq 0). \tag{46}$$

On eliminating the coefficients L_n^+ and L_n^- from (44)–(46), the constants L_n and λ_{n-1} satisfy the system of equations

$$(\gamma_2 b^{2n}-\gamma_1 a^{2n})L_n+(b^2-a^2)(2-n)\overline{L_{2-n}} +(\delta_2 b^{2n}-\delta_1 a^{2n})\frac{\lambda_{n-1}}{n} =\frac{1}{2\pi}\int_0^{2\pi}(b^nF_2(be^{i\theta})-a^nF_1(ae^{i\theta}))e^{-in\theta}d\theta \quad (n\neq 0). \tag{47}$$

Similar to the previous approach, the coefficient M_n associated with the stress function $\psi^*(z)$ can be found from (37) or (38) which satisfy the system of equations

$$(\gamma_2 b^{-2(n+1)}-\gamma_1 a^{-2(n+1)})\overline{L_{-n}}+(b^{-2}-a^{-2})M_n -(\delta_2 b^{-2(n+1)}-\delta_1 a^{-2(n+1)})\frac{\overline{\lambda_{-(n+1)}}}{n} =\frac{1}{2\pi}\int_0^{2\pi}[b^{-(n+2)}\overline{F_2(be^{i\theta})} - a^{-(n+2)}\overline{F_1(ae^{i\theta})}]e^{-in\theta}d\theta \quad (n\neq 0). \tag{48}$$

Once we obtain the coefficients L_n and M_n (see the Appendix), the stress functions $\phi^*(z)$ and $\psi^*(z)$ are completely solved and the components of stress can be determined by substituting (18) and (19) into (3) and (4). Since no analytical solutions for annular problem with a point heat source are available in the literature, only special cases with the absence of a point heat source are considered here for demonstrating the use of the present approach. We first consider the case that the inner and outer boundaries of the annulus are kept at constant temperature, i.e., $T_1=A_0$ on $|z|=a$ and $T_2=A_0'$ on $|z|=b$ and from (12)–(14) and (29)–(30) we have

$$\lambda^*=\frac{A_0'-A_0}{\ln b-\ln a},\quad \lambda_0=\frac{A_0\ln b-A_0'\ln a}{\ln b-\ln a},\quad \lambda_1=0,\quad \lambda_{-1}=0$$

$$A=\frac{-2\mu\beta\lambda^*}{1+\kappa}=\frac{-2\mu\beta(A_0'-A_0)}{(1+\kappa)(\ln b-\ln a)},\quad B=\overline{C}=\frac{-2\mu\beta\lambda_{-1}}{1+\kappa}=0 \tag{49}$$

$$F_1(t)=F_2(t)=\frac{2\mu\beta\lambda^*}{1+\kappa}[t\ln t+t+t\ln\overline{t}].$$

On substituting the above equations into (*A*3) and (*A*5) we obtain

$$L_1=\frac{1}{2}\left[\frac{2A(a^2\ln a-b^2\ln b)}{(b^2-a^2)}-A\right],\quad L_n=0\ \ (n\neq 1)$$
$$M_{-1}=\frac{2A(a^2\ln a-b^2\ln b)}{(b^{-2}-a^{-2})},\quad M_n=0\ \ (n\neq -1) \tag{50}$$

and the components of stress become

$$\sigma_{rr}=\frac{2\mu\beta}{1+\kappa}\frac{A_0'-A_0}{\ln b-\ln a}\left[-\ln\frac{b}{r}-\frac{a^2(r^2-b^2)}{r^2(b^2-a^2)}\ln\frac{b}{a}\right]$$
$$\sigma_{\theta\theta}=\frac{2\mu\beta}{1+\kappa}\frac{A_0'-A_0}{\ln b-\ln a}\left[1-\ln\frac{b}{r}-\frac{a^2(r^2+b^2)}{r^2(b^2-a^2)}\ln\frac{b}{a}\right] \tag{51}$$

which are in accordance with the results given by Timoshenko and Goodier [7]. Next we consider the case that the inner and outer boundaries of the annulus are subjected to angled temperature distributions, i.e., $T_1=A_1\cos\theta$ on $|z|=a$ and $T_2=A_1'\cos\theta$ on $|z|=b$ and from (8)–(10) and (29)–(30) we have

$$\lambda^*=0,\quad \lambda_0=0,\quad \lambda_1=\frac{bA_1'-aA_1}{b^2-a^2},\quad \lambda_{-1}=\frac{a^2b^2}{a^2-b^2}\left(\frac{A_1'}{b}-\frac{A_1}{a}\right)$$
$$A=\frac{-2\mu\beta\lambda^*}{1+\kappa}=0,$$
$$B=\overline{C}=\frac{-2\mu\beta\lambda_{-1}}{1+\kappa}=\frac{-2\mu\beta}{1+\kappa}\frac{a^2b^2}{a^2-b^2}\left(\frac{A_1'}{b}-\frac{A_1}{a}\right) \tag{52}$$
$$F_1(t)=F_2(t)=\frac{2\mu\beta\lambda_{-1}}{1+\kappa}\left[\ln t+\frac{t}{t}+\ln\overline{t}\right].$$

On substituting the above equations into (*A*3) and (*A*5) we obtain

$$L_2=\frac{-\overline{B}}{(a^2+b^2)},\ L_n=0\ \ (n\neq 2)$$
$$M_{-2}=\frac{-a^2b^2B}{a^2+b^2},\ M_n=0\ \ (n\neq -2) \tag{53}$$

and the components of stress are

$$\sigma_{rr}=pr\left(1-\frac{a^2}{r^2}\right)\left(\frac{b^2}{r^2}-1\right)\cos\theta$$
$$\sigma_{\theta\theta}=pr\left(\frac{a^2b^2}{r^4}+\frac{a^2+b^2}{r^2}-3\right)\cos\theta \tag{54}$$
$$\tau_{r\theta}=pr\left(1-\frac{a^2}{r^2}\right)\left(\frac{b^2}{r^2}-1\right)\sin\theta$$

where

$$p=\frac{\alpha E}{2(1-\nu)}\frac{a^2b^2}{b^4-a^4}\left(\frac{A_1}{a}-\frac{A_1'}{b}\right)$$

which are exactly the same as those given by Timoshenko and Goodier [7] for a plane-strain condition.

4 Results and Discussion

For steady-state heat conduction problems the strength q_0 cannot be arbitrarily chosen once the temperature T_1 at the inner boundary and the temperature T_2 at the outer boundary are assumed as known values. The effect of changing the ratio T_2/T_1 and the wall thickness b/a on the dimensionless strength q_0a/T_0k (with the case $r_0=(a+b)/2$, $\theta_0=0$ deg) can be evaluated from (10) and shown graphically in Fig. 3. For convenience of the calculation in (10), we assume the temperature T_1 and T_2 are kept at constant, i.e., $A_0=T_1$, $A_0'=T_2$ from (6) and (7). Once A_0 and A_0' are given, the dimensionless strength q_0a/T_0k can be determined from (10) for different wall thickness b/a. The result indicates that the strength of a point heat source becomes a positive (or negative) value as the temperature at the outer boundary is lower (or higher) than that at the inner boundary. It is then understood that the condition $T_2<T_1$ (or $T_2>T_1$) will accompany with the presence of a heat source (or sink) such that the energy balance within the annular system is preserved. Furthermore, the strength q_0 changes dramatically with the ratio T_2/T_1 for the annulus with a relatively thin wall. The dilatation stress σ_{rr}

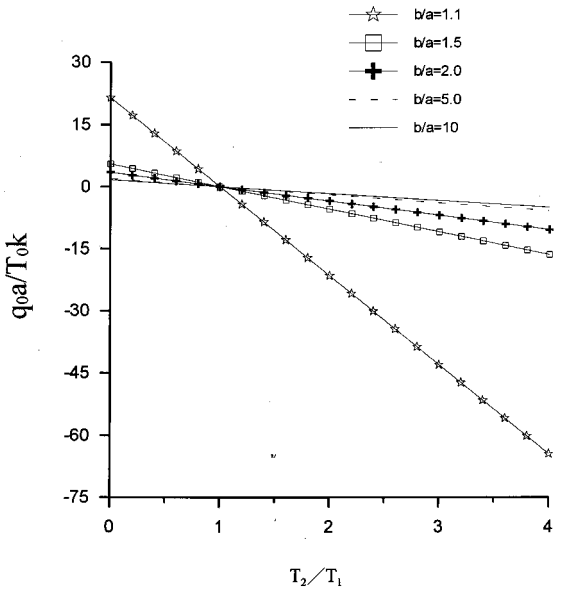

Fig. 3 Relationship between the strength of a point heat source and the temperatures at the boundaries of the annulus

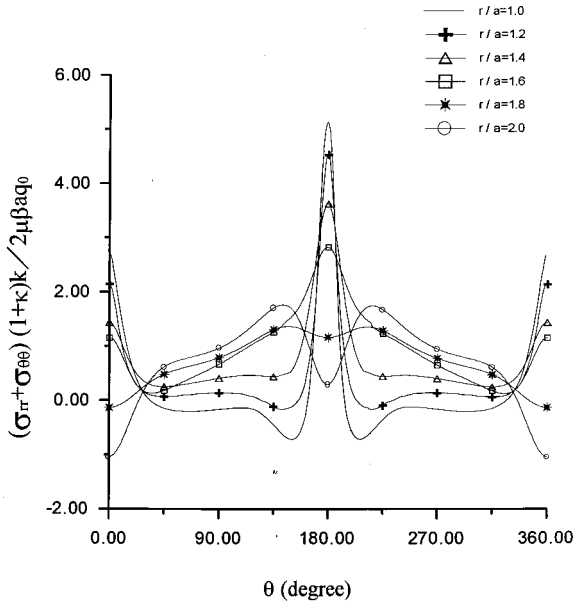

Fig. 5 Dilatation stress in the annulus for the displacement-free and stress-free boundary conditions at the inner and outer boundaries, respectively

$+\sigma_{\theta\theta}$, which is mainly responsible for the result of material failure by fracture, is found for three different cases of boundary value problems as displayed in Figs. 4–6. The conditions $T_2/T_1=3$, $b/a=2$, $r_0/a=1.5$ and $\theta_0=0$ deg are considered for all three cases and the results shown in Figs. 4–6 are based on the series solutions up to the first 20 terms in Eq. (22) which are checked to preserve a good accuracy. It is shown that the maximum dilatation stress always occurs at $\theta_0=180$ deg, which is farthest away from the position where a heat sink resides, for all three cases. For the traction-free boundary condition at both inner and outer boundaries of the annulus, the maximum dilatation stress occurs at the inner boundary with the lower temperature as shown in Fig. 4. For the displacement-free condition (or the traction-free condition) at the inner boundary and traction-free condition (or displacement-free condition) at the outer boundary, the maximum dilatation stress is found to take place at the inner boundary (or outer boundary) as displayed in Fig. 5 (or Fig. 6).

5 Concluding Remarks

In this work we have derived the solutions of the temperature and thermal stresses for an annular region subject to a point heat source. By properly expressing the discrete solutions in terms of explicit functions, the obtained results can be treated as Green's functions which enable us to formulate an integral equation for a crack on the annulus. Since the series solutions derived in this work converge very fast for any wall ratio a/b, the present method is appropriate for analyzing both thin-walled and thick-

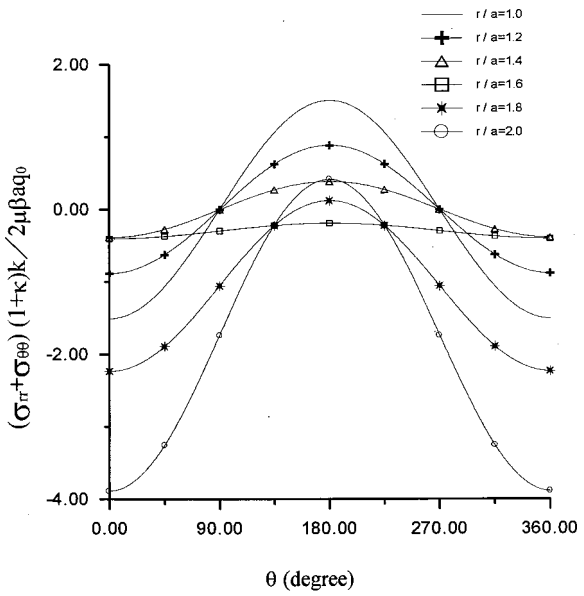

Fig. 4 Dilatation stress in the annulus for the stress-free boundary condition at the inner and outer boundaries

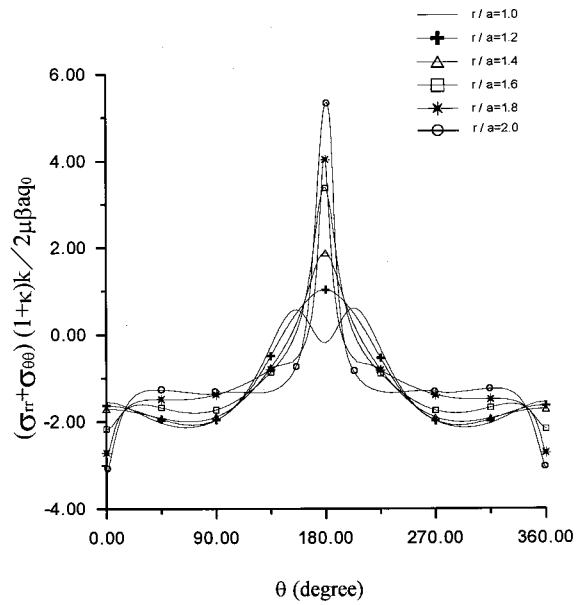

Fig. 6 Dilatation stress in the annulus for the stress-free and displacement-free boundary conditions at the inner and outer boundaries, respectively

walled annuli. In the future study, we will consider the transient behavior of the annular problem in which the consistency condition (10) will not be used.

Acknowledgment

This work was financially supported by the National Science Council, Republic of China, through Grant No. NSC 87-2212-E011-011.

Appendix

Equation (47) can be replaced by

$$(\gamma_2 b^{2n}-\gamma_1 a^{2n})L_n+(b^2-a^2)(2-n)\overline{L_{2-n}} + (\delta_2 b^{2n}-\delta_1 a^{2n})\frac{\lambda_{n-1}}{n}=C_n \tag{A1}$$

or

$$(\gamma_2 b^{2(2-n)}-\gamma_1 a^{2(2-n)})\overline{L_{2-n}}+(b^2-a^2)nL_n + (\delta_2 b^{2(2-n)}-\delta_1 a^{2(2-n)})\frac{\overline{\lambda_{1-n}}}{2-n}=\overline{C_{2-n}}. \tag{A2}$$

On eliminating the coefficients $\overline{L_{2-n}}$ the coefficients L_n satisfy

$$L_n=\Big\{(\gamma_2 b^{2(2-n)}-\gamma_1 a^{2(2-n)})C_n+(n-2)(b^2-a^2)\overline{C_{2-n}} +(b^2-a^2)(\delta_2 b^{2(2-n)}-\delta_1 a^{2(2-n)})\overline{\lambda_{1-n}}-(\gamma_2 b^{2(2-n)} -\gamma_1 a^{2(2-n)})(\delta_2 b^{2n}-\delta_1 a^{2n})\frac{\lambda_{n-1}}{n}\Big\}\Big/\{(\gamma_2 b^{2n}-\gamma_1 a^{2n}) \times(\gamma_2 b^{2(2-n)}-\gamma_1 a^{2(2-n)})+n(n-2)(b^2-a^2)^2\} \quad (n\neq 0). \tag{A3}$$

Similarly, Eq. (48) can be replaced by

$$(\gamma_2 b^{-2(n+1)}-\gamma_1 a^{-2(n+1)})\overline{L_{-n}}+(b^{-2}-a^{-2})M_n -(\delta_2 b^{-2(n+1)}-\delta_1 a^{-2(n+1)})\frac{\overline{\lambda_{-(n+1)}}}{n}=D_n \quad (n\neq 0). \tag{A4}$$

On substituting (*A*3) into (*A*4) we find

$$M_n=\frac{1}{(b^{-2}-a^{-2})}\Big\{(\gamma_1 a^{-2(n+1)}-\gamma_2 b^{-2(n+1)})\Big[(\gamma_2 b^{2(n+2)}-\gamma_1 a^{2(n+2)})\overline{C_{-n}}-(n+2)(b^2-a^2)C_{n+2} +(b^2-a^2)(\delta_2 b^{2(n+2)}-\delta_1 a^{2(n+2)})\lambda_{n+1}+(\gamma_2 b^{2(n+2)}-\gamma_1 a^{2(n+2)})(\delta_2 b^{-2n}-\delta_1 a^{-2n})\frac{\overline{\lambda_{-(n+1)}}}{n}\Big]\Big/[(\gamma_2 b^{-2n}-\gamma_1 a^{-2n}) \times(\gamma_2 b^{2(n+2)}-\gamma_1 a^{2(n+2)})+n(n+2)(b^2-a^2)^2]-(\delta_1 a^{-2(n+1)}-\delta_2 b^{-2(n+1)})\frac{\overline{\lambda_{-(n+1)}}}{n}+D_n\Big\} \quad (n\neq 0) \tag{A5}$$

where the constants C_n and D_n appearing in (*A*1)–(*A*5) are

$$\begin{aligned}
C_n&=\frac{1}{2\pi}\int_0^{2\pi}(b^n F_2(be^{i\theta})-a^n F_1(ae^{i\theta}))e^{-in\theta}d\theta\\
&=\frac{1}{2\pi}\int_0^{2\pi}\{(b^n f_2(be^{i\theta})-a^n f_1(ae^{i\theta}))+(\gamma_1 B+\overline{C}+\delta_2\lambda_{-1})a^n\ln a-(\gamma_2 B+\overline{C}+\delta_2\lambda_{-1})b^n\ln b\\
&\quad+[(\gamma_1 A\ln a+\overline{A}(1+\ln a))a^{n+1}-(\gamma_2 A\ln b+\overline{A}(1+\ln b))b^{n+1}]e^{i\theta}+\overline{B}(a^n-b^n)e^{i2\theta}\\
&\quad+q_0[\delta_2(be^{i\theta}-r_0e^{i\theta_0})[\ln(be^{i\theta}-r_0e^{i\theta_0})-1]b^n-\delta_1(ae^{i\theta}-r_0e^{i\theta_0})[\ln(ae^{i\theta}-r_0e^{i\theta_0})-1]a^n]\\
&\quad+i\theta[\{(\gamma_1 A-\overline{A}+\delta_1 q_0)a^{n+1}-(\gamma_2 A-\overline{A}+\delta_2 q_0)b^{n+1}\}e^{i\theta}+(\gamma_1 B-\overline{C}+\delta_1\lambda_{-1})a^n-(\gamma_2 B+\overline{C}+\delta_2\lambda_{-1})b^n]\}e^{-in\theta}d\theta
\end{aligned} \tag{A6}$$

$$\begin{aligned}
D_n&=\frac{1}{2\pi}\int_0^{2\pi}(b^{-(n+2)}\overline{F_2(be^{i\theta})}-a^{-(n+2)}\overline{F_1(ae^{i\theta})})e^{-in\theta}d\theta\\
&=\frac{1}{2\pi}\int_0^{2\pi}\{(b^{-(n+2)}\overline{f_2(be^{i\theta})}-a^{-(n+2)}\overline{f_1(ae^{i\theta})})+(\gamma_1\overline{B}+C+\delta_1\overline{\lambda_{-1}})a^{-(n+2)}\ln a-(\gamma_2\overline{B}+C+\delta_2\overline{\lambda_{-1}})b^{-(n+2)}\ln b\\
&\quad+[(\gamma_1\overline{A}\ln a+A(1+\ln a))a^{-(n+1)}-(\gamma_2\overline{A}\ln b+A(1+\ln b))b^{-(n+1)}]e^{-i\theta}\\
&\quad+q_0[\delta_2(be^{-i\theta}-r_0e^{-i\theta_0})[\ln(be^{-i\theta}-r_0e^{-i\theta_0})-1]b^{-(n+2)}-\delta_1(ae^{-i\theta}-r_0e^{-i\theta_0})[\ln(ae^{-i\theta}-r_0e^{-i\theta_0})-1]a^{-(n+2)}]\\
&\quad+B(a^n-b^n)e^{-i2\theta}+i\theta[\{(\gamma_2\overline{A}-A)b^{-(n+1)}-(\gamma_1\overline{A}-A)a^{-(n+1)}\}e^{-i\theta}+(\gamma_2\overline{B}-C+\delta_2\overline{\lambda_{-1}})b^{-(n+2)}\\
&\quad-(\gamma_1\overline{B}+C+\delta_1\overline{\lambda_{-1}})a^{-(n+2)}]\}e^{-in\theta}d\theta,
\end{aligned} \tag{A7}$$

respectively. It is interesting to see that, for the stress boundary value problem with $\gamma_1=\gamma_2=1$, $\delta_1=\delta_2=0$, the constants L_n and M_n are only dependent on the coefficients λ^* and λ_{-1} or the coefficients A_0, A_0', B_0, B_0', A_1, A_1', B_1, and B_1'. This gives the conclusion that the temperature distribution along the boundary with the terms in $\cos 2\theta$, $\sin 2\theta$, and higher harmonic in the temperature series do not produce any thermal stress in the annulus.

References

[1] Lamè, G., 1852, *Lecons sur la Thèorie Mathèmatique de l'Elasticitè des Corps Solides*, Gauthier-Villars, Paris.

[2] Michell, J. H., 1899, ''On the Direct Determination of Stress in an Elastic Solid,'' Proc. London Math. Soc., **31**, pp. 100–124.

[3] Bowie, O. L., and Freese, C. E., 1972, ''Elastic Analysis for a Radial Crack in a Circular Ring,'' Eng. Fract. Mech., **4**, pp. 315–321.

[4] Delale, F., and Erdogan, F., 1982, ''Stress Intensity Factors in a Hollow Cylinder Containing a Radial Crack,'' Int. J. Fract., **20**, pp. 251–265.

[5] Worden, R. E., and Keer, L. M., 1991, ''Green's Functions for a Point Load and Dislocation in an Annular Region,'' ASME J. Appl. Mech., **58**, pp. 954–959.

[6] Cheng, W., and Finnie, I., 1989, ''Stress Intensity Factors for Radial Cracks in Circular Cylinders and Other Simply Closed Cylindrical Bodies,'' Eng. Fract. Mech., **32**, pp. 767–774.

[7] Timoshenko, S. P., and Goodier, J. N., 1970, *Theory of Elasticity*, 3rd Ed., McGraw-Hill, New York.

[8] Bogdanoff, J. L., 1954, ''Note on Thermal Stress,'' ASME J. Appl. Mech., **21**, p. 88.

[9] Carslaw, H. S., and Jaeger, J. C., 1965, *Conduction of Heats in Solids*, Clarendon Press, Oxford, UK.

[10] Chao, C. K., and Shen, M. H., 1997, ''On Bonded Circular Inclusions in Plane Thermoelasticity,'' ASME J. Appl. Mech., **64**, pp. 1000–1004.

[11] Muskhelishvili, N. I., 1954, *Some Basic Problems of Mathematical Theory of Elasticity*, P. Noordhoff, Groningen.

On the Characterization of Dynamic Properties of Random Processes by Spectral Parameters

G. Petrucci
Dipartimento di Meccanica e Aeronautica

M. Di Paola
Dipartimento di Ingegneria Strutturale e Geotecnica,
e-mail: dipaola@stru.diseg.unipa.it

B. Zuccarello
Dipartimento di Meccanica e Aeronautica,
e-mail: zuccarello@dima.unipa.it

Universita degli Studi di Palermo,
90128 Palermo, Italy

This paper deals with the general problem of directly relating the distribution of ranges of wide band random processes to the power spectral density (PSD) by means of closed-form expressions. Various attempts to relate the statistical distribution of ranges to the PSD by means of the irregularity factor or similar parameters have been done by several authors but, unfortunately, they have not been fully successful. In the present study, introducing the so-called analytic processes, the reasons for which these parameters are insufficient to an unambiguous determination of the range distribution and the fact that parameters regarding the time-derivative processes are needed have been explained. Furthermore, numerical simulations have shown that the range distributions depend on the irregularity factor and bandwidth parameter of both the process and its derivative. These observations are the basis for the determination of accurate relationships between range distributions and PSDs. [S0021-8936(00)02903-2]

1 Introduction

In a random process the way in which the maxima and the minima of a signal follow one another strongly depends on the distribution of its energy over frequency. This characteristic determinates the statistic distribution of local *extrema* (peaks and valley) and *ranges* (difference between a peak and the consecutive valley). These latter are of great interest in fatigue design, as fatigue damage is mainly related to the stress ranges, and in oceanography where ranges correspond to the heights of waves in the ocean.

The statistic distributions of the extrema has been theoretically addressed ([1,2]) for both narrow-band processes (in which two generic consecutive extrema are almost symmetrically placed with respect to the mean level) and wide-band processes (in which consecutive peaks and valleys can occur without mean level crossing) and involve only the *irregularity factor* α ([1–5]). Concerning the statistic distribution of the ranges, only the case of narrow-band processes has been theoretically solved. In this particular case, in fact, the range distribution coincides with that of the extreme one. In the case of wide-band processes, instead, all attempts to relate the statistical distribution of ranges to the power spectral density (PSD) by means of the irregularity factor ([6–12]) or similar spectral parameters ([13]) have not been fully successful.

In this paper introducing the so-called analytic processes, the time domain interpretation of the irregularity factor and the bandwidth parameter is first given. Then, considering the behavior of analytic processes and their derivatives in the complex plane, the reasons for which the irregularity factor α and the bandwidth parameter q ([14]) are insufficient to give a full probabilistic description of the ranges distribution in a random process are explained. Further considerations on the analytic processes show that analogous parameters relative to the derivative of the process must be introduced in order to obtain the statistical distribution of the ranges. As a confirmation, proper numerical simulations have shown that processes having equal both the spectral parameters of the process can have different range distributions, whereas processes also having the spectral parameters of the time derivative have equal range distributions.

A practical example shows that, although a general closed-form relationship between PSD and range distribution requires further research work, this information can be used at present to obtain useful results in particular cases.

Contributed by the Applied Mechanics Division of THE AMERICAN SOCIETY OF MECHANICAL ENGINEERS for publication in the ASME JOURNAL OF APPLIED MECHANICS. Manuscript received by the ASME Applied Mechanics Division, July 28, 1998; final revision, May 5, 2000. Associate Technical Editor: A. A. Ferri. Discussion on the paper should be addressed to the Technical Editor, Professor Lewis T. Wheeler, Department of Mechanical Engineering, University of Houston, Houston, TX 77204-4792, and will be accepted until four months after final publication of the paper itself in the ASME JOURNAL OF APPLIED MECHANICS.

2 Preliminary Concepts and Definitions

In this section some well-known concepts on analytic processes and spectral parameters are briefly outlined for clarity sake's as well as to introduce appropriate symbologies.

2.1 Analytic Processes. Let $Y(t)$ be a stationary zero mean random process and let $X(t)$ be a complex random process such that its real part is $Y(t)$ whereas its imaginary part is the Hilbert transform of $Y(t)$, that is

$$X(t)=Y(t)+i\hat{Y}(t) \tag{1}$$

where i is the imaginary unit and the accent $\hat{}$ means the Hilbert transform

$$\hat{Y}(t)=\frac{1}{\pi}\int_{-\infty}^{\infty}\frac{Y(t)}{t-\tau}d\tau. \tag{2}$$

The random process $X(t)$ is called the analytic process ([15]) and owns some important characteristics. It is well known that the autocorrelation function $R_X(t)$ of $X(t)$ is related to the autocorrelation function of $Y(t)$ and $\hat{Y}(t)$ by means of the following relationship:

$$R_X(\tau)=R_Y(\tau)+i\hat{R}_Y(\tau) \tag{3}$$

and the one-sided power spectral density (PSD) of the complex process $X(t)$, denoted as $S_X(\omega)$, is related to the two-sided PSD of the real process $Y(t)$, denoted as $S_Y(\omega)$, by means of

$$S_X(\omega)=2U(\omega)S_Y(\omega) \tag{4}$$

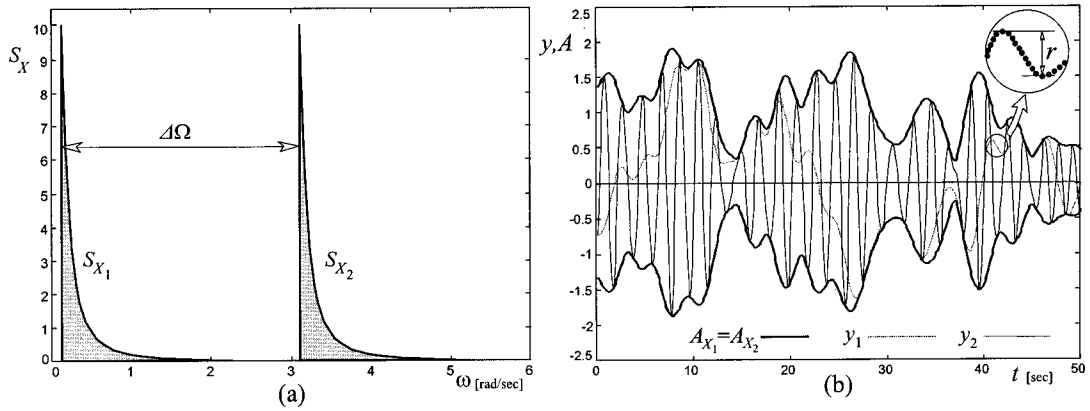

Fig. 1 Power spectral density (PSD) functions S_{X_1} and S_{X_2} (*a*) and corresponding sample functions $y_1(t)$, $y_2(t)$, A_{X_1} and A_{X_2} (*b*).

$U(\omega)$ being the unit step function ($U(\omega)=1 \forall \omega \geq 0$; $U(\omega)=0 \forall \omega < 0$).

The analytic process $X(t)$ can be seen as a vector rotating in the complex plane defined as

$$X(t)=A_X(t)\exp[i\Theta_X(t)] \tag{5}$$

where $A_X(t)$ is the so-called amplitude and $\Theta_X(t)$ is the phase angle respectively defined as

$$A_X(t)=\sqrt{Y^2(t)+\hat{Y}^2(t)} \tag{6a}$$

$$\Theta_X(t)=\tan^{-1}\left[\frac{\hat{Y}(t)}{Y(t)}\right]. \tag{6b}$$

2.2 Spectral Parameters. The statistic distribution of ranges is a feature of great practical significance, especially in oceanography and in fatigue analysis. In a signal a range is defined as the difference in magnitude between a peak (local maximum) and the consecutive valley (local minimum) or, vice versa, between a valley and the consecutive peak (see particular in Fig. 1(*b*)). As previously stated, in a random process, the way in which maxima and minima of a signal follows one another depends on the distribution of the energy over frequency, i.e., on the *bandwidth*. Narrow-band processes are characterized by the fact that two generic consecutive peaks and valleys are almost symmetrically placed with respect to the mean level, while in wide-band processes consecutive peaks and valleys can occur without mean level crossing (Fig. 1(*b*)). The ratio between the mean number of zero crossing and the mean of extrema is called the *irregularity factor* α_X ([3]). The statistic distributions of peaks are well known ([2]) and involve only the α_X parameter, while the conditional distribution function of consecutive peaks and valleys is not known. For these reasons the statistic distribution of the ranges can be theoretically obtained only in the case of narrow-band processes as it coincides with that of the peaks.

Some spectral properties of stochastic processes can be highlighted by using the *spectral moments* ([4,5,14]) defined as

$$\lambda_j=2\int_0^\infty \omega^j S_Y(\omega)d\omega=\int_0^\infty \omega^j S_X(\omega)d\omega \quad (j=1,2\ldots). \tag{7}$$

It has been shown that the spectral moments can be defined in the time domain as the covariance of the analytic process $X(t)$ and its time derivatives by means of the following relationships ([16,17]):

$$\lambda_{2n}=E\left[\frac{d^nX(t)}{dt^n}\,\frac{d^nX^*(t)}{dt^n}\right] \tag{8a}$$

$$i\lambda_{2n+1}=E\left[\frac{d^{n-1}X(t)}{dt^{n-1}}\,\frac{d^nX^*(t)}{dt^n}\right] \tag{8b}$$

where $E[\cdot]$ means stochastic average and the star means complex conjugate.

By means of the spectral moments several spectral parameters, as the distance Ω_X of the centroid of the one-sided PSD from

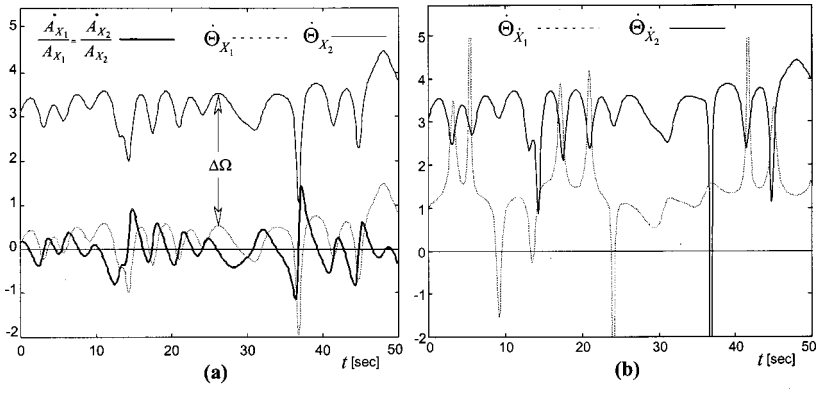

Fig. 2 Sample functions of the processes $\dot{\Theta}_{X_1}, \dot{\Theta}_{X_2}, \dot{A}_{X_1}/A_{X_1}$ coincident with $\dot{A}_{X_2}/A_{X_2}$ (*a*) and $\dot{\Theta}_{\dot{X}_1}$ and $\dot{\Theta}_{\dot{X}_2}$ (*b*)

frequency origin, the radius of gyration ρ_X of the PSD about the frequency origin, and the radius of gyration $\overline{\rho_X}$ of the PSD about its central frequency can be defined ([14,18–20]):

$$\Omega_X = \frac{\lambda_1}{\lambda_0} \tag{9a}$$

$$\rho_X = \sqrt{\frac{\lambda_2}{\lambda_0}} \tag{9b}$$

$$\overline{\rho}_X = \sqrt{\rho_X^2 - \Omega_X^2} = \sqrt{\frac{\lambda_2}{\lambda_0} - \left(\frac{\lambda_1}{\lambda_0}\right)^2}. \tag{10}$$

It is important to note that, considering Eqs. (7), the spectral moments of the analytic process $X(t)$ coincide with those of its real part $Y(t)$ and, consequently, the spectral parameters of $X(t)$ coincide with those of $Y(t)$. This means that the introduction of the imaginary part in analytic processes does not introduce any complication in the numerical evaluation of the spectral parameters whereas, as it will be shown in the following sections, it allows a more complete interpretation of their physical and mathematical meanings.

The bandwidth of a given process has been defined by means of two quantities, the previously introduced *irregularity factor* α_X and the *spectral parameter* q_X introduced by Vanmarcke [14]. It has been shown that α_X ([4]) is defined as

$$\alpha_X = \frac{\lambda_2}{\sqrt{\lambda_0 \lambda_4}} \qquad 0 \leqslant \alpha_X \leqslant 1. \tag{11}$$

It approaches one for narrow-band processes and decreases, approaching zero, when the bandwidth increases.

The spectral parameter q_X is defined as follows:

$$q_X = \frac{\overline{\rho}_X}{\rho_X} = \sqrt{1 - \frac{\lambda_1^2}{\lambda_0 \lambda_2}}; \quad 0 \leqslant q_X \leqslant 1. \tag{12}$$

Unlike the irregularity factor, q_X approaches zero for narrow-band processes and increases, approaching one, when the bandwidth increases.

3 Further Properties of Analytic Processes

In the previous section the spectral parameters have been introduced in the frequency domain. In this section they will be revisited in the time domain taking into account the properties of the analytic processes and using the definitions given in Eqs. (8).

3.1 Time-Domain Properties of Analytic Processes. The time derivatives of the analytic process $X(t)$ defined in Eq. (1) are also analytic processes:

$$\frac{d^n}{dt^n} X(t) = \frac{d^n}{dt^n} Y(t) + i \frac{d^n}{dt^n} \hat{Y}(t). \tag{13}$$

Furthermore, using Eq. (5) it is possible to write

$$\dot{X}(t) = [\dot{A}_X(t) + i\dot{\Theta}_X(t) A_X(t)] \exp[i\Theta_X(t)]$$
$$= \left[\frac{\dot{A}_X(t)}{A_X(t)} + i\dot{\Theta}_X(t)\right] X(t). \tag{14}$$

Equation (14) can also be rewritten as

$$\dot{X}(t) = \omega_X(t) X(t), \tag{15}$$

$\omega_X(t)$ being a complex frequency defined as

$$\omega_X(t) = \frac{\dot{A}_X(t)}{A_X(t)} + i\dot{\Theta}_X(t) = \frac{\dot{X}(t)}{X(t)}. \tag{16}$$

The imaginary part of $\omega_X(t)$ is the angular velocity of the vector $X(t)$ in the complex plane, whereas the real part is related to the time variation of the amplitude.

Relationships similar to Eq. (15) can be written for higher order derivatives of $X(t)$. As an example the second-order derivative of the complex process $X(t)$ can be written as

$$\ddot{X}(t) = \omega_{\dot{X}}(t) \dot{X}(t) = \omega_{\dot{X}}(t) \omega_X(t) X(t) \tag{17}$$

being

$$\omega_{\dot{X}}(t) = \frac{\dot{A}_{\dot{X}}(t)}{A_{\dot{X}}(t)} + i\dot{\Theta}_{\dot{X}}(t) = \frac{\ddot{X}(t)}{\dot{X}(t)}. \tag{18}$$

Let $X_1(t)$ and $X_2(t)$ be two random processes such as the PSD $S_{X_2}(\omega)$ is equal to the PSD $S_{X_1}(\omega)$ but shifted in frequency of a given quantity $\Delta\Omega$ (Fig. 1(*a*)). As an example let

$$S_{X_1}(\omega) = \frac{0.2239}{\omega^2} \quad 0.1 \leqslant \omega \leqslant 2.4 \tag{19}$$

$$S_{X_2}(\omega) = \frac{0.2239}{(\omega - \Delta\Omega)^2} \quad 0.1 + \Delta\Omega \leqslant \omega \leqslant 2.4 + \Delta\Omega \quad (\Delta\Omega = 3); \tag{20}$$

$X_1(t)$ is a broad-band process with $\alpha_{X_1} = 0.36$ and $q_{X_1} = 0.69$, whereas $X_2(t)$ is a narrow-band process with $\alpha_{X_2} = 0.97$ and $q_{X_2} = 0.14$.

The sample functions $x_1(t)$ and $x_2(t)$ of the $X_1(t)$ and $X_2(t)$ processes can be obtained by using the well-known generation formula ([19,20])

$$x_j(t) = y_j(t) + i\hat{y}_j(t) = \sum_{k=1}^{N} \sqrt{2 S_{X_j}(\omega_k) \Delta\omega} \, [\cos(\omega_k t + \Phi_k)$$
$$+ i \operatorname{sen}(\omega_k t + \Phi_k)] \qquad j = 1,2 \tag{21}$$

N being the number of frequency intervals $\Delta\omega$ in which the PSD $S_{X_j}(\omega)$ is discretized and Φ_k the random phase angles uniformly distributed in the range $0 \div 2\pi$. Also, introducing the values obtained by Eq. (21) in Eqs. (6*a*), (16), and (18), the corresponding samples of the amplitude and angular velocity processes can be obtained.

In Fig. 1(*b*) the sample functions $y_1(t)$ and $y_2(t)$ of the processes $Y_1(t)$ and $Y_2(t)$ (obtained using random phase angles equal for both processes) and the corresponding amplitudes are reported; it is possible to note that, although $y_1(t)$ and $y_2(t)$ are entirely different, the amplitudes are exactly coincident. It is also to be noted that the peaks of $y_2(t)$ follow the amplitude, whereas the peaks of $y_1(t)$ are often smaller. It could be shown that if the frequency shift $\Delta\Omega \to \infty$ then all the peaks of $Y_2(t)$ lie in the $A_X(t)$ function.

In Fig. 2(*a*) sample functions of the processes $\omega_{X_j}(t)$, obtained using the $x_j(t)$ functions above defined, are plotted versus time. From this figure it can be noted that the real parts $\dot{A}_{X_j}(t)/A_{X_j}(t)$ of both processes are coincident, whereas the imaginary parts $\dot{\Theta}_{X_j}(t)$ are exactly the same but shifted of a constant quantity equal to $\Delta\Omega$, i.e.,

$$\dot{\Theta}_{X_2}(t) = \dot{\Theta}_{X_1}(t) + \Delta\Omega. \tag{22}$$

Moreover, the sample function of $\dot{\Theta}_{X_1}(t)$ (the broad-band process) fluctuates between positive and negative values, whereas for $\Delta\Omega$ sufficiently large, $\dot{\Theta}_{X_2}(t)$ is always positive. The behavior of the $\dot{\Theta}_{X_j}(t)$ functions implies that the vector $X_2(t)$ always rotates toward the positive direction, whereas the vector $X_1(t)$ sometimes rotates in the negative direction. Obviously the variations of $\dot{\Theta}_{X_j}(t)$ with respect to their mean value become less relevant as $\Delta\Omega$ increases, i.e., when the bandwidth of the process decreases.

Considering that $y_j(t)$ is the projection on the horizontal real axis of the vector $x_j(t)$ rotating in the complex plane, it follows

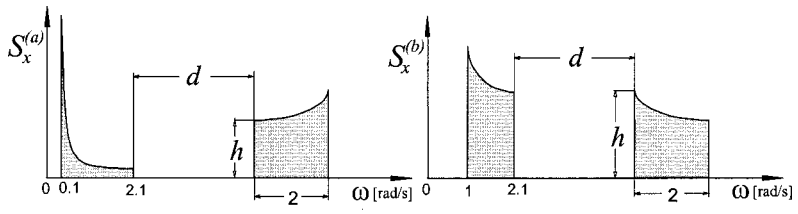

Fig. 3 PSD of type (*a*) and PSD of type (*b*) used in the numerical simulations

that $y_j(t)$ becomes zero, i.e., a zero crossing occurs when $\Theta_{X_j} = \pi/2$ or $3\pi/2$. Moreover, the extrema of $y_j(t)$ occur when their derivative crosses the zero level, i.e., when the derivative of $x_j(t)$ reaches the angular positions $\Theta_{\dot{X}_j} = \pi/2$ or $3\pi/2$.

When the vector $x(t)$ rotates always in the same direction it happens that the maxima of $y(t)$ are always positive, the minima are always negative, and between them a zero crossing always occurs (Fig. 1(*b*)). Two consecutive extrema having the same sign can occur if the vector $x(t)$ changes the direction of rotation two times without crossing the angular position corresponding to the zero level ($\Theta_{X_j} = \pi/2$ or $3\pi/2$); in fact the extrema of $y_j(t)$ also occur near the instants in which $x_j(t)$ changes the direction of rotation.

In the case in which the peak and the valley of a range have the same sign, the amplitude of such a range is related on both the amplitude of the vector and the phase angle covered by the vector between them; if such a phase angle is small, the corresponding range will be small too, independently from the amplitude of the vector. Furthermore, while each range is completed the derivative vector $\dot{x}(t)$ covers half a round in the complex plane reaching the angular positions $\Theta_{\dot{X}_j} = \pi/2$ or $3\pi/2$; this implies that the amplitude of each phase excursion of the vector $x(t)$ (and so the amplitude of the corresponding range) is related to the angular frequency of its derivative. As an example, if $\dot{X}(t)$ is narrow-band so that the $\dot{\Theta}_{\dot{X}}(t)$ function does not own large variations in time, the peaks of the $x(t)$ samples are almost equispaced in time and the ranges have amplitude similar among them.

In Fig. 2(*b*) the sample functions of the processes $\dot{\Theta}_{\dot{X}_1}(t)$ and $\dot{\Theta}_{\dot{X}_2}(t)$ are plotted versus time. Comparing the sample function of $\dot{\Theta}_{\dot{X}_1}(t)$ with that of $\dot{\Theta}_{X_1}(t)$ in Fig. 2(*a*) it can be noted that the two functions are far from each other, but they become closer and closer increasing $\Delta\Omega$, as can be noted comparing the sample functions of $\dot{\Theta}_{\dot{X}_2}(t)$ in Fig. 2(*b*) and $\dot{\Theta}_{X_2}(t)$ in Fig. 2(*a*).

From these observations it is possible to affirm that the succession of the extrema mainly depends on the rotation mode of both the $X(t)$ and $\dot{X}(t)$ processes in the complex plane. In particular:

1 the amplitude of each range not crossing the zero value is strictly related to the amplitude of each phase angle covered by the vector $x_j(t)$ without changing direction, and

2 these phase amplitudes are related to the angular velocity $\dot{\Theta}_{\dot{X}}(t)$ of the derivative vector due to the fact that the extrema occur when the derivative vector reaches the positions $\Theta_{\dot{X}} = \pi/2$ or $3\pi/2$.

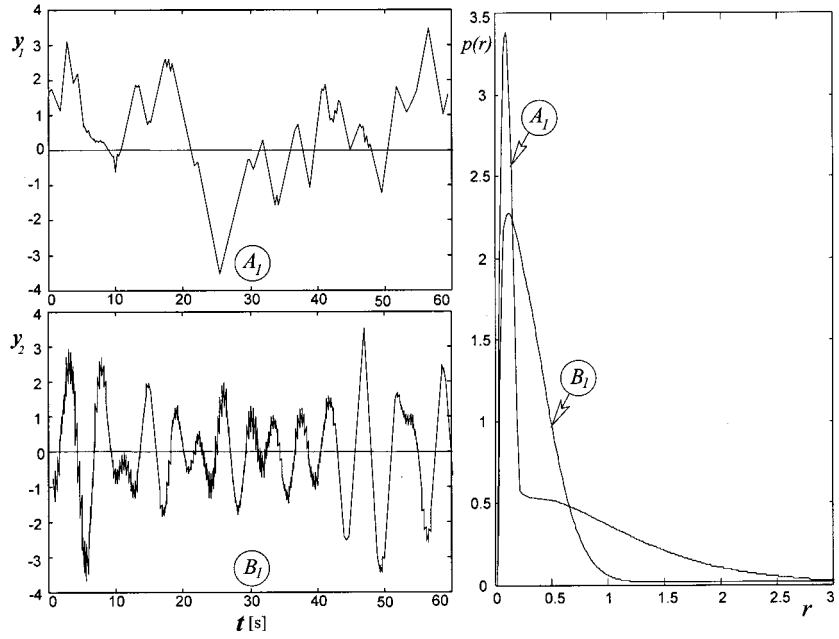

Fig. 4 Sample functions and range distributions of the process A_1 with PSD of type (*a*) and of the process B_1 with PSD of type (*b*) having both the same parameters $\alpha_X = 0.15$ and $q_X = 0.74$

As a confirmation in the next paragraph it will be shown that the spectral parameters are related to mean values of the $\dot{\Theta}_X(t)$ and $\dot{\Theta}_{\dot{X}}(t)$ functions.

3.2 Time-Domain Interpretation of the Spectral Parameters. The physical significance of the two spectral parameters defined above can be better understood by using the definition of analytic process given in Eq. (5). It can be shown that the following relationships hold:

$$\Omega_X = E[\dot{\Theta}_X(t)] \tag{23a}$$

$$\rho_X = E[|\dot{\Theta}_X(t)|] \tag{23b}$$

$$\overline{\rho_X} = \sqrt{(E[|\dot{\Theta}_X(t)|])^2 - (E[\dot{\Theta}_X(t)])^2} \tag{24}$$

where the symbol $|\bullet|$ means absolute value.

These relationships can be obtained by looking at the fact that the probability density of $A_X(t)$, $\Theta_X(t)$, and $\dot{\Theta}_X(t)$ for normal processes can be written as

$$p_{A_X} = \frac{A_X}{\lambda_0} \exp\left(-\frac{A_X^2}{2\lambda_0}\right) \tag{25a}$$

$$p_{\Theta_X} = \begin{cases} \dfrac{1}{2\pi} & 0 \leqslant \Theta_X \leqslant 2\pi \\ 0 & \text{otherwise} \end{cases} \tag{25b}$$

$$p_{\dot{\Theta}_X} = \frac{\overline{\rho}_X^2}{2[(\dot{\Theta}_X - \Omega_X)^2 + \overline{\rho}_X^2]^{3/2}}. \tag{26}$$

Equations (23) to (24) show that

- Ω_X is the mean value of the $\dot{\Theta}_X(t)$ function and it is directly proportional to the phase angle covered by the process $X(t)$ in the positive direction minus that covered in the negative direction,
- ρ_X is the mean value of the absolute value of the $\dot{\Theta}_X(t)$ function and it is directly proportional to the whole phase angle covered by the process $X(t)$ in both the positive and negative direction.
- $\overline{\rho_X}$ is proportional to the double of the whole phase angle covered by the process $X(t)$ in the negative direction.

Moreover, by using the well-known relationship

$$S_{\dot{X}}(\omega) = \omega^2 S_X(\omega) \tag{27}$$

one can write

$$\Omega_{\dot{X}} = \frac{\lambda_3}{\lambda_2} = E[\dot{\Theta}_{\dot{X}}] \tag{28a}$$

$$\rho_{\dot{X}} = \sqrt{\frac{\lambda_4}{\lambda_2}} = E[|\dot{\Theta}_{\dot{X}}|] \tag{28b}$$

$$\overline{\rho_{\dot{X}}} = \sqrt{(E[|\dot{\Theta}_{\dot{X}}(t)|])^2 - (E[\dot{\Theta}_{\dot{X}}(t)])^2}. \tag{29}$$

Then, by means of simple algebra, the spectral parameter q_X and the irregularity parameter α_X can be rewritten in the time domain as

$$q_X = \sqrt{\frac{(E[|\dot{\Theta}_X|])^2 - (E[\dot{\Theta}_X])^2}{(E[|\dot{\Theta}_X|])^2}} \tag{30a}$$

$$\alpha_X = \frac{E[|\dot{\Theta}_X|]}{E[|\dot{\Theta}_{\dot{X}}|]} = \frac{\rho_X}{\rho_{\dot{X}}}. \tag{30b}$$

From these relationships some further considerations on the behavior of stochastic processes can be made.

It has been observed in the previous section that two distinct processes having the same shape of the one-sided PSD but shifted of $\Delta\Omega$ in the frequency domain exhibits the same amplitude but different phase angles $\Theta_X(t)$ and angular frequency $\dot{\Theta}_X(t)$, the latter related by means of Eq. (22). Furthermore, the succession of the extrema mainly depends on the rotation mode of the vector process itself and its derivative. For these reasons it is not a surprise that q_X and α_X are only related to the variation of the phase angle $\Theta_X(t)$, $\dot{\Theta}_X(t)$, and $\dot{\Theta}_{\dot{X}}(t)$ in the time domain.

Equation (30*a*) shows that q_X depends on the ratio between the total phase angle covered in the negative direction and that covered on the whole by the vector $X(t)$; in the case of narrow-band processes it is $\dot{\Theta}_X(t) > 0$, $E[\dot{\Theta}_X(t)] \approx E[|\dot{\Theta}_X(t)|]$ and $q_X \approx 0$.

Equation (30*b*) shows that the α_X parameter is given by the ratio between the absolute values of $\dot{\Theta}_X(t)$ and $\dot{\Theta}_{\dot{X}}(t)$ functions that correspond to the ratio between the total phase angle covered in both the positive and negative directions by the process vector and by its derivative. In the case of narrow-band processes it is $\dot{\Theta}_X(t) \approx \dot{\Theta}_{\dot{X}}(t)$ and $\alpha_X \approx 1$.

Therefore, the spectral parameters are related to the total phase angle covered in the positive and negative directions by the vectors and not to the single excursions (ranges) in each direction; consequently, the q_X and α_X parameters are inadequate to fully describe their statistical distribution.

4 New Parameters for the Characterization of Spectral Contents in Random Processes

In this section new parameters are introduced in order to quantify the bandwidth of processes and their effectiveness is validated by means of proper digital simulations.

As previously stated, all the attempts to directly relate the range distribution of a wide-band processes to its PSD have not been successful. It has been recognized that processes having the same value of α_X (i.e., the same distribution of peaks) have in general a different range distribution, whereas it is self-evident that processes having different dynamic characteristics can own PSDs with the same ratio between the position of the centroid and the radius of gyration about the centroid, i.e., the same parameter q_X. Moreover, it has been observed that the succession of the extrema depends on the rotation mode in the complex plane, not only of the process $X(t)$ but also of its derivative $\dot{X}(t)$. These considerations suggest that parameters involving higher order spectral moments and quantities related to the angular velocities of the first derivative of the process should be introduced in order to quantify more accurately the bandwidth of the process.

By comparing Eqs. (9) and (28) one realizes that the bandwidth parameters of the derivative of a process can be obtained from that of the process given in Eqs. (11) and (12), increasing by two the order of the spectral moments. Taking into account these considerations, the bandwidth parameters relative to the derivative process $\dot{X}(t)$ are introduced:

$$q_{\dot{X}} = \frac{\overline{\rho_{\dot{X}}}}{\rho_{\dot{X}}} = \sqrt{1 - \frac{\lambda_3^2}{\lambda_2 \lambda_4}} = \sqrt{\frac{(E[|\dot{\Theta}_{\dot{X}}|])^2 - (E[\dot{\Theta}_{\dot{X}}])^2}{(E[|\dot{\Theta}_{\dot{X}}|])^2}} \quad 0 \leqslant q_{\dot{X}} \leqslant 1 \tag{31}$$

$$\alpha_{\dot{X}} = \frac{\rho_{\dot{X}}}{\rho_{\ddot{X}}} = \sqrt{\frac{\lambda_3^2}{\lambda_2 \lambda_6}} = \frac{E[|\dot{\Theta}_{\dot{X}}|]}{E[|\dot{\Theta}_{\ddot{X}}|]} \quad 0 \leqslant \alpha_{\dot{X}} \leqslant 1. \tag{32}$$

These parameters are expected to allow a more complete characterization of the spectral properties of random processes.

In order to prove this statement, several numerical simulations have been carried out using different shapes (unimodal, bimodal,

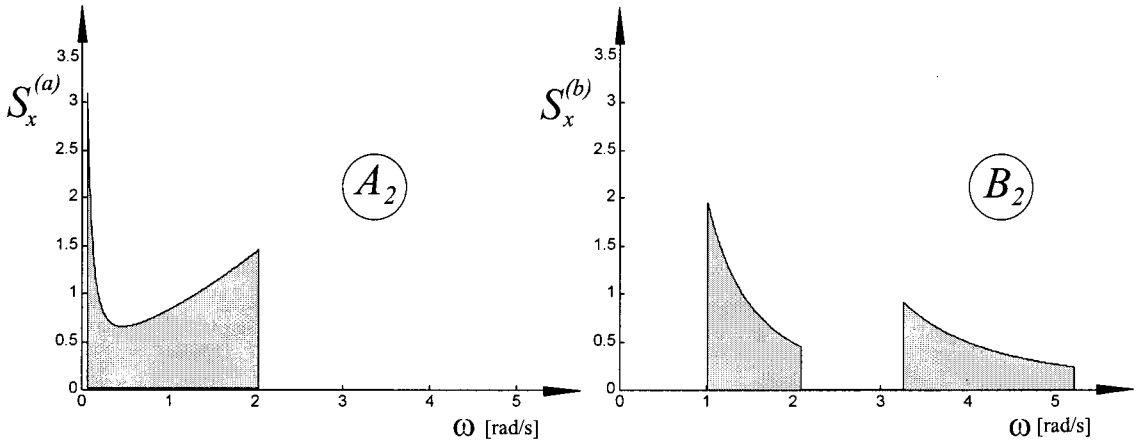

Fig. 5 PSDs of the processes A_2 and B_2 having both $\alpha_X \approx .76$, $q_X \approx .47$ $\alpha_{\dot{X}} \approx .97$ and $q_{\dot{X}} \approx .20$

etc.) of PSDs. As an example, in the following the results relative to the bimodal PSD types (*a*) and (*b*) shown in Fig. 3 and defined as

$$S_X^{(a)} = \begin{cases} (2.1h + 3.4dh + .25hd^2 - .1)/\omega^2 & 0.1 \leqslant \omega \leqslant 2.1 \\ h\omega^2 & 2.1 + d \leqslant \omega \leqslant 4.1 + d \end{cases} \tag{33}$$

$$S_X^{(b)} = \begin{cases} \dfrac{(2h + 6.2d + d^2 + 8.61)}{(0.65d + .105d^2 + .9)\omega^2} & 1.0 \leqslant \omega \leqslant 2.1 \\ h/\omega^2 \quad 2.1 + d \leqslant \omega \leqslant 4.1 + d \end{cases} \tag{34}$$

are shown. The choice of these PSDs is due to the fact that such bimodal spectra not only can assume a wide range of the spectral parameters relative to the process ([20]) but they allow one to obtain different values of the parameters relative to the derivative process, simply varying the two parameters *h* and *d* (Fig. 3). From PSDs, the (*a*) and (*b*) sample functions of processes having different dynamic characteristics have been simulated by means of Eq. (21).

In particular, Fig. 4 shows the sample functions and the range distributions of a couple of processes, one with an (*a*) type PSD ($h = .004$, $d = 7.56$) called A_1 and one with a (*b*) type PSD ($h = .675$, $d = .072$) called B_1, having the same parameters α_X and q_X (equal to 0.15 and 0.74, respectively) relative to the process but with different analogous parameters relative to their derivatives ($q_{\dot{X}} = 0.82$ and $\alpha_{\dot{X}} = 0.78$ for A_1, $q_{\dot{X}} = 0.57$ and $\alpha_{\dot{X}} = 0.31$ for B_1). It can be seen that the process A_1 is characterized by many cycles with intermediate ranges mixed to a few cycles with large and small ranges whereas the process B_1 is characterized by many cycles with large ranges mixed to cycles with very small ranges.

Moreover, Fig. 5 shows two PSDs, one of type (*a*) ($h = 217.4$, $d = -2.17$) called A_2 and one of type (*b*) ($h = 7.51$, $d = 1.14$) called B_2 having a very different shape but the same spectral parameters $\alpha_X \approx .76$, $q_X \approx .47$ $\alpha_{\dot{X}} \approx .97$, $q_{\dot{X}} \approx .20$. Figure 6 shows two corresponding sample functions and the range distributions. From this figure it is possible to see how the equality of the four selected parameters ensures the coincidence of the range distribution since the small deviation observed is negligible for

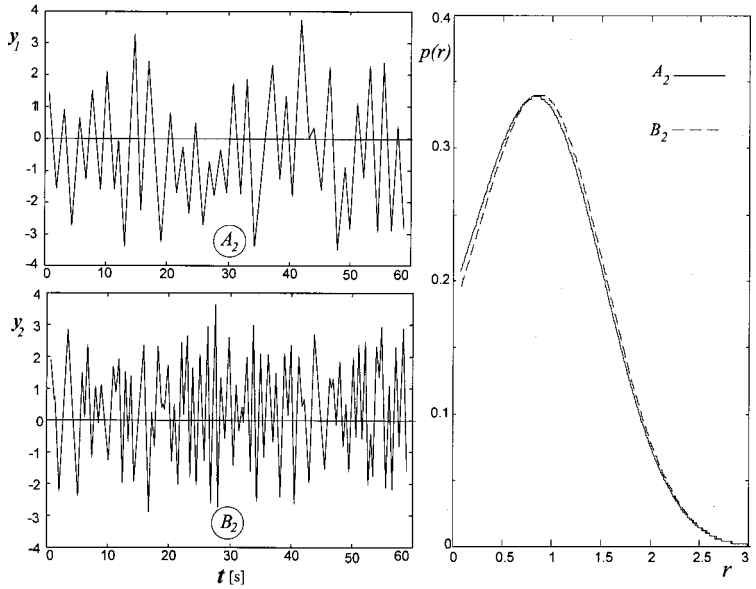

Fig. 6 Sample functions and range distributions of the process A_2 and B_2 having the same parameters $\alpha_X \approx .76$, $q_X \approx .47$, $\alpha_{\dot{X}} \approx .97$ and $q_{\dot{X}} \approx .20$

practical application purposes. In other words, for practical purposes the range distribution is unambiguously related to the parameters α and q of both the process and its time derivative, and consequently accurate relationships between the range distribution and PSD should take into account these four parameters.

The identification of the spectral parameters on which the range distribution of a wide-band process depends is the first step in the detection of the relationships between range distribution and PSD. The second step consists in the determination of closed-form expressions relating the relevant spectral parameters to the range distribution. Obviously, it needs further study, but at this stage of the research some practical results can already be obtained. As an example, closed-form relationships between PSD and the range distribution have been obtained by Petrucci and Zuccarello [21] in the particular case of broad-band processes ($\alpha_x \ll 1,\ q_x \gg 0$) whose time derivative is a narrow-band process ($\alpha_{\dot{x}} \approx 1;\ q_{\dot{x}} \approx 0$). In this case the ranges have a Rayleigh distribution:

$$p(r) = \frac{r}{M_R} \exp\left[-\frac{r^2}{2M_R^2} \right] \tag{35}$$

in which the modal value M_R is related to the the standard deviation σ_X and the spectral parameters α_x and q_x of the process by a third order polynomial, i.e.,

$$M_R = \sigma_X \sum_{w=0}^{3} \sum_{z=0}^{w} g_{wz} \alpha_X^z q_X^{w-z}, \tag{36}$$

being the polynomial coefficients g_{wz} obtained by a best-fitting procedure carried out using the least square technique and given in ([21]).

5 Practical Example

In the following, as a practical example, Eqs. (35)–(36) have been used for the direct evaluation of the range distributions of the displacements that occur in a structure subjected to wind forces. In this case the excitation is the horizontal velocity of the wind that can be represented by a random process $X_w(t)$, whose spectrum is given by ([22]).

$$S_{X_w}(f) = 4K\overline{V}_{10}^2 \frac{L/\overline{V}_{10}}{[2 + (fL/\overline{V}_{10})^2]^{5/6}}, \tag{37}$$

where f is the frequency in Hz, K is a factor in the range $0.005 \leqslant K \leqslant 0.05$ depending on the local wind profile, $\overline{V}_{10}$ is the mean wind speed at 10 ft above the ground, and L is the length scale related to the structural dimensions. For simplicity, a structure represented by a two-degree-of-freedom system (Fig. 7), as an antenna (having mass m_1, stiffness k_1, damping coefficient ζ_1, drag pressure coefficient C and area s_1) joined to a base (having mass m_2, stiffness k_2 and damping coefficient ζ_2) has been considered.

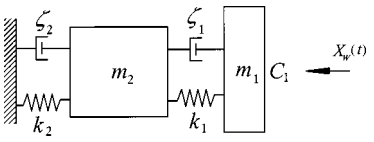

Fig. 7 Two-degree-of freedom system considered in the practical example

Figure 8(*a*) shows the PSD $S_{X_d}(f)$ of the displacement process $X_d(t)$ of the m_1 mass (antenna) obtained by solving the differential equation of motion of the system through the normal mode method ([20]). As an example the following values of the parameters have been assumed: $K = 0.01$, $\overline{V}_{10} = 20$ m/s $L = 60$ m for the wind velocity spectrum and $m_1 = 100$ kg, $m_2 = 1000$ kg, $k_1 = 100$ Nsmm^{-1}, $k_2 = 3000$ Nsmm^{-1}, $\zeta_1 = \zeta_2 = 0.1$, $C = 0.9$, and $s_1 = 1$ m^2 for the system. From the analysis of $S_{X_d}(f)$ follows that $X_d(t)$ is a wide-band displacement process ($\alpha_x \approx 0.58$ and $q_x \approx 0.75$) with narrow-band derivative ($\alpha_{\dot{x}} \approx 1,\ q_{\dot{x}} \approx 0$). Therefore, the corresponding distribution of the range can be calculated directly using the closed-form relationship (35). For comparison Fig. 8(*b*) shows the range distribution obtained by digital simulations along with those obtained using Eqs. (35) and (36). The good agreement between the curves corroborates that for practical purposes, direct relationships between range distribution and PSD can be obtained provided that one take into account the four spectral parameters α_x, q_x, $\alpha_{\dot{x}}$, and $q_{\dot{x}}$.

6 Conclusions

The dynamical properties of random processes are usually described by means of spectral parameters, such as the regularity factor α_X and the spectral parameter q_X, that are defined in the frequency domain. In this paper, using the concept of analytic process, the physical and mathematical meaning of such parameters has been readdressed and a time-domain interpretation has been given. In particular it has been shown that these spectral parameters are related to the angular velocity of the analytic process in the complex plane.

The above interpretations as well as further considerations on the behavior of the analytic processes have shown that the irregularity factor and the bandwidth parameter of the process cannot give a full probabilistic description of the ranges in a random process. As a confirmation it has been shown that processes having the same values of both these parameters can have quite different range distributions.

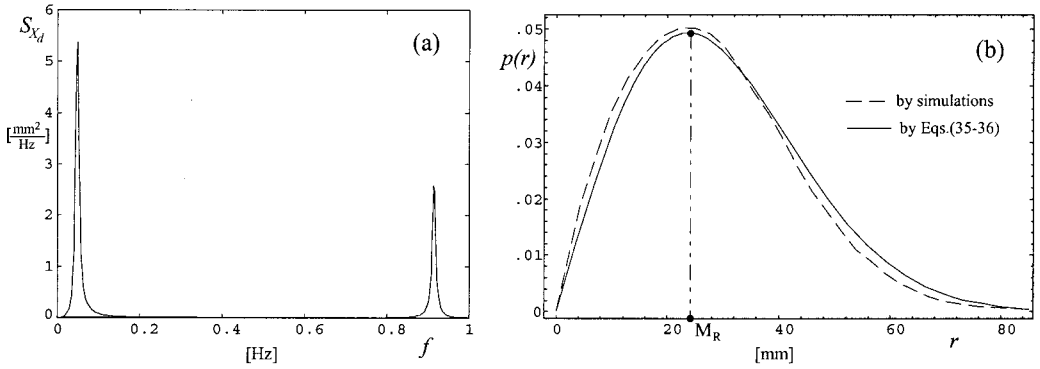

Fig. 8 PSD of the output displacement process X_w (*a*) and relative range distribution (*b*)

Moreover, it has been shown that the range distribution depends not only on the spectral parameters α_X and q_X of the process, but also on the analogous parameters of its derivative $\alpha_{\dot{X}}$ and $q_{\dot{X}}$.

As a conclusion, it is possible to state that to obtain accurate relationships between range distributions and PSD one must take into account both the irregularity factor α_x and the spectral parameter q_x, and the parameters $\alpha_{\dot{x}}$ and $q_{\dot{x}}$ of the derivative of the process.

References

[1] Nigam, N. C., 1983, *Introduction to Random Vibrations*, M.I.T. Press, Cambridge, MA.

[2] Leadbetter, M. R., Lindgren, G., and Rootzen, G., 1983, *Extreme and Related Properties of Random Sequences and Processes*, Springer-Verlag, New York.

[3] Crandall, S. H., and Mark, W. D., 1963, *Random Vibration in Mechanical System*, Academic Press, New York.

[4] Cramer, H., and Leadbetter, M. R., 1967, *Stationary and Related Stochastic Processes*, John Wiley and Sons, New York.

[5] Lin, Y. K., 1967, *Probabilistic Theory of Structural Dynamics*, McGraw-Hill, New York.

[6] Wirsching, P. H., and Light, M. C., 1980, ''Fatigue Under Wide band Random Stresses,'' J. Struct. Div. ASCE, **106**, No. ST7, pp. 1593–1607.

[7] Dowling, N. E., 1983, ''Fatigue Life Prediction for Complex Load Versus Time Histories,'' J. Eng. Mater. Technol., **105**, pp. 206–214.

[8] Tunna, J. M., 1985, ''Random Load Fatigue: Theory and Experiment,'' Proc. Inst. Mech. Eng., **199**, No. C3, pp. 249–257.

[9] Tunna, J. M., 1986, ''Fatigue Life Prediction for Gaussian Random Loads,'' Fatigue Fract. Eng. Mater. Struct., **9**, No. 3, pp. 169–184.

[10] Lindgren, G., and Rychlik, I., 1987, ''Rain Flow Cycle Distributions for Fatigue Prediction Under Gaussian Load Processes,'' Fatigue Fract. Eng. Mater. Struct., **10**, No. 3, pp. 251–260.

[11] Rychlik, I., 1992, ''Rain Flow Cycle in Gaussian Loads,'' Fatigue Fract. Eng. Mater. Struct., **15**, No. 1, pp. 57–72.

[12] Kim, J. J., and Kim, H. Y., 1994, ''Simple Method for Evaluation of Fatigue Damage of Structures in Wide Band Random Vibration,'' Proc. Inst. Mech. Eng., **208**, pp. 65–68.

[13] Lutes, L. D., Corazao, M., Hu, S. J., and Zimmerman, J., 1984, ''Stochastic Fatigue Damage Accumulation,'' J. Struct. Eng., **110**, No. 4, pp. 2585–2601.

[14] Vanmarke, E. H., 1972, ''Properties of Spectral Moments With Applications to Random Vibrations,'' J. Eng. Mech., **98**, pp. 425–446.

[15] Papoulis, A., 1984, *Signal Analysis*, McGraw-Hill, New York.

[16] Di Paola, M., 1985, ''Transient Spectral Moments of Linear System,'' S.M. Arch., **10**, pp. 225–243.

[17] Di Paola, M., and Petrucci, G., 1990, ''Spectral Moments and Pre-envelope Covariances of Nonseparable Processes,'' ASME J. Appl. Mech., **57**, pp. 218–224.

[18] Madsen, H. O., Krenk, S., and Lind, N. C., 1986, *Methods of Structural Safety*, Prentice-Hall, Englewood Cliffs, NJ.

[19] Sobczyk, K., and Spencer, B. F., 1992, *Random Fatigue From Data to Theory*, Academic Press, San Diego.

[20] Wirsching, P. H., Paez, T. L., and Ortiz, K., 1995, *Random Vibrations*, John Wiley and Sons, New York.

[21] Petrucci, G., and Zuccarello, B., 1999, ''On the Estimation of the Fatigue Cycle Distribution From Spectral Density Data,'' J. Mech. Eng. Sci., **213**, pp. 819–831.

[22] Davenport, A. G., and Novak, M., 1988, *Shock & Vibration Handbook*, p. 23, C. M. Harris, ed., McGraw-Hill, New York, Chap. 29.

S. M. Chern
Associate Professor,
Civil Engineering Department,
Chung-Cheng Institute of Technology,
Tahsi, Taoyuan 33509, Taiwan

M. E. Tuttle
Professor,
Mem. ASME,
Mechanical Engineering Department,
University of Washington
MS 352600,
Seattle, WA 98195

On Displacement Fields in Orthotropic Laminates Containing an Elliptical Hole

The classical Savin solution for the stress induced in an orthotropic plate containing an elliptical hole places no restrictions on remote rigid-body rotations. In this paper the Savin procedure is used to obtain a solution for which remote rigid-body rotations are required to be zero. The validity of these new results is demonstrated by comparing predicted displacement fields near a circular hole in specially orthotropic composite panels with those measured using moiré techniques as well as those predicted using the finite element method. [S0021-8936(00)01303-9]

Introduction

Due to the increasing use of polymeric composites in structural applications, there is widespread interest in the mechanical response of thin orthotropic panels containing holes, cutouts, or other irregularities (e.g., see Refs. [1–7]). Several analytical techniques have been developed to study these problems, including the integral transform method ([8]), singular integral equation method ([9,10]), Stroh formalism ([11]), and the classical complex function method ([12,13]). Using a mapping approach, Savin [12] developed a general solution method to determine the stress fields induced in orthotropic plates containing an elliptical hole and subject to remote uniform loading. The corresponding solutions for strain fields can be obtained by substituting Savin's solutions for stress into the orthotropic form of Hooke's Law. One would expect that the displacement fields induced in the plate could then be obtained by integrating the strain fields to obtain displacement fields. However, as mentioned by Savin (see the first footnote which appears on pg. 38 of Ref. [12]), the solutions he derived are based on an incomplete specification of rigid-body rotations. Hence, the displacement fields inferred from the Savin expressions for stress are only valid for a special class of problems. Specifically, (as will be discussed) the displacement fields are only valid for some types of specially orthotropic laminates, and furthermore when such laminates are subjected to remote normal stresses only (i.e., when $\tau_{xy}^{\infty}=0$).

The objective of this article is to reformulate the Savin solution so as to account for rigid-body rotations and therefore obtain expressions for in-plane displacement fields that are valid for any orthotropic plate and for any combination of in-plane loading. The fundamental equations that govern the behavior of orthotropic plates are summarized in the next section. Simplifications that occur if the plate is specially orthotropic rather than generally orthotropic are also discussed. Next, a revised solution based on the Savin approach and which accounts for rigid-body rotations is presented. Finally, predictions based on the revised solution are compared with experimental measurements obtained using moiré techniques as well as with predictions based on the finite element method.

It is appropriate to note that the difficulties associated with the Savin solution are avoided if solutions based on the Stroh formalism are used ([11]). Nevertheless, the Savin solution is still widely employed ([4,14–16]). It is important that the limitation of the solution presented by Savin be appreciated, since several modern experimental methods (for example, those based on the moiré effect) are in essence techniques used to measure displacement fields rather than stress or strain fields. A successful comparison between displacements predicted on the basis of the Savin procedure and experimental measurements requires use of the solution presented herein.

Contributed by the Applied Mechanics Division of THE AMERICAN SOCIETY OF MECHANICAL ENGINEERS for publication in the ASME JOURNAL OF APPLIED MECHANICS. Manuscript received by the ASME Applied Mechanics Division, Jan. 25, 1999; final revision, Apr. 26, 2000. Associate Technical Editor: J. W. Ju. Discussion on the paper should be addressed to the Technical Editor, Professor Lewis T. Wheeler, Department of Mechanical Engineering, University of Houston, Houston, TX 77204-4792, and will be accepted until four months after final publication of the paper itself in the ASME JOURNAL OF APPLIED MECHANICS.

Fundamental Equations

The two-dimensional equilibrium equations (neglecting body forces), the strain-displacement relations, and the compatibility condition are listed below as Eqs. (1)–(3), respectively:

$$\frac{\partial\sigma_x}{\partial x}+\frac{\partial\tau_{xy}}{\partial y}=0,\quad \frac{\partial\sigma_y}{\partial y}+\frac{\partial\tau_{xy}}{\partial x}=0 \tag{1}$$

$$\varepsilon_x=\frac{\partial u}{\partial x},\quad \varepsilon_y=\frac{\partial v}{\partial y},\quad \gamma_{xy}=\frac{\partial v}{\partial x}+\frac{\partial u}{\partial y} \tag{2}$$

$$\frac{\partial^2\varepsilon_x}{\partial y^2}+\frac{\partial^2\varepsilon_y}{\partial x^2}=\frac{\partial^2\gamma_{xy}}{\partial x\partial y} \tag{3}$$

where u, v are in-plane displacements in the x- and y-directions, σ_x, σ_y, τ_{xy} are in-plane stresses, and ε_x, ε_y, and γ_{xy} are in-plane strains. Hooke's law for a generally orthotropic plate can be expressed as

$$\begin{aligned}\varepsilon_x&=a_{11}\sigma_x+a_{12}\sigma_y+a_{16}\tau_{xy}\\ \varepsilon_y&=a_{12}\sigma_x+a_{22}\sigma_y+a_{26}\tau_{xy}\\ \gamma_{xy}&=a_{16}\sigma_x+a_{26}\sigma_y+a_{66}\tau_{xy}\end{aligned} \tag{4}$$

where a_{ij} are elements of reduced compliance matrix. To insure satisfaction of the equilibrium equations, stresses are expressed in terms of an Airy stress function, $U(x,y)$:

$$\sigma_x=\frac{\partial^2U}{\partial y^2},\quad \sigma_y=\frac{\partial^2U}{\partial x^2},\quad \tau_{xy}=-\frac{\partial^2U}{\partial x\partial y}. \tag{5}$$

Substituting Eqs. (4) and (5) into Eq. (3) results in the biharmonic equation for generally orthotropic materials:

$$a_{22}\frac{\partial^4U}{\partial x^4}-2a_{26}\frac{\partial^4U}{\partial x^3\partial y}+(2a_{12}+a_{66})\frac{\partial^4U}{\partial x^2\partial y^2}-2a_{16}\frac{\partial^4U}{\partial x\partial y^3}+a_{11}\frac{\partial^4U}{\partial y^4}=0. \tag{6}$$

The general solution of Eq. (6) depends on the roots of the characteristic equation. Assuming the roots have the general form $F(x+sy)$, the characteristic equation becomes

$$a_{11}s^4-2a_{16}s^3+(2a_{12}+a_{66})s^2-2a_{26}s+a_{22}=0. \tag{7}$$

Through a consideration of potential energy, Lekhnitskii [13] has shown that the characteristic equation has no real roots. Thus, for a generally orthotropic plate the roots of the characteristic equation are always complex and are of the form

$$s_{1,3}=\alpha_1\pm i\beta_1 \quad s_{2,4}=\alpha_2\pm i\beta_2 \tag{8}$$

where α_1, α_2, β_1, and β_2 are real constants and $\beta_1>0$, $\beta_2>0$. For generally orthotropic plates $\alpha_1\neq\alpha_2$ and $\beta_1\neq\beta_2$.

The Airy stress function may be expressed using two distinct roots, and has the general form

$$U=2\ \mathrm{Re}[F_1(x+s_1y)+F_2(x+s_2y)] \tag{9}$$

where Re[ ] denotes the real part of the quantity in brackets. For further simplification, let

$$\phi(z_1)=\frac{\partial F_1(z_1)}{\partial z_1} \quad \psi(z_2)=\frac{\partial F_2(z_2)}{\partial z_2} \tag{10}$$

where $z_1=x+s_1y$, $z_2=x+s_2y$, and $\phi(z_1)$ and $\psi(z_2)$ are complex functions. Substituting Eqs. (9) and (10) into Eq. (5), the stress components may be expressed as

$$\begin{aligned}\sigma_{xx}&=2\ \mathrm{Re}[s_1^2\phi'(z_1)+s_2^2\psi'(z_2)]\\ \sigma_{yy}&=2\ \mathrm{Re}[\phi'(z_1)+\psi'(z_2)]\\ \tau_{xy}&=-2\ \mathrm{Re}[s_1\phi'(z_1)+s_2\psi'(z_2)].\end{aligned} \tag{11}$$

Expressions for the displacement fields can be obtained by applying Hooke's law (Eq. (4)) and integrating, resulting in

$$\begin{aligned}u&=2\ \mathrm{Re}[p_1\phi(z_1)+p_2\psi(z_2)]\\ v&=2\ \mathrm{Re}[q_1\phi(z_1)+q_2\psi(z_2)]\end{aligned} \tag{12}$$

where

p_1, p_2, q_1, q_2 are complex constants, defined as follows:

$$\begin{aligned}p_1&=a_{11}s_1^2+a_{12}-a_{16}s_1\\ p_2&=a_{11}s_2^2+a_{12}-a_{16}s_2\\ q_1&=a_{12}s_1+\frac{a_{22}}{s_1}-a_{26}\\ q_2&=a_{12}s_2+\frac{a_{22}}{s_2}-a_{26}.\end{aligned} \tag{13}$$

The preceding results are simplified if the plate is specially orthotropic (i.e., if $a_{16}=a_{26}=0$). In this case the biharmonic and characteristic equations (Eqs. (6) and (7), respectively) reduce to

$$a_{22}\frac{\partial^4U}{\partial x^4}+(2a_{12}+a_{66})\frac{\partial^4U}{\partial x^2\partial y^2}+a_{11}\frac{\partial^4U}{\partial y^4}=0 \tag{14}$$

$$a_{11}s^4+(2a_{12}+a_{66})s^2+a_{22}=0. \tag{15}$$

The characteristic equation can alternatively be written as

$$s^4+2\chi s^2+\lambda^2=0 \tag{16}$$

where

$$\chi=\left(\frac{E_{xx}}{2G_{xy}}-\nu_{xy}\right), \quad \lambda=\sqrt{\frac{E_{xx}}{E_{yy}}}. \tag{17}$$

For specially orthotropic materials $\alpha_1=\alpha_2=\alpha$. Hence, if $a_{16}=a_{26}=0$, then the form of the roots of the characteristic equation may be grouped into three possible cases (compare with Eq. (8)).

Case I. $\chi<\lambda$: In this case $\alpha\neq0$, $\beta_1=\beta_2=\beta$, and the roots are complex and of the form

$$s_{1,3}=\alpha\pm i\beta \quad s_{2,4}=-\alpha\pm i\beta$$

Case II. $\chi>\lambda$: In this case $\alpha=0$, $\beta_1\neq\beta_2$, and the roots are purely imaginary and of the form

$$s_{1,3}=\pm i\beta_1 \quad s_{2,4}=\pm i\beta_2.$$

Case III. $\chi=\lambda$: In this case $\alpha=0$, $\beta_1=\beta_2=\beta$, and the roots are repeated and purely imaginary:

$$s_{1,2,3,4}=\pm i\beta.$$

For Cases I and II the Airy stress function can again be expressed using two distinct roots, in accordance with Eq. (9). Equation (9) is not valid for Case III, however, since in this case the roots are repeated. Isotropic plates (or symmetric quasi-isotropic composite plates) correspond to Case III, since in these instances $E_{xx}=E_{yy}=E$, $\nu_{xy}=\nu_{yx}=\nu$, $G_{xy}=G_{yx}=G=E/2(1+\nu)$, and therefore $\chi=\lambda=1$, satisfying the conditions for Case III. The response of isotropic or quasi-isotropic plates is not the focus of this paper and will not be further discussed. The interested reader is referred to Refs. ([11,17]).

In summary, the solution for a thin orthotropic plate subjected to in-plane loading involves finding complex function $\phi(z_1)$ and $\psi(z_2)$ which satisfy the appropriate biharmonic equation (e.g., Eqs. (6) or (14)) and the prevailing boundary conditions. Once these functions are found the problem is solved.

Application of the Savin Solution Procedure

A plate containing an elliptical hole with major and minor axes a and b, respectively, and referenced to an in-plane $x-y$ coordinate system is shown in Fig. 1. Savin found that the following complex functions are applicable in this case:

$$\begin{aligned}\phi(z_1)&=(B^*+iC^*)z_1+\phi_0\\ \psi(z_2)&=(B'^*+iC'^*)z_2+\varphi_0\end{aligned} \tag{18}$$

where B^*, C^*, B'^*, and C'^* are real constants and $\phi_0(z_1)$ and $\psi_0(z_2)$ are holomorphic functions of the following form:

$$\begin{aligned}\phi_0(z_1)&=a_0+\frac{a_{-1}}{z_1}+\frac{a_{-2}}{z_1^2}+\frac{a_{-3}}{z_1^3}+\ldots\\ \psi_0(z_2)&=b_0+\frac{b_{-1}}{z_2}+\frac{b_{-2}}{z_2^2}+\frac{b_{-3}}{z_2^3}+\ldots.\end{aligned} \tag{19}$$

To satisfy the stress boundary conditions at infinity, Savin substituted Eq. (18) into Eq. (11) and let $z_1, z_2\to\infty$, resulting in the following three equations:

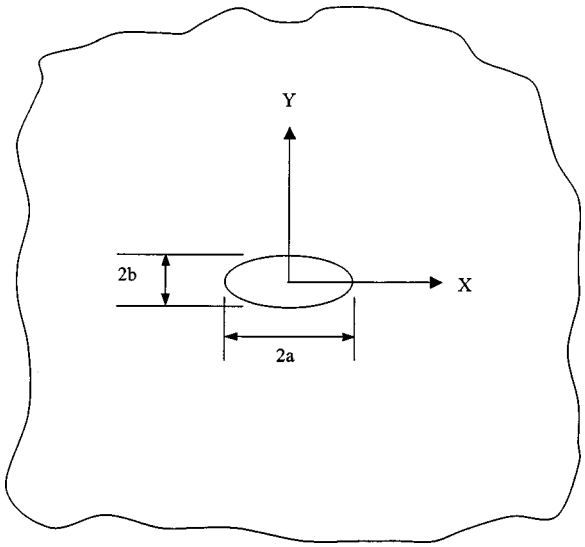

Fig. 1 Schematic of infinite orthotropic plate with elliptical hole

$$\sigma_x^\infty = s_1^2(B^*+iC^*)+\overline{s_1^2(B'^*+iC'^*)}+s_2^2(B^*+iC^*)+\overline{s_2^2(B'^*+iC'^*)}$$

$$\sigma_y^\infty = (B^*+iC^*)+\overline{(B^*+iC^*)}+(B'^*+iC'^*)+\overline{(B'^*+iC'^*)} \tag{20}$$

$$-\tau_{xy}^\infty = s_1(B^*+iC^*)+\overline{s_1(B^*+iC^*)}+s_2(B'^*+iC'^*)+\overline{s_2(B'^*+iC'^*)}$$

where σ_x^∞, σ_y^∞, and τ_{xy}^∞ are remote in-plane stresses. Since Eqs. (20) represent three equations in four unknowns, a fourth equation is needed to uniquely determine the four constants B^*, C^*, B'^*, and C'^*. Savin simply assumed $C^*=0$, while acknowledging that by doing so displacement boundary conditions associated with rigid-body rotations are not necessarily satisfied. The following relatively simple expressions for the remaining three constants are obtained if it is assumed that $C^*=0$:

$$B^* = \frac{\sigma_x^\infty+(\alpha_2^2+\beta_2^2)\sigma_y^\infty+2\alpha_2\tau_{xy}^\infty}{2[(\alpha_2-\alpha_1)^2+(\beta_2^2-\beta_1^2)]}$$

$$B'^* = \frac{-\sigma_x^\infty+(\alpha_1^2-\beta_1^2-2\alpha_1\alpha_2)\sigma_y^\infty-2\alpha_2\tau_{xy}^\infty}{2[(\alpha_2-\alpha_1)^2+(\beta_2^2-\beta_1^2)]} \tag{21}$$

$$C'^* = \frac{(\alpha_1-\alpha_2)\sigma_x^\infty+[\alpha_2(\alpha_1^2-\beta_1^2)-\alpha_1(\alpha_2^2-\beta_2^2)]\sigma_y^\infty}{2\beta_2[(\alpha_2-\alpha_1)^2+(\beta_2^2-\beta_1^2)]} + \frac{[(\alpha_1^2-\beta_1^2)-(\alpha_2^2-\beta_2^2)]\tau_{xy}^\infty}{2\beta_2[(\alpha_2-\alpha_1)^2+(\beta_2^2-\beta_1^2)]}.$$

However, if rigid-body rotations are taken into account, then in general $C^*\neq 0$ and therefore Eqs. (21) do not correspond to any particular level of rigid-body rotation. Savin noted (see the first footnote which appears on pg. 38 of Ref. [12]) that the needed fourth equation can be obtained through consideration of the rigid-body rotation at infinitely distant points of the plate. Rigid-body rotation is related to in-plane displacement fields according to

$$\overline{\omega} = \frac{1}{2}\left(\frac{\partial v}{\partial x}-\frac{\partial u}{\partial y}\right).$$

It is herein assumed that rigid-body rotations are zero at infinity, which implies

$$\left.\frac{\partial v}{\partial x}\right|_\infty = \left.\frac{\partial u}{\partial y}\right|_\infty. \tag{22}$$

Equations (20) and (22) form a system of four equations, and were used to determine the four unknown real constants B^*, C^*, B'^*, and C'^*. Since the associated algebra is extensive, Eqs. (20), (22) were solved symbolically using MAPLE. The generalized expressions for the constants B^*, C^*, B'^*, and C'^* are lengthy and appear as Eqs. (A1)–(A4) in the Appendix. In all of the following discussion the constants B^*, C^*, B'^*, and C'^* are those given by Eqs. (A1)–(A4) rather than Eqs. (21).

The remaining solution steps are identical to those described by Savin [12], although intermediate and final results differ somewhat due to the revised form of B^*, C^*, B'^*, and C'^*. In order to find the holomorphic functions, $\phi_0(z_1)$ and $\psi_0(z_2)$, a mapping is used that transfers the physical area outside the elliptical hole into a unit circle according to

$$z_1=\omega_1(\zeta_1)=\frac{a+is_1b}{2}\zeta_1+\frac{a-is_1b}{2}\frac{1}{\zeta_1}$$

$$z_2=\omega_2(\zeta_2)=\frac{a+is_2b}{2}\zeta_2+\frac{a-is_2b}{2}\frac{1}{\zeta_2}. \tag{23}$$

After inversion, the functions become (Savin showed only negative sign here)

$$\zeta_1=\frac{z_1\pm\sqrt{z_1^2-(a^2+s_1^2b^2)}}{a+is_1b}$$

$$\zeta_2=\frac{z_2\pm\sqrt{z_2^2-(a^2+s_2^2b^2)}}{a+is_2b}.$$

The sign is taken such that ζ_1 and ζ_2 are inside a unit circle, i.e.,

$$|\zeta_1|\leqslant 1 \quad \text{and} \quad |\zeta_2|\leqslant 1$$

Traction-free boundary conditions are enforced around the boundary of the hole to solve for the holomorphic functions $\phi_0(z_1)$ and $\psi_0(z_2)$. The boundary conditions around an elliptical hole are

$$\frac{\partial U}{\partial x}=-\int_0^s Y_n ds+C_1, \quad \frac{\partial U}{\partial y}=\int_0^s X_n ds+C_2 \tag{24}$$

where C_1 and C_2 are arbitrary real constants, X_n and Y_n are resulting forces along the elliptical hole acting in x and y direction, and s is an arc measured from an arbitrarily chosen point on the contour of the hole. Inserting Eq. (9) into Eq. (24), the boundary conditions may be expressed in terms of the complex functions $\phi(z_1)$ and $\psi(z_2)$:

$$f_1=-\int_0^s Y_n ds+C_1=2\,\mathrm{Re}[\phi(z_1)+\psi(z_2)]$$

$$f_2=\int_0^s X_n ds+C_2=2\,\mathrm{Re}[s_1\phi(z_1)+s_2\psi(z_2)]. \tag{25}$$

Inserting Eq. (18) into Eq. (25), the boundary conditions can be expressed in terms of the functions $\phi_0(z_1)$ and $\psi_0(z_2)$:

$$2\,\mathrm{Re}[\phi_0(z_1)+\psi_0(z_2)]=f_1-2\,\mathrm{Re}[(B^*+iC^*)z_1+B\ln z_2+(B'^*+iC'^*)z_2]=f_1^0$$

$$2\,\mathrm{Re}[s_1\phi_0(z_1)+s_2\psi_0(z_2)]=f_2-2\,\mathrm{Re}[s_1(B^*+iC^*)z_1+s_2(B'^*+iC'^*)z_2]=f_2^0. \tag{26}$$

Now, solving the problem by finding functions $\phi(z_1)$ and $\psi(z_2)$ reduces to finding the holomorphic functions $\phi_0(z_1)$ and $\psi_0(z_2)$. The Schwartz formula is applied and the following notation is introduced:

$$K_1=\frac{(B^*+iC^*)(a+is_1b)+(B'^*+iC'^*)(a+is_2b)}{2}$$

$$K_2=\frac{(B^*+iC^*)(a-is_1b)+(B'^*+iC'^*)(a-is_2b)}{2}$$

$$K_3=\frac{s_1(B^*+iC^*)(a+is_1b)+s_2(B'^*+iC'^*)(a+is_2b)}{2} \tag{27}$$

$$K_4=\frac{s_1(B^*+iC^*)(a-is_1b)+s_2(B'^*+iC'^*)(a-is_2b)}{2}$$

There results

$$\phi_0(\zeta_1)=-\frac{(K_3+\overline{K_4})-s_2(K_1+\overline{K_2})}{s_1-s_2}\zeta_1+\lambda_1$$

$$\psi_0(\zeta_2)=\frac{(K_3+\overline{K_4})-s_1(K_1+\overline{K_2})}{s_1-s_2}\zeta_2+\lambda_2 \tag{28}$$

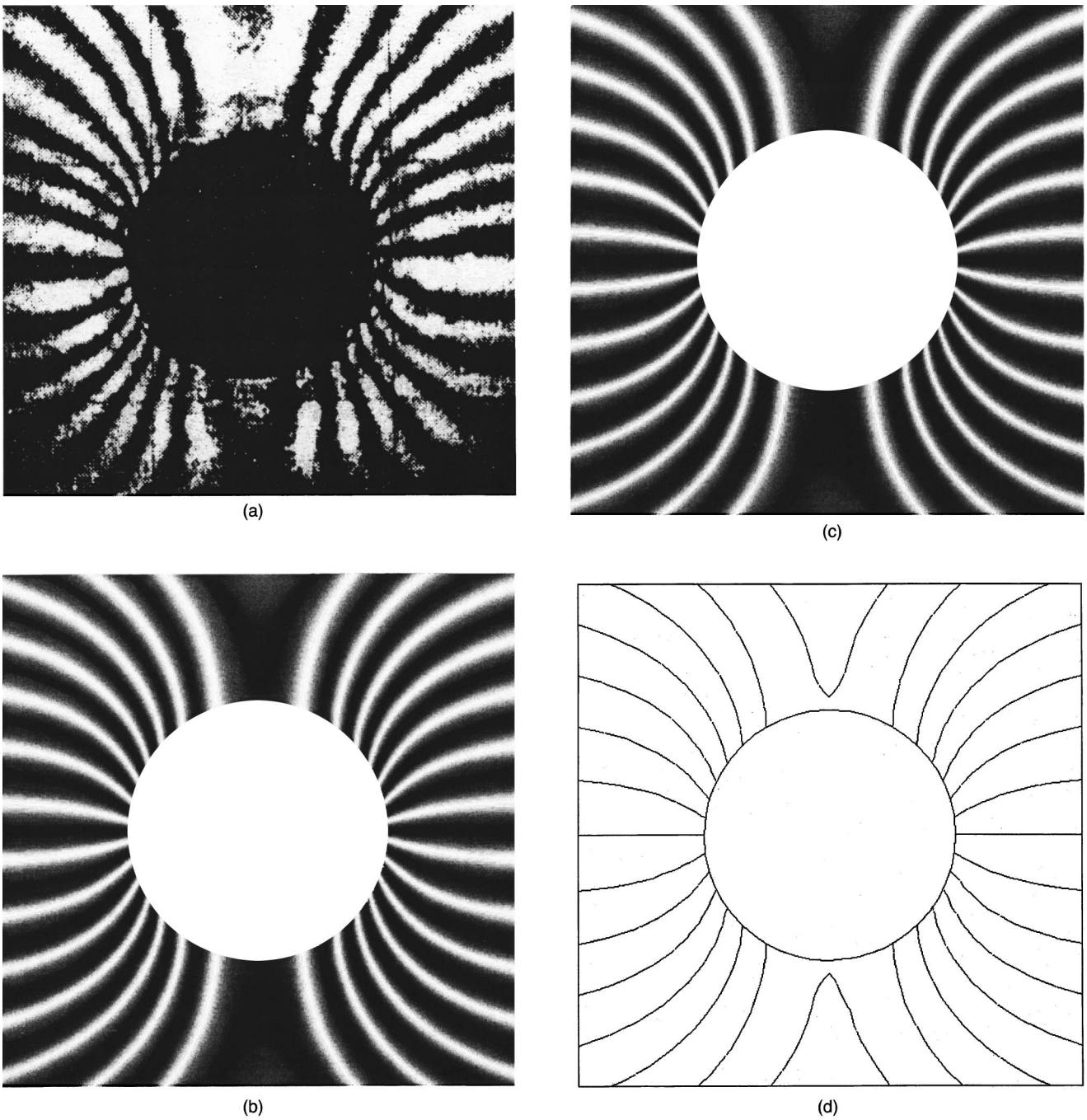

Fig. 2 (*a*) **Measured *v*-displacement fringe pattern induced in a $[0/\pm 45/\overline{90}]_s$ boron-epoxy panel containing a 25.4-mm-dia circular hole, subjected to $\sigma_y^\infty = 93$ MPa ([6]). (*b*) *v*-displacement fringe pattern for a $[0/\pm 45/\overline{90}]_s$ boron-epoxy panel containing a 25.4-mm-dia circular hole, subjected to $\sigma_y^\infty = 93$ MPa, predicted according to the original Savin solution. (*c*) *v*-displacement fringe pattern for a $[0/\pm 45/\overline{90}]_s$ boron-epoxy panel containing a 25.4-mm-dia circular hole, subjected to $\sigma_y^\infty = 93$ MPa, predicted according to the revised solution. (*d*) *v*-displacement fringe pattern for a $[0/\pm 45/\overline{90}]_s$ boron-epoxy panel containing a 25.4-mm-dia circular hole, subjected to $\sigma_y^\infty = 93$ MPa, predicted by a finite element method (ANSYS) analysis.**

where λ_1 and λ_2 are arbitrary constants of integration and were ignored by Savin. Finally, the holomorphic functions are obtained as

$$\phi_0(z_1) = \frac{-i[b\sigma_x^\infty + ias_2\sigma_y^\infty + (bs_2 + ia)\tau_{xy}^\infty]}{2(s_1 - s_2)}\zeta_1$$
$$\psi_0(z_2) = \frac{-i[b\sigma_x^\infty + ias_1\sigma_y^\infty + (bs_1 + ia)\tau_{xy}^\infty]}{2(s_1 - s_2)}\zeta_2. \tag{29}$$

This completes the solution of the problem. The expressions for in-plane stresses and displacements (Eqs. (11) and (12)) can now be expressed in more physically meaningful forms, as follows:

$$\sigma_x = \sigma_x^\infty + 2\,\mathrm{Re}[s_1^2\phi_0'(z_1) + s_2^2\psi_0'(z_2)]$$
$$\sigma_y = \sigma_y^\infty + 2\,\mathrm{Re}[\phi_0'(z_1) + \psi_0'(z_2)] \tag{30}$$
$$\tau_{xy} = \tau_{xy}^\infty - 2\,\mathrm{Re}[s_1\phi_0'(z_1) + s_2\psi_0'(z_2)]$$

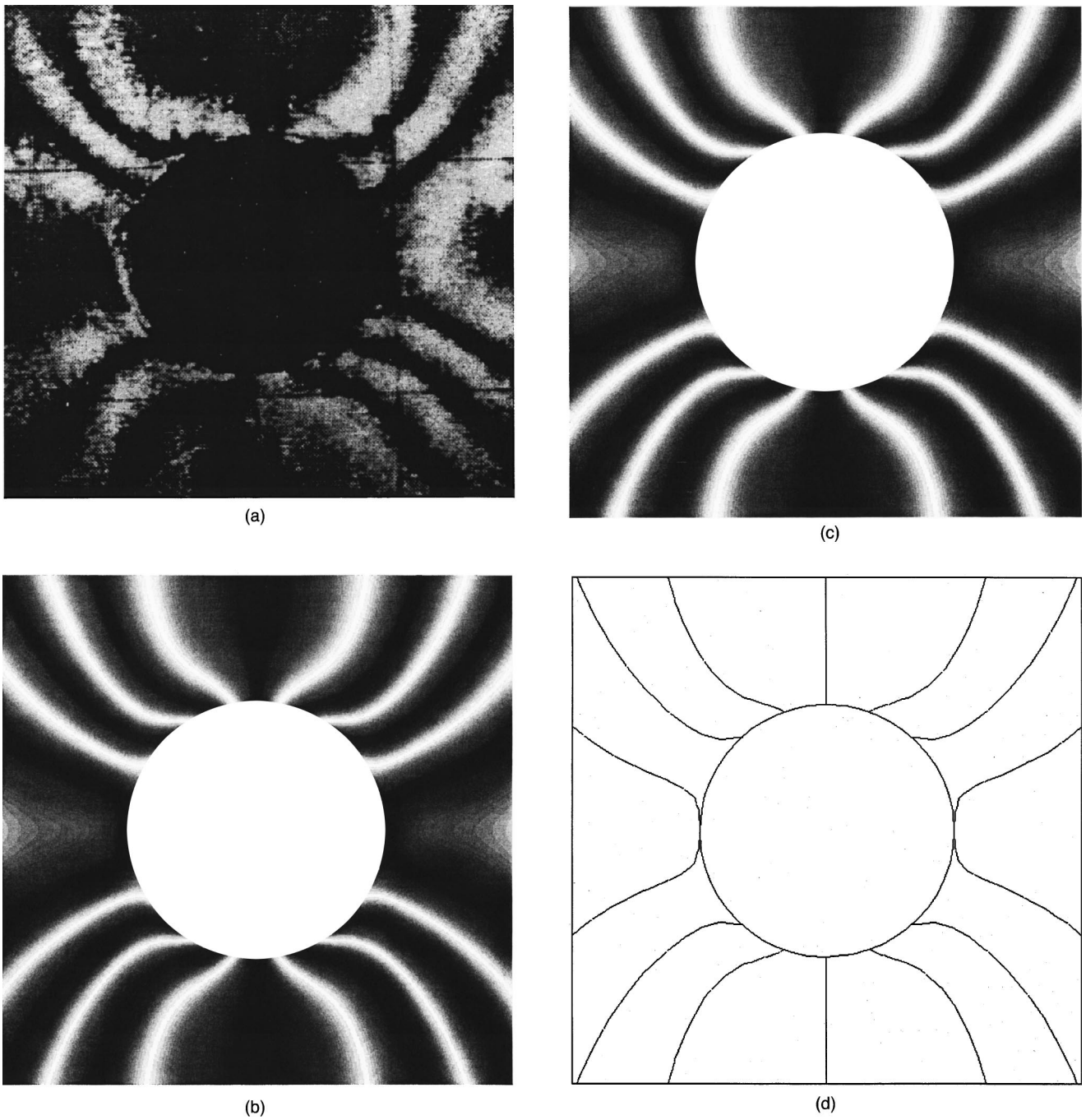

Fig. 3 (*a*) **Measured** u**-displacement fringe pattern induced in a** $[0/\pm 45/\overline{90}]_s$ **boron-epoxy panel containing a 25.4-mm-dia circular hole, subjected to** $\sigma_y^\infty = 93$ **MPa ([6]).** (*b*) u**-displacement fringe pattern for a** $[0/\pm 45/\overline{90}]_s$ **boron-epoxy panel containing a 25.4-mm-dia circular hole, subjected to** $\sigma_y^\infty = 93$ **MPa, predicted according to the original Savin solution.** (*c*) u**-displacement fringe pattern for a** $[0/\pm 45/\overline{90}]_s$ **boron-epoxy panel containing a 25.4-mm-dia circular hole, subjected to** $\sigma_y^\infty = 93$ **MPa, predicted according to the revised solution.** (*d*) u**-displacement fringe pattern for a** $[0/\pm 45/\overline{90}]_s$ **boron-epoxy panel containing a 25.4-mm-dia circular hole, subjected to** $\sigma_y^\infty = 93$ **MPa, predicted by the finite element method (ANSYS) analysis.**

and

$$u = u^\infty + 2\,\mathrm{Re}[p_1\phi_0(z_1) + p_2\psi_0(z_2)]$$
$$= x(a_{11}\sigma_x^\infty + a_{12}\sigma_y^\infty + a_{16}\tau_{xy}^\infty) + \frac{y}{2}(a_{16}\sigma_x^\infty + a_{26}\sigma_y^\infty + a_{66}\tau_{xy}^\infty)$$
$$+ 2\,\mathrm{Re}[p_1\phi_0(z_1) + p_2\psi_0(z_2)] \quad (31)$$

$$v = v^\infty + 2\,\mathrm{Re}[q_1\phi_0(z_1) + q_2\psi_0(z_2)]$$
$$= y(a_{12}\sigma_x^\infty + a_{22}\sigma_y^\infty + a_{26}\tau_{xy}^\infty) + \frac{x}{2}(a_{16}\sigma_x^\infty + a_{26}\sigma_y^\infty + a_{66}\tau_{xy}^\infty)$$
$$+ 2\,\mathrm{Re}[q_1\phi_0(z_1) + q_2\psi_0(z_2)]$$

where u^∞ and v^∞ are remote in-plane displacements. Note from

Table 1 Comparison of the predicted response at the point $x=377$ mm, $y=1085$ mm for a $[0/\pm 45/\overline{90}]_s$ boron-epoxy panel containing a 25.4-mm-dia circular hole, subjected to $\sigma_y^\infty=90.3$ MPa (13,100 psi)

	Savin	Revised	ANSYS
u (mm)	−0.136	−0.136	−0.136
v (mm)	1.86	1.86	1.92
σ_x (MPa)	≈0	≈0	≈0
σ_y (MPa)	90.3	90.3	90.3
τ_{xy} (MPa)	≈0	≈0	≈0
ε_x (μm/m)	−359	−359	−359
ε_y (μm/m)	1713	1713	1666
γ_{xy} (μrad)	0	0	0

Eq. (19) that all terms within Re [ ] in Eqs. (30) and (31) approach zero as $z_1, z_2 \to \infty$. Hence, these terms represent the disturbance in the stress and displacement fields due to the presence of the elliptical hole.

Comparisons Between Experimental Measurements and Analytical/Numerical Predictions

Displacement fields near a 25.4-mm-diameter circular hole in composite panels have been measured using geometric moiré, as reported in Refs. ([6,7]). In this paper these previously reported experimental measurements will be compared to (a) predictions based on the original Savin solution, (b) the revised solution as presented above, and (c) predictions obtained using the finite element code ANSYS. Specially orthotropic $[0/\pm 45/\overline{90}]_s$ laminates subjected to uniaxial tensile loadings were considered in both

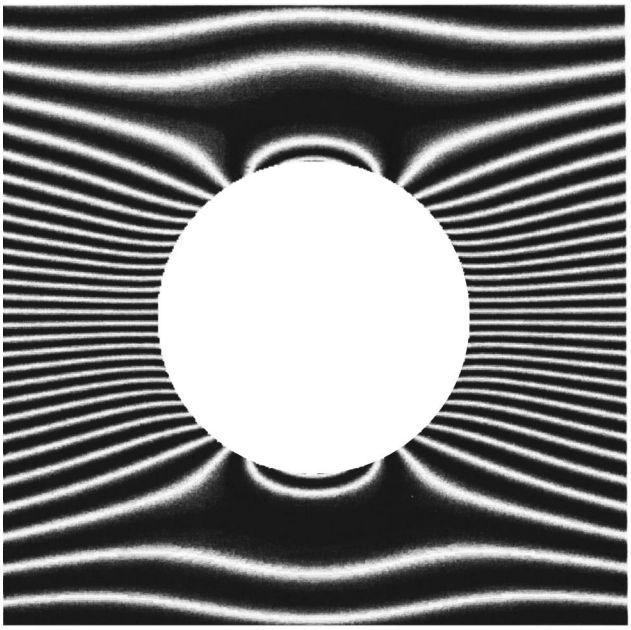

(a)

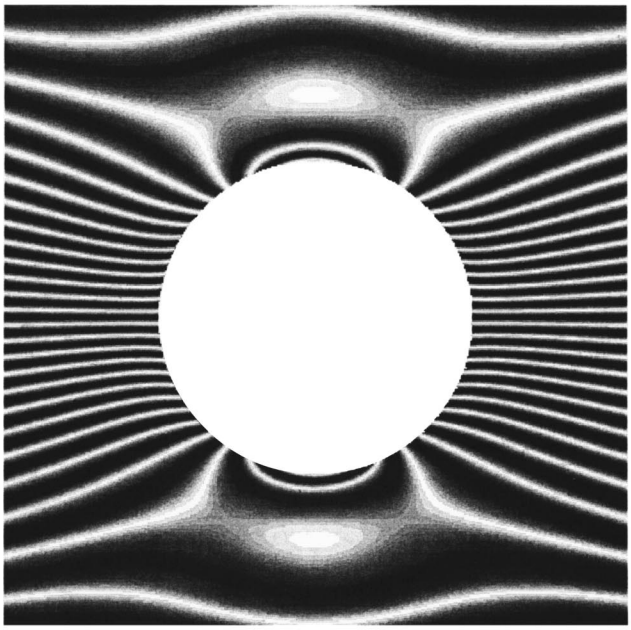

(b)

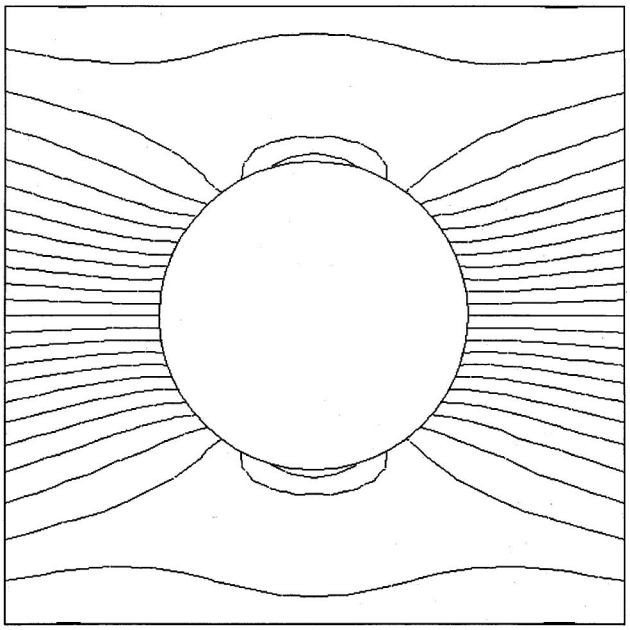

(c)

Fig. 4 (*a*) *v*-displacement fringe pattern for a $[0/\pm 45/\overline{90}]_s$ boron-epoxy panel containing a 25.4-mm-dia circular hole, subjected to $\tau_{xy}^\infty=17.2$ MPa, predicted according to the original Savin solution. (*b*) *v*-displacement fringe pattern for a $[0/\pm 45/\overline{90}]_s$ boron-epoxy panel containing a 25.4-mm-dia circular hole, subjected to $\tau_{xy}^\infty=17.2$ MPa, predicted according to the revised solution. (*c*) *v*-displacement fringe pattern for a $[0/\pm 45/\overline{90}]_s$ boron-epoxy panel containing a 25.4-mm-dia circular hole, subjected to $\tau_{xy}^\infty=17.2$ MPa, predicted by the finite element method (ANSYS) analysis.

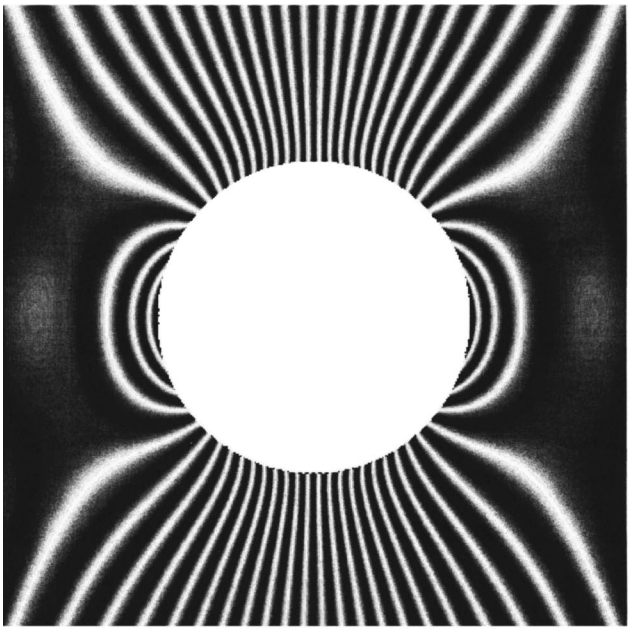

(a)

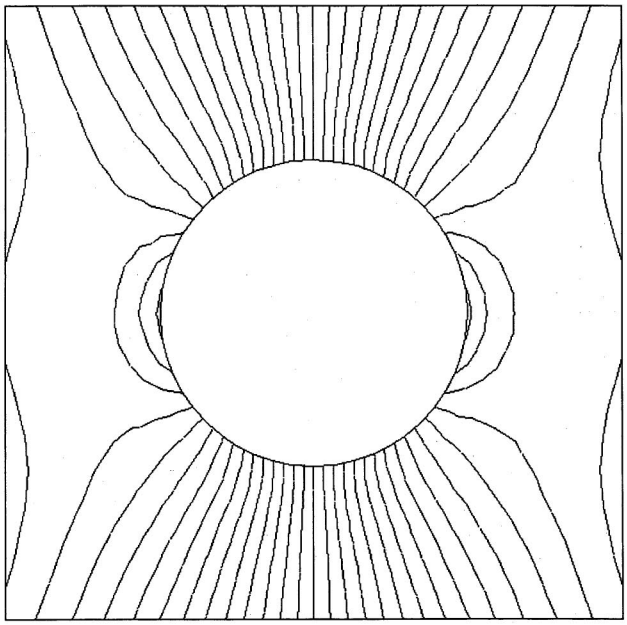

(c)

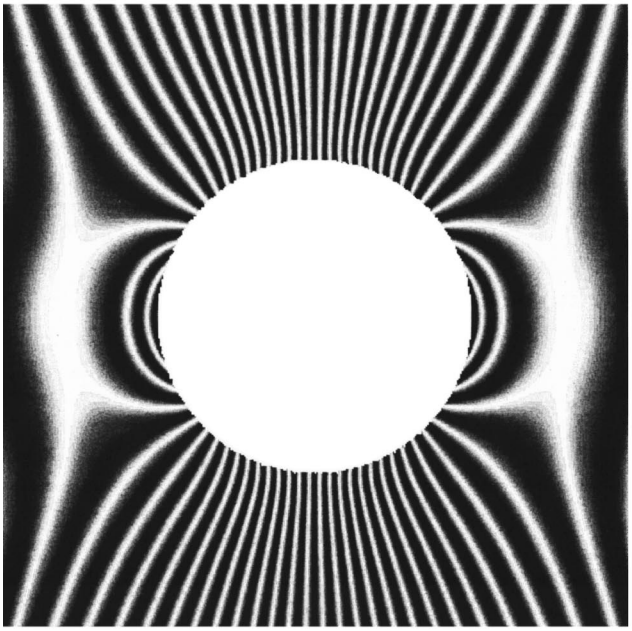

(b)

Fig. 5 (*a*) ***u*-displacement fringe pattern for a $[0/\pm 45/\overline{90}]_s$ boron-epoxy panel containing a 25.4-mm-dia circular hole, subjected to $\tau_{xy}^{\infty}=17.2$ MPa, predicted according to the original Savin solution.** (*b*) ***u*-displacement fringe pattern for a $[0/\pm 45/\overline{90}]_s$ boron-epoxy panel containing a 25.4-mm-dia circular hole, subjected to $\tau_{xy}^{\infty}=17.2$ MPa, predicted according to the revised solution.** (*c*) ***u*-displacement fringe pattern for a $[0/\pm 45/\overline{90}]_s$ boron-epoxy panel containing a 25.4-mm-dia circular hole, subjected to $\tau_{xy}^{\infty}=17.2$ MPa, predicted by the finite element method (ANSYS) analysis.**

([6,7]). However, in ([6]) the composite panel tested was composed of a boron-epoxy material system, whereas in ([7]) the panel tested was a glass-epoxy panel. Although an identical stacking sequence was used in both studies, the material properties involved are such that the panel tested in ([6]) corresponds to Case II (i.e., the roots of the characteristic equation are purely imaginary), whereas the panel tested in ([7]) corresponds to Case I (i.e., the roots of the characteristic equation are complex).

Comparisons will also be made for pure shear loadings, i.e., for $\sigma_x^{\infty}=\sigma_y^{\infty}=0$, $\tau_{xy}^{\infty}\neq 0$. Since experimental measurements are not available for this second loading condition, in this second case comparisons will be made between (a) the original Savin solution, (b) the revised solution, and (c) finite element predictions.

Geometric moiré is an optical technique that reveals in-plane

Table 2 Comparison of the predicted response at the point $x=599$ mm, $y=161$ mm for a $[0/\pm 45/\overline{90}]_s$ boron-epoxy panel containing a 25.4-mm-dia circular hole, subjected to $\tau_{xy}^{\infty}=17.2$ MPa (2500 psi)

	Savin	Revised	ANSYS
u (mm)	0.060	0.049	0.049
v (mm)	0.130	0.169	0.169
σ_x (MPa)	−0.04	−0.04	−.04
σ_y (MPa)	≈0	≈0	≈0
τ_{xy} (MPa)	17.2	17.2	17.2
ε_x (μm/m)	≈0	≈0	≈0
ε_y (μm/m)	≈0	≈0	≈0
γ_{xy} (μrad)	605	605	606

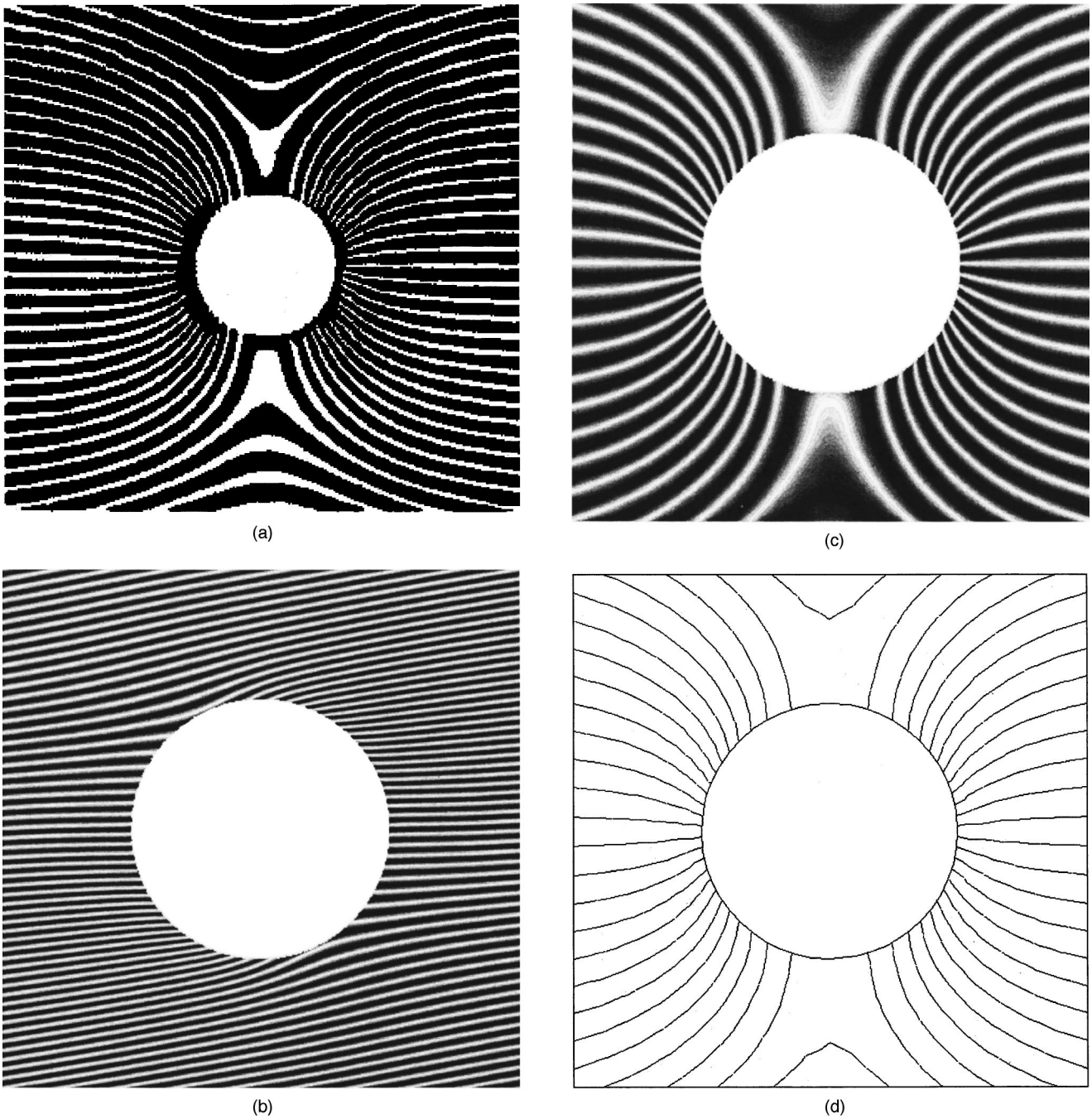

Fig. 6 (*a*) **Measured *v*-displacement fringe pattern induced in a $[0/\pm 45/\overline{90}]_s$ glass-epoxy panel containing a 25.4-mm-dia circular hole, subjected to $\sigma_y^\infty = 198$ MPa ([7]).** (*b*) ***v*-displacement fringe pattern for a $[0/\pm 45/\overline{90}]_s$ glass-epoxy panel containing a 25.4-mm-dia circular hole, subjected to $\sigma_y^\infty = 198$ MPa, predicted according to the original Savin solution (resolution reduced to 50.8 μm).** (*c*) ***v*-displacement fringe pattern for a $[0/\pm 45/\overline{90}]_s$ glass-epoxy panel containing a 25.4-mm-dia circular hole, subjected to $\sigma_y^\infty = 198$ MPa, predicted according to the revised solution.** (*d*) ***v*-displacement fringe pattern for a $[0/\pm 45/\overline{90}]_s$ glass-epoxy panel containing a 25.4-mm-dia circular hole, subjected to $\sigma_y^\infty = 198$ MPa, predicted by the finite element method (ANSYS) analysis.**

displacements in the form of alternating light-and-dark lines called ''fringes.'' To facilitate a direct whole-field comparison between measured and predicted displacement fields, a program was written in-house and used to plot the fringe patterns predicted by the original and revised Savin solutions. Similarly, in-plane displacement fields predicted using ANSYS were plotted as contour lines of constant displacement. This procedure allows a direct whole-field comparison between measured and predicted displacement fields. In addition, displacements calculated according to the original solution, the revised solution, and the finite element method analysis, will be compared at a particular point far removed from the circular hole.

Details of the geometric moiré method are given elsewhere ([18]). In simplest form, a grating (called the specimen grating) is bonded to the specimen surface. The specimen grating is then viewed through a second grating (called the reference grating). When a load is applied the specimen grating is deformed, and an interference pattern (i.e., a fringe pattern) develops which repre-

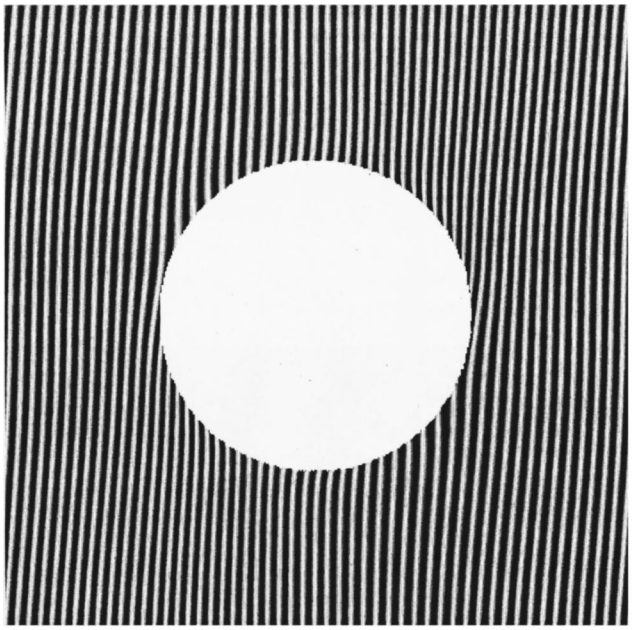

(a)

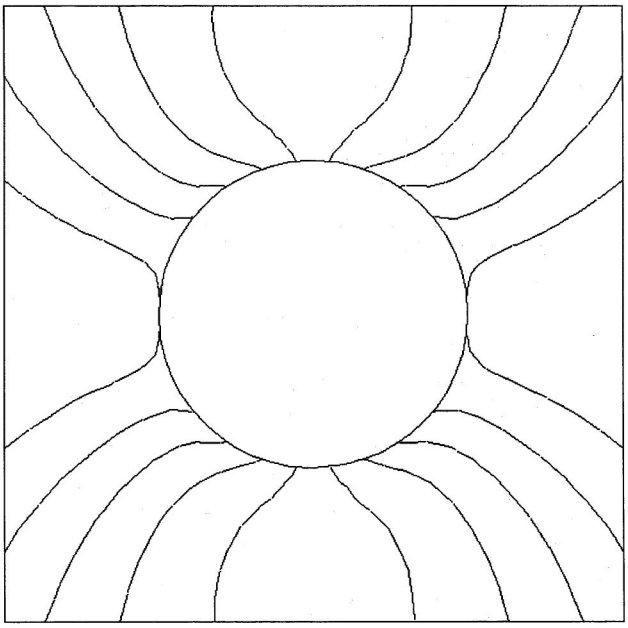

(c)

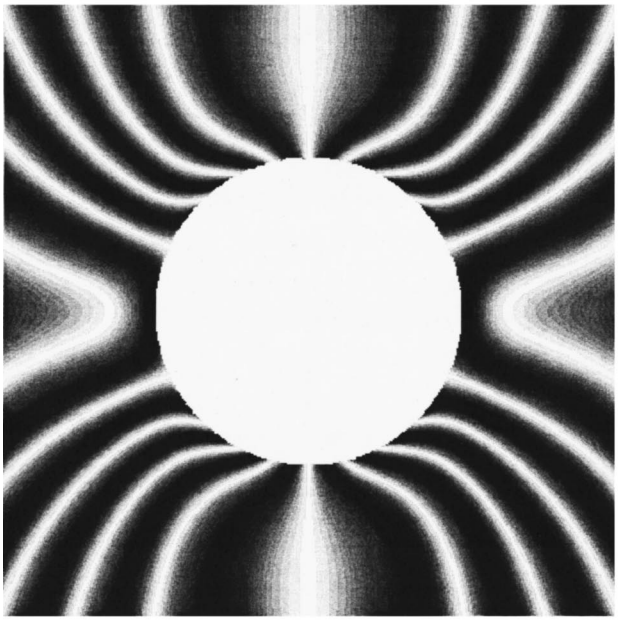

(b)

Fig. 7 (*a*) ***u*-displacement fringe pattern for a $[0/\pm 45/\overline{90}]_s$ glass-epoxy panel containing a 25.4-mm-dia circular hole, subjected to $\sigma_y^\infty = 198$ MPa, predicted according to the original Savin solution (resolution reduced to 50.8 μm).** (*b*) ***u*-displacement fringe pattern for a $[0/\pm 45/\overline{90}]_s$ glass-epoxy panel containing a 25.4-mm-dia circular hole, subjected to $\sigma_y^\infty = 198$ MPa, predicted according to the revised solution.** (*c*) ***u*-displacement fringe pattern for a $[0/\pm 45/\overline{90}]_s$ glass-epoxy panel containing a 25.4-mm-dia circular hole, subjected to $\sigma_y^\infty = 198$ MPa, predicted by the finite element method (ANSYS) analysis.**

sents in-plane displacements. Measurement resolution depends on the grating frequency. Different grating frequencies were used in ([6,7]), and hence the fringe patterns reported in ([6,7]) were obtained at two different levels of resolution. The predicted fringe patterns presented in the following sections were therefore generated using different resolution levels, i.e., the resolution assumed to create the predicted fringe patterns is varied from one subsection to the next, as appropriate.

For brevity, the finite element meshes used will not be described in detail. Briefly, six-node triangular elements were used during the finite element method analyses. Convergence studies were performed to insure that the mesh densities used were sufficient to accurately capture details of the predicted stress/displacement fields. At least 800 elements were used in all cases.

Table 3 Comparison of the predicted response at the point $x = 377$ mm, $y = 1085$ mm for a $[0/\pm 45/\overline{90}]_s$ glass-epoxy panel containing a 25.4-mm-dia circular hole, subjected to $\sigma_y^\infty = 198$ MPa (28,700 psi)

	Savin	Revised	ANSYS
u (mm)	−62.7	−1.04	−1.04
v (mm)	32.3	11.0	11.0
σ_x (MPa)	≈0	≈0	≈0
σ_y (MPa)	198	198	198
τ_{xy} (MPa)	≈0	≈0	≈0
ε_x (μm/m)	−2760	−2760	−2760
ε_y (μm/m)	10,150	10,150	10,150
γ_{xy} (μrad)	0	0	0

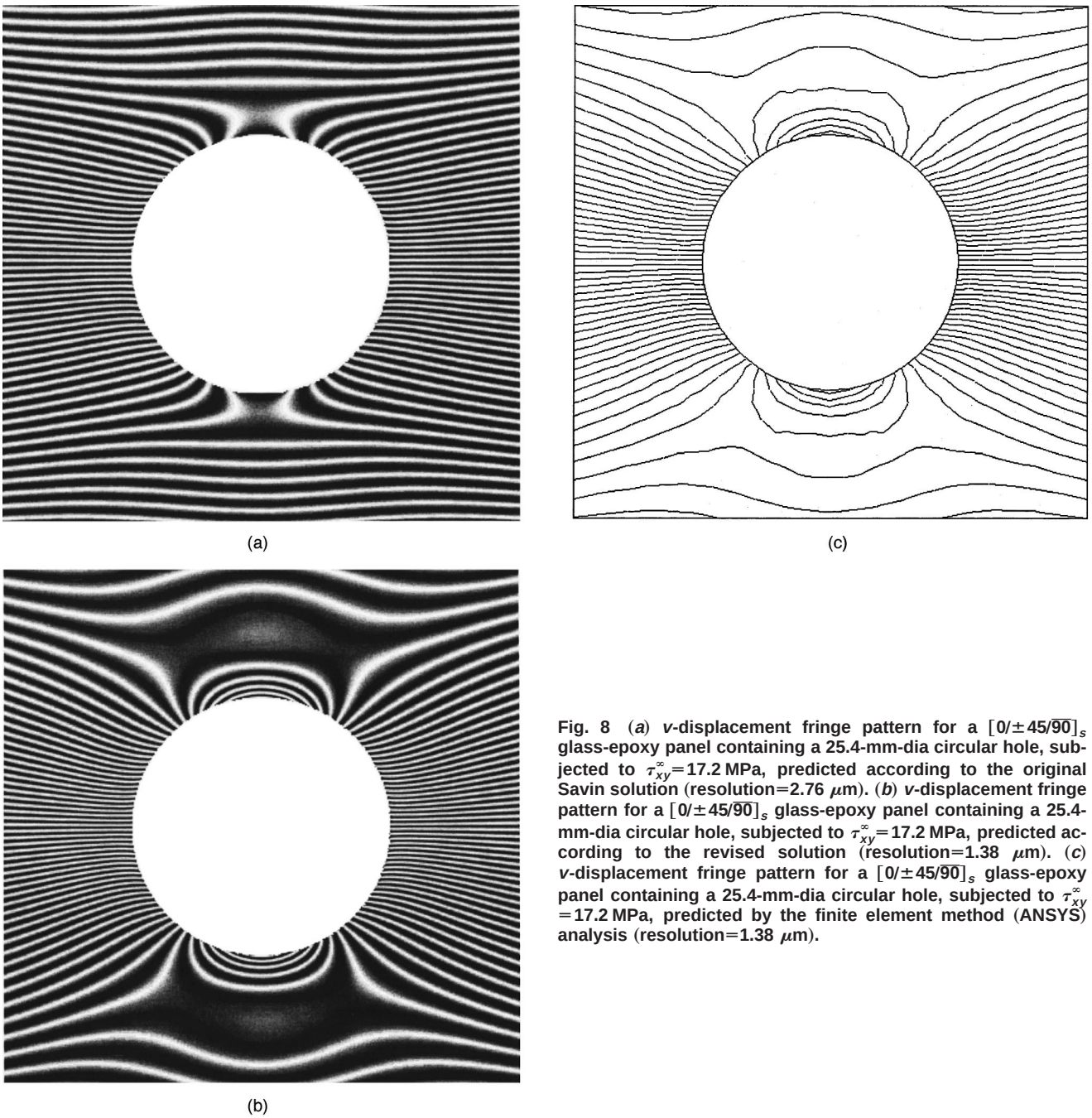

Fig. 8 (*a*) ***v*-displacement fringe pattern for a $[0/\pm 45/\overline{90}]_s$ glass-epoxy panel containing a 25.4-mm-dia circular hole, subjected to $\tau_{xy}^{\infty}=17.2$ MPa, predicted according to the original Savin solution (resolution=2.76 μm).** (*b*) ***v*-displacement fringe pattern for a $[0/\pm 45/\overline{90}]_s$ glass-epoxy panel containing a 25.4-mm-dia circular hole, subjected to $\tau_{xy}^{\infty}=17.2$ MPa, predicted according to the revised solution (resolution=1.38 μm).** (*c*) ***v*-displacement fringe pattern for a $[0/\pm 45/\overline{90}]_s$ glass-epoxy panel containing a 25.4-mm-dia circular hole, subjected to $\tau_{xy}^{\infty}=17.2$ MPa, predicted by the finite element method (ANSYS) analysis (resolution=1.38 μm).**

Composite Panel With Purely Imaginary Roots

The material properties for the boron-epoxy panel studied in ([6]) were reported to be $E_{xx}=113$ GPa (16.40 Msi), $E_{yy}=52.7$ GPa (7.65 Msi), $G_{xy}=28.5$ GPa (4.13 Msi), and $\nu_{xy}=0.45$. The roots (s_1, s_2) of the characteristic equation for this material are purely imaginary and equal $1.0358i$ and $1.4135i$, respectively. Hence, this panel corresponds to Case II.

Uniaxial Tensile Loading. Measured v and u-displacement fields induced by a remote tensile stress of $\sigma_y^{\infty}=90.3$ MPa (13,100 psi) are shown in Figs. 2(*a*) and 3(*a*), respectively. These images were obtained using a fringe multiplication technique ([6]), resulting in an effective grating frequency of 197 lines/mm (5000 lines/in.). This frequency corresponds to a displacement measurement resolution of 5.08 μm. The corresponding predicted displacement fields are plotted in Figs. 2(*b–d*) and 3(*b–d*). The predicted displacement fields are all essentially identical, and closely resemble the measured moiré patterns. Also, numerical comparison of predicted displacements, strains, and stresses at the point ($x=377$ mm, $y=1085$ mm), a point picked randomly from among the nodal point positions in the finite element method mesh, is made in Table 1. Excellent agreement is obtained in all cases. It is concluded that, for this loading condition and material system/stacking sequence, predictions obtained using the original Savin solution, the revised solution, and the finite element method analysis are all essentially equivalent.

Pure Shear Loading. Comparisons between predicted v and u-displacement fields caused by a remote pure shear stress of $\tau_{xy}^{\infty}=17.2$ MPa (2500 psi) are made in Figs. 4 and 5, respectively (as previously mentioned, experimental results are not available for a pure shear loading). In these figures the (simulated) fringe

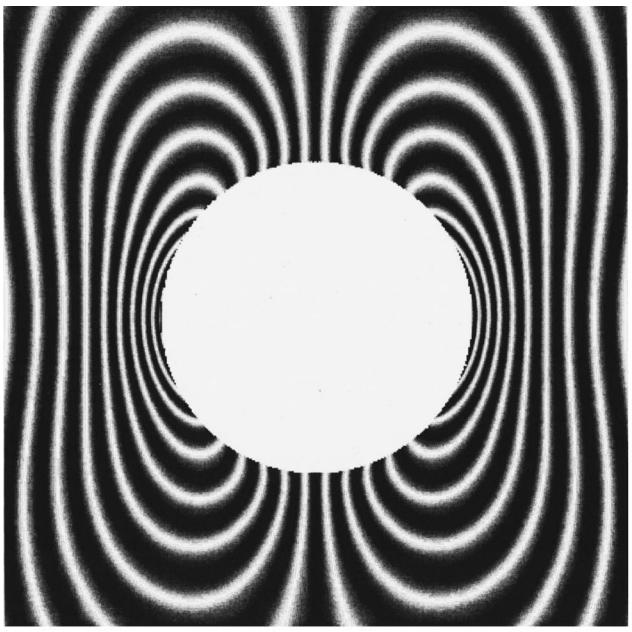

(a)

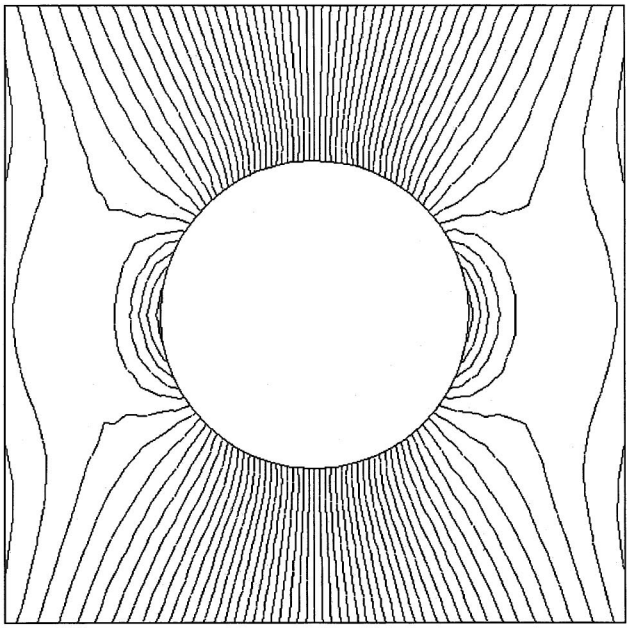

(c)

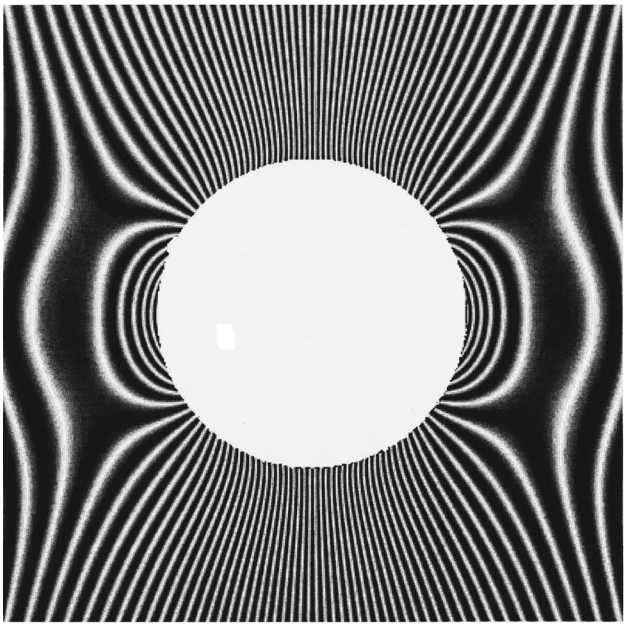

(b)

Fig. 9 (*a*) ***u*-displacement fringe pattern for a $[0/\pm 45/\overline{90}]_s$ glass-epoxy panel containing a 25.4-mm-dia circular hole, subjected to $\tau_{xy}^{\infty}=17.2$ MPa, predicted according to the original Savin solution (resolution=2.76 μm).** (*b*) ***u*-displacement fringe pattern for a $[0/\pm 45/\overline{90}]_s$ glass-epoxy panel containing a 25.4-mm-dia circular hole, subjected to $\tau_{xy}^{\infty}=17.2$ MPa, predicted according to the revised solution (resolution=1.38 μm).** (*c*) ***v*-displacement fringe pattern for a $[0/\pm 45/\overline{90}]_s$ glass-epoxy panel containing a 25.4-mm-dia circular hole, subjected to $\tau_{xy}^{\infty}=17.2$ MPa, predicted by the finite element method (ANSYS) analysis (resolution=1.38 μm).**

patterns correspond to a resolution of 0.833 μm. Both figures contain images which were (a) predicted by the original Savin solution, (b) predicted by the revised solution, and (c) predicted using ANSYS. A careful inspection of these figures reveals that for this loading condition the displacement fields predicted by the original Savin solution differs markedly from that predicted by the revised solution and the finite element method analysis. In Fig. 4 the differences are particularly noticeable at the 12 o'clock and 6 o'clock positions around the hole circumference, whereas in Fig. 5 the differences are most noticeable at the 3 o'clock and 9 o'clock positions. The discrepancy is further highlighted by a numerical comparison of predicted displacements, strains, and stresses, again at the far-field point ($x=599$ mm, $y=161$ mm). This comparison is made in Table 2. It is seen that predicted strains and stresses are identical in all cases, but the displacements

Table 4 Comparison of the predicted response at the point $x=599$ mm, $y=161$ mm for a $[0/\pm 45/\overline{90}]_s$ glass-epoxy panel containing a 25.4-mm-dia circular hole, subjected to $\tau_{xy}^{\infty}=17.2$ MPa (2500 psi)

	Savin	Revised	ANSYS
u (mm)	0.396	0.156	0.156
v (mm)	−0.295	0.544	0.544
σ_x (MPa)	−0.03	−0.03	−0.03
σ_y (MPa)	≈0	≈0	≈0
τ_{xy} (MPa)	17.2	17.2	17.2
ε_x (μm/m)	−1	−1	−1
ε_y (μm/m)	0	0	0
γ_{xy} (μrad)	1940	1940	1940

predicted by the original Savin solution do not agree with predictions based on the revised solution or the finite element method analysis.

Composite Panel With Complex Roots

The material properties for the glass-epoxy panel studied in ([7]) were reported to be $E_{xx}=25.9$ GPa (3.75 Msi), $E_{yy}=19.5$ GPa (2.83 Msi), $G_{xy}=8.89$ GPa (1.29 Msi), and $\nu_{xy}=0.36$. The roots (s_1, s_2) of the characteristic equation for this material are complex and equal $-0.1698+1.0594i$ and $0.1698+1.0594i$, respectively. Hence, this panel corresponds to Case I.

Uniaxial Tensile Loading. The measured v-displacement field induced by a remote tensile stress of $\sigma_y^\infty=198$ MPa (28,700 psi) is shown in Fig. 6(*a*). This image was obtained using a grating frequency of 39.4 lines/mm (1000 lines/in.) corresponding to a measurement resolution of 25.4 μm. The corresponding predicted displacement fields are plotted in Figs. 6(*b–d*). If a resolution of 25.4 μm is used to plot the fringe patterns predicted by the original Savin solution, the resulting fringes are too dense to be plotted. For present purposes the displacement fields predicted by the original Savin solution (Fig. 6(*b*)) have therefore been generated based on a reduced resolution of 50.8 μm. The fringe patterns predicted by the revised solution and the finite element method analysis (Figs. 6(*c,d*)) have been generated using a resolution of 25.4 μm. Excellent agreement was achieved between predictions based on the revised solution and the finite element method analysis, and furthermore these results closely resemble the experimental fringe pattern. In contrast, the displacement field predicted by the original Savin solution is grossly distorted, since rigid-body rotations have not been properly accounted for, as previously discussed.

The transverse u-displacement field was not measured in ([7]). A comparison between predicted u-displacement fields is made in Figs. 7(*a–c*). Once again, excellent agreement is achieved between the revised solution and the finite element method analysis, whereas the u-displacement field predicted by the original Savin solution is distorted due to rigid-body rotations.

A numerical comparison of predicted displacements, strains, and stresses, again at the far-field point ($x=377$ mm, $y=1085$ mm), is made in Table 3. It is seen that the predicted strains and stresses are identical in all cases, but the displacements predicted by the original Savin solution do not agree with predictions based on the revised solution or the finite element method analysis.

Pure Shear Loading. Comparisons between predicted v and u-displacement fields caused by a remote pure shear stress of $\tau_{xy}^\infty=17.2$ MPa (2500 psi) are made in Figs. 8 and 9, respectively (as previously mentioned, experimental results are not available for a pure shear loading). In Figs. 8(*a*) and 9(*a*) the simulated fringe patterns correspond to a resolution of 2.76 μm, whereas in Figs. 8(*b,c*) and 9(*b,c*) the resolution was increased to 1.38 μm. As before, a lower resolution was required to plot the fringe pattern predicted by the original Savin solution. Also as before, the revised solution and the finite element method analysis are in close agreement, and differ substantially from predictions based on the original Savin solution. A numerical comparison that confirms these discrepancies is made in Table 4.

Summary and Conclusions

The classical Savin solution for the stress induced in an orthotropic plate containing an elliptical hole places no restrictions on remote rigid-body rotations. In this paper the Savin procedure is used to obtain a solution for which remote rigid-body rotations are required to be zero. The validity of the revised solution is demonstrated by comparing predicted displacement fields induced in composite panels with those measured using geometric moiré as well as those predicted using the finite element method.

It is concluded that stress and strain fields are properly predicted by the original Savin solution in all cases. This would be expected, since the stress boundary conditions were satisfied in the original solution formulated by Savin. However, in most cases the displacements inferred from the original Savin solution are incorrect, in the sense that the predicted values contain an unknown level of rigid-body rotations. The only case in which displacements inferred from the original Savin solution do not include rigid-body rotations is for specially orthotropic panels with purely imaginary roots, subjected to remote in-plane normal stresses only (i.e., when $\tau_{xy}^\infty=0$).

The revised solution presented herein can be used to accurately predict the stress, strain and displacement fields induced in any orthotropic panel containing an elliptical hole and subjected to any combination of remote in-plane stresses, σ_x^∞, σ_y^∞, and τ_{xy}^∞.

Appendix

Expressions for the four constants B^*, C^*, B'^*, and C'^* are listed below:

$$B'^*=\frac{1}{2D}\{[2a_{11}|s_1||s_2|(3\alpha_1\alpha_2^2-3\alpha_1^2\alpha_2+\alpha_2\beta_1^2-\alpha_1\beta_2^2)+a_{22}(-2\alpha_2^3-2\alpha_2\beta_2^2+2\alpha_1\beta_1^2+2\alpha_1^3)]\tau_{xy}$$
$$+[a_{11}|s_1|^2|s_2|(3\alpha_2^2-4\alpha_1\alpha_2+\beta_1^2-\beta_2^2+\alpha_1^2)+a_{22}(\alpha_1^4-\alpha_2^2\beta_1^2-\beta_1^2\beta_2^2+3\alpha_1^2\beta_2^2-4\alpha_1\alpha_2\beta_2^2+\beta_1^4+3\alpha_1^2\alpha_2^2+2\alpha_1^2\beta_1^2-4\alpha_1\alpha_2^3)$$
$$+2a_{26}|s_1||s_2|(\alpha_2-\alpha_1)]\sigma_y+[a_{11}|s_1||s_2|(3\alpha_2^2-\beta_2^2-3\alpha_1^2+\beta_1^2)+a_{22}(-\alpha_2^2-\beta_2^2+\alpha_1^2+\beta_1^2)-2a_{16}|s_1||s_2|(\alpha_2-\alpha_1)]\sigma_x\} \quad (A1)$$

$$B^*=\frac{1}{2D}\{-[2a_{11}|s_1||s_2|(3\alpha_1\alpha_2^2-3\alpha_1^2\alpha_2+\alpha_2\beta_1^2-\alpha_1\beta_2^2)+a_{22}(-2\alpha_2^3-2\alpha_2\beta_2^2+2\alpha_1\beta_1^2+2\alpha_1^3)]\tau_{xy}$$
$$+[a_{11}|s_1||s_2|^2(3\alpha_1^2-4\alpha_1\alpha_2+\beta_2^2-\beta_1^2+\alpha_2^2)+a_{22}(\alpha_2^4-\alpha_1^2\beta_2^2-\beta_1^2\beta_2^2+3\alpha_2^2\beta_1^2-4\alpha_1\alpha_2\beta_1^2+\beta_2^4+3\alpha_1^2\alpha_2^2+2\alpha_2^2\beta_2^2-4\alpha_1^3\alpha_2)$$
$$+2a_{26}|s_1||s_2|(\alpha_1-\alpha_2)]\sigma_y-[a_{11}|s_1||s_2|(3\alpha_2^2-\beta_2^2-3\alpha_1^2+\beta_1^2)+a_{22}(-\alpha_2^2-\beta_2^2+\alpha_1^2+\beta_1^2)-2a_{16}|s_1||s_2|(\alpha_2-\alpha_1)]\sigma_x\} \quad (A2)$$

$$C'^*=\frac{1}{2\beta_2 D}\{[a_{11}|s_1||s_2|(2\alpha_1\alpha_2^3-3\alpha_1^2\alpha_2^2+\alpha_2^2\beta_1^2-6\alpha_1\alpha_2\beta_2^2+\alpha_1^4+2\alpha_1^2\beta_1^2+\beta_1^4+3\alpha_1^2\beta_2^2-\beta_1^2\beta_2^2)$$
$$+a_{22}(\beta_2^4-\alpha_2^4-\alpha_2^2\beta_1^2-2\alpha_1^3\alpha_2-2\alpha_1\alpha_2\beta_1^2+3\alpha_1^2\alpha_2^2+3\alpha_1^2\beta_2^2-\beta_1^2\beta_2^2)]\tau_{xy}+[a_{11}|s_1|^2|s_2|(\alpha_2^3-2\alpha_1\alpha_2^2+\alpha_1^2\alpha_2+\alpha_2\beta_1^2-3\alpha_2\beta_2^2$$
$$+2\alpha_1\beta_2^2)+a_{22}(-\alpha_1^4\alpha_2-\alpha_2^3\beta_1^2+2\alpha_1\beta_2^4-\alpha_2\beta_1^4-2\alpha_1\alpha_2^4-\alpha_2\beta_1^2\beta_2^2+3\alpha_1^2\alpha_2\beta_2^2+3\alpha_1^2\alpha_2^3-2\alpha_1^2\alpha_2\beta_1^2)$$
$$+a_{26}|s_1||s_2|(\alpha_2^2-2\alpha_1\alpha_2+\beta_1^2+\alpha_1^2-\beta_2^2)]\sigma_y+[a_{11}|s_1||s_2|(\alpha_2^3-3\alpha_1^2\alpha_2+\alpha_2\beta_1^2-3\alpha_2\beta_2^2+2\alpha_1^3+2\alpha_1\beta_1^2)$$
$$+a_{22}(-\alpha_2\beta_2^2-\alpha_2^3-\alpha_2\beta_1^2-\alpha_1^2\alpha_2+2\alpha_1\beta_2^2+2\alpha_1\alpha_2^2)-a_{16}|s_1||s_2|(\alpha_2^2-2\alpha_1\alpha_2+\beta_1^2+\alpha_1^2-\beta_2^2)]\sigma_x\} \quad (A3)$$

$$C^* = \frac{1}{2\beta_1 D}\{[a_{11}|s_1||s_2|(2\alpha_1^3\alpha_2 - 3\alpha_1^2\alpha_2^2 + \alpha_1^2\beta_2^2 - 6\alpha_1\alpha_2\beta_1^2 + \alpha_2^4 + 2\alpha_2^2\beta_2^2 + \beta_2^4 + 3\alpha_2^2\beta_1^2 - \beta_1^2\beta_2^2)$$
$$+ a_{22}(\beta_1^4 - \alpha_1^4 - \alpha_1^2\beta_2^2 - 2\alpha_1\alpha_2^3 - 2\alpha_1\alpha_2\beta_2^2 + 3\alpha_1^2\alpha_2^2 + 3\alpha_2^2\beta_1^2 - \beta_1^2\beta_2^2)]\tau_{xy} + [a_{11}|s_1||s_2|^2(\alpha_1^3 - 2\alpha_1^2\alpha_2 + \alpha_1\alpha_2^2 + \alpha_1\beta_2^2 - 3\alpha_1\beta_1^2$$
$$+ 2\alpha_2\beta_1^2) + a_{22}(-\alpha_1\alpha_2^4 - \alpha_1^3\beta_2^2 + 2\alpha_2\beta_1^4 - \alpha_1\beta_2^4 - 2\alpha_1^4\alpha_2 - \alpha_1\beta_2^2\beta_1^2 + 3\alpha_1\alpha_2^2\beta_1^2 + 3\alpha_1^3\alpha_2^2 - 2\alpha_1\alpha_2^2\beta_2^2)$$
$$+ a_{26}|s_1||s_2|(\alpha_1^2 - 2\alpha_1\alpha_2 + \beta_2^2 + \alpha_2^2 - \beta_1^2)]\sigma_y + [a_{11}|s_1||s_2|(\alpha_1^3 - 3\alpha_1\alpha_2^2 + \alpha_1\beta_2^2 - 3\alpha_1\beta_1^2 + 2\alpha_2^3 + 2\alpha_2\beta_2^2)$$
$$+ a_{22}(-\alpha_1\beta_1^2 - \alpha_1^3 - \alpha_1\beta_2^2 - \alpha_1\alpha_2^2 + 2\alpha_2\beta_1^2 + 2\alpha_1^2\alpha_2) - a_{16}|s_1||s_2|(\alpha_1^2 - 2\alpha_1\alpha_2 + \beta_2^2 + \alpha_2^2 - \beta_1^2)]\sigma_x\} \quad (A4)$$

where

$$|s_i| = \alpha_i^2 + \beta_i^2$$
$$\%1 = a_{11}(\alpha_1^2 + \beta_1^2)(\alpha_2^2 + \beta_2^2) + a_{22}$$
$$\%2 = \alpha_1^2 - 2\alpha_1\alpha_2 + \alpha_2^2 + \beta_1^2 + 2\beta_1\beta_2 + \beta_2^2$$
$$\%3 = \alpha_1^2 - 2\alpha_1\alpha_2 + \alpha_2^2 + \beta_1^2 - 2\beta_1\beta_2 + \beta_2^2$$
$$D = \%1\%2\%3.$$

References

[1] Green, A. E., and Taylor, G. I., 1945, ''Stress Systems in Aeolotropic Plates III,'' Proc. R. Soc. London, Ser. A, **184**, pp. 181–195; pp. 218–219.

[2] Bonora, N., Costanzi, M., and Marchetti, M., 1993, ''On Closed Form Solution for the Elastic Stress Field Around Holes in Orthotropic Composite Plates Under in-Plane Stress Conditions,'' Composite Structures, **25**, pp. 139–156.

[3] Sampath, S. G., and Hulbert, L. E., 1975, ''Analysis of Multiholed Orthotropic Laminated Plates by the Boundary-Point-Squares Methods,'' ASME J. Pressure Vessel Technol., **75**, pp. 118–122.

[4] Hayashi, T., 1986, ''Stress Analysis of the Anisotropic Plate With a Hole Under the Uniaxial Loading,'' *Composite '86: Recent Advances in Japan and the United States, Proc. Japan-U.S. CCM-III*, K. Kawata, S. Umekawa, and A. Kobayashi, eds., Japan Society of Composite Materials, Tokyo, pp. 197–204.

[5] Kaltakci, M. Y., 1996, ''Stress Concentrations and Failure Criteria in Anisotropic Plates With Circular Holes Subjected to Tension or Compression,'' Comput. Struct., **61**, pp. 67–78.

[6] Daniel, I. M., Rowlands, R. E., and Whiteside, J. B., 1973, ''Deformation and Failure of Boron-Epoxy Plate With Circular Hole,'' *Analysis of the Test Methods for High Modulus Fibers and Composites*, ASTM STP 521, American Society for Testing and Materials, Philadelphia, PA, pp. 143–164.

[7] Rowlands, R. E., Daniel, I. M., and Whiteside, J. B., 1973, ''Stress and Failure Analysis of a Glass-Epoxy Composite Plate With a Circular Hole,'' Exp. Mech., **13**, No. 1, pp. 31–37.

[8] Sneddon, I. N., 1975, ''Integral Transform Methods for the Solution of Mixed Boundary Value Problems in the Classical Theory of Elastostatics,'' *Application of Integral Transforms in the Theory of Elasticity* (CISM Courses and Lectures No. 220), I. N Sneddon, ed., Springer-Verlag, New York.

[9] Gilbert, R. P., and Schneider, M., 1987, ''The Boundary Integral Method for Two-Dimensional Orthotropic Materials,'' J. Elast., **18**, pp. 61–82.

[10] Ladopoulas, E. G., 1989, ''Singular Integral Operators Method for Two-Dimensional Plasticity Problems,'' Comput. Struct., **33**, pp. 859–865.

[11] Ting, T. C. T., 1996, *Anisotropic Elasticity: Theory and Applications*, Oxford University Press, New York.

[12] Savin, G. N., 1961, *Stress Concentration Around Holes*, Pergamon Press, New York.

[13] Lekhnitskii, S. G., 1963, *Theory of Elasticity of an Anisotropic Body*, Holden-Day, San Francisco.

[14] Bonora, N., Costanzi, M., and Marchetti, M., 1994, ''A Computational Procedure to Calculate Stress-Strain Field Around Simple Shape Holes in Composite Laminates,'' Comput. Struct., **53**, No. 5, pp. 1167–1179.

[15] Ukadgaonker, V. G., and Rao, D. K. N., 1999, ''Stress Distribution Around Triangular Holes in Anisotropic Plates,'' Comput. Struct., **45**, No. 1, pp. 171–183.

[16] Jen, M.-H. R., Kau, Y. S., and Hsu, J. M., 1993, ''Interlaminar Stresses in a Centrally Notched Composite Laminate,'' Int. J. Solids Struct., **30**, No. 21, pp. 2911–2928.

[17] Muskhelishvili, N. I., 1953, *Some Basic Problems of the Mathematical Theory of Elasticity: Fundamental Equations, Plane Theory of Elasticity, Torsion, and Bending*, P. Noordhoff, Groningen (translated from the Russian by J. R. M. Radok).

[18] Kobayashi, Albert S., ed., 1993, *Handbook on Experimental Mechanics*, 2nd Ed., Society for Experimental Mechanics, Bethel, CT.

Surveillance of Mechanical Systems on the Basis of Vibration Signature Analysis

A. W. Smyth
School of Engineering and Applied Science,
Columbia University,
New York, NY 10027-6699

S. F. Masri
School of Engineering,
University of Southern California,
Los Angeles, CA 90089-2531

T. K. Caughey
Division of Engineering and Applied Science,
California Institute of Technology,
Pasadena, CA 91125

N. F. Hunter
Analysis and Testing,
Los Alamos National Laboratory,
Los Alamos, NM 87545

A comprehensive experimental study is presented to assess the utility of a proposed structural health monitoring and damage detection methodology based on vibration signature analysis of the test article. The approach uses a time-domain least-squares-based method to identify the reduced-order system matrices of an equivalent linear model whose order matches the number of available sensors. A quantification of the level of the system nonlinearity is obtained by determining the residual nonlinear forces involved in the system dynamics. The approach is applied to an intricate mechanical system about which virtually no information was available; i.e., the system was essentially a ''black box.'' By using similar measurements from a reference version of the test article and two subsequently modified versions, it is shown that through the use of higher-order statistics involving the probability density functions of key system parameters, a reliable measure of the extent of variation of the system influence functions may be obtained. The use of measures of the identified quantities' dispersion offers a practical method for quantifying the reliability of the estimated changes involved in dealing with real-world (i.e., not noise-free) measurements that result in uncertain estimates of the physical changes in the article being monitored. [S0021-8936(00)03303-1]

1 Introduction

1.1 Motivation. An important engineering field and research area, which has been receiving an increasing amount of attention for many years, is the general field of structural health monitoring. Health monitoring refers to the use of in situ nondestructive sensing and analysis of system characteristics, including structural response, for the purposes of detecting changes in the underlying system which may indicate damage or degradation. Applications of this field span a very broad range of systems from dispersed civil infrastructure components, to high-performance aerospace systems, to delicate medical devices.

Representative publications in this field include *Mechanical Signature Analysis* ([1]) and others ([2–5]).

1.2 Technical Challenges. While there is a definite consensus about the great potential of the structural health monitoring field, there is also a general agreement that, in view of the numerous considerations that influence the choice and effectiveness of a structural health monitoring method ([6]), no one approach is likely to be suitable for dealing with all the situations and systems that are encountered in practical cases to detect, locate and quantify the extent of damage or deterioration in a target system. Consequently, there is a need for a ''toolkit'' of methods to deal with the variety of approaches required to cope with all the potential applications.

1.3 Literature Review. The most common approach to the problem of structural health monitoring and damage detection through response signature analysis is by the model updating procedure. The basic idea is to use dynamic test data (usually modal parameters or acceleration time histories) to continually update the stiffness distribution of a model of the structure. In practice, the model updating approach to infer damage is often an ill-conditioned, even nonunique, inverse problem. To overcome these difficulties (associated with measurement noise and other uncertainties), researchers have made advances through the use of statistical approaches ([7–9]). Although some research has been conducted using nonparametric modeling (artificial neural networks, etc.) for the health monitoring problem, it has proven difficult to locate and quantify damage from nonparametric system models. Therefore, almost all of the work in this area has involved, in some form or other, the modeling of systems with an equivalent linear model through least-squares-based identification methods. Notable contributions in this class of approaches include Agbabian et al. [10], Ghanem and Shinozuka [11], Loh and Tou [12], and Juang et al. [13]. In addition, experimental application studies include Farrar and Jauregui [14], Zimmerman et al. [15], Loh and Wu [16], and Shinozuka and Ghanem [17]. Most damage detection studies have concentrated on off-line (i.e., batch mode) identification, but progress has also been made in the on-line identification and damage detection problem (which is useful for real-time active control applications) for general dynamic systems ([18–20]).

1.4 Scope. This paper is focused on the development and implementation of a diagnostic approach for monitoring the condition of intricate mechanical systems on the basis of vibration signature analysis. While the proposed method is applicable to general structural systems, it is ideal for situations where the complexity or the inaccessibility of the target system components precludes the use of traditional parametric system identification approaches for model-based diagnostic applications. In this paper, a system identification technique will be explored not only with regard to its dynamic response modeling capabilities, but also for its usefulness in the context of damage detection or health monitoring. The effectiveness of the approach is studied by analyzing actual experimental dynamic response data from an unknown physical system at various stages of structural modification.

This study is focused on evaluating a time-domain approach for determining an optimum reduced-order linear as well as nonlinear system from vibration response measurements. The nonlinear component of the dynamic response is not treated as residual er-

Contributed by the Applied Mechanics Division of THE AMERICAN SOCIETY OF MECHANICAL ENGINEERS for publication in the ASME JOURNAL OF APPLIED MECHANICS. Manuscript received by the ASME Applied Mechanics Division, Mar. 9, 1999; final revision, May 5, 2000. Associate Technical Editor: A. A. Ferri. Discussion on the paper should be addressed to the Technical Editor, Professor Lewis T. Wheeler, Department of Mechanical Engineering, University of Houston, Houston, TX 77204-4792, and will be accepted until four months after final publication of the paper itself in the ASME JOURNAL OF APPLIED MECHANICS.

ror, but rather as a significant component of the system's response, which may be more sensitive to certain classes of damage and deterioration. Section 2 of the paper presents an overview of the formulation of the approach. Section 3 describes the experimental setup, instrumentation, and preliminary data processing. Section 4 applies the proposed approach to three physical systems with intentional variation in their internal components. Section 5 discusses the results and indicates the potential advantages as well as the limitations of the methodology.

2 Formulation of Time-Domain Identification Approach

2.1 Overview of Time-Domain Identification of Equivalent System Matrices. Consider a discrete nonlinear multi-degree-of-freedom system which is subjected to directly applied excitation forces $\mathbf{f}_1(t)$ as well as prescribed support motions $\mathbf{x}_0(t)$. The motion of this multi-input/multi-output nonlinear system is governed by the set of equations

$$\mathbf{M}_{11}^e\ddot{\mathbf{x}}_1(t)+\mathbf{C}_{11}^e\dot{\mathbf{x}}_1(t)+\mathbf{K}_{11}^e\mathbf{x}_1(t)+\mathbf{M}_{10}^e\ddot{\mathbf{x}}_0(t)+\mathbf{C}_{10}^e\dot{\mathbf{x}}_0(t)+\mathbf{K}_{10}^e\mathbf{x}_0(t)+\mathbf{f}_{NL}(t)=\mathbf{f}_1(t), \quad (1)$$

where $\mathbf{f}_1(t)$=an n_1 column vector of directly applied forces; $\mathbf{x}(t)=(\mathbf{x}_1(t),\mathbf{x}_0(t))^T$=system displacement vector of order (n_1+n_0); $\mathbf{x}_1(t)$=active degree-of-freedom displacement vector of order n_1; and $\mathbf{x}_0(t)$=prescribed support displacement vector of order n_0; $\mathbf{M}_{11}^e$, $\mathbf{C}_{11}^e$, $\mathbf{K}_{11}^e$=constant matrices that characterize the inertia, damping, and stiffness forces associated with the unconstrained degree-of-freedom of the system, each of order $n_1\times n_1$; $\mathbf{M}_{10}^e$, $\mathbf{C}_{10}^e$, $\mathbf{K}_{10}^e$=constant matrices that characterize the inertia, damping, and stiffness forces associated with the support motions, each of order $n_1\times n_0$; and $\mathbf{f}_{NL}(t)$=an n_1 column vector of nonlinear nonconservative forces involving $\mathbf{x}_1(t)$ as well as $\mathbf{x}_0(t)$. This section is concerned with a time-domain method for the identification of the system matrices appearing in Eq. (1) as well as the nonlinear forces acting on the system. The representation of the identified system will be in a form that allows the prediction of its transient response under arbitrary excitations, by using conventional numerical techniques for initial value problems in ordinary differential equations.

Consider a linearized version of the system under discussion and assume it is governed by

$$\mathbf{M}_{11}^e\ddot{\mathbf{x}}_1(t)+\mathbf{C}_{11}^e\dot{\mathbf{x}}_1(t)+\mathbf{K}_{11}^e\mathbf{x}_1(t)+\mathbf{M}_{10}^e\ddot{\mathbf{x}}_0(t)+\mathbf{C}_{10}^e\dot{\mathbf{x}}_0(t)+\mathbf{K}_{10}^e\mathbf{x}_0(t)=\mathbf{f}_1(t). \quad (2)$$

Let the response vector $\mathbf{r}(t)$ of order $3(n_1+n_0)$ be defined as

$$\mathbf{r}(t)=(\ddot{\mathbf{x}}_1^T(t),\dot{\mathbf{x}}_1^T(t),\mathbf{x}_1^T(t),\ddot{\mathbf{x}}_0^T(t),\dot{\mathbf{x}}_0^T(t),\mathbf{x}_0^T(t))^T. \quad (3)$$

Introducing matrix $\mathbf{R}$

$$\mathbf{R}=\begin{bmatrix}\mathbf{r}^T(t_1)\\ \mathbf{r}^T(t_2)\\ \vdots\\ \mathbf{r}^T(t_N)\end{bmatrix} \quad (4)$$

and using the notation above, the grouping of the measurements can be expressed concisely as

$$\hat{\mathbf{R}}\hat{\boldsymbol{\alpha}}=\hat{\mathbf{b}} \quad (5)$$

where $\hat{\mathbf{R}}$ is a block diagonal matrix whose diagonal elements are equal to $\mathbf{R}$, $\hat{\boldsymbol{\alpha}}=[\boldsymbol{\alpha}_1^T,\boldsymbol{\alpha}_2^T,\ldots,\boldsymbol{\alpha}_{n_1}^T]^T$ and $\hat{\mathbf{b}}$ is the corresponding vector of excitation measurements. Keeping in mind that $\hat{\mathbf{R}}$ is of order $m\times n$ where $m=Nn_1$, and $n=3n_1(n_1+n_0)$, then if a sufficient number of measurements is taken, this will result in $m>n$. Under these conditions, least-squares procedures can be used to solve for all the system parameters that constitute the entries in $\hat{\boldsymbol{\alpha}}$:

$$\hat{\boldsymbol{\alpha}}=\hat{\mathbf{R}}^{\dagger}\hat{\mathbf{b}} \quad (6)$$

where $\hat{\mathbf{R}}^{\dagger}$ is the pseudo-inverse of $\hat{\mathbf{R}}$ ([21]). In the more general case where the measurements associated with certain degrees-of-freedom are more reliable than others and/or measurements accumulated over certain time periods are to be emphasized differently from the others, a symmetric, nonsingular, usually diagonal error weighting matrix $\mathbf{W}$ can be used with the overdetermined set of equations in Eq. (5), thus resulting in the approximate solution ([22])

$$\hat{\boldsymbol{\alpha}}=(\hat{\mathbf{R}}^T\mathbf{W}\hat{\mathbf{R}})^{-1}\hat{\mathbf{R}}^T\mathbf{W}\hat{\mathbf{b}}. \quad (7)$$

2.2 Application to Example Four-Degree-of-Freedom System With a Single Excitation. Consider an example four-degree-of-freedom system governed by

$$\mathbf{M}\ddot{\mathbf{y}}(t)+\mathbf{C}\dot{\mathbf{y}}(t)+\mathbf{K}\mathbf{y}(t)=\mathbf{g}(t). \quad (8)$$

For clarity of presentation (simplified subscript notation) vector $\mathbf{y}$ is used to represent the system's absolute displacement $\mathbf{x}_1(t)$, and $\mathbf{g}(t)$ is used to represent the excitation $\mathbf{f}_1(t)$. It is assumed that no support motion is involved (i.e., $\mathbf{x}_0(t)=0$). Furthermore, matrices $\mathbf{M}_{11}$, $\mathbf{C}_{11}$, and $\mathbf{K}_{11}$ are denoted by $\mathbf{M}$, $\mathbf{C}$, and $\mathbf{K}$, respectively. Noting that in this case $n_1=4$ and $n_0=0$, in expanded form Eq. (8) becomes

$$m_{i1}\ddot{y}_1+m_{i2}\ddot{y}_2+m_{i3}\ddot{y}_3+m_{i4}\ddot{y}_4+c_{i1}\dot{y}_1+c_{i2}\dot{y}_2+c_{i3}\dot{y}_3+c_{i4}\dot{y}_4+k_{i1}y_1+k_{i2}y_2+k_{i3}y_3+k_{i4}y_4=g_i(t)\quad i=1,2,3,4. \quad (9)$$

Note that the response vector $\mathbf{r}(t)$ in this case is

$$\mathbf{r}(t)=[\ddot{y}_1,\ddot{y}_2,\ddot{y}_3,\ddot{y}_4,\dot{y}_1,\dot{y}_2,\dot{y}_3,\dot{y}_4,y_1,y_2,y_3,y_4]^T. \quad (10)$$

If response measurements at times $t_1,t_2,\ldots,t_N$ are made, then the observation matrix $\mathbf{R}$ becomes

$$\mathbf{R}=\begin{bmatrix}\ddot{y}_1(t_1) & \ddot{y}_2(t_1) & \ddot{y}_3(t_1) & \ddot{y}_4(t_1) & \dot{y}_1(t_1) & \dot{y}_2(t_1) & \dot{y}_3(t_1) & \dot{y}_4(t_1) & y_1(t_1) & y_2(t_1) & y_3(t_1) & y_4(t_1)\\ \ddot{y}_1(t_2) & \ddot{y}_2(t_2) & \ddot{y}_3(t_2) & \ddot{y}_4(t_2) & \dot{y}_1(t_2) & \dot{y}_2(t_2) & \dot{y}_3(t_2) & \dot{y}_4(t_2) & y_1(t_2) & y_2(t_2) & y_3(t_2) & y_4(t_2)\\ \ddot{y}_1(t_3) & \ddot{y}_2(t_3) & \ddot{y}_3(t_3) & \ddot{y}_4(t_3) & \dot{y}_1(t_3) & \dot{y}_2(t_3) & \dot{y}_3(t_3) & \dot{y}_4(t_3) & y_1(t_3) & y_2(t_3) & y_3(t_3) & y_4(t_3)\\ \vdots & \vdots & \vdots & \vdots & \vdots & \vdots & \vdots & \vdots & \vdots & \vdots & \vdots & \vdots\\ \ddot{y}_1(t_N) & \ddot{y}_2(t_N) & \ddot{y}_3(t_N) & \ddot{y}_4(t_N) & \dot{y}_1(t_N) & \dot{y}_2(t_N) & \dot{y}_3(t_N) & \dot{y}_4(t_N) & y_1(t_N) & y_2(t_N) & y_3(t_N) & y_4(t_N)\end{bmatrix} \quad (11)$$

and the $n_1=4$ parameter vectors $\boldsymbol{\alpha}_1$, $\boldsymbol{\alpha}_2$, $\boldsymbol{\alpha}_3$, and $\boldsymbol{\alpha}_4$ are

$$\boldsymbol{\alpha}_i=[m_{i1},m_{i2},m_{i3},m_{i4},c_{i1},c_{i2},c_{i3},c_{i4},k_{i1},k_{i2},k_{i3},k_{i4}]^T\quad i=1,2,3,4. \quad (12)$$

Note from Eq. (11) that the number of rows in $\mathbf{R}$ is equal to N, the number of time samples used to observe the response, and the number of columns of $\mathbf{R}$ equals three times n_1, where $n_1=4$, is the number of the system degrees-of-freedom. The excitation measurements $\mathbf{b}_1(t)$, $\mathbf{b}_2(t)$, $\mathbf{b}_3(t)$, and $\mathbf{b}_4(t)$ are

$$\mathbf{b}_i(t)=[g_i(t_1),g_i(t_2),\ldots,g_i(t_N)]^T \quad i=1,2,3,4. \tag{13}$$

If a number $N\geqslant 3n_1$ of time sample measurements is used to construct $\mathbf{R}$ in the manner indicated in Eq. (11), then one obtains

$$\hat{\mathbf{R}}\hat{\boldsymbol{\alpha}}=\hat{\mathbf{b}} \tag{14}$$

where

$$\hat{\mathbf{R}}=\begin{bmatrix}\mathbf{R}&0&0&0\\0&\mathbf{R}&0&0\\0&0&\mathbf{R}&0\\0&0&0&\mathbf{R}\end{bmatrix},\quad \hat{\boldsymbol{\alpha}}=\begin{bmatrix}\boldsymbol{\alpha}_1\\\boldsymbol{\alpha}_2\\\boldsymbol{\alpha}_3\\\boldsymbol{\alpha}_4\end{bmatrix},\quad \hat{\mathbf{b}}=\begin{bmatrix}\mathbf{b}_1\\\mathbf{b}_2\\\mathbf{b}_3\\\mathbf{b}_4\end{bmatrix} \tag{15}$$

or alternatively

$$\mathbf{R}\boldsymbol{\alpha}_i=\mathbf{b}_i, \quad i=1,n_1. \tag{16}$$

Note that the order of $\mathbf{R}$ is $(N\times 3n_1)$, the order of $\boldsymbol{\alpha}_i$ is $(3n_1\times 1)$, and the order of $\mathbf{b}_i$ is $(N\times 1)$. Now if *none* of the excitation forces is identically equal to zero, then the rank of $\mathbf{R}$ is rank$(\mathbf{R})=3n_1$, and least-squares methods can be used in the manner discussed above to uniquely determine $\hat{\boldsymbol{\alpha}}$:

$$\hat{\boldsymbol{\alpha}}=\hat{\mathbf{R}}^{\dagger}\hat{\mathbf{b}}, \tag{17}$$

or

$$\boldsymbol{\alpha}_i=\mathbf{R}^{\dagger}\mathbf{b}_i, \quad i=1,n_1. \tag{18}$$

On the other hand, if *one* of the excitation forces, e.g., $g_2(t)=0$, then the number of independent *columns* of $\mathbf{R}$ is $(3n_1-1)$. This fact can be easily established from Eq. (9) with $i=2$, since the RHS being zero indicates that the 12 measurements $\ddot{y}_1(t),\ddot{y}_2(t),\ddot{y}_3(t),\ddot{y}_4(t),\ldots,y_1(t),y_2(t),y_3(t),y_4(t)$ are linearly dependent. The rank of $\mathbf{R}$ in this situation becomes rank$(\mathbf{R})=3n_1-1$.

Returning to the example under discussion, it is clear that unless *all* components of the excitation vector $\mathbf{g}(t)$ are $\neq 0$, the rank of $\mathbf{R}$ will be less than the dimension of the corresponding parameter vector $\boldsymbol{\alpha}$, consequently the system parameter $\hat{\boldsymbol{\alpha}}$ cannot be uniquely determined. In general, for an n_1 degree-of-freedom system governed by Eq. (2), the rank of $\mathbf{R}$ is

$$\text{rank}(\mathbf{R})=3(n_1+n_0)-(n_1-n_f) \tag{19}$$

where n_f=the number of active (nonzero) components of the excitation vector. Thus, unless $n_f=n_1$, the $3n_1(n_1+n_0)$ components of the system parameter vector $\hat{\boldsymbol{\alpha}}$ cannot be uniquely determined without imposing some restrictions (such as symmetry) on the nature of components.

Later in the experimental phase of this study, the symmetry restriction on the system matrices will be imposed because the excitation forces are not applied to all of the degrees-of-freedom. The implementation of this still involves the basic least-squares solution of the form $\hat{\mathbf{R}}\hat{\boldsymbol{\alpha}}=\hat{\mathbf{b}}$ but here the $\hat{\mathbf{R}}$ and the $\hat{\boldsymbol{\alpha}}$ (which will have fewer parameters) will be organized in a special way. In this case specifically, where only degree-of-freedom #4 is directly excited, the $\hat{\mathbf{R}}\hat{\boldsymbol{\alpha}}=\hat{\mathbf{b}}$ expression which guarantees symmetric system matrices will be written as follows:

$$\begin{bmatrix}
\ddot{\mathbf{y}}_1&\ddot{\mathbf{y}}_2&\ddot{\mathbf{y}}_3&\ddot{\mathbf{y}}_4&\dot{\mathbf{y}}_1&\dot{\mathbf{y}}_2&\dot{\mathbf{y}}_3&\dot{\mathbf{y}}_4&\mathbf{y}_1&\mathbf{y}_2&\mathbf{y}_3&\mathbf{y}_4&0&0&0&0&0&0&0&0&0&0&0&0&0&0&0&0&0&0\\
0&\ddot{\mathbf{y}}_1&0&0&0&\dot{\mathbf{y}}_1&0&0&0&\mathbf{y}_1&0&0&\ddot{\mathbf{y}}_2&\ddot{\mathbf{y}}_3&\ddot{\mathbf{y}}_4&\dot{\mathbf{y}}_2&\dot{\mathbf{y}}_3&\dot{\mathbf{y}}_4&\mathbf{y}_2&\mathbf{y}_3&\mathbf{y}_4&0&0&0&0&0&0&0&0&0\\
0&0&\ddot{\mathbf{y}}_1&0&0&0&\dot{\mathbf{y}}_1&0&0&0&\mathbf{y}_1&0&0&\ddot{\mathbf{y}}_2&0&0&\dot{\mathbf{y}}_2&0&0&\mathbf{y}_2&0&\ddot{\mathbf{y}}_3&\ddot{\mathbf{y}}_4&\dot{\mathbf{y}}_3&\dot{\mathbf{y}}_4&\mathbf{y}_3&\mathbf{y}_4&0&0&0\\
0&0&0&\ddot{\mathbf{y}}_1&0&0&0&\dot{\mathbf{y}}_1&0&0&0&\mathbf{y}_1&0&0&\ddot{\mathbf{y}}_2&0&0&\dot{\mathbf{y}}_2&0&0&\mathbf{y}_2&0&\ddot{\mathbf{y}}_3&0&\dot{\mathbf{y}}_3&0&\mathbf{y}_3&\ddot{\mathbf{y}}_4&\dot{\mathbf{y}}_4&\mathbf{y}_4
\end{bmatrix}
\begin{bmatrix}m_{11}\\m_{12}\\m_{13}\\m_{14}\\c_{11}\\c_{12}\\c_{13}\\c_{14}\\k_{11}\\k_{12}\\k_{13}\\k_{14}\\m_{22}\\m_{23}\\m_{24}\\c_{22}\\c_{23}\\c_{24}\\k_{22}\\k_{23}\\k_{24}\\m_{33}\\m_{34}\\c_{33}\\c_{34}\\k_{33}\\k_{34}\\m_{44}\\c_{44}\\k_{44}\end{bmatrix}=\begin{bmatrix}0\\0\\0\\\mathbf{f}_4\end{bmatrix}.$$

Due to space limitations, the $\hat{\mathbf{R}}$ matrix is not written more explicitly; however, each row in this expression is meant to represent multiple rows corresponding to the considered time steps. In other words each element is a column vector, for example $\mathbf{y}_1 = [y_1(t_1), y_1(t_2), \ldots, y_1(t_N)]^T$. Notice also that, because the constraint of symmetric system matrices is imposed, the $\hat{\boldsymbol{\alpha}}$ vector has only 30 parameters as opposed to the full 48 which would normally describe the general **M**, **C**, and **K** matrices for a four-degree-of-freedom linear system.

2.3 Identification of Nonlinear Residual Terms. Once the linear portion of the system response has been identified, there are several approaches using hybrid (parametric/nonparametric) identification techniques which can be used to identify the nonlinear residual response. For example, the residual could be least-squares fitted in much the same way as done previously, however, with a set of basis functions generated from a series expansion of various products of $x(t)$, $\dot{x}(t)$, and $\ddot{x}(t)$ system response terms ([23]). Alternatively, the authors have found artificial neural network identification approaches to be quite effective in identifying nonlinear system dynamics ([23,24]). Further background information and references on the use of neural networks to model system dynamics can be found in Housner et al. [6].

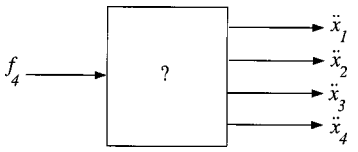

Fig. 1 "Black box" experimental mechanical system with single force input and four acceleration outputs

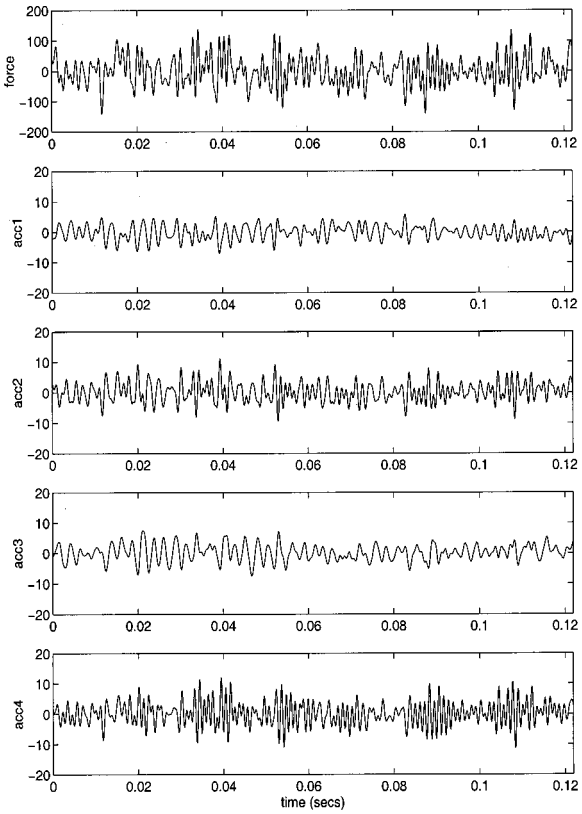

Fig. 2 The first 1000 samples (or 0.122 seconds) for each channel from the "black box" experimental reference data set

Table 1 The four equivalent linear identification cases and their parameters for the analysis of the reference system data

Case Number	*Total Number of Pts.*	*Starting Pt.*	*Ending Pt.*	*Incr.*
Case 1	1000	1	2000	2
Case 2	5000	1	10000	2
Case 3	10000	1	20000	2
Case 4	20480	1	20480	1

3 Experimental Data Sets

3.1 Experimental Setup. The test article is a mechanical system composed of numerous internal components and materials with significant nonlinear characteristics. Information concerning the system's shape, size, material, location of sensors, etc., was not available. Therefore the test situation is as close as one would get to a ''black box'' experiment. The system was monitored by means of four accelerometers and a single force gauge in the proximity of one of the sensors. A block diagram of the dynamic system representation is shown in Fig. 1, indicating one input and four outputs. The excitation source consisted of an electrodynamic exciter which furnished a wide-band excitation to the system. Note that the proposed monitoring approach imposes no restrictions on the test signal, provided it is persistent enough to yield an applicable mathematical model.

3.2 Data Acquisition. The sensor data was digitally sampled and recorded at a rate of 8192 Hz, in other words every 1.2204×10^{-4} seconds. The total duration of the recordings was 2.5 seconds, thus resulting in 20,480 samples per recording channel. A sampling of the unprocessed recorded data is shown in Fig. 2. It can be clearly seen from Fig. 2 that the frequency content in the force record most clearly resembles that in the acceleration record of channel #4. Therefore it is not surprising to find that the force is applied at the channel #4 location.

3.3 Preliminary Data Processing. Before doing any system identification analysis, the supplied data was further processed to obtain the displacement and velocity records corresponding to the available acceleration records. The suggested frequencies of interest were also given to be above 150 Hz, so therefore high-pass filtering was also performed. The following step-by-step approach was adopted for the integration procedure from acceleration to velocity and then to displacement: (1) high-pass filter the acceleration record, (2) numerically integrate the

Table 2 Estimates of equivalent linear system matrices for Case 1

Mass Matrix ($\mathbf{M}^e$)

0.564	2.205	-0.085	4.061
2.205	5.032	-1.068	-2.197
-0.085	-1.068	-3.677	-0.398
4.061	-2.197	-0.398	-3.866

Damping Matrix ($\mathbf{C}^e$)

$10^3 \times$

-0.276	-2.300	-2.156	6.241
-2.300	-0.481	-0.685	0.128
-2.156	-0.685	-1.714	-1.245
6.241	0.128	-1.245	8.087

Stiffness Matrix ($\mathbf{K}^e$)

$10^8 \times$

1.382	0.356	-0.390	1.384
0.356	0.202	-0.139	0.271
-0.390	-0.139	-0.025	-0.146
1.384	0.271	-0.146	1.292

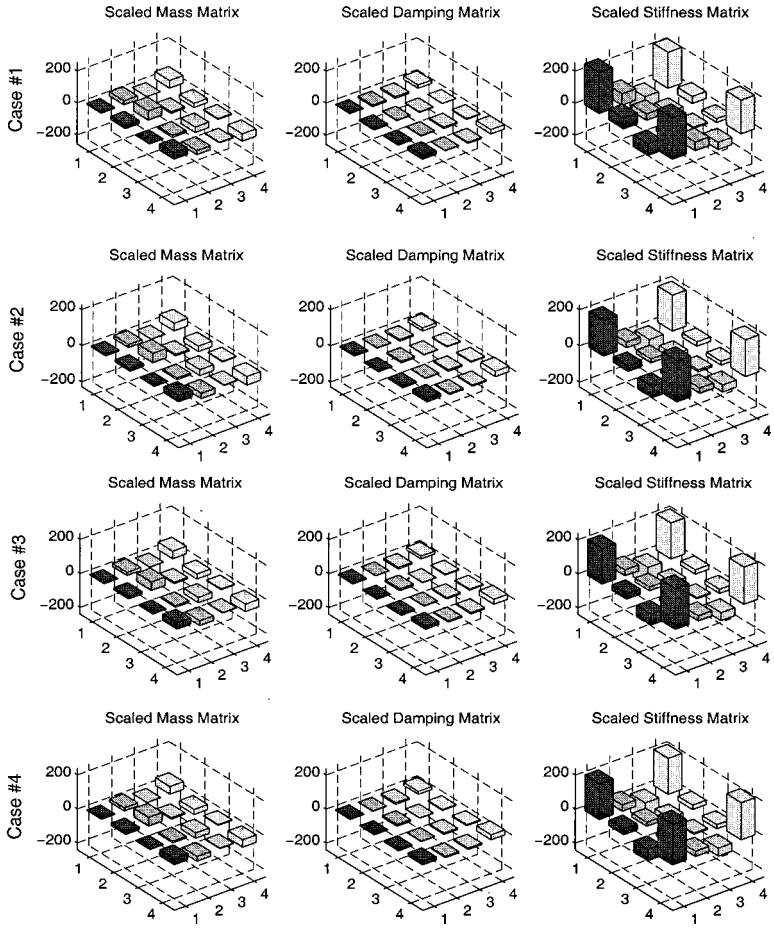

Fig. 3 Comparison of scaled estimates of system matrices for reference system—Cases 1 through 4

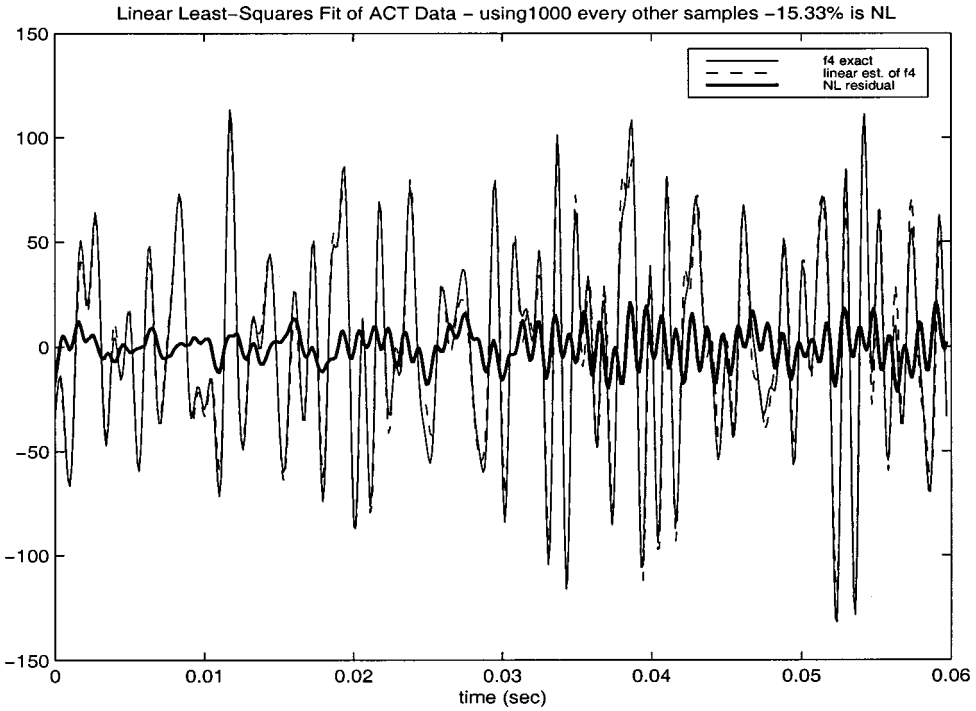

Fig. 4 Time history comparison of excitation force (solid line), linear least-squares estimated force (dashed line), and the nonlinear residual force (thick line) for Case 1 identification of the reference system

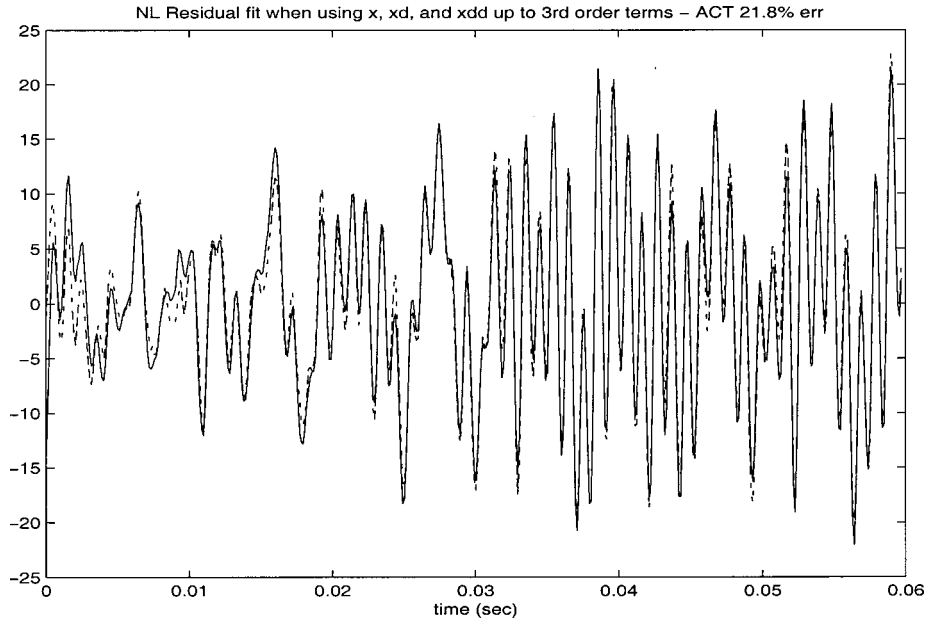

Fig. 5 Time history comparison of the nonlinear residual force (solid line) and the residual force estimate (dashed line), modeled with combinations of $x(t)$, $\dot{x}(t)$, and $\ddot{x}(t)$ up to third-order powers for the reference system

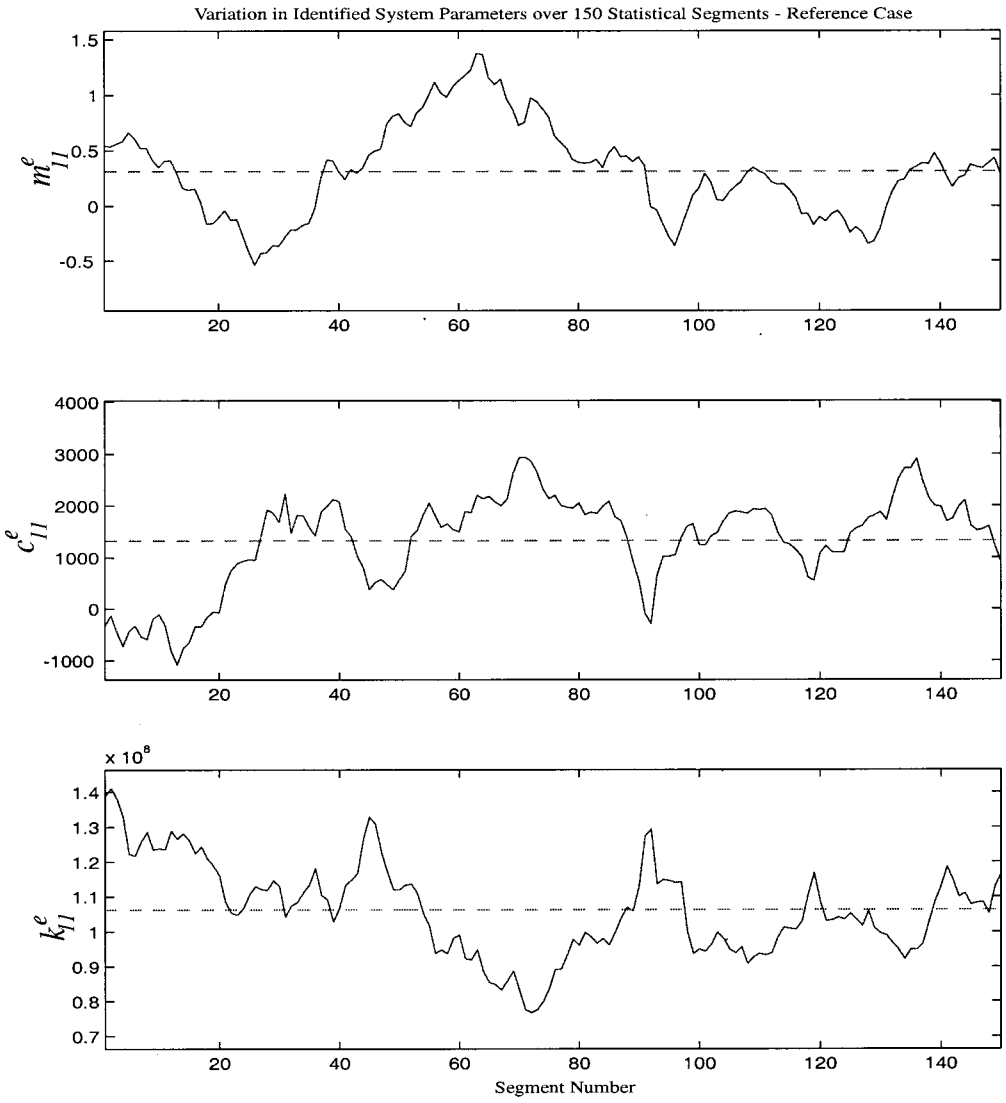

Fig. 6 Sample identification results for the reference system corresponding to (*a*) m_{11}; (*b*) c_{11}; (*c*) k_{11}. In each plot, the dashed line represents the mean value of the parameter.

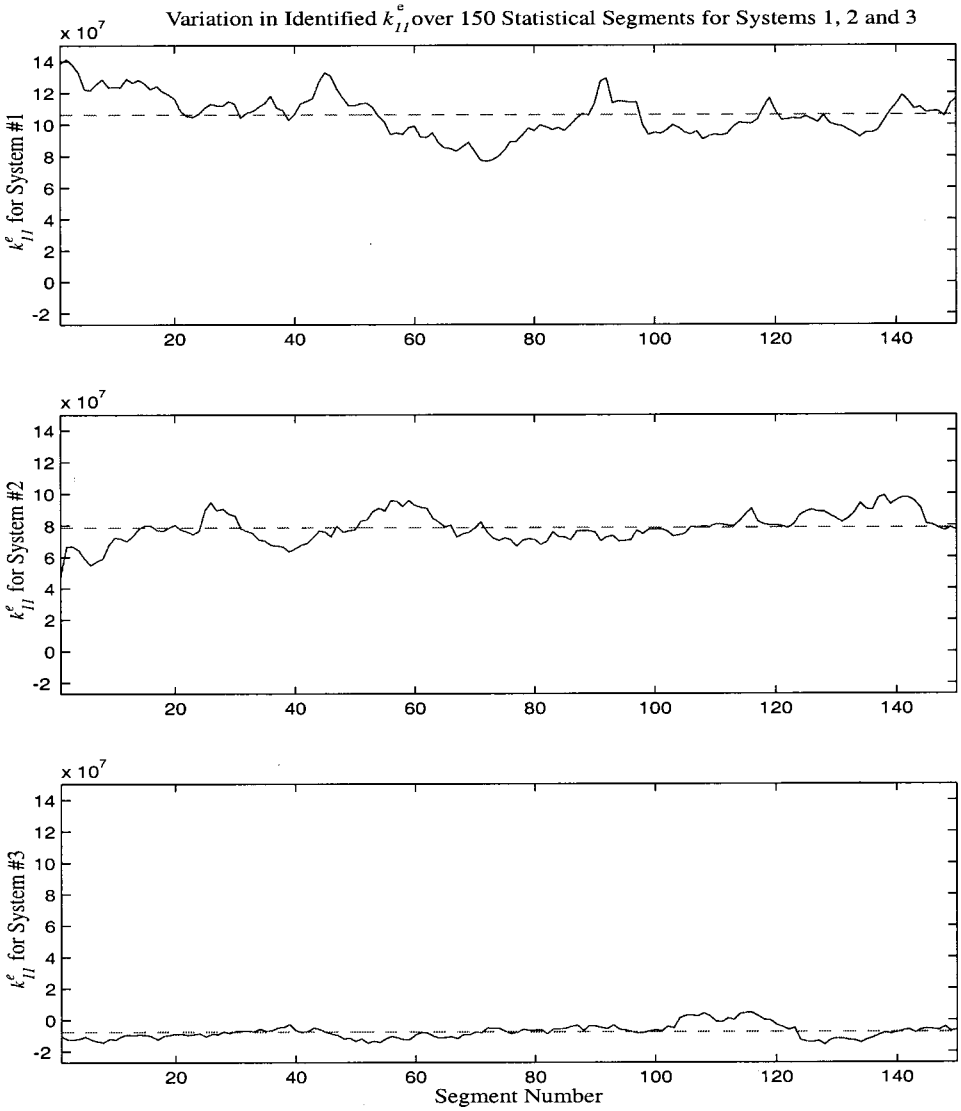

Fig. 7 Sample identification results for k_{11} corresponding to (*a*) the reference system (system #1); (*b*) system #2; (*c*) system #3. In each plot, the dashed line represents the mean value of the parameter.

resulting processed acceleration, (3) high-pass filter the result, (4) numerically integrate the processed velocity, and (5) high-pass filter the result. Note that the high-pass filtering at each stage takes care of the removal of a nonzero offset or linear trend often required after integration of acceleration records. The pass-band filtering was performed with no phase distortion.

As previously mentioned, the experiments were conducted three times with the same test configuration and amplitude of excitation. The test organization reported that structural modifications were made between tests. Therefore this collection of data provides an excellent platform to perform health monitoring analysis to detect system changes. The data from System #1 will be referred to as the reference system, and more in depth analysis done on this system is reported in the following section.

4 Analysis of Reference System

4.1 Identification of System Matrices. Using the formulation of Section 2, the optimum equivalent system matrices and the residual nonlinear force, based on the assumption of a single excitation and three symmetric system matrices, was determined. The least-squares identification was performed four times with different numbers of time samples used for each case. Table 1 shows the four cases and the corresponding time samples used. Note that increasing the number of points used in the least-squares solution changes the aspect ratio (i.e., an increase in the number of rows) of the $\mathbf{R}$ observation matrix, and hence leads to a more overdetermined set of linear equations.

The resulting system matrix estimates for Case 1 from the least-squares fitting process are shown in Table 2. Similar results are obtained for Cases 2–4 ([23]). The first noticeable feature of these dynamic system matrices is the presence of negative terms along the diagonal of the matrices, in other words, the matrices are not positive-definite. Of course, negative mass, negative damping, or negative stiffness does not (physically) exist. These fictitious terms are attributable to the equivalent linearization of nonlinearities. This difficulty is quite intuitive, i.e., that physically unusual terms may arise from an equivalent linear fitting of a truly nonlinear system response. Other than noticing the nonpositive definiteness of the identified system matrices, little intuitive sense can be gained from the listing of the matrix coefficients. Therefore, an alternative representation follows in Fig. 3. Here the elements of the system matrices have been scaled columnwise by

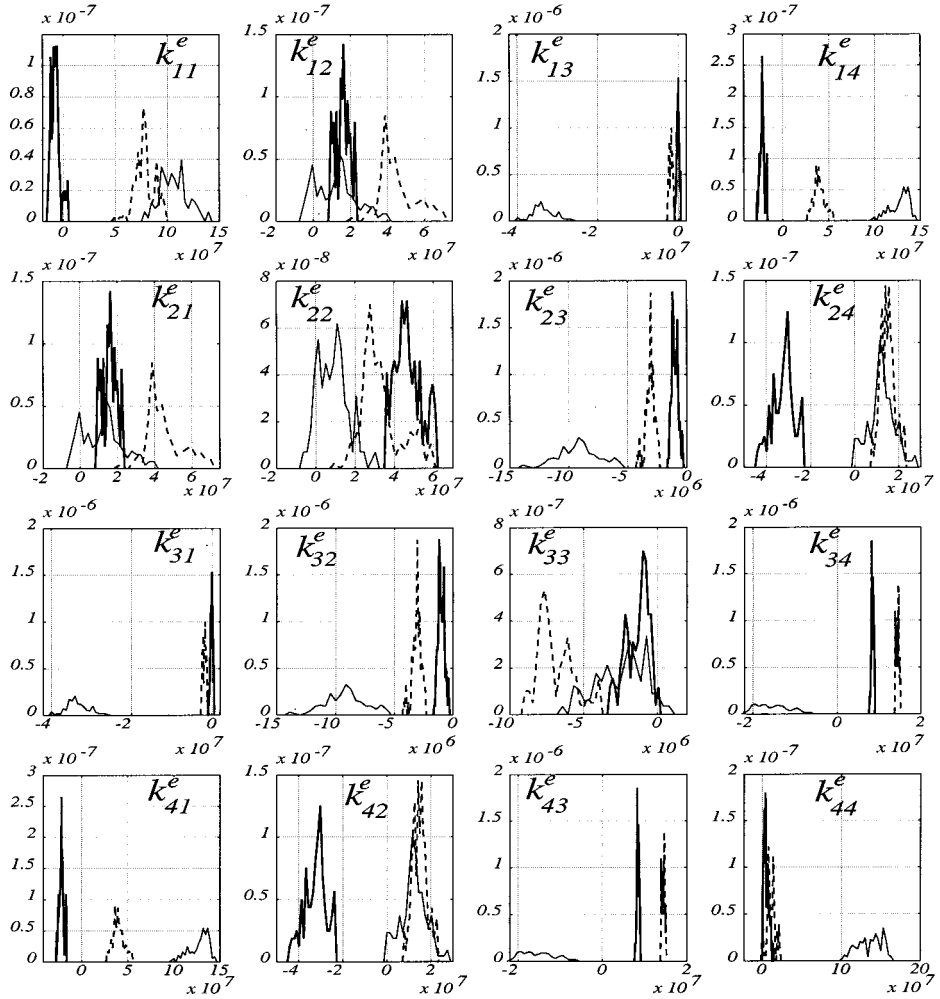

Fig. 8 Probability densities of stiffness matrix coefficients for 150 statistical averages of the equivalent linear identification of the three different systems. System #1 (solid line), system #2 (dotted line), system #3 (dash-dot line).

multiplying by the maximum value of the response variable to which they correspond.

This figure better illustrates the similarity in the estimated system influence coefficients obtained using different numbers of discrete samples in the least-squares solution. One may conclude, that for this system response, 1000 points (corresponding to about 30 periods of the lowest dominant frequency) is sufficient to obtain an accurate equivalent linear system estimate. One may also conclude that the response over the duration of the measurements is reasonably stationary, because the estimates vary little depending upon the window length used for fitting. Under more suitable conditions for the application of this method ([10]), natural frequency and damping estimates could be obtained from the complex eigenvalue solution associated with the estimated linear system equation. However, due to the nonpositive definiteness of the estimated system matrices in this case, this proved to be futile. From the poor physical interpretation of the coefficients in the linear system matrices one may conclude that the linear system model could not accurately capture the true dynamics of this system.

4.2 Determination of Nonlinear Residual Force $\mathbf{f}_{NL}$. From the results of the previous section, a best-fit linear force $\mathbf{f}^e_L$ may be determined for each set of estimated parameters. Taking the difference of this from the excitation force $\mathbf{f}_1(t)$, as in Eq. (1), a nonlinear residual force $\mathbf{f}_{NL}$ is obtained:

$$\mathbf{f}_{NL}(t)=\mathbf{f}_1(t)-\mathbf{f}^e_L(t)=\mathbf{f}_1(t)-\mathbf{M}^e\ddot{\mathbf{x}}(t)-\mathbf{C}^e\dot{\mathbf{x}}(t)-\mathbf{K}^e\mathbf{x}(t). \tag{21}$$

A representative time history comparison (from the Case 1 estimation) of the excitation force $\mathbf{f}_4$, the linear estimate, and the nonlinear residual is shown in Fig. 4. Clearly, the fitting results are quite good—the large as well as small peaks are well estimated and all frequencies are tracked fairly accurately.

For the Case 1 simulation, which involved a least-squares fit with 1000 points, the norm of the dimensionless error ratio is 15.33 percent. Comparable error values are obtained for Case 2–4. It is worth noting that the nonlinear component is not just ''noise,'' but contains a characteristic signature of the underlying system nonlinearities. Sophisticated analysis of this component may aid in understanding the physics of the nonlinear system characteristics ([25]). It is noteworthy that the testing organization that furnished the data stated that the article incorporated components with significant nonlinear characteristics. Furthermore, the fact that $\mathbf{f}_{NL}$ is not random noise, but rather a highly correlated nonlinear function of the system response is demonstrated in Fig. 5. Using the nonparametric approach of Smyth [23], it is seen that $\mathbf{f}_{NL}$ can be reasonably estimated by a series of nonlinear functions involving primarily the physical system accelerations and velocities as basis functions. Note that for added resolution, the scale of the ordinate in Fig. 5 is about five times more sensitive than the corresponding scale of Fig. 4.

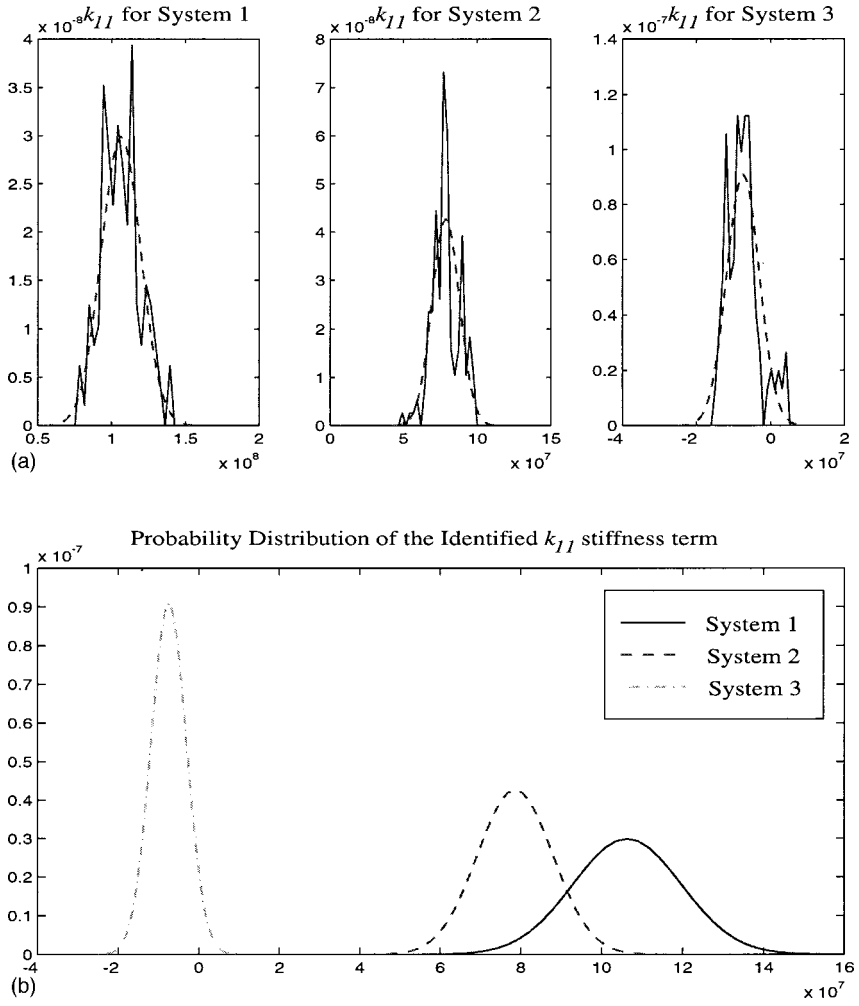

Fig. 9 (*a*) Probability densities of the k_{11} stiffness coefficient for 150 statistical averages of the equivalent linear identification of the three different systems. Each plot has a superimposed Gaussian distribution. (*b*) System #1 (thin solid line), system #2 (dotted line), system #3 (thick solid line) comparison.

To further support the assertion, that the residual is the result of response nonlinearities (and of course, measurement noise), rather than unmodeled linear dynamics, the entire system was also modeled using the Observer Kalman Filter Identification (OKID) method ([13]) and an assumed linear model with 20 general modes. The rms of the residual, was only reduced by a fraction of a percent from the rms of the residual obtained with a four-mode linear model (similar to that used in this study). In other words, increasing the fidelity of the linear model aids little in reducing the residual component of the response. It should be noted, that other techniques, which rely on the comparison between the Hilbert Transform of the system dynamics and the frequency response function, can also be employed to indicate the presence of nonlinearities ([26,27]).

5 Detection of Changes in System Parameters

In this section, the identification results from the reference system are compared with results obtained from the same methods on Systems #2 and #3. The test organization stated that these systems are (physically) modified versions of the reference system, i.e., the detection results of this study are not associated with ''false positive'' indications. The goal of this section is to evaluate the identification method for its usefulness as a structural health monitoring tool.

5.1 Comparison of PDF's of Influence Coefficients. The equivalent linear analysis was repeated for all three systems, however, this time statistical averaging was used to get a sense of the distribution of the system matrix coefficients. This statistical analysis could provide a means to assess and calibrate the sensitivity of identification approaches to detect, locate and quantify levels of structural changes. The averaging was conducted using 150 time history windows, of 2000 points each, staggered by 100 points each time. Figure 6 shows representative samples of m_{11}^e, c_{11}^e, and k_{11}^e corresponding to the reference system. The mean value of each parameter is indicated by a dashed line. Note that the fluctuation in the values of the identified parameters have the appearance of a random process. Similar results are obtained for all the identified influence coefficients.

Figure 7 shows representative samples of k_{11}^e corresponding to the reference system and the other two modified systems. For ease of comparison, identical scales are used in the three plots shown in Fig. 7. Note that the dashed lines, which indicate the mean values of the respective parameters, show a significant change in the mean value of k_{11} among the three tested systems. Furthermore, it is worth noting that the level of the dispersion of the fluctuations with respect to their respective mean shows a marked difference among the three systems.

Figure 8 shows the probability densities of the coefficients of

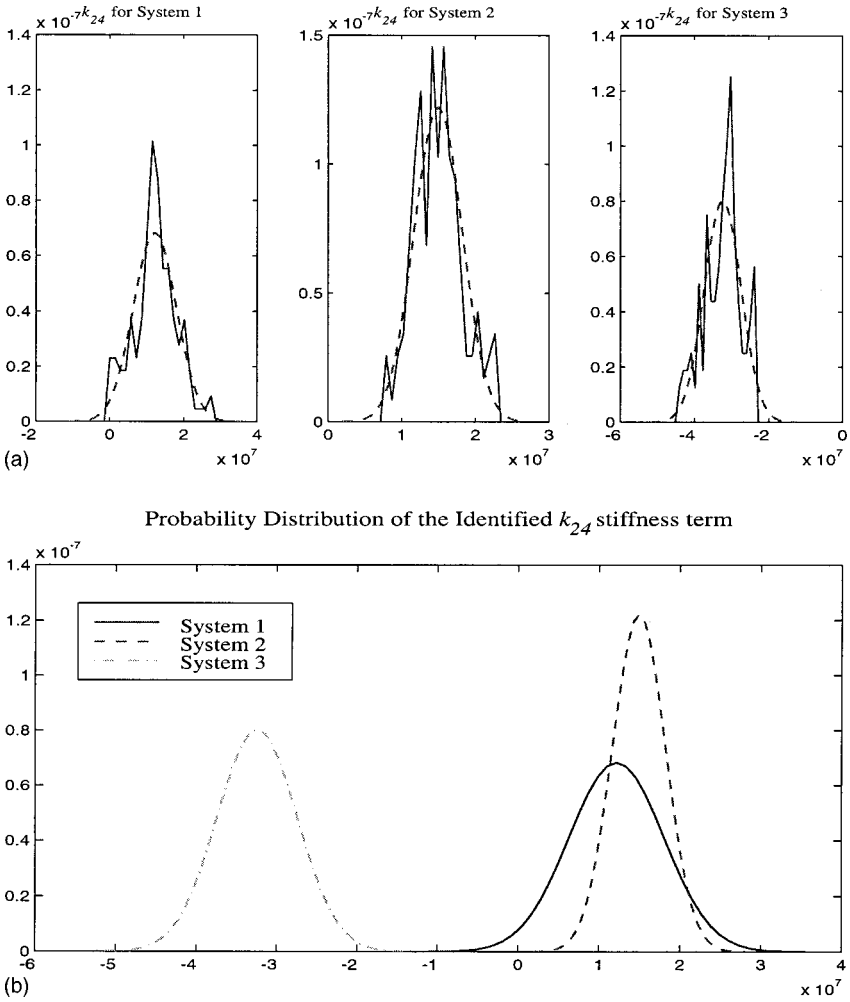

Fig. 10 (*a*) Probability densities of the k_{24} stiffness coefficient for 150 statistical averages of the equivalent linear identification of the three different systems. Each plot has a superimposed Gaussian distribution. (*b*) System #1 (solid line), system #2 (dotted line), system #3 (dash-dot line) comparison.

the estimated stiffness matrices for all three systems. Although the distributions appear somewhat rough due to the relatively small number (150) of statistical averages taken, one can see striking differences in the mean values of the coefficients, and often differences in the variance of the estimated coefficients. The solid line, representing the density of the estimated coefficients for the reference system, generally shows greater variance than the other two-system parameter estimates. It is difficult to pinpoint the cause of this difference, given the standardization of the test procedure, other than to suggest that it could be related to what appears, from the ''transfer function'' representation, to be more complex dynamics. Note that similar results were obtained for the mass and damping matrix coefficient estimates.

Figure 8 contains a large amount of comparative information on the identification results for the reference and the two modified systems. It is helpful, however, to focus on individual elements and how their identified values change with respect to the system modifications. Figure 9 highlights the differences between the identified results for the k_{11}^e stiffness term. As is shown in the previous figure, the solid line in the top three plots shows the probability distributions of the identified k_{11}^e values over 150 identifications of partially overlapping response segments. This time, however, an equivalent Gaussian distribution with the mean and standard deviation of the identification results is superimposed over the actual (experimental) results. These distributions are then compared in the lower plot in Fig. 9. This type of figure clearly shows the shift in the average identified result for the three identified systems, as well as showing a variation in the level of uncertainty associated with the identified values. It is important to note here that, because all of the experiments were conducted with the same level of input excitation and presumably noise levels in the measurements, it is justifiable to make these kind of comparisons across experiments. A similar comparison of the statistical results for the identification of coefficient k_{24}^e (which is of course the same as k_{42}^e because of the prescribed symmetry assumption) is shown in Fig. 10. Again, variations in the standard deviation of the identified results can be clearly seen; however, there is only a

Table 3 The mean value of the equivalent linear system stiffness matrix for the reference system (i.e., system #1), and its standard deviation over the 150 identification cases

Mean Stiffness Matrix ($\bar{\mathbf{K}}^{(0)}$)

$10^8\times$

1.063	0.122	-0.335	1.273
0.122	0.087	-0.092	0.122
-0.335	-0.092	-0.025	-0.153
1.273	0.122	-0.153	1.355

Std. Dev. of Stiffness Matrix ($\mathbf{S}$)

$10^8\times$

0.133	0.108	0.028	0.106
0.108	0.077	0.017	0.058
0.028	0.017	0.017	0.039
0.106	0.058	0.039	0.155

Table 4 The mean value of the equivalent linear system stiffness matrix for system #2 (left column) and for system #3 (right column), and the respective standard deviation over the 150 identification cases. The dimensionless error matrices are also presented relative to the reference case.

System #2

$\bar{\mathbf{K}}^e$ - Mean Stiffness Matrix

$10^8\times$

0.786	0.453	-0.019	0.398
0.453	0.333	-0.031	0.149
-0.019	-0.031	-0.069	0.144
0.398	0.149	0.144	0.111

S - Std. Dev. of Stiffness Matrix

$10^8\times$

0.093	0.099	0.004	0.064
0.099	0.105	0.004	0.033
0.004	0.004	0.012	0.004
0.064	0.033	0.004	0.054

V - Dim. Error of Stiffness Matrix

-0.261	2.708	-0.943	-0.687
2.708	2.845	-0.663	0.226
-0.943	-0.663	1.788	-1.945
-0.688	0.226	-1.945	-0.918

D - Dim. Err. of Stiffness Mat. wrt to **S**

-2.080	3.056	11.282	-8.302
3.056	3.193	3.511	0.473
11.282	3.511	-2.630	7.661
-8.302	0.473	7.661	-8.024

System #3

$\bar{\mathbf{K}}^e$ - Mean Stiffness Matrix

$10^8\times$

-0.075	0.158	-0.001	-0.224
0.158	0.472	-0.010	-0.325
-0.001	-0.010	-0.014	0.084
-0.224	-0.325	0.084	0.054

S - Std. Dev. of Stiffness Matrix

$10^8\times$

0.044	0.039	0.003	0.025
0.039	0.069	0.003	0.050
0.003	0.003	0.008	0.003
0.025	0.050	0.003	0.030

V - Dim. Error of Stiffness Matrix

-1.071	0.291	-0.997	-1.176
0.291	4.454	-0.889	-3.663
-0.997	-0.889	-0.448	-1.553
-1.176	-3.663	-1.553	-0.960

D - Dim. Err. of Stiffness Mat. wrt to **S**

-8.542	0.329	11.918	-14.192
0.329	4.999	4.712	-7.656
11.918	4.712	0.658	6.115
-14.192	-7.656	6.115	-8.387

minor change in the average identified coefficient between the reference system (i.e., system # 1) and system #2.

A summary of the identification results for the three systems is shown in Tables 3 and 4. The numerical values for the following matrices are given: (1) the mean identified stiffness matrices $\bar{\mathbf{K}}^e$; (2) the standard deviation matrix **S** of the identified stiffness matrix; (3) the matrix **V** whose elements correspond to the dimensionless error between the mean of the identified values for the modified system with the ''undamaged'' reference system; and (4) the matrix **D** whose elements correspond with the dimensionless change in the mean of the identified values for the modified system with respect to the reference system expressed as a multiple of the corresponding standard deviation. In other words the coefficients of **V** and **D** are defined as follows:

$$v_{ij}=(\bar{k}^e_{ij}-\bar{k}^{(0)}_{ij})/\bar{k}^{(0)}_{ij} \quad \text{and} \quad d_{ij}=(\bar{k}^e_{ij}-\bar{k}^{(0)}_{ij})/\bar{s}_{ij} \qquad (22)$$

where $\bar{k}^{(0)}_{ij}$ is just the mean of the effective linear stiffness coefficient (i.e., $\bar{k}^e_{ij}$) obtained for the identification of the reference system. Notice, for example, the small value of v_{24} for system #2 relative to that for system #3, and how it captures the nature of the lower plot in Fig. 10. It should of course be noted that these types of results on the change in mean and standard deviation are also available for the identified mass and damping coefficients.

6 Discussion

To better calibrate and evaluate the sensitivity to detecting slight changes in the system parameters for this type of method, there is still a need for knowledge of the nature of changes made in the test article. However, despite the lack of detailed knowledge of the structural modifications, clear changes are detected in the reduced-order equivalent linear model parameters. One of the drawbacks of the method, when applied to structural systems which have a significant nonlinear component to their dynamic response, is that the comparison in identification results should be made for similar levels of broad-band excitation and with similar levels of measurement noise.

The time-domain identification method presented here could be slightly modified in several ways by using recursive techniques or changing the manner in which the segmentation is performed during the statistical averaging. Also, the level of structural nonlinearity in the ''undamaged'' structure is potentially of critical importance to the success of this equivalent linearization-based identification method. These issues and their potential for altering the results have yet to be explored. Furthermore, in order to gauge the sensitivity of the approach under discussion to detect slight changes in the target system, a study is needed to correlate the magnitude of the dimensionless v_{ij} parameters with a range of measured changes in the test article.

7 Summary and Conclusions

An experimental study is presented to evaluate the effectiveness of a time-domain parametric identification approach for monitoring the ''health'' of intricate, nonlinear systems. The method of approach requires the use of excitation and acceleration response records, to develop an equivalent multi-degree-of-freedom mathematical model whose order is compatible with the number of sensors used. Application of the identification procedure under discussion yields the optimum value of the elements of the equivalent linear system matrices. By performing the identification task before and after potential structural changes (damage) in the physical system have occurred, quantifiable changes in the identified mathematical model can be detected.

The potential usefulness of the identification procedure under discussion for damage detection is demonstrated by means of tests on a complex mechanical system exhibiting significant nonlinear characteristics. This system is used to conduct experiments to generate high-quality data sets that are subsequently analyzed to determine the mean, variance, and probability density functions corresponding to each element of the identified system matrices. To gain some insight into the reliability of the proposed detection scheme, physically different versions of the test article were investigated, in which the location as well as the magnitude of the ''damage'' was varied.

The method provided clear indication of structural alteration through changes in the identified parameters. The dimensionless measures like **V** and **D**, which use the built-in uncertainty scale furnished by the estimated variance of the identification results, prove to be particularly useful in detecting dominant changes. Because the method presented here is a parametric identification scheme based on a linearized model, its ability to capture the overall dynamic response of nonlinear systems is of course limited. Further parametric or nonparametric nonlinear identification techniques can be employed to obtain a complete linear/nonlinear dynamic model of the system dynamics by either treating the residual error as the nonlinear response component or by treating the entire dynamic response generally.

On the basis of this exploratory study, it appears that determining the probability density functions of the identified system matrices may furnish useful indices, that can be conveniently extracted during an experimental test, to quantify changes in the characteristics of physical systems without the need for virtually any information about the topology of the system or the nature of the underlying physical phenomena that are being observed.

Acknowledgments

This study was supported in part by grants from the Air Force Office of Scientific Research, the National Science Foundation, and the Federal Emergency Management Agency.

References

[1] Braun, S. G., ed., 1986, *Mechanical Signature Analysis: Theory and Applications*, Academic Press.

[2] Chang, F.-K., ed., 1997, ''Structural Health Monitoring, Current Status and Perspectives,'' *Proceedings of the International Workshop on Structural*

Health Monitoring, Stanford University, Stanford, CA, Sept. 18–20, Technomic, Lancaster, PA.
[3] Natke, H. G., Tomlinson, G. R., and Yao, J. T. P., eds., 1993, *Safety Evaluation Based on Identification Approaches Related to Time-Variant and Nonlinear Structures*, Friedr. Vieweg & Sohn.
[4] Doebling, S. W., Farrar, C. H., Prime, M. B., and Shevitz, D. W., 1996, ''Damage Identification and Health Monitoring of Structural and Mechanical Systems from Changes in their Vibration Characteristics: A Literature Review,'' Tech. Report LA-13070-MS, Los Alamos National Laboratory Report.
[5] Tomlinson, G. R., and Worden, K., 1994, ''Modeling and Classification of Non-linear Systems Using Neural Networks. Part I: Simulation,'' J. Mech. Syst. Signal Process., **8**, pp. 319–356.
[6] Housner, G. W., Bergman, L. A., Caughey, T. K., Chassiakos, A. G., Claus, R. O., Masri, S. F., Skelton, R. E., Soong, T. T., Spencer, B. F., and Yao, J. T. P., 1997, ''Structural Control: Past, Present and Future,'' ASCE J. Eng. Mech., (Special Issue), **123**, No. 9, pp. 897–971.
[7] Beck, J. L., and Katafygiotis, L. S., 1992, ''Probabilistic System Identification and Health Monitoring of Structures.'' *Proc. 10th World Conference on Earthquake Engineering*, Madrid, Spain.
[8] Beck, J. L., and Katafygiotis, L. S., 1998, ''Updating Models and their Uncertainties. I: Bayesian Statistical Framework,'' ASCE J. Eng. Mech., **124**, pp. 455–461.
[9] Sohn, H., and Law, K. H., 1997, ''Bayesian Probabilistic Approach for Structural Damage Detection,'' J. Earthquake Eng. Struct. Dyn., **26**, pp. 1259–1281.
[10] Agbabian, M. S., Masri, S. F., Miller, R. F., and Caughey, T. K., 1990, ''System Identification Approach to Detection of Structural Changes,'' ASCE J. Eng. Mech., **117**, No. 2, pp. 370–390.
[11] Ghanem, R., and Shinozuka, M., 1995, ''Structural-System Identification. I: Theory,'' ASCE J. Eng. Mech., **121**, pp. 255–264.
[12] Loh, C.-H., and Tou, I.-C., 1995, ''A System Identification Approach to the Detection of Changes in Both Linear and Nonlinear Structural Parameters,'' J. Earthquake Eng. Struct. Dyn., **24**, p. 85–97.
[13] Juang, J. N., Phan, M., Horta, L. G., and Longman, R. W., 1993, ''Identification of Observer/Kalman Filter Markov Parameters: Theory and Experiments,'' J. Guid. Control Dyn., **16**, No. 2, pp. 320–329.
[14] Farrar, C. R., and Jauregui, D., 1996, ''Damage Detection Algorithms Applied to Experimental and Numerical Modal Data from the I-40 Bridge,'' Report No. LA-13074-MS, Los Alamos National Laboratory, Los Alamos, NM.
[15] Zimmerman, D. C., Smith, S. W., Kim, H. M., and Bartkowicz, T. J., 1996, ''An Experimental Study of Structural Health Monitoring using Incomplete Measurements,'' ASME J. Vibr. Acoust., **118**, pp. 543–550.
[16] Loh, C.-H., and Wu, T.-C., 1999, ''System Identification of Fei-Tsui Arch Dam from Forced Vibration and Seismic Response Data,'' J. Earthquake Eng. Struct. Dyn., (to appear).
[17] Shinozuka, M., and Ghanem, R., 1995, ''Structural System Identification. II: Experimental Verification,'' ASCE J. Eng. Mech., **121**, p. 265–273.
[18] Loh, C.-H., and Lin, H.-M., 1996, ''Application of Off-Line and On-Line Identification Techniques to Building Seismic Response Data,'' J. Earthquake Eng. Struct. Dyn., **25**, pp. 269–90.
[19] Smyth, A. W., Masri, S. F., Chassiakos, A. G., and Caughey, T. K., 1999, ''On-Line Parametric Identification of MDOF Nonlinear Hysteretic Systems,'' ASCE J. Eng. Mech., **125**, No. 2, pp. 133–142.
[20] Sato, T., and Qi, K., 1998, ''Adaptive H_∞ Filter: Its Applications to Structural Identification,'' ASCE J. Eng. Mech., **124**, No. 11, pp. 1233–1240.
[21] Golub, G. H., and Van Loan, C. F., 1983, *Matrix Computations*, Johns Hopkins University Press, Baltimore, MD.
[22] Brogan, W. L., 1985, *Modern Control Theory*, 2nd Ed., Quantum Publishers, New York.
[23] Smyth, A. W., 1998, ''Experimental and Analytical Studies in Nonlinear System Identification and Modeling for Structural Control,'' Ph.D. thesis, University of Southern California, Los Angeles, CA.
[24] Masri, S. F., Smyth, A. W., Chassiakos, A. G., Nakamura, M., and Caughey, T. K., 1999, ''Training Neural Networks by Adaptive Random Search Techniques,'' ASCE J. Eng. Mech., **125**, No. 2, pp. 123–132.
[25] Masri, S. F., Miller, R. W., Saud, A. F., and Caughey, T. K., 1987, ''Identification of Nonlinear Vibrating Structures,'' ASME J. Appl. Mech., **54**, pp. 918–929.
[26] Worden, K., 1989, ''Parametric and Nonparametric Identification of Nonlinearity in Structural Dynamics,'' Ph.D. thesis, Department of Mechanical Engineering, Heriot-Watt University, Edinburgh.
[27] Loh, C.-H., and Duh, G.-Y., 1996, ''Frequency Domain and Time Domain Identification on Nonlinear Structural System,'' *Proceedings of the 11th World Conference on Earthquake Engineering*, Acapulco, Mexico, Pergamon, Oxford, UK, p. 653.
[28] IMAC, 1998, *Proceedings of the 16th International Modal Analysis Conference*, Santa Barbara, CA, Society of Experimental Mechanics.
[29] IMAC, 1999, *Proceedings of the 17th International Modal Analysis Conference*, Kissimmee, FL, Society of Experimental Mechanics.

Plastic Bifurcation in the Triaxial Confining Pressure Test

D. Durban
Mem. ASME,
Faculty of Aerospace Engineering,
Technion, Haifa 32000, Israel

P. Papanastasiou[1]
Schlumberger Cambridge Research Ltd.,
High Cross, Madingley Road,
Cambridge CB3 0EL
England

Bifurcations of a circular cylinder are studied, within the context of the triaxial confining pressure test, for pressure sensitive solids. Material response is modeled by large strain versions of flow and deformation theories of plasticity in conjunction with the Drucker-Prager solid. An axially symmetric deformation pattern is assumed prior to bifurcation and only diffuse modes within the elliptic regime are considered. The governing equations are solved analytically in terms of Bessel functions and a search procedure is employed to trace bifurcation loads. Deformation theory predicts critical stresses which are consistently below flow theory results, and provides practical upper bounds on experimentally observed values of peak stresses. [S0021-8936(00)01403-3]

1 Introduction

The confining pressure triaxial calibration test has traditionally served as the fundamental material characterization experiment in geomechanics. The procedure centers on applying hydrostatic pressure on a circular cylindrical specimen, followed by increasing the axial component of stress up to failure. In metal plasticity, Cheng et al. [1] first studied bifurcations of elastoplastic cylinders in axisymmetric conditions for the problems of tension and compression. Hutchinson and Miles [2] examined necking bifurcation of cylinders under tension for an incompressible material with transverse anisotropy. Miles and Nuwayhid [3] extended the analysis to include compressibility. Axisymmetric bifurcations in frictional materials were studied by Drescher and Vardoulakis [4], Vardoulakis [5], and Chau [6] for various constitutive models. The Cam-Clay model has been employed in a recent bifurcation analysis by Yatomi and Shibi [7]. Sulem and Vardoulakis [8] analyzed axisymmetric bifurcations for a polar material with Cosserat microstructure. Chau [9] considered nonaxisymmetric bifurcations of cylindrical specimen along with a further extension [10] to include all higher circumferential modes. Despite an intensive research effort in recent years (essential studies have been reviewed by Vardoulakis and Sulem [11]), the exact details of the near failure behavior are not fully understood. Particularly, the onset of bifurcation modes and possible emergence of shear bands in the vicinity of peak stress, experimentally observed, pose major challenges for further study. While only diffuse mode bifurcations are examined in this work it is worth mentioning that shear banding can also be considered as a form of bifurcation from the primary state of stress.

The present paper, which is a sequel to Papanastasiou and Durban [12], focuses on one aspect of that calibration test: the reliability of bifurcation predictions obtained with available material models. We examine a circular cylinder strained axially—symmetrically by an all round pressure and then compressed axially up to bifurcation. Material response is modeled by the large strain flow and deformation theories of the Drucker-Prager type [12].

The governing equations are presented in the next section along with a separation of variables representation of possible eigenmodes. The system of ordinary differential equations for the radial profiles of perturbed velocities admits an analytical solution in terms of Bessel functions (Section 3) which in turn leads to a transcendental algebraic eigenvalue equation for critical stresses. Sample calculations are presented in Section 4 and compared with experimental data for two geomaterials (Castlegate sandstone and Jurrasic shale).

The main findings of this study confirm that deformation theory predictions for bifurcation loads are lower than those obtained with flow theory. The difference between the results of the two theories increase with increasing plastification. The levels of experimental peak stresses are below deformation theory predictions for bifurcation loads, with an average overestimation by the latter of about 9.6 percent for Castlegate sandstone and about 3.6 percent for the Jurassic shale. It would appear from that comparison that the Drucker-Prager deformation theory can provide reliable predictions in the analysis of the triaxial calibration test for pressure sensitive solids.

2 Problem Formulation

A circular cylinder $(0\leqslant r\leqslant a, 0\leqslant z\leqslant l)$, is uniformly stressed by external compressive loads which induce the primary state of stress

$$\sigma_{rr}=\sigma_{\theta\theta}=-p \qquad \sigma_{zz}=-\sigma \tag{1}$$

with both p, σ being positive. Here (r,θ,z) denote an instantaneous Eulerian polar system of coordinates. The original, undeformed dimensions of the cylinder are (a_0, l_0) and an axially symmetric strain pattern is assumed over the entire loading history.

We examine possible modes of bifurcation, along the primary path (1), described by the separation of variables solution ([12])

$$u=U(r)\cos m\theta\cos\frac{k\pi z}{l} \tag{2}$$

$$v=V(r)\sin m\theta\cos\frac{k\pi z}{l} \tag{3}$$

$$w=W(r)\cos m\theta\sin\frac{k\pi z}{l} \tag{4}$$

where (u,v,w) are the (r,θ,z) components of the perturbed velocity field, (m, k) are the corresponding wave numbers, and the radial profiles U,V,W are as yet unknown.

Material behavior is modeled by two particular cases of the family

$$\overset{\nabla}{\boldsymbol{\sigma}}=\mathcal{L}\cdot\cdot\,\mathbf{D} \tag{5}$$

where $\overset{\nabla}{\boldsymbol{\sigma}}$ is the Jaumann stress rate of the Cauchy stress, $\mathbf{D}$ is the Eulerian strain rate, and $\mathcal{L}$ denotes the fourth-order tensor of in-

[1]To whom correspondence should be addressed.

Contributed by the Applied Mechanics Division of THE AMERICAN SOCIETY OF MECHANICAL ENGINEERS for publication in the ASME JOURNAL OF APPLIED MECHANICS. Manuscript received by the ASME Applied Mechanics Division, March 9, 1999; final revision, January 31, 2000. Associate Technical Editor: K. T. Ramesh. Discussion on the paper should be addressed to the Technical Editor, Professor Lewis T. Wheeler, Department of Mechanical Engineering, University of Houston, Houston, TX 77204-4792, and will be accepted until four months after final publication of the paper itself in the ASME JOURNAL OF APPLIED MECHANICS.

stantaneous moduli. Here we employ the large strain flow and deformation Drucker-Prager theories, with the effective stress σ_e and plastic potential ϕ defined by

$$\sigma_e = Q + \mu\sigma_h \qquad \phi = Q + \eta\sigma_h \tag{6}$$

where $Q=(3/2\mathbf{S}\cdot\cdot\mathbf{S})$ is the Mises effective stress with $\mathbf{S}$ denoting the stress deviator, σ_h is the hydrostatic stress and (μ,η) are pressure sensitive parameters. The standard Mises model is obtained with $\mu=\eta=0$, while for associated solids in general $\mu=\eta$. A complete derivation of the instantaneous moduli tensor $\mathcal{L}$, for both flow and deformation theories which originate from (6), has been given in Papanastasiou and Durban [12] and here we shall just recapitulate the essential relations that correspond to the field (1). Thus, with due account of material symmetry we have the scalar specification of (5) as

$$\begin{aligned}
&\overset{\nabla}{\sigma}_{rr} = L_{rr}d_{rr} + L_{r\theta}d_{\theta\theta} + L_{rz}d_{zz}\\
&\overset{\nabla}{\sigma}_{\theta\theta} = L_{r\theta}d_{rr} + L_{rr}d_{\theta\theta} + L_{rz}d_{zz}\\
&\overset{\nabla}{\sigma}_{zz} = L_{zr}d_{rr} + L_{zr}d_{\theta\theta} + L_{zz}d_{zz}\\
&\overset{\nabla}{\sigma}_{r\theta} = 2G_{r\theta}d_{r\theta} \qquad \overset{\nabla}{\sigma}_{\theta z} = 2G_{\theta z}d_{\theta z} \qquad \overset{\nabla}{\sigma}_{zr} = 2G_{\theta z}d_{zr}
\end{aligned} \tag{7}$$

where d_{ij} $(i,j=r,\theta,z)$ are the Eulerian strain rate components. The instantaneous moduli L_{ij}, G_{ij} $(i,j=r,\theta,z)$ are defined by

$$\begin{aligned}
&L_{rr} = 2G + \lambda - \Gamma_t N_r M_r \qquad L_{r\theta} = L_{rr} - 2G \qquad L_{rz} = \lambda - \Gamma_t N_r M_z\\
&L_{zr} = \lambda - \Gamma_t N_z M_r \qquad L_{zz} = 2G + \lambda - \Gamma_t N_z M_z \qquad G_{r\theta} = G_{\theta z} = G
\end{aligned} \tag{8}$$

where (G,λ) are the Lame constants, and Γ_t is the flow theory plastic parameter

$$\Gamma_t = \frac{4(G-G_t)/3}{1+(K/K_t-1)G_t/G} \tag{9}$$

with (G_t,K_t) denoting the tangent shear and bulk moduli, respectively, defined as

$$\frac{1}{G_t} = \frac{1}{G} + 3\left(\frac{\sigma_e}{\phi}\right)\frac{d\epsilon_p}{d\sigma_e} \qquad \frac{1}{K_t} = \frac{1}{K} + \mu\eta\left(\frac{\sigma_e}{\phi}\right)\frac{d\epsilon_p}{d\sigma_e} \tag{10}$$

K being the elastic bulk modulus, and the effective stress σ_e is a known function of the total plastic strain ϵ_p. The plastic strain is defined by the principle of plastic power equivalence ([13])

$$\dot{\epsilon}_p\sigma_e = \sigma_{ij}\dot{\epsilon}^p_{ij}. \tag{11}$$

Also, in (8)

$$M_i = \frac{3S_{ii}}{2Q} + \frac{\mu K}{2G} \qquad N_i = \frac{3S_{ii}}{2Q} + \frac{\eta K}{2G} \qquad i=r,\theta,z \qquad \textit{no sum} \tag{12}$$

where S_{ii} are the normal deviatoric stress components.

Likewise, the deformation theory relations are given by (7) with

$$\begin{aligned}
&L_{rr} = 2G_s + \lambda_d - \Gamma_d N_r M_r \qquad L_{r\theta} = L_{rr} - 2G_s\\
&L_{rz} = \lambda_d - \Gamma_d N_r M_z\\
&L_{zr} = \lambda_d - \Gamma_d N_z M_r \qquad L_{zz} = 2G_s + \lambda_d - \Gamma_d N_z M_z \qquad G_{r\theta} = G_s
\end{aligned} \tag{13}$$

$$G_{\theta z} = G_{zr} = \left(\frac{a_r^2 + a_z^2}{a_r^2 - a_z^2}\ln\frac{a_r}{a_z}\right)G_s$$

where G_s is the secant shear modulus

$$\frac{1}{G_s} = \frac{1}{G} + \frac{3\sigma_e\epsilon_p}{\phi Q}. \tag{14}$$

(λ_d,Γ_d) are the deformation theory parameters

$$\lambda_d = \frac{(1-G_d/G_s)K}{1+(G_d/G)(K/K_d-1)-(G_dK)/(G_sK_d)} - \frac{2}{3}G_s$$

$$\Gamma_d = \frac{(4G_s/3)[1+(G_d/G)(K/K_d-1)-(G_dK)/(G_sK_d)]}{1+(G_d/G)(K/K_d-1)} \tag{15}$$

with

$$\frac{1}{G_d} = \frac{1}{G} + 3\left[\left(\frac{1}{\phi}\right)\frac{d(\sigma_e\epsilon_p)}{d\sigma_e} - \frac{\sigma_e\epsilon_p}{\phi^2}\right]$$

$$\frac{1}{K_d} = \frac{1}{K} + \eta\left[\left(\frac{\mu}{\phi}\right)\frac{d(\sigma_e\epsilon_p)}{d\sigma_e} - \eta\frac{\sigma_e\epsilon_p}{\phi^2}\right]. \tag{16}$$

Also in (13), the principal stretches in directions (r,z) are denoted by (a_r,a_z), respectively, and in analogy with (12)

$$M_i = \frac{3S_{ii}}{2Q} + \frac{\mu_d K}{2G_s} \qquad N_i = \frac{3S_{ii}}{2Q} + \frac{\eta_d K}{2G_s} \qquad i=r,\theta,z \qquad \textit{no sum} \tag{17}$$

where

$$\mu_d = \frac{(3/\eta)G_d(1/K_d-1/K)}{1+(G_d/G)(K/K_d-1)-(G_dK)/(G_sK_d)}$$

$$\eta_d = \frac{\eta(1-G_d/G)}{1+(G_d/G)(K/K_d-1)-(G_dK)/(G_sK_d)}. \tag{18}$$

Clearly, the instantaneous moduli (7) are load dependent, though spatially homogeneous, and vary with (p,σ) along the deformation path according to the hardening (softening) response $\epsilon_p(\sigma_e)$. It is worth mentioning that the instantaneous moduli in (8) and (13) admit the identity $2G_{r\theta}=L_{rr}-L_{r\theta}$ thus implying that relations (7) resemble the stress-strain relations for transversely isotropic elastic solids ([14]). It is worth to observe if the degree of strain-induced anisotropy inherent to deformation theory, (13), is sufficient to predict bifurcations at realistic load levels for the triaxial validation test. Supporting the use of a noncoaxial plasticity model for such predictions, Vardoulakis [5] claimed that the shear modulus for the difference of radial and hoop stress increment $L_{rr}-L_{r\theta}=2G_s$ should be significantly different than the modulus (G_{rz}) for the shear stress increment. Apparently such a condition can be met for deformation theory in the plastic region where the dependent on the stretches instantaneous modulus G_{rz}, in $(13)_c$, reduces significantly.

Inserting now the perturbed velocity field (2)–(4) in the rate equilibrium equations ([12]), and accounting for (7), gives the three equations, for the radial profiles U,V,W,

$$\begin{aligned}
&L_{rr}\left(U'' + \frac{U'}{r}\right) - (L_{rr} + m^2G_{r\theta})\frac{U}{r^2} - \left(\frac{k\pi}{l}\right)^2\left[G_{\theta z} - \frac{1}{2}(p-\sigma)\right]U\\
&+ m(L_{r\theta} + G_{r\theta})\frac{V'}{r} - m(L_{rr} + G_{r\theta})\frac{V}{r^2} + \left(\frac{k\pi}{l}\right)\\
&\times\left[L_{\theta z} + G_{\theta z} - \frac{1}{2}(p-\sigma)\right]W' = 0
\end{aligned} \tag{19}$$

$$\begin{aligned}
&-m(L_{r\theta} + G_{r\theta})\frac{U'}{r} - m(L_{rr} + G_{r\theta})\frac{U}{r^2} + G_{r\theta}\left(V'' + \frac{V'}{r^2}\right)\\
&-(G_{r\theta} + m^2L_{rr})\frac{V}{r^2} - \left(\frac{k\pi}{l}\right)^2\left[G_{\theta z} + \frac{1}{2}(p-\sigma)\right]V\\
&-m\left(\frac{k\pi}{l}\right)\left[L_{\theta z} + G_{\theta z} - \frac{1}{2}(p-\sigma)\right]\frac{W}{r} = 0
\end{aligned} \tag{20}$$

$$-\left(\frac{k\pi}{l}\right)\left[L_{zr}+G_{\theta z}+\frac{1}{2}(p-\sigma)\right]\left(U'+\frac{U}{r}+m\frac{V}{r}\right)$$
$$+\left[G_{\theta z}-\frac{1}{2}(p-\sigma)\right]\mathcal{L}_m(W)-\left(\frac{k\pi}{l}\right)^2 L_{zz}W=0 \quad (21)$$

where the prime denotes differentiation with respect to r, and $\mathcal{L}_m(\cdot)$ is the Bessel operator

$$\mathcal{L}_m(\cdot)=(\cdot)''+\frac{(\cdot)'}{r}-m^2\frac{(\cdot)'}{r^2}. \quad (22)$$

These equations are supplemented by the conditions of vanishing traction rates, at $r=a$, which take here the form

$$L_{rr}U'+L_{r\theta}\frac{U}{r}+mL_{r\theta}\frac{V}{r}+\left(\frac{k\pi}{l}\right)L_{\theta z}W=0$$
$$-m(G_{r\theta}+p)\frac{U}{r}+G_{r\theta}V'-(G_{r\theta}+p)\frac{V}{r}=0 \quad (23)$$
$$-\left(\frac{k\pi}{l}\right)\left[G_{\theta z}+\frac{1}{2}(p+\sigma)\right]U+\left[G_{\theta z}-\frac{1}{2}(p-\sigma)\right]W'=0.$$

At the faces $z=0,l$ we have by (2)–(4) that the axial velocity W and the shear traction rates vanish ([12]).

Thus, the problem lies in solving the eigensystem (19)–(21) along with the boundary data (23). Axially symmetric modes are recovered from the general solution with $m=0$ and $V=0$.

3 Continuous Eigenfunctions

Equations (19)–(21) resemble, for any loading state (p,σ), the analogous equations for transversely isotropic cylindrical tubes ([14]). Accordingly, available analytical solutions (e.g., [15]) can be adapted, as in Chau [6], to facilitate a closed-form solution of the governing equations. For the sake of completeness, however, we summarize here the essential details of a solution method.

Motivated by the Bessel-like structure of Eqs. (19)–(21) we seek solutions of the form

$$U=m\frac{F_1}{r} \qquad V=-F_1' \quad (24)$$

where F_1 is an unknown function of r.

Inserting (24) in (19)–(21), respectively, we get the equations

$$m\left[\mathcal{L}_m(F_1)-\left(\frac{k\pi}{l}\right)^2\gamma_1^2F_1\right]+\left(\frac{k\pi}{l}\right)\alpha_0 rW'=0 \quad (25)$$

$$\mathcal{L}_m'(F_1)-\left(\frac{k\pi}{l}\right)^2\gamma_1^2F_1'+m\left(\frac{k\pi}{l}\right)\alpha_0\frac{W}{r}=0 \quad (26)$$

$$\beta_1\mathcal{L}_m(W)-\left(\frac{k\pi}{l}\right)^2 W=0 \quad (27)$$

where

$$\gamma_1^2=\frac{G_{\theta z}+(p-\sigma)/2}{G_{r\theta}} \qquad \alpha_0=\frac{L_{\theta z}+G_{\theta z}-(p-\sigma)/2}{G_{r\theta}}$$
$$\beta_1=\frac{G_{\theta z}-(p-\sigma)/2}{L_{zz}}. \quad (28)$$

Clearly, Eqs. (25)–(26) are compatible only if $(rW')'=m^2W/r$ implying that $\mathcal{L}_m(W)=0$ and hence, by (27), $W\equiv 0$. The solution for F_1 from (25) is then simply

$$F_1=A_1I_m\left(k\pi\gamma_1\frac{r}{l}\right)+B_1K_m\left(k\pi\gamma_1\frac{r}{l}\right)=0 \quad (29)$$

where I_m, K_m are the modified Bessel functions of order m and A_1, B_1 are the integration constants. The radial profiles U and V follow now at once from (24).

To find the remaining solutions we assume that U and V are derived from a potential function $F_2(r)$ by

$$U=F_2' \qquad V=-m\frac{F_2}{r} \quad (30)$$

which may be compared to (24). Substituting (30) in (19)–(20) we find that both equations are reduced to the common form

$$\alpha_2\mathcal{L}_m(F_2)-\left(\frac{k\pi}{l}\right)^2\beta_2F_2+\left(\frac{k\pi}{l}\right)W=0 \quad (31)$$

where

$$\alpha_2=\frac{L_{rr}}{L_{\theta z}+G_{\theta z}-(p-\sigma)/2} \qquad \beta_2=\frac{G_{\theta z}+(p-\sigma)/2}{L_{\theta z}+G_{\theta z}-(p-\sigma)/2}. \quad (32)$$

Similarly, Eq. (21) becomes

$$-\left(\frac{k\pi}{l}\right)\alpha_1\mathcal{L}_m(F_2)+\beta_1\mathcal{L}_m(W)-\left(\frac{k\pi}{l}\right)^2W=0 \quad (33)$$

where

$$\alpha_1=\frac{L_{zr}+G_{\theta z}+(p-\sigma)/2}{L_{zz}} \quad (34)$$

Substituting W from (31) in (33) results in the equation

$$\left[\mathcal{L}_m+\left(\frac{k\pi}{l}\right)^2\gamma_2^2\right]\left[\mathcal{L}_m+\left(\frac{k\pi}{l}\right)^2\gamma_3^2\right]F_2=0 \quad (35)$$

where γ_2^2, γ_3^2 are the roots of the characteristic equation

$$\alpha_2\beta_1\gamma^4+(\beta_1\beta_2+\alpha_2-\alpha_1)\gamma^2+\beta_2=0 \quad (36)$$

namely

$$\left\{\begin{matrix}\gamma_2^2\\ \gamma_3^2\end{matrix}\right\}=-\frac{\beta_1\beta_2+\alpha_2-\alpha_1\{\pm\}\sqrt{(\beta_1\beta_2+\alpha_2-\alpha_1)^2-4\alpha_2\beta_1\beta_2}}{2\alpha_2\beta_1}. \quad (37)$$

The solution of (35) can be written as

$$F_2=A_2J_m\left(k\pi\gamma_2\frac{r}{l}\right)+B_2Y_m\left(k\pi\gamma_2\frac{r}{l}\right)+A_3J_m\left(k\pi\gamma_3\frac{r}{l}\right)$$
$$+B_3Y_m\left(k\pi\gamma_3\frac{r}{l}\right) \quad (38)$$

where J_m, Y_m are the ordinary Bessel functions and A_2, A_3, B_2, B_3 are integration constants. The velocities U, V follow from (30) while the axial velocity profile W is obtained from (31) as

$$W=(\alpha_2\gamma_2^2+\beta_2)\left[A_2J_m\left(k\pi\gamma_2\frac{r}{l}\right)+B_2Y_m\left(k\pi\gamma_2\frac{r}{l}\right)\right]+(\alpha_3\gamma_3^2$$
$$+\beta_2)\left[A_3J_m\left(k\pi\gamma_3\frac{r}{l}\right)+B_3Y_m\left(k\pi\gamma_3\frac{r}{l}\right)\right]. \quad (39)$$

Thus, the complete solution of Eqs. (19)–(21) is the linear combination of U and V, derived from (29) and (38), with W given by (39). Axially symmetric modes of bifurcation are recovered from the general solution with $m=0$ and $A_1=B_1=0$.

While the complete solution of the governing system (19)–(21) is applicable for a uniformly stressed (1) hollow cylinder, only full cylinders bifurcations are addressed in this study. Thus, we need to consider the restricted version of (29) and (38)–(39) with $B_1=B_2=B_3=0$ in order to avoid the unbounded values of the Bessel functions, K_m and Y_m, along the axis $r=0$. It follows that the complete solution of continuous bifurcations for a full cylinder reads

$$U=A_1\frac{m}{r}I_m\left(k\pi\gamma_1\frac{r}{l}\right)+A_2J'_m\left(k\pi\gamma_2\frac{r}{l}\right)+A_3J'_m\left(k\pi\gamma_3\frac{r}{l}\right) \tag{40}$$

$$V=-A_1I'_m\left(k\pi\gamma_1\frac{r}{l}\right)-A_2\frac{m}{r}J_m\left(k\pi\gamma_2\frac{r}{l}\right)-A_3\frac{m}{r}J_m\left(k\pi\gamma_3\frac{r}{l}\right) \tag{41}$$

$$W=A_2(\alpha_2\gamma_2^2+\beta_2)J_m\left(k\pi\gamma_2\frac{r}{l}\right)+A_3(\alpha_2\gamma_3^2+\beta_2)J_m\left(k\pi\gamma_3\frac{r}{l}\right). \tag{42}$$

Compliance with the boundary data (23), over the outer surface $r=a$, leads to three linear algebraic homogeneous equations for the integration constants A_1,A_2,A_3. A nontrivial solution (bifurcation) is possible for discrete pairs (p,σ) at which the determinant of that system vanishes. The smallest value of bifurcation loads (eigenvalues) is determined via a search procedure for the minimizing values of wave number (m, k).

The diffuse bifurcation modes discussed here are expected to develop, for common geomaterials, in the elliptic range of governing equations. An available regime classification [10,11] states, with the present notation, that the various regimes are

(a) elliptic imaginary when

$$(\beta_1\beta_2+\alpha_2-\alpha_1)^2-4\alpha_2\beta_1\beta_2>0,\quad \alpha_2\beta_1\beta_2>0,$$
$$\beta_1\beta_2+\alpha_2-\alpha_1>0$$

(b) elliptic complex when

$$(\beta_1\beta_2+\alpha_2-\alpha_1)^2-4\alpha_2\beta_1\beta_2<0,\quad \alpha_2\beta_1\beta_2>0$$

(c) hyperbolic when

$$(\beta_1\beta_2+\alpha_2-\alpha_1)^2-4\alpha_2\beta_1\beta_2>0,\quad \alpha_2\beta_1\beta_2>0,$$
$$\beta_1\beta_2+\alpha_2-\alpha_1<0$$

(d) parabolic when

$$\alpha_2\beta_1\beta_2<0.$$

The first calculations were performed for Castlegate sandstone characterized by (6) with $\mu=\eta=1.311$, elastic constants $E=8.1$ GPa and $\nu=0.35$, and plastic response function

$$\epsilon_p=K(\sigma_e-Y)^n,\quad \sigma_e\geqslant Y \tag{43}$$

with $K=1.3\cdot10^{-6}\,[\mathrm{MPa}]^{1/n}$, $n=3.547$, and $Y=14.08$ MPa. We emphasize here that although the presented flow and deformation theory models were derived for the general cases of nonassociated Drucker-Prager solids, in this particular example we assumed associative behavior, $\mu=\eta$, because the Castlegate sandstone exhibited pronounced dilation (even higher than the friction angle at low confining pressures) in the triaxial tests; the experimental stress-strain and volumetric strain curves can be found in Papanastasiou and Durban [16].

Figure 1 displays the variation of the deformation theory characteristics roots (γ_2,γ_3), as evaluated from (37), with increasing axial pressure σ and with different levels of confining pressure p. The characteristic root γ_2 is looping and then moving to the right whereas γ_3 is looping and moving to the left along the x-axis. It is apparent from Fig. 1 that in the practical range of interest the field equations are elliptic complex with (γ_2,γ_3) being complex conjugates. Similar observations have been verified for other types of common geomaterials. Accordingly, we proceed in this study with investigating the diffuse modes of bifurcation (2)–(4) within the elliptic regime.

Notice that the eigenvalue equation has roots which depend continuously on the parameter $k\pi a/l$. Here, the ratio a/l may depend on loading history and current state of stress at the onset of bifurcation. Just to give an example, it can be shown [13] that with the deformation theory, in the deep plastic range,

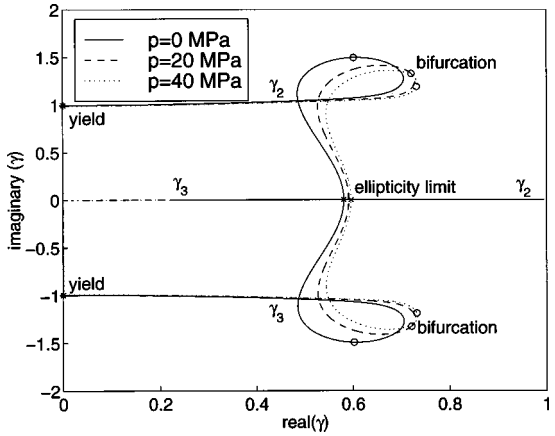

Fig. 1 Variation of characteristic roots γ_2,γ_3 with axial stress σ for different levels of confining pressure p. Results are for Castlegate sandstone and with deformation theory. The roots γ_2,γ_3 are complex conjugates from initial yield onwards up to the ellipticity limit where the equations become hyperbolic.

$$\frac{l}{a}=\frac{l_0}{a_0}e^{-(3/2)\epsilon_p} \tag{44}$$

with ϵ_p being a known function of the effective stress σ_e.

4 Calculation of Bifurcation Loads

Sample calculation have been performed for Castlegate sandstone (43) over a range of confining pressures. The transcendental equation resulting from the boundary data (40)–(42) has been solved numerically to trace the lowest eigenvalue for applied axial stress σ. Typical results are shown in Fig. 2 with zero confining pressure, different circumferential wave numbers m, and upon regarding the normalized axial wave number $k\pi a/l$ as a continuous variable. All results in Fig. 2 are for the deformation theory model and broadly resemble those of Chau [10] albeit his assumption of stress independent moduli ratio. As expected (Fig. 2), tapered specimen with small values of a/l, will bifurcate with the buckling mode $(m=1)$ while the axially symmetric mode $(m=0)$ becomes dominant at a specific value of $k\pi a/l$ (Fig. 2). Notice also the ellipticity limit (e.l.) in Fig. 2 which indicates here the elliptic/hyperbolic boundary beyond which the emergence of shear bands becomes possible.

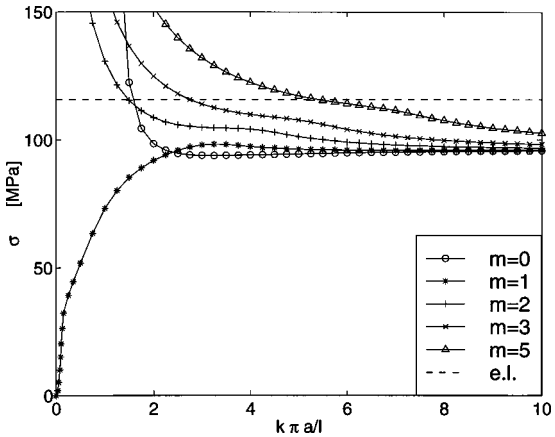

Fig. 2 Lowest bifurcation stresses for Castlegate sandstone with zero confining pressure $(p=0)$ under axial compression σ. Results are with deformation theory and the ellipticity limit (e.l.) is indicated by a broken line.

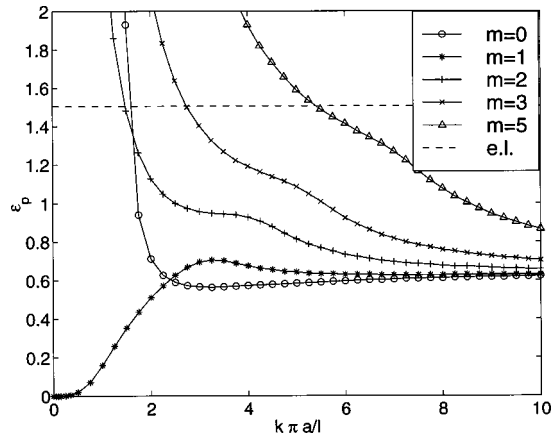

Fig. 3 Levels of effective plastic strain ϵ_p at bifurcation. Data as in Fig. 2.

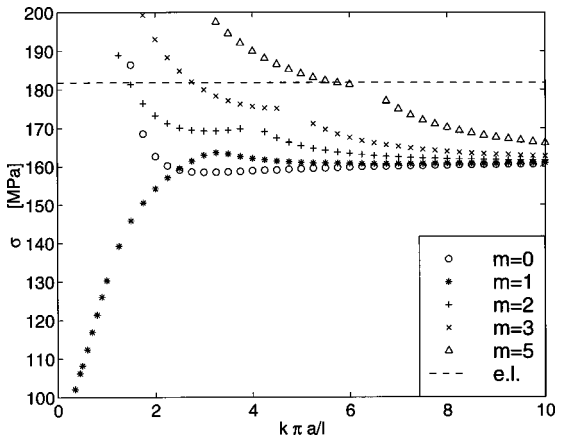

Fig. 4 Bifurcation stresses. Data as in Fig. 2 but with confining pressure $p=20$ MPa.

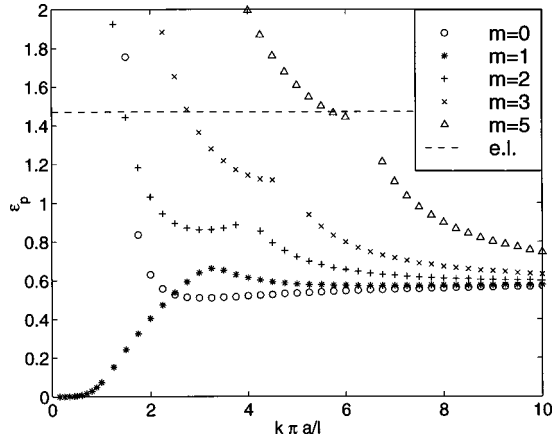

Fig. 5 Effective plastic strain at bifurcation. Data as in Fig. 4.

The bifurcation data of Fig. 2 is reproduced in Fig. 3 for critical values of the effective plastic strain ϵ_p. The gap between the various circumferential eigenmodes in now wider, in comparison with Fig. 2, and the practical significance of eigenmodes associated with circumferential wave numbers $m=1$ and $m=0$ is more apparent.

Figures 4 and 5 present bifurcation results analogous to those of Figs. 2 and 3 but with a confining pressure of $p=20$ MPa. Higher axial stress levels were required to initiate bifurcation (Fig. 4) though the corresponding effective plastic strains (Fig. 5) do not differ much from those at pure axial compression (Fig. 3). Convergence difficulties have been encountered for modes with $m>2$ at intermediate values of parameter $k\pi a/l$.

Representative calculations have been performed for nonassociated solids, with $\eta \neq \mu$ in (6), but no substantial sensitivity was found within the range of parameters considered here. Flow theory predictions for bifurcation loads are consistently higher than those obtained with deformation theory—a comparison is to be provided below in the context of assessing experimental results.

Ideally, the theoretical predictions should be compared with the load level at the onset of bifurcation in the triaxial experiments. It is also known that in the triaxial tests bifurcation takes place in the near post-peak regime. Therefore, the easily detected peak stress in the experiments provides a lower bound to the bifurcation loads and it will be used next as a base for comparison. Table 1 shows values of peak stresses (i.e., maximum value of σ) measured in the triaxial compression tests over a range of confining pressures of 5 to 40 MPa. The experiments were performed on specimens with original, undeformed, length to radius ratio of $l_0/a_0=4$. The corresponding bifurcation points are indicated in Fig. 1. Also shown in Table 1 are numerical results for bifurcation stresses and failure of ellipticity, as obtained from the present analysis, for both deformation and flow theories. Similar results are given in Table 2, with specimens of the same geometrical ratio of $l_0/a_0=4$, for Jurrasic shale characterized by elastic parameters $E=3.7$ GPa, $\nu=0.35$ and plastic response function given by (43) with $K=1.605\cdot 10^{-6}[\text{MPa}]^{1/n}$, $n=2.857$ and $Y=11.76$ MPa, and $\mu=\eta=0.648$. The calibration data for the Jurrasic shale supported an associated behavior, mainly due to the low value of its internal friction. All bifurcation modes in Tables 1 and 2 are for wave numbers $m=1$, $k=1$, associated with buckling.

Judging from the data presented in Tables 1 and 2 it may be concluded that deformation theory predicts bifurcation loads that are below flow theory results but above experimental peak stresses (except for the shale peak stress at $p=60$ MPa). The dif-

Table 1 Comparison of flow and deformation theories predictions with triaxial compression tests on Castlegate sandstone (results in MPa)

Experiment		Deformation Theory		Flow Theory	
Confining pressure	Peak stress	Bifurcation	Ellipticity limit	Bifurcation	Ellipticity limit
5	52.85	77.80	132.30	218.1	6005
10	73.84	96.60	148.80	200.9	6010
20	114.56	120.80	181.80	170.9	6020
25	123.46	135.80	198.40	165.0	6025
30	138.31	151.10	214.90	168.3	6030
35	145.82	166.50	231.50	177.4	6035
40	159.43	182.00	248.10	189.2	6040

Table 2 Comparison of flow and deformation theories predictions with triaxial compression tests on Jurassic shale (results in MPa)

Experiment		Deformation Theory		Flow Theory	
Confining pressure	Peak stress	Bifurcation	Ellipticity limit	Bifurcation	Ellipticity limit
5	32.05	69.60	166.7	78.6	2741
25	89.10	95.20	202.4	98.7	2760
40	116.50	117.00	229.1	118.9	2775
60	164.00	148.50	264.9	148.9	2796

ference in bifurcation results obtained from the two theories decreases with increasing confining pressure due to the delay in plastification, via σ_e in (6), at higher levels of the confining pressure. Recall that the effective stress (6) in the triaxial compression test is given by

$$\sigma_e = \left(1 - \frac{1}{3}\mu\right)\sigma - \left(1 + \frac{2}{3}\mu\right)p \tag{45}$$

implying, by (43), that the confining pressure reduces the level of plastic strains in the specimen for this particular model.

Over the intermediate range of p deformation theory appears to provide a useful upper bound on the peak stress with an average overestimation of about 9.6 percent for Castlegate sandstone and about 3.6 percent for Jurassic shale. Failure of ellipticity is predicted by deformation theory in all cases to be above bifurcation stress, and is unrealistically high with flow theory.

It is likely that a more refined theoretical model can improve the theoretical predictions by accounting for strain softening in the post peak zone and, possibly, considering stress dependence of some of the material parameters. Further improvements can be made by resorting to a noncoaxial plasticity model along the lines followed by Papamichos and Vardoulakis [17] and Yatomi and Shibi [7]. However, even with its present restricted validity the Drucker-Prager deformation theory appears to provide useful and reliable results in the bifurcation analysis of pressure sensitive solids.

Acknowledgments

The authors wish to thank Schlumberger for supporting this research. Part of this study was supported by the fund for promotion of research at the Technion. D. D. is grateful for the kind assistance of the Sydney Goldstein Chair in Aeronautical Engineering.

References

[1] Cheng, S. Y., Ariaratnam, S. T., and Dubey, R. N., 1971, ''Axisymmetric Bifurcation in an Elastic-Plastic Cylinder Under Axial Load and Lateral Hydrostatic Pressure,'' Q. Appl. Math., **21**, pp. 41–51.

[2] Hutchinson, J. W., and Miles, J. P., 1974, ''Bifurcation Analysis of the Onset of Necking in an Elastic-Platic Cylinder Under Uniaxial Tension,'' J. Mech. Phys. Solids, **22**, pp. 61–71.

[3] Miles, J. P., and Nuwayhid, U. A., 1985, ''Bifurcation in Compressible Elastic-Plastic Cylinder Under Uniaxial Tension,'' Appl. Sci. Res., **42**, pp. 33–54.

[4] Drescher, A., and Vardoulakis, I., 1982, ''Geometric Softening in Triaxial Tests on Granular Material,'' Geotechnique, **32**, pp. 291–303.

[5] Vardoulakis, I., 1983, ''Rigid Granular Plasticity Model and Bifurcation in the Triaxial Test,'' Acta Mech., **49**, pp. 57–79.

[6] Chau, K.-T., 1992, ''Non-Normality and Bifurcation in a Compressible Pressure-Sensitive Circular Cylinder Under Axially Symmetric Tension and Compression,'' Int. J. Solids Struct., **29**, pp. 801–824.

[7] Yatomi, C., and Shibi, T., 1997, ''Antisymmetric Bifurcation Analysis in a Circular Cylinder of a Non-Coaxial Cam-Clay Model,'' *Deformation and Progressive Failure in Geomechanics*, IS-Nagoya, 1997, Pergamon, Elsevier, Oxford, UK, pp. 9–14.

[8] Sulem, J., and Vardoulakis, I., 1990, ''Bifurcation Analysis of the Triaxial Test on Rock Specimens: A Theoretical Model for Shape and Size Effect,'' Acta Mech., **83**, pp. 195–212.

[9] Chau, K.-T., 1993, ''Antisymmetric Bifurcation in a Compressible Pressure-Sensitive Circular Cylinder Under Axisymmetric Tension and Compression,'' ASME J. Appl. Mech., **60**, pp. 282–289.

[10] Chau, K.-T., 1995, ''Buckling, Barelling, and Surface Instabilities of a Finite, Transversely Isotropic Circular Cylinder,'' Q. Appl. Math., **53**, pp. 225–244.

[11] Vardoulakis, I., and Sulem, J., 1995, ''Bifurcation Analysis in Geomechanics,'' Blackie A & P, Chapman & Hall, London.

[12] Papanastasiou, P., and Durban, D., 1999, ''Bifurcation of Elastoplastic Pressure Sensitive Hollow Cylinders,'' ASME J. Appl. Mech., **66**, pp. 117–123.

[13] Durban, D., and Papanastasiou, P., 1997, ''Cylindrical Cavity Expansion and Contraction in Pressure Sensitive Geomaterials,'' Acta Mech., **122**, pp. 99–122.

[14] Kardomateas, G. A., 1993, ''Stability Loss in Thick Transversely Isotropic Cylindrical Shells Under Axial Compression,'' ASME J. Appl. Mech., **60**, pp. 506–513.

[15] Elliot, H. A., 1948, ''Three-Dimensional Stress Distribution in Hexagonal Aelotropic Crystals,'' Proc. Cambridge Philos. Soc., **44**, pp. 522–533.

[16] Papanastasiou, P., and Durban, D., 1997, ''Elastoplastic Analysis of Cylindrical Cavity Problems in Geomaterials,'' Int. J. Num. Anal. Meth. Geomech., **21**, pp. 121–132.

[17] Papamichos, E., and Vardoulakis, I., 1995, ''Shear Band Formation in Sand According to Non-Coaxial Plasticity Model,'' Geotechnique, **45**, pp. 649–661.

Three-Dimensional Analytical Solution for Hybrid Multilayered Piezoelectric Plates

S. S. Vel
Postdoctoral Research Associate,
Mem. ASME

R. C. Batra
Clifton C. Garvin Professor,
Fellow ASME

Department of Engineering Science
and Mechanics,
Virginia Polytechnic Institute
and State University,
Blacksburg, VA 24061-0219

Analytical solutions for the static three-dimensional deformations of multilayered piezoelectric rectangular plates are obtained by using the Eshelby-Stroh formalism. The laminated plate consists of homogeneous elastic or piezoelectric laminae of arbitrary thicknesses. The equations of static, linear, piezoelectricity are exactly satisfied at every point in the body. The analytical solution is in terms of an infinite series; the continuity conditions at the interfaces and boundary conditions at the edges are used to determine the coefficients. The formulation admits different boundary conditions at the edges and is applicable to thick and thin laminated plates. Results are presented for thick piezoelectric plates with two opposite edges simply supported and the other two subjected to various boundary conditions. [S0021-8936(00)01803-1]

1 Introduction

In recent years, piezoelectric materials have been integrated with structural systems to form a class of ''smart structures.'' The piezoelectric materials are capable of altering the structure's response through sensing, actuation and control. By integrating surface-bonded and embedded actuators into structural systems, desired localized strains may be induced by applying the appropriate voltage to the actuators.

In order to successfully incorporate piezoelectric actuators into structures, the mechanical interaction between the actuators and the base structure must be fully understood. Mechanical models were developed by Crawley and de Luis [1], Im and Atluri [2], Crawley and Anderson [3], and others for piezoelectric patches mounted to top and/or bottom surfaces of a beam. Lee [4] developed a theory for laminated plates with distributed piezoelectric layers based on the classical lamination theory. Wang and Rogers [5] applied the classical lamination theory to plates with surface-bonded or embedded piezoelectric patches. A coupled first-order shear deformation theory for multilayered piezoelectric plates was presented by Huang and Wu [6]. Mitchell and Reddy's [7] coupled higher-order theory is based on an equivalent single-layer theory for the mechanical displacements and layerwise discretization of the electric potential. Numerous finite element studies have also been conducted (e.g., see Robbins and Reddy [8], Ha et al. [9], Heyliger et al. [10], and Batra and Liang [11]).

Vlasov [12], Pagano [13,14], and Srinivas and Rao [15] obtained three-dimensional analytical solutions for simply supported, laminated anisotropic elastic plates. Their method has been extended by Ray et al. [16] and Heyliger and Brooks [17] to study the cylindrical bending of laminated piezoelectric plates. Analytical solutions for the static behavior of a homogeneous simply supported, piezoelectric rectangular plate was given by Bisegna and Maceri [18] and Lee and Jiang [19]. Heyliger [20,21] provided a three-dimensional solution for the static behavior of multilayered piezoelectric rectangular plates. All the aforementioned three-dimensional solutions are restricted to piezoelectric laminates whose edges are simply supported and electrically grounded. Such solutions are useful for validating new or improved plate theories ([22]) and finite element formulations ([10,23]). However, simply supported boundary conditions are less frequently realized in practice and they do not exhibit the well-known singular effects observed near clamped or traction-free edges. The available analytical solution techniques for three-dimensional deformations are incapable of analyzing laminates with clamped or traction-free edges and/or when the edges are electrically in contact with a low-permittivity medium like air, wherein the normal component of the electrical displacement vanishes.

The Eshelby-Stroh formalism ([24–26]) provides exact solutions to the governing differential equations of anisotropic materials under generalized plane-strain deformations in terms of arbitrary analytical functions. Vel and Batra [27,28] adopted a series solution for the analytic functions to analyze the generalized plane-strain deformation of laminated elastic plates subjected to arbitrary boundary conditions, and the cylindrical bending of a laminated elastic plate with embedded or surface mounted piezoceramic patches. Recently, Vel and Batra [29] generalized the Eshelby-Stroh formalism to study the three-dimensional deformations of laminated elastic rectangular plates with arbitrary boundary conditions. Here we extend this method to multilayered piezoelectric plates subjected to arbitrary boundary conditions. The edges of each lamina may be subjected to mechanical and electrical boundary conditions different from those on the adjoining laminae. The governing differential equations are solved exactly and various constants in the resulting series solution are determined from the boundary conditions at the edges and the continuity conditions at the interfaces. This results in an infinite system of equations in infinitely many unknowns. By retaining a large number of terms in the series solution, the mechanical displacements, stresses, electric potential, and electric displacement can be computed to any desired degree of accuracy. Results are presented for thick piezoelectric plates with two edges simply supported and the other two edges subjected to arbitrary boundary conditions. These results can be used to assess the accuracy of different plate theories and finite element formulations.

Contributed by the Applied Mechanics Division of THE AMERICAN SOCIETY OF MECHANICAL ENGINEERS for publication in the ASME JOURNAL OF APPLIED MECHANICS. Manuscript received by the ASME Applied Mechanics Division, June 2, 1999; final revision, Nov. 23, 1999. Associate Technical Editor: I. M. Daniels. Discussion on the paper should be addressed to the Technical Editor, Professor Lewis T. Wheeler, Department of Mechanical Engineering, University of Houston, Houston, TX 77204-4792, and will be accepted until four months after final publication of the paper itself in the ASME JOURNAL OF APPLIED MECHANICS.

2 Formulation of the Problem

We use a rectangular Cartesian coordinate system, shown in Fig. 1, to describe the infinitesimal quasi-static deformations of an N-layer piezoelectric laminated plate occupying the region $[0,L_1]\times[0,L_2]\times[0,L_3]$ in the unstressed reference configuration.

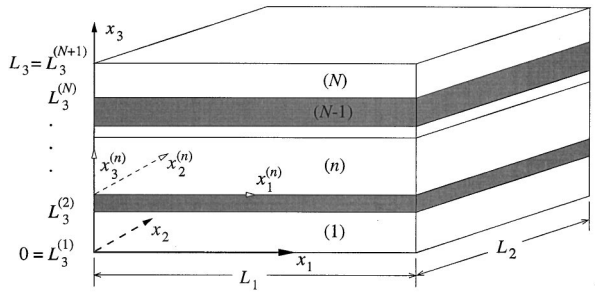

Fig. 1 An *N*-layer laminated piezoelectric plate

The vertical positions of the bottom and top surfaces as well as of the $N-1$ interfaces between the laminae are denoted by $L_3^{(1)}=0$, $L_3^{(2)}, \ldots, L_3^{(n)}, \ldots, L_3^{(N)}$, $L_3^{(N+1)}=L_3$.

The equilibrium equations and charge equations of electrostatics in the absence of body forces and free charges are

$$\sigma_{jm,m}=0, \quad D_{m,m}=0, \quad (j,m=1,2,3), \tag{1}$$

where σ_{jm} are the components of the Cauchy stress tensor and D_m the electric displacement. A comma followed by index m indicates partial differentiation with respect to the present position x_m of a material particle, and a repeated index implies summation over the range of the index.

The constitutive equations of a linear piezoelectric medium are ([30])

$$\sigma_{jm}=C_{jmqr}\varepsilon_{qr}-e_{rjm}E_r, \quad D_m=e_{mqr}\varepsilon_{qr}+\epsilon_{mr}E_r, \quad (q,r=1,2,3), \tag{2}$$

where ε_{qr} are the components of the infinitesimal strain tensor, E_r the electric field, C_{jmqr} the elasticity constants, e_{rjm} the piezoelectric moduli, and ϵ_{mr} the electric permittivity. The infinitesimal strain tensor and electric field are related to the mechanical displacement u_q and electric potential ϕ by

$$\varepsilon_{qr}=\frac{1}{2}(u_{q,r}+u_{r,q}), \quad E_j=-\phi_{,j}. \tag{3}$$

We will interchangeably use the direct and indicial notation. The stored energy density W for a piezoelectric medium is given by ([30])

$$W=\frac{1}{2}(\sigma_{jm}\varepsilon_{jm}+D_mE_m)=\frac{1}{2}(C_{jmqr}\varepsilon_{jm}\varepsilon_{qr}+\epsilon_{mr}E_mE_r). \tag{4}$$

The symmetry of the stress and strain tensors and the existence of the stored energy function imply the following symmetry conditions:

$$C_{jmqr}=C_{mjqr}=C_{qrjm}, \; e_{rjm}=e_{rmj}, \; \epsilon_{mr}=\epsilon_{rm}. \tag{5}$$

In the most general case, there are 21 independent elastic constants, 18 independent piezoelectric moduli, and 6 independent dielectric permittivities. Material elasticities are assumed to yield a positive stored energy density for every nonrigid deformation and/or nonzero electric field. That is,

$$C_{jmqr}u_{j,m}u_{q,r}>0, \quad \epsilon_{mr}E_mE_r>0, \tag{6}$$

for every real nonzero ε_{jm} and E_m. The total stored energy U of the piezoelectric laminate is given by

$$U=\int_{\mathcal{R}} W dv, \tag{7}$$

where $\mathcal{R}=[0,L_1]\times[0,L_2]\times[0,L_3]$. The displacement or traction components and electric potential or normal component of the electric displacement on the edges $x_1=0$, L_1; $x_2=0$, L_2; and on the bottom and top surfaces are specified as

$$\mathbf{I}_{u\phi}^{(s)}\begin{bmatrix}\mathbf{u}\\ \phi\end{bmatrix}+\mathbf{I}_{\sigma D}^{(s)}\begin{bmatrix}\boldsymbol{\sigma}_s\\ D_s\end{bmatrix}=\mathbf{f}^{(s)} \quad \text{on } x_s=0,$$

$$\mathbf{J}_{u\phi}^{(s)}\begin{bmatrix}\mathbf{u}\\ \phi\end{bmatrix}+\mathbf{J}_{\sigma D}^{(s)}\begin{bmatrix}\boldsymbol{\sigma}_s\\ D_s\end{bmatrix}=\mathbf{g}^{(s)} \quad \text{on } x_s=L_s, \quad (s=1,2,3), \tag{8}$$

where $(\boldsymbol{\sigma}_s)_i=\sigma_{is}$. The functions $\mathbf{f}^{(s)}, \mathbf{g}^{(s)}$ are known and $\mathbf{I}_{u\phi}^{(s)}, \mathbf{I}_{\sigma D}^{(s)}, \mathbf{J}_{u\phi}^{(s)}, \mathbf{J}_{\sigma D}^{(s)}$ are 4×4 diagonal matrices. For most applications, these diagonal matrices have entries either zero or one such that

$$\mathbf{I}_{u\phi}^{(s)}+\mathbf{I}_{\sigma D}^{(s)}=\mathbf{J}_{u\phi}^{(s)}+\mathbf{J}_{\sigma D}^{(s)}=\mathbf{I} \quad (s=1,2,3), \tag{9}$$

with $\mathbf{I}$ being the 4×4 identity matrix. For example, if the surface $x_1=0$ is rigidly clamped and electrically grounded then $\mathbf{I}_{u\phi}^{(1)}=\mathbf{I}$, $\mathbf{I}_{\sigma D}^{(1)}=\mathbf{0}$ and $\mathbf{f}^{(1)}(x_2,x_3)=\mathbf{0}$, i.e., $u_1=u_2=u_3=0$, $\phi=0$. If the surface is rigidly clamped and the normal component of the electric displacement is zero, then $\mathbf{I}_{u\phi}^{(1)}=\text{diag}[1,1,1,0]$, $\mathbf{I}_{\sigma D}^{(1)}=\text{diag}[0,0,0,1]$. Boundary conditions at an electrically grounded simply supported edge $x_1=0$ may be simulated by $\mathbf{I}_{u\phi}^{(1)}=\text{diag}[0,1,1,1]$, $\mathbf{I}_{\sigma D}^{(1)}=\text{diag}[1,0,0,0]$ and $\mathbf{f}^{(1)}(x_2,x_3)=\mathbf{0}$, i.e., $u_2=u_3=0$, $\phi=0$ and $\sigma_{11}=0$. The method is valid even when the elements of matrices $\mathbf{I}_{u\phi}^{(s)}$, $\mathbf{I}_{\sigma D}^{(s)}$, $\mathbf{J}_{u\phi}^{(s)}$ and $\mathbf{J}_{\sigma D}^{(s)}$ are functions of coordinates only.

The interface conditions on the material surfaces $x_3=L_3^{(2)}, \ldots, L_3^{(n)}, \ldots, L_3^{(N)}$ may be specified as follows:

(a) If the surface $x_3=L_3^{(n)}$ is an interface between two laminae, the mechanical displacements, surface tractions, electric potential, and the normal component of the electric displacement between them are taken to be continuous. That is

$$[\![\mathbf{u}]\!]=\mathbf{0}, [\![\boldsymbol{\sigma}_3]\!]=\mathbf{0}, [\![\phi]\!]=0, [\![D_3]\!]=0 \quad \text{on } x_3=L_3^{(n)}. \tag{10}$$

Here $[\![\mathbf{u}]\!]$ denotes the jump in the value of $\mathbf{u}$ across an interface. Thus the adjoining laminae are presumed to be perfectly bonded together.

(b) If the surface $x_3=L_3^{(n)}$ is an electroded interface, then the potential on this surface is a known function $f(x_1,x_2)$ while the normal component of the electric displacement need not be continuous across this interface, i.e.,

$$[\![\mathbf{u}]\!]=\mathbf{0}, [\![\boldsymbol{\sigma}_3]\!]=\mathbf{0}, \; \phi=f(x_1,x_2) \text{ on } x_3=L_3^{(n)}. \tag{11}$$

We assume that the electrode is of infinitesimal thickness and ignore its influence on the mechanical deformations of the structure.

3 A Solution of the Governing Differential Equations

We construct a local coordinate system $x_1^{(n)}, x_2^{(n)}, x_3^{(n)}$ with local axes parallel to the global axes and the origin at the point where the global x_3-axis intersects the bottom surface of the nth lamina. In this local coordinate system, the nth lamina occupies the region $[0,l_1]\times[0,l_2]\times[0,l_3^{(n)}]$, where $l_1=L_1$, $l_2=L_2$ and $l_3^{(n)}=L_3^{(n+1)}-L_3^{(n)}$. We drop the superscript n for convenience with the understanding that all material constants and variables belong to this lamina.

The Eshelby-Stroh formalism ([24–26]) provides a solution for the generalized plane-strain deformations of a linear elastic/piezoelectric anisotropic material. We extend it to three-dimensional deformations by assuming that

$$\begin{bmatrix}\mathbf{u}\\ \phi\end{bmatrix}=\mathbf{a}\exp\left[i\left(\frac{k_1\pi}{l_1}x_1+\frac{k_2\pi}{l_2}x_2+p\frac{x_3}{l_3}\right)\right], \tag{12}$$

where $\mathbf{a}$ and p are possible complex constants to be determined, k_1 and k_2 are known integers, and $i=\sqrt{-1}$. The chosen displacement and potential field has a sinusoidal variation on the x_1-x_2

plane with an arbitrary exponential variation in the x_3-direction; k_1 and k_2 determine the period of the sinusoidal terms in the x_1 and x_2-directions respectively.

From Eqs. (12), (3), and (2) we obtain

$$\sigma_{jm}=i(C_{jmqr}a_q+e_{rjm}a_4)\left(\frac{k_1\pi}{l_1}\delta_{r1}+\frac{k_2\pi}{l_2}\delta_{r2}+p\frac{\delta_{r3}}{l_3}\right)\times\exp\left[i\left(\frac{k_1\pi}{l_1}x_1+\frac{k_2\pi}{l_2}x_2+p\frac{x_3}{l_3}\right)\right],$$
$$D_m=i(e_{mqr}a_q-\epsilon_{mr}a_4)\left(\frac{k_1\pi}{l_1}\delta_{r1}+\frac{k_2\pi}{l_2}\delta_{r2}+p\frac{\delta_{r3}}{l_3}\right)\times\exp\left[i\left(\frac{k_1\pi}{l_1}x_1+\frac{k_2\pi}{l_2}x_2+p\frac{x_3}{l_3}\right)\right]. \tag{13}$$

Here δ_{ij} is the Kronecker delta ([30]). Substitution of (13) into (1) gives equations which can be written as

$$\{\mathbf{Q}^C+p[\mathbf{R}^C+(\mathbf{R}^C)^T]+p^2\mathbf{T}^C\}\mathbf{a}^C+\{\mathbf{q}^e+p[\mathbf{r}^e+\mathbf{s}^e]+p^2\mathbf{t}^e\}a_4=\mathbf{0},$$
$$\{(\mathbf{q}^e)^T+p[(\mathbf{r}^e)^T+(\mathbf{s}^e)^T]+p^2(\mathbf{t}^e)^T\}\mathbf{a}^C-\{q^\epsilon+p[r^\epsilon+s^\epsilon]+p^2t^\epsilon\}a_4=0, \tag{14}$$

where $\mathbf{a}^C=[a_1,a_2,a_3]^T$, the matrices $\mathbf{Q}^C,\mathbf{R}^C,\mathbf{T}^C$ are related to the elastic constants C_{jmqr} by

$$Q^C_{jq}=\frac{k_1^2\pi^2}{l_1^2}C_{j1q1}+\frac{k_1k_2\pi^2}{l_1l_2}(C_{j1q2}+C_{j2q1})+\frac{k_2^2\pi^2}{l_2^2}C_{j2q2},$$
$$R^C_{jq}=\frac{k_1\pi}{l_3l_l}C_{j3q1}+\frac{k_2\pi}{l_3l_2}C_{j3q2},\quad T^C_{jq}=\frac{1}{l_3^2}C_{j3q3}, \tag{15}$$

the vectors $\mathbf{q}^e$, $\mathbf{r}^e$, $\mathbf{s}^e$, and $\mathbf{t}^e$ are related to the piezoelectric moduli e_{rjm} by

$$q^e_j=\frac{k_1^2\pi^2}{l_1^2}e_{1j1}+\frac{k_1k_2\pi^2}{l_1l_2}(e_{1j2}+e_{2j1})+\frac{k_2^2\pi^2}{l_2^2}e_{2j2},$$
$$r^e_j=\frac{k_1\pi}{l_3l_1}e_{3j1}+\frac{k_2\pi}{l_3l_2}e_{3j2},\quad s^e_j=\frac{k_1\pi}{l_3l_1}e_{1j3}+\frac{k_2\pi}{l_3l_2}e_{2j3},\quad t^e_j=\frac{1}{l_3^2}e_{3j3}, \tag{16}$$

and the scalars q^ϵ, r^ϵ, s^ϵ, and t^ϵ are related to the electric permittivity ϵ_{jr} by

$$q^\epsilon=\frac{k_1^2\pi^2}{l_1^2}\epsilon_{11}+\frac{k_1k_2\pi^2}{l_1l_2}(\epsilon_{12}+\epsilon_{21})+\frac{k_2^2\pi^2}{l_2^2}\epsilon_{22},$$
$$r^\epsilon=\frac{k_1\pi}{l_3l_1}\epsilon_{31}+\frac{k_2\pi}{l_3l_2}\epsilon_{32},\quad s^\epsilon=\frac{k_1\pi}{l_3l_1}\epsilon_{13}+\frac{k_2\pi}{l_3l_2}\epsilon_{23},\quad t^\epsilon=\frac{1}{l_3^2}\epsilon_{33}. \tag{17}$$

It should be noted that $s^\epsilon=r^\epsilon$ due to the symmetry restriction $(5)_3$ on the electric permittivity tensor. The two equations in (14) can be combined as

$$\{\mathbf{Q}+p[\mathbf{R}+\mathbf{R}^T]+p^2\mathbf{T}\}\mathbf{a}=\mathbf{0}, \tag{18}$$

where

$$\mathbf{Q}=\begin{bmatrix}\mathbf{Q}^C & \mathbf{q}^e\\ (\mathbf{q}^e)^T & -q^\epsilon\end{bmatrix},\quad \mathbf{R}=\begin{bmatrix}\mathbf{R}^C & \mathbf{r}^e\\ (\mathbf{s}^e)^T & -r^\epsilon\end{bmatrix},\quad \mathbf{T}=\begin{bmatrix}\mathbf{T}^C & \mathbf{t}^e\\ (\mathbf{t}^e)^T & -t^\epsilon\end{bmatrix}. \tag{19}$$

Following the method used by Suo et al. [31] for generalized plane deformations of piezoelectric materials, we can prove that the eigenvalues p of (18) cannot be real. Since the matrices $\mathbf{Q}$, $\mathbf{R}$, and $\mathbf{T}$ in (18) are real, there are four pairs of complex conjugate values for p. Let $(p_\alpha,\mathbf{a}_\alpha)$ $(\alpha=1,2,\ldots,8)$ be eigensolutions of (18) such that

$$\mathrm{Im}(p_\alpha)>0,\quad p_{\alpha+4}=\overline{p}_\alpha,\quad \mathbf{a}_{\alpha+4}=\overline{\mathbf{a}}_\alpha\quad(\alpha=1,\ldots,4), \tag{20}$$

where a bar superimposed on a quantity denotes its complex conjugate. For distinct p_α we can superpose eight solutions of the form (12) to obtain

$$\begin{bmatrix}\mathbf{u}\\ \phi\end{bmatrix}=\mathbf{A}\left\langle\exp\left[i\left(\frac{k_1\pi}{l_1}x_1+\frac{k_2\pi}{l_2}x_2+p_*\frac{x_3}{l_3}\right)\right]\right\rangle\mathbf{c}+\text{conjugate}, \tag{21}$$

where $\mathbf{A}=[\mathbf{a}_1,\mathbf{a}_2,\mathbf{a}_3,\mathbf{a}_4]$, $\mathbf{c}$ is an arbitrary 4×1 vector of unknown complex coefficients, $\langle\psi(p_*)\rangle=\mathrm{diag}[\psi(p_1),\psi(p_2),\psi(p_3),\psi(p_4)]$, and conjugate stands for the complex conjugate of the explicitly stated term. We obtain the following expressions for the stress tensor and electric displacement by superposing eight solutions of the form (13),

$$\begin{bmatrix}\boldsymbol{\sigma}_m\\ D_m\end{bmatrix}=\mathbf{S}_m\left\langle\exp\left[i\left(\frac{k_1\pi}{l_1}x_1+\frac{k_2\pi}{l_2}x_2+p_*\frac{x_3}{l_3}\right)\right]\right\rangle\mathbf{c}+\text{conjugate}, \tag{22}$$

where

$$\mathbf{S}_m=[\mathbf{V}_{(m,1)}\mathbf{a}_1,\mathbf{V}_{(m,2)}\mathbf{a}_2,\mathbf{V}_{(m,3)}\mathbf{a}_3,\mathbf{V}_{(m,4)}\mathbf{a}_4],$$
$$\mathbf{V}_{(m,\alpha)}=\begin{bmatrix}\mathbf{V}^C_{(m,\alpha)} & \mathbf{v}^e_{(m,\alpha)}\\ (\mathbf{w}^e_{(m,\alpha)})^T & -v^\epsilon_{(m,\alpha)}\end{bmatrix},$$
$$(\mathbf{V}^C_{(m,\alpha)})_{jq}=i\left(\frac{k_1\pi}{l_1}C_{jmq1}+\frac{k_2\pi}{l_2}C_{jmq2}+p_\alpha\frac{C_{jmq3}}{l_3}\right), \tag{23}$$
$$(\mathbf{v}^e_{(m,\alpha)})_j=i\left(\frac{k_1\pi}{l_1}e_{1jm}+\frac{k_2\pi}{l_2}e_{2jm}+p_\alpha\frac{e_{3jm}}{l_3}\right),$$
$$(\mathbf{w}^e_{(m,\alpha)})_j=i\left(\frac{k_1\pi}{l_1}e_{mj1}+\frac{k_2\pi}{l_2}e_{mj2}+p_\alpha\frac{e_{mj3}}{l_3}\right),$$
$$v^\epsilon_{(m,\alpha)}=i\left(\frac{k_1\pi}{l_1}\epsilon_{m1}+\frac{k_2\pi}{l_2}\epsilon_{m2}+p_\alpha\frac{\epsilon_{m3}}{l_3}\right).$$

The expressions (21) and (22) are valid when the eigenvalues p_α are distinct, or if they are not, there exist eight independent eigenvectors $\mathbf{a}_\alpha$. If an eigenvalue is repeated r times $(2\leqslant r\leqslant4)$ and it does not have r corresponding independent eigenvectors, then (21) and (22) need to be modified appropriately. The procedure is similar to that given for elastic laminates by Vel and Batra [29].

4 A Series Solution

The complete double Fourier series expansion constructed to satisfy the boundary/interface conditions on the surfaces $x_3^{(n)}=0$, $l_3^{(n)}$ is obtained by superposing solutions of the form (21). In the following equations the first superscript n denotes the nth lamina and the second superscript 3 indicates that the series terms have a double Fourier series expansion on the planes $x_3^{(n)}=0$ and $l_3^{(n)}$. The dependence of the eigenvalues and eigenvectors on k_1 and k_2 is indicated by the subscripts.

$$\begin{aligned}\begin{bmatrix}\mathbf{u}^{(n,3)}\\ \phi^{(n,3)}\end{bmatrix}&=\mathbf{A}^{(n,3)}_{(k_0,k_0)}[\boldsymbol{\eta}^{(n,3)}_{(k_0,k_0)}\mathbf{c}^{(n,3)}_{(k_0,k_0)}+\boldsymbol{\xi}^{(n,3)}_{(k_0,k_0)}\mathbf{d}^{(n,3)}_{(k_0,k_0)}]+\sum_{k_1=1}^{\infty}\mathbf{A}^{(n,3)}_{(k_1,0)}\\ &\times[\boldsymbol{\eta}^{(n,3)}_{(k_1,0)}\mathbf{c}^{(n,3)}_{(k_1,0)}+\boldsymbol{\xi}^{(n,3)}_{(k_1,0)}\mathbf{d}^{(n,3)}_{(k_1,0)}]+\sum_{k_2=1}^{\infty}\mathbf{A}^{(n,3)}_{(0,k_2)}[\boldsymbol{\eta}^{(n,3)}_{(0,k_2)}\mathbf{c}^{(n,3)}_{(0,k_2)}\\ &+\boldsymbol{\xi}^{(n,3)}_{(0,k_2)}\mathbf{d}^{(n,3)}_{(0,k_2)}]+\sum_{k_1,k_2=1}^{\infty}\{\mathbf{A}^{(n,3)}_{(k_1,k_2)}[\boldsymbol{\eta}^{(n,3)}_{(k_1,k_2)}\mathbf{c}^{(n,3)}_{(k_1,k_2)}\\ &+\boldsymbol{\xi}^{(n,3)}_{(k_1,k_2)}\mathbf{d}^{(n,3)}_{(k_1,k_2)}]+\mathbf{A}^{(n,3)}_{(k_1,-k_2)}[\boldsymbol{\eta}^{(n,3)}_{(k_1,-k_2)}\mathbf{c}^{(n,3)}_{(k_1,-k_2)}\\ &+\boldsymbol{\xi}^{(n,3)}_{(k_1,-k_2)}\mathbf{d}^{(n,3)}_{(k_1,-k_2)}]\}+\text{conjugate}.\end{aligned} \tag{24}$$

The terms involving $k_0 \in (0,1)$ play the role of the constant term in the double Fourier series expansion and

$$\boldsymbol{\eta}^{(n,3)}_{(k_1,k_2)}(x_1^{(n)},x_2^{(n)},x_3^{(n)}) = \left\langle \exp\left[i\left(\frac{k_1\pi}{l_1}x_1^{(n)} + \frac{k_2\pi}{l_2}x_2^{(n)} + p^{(n,3)}_{(k_1,k_2,*)}\frac{x_3^{(n)}}{l_3^{(n)}}\right)\right]\right\rangle,$$

$$\boldsymbol{\xi}^{(n,3)}_{(k_1,k_2)}(x_1^{(n)},x_2^{(n)},x_3^{(n)}) = \left\langle \exp\left[-i\left(\frac{k_1\pi}{l_1}x_1^{(n)} + \frac{k_2\pi}{l_2}x_2^{(n)} + p^{(n,3)}_{(k_1,k_2,*)}\left(\frac{x_3^{(n)}}{l_3^{(n)}}-1\right)\right)\right]\right\rangle. \tag{25}$$

The functions $\boldsymbol{\eta}^{(n,3)}_{(k_1,k_2)}(x_1^{(n)},x_2^{(n)},x_3^{(n)})$ and $\boldsymbol{\xi}^{(n,3)}_{(k_1,k_2)}(x_1^{(n)},x_2^{(n)},x_3^{(n)})$ vary sinusoidally on the surfaces $x_3^{(n)}=0$, $l_3^{(n)}$ and exponentially in the $x_3^{(n)}$-direction. The inequality $(20)_1$ ensures that all functions decay exponentially towards the interior of the nth lamina.

Similar expressions can be written for $[\mathbf{u}^{(n,1)},\phi^{(n,1)}]^T$ and $[\mathbf{u}^{(n,2)},\phi^{(n,2)}]^T$ which have a complete double Fourier series expansion on the side surfaces $x_1^{(n)}=0,l_1$ and $x_2^{(n)}=0,l_2$ respectively. The mechanical displacement, electric potential, stress, and electric displacement fields for the nth lamina are

$$\begin{bmatrix}\mathbf{u}^{(n)}\\ \phi^{(n)}\end{bmatrix} = \sum_{s=1}^{3}\begin{bmatrix}\mathbf{u}^{(n,s)}\\ \phi^{(n,s)}\end{bmatrix}, \quad \begin{bmatrix}\boldsymbol{\sigma}_m^{(n)}\\ D_m^{(n)}\end{bmatrix} = \sum_{s=1}^{3}\begin{bmatrix}\boldsymbol{\sigma}_m^{(n,s)}\\ D_m^{(n,s)}\end{bmatrix}. \tag{26}$$

The unknowns $\mathbf{c}^{(n,s)}_{(k_1,k_2)}$ and $\mathbf{d}^{(n,s)}_{(k_1,k_2)}$ in (26) are assumed to be complex, except for $\mathbf{c}^{(n,s)}_{(k_0,k_0)}$ and $\mathbf{d}^{(n,s)}_{(k_0,k_0)}$ which are real.

5 Satisfaction of Boundary and Interface Conditions

The boundary conditions (8) on the surfaces $x_s=0$, L_s and continuity conditions (10) or (11) on the interfaces $x_3=L_3^{(2)}$, $L_3^{(3)},\ldots,L_3^{(N)}$ are satisfied by the classical Fourier series method, resulting in a system of linear algebraic equations for the unknown coefficients $\mathbf{c}^{(n,s)}_{(k_1,k_2)}$ and $\mathbf{d}^{(n,s)}_{(k_1,k_2)}$. On the bottom surface $x_3^{(1)}=0$, we extend the component functions in (26) defined on $[0,l_1]\times[0,l_2]$ to the interval $[-l_1,l_1]\times[-l_2,l_2]$. The functions $\boldsymbol{\eta}^{(1,3)}_{(k_1,k_2)}$ and $\boldsymbol{\xi}^{(1,3)}_{(k_1,k_2)}$ which have a sinusoidal variation on the plane $x_3^{(1)}=0$ are extended without modification since they form the basis functions for this surface, except for terms involving k_0 which are extended as even functions. The functions $\boldsymbol{\eta}^{(1,1)}_{(k_1,k_2)}$ and $\boldsymbol{\xi}^{(1,1)}_{(k_1,k_2)}$ which have an exponential variation in the $x_1^{(1)}$-direction and a sinusoidal variation in the $x_2^{(1)}$-direction are extended as even functions in the $x_1^{(1)}$-direction and without modification in the $x_2^{(1)}$-direction. The functions $\boldsymbol{\eta}^{(1,2)}_{(k_1,k_2)}$ and $\boldsymbol{\xi}^{(1,2)}_{(k_1,k_2)}$ are extended as even functions in the $x_2^{(1)}$-direction and without modification in the $x_1^{(1)}$-direction. The prescribed function $\mathbf{f}^{(3)}(x_1^{(1)},x_2^{(1)})$ is suitably extended. We multiply $(8)_1$ corresponding to $s=3$ by $\exp[i(\tilde{k}_1\pi x_1^{(1)}/l_1+\tilde{k}_2\pi x_2^{(1)}/l_2]$ and integrate the result with respect to $x_1^{(1)}$ and $x_2^{(1)}$ over the interval $[-l_1,l_1]\times[-l_2,l_2]$ to obtain

$$\int_{-l_2}^{l_2}\int_{-l_1}^{l_1}\left\{\mathbf{I}^{(3)}_{u\phi}\begin{bmatrix}\mathbf{u}^{(1)}\\ \phi^{(1)}\end{bmatrix} + \mathbf{I}^{(3)}_{\sigma D}\begin{bmatrix}\boldsymbol{\sigma}_3^{(1)}\\ D_3^{(1)}\end{bmatrix} - \mathbf{f}^{(3)}\right\} \times \exp\left[i\left(\frac{\tilde{k}_1\pi x_1^{(1)}}{l_1}+\frac{\tilde{k}_2\pi x_2^{(1)}}{l_2}\right)\right] dx_1^{(1)}dx_2^{(1)} = \mathbf{0} \ \text{ at } \ x_3^{(1)}=0, \tag{27}$$

for all $(\tilde{k}_1,\tilde{k}_2)\in(\{0\},\{0\})\cup(\mathcal{Z}^+\times\{0\})\cup(\{0\}\times\mathcal{Z}^+)\cup(\mathcal{Z}^+\times\mathcal{Z}^+)\cup(\mathcal{Z}^+\times\mathcal{Z}^-)$, where $\mathcal{Z}^+$ and $\mathcal{Z}^-$ denote the sets of positive and negative integers, respectively. The same procedure is repeated for the boundary condition $(8)_2$ on the top surface of the Nth lamina with $s=3$ and the interface continuity conditions (10) or (11) between the various laminae.

On the side surfaces $x_1^{(n)}=0,l_1$ the functions are extended over the interval $[-l_2,l_2]\times[-l_3^{(n)},l_3^{(n)}]$ in the $x_2^{(n)}-x_3^{(n)}$ plane. We then multiply (8) corresponding to $s=1$ by $\exp[i(\tilde{k}_2\pi x_2^{(n)}/l_2+\tilde{k}_3\pi x_3^{(n)}/l_3^{(n)})]$ and integrate the result with respect to $x_2^{(n)}$ and $x_3^{(n)}$ over $[-l_2,l_2]\times[-l_3^{(n)},l_3^{(n)}]$. A similar procedure is used to satisfy the boundary conditions (8) corresponding to $s=2$ on the surfaces $x_2^{(n)}=0,l_2$.

Substitution from (26) into (27) and the other equations that enforce the boundary conditions on the top surface, the interfaces between adjoining laminae and the side surfaces leads to an infinite set of linear algebraic equations for the infinitely many unknown coefficients $\mathbf{c}^{(n,s)}_{(k_1,k_2)}$ and $\mathbf{d}^{(n,s)}_{(k_1,k_2)}$. A general theory for the solution of the resulting infinite system of equations does not exist. However, reasonably accurate results can be obtained by truncating k_1 and k_2 in (24) to K_1 and K_2 terms, respectively. The series involving summations over k_1 and k_2 in the expression for $[\mathbf{u}^{(n,1)},\phi^{(n,1)}]$ are truncated to K_2 and $K_3^{(n)}$ while those for $[\mathbf{u}^{(n,2)},\phi^{(n,2)}]$ are truncated to $K_3^{(n)}$ and K_1 terms. In general, we try to maintain approximately the same period of the largest harmonic on all interfaces and boundaries by choosing $K_3^{(n)}=\text{Ceil}(K_1 l_3^{(n)}/l_1)$ and $K_2=\text{Ceil}(K_1 l_2/l_1)$, where $\text{Ceil}(y)$ equals the smallest integer greater than or equal to y. Thus, the size of the truncated matrix will depend solely on the choice of K_1.

6 Results and Discussion

Problems studied by Heyliger [20] and Heyliger et al. [10] were analyzed by the present method with $K_1=200$, and the two sets of results matched very well. As shown below, satisfactory results can be computed even with $K_1=50$.

We present results for laminated plates with each lamina made of either graphite-epoxy ([22]), PVDF ([10,32]) or PZT-5A ([22]) with nonzero values of material variables listed in Table 1. We treat the graphite-epoxy layer as a piezoelectric material with the piezoelectric moduli set equal to zero, and solve for the electric field in the graphite-epoxy layer which is uncoupled from the elastic field. In this section we denote the thickness of the laminate by $H(=L_3)$.

Although our solution is applicable to laminates with general boundary conditions on all four edges, here we consider laminated piezoelectric plates that are simply supported and electrically grounded on the opposite edges $x_2=0$ and L_2, i.e., $u_1=u_3=0$, $\sigma_{22}=0$, $\phi=0$, and the other two edges subjected to various boundary conditions. The reason for this choice is that if each

Table 1 Nonvanishing material properties of the graphite-epoxy, PVDF, and PZT-5A

Property	0° Graphite-epoxy	0° PVDF	PZT-5A
C_{1111}(GPa)	183.443	238.24	99.201
C_{2222}(GPa)	11.662	23.60	99.201
C_{3333}(GPa)	11.662	10.64	86.856
C_{1122}(GPa)	4.363	3.98	54.016
C_{1133}(GPa)	4.363	2.19	50.778
C_{2233}(GPa)	3.918	1.92	50.778
C_{2323} (GPa)	2.870	2.15	21.100
C_{3131}(GPa)	7.170	4.40	21.100
C_{1212}(GPa)	7.170	6.43	22.593
e_{311} (Cm^{-2})	0	-0.130	-7.209
e_{322} (Cm^{-2})	0	-0.145	-7.209
e_{333} (Cm^{-2})	0	-0.276	15.118
e_{223} (Cm^{-2})	0	-0.009	12.322
e_{113} (Cm^{-2})	0	-0.135	12.322
$\epsilon_{11}(10^{-10}$ F/m)	153.0	1.1068	153.0
$\epsilon_{22}(10^{-10}$ F/m)	153.0	1.0607	153.0
$\epsilon_{33}(10^{-10}$ F/m)	153.0	1.0607	150.0

Table 2 Convergence study for a [0 deg PVDF/90 deg PVDF] square laminate subjected to mechanical load, $L_1/H=5$

K_1	$\tilde{u}_1(H)$	$\tilde{u}_3(H^{\pm}/2)$	$\tilde{\sigma}_{11}(H)$	$\tilde{\sigma}_{13}(H^{\pm}/2)$	$\tilde{\phi}(3H/4)$	$\tilde{D}_3(H)$	$\tilde{U}$
25	−0.244 744	6.803 677 6.803 467	1.690 039	0.232 611 0.232 731	−0.221 222	2.784 989	1.028 037
50	−0.244 314	6.803 253 6.803 291	1.676 032	0.233 188 0.233 036	−0.220 854	2.758 772	1.028 027
100	−0.244 253	6.803 264 6.803 255	1.681 768	0.232 722 0.232 736	−0.220 854	2.772 986	1.028 026
150	−0.244 243	6.803 245 6.803 250	1.678 181	0.232 879 0.232 921	−0.220 851	2.764 628	1.028 026
200	−0.244 237	6.803 248 6.803 245	1.680 697	0.233 243 0.233 243	−0.220 850	2.770 503	1.028 025

lamina is made of a monoclinic material of crystal class m (see [33]), then the boundary conditions at the edges $x_2=0,L_2$ are identically satisfied by the following mechanical displacement and electric potential distributions:

$$\mathbf{u}=[f_1(x_1,x_3)\sin(\lambda\pi x_2/L_2),f_2(x_1,x_3)\times\cos(\lambda\pi x_2/L_2),f_3(x_1,x_3)\sin(\lambda\pi x_2/L_2)]^T$$
$$\phi=f_4(x_1,x_3)\sin(\lambda\pi x_2/L_2). \tag{28}$$

The equilibrium and charge equations will yield coupled partial differential equations for $f_\alpha(x_1,x_3)$, $(\alpha=1,\ldots,4)$. Thus, we need only one term, namely $k_2=\lambda$, in the x_2-direction in the double Fourier series expansion and the size of the truncated matrix is greatly reduced. PVDF and graphite-epoxy are orthorhombic materials of crystal class mm2 and PZT-5A is a hexagonal material of crystal class 6mm, all of which belong to the group of monoclinic materials of crystal class m.

The edges $x_1=0,L_1$ may be either clamped (C) with $u_1=u_2=u_3=0$, or free of traction (F) with $\sigma_{11}=\sigma_{12}=\sigma_{13}=0$ or simply supported (S) with $u_1=u_3=0$, $\sigma_{11}=0$. We append P when the edge is electrically grounded ($\phi=0$) or D when the normal component of the electric displacement is set to zero, i.e., $D_1=0$. For example, FP-FP denotes a laminated plate that is traction-free and electrically grounded on the edges $x_1=0$ and L_1. In this notation, all analytical three-dimensional solutions available to date ([18–21]) are for piezoelectric laminates that have all four edges subjected to SP boundary conditions.

6.1 PVDF Cross-Ply Laminate. Consider a two-ply square laminate with the bottom and top layers made of 0 deg PVDF and 90 deg PVDF, respectively. The material properties of the 90 deg PVDF may be inferred from those of the 0 deg PVDF given in Table 1. Both layers are of equal thickness, $L_1/H=5$ and $L_1=1.0$ m. The interface is electroded and conditions (11) are enforced with $f(x_1,x_2)=0$ on $x_3=H/2$. The following two electromechanical loading cases are considered:

(i) Mechanical load:

$$\boldsymbol{\sigma}_3(x_1,x_2,H)=[0,0,q_0/2]^T\sin(\pi x_1/L_1)\sin(\pi x_2/L_2) \tag{29}$$
$$\boldsymbol{\sigma}_3(x_1,x_2,0)=[0,0,-q_0/2]^T\sin(\pi x_1/L_1)\sin(\pi x_2/L_2)$$
$$\phi(x_1,x_2,H)=\phi(x_1,x_2,0)=0;$$

(ii) Electrical load:

$$\phi(x_1,x_2,H)=\phi(x_1,x_2,0)=0.5\phi_0\sin(\pi x_1/L_1)\sin(\pi x_2/L_2),$$
$$\boldsymbol{\sigma}_3(x_1,x_2,H)=\boldsymbol{\sigma}_3(x_1,x_2,0)=\mathbf{0}. \tag{30}$$

Results for combined mechanical and electrical loads can be obtained by superposition of the solutions corresponding to loads (i) and (ii).

The effect of truncation of the series on the accuracy of the solution is investigated for the two-ply laminated plate with two opposite edges simply supported and grounded and the other two edges subjected to FD-FD boundary conditions. Computed results for various quantities at specific points in the laminate are listed in Table 2 for the case of the mechanical loading. The following nondimensionalization has been used:

$$[\tilde{u}_1(x_3),\tilde{u}_3(x_3)]=\frac{C_0}{L_1q_0}\left[u_1\left(\frac{L_1}{4},\frac{L_2}{2},x_3\right),u_3\left(\frac{L_1}{2},\frac{L_2}{2},x_3\right)\right],$$
$$[\tilde{\sigma}_{11}(x_3),\tilde{\sigma}_{13}(x_3)]=\frac{1}{q_0}\left[\sigma_{11}\left(\frac{L_1}{2},\frac{L_2}{2},x_3\right),\sigma_{13}\left(\frac{L_1}{8},\frac{L_2}{2},x_3\right)\right],$$
$$[\tilde{\sigma}_{23}(x_3),\tilde{\sigma}_{33}(x_3)]=\frac{1}{q_0}\left[\sigma_{23}\left(\frac{L_1}{8},0,x_3\right),\sigma_{33}\left(\frac{L_1}{2},\frac{L_2}{2},x_3\right)\right],$$
$$\tilde{\phi}(x_3)=\frac{1000e_0}{L_1q_0}\phi\left(\frac{L_1}{2},\frac{L_2}{2},x_3\right), \tag{31}$$
$$\tilde{D}_3(x_3)=\frac{C_0}{e_0q_0}D_3\left(\frac{L_1}{2},\frac{L_2}{2},x_3\right),$$
$$\tilde{U}=\frac{UC_0}{q_0^2L_1^3},$$

where $C_0=23.60$ GPa and $e_0=-0.145\,\mathrm{Cm}^{-2}$ are representative values of the elastic and piezoelectric moduli for a PVDF (Table

Table 3 Convergence study for a [0 deg PVDF/90 deg PVDF] square laminate subjected to electrical load, $L_1/H=5$

K_1	$\hat{u}_1(H)$	$\hat{u}_3(H^{\pm}/2)$	$\hat{\sigma}_{11}(0)$	$\hat{\sigma}_{13}(H^{\pm}/2)$	$\hat{\phi}(3H/4)$	$\hat{D}_3(H)$	$\hat{U}$
25	0.664 816	−1.541 948 −1.540 149	2.454 258	0.362 439 0.362 538	0.244 276	−6.727 594	0.708 785
50	0.665 182	−1.541 010 −1.541 439	2.440 661	0.359 968 0.360 036	0.244 286	−6.791 965	0.708 884
100	0.665 181	−1.541 428 −1.541 314	2.454 716	0.362 149 0.361 994	0.244 286	−6.757 952	0.708 908
150	0.665 180	−1.541 397 −1.541 450	2.447 524	0.361 835 0.361 693	0.244 286	−6.777 602	0.708 913
200	0.665 201	−1.541 454 −1.541 424	2.453 644	0.360 644 0.360 642	0.244 286	−6.763 651	0.708 914

1). These results show that the mechanical displacements $\tilde{u}_1$ and $\tilde{u}_3$, transverse shear stress $\tilde{\sigma}_{13}$ and electric potential $\tilde{\phi}$ converge rapidly, but the axial stress $\tilde{\sigma}_{11}$ and transverse component $\tilde{D}_3$ of the electric displacement converge slowly. The upper and lower values of the transverse displacement $\tilde{u}_3$ and transverse shear stress $\tilde{\sigma}_{13}$ are at corresponding points on the two sides of the interface between the laminae. As is evident, the interface continuity conditions are also satisfied very well with increasing K_1. The difference in the values of $\tilde{\sigma}_{11}(H)$ and $\tilde{\sigma}_{13}(H^+/2)$ for $K_1 = 150$ and 200 is 0.15 percent and 0.16 percent, respectively. The total stored energy $\tilde{U}$ exhibits monotonic convergence from above and has converged to four decimal places for $K_1 = 50$. While k_0 in (24) was chosen to be 0.5 for this study, a similar convergence behavior was observed for other values of k_0. Table 3 presents a convergence study for the case of electric loading wherein the nondimensional variables are defined as

$$[\hat{u}_1(x_3), \hat{u}_3(x_3)] = \frac{C_0}{e_0 \phi_0}\left[u_1\left(\frac{L_1}{4}, \frac{L_2}{2}, x_3\right), u_3\left(\frac{L_1}{2}, \frac{L_2}{2}, x_3\right)\right],$$

$$[\hat{\sigma}_{11}(x_3), \hat{\sigma}_{13}(x_3)] = \frac{L_1}{e_0 \phi_0}\left[\sigma_{11}\left(\frac{L_1}{2}, \frac{L_2}{2}, x_3\right), \sigma_{13}\left(\frac{L_1}{8}, \frac{L_2}{2}, x_3\right)\right],$$

$$[\hat{\sigma}_{23}(x_3), \hat{\sigma}_{33}(x_3)] = \frac{L_1}{e_0 \phi_0}\left[\sigma_{23}\left(\frac{L_1}{8}, 0, x_3\right), \sigma_{33}\left(\frac{L_1}{8}, \frac{L_2}{2}, x_3\right)\right],$$

$$\hat{\phi}(x_3) = \frac{1}{\phi_0}\phi\left(\frac{L_1}{2}, \frac{L_2}{2}, x_3\right), \tag{32}$$

$$\hat{D}_3(x_3) = \frac{L_1 C_0}{100 e_0^2 \phi_0} D_3\left(\frac{L_1}{2}, \frac{L_2}{2}, x_3\right), \quad \hat{U} = \frac{U}{\phi_0^2 \epsilon_0 L_1}.$$

Here $\epsilon_0 = 1.0607 \times 10^{-10}$ F/m is the typical magnitude of the electric permittivity of a PVDF. In this case too, the mechanical displacements, electric potential, and transverse shear stress converge faster than the longitudinal stress and transverse component of the electric displacement. The total stored energy for the electrical loading converges monotonically from below, in contrast to the case of the mechanical loading where the convergence is from above. Thus for the combined mechanical and electrical loading, the total stored energy may not converge monotonically. Results presented below are for $K_1 = 200$.

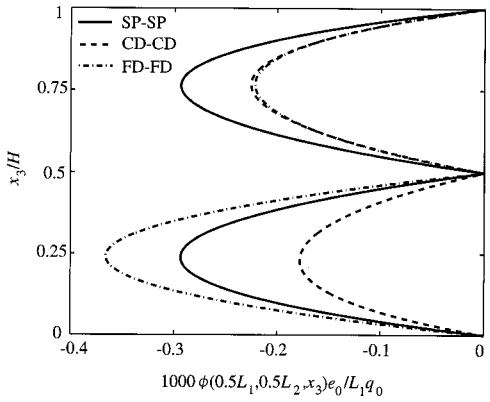

Fig. 2 Influence of the boundary conditions on the through-thickness distribution of the potential due to a mechanical load for the [0 deg PVDF/90 deg PVDF] laminate

Electric potential is induced in the laminate due to the application of the mechanical load. The through-thickness distribution of the electric potential at the midspan is shown in Fig. 2 corresponding to three different boundary conditions. The electric potential distribution within each layer is parabolic and the magnitude depends on the boundary condition at the edge. Figure 3 depicts for the mechanical and electric loading the through-thickness distribution of the transverse displacement, longitudinal stress, and transverse shear stress for three different sets of boundary conditions at the edges $x_1 = 0, L_1$. The transverse displacement essentially remains independent of the thickness coordinate for mechanical loading, as is usually assumed in the theory of laminated elastic plates. When subjected to an electric load, the top and bottom surfaces exhibit larger transverse displacement than the midplane. The longitudinal stress σ_{11} is discontinuous across the

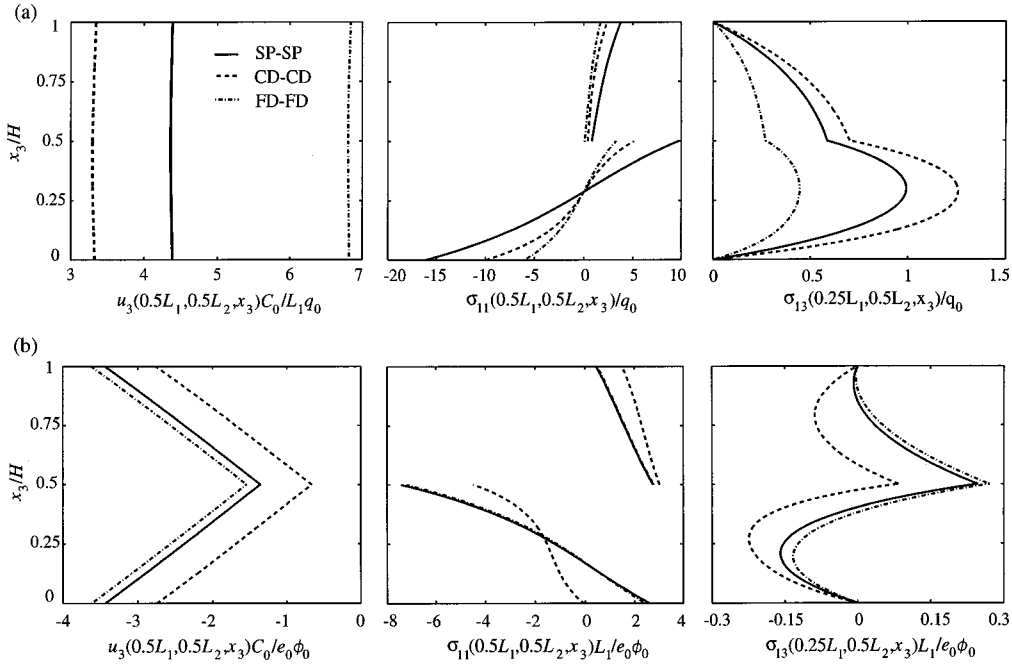

Fig. 3 Influence of the boundary conditions on the through-thickness distribution of the transverse displacement, longitudinal stress, and transverse shear stress for the [0 deg PVDF/90 deg PVDF] laminate subjected to (*a*) mechanical load and (*b*) electrical load

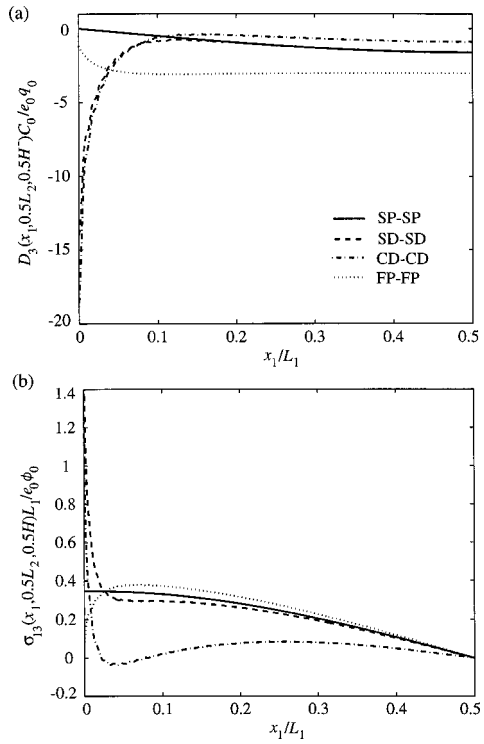

Fig. 4 Axial variation on the interface of the [0 deg PVDF/90 deg PVDF] laminate (*a*) transverse electric displacement for the mechanical load and (*b*) transverse shear stress for the electric load

interface due to the change in material properties between the laminae. The longitudinal stress is largest in magnitude on the bottom surface for the mechanical loading and on the 0 deg PVDF side of the interface for the electrical loading. The maximum transverse shear stress σ_{13} occurs at about $x_3 \simeq 0.3H$ for the case of the mechanical loading and is largest when the edges are clamped. When subjected to the electrical load, the maximum transverse shear stress occurs on the interface when the edges are simply supported or traction-free and at $x_3 \simeq 0.3H$ when the edges are clamped.

The axial variation of the induced electric displacement component D_3 on the 0 deg PVDF side of the interface is shown in Fig. 4(*a*) for the mechanical loading. The result is plotted over only half the span since it is symmetric about the midspan. When the edges are simply supported and grounded, i.e., SP boundary conditions, D_3 is largest at the midspan and vanishes at the edges $x_1 = 0, L_1$. In the case of SD and CD boundary conditions, D_3 is essentially uniform over the middle eight-tenth of the span but varies from -19 at $x_1 = 0$ to -1 at $x_1 = 0.1L_1$. This rapid change in D_3 near the edges has not been investigated in detail. The large electric displacements could lead to dielectric failure at the edges when the laminate is subjected to only a moderate mechanical load. The shear stress σ_{13} on the interface due to an electric load is antisymmetric about the midspan and is shown in Fig. 4(*b*). A thorough study of this rapid change in σ_{13} at the edges except when they are simply supported and grounded, necessitates the use of special functions and has not been pursued here. The shear stress at the edges seems to be singular for SD and CD boundary conditions and could lead to delamination failure at the edges even for moderate electrical loads. Such large stresses were also observed at the edges of piezoelectric layers by Batra et al. [34] and Robbins and Reddy [8].

Figures 5(*a*) and (*b*) show the transverse deflection of the midplane for the case of the mechanical and electrical load, respectively, when two of the edges are clamped or traction-free. The transverse deflection of a laminate that is simply supported and electrically grounded on all four edges has the double-sinusoidal shape of the applied mechanical (29) or the electrical load (30), and is not depicted. This is not true when two of the edges are clamped or traction-free. The transverse deflection at the center of the plate is largest when two edges are traction-free and smallest when they are clamped. The transverse deflection near the clamped edges is opposite in direction to that at the center of a

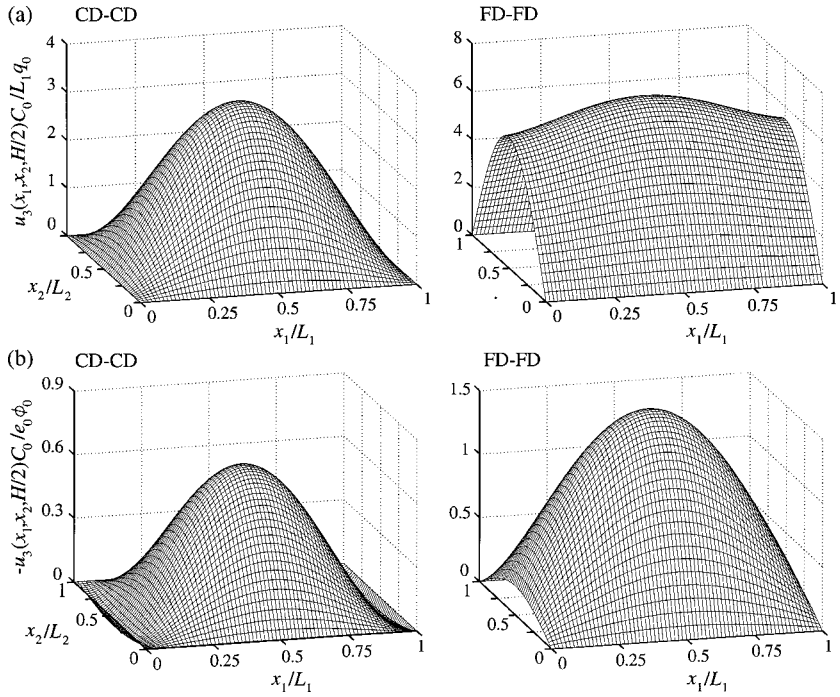

Fig. 5 Influence of the boundary conditions on the midplane transverse displacement of the [0 deg PVDF/90 deg PVDF] laminate for (*a*) mechanical load and (*b*) electrical load

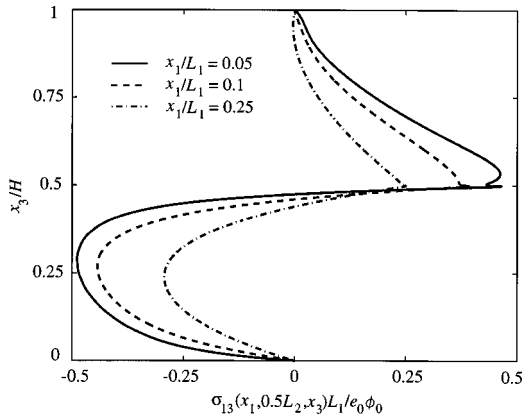

Fig. 6 Through-thickness variation of the transverse shear stress on three sections of a [0 deg PVDF/90 deg PVDF] laminate with layerwise variation of boundary conditions

Table 4 Mechanical displacement, stresses, electric potential, and electric displacement at specific locations of a square [0 deg PVDF/90 deg PVDF] laminate for various boundary conditions, $L_1/H=5$

Variable	SP-SP	CD-CD	FD-FD	(CD,FD)-(CD,FD)
$\tilde{u}_1(H)$	-0.785	-0.406	-0.244	-0.617
$\hat{u}_3(H/2)$	4.360	3.298	6.803	3.676
$\tilde{\sigma}_{11}(H)$	3.770	2.361	1.681	3.080
$\tilde{\sigma}_{13}(H/2)$	0.766	0.902	0.233	0.600
$\tilde{\sigma}_{23}(H/2)$	0.317	0.186	0.908	0.239
$\tilde{\sigma}_{33}(H/2)$	0.000	0.051	-0.089	0.057
$\tilde{\phi}(H/4)$	-0.293	-0.177	-0.365	-0.205
$\tilde{D}_3(0)$	-3.432	-3.147	-4.157	-3.247
$\hat{u}_1(H)$	0.676	0.382	0.665	0.620
$\hat{u}_3(H/2)$	-1.357	-0.664	-1.541	-1.046
$\hat{\sigma}_{11}(0)$	2.642	-0.017	2.454	0.738
$\hat{\sigma}_{13}(H/2)$	0.321	0.042	0.361	0.376
$\hat{\sigma}_{23}(H/2)$	0.133	0.232	0.170	0.183
$\hat{\sigma}_{33}(H/2)$	0.000	0.039	-0.004	-0.094
$\hat{\phi}(3H/4)$	0.244	0.244	0.244	0.244
$\hat{D}_3(H)$	-6.770	-6.758	-6.764	-6.762

CD-CD laminate when subjected to the electric load.

The present method can also analyze laminated plates when the edges of each lamina are subjected to boundary conditions different from those on the corresponding edge of the adjoining laminae. As an example, consider the configuration denoted by (CD, FD)-(CD,FD) wherein the bottom lamina of the two-ply laminated plate is clamped at $x_1=0$ and L_1 and the corresponding edges of the top lamina are traction-free with the normal component of the electric displacement set equal to zero for both laminae. Figure 6 depicts the through-thickness distribution of the transverse shear stress σ_{13} on three sections when the laminate is subjected to the electric load. As we approach the edge, the point of the maximum transverse shear stress in the 0 deg PVDF lamina shifts closer to the interface and it is accompanied by large gradients. Numerical results at specific points in the laminate for four sets of boundary conditions given in Table 4 can be used to compare predictions from various plate theories and finite element solutions.

6.2 Graphite-Epoxy and PZT-5A Hybrid Laminate. Consider a three-ply square laminate with the bottom and middle layers made of graphite-epoxy with fibers parallel to the x_1 and x_2 directions, respectively, and the topmost layer made of PZT-5A, i.e., [0 deg GE/90 deg GE/PZT-5A]. The graphite-epoxy layers are of thickness $0.4H$, the PZT-5A layer is of thickness $0.2H$, $L_1/H=5$ and $L_1=1.0$ m. Interface conditions (10) are assumed between the graphite-epoxy laminae. The interface between the PZT-5A and its neighboring graphite-epoxy lamina is electroded and grounded. The bottom surface of the laminate is traction-free and the following two electromechanical loadings are considered for the top surface:

(i) Mechanical load: $\boldsymbol{\sigma}_3(x_1,x_2,H)=[0,0,q_0]^T \sin(\pi x_1/L_1)\times\sin(\pi x_2/L_2), \phi(x_1,x_2,H)=0$,

(ii) Electrical load: $\phi(x_1,x_2,H)=\phi_0 \sin(\pi x_1/L_1)\times\sin(\pi x_2/L_2)$, $\boldsymbol{\sigma}_3(x_1,x_2,H)=\mathbf{0}$.

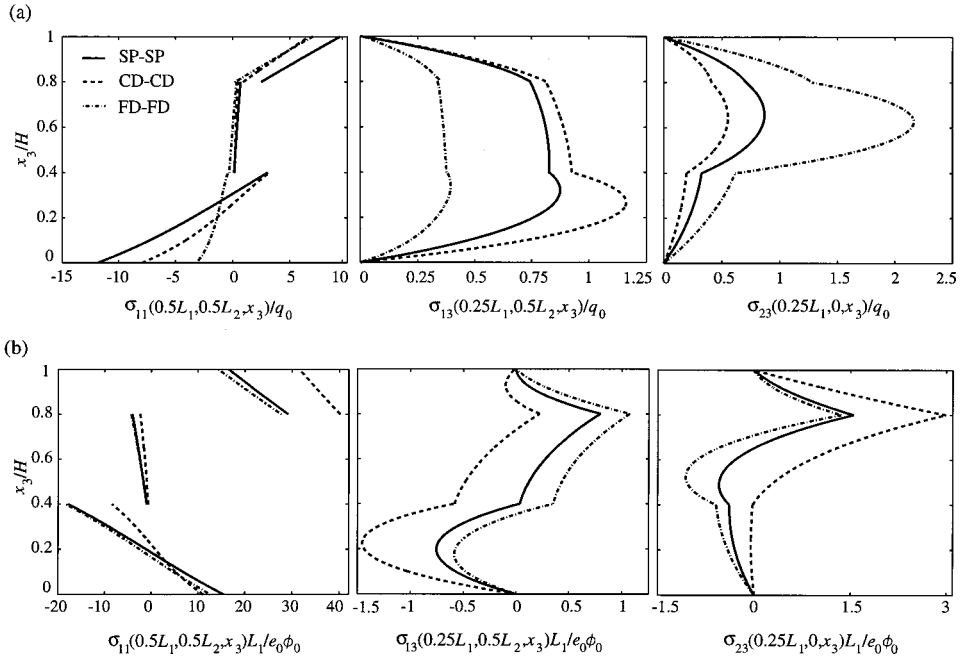

Fig. 7 Influence of the boundary conditions on the through-thickness distribution of the stresses for the [0 deg GE/90 deg GE/PZT-5A] laminate, (*a*) mechanical load and (*b*) electrical load

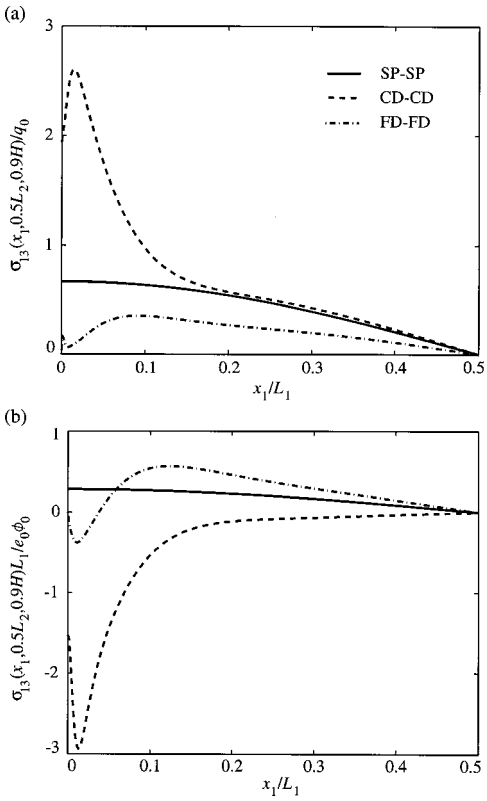

Fig. 8 Axial variation of the transverse shear stress on the midsurface of the PZT-5A lamina of the [0 deg GE/90 deg GE/PZT-5A] laminate for (*a*) mechanical load and (*b*) electrical load

The nondimensionalizations (31) and (32) are used with $C_0 = 99.201$ GPa and $e_0 = -7.209\ \mathrm{Cm}^{-2}$; they are representative values of the elastic and piezoelectric moduli of a PZT-5A. Figure 7(*a*) depicts the through-thickness distribution of stresses for the mechanical loading. The longitudinal stress is approximately piecewise affine. The transverse shear stress σ_{13} is larger when the edges are clamped than when they are simply supported or traction-free. The shear stress σ_{23} attains the maximum value in the 90 deg GE lamina and is largest when the edges are traction-free. The corresponding through-thickness variation of the stresses for the electric loading is shown in Fig. 7(*b*). The longitudinal stress σ_{11} on the PZT-5A side of the interface is larger than that at other points. The maximum value of the transverse shear stress σ_{13} is at the interface between the PZT and the substrate for simply supported and traction-free boundary conditions and occurs in the 0 deg GE lamina for the clamped boundary condition. The maximum value of the transverse shear stress σ_{23} is at the interface between the PZT and the substrate for all three boundary conditions. Figures 8(*a*) and (*b*) show the axial variation of the transverse shear stress σ_{13} on the mid-surface of the PZT-5A layer for three different boundary conditions. They exhibit rapid variations at the edges except when the edges are simply supported and electrically grounded. Further results at specific points are given in Table 5 for the three sets of boundary conditions.

Table 5 Mechanical displacement, stresses, electric potential, and electric displacement at specific locations of a square [0 deg GE/90 deg GE/PZT-5A] laminate for various boundary conditions, $L_1/H=5$

Variable	SP-SP	CD-CD	FD-FD
$\tilde{u}_1(H)$	-1.933	-1.082	0.322
$\hat{u}_3(H/2)$	14.325	10.851	35.728
$\tilde{\sigma}_{11}(H)$	9.329	6.652	6.991
$\tilde{\sigma}_{13}(0.8H)$	0.972	1.056	0.388
$\tilde{\sigma}_{23}(0.8H)$	0.384	0.096	1.216
$\tilde{\sigma}_{33}(H/2)$	0.419	0.462	0.356
$\tilde{\phi}(0.9H)$	-3.668	-3.020	-5.117
$\tilde{D}_3(H)$	21.563	13.301	29.818
$\hat{u}_1(H)$	10.161	4.774	10.326
$\hat{u}_3(H/2)$	-25.862	-14.205	-36.291
$\hat{\sigma}_{11}(0)$	15.517	11.115	12.631
$\hat{\sigma}_{13}(0.8H)$	1.042	0.057	1.389
$\hat{\sigma}_{23}(0.8H)$	0.836	2.184	1.419
$\hat{\sigma}_{33}(H/2)$	-0.119	-0.012	-0.112
$\hat{\phi}(0.9H)$	0.505	0.502	0.506
$\hat{D}_3(H)$	-9.878	-9.440	-10.000

7 Conclusions

We have extended the Eshelby-Stroh formalism to study the three-dimensional deformations of thick piezoelectric laminates subjected to arbitrary boundary conditions at the edges. The equations of static, linear, piezoelectricity are satisfied at every point of the body. The analytical solution is in terms of an infinite series; the boundary conditions and the continuity conditions at the interfaces between the laminae are used to determine the unknown coefficients. By keeping a large number of terms in the series solution, the mechanical displacements, stresses, electric potential, and electric displacement can be computed to any desired degree of accuracy.

We have computed results for a two-ply [0 deg PVDF/90 deg PVDF] laminate and a three ply [0 deg GE/90 deg GE/PZT-5A] hybrid laminate that is simply supported and electrically grounded on two opposite edges and subjected to various mechanical and electrical boundary conditions at the remaining two edges. The effect of either mechanically clamping the edges, simply supporting them or leaving them traction free and prescribing either the electric potential or the normal component of the electric displacement to vanish, has been delineated. It is observed that the solution, valid for thick plates, exhibits sharp variations near the edges except when they are simply supported and electrically grounded.

It is found that for the two-ply laminate, the total stored energy converges monotonically from above for the mechanical loading and from below for the electric loading. When the normal component of the electric displacement is prescribed to be zero at the edges, the longitudinal distribution of the component of the electric displacement in the thickness direction exhibits, near the edges, rapid variations in a region of width $0.1L$ where L equals the span of the square plate. However, the width of such a layer equals $0.02L$ for the longitudinal distribution of the transverse shear stress. For a sinusoidal loading on the top surface, the deflected shape of the midsurface is sinusoidal only when all four edges are simply supported. When the two opposite edges of the upper PZT layer are free but that of the lower one are clamped, most severe deformations occur at points on the interface where the free edge meets it.

For the three-ply hybrid laminate, the axial variation of the transverse shear stress on the midsurface of the PZT layer exhibits sharp variations in a region of width $0.1L$ near the clamped and traction free edges. The maximum value of the transverse shear stress occurs at a point on the interface between the PZT and the substrate when the edges are either simply supported or traction-free but at a point within the 0 deg graphite-epoxy lamina when the edges are clamped. The tabulated results presented herein should help establish the validity of various approximate theories. Finally we note that edge singularities, if any, have not been delineated by using special functions. The present technique seems to capture adequately the sharp variations in the fields near the clamped and traction-free edges but neither gives the order of the singularity nor its precise width. The interested reader should consult Ting [26]; Vel and Batra [27] have commented on this for a generalized plane-strain problem.

Acknowledgments

This work was partially supported by the NSF grant CMS9713453 and the ARO grant DAAG55-98-1-0030 to Virginia Polytechnic Institute and State University. R. C. Batra was also supported by an Alexander von Humboldt Award.

References

[1] Crawley, E. F., and de Luis, J., 1987, ''Use of Piezoelectric Actuators as Elements of Intelligent Structures,'' AIAA J., **25**, pp. 1373–1385.
[2] Im, S., and Atluri, S. N., 1989, ''Effects of a Piezo-Actuator on a Finitely Deformed Beam Subjected to General Loading,'' AIAA J., **27**, pp. 1801–1807.
[3] Crawley, E. F., and Anderson, E. H., 1990, ''Detailed Models of Piezoceramic Actuation of Beams,'' J. Intell. Mater. Syst. Struct., **1**, pp. 4–25.
[4] Lee, C. K., 1990, ''Theory of Laminated Piezoelectric Plates for the Design of Distributed Sensors/Actuators. Part 1: Governing Equations and Reciprocal Relationships,'' J. Acoust. Soc. Am., **87**, pp. 1144–1158.
[5] Wang, B. T., and Rogers, C. A., 1991, ''Laminate Plate Theory for Spatially Distributed Induced Strain Actuators,'' J. Compos. Mater., **25**, pp. 433–452.
[6] Huang, J. H., and Wu, T. L., 1996, ''Analysis of Hybrid Multilayered Piezoelectric Plates,'' Int. J. Eng. Sci., **34**, pp. 171–181.
[7] Mitchell, J. A., and Reddy, J. N., 1995, ''A Refined Hybrid Plate Theory for Composite Laminates With Piezoelectric Laminae,'' Int. J. Solids Struct., **32**, pp. 2345–2367.
[8] Robbins, D. H., and Reddy, J. N., 1991, ''Analysis of Piezoelectrically Actuated Beams Using a Layer-Wise Displacement Theory,'' Comput. Struct., **41**, pp. 265–279.
[9] Ha, S. K., Keilers, C., and Chang, F. K., 1992, ''Finite Element Analysis of Composite Structures Containing Piezoceramic Sensors and Actuators,'' AIAA J., **30**, pp. 772–780.
[10] Heyliger, P., Ramirez, G., and Saravanos, D., 1994, ''Coupled Discrete-Layer Finite Elements for Laminated Piezoelectric Plates,'' Commun. Numer. Meth. Eng., **10**, pp. 971–981.
[11] Batra, R. C., and Liang, X. Q., 1997, ''Finite Dynamic Deformations of Smart Structures,'' Comput. Mech., **20**, pp. 427–438.
[12] Vlasov, B. F., 1957, ''On One Case of Bending of Rectangular Thick Plates,'' *Vestnik Moskovskogo Universiteta. Seriëiìa Matematiki, mekhaniki, astronomii, fiziki, khimii*, No. 2, pp. 25–34, (in Russian).
[13] Pagano, N. J., 1969, ''Exact Solutions for Composite Laminates in Cylindrical Bending,'' J. Compos. Mater., **3**, pp. 398–411.
[14] Pagano, N. J., 1970, ''Exact Solutions for Rectangular Bidirectional Composites and Sandwich Plates,'' J. Compos. Mater., **4**, pp. 20–34.
[15] Srinivas, S., and Rao, A. K., 1970, ''Bending, Vibration and Buckling of Simply Supported Thick Orthotropic Rectangular Plates and Laminates,'' Int. J. Solids Struct., **6**, pp. 1463–1481.
[16] Ray, M. C., Rao, K. M., and Samanta, B., 1993, ''Exact Solution for Static Analysis of Intelligent Structures Under Cylindrical Bending,'' Comput. Struct., **47**, pp. 1031–1042.
[17] Heyliger, P., and Brooks, S., 1996, ''Exact Solutions for Laminated Piezoelectric Plates in Cylindrical Bending,'' ASME J. Appl. Mech., **63**, pp. 903–910.
[18] Bisegna, P., and Maceri, F., 1996, ''An Exact Three-Dimensional Solution for Simply Supported Rectangular Piezoelectric Plates,'' ASME J. Appl. Mech., **63**, pp. 628–638.
[19] Lee, J. S., and Jiang, L. Z., 1996, ''Exact Electroelastic Analysis of Piezoelectric Laminae via State Space Approach,'' Int. J. Solids Struct., **33**, pp. 977–990.
[20] Heyliger, P., 1994, ''Static Behavior of Laminated Elastic/Piezoelectric Plates,'' AIAA J., **32**, pp. 2481–2484.
[21] Heyliger, P., 1997, ''Exact Solutions for Simply Supported Laminated Piezoelectric Plates,'' ASME J. Appl. Mech., **64**, pp. 299–306.
[22] Tang, Y. Y., Noor, A. K., and Xu, K., 1996, ''Assessment of Computational Models for Thermoelectroelastic Multilayered Plates,'' Comput. Struct., **61**, pp. 915–933.
[23] Saravanos, D. A., Heyliger, P. R., and Hopkins, D. A., 1997, ''Layerwise Mechanics and Finite Element for the Dynamic Analysis of Piezoelectric Composite Plates,'' Int. J. Solids Struct., **34**, pp. 359–378.
[24] Eshelby, J. D., Read, W. T., and Shockley, W., 1953, ''Anisotropic Elasticity With Applications to Dislocation Theory,'' Acta Metall., **1**, pp. 251–259.
[25] Stroh, A. N., 1958, ''Dislocations and Cracks in Anisotropic Elasticity,'' Philos. Mag., **3**, pp. 625–646.
[26] Ting, T. C. T., 1996, *Anisotropic Elasticity. Theory and Applications*, Oxford University Press, New York.
[27] Vel, S. S., and Batra, R. C., 2000, ''The Generalized Plane Strain Deformations of Thick Anisotropic Composite Laminated Plates,'' Int. J. Solids Struct., **37**, pp. 715–733.
[28] Vel, S. S., and Batra, R. C., 2000, ''Cylindrical Bending of Laminated Plates With Distributed and Segmented Piezoelectric Actuators/Sensors,'' AIAA J., **38**, pp. 857–867.
[29] Vel, S. S., and Batra, R. C., 1999, ''Analytical Solution for Rectangular Thick Laminated Plates Subjected to Arbitrary Boundary Conditions,'' AIAA J., **37**, pp. 1464–1473.
[30] Tiersten, H. F., 1969, *Linear Piezoelectric Plate Vibrations*, Plenum Press, New York.
[31] Suo, Z., Kuo, C.-M., Barnett, D. M., and Willis, J. R., 1992, ''Fracture Mechanics for Piezoelectric Ceramics,'' J. Mech. Phys. Solids, **40**, pp. 739–765.
[32] Tashiro, K., Tadokoro, H., and Kobayashi, M., 1981, ''Structure and Piezoelectricity of Poly(Vinylidene Flouride),'' Ferroelectrics, **32**, pp. 167–175.
[33] Nye, J. F., 1985, *Physical Properties of Crystals*, Oxford University Press, New York.
[34] Batra, R. C., Liang, X. Q., and Yang, J. S., 1996, ''The Vibration of a Simply Supported Rectangular Elastic Plate Due to Piezoelectric Actuators,'' Int. J. Solids Struct., **33**, pp. 1597–1618.

Combinations for the Free-Vibration Behaviors of Anisotropic Rectangular Plates Under General Edge Conditions

Y. Narita
Mem. ASME
Department of Mechanical Engineering,
Hokkaido Institute of Technology,
7-15 Maeda, Teine,
Sapporo 006-8585, Japan
e-mail: narita@hit.ac.jp

The free-vibration behavior of rectangular plates constitutes an important field in applied mechanics, and the natural frequencies are known to be primarily affected by the boundary conditions as well as aspect and thickness ratios. Any one of the three classical edge conditions, i.e., free, simply supported, and clamped edges, may be used to model the constraint along an edge of the rectangle. Along the entire boundary with four edges, there exist a wide variety of combinations in the edge conditions, each yielding different natural frequencies and mode shapes. For counting the total number of possible combinations the present paper introduces the Polya counting theory in combinatorial mathematics. Formulas are derived for counting the exact numbers. A modified Ritz method is then developed to calculate natural frequencies of anisotropic rectangular plates under any combination of the three classical edge conditions and is used to numerically verify the numbers. In this numerical study the number of combinations in the free-vibration behavior is determined for some plate models by using the derived formulas. Results are corroborated by counting the numbers of different sets of the natural frequencies that are obtained from the modified Ritz method. [S0021-8936(00)02203-0]

1 Introduction

The free-vibration analysis of rectangular plates has been of academic and practical interest for many decades, and their free-vibration behavior (i.e., natural frequencies and mode shapes) is considered to be essentially important technical information in structural design. Various books and monographs ([1–4]) reveal that there exist many published papers since the 1960s on the vibration analysis of *isotropic* rectangular plates and that there are also a reasonable number of results for *anisotropic* and *laminated* plates published in the last two decades.

It is well known that the free-vibration behavior of plates is significantly affected by edge constraints, which are modeled typically by using one of the classical conditions of free, simply supported, and clamped edges. There are a wide variety of combinations along the entire boundary of a rectangle when edge conditions are independently assumed along each of four edges. When one fixes the position of the plate and does not allow it to rotate or flip, there can be $3^4=81$ different combinations of boundary conditions (i.e., three different edge conditions along four edges). If the position is not fixed, however, one case is obtained only by rotating or flipping the plate from the original position, and some cases are possible which yield the identical set of natural frequencies.

It is sometimes necessary to grasp the number of possible combinations of structural response in the design situation, and the same is true when the management of structural design data is considered. The theory of counting has advanced in the area of combinatorial mathematics and has potential applications in engineering and physical sciences. Among the combinatorial theories is Polya's theory of counting ([5,6]) which is well known as a classical and basic theory for counting problems involving symmetry.

In connection with this topic in the field of structural vibration, Leissa [7] presented the natural frequencies of isotropic rectangular plates having all possible boundary conditions. It is expected that the number of different combinations increases as complicating effects such as orthotropy or anisotropy are included and the degree of symmetry reduces with the appearance of the principal material axes that are not parallel to the edges. To the author's best knowledge, there are no papers dealing with this kind of counting problem in applied mechanics, although the technical need for solutions of such counting in mechanics seems to be increasing as mentioned.

The present paper deals with the free-vibration analysis of isotropic and anisotropic thin plates having square or rectangular shapes subjected to general boundary conditions by using a modified Ritz method, and introduces the Polya counting method for calculating the number of combinations in the free-vibration behavior. The underlying notion and definition in the counting theory are explained first, and then formulas, called cyclic polynomials, are introduced to actually figure out the numbers for various plate models. A Ritz method is modified and used to incorporate arbitrary combinations of the three classical edge conditions, and computer code is developed to calculate natural frequencies of the plates for some different models. The validity of the present approach is established by showing the exact match between the classified number of calculated frequencies and that of the Polya counting estimates.

2 Polya Counting Theory and Application

2.1 Polya Counting Theory. The basic concept in Polya's theory of counting ([5,6]) is explained first. Consider a ''permutation'' which is a one-to-one mapping from a set D onto D. For an illustrative purpose, a set D is defined as $D=\{1,2,3,4\}$, and a permutation of transposing $1\rightarrow1$, $2\rightarrow4$, $3\rightarrow2$, and $4\rightarrow3$ is expressed as $P=\left(\begin{smallmatrix}1&2&3&4\\1&4&2&3\end{smallmatrix}\right)$. The identical permutation can be ex-

Contributed by the Applied Mechanics Division of THE AMERICAN SOCIETY OF MECHANICAL ENGINEERS for publication in the ASME JOURNAL OF APPLIED MECHANICS and presented at the ASME 17th Biennial Conference on Mechanical Vibration and Noise, Sept. 12–15, 1999, Las Vegas, NV. Manuscript received by the ASME Applied Mechanics Division, June 24, 1999; final revision, Dec. 2, 1999. Associate Technical Editor: J. R. Barber. Discussion on the paper should be addressed to the Technical Editor, Professor Lewis T. Wheeler, Department of Mechanical Engineering, University of Houston, Houston, TX 77204-4792, and will be accepted until four months after final publication of the paper itself in the ASME JOURNAL OF APPLIED MECHANICS.

pressed as $P=(1)(243)$ to mean $(1\rightarrow1)$ and $(2\rightarrow4\rightarrow3\rightarrow2)$, and this cycle notation (see, e.g., [8]) is used hereafter. When P_1 and P_2 are such two permutations, a composition (product) P_1P_2 of P_1 and P_2 also becomes a permutation.

A set G, which is composed of all permutations applicable to a set D, can be considered as a finite group, because it satisfies the associative law and there are a unit and inverse elements in G. A kind of set, which is composed of all possible rotations and flippings of a plate geometry, becomes such a permutation group.

The next important notion in counting is ''class,'' which is explained below by using a simple example. Figure 1(a) shows an isotropic square plate whose edges are numbered as 1 (left-hand edge), 2 (lower edge), 3 (right-hand edge), and 4 (upper edge). Free, simply supported, and clamped edges are denoted hereafter by F, S, and C, respectively, and for example, two plates shown in Fig. 1(b) are represented by CSFF and FCSF.

Suppose that these numbered edges 1, 2, 3, and 4 are fixed in the space. The number of combinations in the boundary condition becomes $3^4=81$ when one of the three edge conditions is applied along each edge. From a viewpoint of structural behaviors, however, two square plates shown in Fig. 1(b) are identical because one case is obtained just by the rotation of ninety-degree from the other. In contrast, one of the plates shown in Fig. 1(c) can be represented by neither rotating nor flipping the other. The two plates shown in Fig. 1(b) are claimed to belong in the same ''class,'' while the two in Fig. 1(c) are said to be ''not in the class.'' In mathematical words, the present paper deals with counting the number of classes when a cyclic permutation group

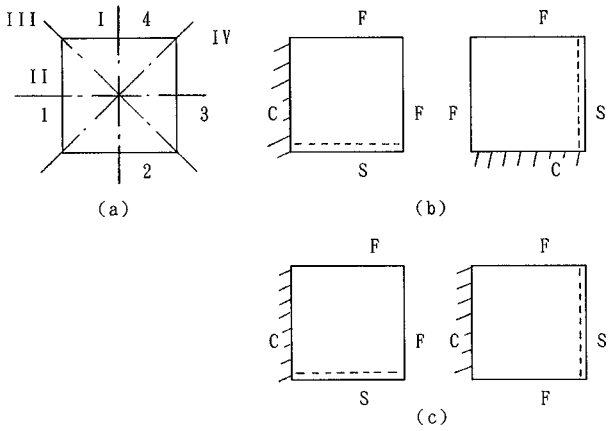

Fig. 1 Class and nonclass of plates with boundary conditions

G acts on a set D. Definitions of finite group, cyclic group, permutation, and others are given, for example, in books by Cohen [9] and Dornhoff and Hohn [6].

In the Polya counting theory, a kind of polynomial called ''cyclic polynomial'' is used to calculate the number of combinations. When a cyclic group, which acts on a finite group D, is denoted by G and $C_k(G)$ is a number of elements in G which have the cyclic number k, then the cyclic polynomial for a group G acting on D is given by

$$Z_G(x)=\frac{1}{|G|}\sum_{k=1}^{|D|}C_k(G)x^k. \tag{1}$$

By using the terminology in the following examples, G is a set of actions of rotation and flipping over the geometry, and $|G|$ is the order of a group which is the number of elements in G. The x represents the number of the different edge conditions applied to each edge.

2.2 Application of the Theory. Figure 2 shows various plate models used in numerical examples. Plate (a) is an isotropic square plate, plate (b) is an isotropic rectangular plate and plate (c) is a specially orthotropic square plate where the principle material axes are parallel to the edges. Plate (d) is a specially orthotropic rectangular plate and plate (e) is a diagonally orthotropic square plate with the principle material axes being parallel to the diagonals. Plate (f) is a skew orthotropic (anisotropic) square plate and plate (g) is a skew orthotropic rectangular plate, where the principal material axis has a certain angle ($\theta\neq0$ deg, 45 deg, 90 deg) with respect to the straight edges. The four edges of the plates are numbered 1 through 4, as explained in Fig. 1(a), and the set of four edges is given by $D=\{1,2,3,4\}$.

For an isotropic square plate (a), a group of actions in which the mapped configurations coincide with the original one by rotation is

$$G_r=\{(1)(2)(3)(4),(1234),(13)(24),(1432)\} \tag{2}$$

where four elements represent counterclockwise rotations of 0 deg, 90 deg, 180 deg, and 270 deg, respectively. Similarly, a group generated by flipping is

$$G_f=\{(1)(3)(24),(2)(4)(13),(12)(34),(14)(23)\} \tag{3}$$

where the four elements represent flipping with respect to the axes II, I, IV, and III, respectively, in Fig. 1(a).

A union $G=G_r+G_f$ is a cyclic group with a unit element $(1)(2)(3)(4)$ and G_r is a subgroup of G. By substitution of G with Eqs. (2), (3) into Eq. (1), one gets a cyclic polynomial for plate (a) as

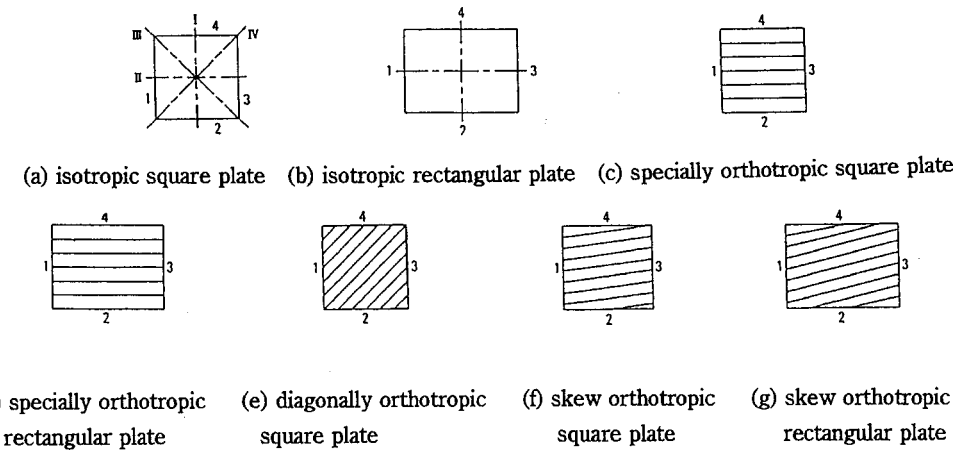

Fig. 2 Numerical examples (solid lines indicate the major principal material axis)

Table 1 Cyclic polynomials and the number of combinations for plate models shown in Fig. 2.

Plate Model	Cyclic Polynomial	$Z_G(x)$ x=2	x=3	x=4
(a)	$Z_G(x)=\frac{1}{8}(x^4+2x^3+3x^2+2x)$	6	21	55
(b)(c)(d)	$Z_G(x)=\frac{1}{4}(x^4+2x^3+x^2)$	9	36	100
(e)	$Z_G(x)=\frac{1}{4}(x^4+3x^2)$	7	27	76
(f)(g)	$Z_G(x)=\frac{1}{2}(x^4+x^2)$	10	45	136

$$Z_G(x)=\frac{1}{8}(x^4+2x^3+3x^2+2x) \tag{4}$$

where $C_4(G)=1$, a coefficient of x^4, is determined from *one* element (with $k=4$) of (1)(2)(3)(4) in Eq. (2), $C_3(G)=2$ is from *two* elements ($k=3$) of (1)(3)(24) and (2)(4)(13) in Eq. (3), and so on.

When one considers combinations for two different kinds of conditions along each edge, for instance free edge and clamped edge, $Z_G(2)=6$ is obtained from Eq. (4) for $x=2$. Likewise, combinations of $Z_G(3)=21$ and $Z_G(4)=55$ can be calculated for three (e.g., F, S, and C) and four (e.g., F, S, C, and an elastic constraint of some degree) edge conditions, respectively.

For plate (*b*), the axial symmetry about the III and IV axes disappear and G_r and G_f become

$$G_r=\{(1)(2)(3)(4),(13)(24)\} \tag{5a}$$

$$G_f=\{(1)(3)(24),(2)(4)(13)\} \tag{5b}$$

The union of $G=G_r+G_f$ determines a cyclic polynomial for this plate, and $Z_G(3)=36$ is given for $x=3$. Although the reference of Leissa [7] claims that 21 cases (not 36 cases) exist for a rectangular plate, the aspect ratio a/b is varied as necessary in that paper, while the aspect ratio is fixed in the present result of $Z_G(3)=36$. For example, a FSSF plate with aspect ratio $a/b=2$ is regarded as identical as FFSS plate with $a/b=0.5$ in the reference ([7]).

Group (5) is also applicable to plate (*c*) (specially orthotropic square plate) and plate (*d*) (specially orthotropic rectangular plate). It is interesting to note that the number of combinations for isotropic plates differs between the square ($a=b$) and rectangular ($a\neq b$) plates, but the specially orthotropic plates show no difference in the number of combination between the two plates.

For diagonally orthotropic square plate (*e*) where the principal material axes coincide with diagonals, G_r and G_f are

$$G_r=\{(1)(2)(3)(4),(13)(24)\} \tag{6a}$$

$$G_f=\{(12)(34),(14)(23)\} \tag{6b}$$

and $G=G_r+G_f$ yields a fewer number of combinations than that of plate (*c*).

In both plates (*f*) and (*g*), where skew orthotropy is assumed (not diagonally), flipping does not exist, i.e., $G_f=\phi$ (empty set). All these cyclic polynomials and values of $Z_G(x)$ with $x=2$, 3 and 4 are presented in Table 1 for plates (*a*) through (*g*).

3 Free-Vibration Analysis of Anisotropic Plates

A semi-analytical solution is developed here by using the method of Ritz for the verification of the counting results in this numerical study, because such an analysis-based solution has a low computational cost and easiness in varying parameters, in contrast to numerical methods such as the finite element method. Figure 3 shows an anisotropic rectangular plate and the coordinate system where the major and minor principal axes are denoted by the L and T axes. The dimension of the plate is given by $a\times b\times h$ (thickness). The stress and strain relation is given by

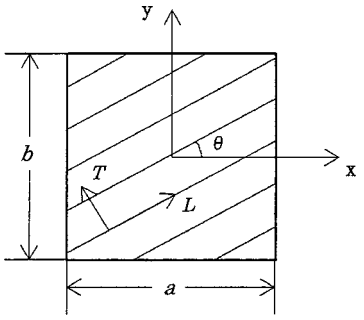

Fig. 3 Rectangular plate and coordinate system

$$\begin{Bmatrix}\sigma_L\\ \sigma_T\\ \tau_{LT}\end{Bmatrix}=\begin{bmatrix}Q_{11}&Q_{12}&0\\ Q_{12}&Q_{22}&0\\ 0&0&Q_{66}\end{bmatrix}\begin{Bmatrix}\varepsilon_L\\ \varepsilon_T\\ \gamma_{LT}\end{Bmatrix} \tag{7}$$

where the matrix elements are given by

$$Q_{11}=\frac{E_L}{1-\nu_{LT}\nu_{TL}},\quad Q_{22}=\frac{E_T}{1-\nu_{LT}\nu_{TL}},$$

$$Q_{12}=\frac{\nu_{TL}E_L}{1-\nu_{LT}\nu_{TL}},\quad Q_{66}=G_{LT} \tag{8}$$

with E_L and E_T are moduli of longitudinal elasticity in the L and T directions, respectively, G_{LT} is a shear modulus and ν_{LT} is a Poisson's ratio. Relation (7) can be transferred to

$$\begin{Bmatrix}\sigma_x\\ \sigma_y\\ \tau_{xy}\end{Bmatrix}=\begin{bmatrix}\overline{Q}_{11}&\overline{Q}_{12}&\overline{Q}_{16}\\ \overline{Q}_{12}&\overline{Q}_{22}&\overline{Q}_{26}\\ \overline{Q}_{16}&\overline{Q}_{26}&\overline{Q}_{66}\end{bmatrix}\begin{Bmatrix}\varepsilon_x\\ \varepsilon_y\\ \gamma_{xy}\end{Bmatrix} \tag{9}$$

where the stresses and strains are given with respect to the x and y-axes ([10,11]).

If one considers the small-amplitude (linear) free vibration of a thin plate, the deflection w may be written by

$$w(x,y,t)=W(x,y)\sin\omega t \tag{10}$$

where W is the amplitude and ω is a radian frequency of the plate. Then, the maximum strain energy due to the bending is expressed by

$$U_{\max}=\frac{1}{2}\int\int_A\{\kappa\}^T\begin{bmatrix}D_{11}&D_{12}&D_{16}\\ D_{12}&D_{22}&D_{26}\\ D_{16}&D_{26}&D_{66}\end{bmatrix}\{\kappa\}dA \tag{11}$$

where the D_{ij} are the bending stiffnesses defined by $D_{ij}=(h^3/12)\overline{Q}_{ij}$ and $\{\kappa\}$ is a curvature vector

$$\{\kappa\}=\left\{-\frac{\partial^2W}{\partial x^2}-\frac{\partial^2W}{\partial y^2}-2\frac{\partial^2W}{\partial x\partial y}\right\}^T. \tag{12}$$

The maximum kinetic energy is given by

$$T_{\max}=\frac{1}{2}\rho\omega^2\int\int_A W^2dA \tag{13}$$

where ρ is the mass per unit area.

For the sake of simplicity, nondimensional quantities are introduced as

$$\xi=\frac{2x}{a},\quad \eta=\frac{2y}{b}\ \text{(nondimensional coordinates)},$$

$$\alpha = \frac{a}{b} \text{ (aspect ratio)},$$

$$D_0 = \frac{E_T h^3}{12(1-\nu_{LT}\nu_{TL})} \text{ (reference stiffness)}, \tag{14}$$

$$d_{ij} = \frac{D_{ij}}{D_0} \text{ (nondimensional stiffness)}$$

$$\Omega = \omega a^2 \sqrt{\frac{\rho}{D_0}} \text{ (frequency parameter)}.$$

The next step in the Ritz method is to assume that the amplitude is

$$W(\xi,\eta) = \sum_{m=0}^{M-1}\sum_{n=0}^{N-1} A_{mn} X_m(\xi) Y_n(\eta) \tag{15}$$

where A_{mn} are unknown coefficients, and $X_m(\xi)$ and $Y_n(\eta)$ are the functions modified later so that any kinematical boundary conditions are satisfied at the edges ([12,13]).

After substituting Eq. (15) into the energies (11) and (13), the stationary value is obtained by

$$\frac{\partial}{\partial A_{\bar{m}\bar{n}}}(T_{\max} - U_{\max}) = 0 \quad (\bar{m} = 0,1,2,\ldots;\ \bar{n} = 0,1,2,\ldots). \tag{16}$$

Then the eigenvalue equation that contains the frequency parameter Ω is derived as

$$\sum_{m=0}^{M-1}\sum_{n=0}^{N-1} [d_{11} I^{(2200)} + \alpha^2 d_{12}(I^{(2002)} + I^{(0220)}) + \alpha^4 I^{(0022)} + 2\alpha d_{16}(I^{(2101)} + I^{(1210)}) + 2\alpha^3 d_{26}(I^{(0121)} + I^{(1012)}) + 4\alpha^2 d_{66} I^{(1111)} - \Omega^2 I^{(0000)}]_{m\bar{m}n\bar{n}} \cdot A_{mn} = 0$$
$$(\bar{m} = 0,1,2,\ldots;\ \bar{n} = 0,1,2,\ldots) \tag{17}$$

where I are the products

$$I^{(pqrs)}_{mmnn} = \phi^{(pq)}_{mm} \cdot \phi^{(rs)}_{nn} \tag{18}$$

of the two integrals defined by

$$\phi^{(pq)}_{mm} = \int_{-1}^{1} \frac{\partial^{(p)} X_m}{\partial \xi^{(p)}} \frac{\partial^{(q)} X_{\bar{m}}}{\partial \xi^{(q)}} d\xi. \tag{19}$$

Equation (17) is a set of linear simultaneous equations in terms of the coefficients A_{mn}, and the eigenvalues Ω may be extracted by using existing computer subroutines.

The analytical procedure developed thus far is a standard routine of the Ritz method, and the modification is explained next so as to incorporate arbitrary edge conditions into the amplitude $W(\xi,\eta)$. In the traditional approach, for example, using the beam functions for $X_m(\xi)$ and $Y_n(\eta)$, many different products of regular and hyper trigonometric functions exist for arbitrary conditions and it is difficult to make a unified subroutine to calculate all of the various kinds of integrals.

The present approach introduces a kind of polynomial

$$X_m(\xi) = \xi^m (\xi+1)^{B1} (\xi-1)^{B3}$$
$$Y_n(\eta) = \eta^n (\eta+1)^{B2} (\eta-1)^{B4} \tag{20}$$

where B_1, B_2, B_3, and B_4 are ''boundary indices'' ([12,13]) which are added to satisfy the kinematical boundary conditions and are used in such a way as $B_1 = 0$ for F (free edge), 1 for S (simply supported edge), and 2 for C (clamped edge). To the CSFF plate shown in Fig. 1(*b*), for instance, $B_1 = 2$, $B_2 = 1$ and $B_3 = B_4 = 0$ are applied. With the boundary indices B_i's and Eqs. (20), the method of Ritz can accommodate arbitrary sets of the edge conditions, and the integrals (19) can be exactly evaluated.

4 Results and Discussions

4.1 Accuracy of the Ritz Solution. Frequency parameters are calculated by using Eq. (17), and accuracy of the solutions should be tested before counting different sets of natural frequencies to estimate the number of combinations. The material constants used in the examples are taken ([11]) for graphite/epoxy composite as

G/E material: $E_L = 138$ Gpa, $E_T = 8.96$ Gpa,

$G_{LT} = 7.1$ Gpa, $\nu_{LT} = 0.30$

Table 2 presents a convergence study for the frequency parameters $\Omega_1 \sim \Omega_4$ (lowest four modes) of Plate (*f*), i.e., a skew orthotropic square plate with the major principal axis of $\theta = 30$ deg. Four different boundary conditions, FFFF, SSSS, CCCC, and CFFF (cantilever), are considered. It is clearly seen that the frequencies monotonically decrease from above as the number of terms is increased in Eq. (15), and converge almost with the four significant figures when the terms $M = N = 10$ in the series are taken. Based on the test results, the frequencies are calculated hereafter by using the $M \times N = 10 \times 10$ solutions.

The solution accuracy is also validated by comparison of the present values with others for plate (*a*). Table 3 compares the present results with the series solutions of Gorman [14–16] and the exact solution ([7]) for isotropic square plates. As shown in the table, the agreement is excellent for all the results compared, and the validity of the analytical method is established.

4.2 Verification of the Polya Theory With Numerical Experiment. Considering the edge conditions of F, S, and C, natural frequencies are calculated for the plate models shown in Figs. 2(*a*)–(*g*). Calculations of frequencies are done for all the $3^4 = 81$

Table 2 Convergence study of frequency parameters Ω of skew orthotropic square plates (plate (*f*) in Fig. 2, $\theta = 30$ deg, G/E material)

B.C.	Num.of terms	1 st.	2 nd.	3 rd.	4 th.
FFFF	6×6	20.21	22.50	47.74	63.37
	8×8	20.21	22.31	46.90	61.53
	10×10	20.21	22.31	46.89	61.52
SSSS	6×6	44.31	67.23	113.9	159.9
	8×8	44.31	67.23	112.6	159.9
	10×10	44.31	67.23	112.6	159.9
CCCC	6×6	93.61	116.6	163.9	236.4
	8×8	93.61	116.6	163.8	235.4
	10×10	93.61	116.6	163.8	235.4
CFFF	6×6	13.79	18.61	36.16	74.20
	8×8	13.79	18.60	35.78	72.04
	10×10	13.79	18.60	35.77	72.02

Table 3 Comparison of frequency parameters Ω of isotropic square plates (plate (*a*) in Fig. 2)

B.C.	Reference	1 st.	2 nd.	3 rd.	4 th.
FFFF	Present	13.17	19.22	24.42	34.23
(ν=0.333)	Gorman(1978)	13.17	19.22	24.42	34.23
SSSS	Present	19.74	49.35	78.96	98.70
(ν=0.3)	Leissa(1973)	19.74	49.35	78.96	98.70
CCCC	Present	35.99	73.39	108.2	131.6
(ν=0.3)	Gorman(1977)	35.98	73.40	108.2	131.6
CFFF	Present	3.460	8.358	21.09	27.06
(ν=0.333)	Gorman(1976)	3.459	8.356	21.09	27.06

Table 4 Classified boundary conditions by numerical study for various plate models shown in Fig. 2

Plate (a)

```
( 1)----------
      F F F F
( 2)----------
      F F F S
      F F S F
      F S F F
      S F F F
( 3)----------
      F F F C
      F F C F
      F C F F
      C F F F
( 4)----------
      F F S S
      F S S F
      S F F S
      S S F F
( 5)----------
      F F S C
      F F C S
      F S C F
      F C S F
      S F F C
      S C F F
      C F F S
      C S F F
( 6)----------
      F F C C
      F C C F
      C F F C
      C C F F
( 7)----------
      F S F S
      S F S F
( 8)----------
      F S F C
      F C F S
      S F C F
      C F S F
( 9)----------
      F S S S
      S F S S
      S S F S
      S S S F
(10)----------
      F S S C
      F C S S
      S F C S
      S S F C
      S S C F
      S C F S
      C F S S
      C S S F
(11)----------
      F S C S
      S F S C
      S C S F
      C S F S
```

```
(12)----------
      F S C C
      F C C S
      S F C C
      S C C F
      C F S C
      C S F C
      C C F S
      C C S F
(13)----------
      F C F C
      C F C F
(14)----------
      F C S C
      S C F C
      C F C S
      C S C F
(15)----------
      F C C C
      C F C C
      C C F C
      C C C F
(16)----------
      S S S S
(17)----------
      S S S C
      S S C S
      S C S S
      C S S S
(18)----------
      S S C C
      S C C S
      C S S C
      C C S S
(19)----------
      S C S C
      C S C S
(20)----------
      S C C C
      C S C C
      C C S C
      C C C S
(21)----------
      C C C C
```

Plate (b)(c)(d)

```
( 1)----------
      F F F F
( 2)----------
      F F F S
      F S F F
( 3)----------
      F F F C
      F C F F
( 4)----------
      F F S F
      S F F F
( 5)----------
      F F S S
      F S S F
      S F F S
      S S F F
( 6)----------
      F F S C
      F C S F
      S F F C
      S C F F
( 7)----------
      F F C F
      C F F F
( 8)----------
      F F C S
      F S C F
      C F F S
      C S F F
( 9)----------
      F F C C
      F C C F
      C F F C
      C C F F
(10)----------
      F S F S
(11)----------
      F S F C
      F C F S
(12)----------
      F S S S
      S S F S
(13)----------
      F S S C
      F C S S
      S S F C
      S C F S
(14)----------
      F S C S
      C S F S
(15)----------
      F S C C
      F C C S
      C S F C
      C C F S
(16)----------
      F C F C
(17)----------
      F C S C
      S C F C
```

```
(18)----------
      F C C C
      C C F C
(19)----------
      S F S F
(20)----------
      S F S S
      S S S F
(21)----------
      S F S C
      C S S F
(22)----------
      S F C F
      C F S F
(23)----------
      S F C S
      S S C F
      C F S S
      C S S F
(24)----------
      S F C C
      S C C F
      C F S C
      C C C F
(25)----------
      S S S S
(26)----------
      S S S C
      S C S S
(27)----------
      S S C S
      C S S S
(28)----------
      S S C C
      S C C S
      C S S C
      C C S S
(29)----------
      S C S C
(30)----------
      S C C C
      C C S C
(31)----------
      C F C F
(32)----------
      C F C S
      C S C F
(33)----------
      C F C C
      C C C F
(34)----------
      C S C S
(35)----------
      C S C C
      C C C S
(36)----------
      C C C C
```

Table 4 (Continued)

Plate (e)

```
( 1)----------
      F F F F
( 2)----------
      F F F S
      F F S F
      F S F F
      S F F F
( 3)----------
      F F F C
      F F C F
      F C F F
      C F F F
( 4)----------
      F F S S
      S S F F
( 5)----------
      F F S C
      F F C S
      S C F F
      C S F F
( 6)----------
      F F C C
      C C F F
( 7)----------
      F S F S
      S F S F
( 8)----------
      F S F C
      F C F S
      S F C F
      C F S F
( 9)----------
      F S S F
      S F F S
(10)----------
      F S S S
      S F S S
      S S F S
      S S S F
(11)----------
      F S S C
      S F C S
      S C F S
      C S S F
(12)----------
      F S C F
      F C S F
      S F F C
      C F F S
(13)----------
      F S C S
      S F S C
      S C S F
      C S F S
(14)----------
      F S C C
      S F C C
      C C F S
      C C S F
```

```
(15)----------
      F C F C
      C F C F
(16)----------
      F C S S
      S S F C
      S S C F
      C F S S
(17)----------
      F C S C
      S C F C
      C F C S
      C S C F
(18)----------
      F C C F
      C F F C
(19)----------
      F C C S
      S C C F
      C F S C
      C S F C
(20)----------
      F C C C
      C F C C
      C C F C
      C C C F
(21)----------
      S S S S
(22)----------
      S S S C
      S S C S
      S C S S
      C S S S
(23)----------
      S S C C
      C C S S
(24)----------
      S C S C
      C S C S
(25)----------
      S C C S
      C S S C
(26)----------
      S C C C
      C S C C
      C C S C
      C C C S
(27)----------
      C C C C
```

Plate (f)(g)

```
( 1)----------
      F F F F
( 2)----------
      F F F S
      F S F F
( 3)----------
      F F F C
      F C F F
( 4)----------
      F F S F
      S F F F
( 5)----------
      F F S S
      S S F F
( 6)----------
      F F S C
      S C F F
( 7)----------
      F F C F
      C F F F
( 8)----------
      F F C S
      C S F F
( 9)----------
      F F C C
      C C F F
(10)----------
      F S F S
(11)----------
      F S F C
      F C F S
(12)----------
      F S S F
      S F F S
(13)----------
      F S S S
      S S F S
(14)----------
      F S S C
      S C F S
(15)----------
      F S C F
      C F F S
(16)----------
      F S C S
      C S F S
(17)----------
      F S C C
      C C F S
(18)----------
      F C F C
(19)----------
      F C S F
      S F F C
(20)----------
      F C S S
      S S F C
(21)----------
      F C S C
      S C F C
```

```
(22)----------
      F C C F
      C F F C
(23)----------
      F C C S
      C S F C
(24)----------
      F C C C
      C C F C
(25)----------
      S F S F
(26)----------
      S F S S
      S S S F
(27)----------
      S F S C
      S C S F
(28)----------
      S F C F
      C F S F
(29)----------
      S F C S
      C S S F
(30)----------
      S F C C
      C C S F
(31)----------
      S S S S
(32)----------
      S S S C
      S C S S
(33)----------
      S S C F
      C F S S
(34)----------
      S S C S
      C S S S
(35)----------
      S S C C
      C C S S
(36)----------
      S C S C
(37)----------
      S C C F
      C F S C
(38)----------
      S C C S
      C S S C
(39)----------
      S C C C
      C C S C
(40)----------
      C F C F
(41)----------
      C F C S
      C S C F
(42)----------
      C F C C
      C C C F
(43)----------
      C S C S
(44)----------
      C S C C
      C C C S
(45)----------
      C C C C
```

cases, and each new set of frequencies is numerically compared to the previously calculated values to identify whether these sets of boundary conditions belong to the same class.

Table 4 presents classified boundary conditions obtained in the numerical study. For plate (*a*), 21 classes are obtained starting from (1) FFFF. The class is numbered up to the most constrained case of (21) CCCC. This number of 21 is identical with $Z_G(3)=21$ in Table 1. It is easily understood that (2) FFFS, FFSF, FSFF, SFFF yield the identical frequency values for a square isotropic plate. It is also interesting to know that eight sets of edge conditions give the identical frequency values for (5), (10), and (12). For plates (*b*), (*c*), and (*d*), where some axes of symmetry are lost, the frequencies for (2) FFFS, FSFF are no longer the same as (4) FFSF, SFFF, and 36 different classes are obtained.

In contrast, for plate (*e*) where there are the principal material axes on the diagonals, the number of classes reduces to 27, however, this number is still more than plate (*a*) due to the diagonal orthotropy. This difference is seen by observing that (4) FFSS, FSSF, SFFS, SSFF (two edges simply supported) in plate (*a*) splits into (4) FFSS, SSFF (i.e., the major material axis is located so as to bisect the right angle at the corner of the adjacent SS edges) and (9) FSSF, SFFS (i.e., the major material axis is in the direction of a diagonal connecting two corners made by the F and S edges) in plate (*e*).

The maximum number of combinations is found for plates (*f*) and (*g*). Each class in these plates has at most two sets, wherein the first two symbols are interchanged with the last two symbols, such as FF and FS in (2) FFFS, FSFF, FF and FC in (3) FFFC, FCFF, and so on.

As is clearly seen, the numbers of combinations for plate (*a*), plates (*b*), (*c*), (*d*), plate (*e*) and plates (*f*), (*g*) are 21, 36, 27, and 45, respectively, and exactly coincide with the numbers for $x=3$ in Table 1 estimated by using the Polya counting theory.

Table 5 presents frequency parameters Ω of the specially orthotropic plate (plate (*c*) in Fig. 2) obtained for the 36 combinations classified in Table 4. The lowest six frequencies are tabulated for future comparison in the order listed in Table 4. Three frequencies are zero due to rigid-body motions of translation and rotations for (1) FFFF, and the first frequency is zero due to that of rotation for (2) FFFS, FSFF and (4) FFSF, SFFF. The frequencies tend to increase, as one sees rows going down from the top row of (1) FFFF to the bottom of (36) CCCC in the table and the total constraints along the edges are gradually strengthened.

5 Conclusions

The Polya counting theory in combinatorial mathematics is introduced in order to solve a type of mechanics problem which may be encountered in plate structural design. The counting method, which is based on the group theory, is used to determine the number of combinations in the boundary conditions in connection with the plate vibration behaviors. For various square and rectangular plate models with isotropic, specially orthotropic, and skew orthotropic material properties, the number of combinations obtained by the counting theory is numerically verified by calculating natural frequencies of the plates. It is hoped that this ap-

Table 5 Frequency parameters Ω of specially orthotropic square plates (plate (*c*) in Fig. 2, G/E material)

B.C.		1st.	2nd.	3rd.	4th.	5th	6th
(1)	FFFF	0	0	0	20.21	22.31	46.89
(2)	FFFS, FSFF	0	9.858	15.38	34.13	49.86	70.90
(3)	FFFC, FCFF	3.510	11.69	21.99	39.62	61.58	80.97
(4)	FFSF,SFFF	0	10.24	30.35	60.47	66.85	69.55
(5)	FFSS,FSSF,SFFS,SSFF						
		5.053	21.77	55.72	62.37	77.67	109.2
(6)	FFSC,FCSF,SFFC,SCFF						
		6.977	27.64	62.68	66.92	81.11	117.8
(7)	FFCF,CFFF	13.79	18.60	35.77	72.02	86.42	92.65
(8)	FFCS,FSCF,CFFS,CSFF						
		15.11	27.67	59.30	87.98	101.1	112.0
(9)	FFCC,FCCF,CFFC,CCFF						
		15.98	32.70	69.87	88.32	104.0	127.8
(10)	FSFS	9.845	21.66	39.41	55.03	88.71	97.03
(11)	FSFC,FCFS	15.39	25.70	49.89	63.92	98.57	104.1
(12)	FSSS,SSFS	13.76	43.78	68.33	93.17	93.88	139.6
(13)	FSSC,FCSS,SSFC,SCFS						
		18.54	53.70	70.11	100.1	108.2	151.3
(14)	FSCS,CSFS	20.55	47.41	93.04	95.52	115.3	157.2
(15)	FSCC,FCCS,CSFC,CCFS						
		24.12	56.77	94.42	110.2	120.6	167.9
(16)	FCFC	22.35	30.88	61.61	74.16	100.5	120.8
(17)	FCSC,SCFC	24.78	64.95	72.45	107.6	124.5	164.4
(18)	FCCC,CCFC	29.24	67.57	96.23	126.3	127.0	180.0
(19)	SFSF	38.69	43.11	59.67	94.33	150.1	154.8
(20)	SFSS,SSSF	39.84	51.05	80.20	130.8	156.0	166.0
(21)	SFSC,SCSF	40.28	54.76	89.20	145.4	156.2	168.0
(22)	SFCF,CFSF	60.47	63.85	77.19	107.6	159.9	196.0
(23)	SFCS,SSCF,CFSS,CSSF						
		61.33	70.01	94.63	141.2	197.0	205.6
(24)	SFCC,SCCF,CFSC,CCSF						
		61.64	72.88	102.5	154.9	197.2	207.2
(25)	SSSS	44.31	67.23	112.6	159.9	177.2	179.7
(26)	SSSC,SCSS	46.41	74.70	125.9	160.8	181.0	198.5
(27)	SSCS,CSSS	64.69	83.14	123.8	187.8	200.3	215.3
(28)	SSCC,SCCS,CSSC,CCSS						
		66.20	89.38	136.1	201.1	205.9	218.5
(29)	SCSC	49.47	83.64	140.6	162.0	185.7	218.6
(30)	SCCC,CCSC	68.41	97.05	149.9	202.0	222.4	225.5
(31)	CFCF	87.77	90.29	100.6	126.1	173.6	242.0
(32)	CFCS,CSCF	88.41	94.96	114.9	156.1	221.6	242.8
(33)	CFCC,CCCF	88.63	97.14	121.5	168.7	239.8	243.0
(34)	CSCS	90.89	105.3	140.2	199.5	245.7	258.7
(35)	CSCC,CCCS	91.99	110.3	151.2	216.7	246.4	261.5
(36)	CCCC	93.61	116.6	163.8	235.4	247.1	264.8

proach may be extended to counting problems of more complicated geometry, modeling, and material properties in mechanics.

References

[1] Leissa, A. W., 1969, ''Vibration of Plates,'' NASA-160, U.S. Government Printing Office, Washington, D.C.

[2] Blevins, R. D., 1979, *Formulas for Natural Frequency and Mode Shape*, Van Nostrand Reinhold, New York.

[3] Gorman, D. J., 1982, *Free Vibration Analysis of Rectangular Plates*, Elsevier, New York.

[4] Sekiya, S., Hamada, M., and Sumi, S., 1982, *Handbook for Strength and Design for Plate Structures*, Asakura Publishing Co., Tokyo (in Japanese).

[5] Liu, C. L., 1968, *Introduction of Combinatorial Mathematics*, McGraw-Hill, New York, pp. 126–166.

[6] Dornhoff, L. L., and Hohn, F. E., 1978, *Applied Modern Algebra*, Macmillan, New York, pp. 242–255.

[7] Leissa, A. W., 1973, ''The Free Vibration of Rectangular Plates,'' J. Sound Vib., **31**, pp. 257–293.

[8] Slomson, A., *An Introduction to Combinatorics*, Chapman and Hall, London, pp. 109–112.

[9] Cohen, H., 1992, *Mathematics for Scientists and Engineers*, Prentice-Hall, Englewood Cliffs, NJ, pp. 515–521.

[10] Jones, R. M., 1975, *Mechanics of Composite Materials*, Scripta, Washington D.C.

[11] Vinson, J. R., and Sierakowski, R. L., 1986, *The Behavior of Structures Composed of Composite Materials*, Martinus Nijhoff, Dordrecht.

[12] Narita, Y., Ohta, Y., Yamada, G., and Kobayashi, Y., 1992, ''Analytical Method for Vibration of Angle-Ply Cylindrical Shells Having Arbitrary Edges,'' Am. Inst. Aeronaut. Astronaut. J., **30**, pp. 790–796.

[13] Narita, Y., 1995, ''Series and Ritz-Type Buckling Analysis,'' *Buckling and Postbuckling of Composite Plates*, edited by G. J. Turvey and I. H. Marshall, eds., Chapman and Hall, London, pp. 33–57.

[14] Gorman, D. J., 1976, ''Free Vibration Analysis of Cantilever Plates by the Method of Superposition,'' J. Sound Vib., **49**, pp. 453–467.

[15] Gorman, D. J., 1977, ''Free-Vibration Analysis of Rectangular Plates With Clamped-Simply Supported Edge Conditions by the Method of Superposition,'' ASME J. Appl. Mech., **44**, pp. 743–749.

[16] Gorman, D. J., 1978, ''Free Vibration Analysis of the Completely Free Rectangular Plate by the Method of Superposition,'' J. Sound Vib., **57**, pp. 437–447.

Numerical Computation of Differential-Algebraic Equations for the Approximation of Artificial Satellite Trajectories and Planetary Ephemerides

B. Fox
Parallel Computing Research Laboratory,
Department of Electrical and
Electronic Engineering,
e-mail: budfox@ee.uwa.edu.au

L. S. Jennings
Centre for Applied Dynamics
and Optimization,
e-mail: les@maths.uwa.edu.au

A. Y. Zomaya
Parallel Computing Research Laboratory,
The University of Western Australia,
Perth, WA 6907, Australia
e-mail: zomaya@ee.uwa.edu.au

The principle of virtual work and Lagrange's equations of motion are used to construct a system of differential equations for constrained spatial multibody system modeling. The differential equations are augmented with algebraic constraints representing the system being modeled. The resulting system is a high index differential-algebraic equation (DAE) which is cast as an ordinary differential equation (ODE) by differentiating the constraint equations twice. The initial conditions are the heliocentric rectangular equatorial generalized coordinates and their first time derivatives of the planets of the solar system and an artificial satellite. The ODE is computed using the integration subroutine LSODAR to generate the body generalized coordinates and time derivatives and hence produce the planetary ephemerides and satellite trajectories for a time interval. Computer simulation and graphical output indicate the satellite and planetary positions and the latter may be compared with those provided in the Astronomical Almanac. Constraint compliance is investigated to establish the accuracy of the computation. [S0021-8936(00)03403-6]

1 Introduction

Planar and spatial multibody modeling and constrained variational dynamics have been pursued substantially since 1980. Authors such as Haug [1], Nikravesh [2], and Shabana [3,4] have studied rigid and flexible planar and spatial systems using various software tools, for example, ADAMS (Automatic Dynamic Analysis of Mechanical Systems) ([5,6]) DADS (Dynamic Analysis and Design System) ([7]), and MADYMO (MAthematical DYnamical MOdels) ([8]) and have contributed modeling, computation, and software design techniques to the field. Here the authors use their own planar and spatial constrained variational system software, *Multibody System* ([9,10]), for computing satellite motion and planetary ephemerides of the solar system and recording the accuracy of the integration method employed.

Multibody system equations may be cast as differential-algebraic equations (DAEs), since the system equations are augmented with algebraic constraints defining the geometry of the system. Simeon et al. [11] investigates thoroughly the theory and computation of DAEs. The integration package used by Simeon is ODASSL ([12]) and differs from LSODAR in that the constraint equations need not be differentiated thereby reducing numerical inaccuracy.

Brenan et al. [12] introduce the basic types of DAEs, constrained variational problems, the theory, solvability and index concept, linear and nonlinear systems, numerical methods involving order reduction and stiffness, software including DASSL based on the BDF methods for DAE computation, algorithms, applications, and examples of DAEs in problems involving rigid-body systems, trajectory control, electrical networks, and the method of lines.

Contributed by the Applied Mechanics Division of THE AMERICAN SOCIETY OF MECHANICAL ENGINEERS for publication in the ASME JOURNAL OF APPLIED MECHANICS. Manuscript received by the ASME Applied Mechanics Division, March 31, 1999; final revision, May 5, 1999. Associate Technical Editor: A. A. Ferri. Discussion on the paper should be addressed to the Technical Editor, Professor Lewis T. Wheeler, Department of Mechanical Engineering, University of Houston, Houston, TX 77204-4792, and will be accepted until four months after final publication of the paper itself in the ASME JOURNAL OF APPLIED MECHANICS.

Studies concerning the theory and computation of DAEs have been documented in [11–22]. Involved mechanical examples of DAEs may be found in [23–26].

Planetary ephemerides have been computed by various research groups including space agencies and J.P.L. and this information is made available in the public domain see [27] and the Astronomical Almanac [28]. The data is accurately provided and involves computing phenomena such as planetary aberration, nutations and liberations into consideration; see [29] for further details about spherical astronomy. Software developed by J.P.L., see [30] and [31], provides detail about computation of planetary ephemerides and has evolved to produce the more recent DE200 (Development Ephemeris 200), DE202, DE405, and DE406 lunar and planetary ephemerides.

The purpose of this work is to investigate the numerical accuracy of integrating multibody system equations, by computing the motion of an artificial satellite and ephemerides of the planets of the solar system (that of the Earth is in fact the Earth-Moon barycenter) given initial ecliptic orbital elements or heliocentric rectangular equatorial coordinates provided in the Astronomical Almanac [28]. The computation of the generalized coordinates and their time derivatives results in the ephemerides and is achieved through integration of the governing multibody system ODE. The software, *Multibody System*, used to compute the trajectories employs the use of generalized Cartesian coordinates and publicly available code found in the packages LAPACK/LINPACK [32] and the numerical integration subroutine LSODAR [21]; this allows automatic step-size selection to control local error tolerances, method switching, singularity detection, number of function evaluations, and additional information to be obtained in order that efficiency and accuracy of the numerical computation may be compared against other schemes.

The main aim is to investigate constraint compliance throughout the computation to determine the *drift* of the constraint equations; for different choices of relative error tolerance one may observe better constraint compliance. Earlier work, Fox et al. [9], involving collision of hard and soft bodies indicated particular

numerical difficulties with constraint compliance. This study was chosen because the dynamics are very smooth, but there are still theoretical constraints that need to be satisfied.

The rest of the paper is divided as follows. Section 2 provides the multibody system equations using the principle of virtual work and Lagrange's equations. Section 3 shows how a high index DAE may be cast as the underlying ODE suitable for numerical integration. Section 4 introduces the spherical astronomy concerning calculation of planetary ephemerides and satellite trajectories. Section 5 presents the numerical results and computational details concerning the integration of the underlying ODE of the orbital system and finally Section 6 reviews the researched ideas.

2 Spatial Multibody System Equations

The general equations of dynamic equilibrium for multibody systems can be formulated using generalized Cartesian coordinates, the principle of virtual work and Lagrange's equations of motion. The following derivation follows closely the work of Nikravesh [2] and Shabana [3,4] whose formulations of the resulting differential equations of motion can, in fact, be shown to be equivalent.

The Euler parameter method involves Euler parameters rather than Euler angles and is discussed thoroughly in [33–36] and [3]. The standard Cartesian generalized coordinates are used to describe the position of a local body coordinate system which moves with the body, and the Euler parameters may be used as the generalized coordinates for the orientation of a body coordinate system with respect to the global frame, that is

$$\Theta_i=(\theta_0,\theta_1,\theta_2,\theta_3)_i^T \tag{2.1}$$

and the complete set of generalized coordinates are

$$\mathbf{q}_i=[R_x\ \ R_y\ \ R_z\ \ \theta_0\ \ \theta_1\ \ \theta_2\ \ \theta_3]_i^T. \tag{2.2}$$

The theoretical constraint equation for body i is

$$\mathbf{C}(\mathbf{q}_i,t)=\Theta_i^T\Theta_i-1=0. \tag{2.3}$$

The kinetic energy of body i is an integral over the volume V_i

$$T_i=\frac{1}{2}\int_{V_i}\rho_i\dot{\mathbf{r}}_i^T\dot{\mathbf{r}}_i dV_i \tag{2.4}$$

where $\mathbf{r}_i$ is the global position vector of the body i coordinate system, and it may be shown that

$$T_i=\frac{1}{2}\dot{\mathbf{R}}_i\mathbf{m}_{\mathbf{RR},i}\dot{\mathbf{R}}_i+\frac{1}{2}\dot{\Theta}_i\mathbf{m}_{\Theta\Theta,i}\dot{\Theta}_i. \tag{2.5}$$

On substitution of this expression into the Lagrange equations of motion

$$\frac{d}{dt}\left(\frac{\partial T_i}{\partial\dot{\mathbf{q}}_i}\right)-\frac{\partial T_i}{\partial\dot{\mathbf{q}}_i}=\overline{\mathbf{Q}}_i^T \tag{2.6}$$

one arrives at the equations of motion for body i, which are

$$\begin{bmatrix}\mathbf{m}_{\mathbf{RR},i} & 0\\ 0 & \mathbf{m}_{\Theta\Theta,i}\end{bmatrix}\begin{bmatrix}\ddot{\mathbf{R}}_i\\ \ddot{\Theta}_i\end{bmatrix}=\begin{bmatrix}\overline{\mathbf{Q}}_{\mathbf{R}_i}\\ \overline{\mathbf{Q}}_{\Theta_i}\end{bmatrix}+\begin{bmatrix}0\\ -2\tilde{\overline{\mathbf{G}}}_i^T\overline{\mathbf{I}}_{\Theta\Theta,i}\overline{\omega}_i\end{bmatrix}. \tag{2.7}$$

Augmenting these equations with the constraint equations yields the spatial augmented system equations for body i

$$\begin{bmatrix}\begin{bmatrix}\mathbf{m}_{\mathbf{RR},i} & 0\\ 0 & \mathbf{m}_{\Theta\Theta,i}\end{bmatrix} & \begin{bmatrix}0\\ 2\Theta_i^T\end{bmatrix}\\ [0\quad 2\Theta_i] & 0\end{bmatrix}\begin{bmatrix}\ddot{\mathbf{R}}_i\\ \ddot{\Theta}_i\\ \lambda_i\end{bmatrix}=\begin{bmatrix}\mathbf{Q}_{e,\mathbf{R}_i}\\ \mathbf{Q}_{e,\Theta_i}\\ -2\dot{\Theta}_i^T\dot{\Theta}_i\end{bmatrix}+\begin{bmatrix}0\\ \mathbf{Q}_{v,\Theta_i}\\ 0\end{bmatrix} \tag{2.8}$$

from which one may assemble the complete system of equations, repeated here as

$$\begin{bmatrix}\mathbf{M} & \mathbf{C}_\mathbf{q}^T\\ \mathbf{C}_\mathbf{q} & 0\end{bmatrix}\begin{bmatrix}\ddot{\mathbf{q}}\\ \lambda\end{bmatrix}=\begin{bmatrix}\mathbf{Q}_e\\ \mathbf{Q}_d\end{bmatrix}. \tag{2.9}$$

For further information on the this technique one may consult [2] and [3].

3 Differential Algebraic Equations

Constrained variational systems usually involve differential equations augmented with algebraic constraints involving system variables for which the equations are being computed and hence these systems can be represented by DAEs. Petzold and coauthors have performed substantial research on the solvability and computation of DAEs, [12] address the foundations of the theory, computation and applications of DAEs and include many references on earlier work in this field; other important contributions to the study of DAEs were given in the introduction. A DAE may be of the form

$$\mathbf{F}(\dot{\mathbf{x}},\mathbf{x},t)=0. \tag{3.1}$$

The DAE of the multibody system considered here is of the form

$$\begin{bmatrix}\mathbf{I} & 0 & 0\\ 0 & \mathbf{M} & \dfrac{\partial\mathbf{C}^T}{\partial\mathbf{q}}\\ 0 & 0 & 0\end{bmatrix}\begin{bmatrix}\dot{\mathbf{q}}\\ \dot{v}\\ \dot{\mu}\end{bmatrix}=\mathbf{f}(\mathbf{q},t)=\begin{bmatrix}v\\ \mathbf{Q}_e\\ \mathbf{C}(\mathbf{q},t)\end{bmatrix}, \tag{3.2}$$

where $\dot{\mu}=\lambda$ and $\dot{v}=\ddot{q}$. The matrix on the left-hand side is, however, singular, differentiating the third equation above with respect to time twice, yields

$$\begin{bmatrix}\mathbf{I} & 0 & 0\\ 0 & \mathbf{M} & \left(\dfrac{\partial\mathbf{C}}{\partial\mathbf{q}}\right)^T\\ 0 & \dfrac{\partial\mathbf{C}}{\partial\mathbf{q}} & 0\end{bmatrix}\begin{bmatrix}\dot{\mathbf{q}}\\ \dot{v}\\ \dot{\mu}\end{bmatrix}=\mathbf{f}(\mathbf{q},\dot{\mathbf{q}},t)=\mathbf{f}(\mathbf{q},v,t), \tag{3.3}$$

which has a nonsingular leading matrix providing $\partial\mathbf{C}/\partial\mathbf{q}$ is of full rank for all time. The following definition classifies a DAE with respect to differentiation of the system equations given by Eq. (3.1).

Definition: The minimum number of times that all or part of the DAE $\mathbf{F}(\dot{\mathbf{x}},\mathbf{x},t)=0$ *must be differentiated with respect to t in order to determine* $\dot{\mathbf{x}}$ *as a continuous function of* $\mathbf{x}$ *and t, for t in some interval, is the index of the DAE* ([12]).

The original system has been differentiated twice and the substitution of $\dot{\boldsymbol{\mu}}=\lambda$ can be considered as an additional differentiation. This results in the ODE shown in Eq. (3.3) and hence the original system Eq. (3.2) is regarded as a DAE of index three. Note that here $\mu(t)=\int_0^t\lambda(\tau)d\tau$ (and hence $\mu(0)=0$) is computed by the ODE software. To find $\lambda(t)$, $\mu(t)$ must be differentiated, this is, however, a slightly unstable process. Note that $\lambda(t)$ does not need to be treated this way, as its value can be obtained directly by solving Eq. (2.9), at each time-step. Recording the value of $\lambda(t)$ at the requested time values passed to standard ODE software requires modifications to the software. Purpose-built software (DAE-index 2) can be made to handle this.

Petzold et al. [12] discuss the computational/numerical difficulties that may arise as a result of differentiating the constraint equations; the constraint equations may not be satisfied as the integration progresses and excessive differentiation of the constraints is not recommended. Other computational software such as DASSL, see [15] and [16], is also introduced in [12] and requires only the constraint equations $\mathbf{C}(\mathbf{q},t)=0$, be augmented to the differential equation, rather than the user having to supply the twice differentiated constraint equations $\mathbf{Q}_d$ as in Eq. (3.3) and Eq. (2.8). This software differs from the LSODA line of integration subroutines of [20] in (1) the interpolation method of previous solution points required by BDF formulas, (2) the implemen-

tation of these formulas, and (3) the time-step size method order determination and constraint compliance or error control used. For further information regarding algorithms and numerical strategies see [12].

4 Spherical Astronomy

Green [29] and Danby [37] provide a detailed introduction to spherical astronomy which includes information on spherical geometry, the celestial sphere, reference frames, planetary orbits, heliocentric and geocentric coordinate systems, nutation, libration, and time. Carroll and Ostlie [38] provide an introduction to astrophysics and discuss the celestial sphere, celestial mechanics, including Newtonian mechanics, and Kepler's Laws. Kibble [39] pursues the laws of conservation of energy and the radial energy equation in his introduction of gravitational force and orbital mechanics and finally [40] provides a modern proof of the Law of Gravity and shows how this implies Kepler's Second Law that ''a planetary orbit is an ellipse with the sun at one focus'' (although this is regarded as Kepler's First Law by [38]). The following material is based on the work of the authors stated above and provides a brief introduction to the theory of celestial mechanics required in the extension of the code *Multibody System*, used to mathematically model and numerically compute the ODE introduced in Sections 2 and 3.

The code *Multibody System* is a body of code written in C, referencing appropriate mathematical software like LSODAR, and parts of LAPACK. A user adds the appropriate dynamical equations and twice differentiated constraint equations, in the form of the matrices of Eq. (2.9) and allows computation of the system for the variables of interest.

The Encyclopedia of Planetary Sciences [41] provides the following definition; ''An ephemeris (plural: ephemerides) is defined to be a tabular listing of the position of a celestial body at regular intervals.'' Nutation is defined by [29] as ''the periodic variations in the position of the true pole (of the orbiting body) about its mean position'' and physical libration is defined by [29] as the oscillation of the mean rotation axis of a body. As mentioned earlier, work at JPL see [27], [42], [30], and [31] has resulted in the production of planetary ephemerides including: DE102, DE200, DE202 involving nutations but not liberations, DE405 involving nutations and liberations and DE406 including neither nutations nor liberations. Here no liberations or nutations of any orbiting body will be taken into consideration in the computation of the body generalized coordinates and their time derivatives.

4.1 Coordinate Systems. In order to compute the planetary and satellite trajectories a reference frame or coordinate system is required. Here the heliocentric celestial sphere is chosen, upon which astronomical quantities of the celestial bodies concerned, may be measured. Illustrated in Fig. 1 is such a sphere, where ξ, η, and ζ, are the heliocentric rectangular ecliptic coordinates. The first point of Aires, or the vernal equinox is Ψ. The ascending node L, defines the position on the ecliptic where the planetary/body orbit progresses from south to north and if the inclination of the orbital plane i, with respect to the ecliptic is between 0 and 90 deg, then the orbit is regarded as direct, otherwise it is known as retrograde. The longitude of the ascending node L, is Ω and is measured eastward from the vernal equinox Ψ, along the ecliptic. A is the position of the orbiting body at the time of perihelion, P is the position of the orbiting body at some time t. Ψ, U, and K, form an orthogonal triad, the argument of perihelion is $\omega = \angle LA$ and finally $\nu = \angle PSA$ is the true anomoly, that is, the angle from the point of perihelion to the orbiting body located at P at some time t. The Astronomical Almanac [28] provides the parameters (a,e,i,Ω,ω) for the purpose of calculation of planetary ephemerides. The semimajor axis of the orbital ellipse is a, e is the orbital eccentricity, the mean anomoly is $M = L - (\omega + \Omega)$, the true anomoly may be computed as

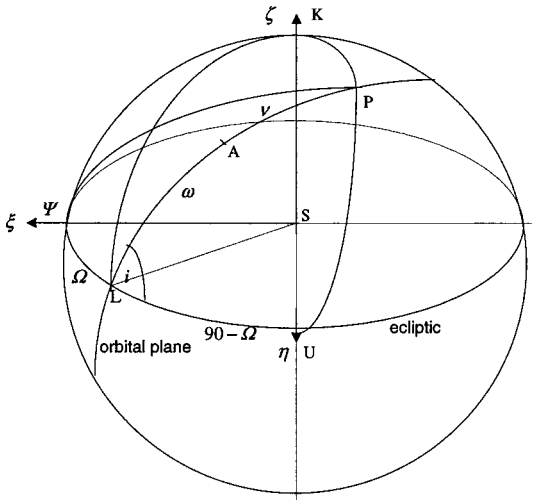

Fig. 1 Heliocentric celestial sphere

$$\nu = M + \left(2e - \frac{e^3}{4}\right)\sin(M) + \left(\frac{5e^2}{4}\right)\sin(2M) + \left(\frac{13e^3}{12}\right)\sin(3M) + \ldots \tag{4.1}$$

and the true distance of the orbiting body from the sun is

$$r = \frac{a(1-e^2)}{(1+e\cos\nu)}. \tag{4.2}$$

Using the cosine formula one obtains the heliocentric rectangular ecliptic coordinates of an orbiting body as follows:

$$\mathbf{r} = \begin{bmatrix} \xi \\ \eta \\ \zeta \end{bmatrix} = r \begin{bmatrix} \cos(\Psi P) \\ \cos(UP) \\ \cos(KP) \end{bmatrix} = r \begin{bmatrix} \cos(\nu+\omega)\cos(\Omega) - \sin(\nu+\omega)\sin(\Omega)\cos(i) \\ \cos(\nu+\omega)\sin(\Omega) + \sin(\nu+\omega)\cos(\Omega)\cos(i) \\ \sin(\nu+w)\sin(i) \end{bmatrix}. \tag{4.3}$$

If the heliocentric rectangular equatorial coordinates are required then these may be obtained from the ecliptic coordinates determined above using the following approach. Figure 2 may be found in [29] and indicates an angular tilt of the ecliptic plane and the equatorial plane known as the obliquity of the ecliptic, de-

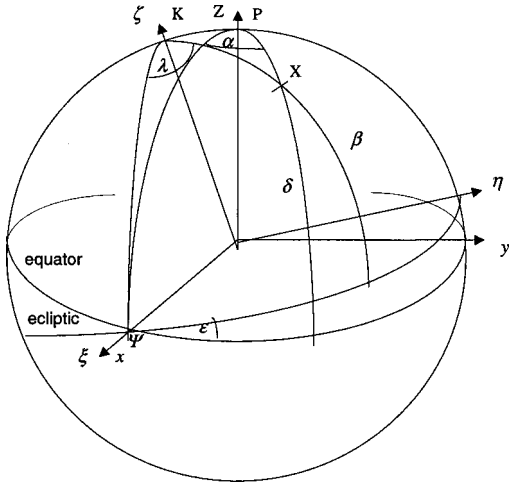

Fig. 2 Relation between equatorial and ecliptic coordinates

Table 1 Heliocentric initial coordinates (AU) and velocity components (AU d^{-1}) of an artificial satellite

R_x	R_y	R_z	$\dot{R}_x$	$\dot{R}_y$	$\dot{R}_z$
- 0.590 499 4	+ 0.722 747 8	+ 0.313 354 4	- 0.014 043 9	- 0.007 755 9	- 0.004 131 8

noted $\boldsymbol{\varepsilon}$. The ecliptic spherical coordinates λ and β are the ecliptic longitude and latitude, respectively, and the equatorial spherical coordinates α and δ are the equatorial right ascension and declination, respectively. The heliocentric rectangular ecliptic coordinates are ξ, η, and ζ and the heliocentric rectangular equatorial coordinates are x, y and z; these are related by the following equation:

$$\begin{bmatrix} x \\ y \\ z \end{bmatrix} = \mathbf{A}_x(\boldsymbol{\varepsilon}) \begin{bmatrix} \xi \\ \eta \\ \zeta \end{bmatrix} = \begin{bmatrix} 1 & 0 & 0 \\ 0 & \cos\boldsymbol{\varepsilon} & -\sin\boldsymbol{\varepsilon} \\ 0 & \sin\boldsymbol{\varepsilon} & \cos\boldsymbol{\varepsilon} \end{bmatrix} \begin{bmatrix} \xi \\ \eta \\ \zeta \end{bmatrix} \tag{4.4}$$

where $\mathbf{A}_x(\boldsymbol{\varepsilon})$ is the rotation matrix of a vector through the angle $\boldsymbol{\varepsilon}$ about the $x \equiv \xi$-axis.

It may be necessary to obtain the geocentric (Earth centered) coordinates of the orbiting bodies rather than use the heliocentric coordinates. Now, $\mathbf{r}_{P,S} = \mathbf{r}_{E,S} + \mathbf{r}_{P,E}$, where $\mathbf{r}_{P,S}$ is the heliocentric position vector of the planet under consideration with respect to the Sun, $\mathbf{r}_{E,S}$ is the heliocentric position vector of the Earth with respect to the Sun and $\mathbf{r}_{P,E}$ is the geocentric position vector of the planet with respect to the Earth; naturally $-\mathbf{r}_{E,S} = \mathbf{r}_{S,E}$. Finally if the geocentric right ascension and declination, α and δ, respectively, of the orbiting body are known together with the radial distance $\|\mathbf{r}\|$ (obtainable by Pythagoras's theorem), then

$$\mathbf{r}_{P,E} = \mathbf{r}_{P,S} - \mathbf{r}_{E,S} = \|\mathbf{r}\| \begin{bmatrix} \cos\delta\cos\alpha \\ \cos\delta\sin\alpha \\ \sin\delta \end{bmatrix}. \tag{4.5}$$

Section E3 of the Astronomical Almanac [28] provides both the orbital elements and the heliocentric rectangular equatorial coordinates for the planets of the solar system on a particular Julian day, here Julian day 2450840.5 is considered; these coordinates form the initial conditions of the multibody system equations.

4.2 System Forces. Newton used Kepler's first two laws to show that they implied his Law of Universal Gravitation. Kepler's First Law (a planet orbits the Sun in an ellipse, with the Sun at one focus of the ellipse) and Kepler's Second Law (a line connecting a planet to the Sun sweeps out equal area in equal time intervals) are derived in [38]. For details and proofs of the relation between Kepler's Laws and Newton's Law of Universal Gravitation, see [40]. The magnitude of the gravitational force is

$$F_{c_{ij}} = \frac{G m_i m_j}{\|\mathbf{r}_{p_{ij}}\|^2}. \tag{4.6}$$

the gravitational constant $G = 6.672 \times 10^{-11}\,\mathrm{m^3\,kg^{-1}\,s^{-2}}$, m_i, $i = 1, \ldots, NB$, are the masses, $\mathbf{r}_{p_{ij}}$ is the position vector joining the center of masses of the bodies concerned.

The points on the bodies between which the gravitational force is acting are the centroids of the bodies, hence the local position vectors $\overline{\mathbf{u}}_{p_i}$ and $\overline{\mathbf{u}}_{p_j}$ of these centroids are identically zero; centroidal body coordinates are used. From the modeling performed in [9], [10], and [4] the generalized forces $\mathbf{Q}_{e,i}$ and $\mathbf{Q}_{e,j}$ acting on bodies i and j are, respectively,

$$\mathbf{Q}_{e,i} = \begin{bmatrix} \mathbf{Q}_{\mathbf{R},i} \\ \mathbf{Q}_{\theta,i} \end{bmatrix} = F_{c_{ij}} \begin{bmatrix} \mathbf{I} \\ \overline{\mathbf{u}}_{P_i}^T \mathbf{A}_{\theta,i}^T \end{bmatrix} \frac{\mathbf{r}_{p_{ij}}}{\|\mathbf{r}_{p_{ij}}\|}$$

and

$$\mathbf{Q}_{e,j} = \begin{bmatrix} \mathbf{Q}_{R,j} \\ \mathbf{Q}_{\theta,j} \end{bmatrix} = -F_{c_{ij}} \begin{bmatrix} \mathbf{I} \\ \overline{\mathbf{u}}_{P_j}^T \mathbf{A}_{\theta,j}^T \end{bmatrix} \frac{\mathbf{r}_{p_{ij}}}{\|\mathbf{r}_{p_{ij}}\|}, \tag{4.7}$$

which can be suitably simplified as $\overline{\mathbf{u}}_{p_i} = \overline{\mathbf{u}}_{p_j} = 0$.

5 Results

The authors' general, spatial, multibody dynamics software *Multibody System* can be employed to produce planetary ephemerides and satellite trajectories with arbitrary accuracy given the number of significant figures found in the provided initial conditions and physical planetary data. The software can also be used for animation purposes, but here graphical and tabular output is more convenient and found below are graphs of planetary and satellite positions and tables comparing computed data to that found in the Astronomical Almanac of 1998.

The multibody model involves 11 bodies: Sun, Mercury, Venus, Earth-Moon barycenter, Mars, Jupiter, Saturn, Uranus, Neptune, Pluto, and one artificial geosynchronous satellite. The initial conditions for the planets are provided by the Astronomical Almanac [28] and the satellite initial conditions are given in Table 1 in AU (Astronomical Unit) and AU d^{-1}.

The satellite moves in a geosynchronous orbit with an orbital period of 86,400 seconds and a rotational angular velocity $\omega = 2\pi/86400\,\mathrm{rad\,s^{-1}}$, allowing equipment to be continuously facing a fixed location on Earth. The satellite velocity v at perihelion, is found using

$$v = \left(\frac{G M_E (1+e)}{a(1-e)} \right)^{1/2}, \tag{5.1}$$

where the semimajor axis a, is given by

$$a = \left(\frac{G(M_E + M_{\mathrm{sat}}) P^2}{4\pi^2} \right)^{1/3}, \tag{5.2}$$

the orbital period P is 86,400 s, the eccentricity $e = 0$ for a geosynchronous orbit and the radial distance of an orbiting body at perihelion is $r = a(1-e)$. The angular coordinates of the satellite are given by Eq. (2.1) where the angle through which the satellite rotates about its axis of rotation is $\theta = \omega t$ rad.

The constraint equations to be augmented to the system equations are given by Eq. (2.3), where Θ is the vector of Euler parameters introduced in Section 2. Constraint compliance investigated here involves checking the following equality:

$$\|\mathbf{C}(\mathbf{q},t) - \mathbf{C}(\mathbf{q},0)\| = 0 \tag{5.3}$$

Table 2 Constraint compliance norms, for differing values of RTOL over time

	t = 50 days	t = 100 days	t = 200 days	t = 360 days
RTOL = 10^{-5}	0.001 104 155 8	0.000 346 266 7	0.003 679 671 1	0.297 395 551 8
RTOL = 10^{-10}	0.000 000 002 3	0.000 000 004 7	0.000 000 357 8	0.000 000 941 8

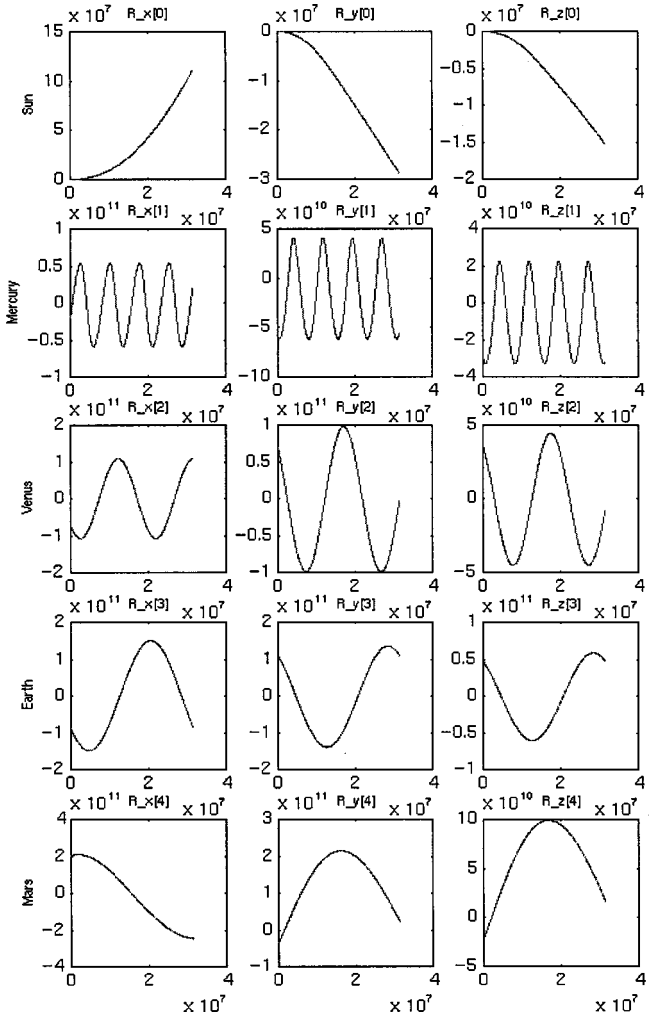

Fig. 3 Planetary trajectories for 365 days

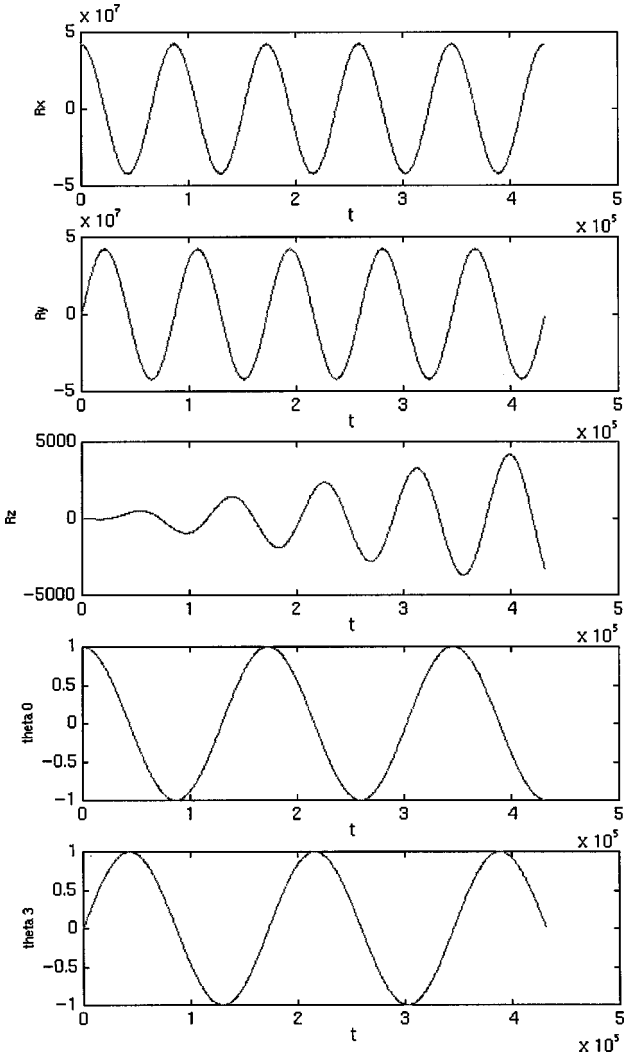

Fig. 4 Satellite periodicity about Earth

for the duration of the computation. Table 2 indicates the value of the norm shown in Eq. (5.3) after a time interval.

If x_{app} is the approximate value of a variable whose true value is x_{tr} then [41] indicates that the absolute error is $e_{\text{abs}}=x_{\text{app}}-x_{tr}$ and the relative error is $e_{\text{rel}}=(x_{\text{app}}-x_{tr})/x_{tr}$. Given the value of the relative error tolerance parameter RTOL, one can determine the absolute error tolerance parameter for body i as

$$ATOL_i=RTOL_i(R_{x,i}+R_{y,i}+R_{z,i})^{1/2} \tag{5.4}$$

where $R_{x,i}$, $R_{y,i}$, and $R_{z,i}$ are the heliocentric rectangular equatorial coordinates of the center of mass of the ith planetary body.

Figure 3 shows the planetary trajectories for the Sun, Mercury, Venus, Earth-Moon barycenter, and Mars for 365 days, computed with a time-step size of 1000 seconds. The sidereal orbital periods (years) provided by [38] are: Mercury 0.2408, Venus 0.6152, Earth 1.0000, and Mars 1.8809. The periodicity of the inner planets is shown and it may be observed that the Sun is pulled away from its initial position by the other orbiting bodies.

The periodicity of the satellite is shown in Fig. 4 to be 24 hours over a five-day time interval. The position of the satellite with respect to the Earth is clearly sinusoidal in the x and y-coordinates but grows linearly in a sinusoidal fashion in the z-coordinate; this is predominantly due to the force of the sun. The satellite Euler parameters $\theta_0=\cos(\theta/2)$ and $\theta_3=v_3\sin(\theta/2)$ show the rotation of the satellite about its axis of rotation v and are sinusoidal as expected; the angular velocity $\dot{\theta}=\omega$ and hence $\theta=\omega t$.

The final positions and velocities of the ten major planets is recorded after 200 and 360 days of computation and are shown in Table 3. Computation began at Julian day 2450840.5 and after 200 days at Julian day 2451040.5 and after 360 days Julian day 2451200.5, the accuracy of the computed data, coincident with that of the Astronomical Almanac [28] is shown in bold. The initial conditions for position and velocity are given to seven significant figures in the Astronomical Almanac [28], but the masses used are given at worst to only four significant figures. Hence the accuracy reached by the software *Multibody System* is satisfactory given the data used.

In order to reduce numerical inaccuracy in the computation, one should divide the system equations by the body mass m_i or the body inertia tensor $\bar{\mathbf{I}}_{\theta\theta,i}$ since it is a diagonal matrix (uniform spherical bodies have been used). Equation (2.8) indicates the dynamics of the position and angular components as a system of differential algebraic equations.

One may also note that for certain values of time and angular velocity ω, the submatrix $\mathbf{m}_{\theta\theta,i}$ may not be invertible and hence the mass matrix $\mathbf{M}_i$ alone, may not be invertible, although the coefficient matrix shown in Eq. (2.9) is still invertible. The following matrix inversion technique for the computation of the system equations may not be used since it requires that the upper left block $\mathbf{A}$, be invertible for all time.

Table 3 (a) Heliocentric coordinates (AU) and velocity components (AU d^{-1}) of orbiting bodies at Julian day 2451040.5; (b) Heliocentric coordinates (AU) and velocity components (AU d^{-1}) of orbiting bodies at Julian day 2451200.5

	R_x	R_y	R_z	$\dot{R}_x$	$\dot{R}_y$	$\dot{R}_z$
Mercury	+ 0.326 588 8	- 0.192 603 2	- 0.136 729 2	+ 0.010 718 8	+ 0.021 866 1	+ 0.010 568 5
Venus	- 0.039 522 2	+ 0.654 109 7	+ 0.296 780 7	- 0.020 262 2	- 0.001 583 8	+ 0.000 569 8
Earth-Moon	+ 0.798 315 4	- 0.572 412 6	- 0.248 179 8	+ 0.010 315 8	+ 0.012 375 6	+ 0.005 365 4
Mars	- 0.283 530 9	+ 1.422 970 9	+ 0.660 340 5	- 0.013 234 7	- 0.001 315 5	- 0.000 245 5
Jupiter	+ 4.898 709 8	- 0.738 001 3	- 0.435 699 8	+ 0.001 194 0	+ 0.007 175 1	+ 0.003 046 5
Saturn	+ 8.230 425 3	+ 4.126 769 9	+ 1.350 482 6	- 0.002 887 3	+ 0.004 516 8	+ 0.001 989 8
Uranus	+13.012 783 2	-13.687 289 0	- 6.178 842 9	+ 0.002 946 7	+ 0.002 214 1	+ 0.000 927 9
Neptune	+15.487 039 6	-23.790 305 7	-10.123 130 5	+ 0.002 675 7	+ 0.001 541 4	+ 0.000 564 4
Pluto	-11.390 982 8	-27.372 834 9	- 5.108 077 2	+ 0.002 978 8	- 0.001 277 6	- 0.001 294 5

(a)

	R_x	R_y	R_z	$\dot{R}_x$	$\dot{R}_y$	$\dot{R}_z$
Mercury	+ 0.033 732 2	- 0.404 824 8	- 0.219 664 1	+ 0.022 423 9	+ 0.003 886 7	- 0.000 249 1
Venus	+ 0.714 550 5	- 0.104 345 0	- 0.092 134 3	+ 0.003 586 4	+ 0.018 136 2	+ 0.007 932 3
Earth-Moon	- 0.513 233 2	+ 0.769 820 9	+ 0.333 742 8	- 0.014 947 2	- 0.008 303 9	- 0.003 600 3
Mars	- 1.641 370 7	+ 0.198 748 8	+ 0.135 546 7	- 0.001 466 2	- 0.011 521 4	- 0.005 244 8
Jupiter	+ 4.937 056 1	+ 0.420 936 7	+ 0.060 135 2	- 0.000 720 6	+ 0.007 236 7	+ 0.003 119 5
Saturn	+ 7.730 294 7	+ 4.828 775 7	+ 1.661 950 2	- 0.003 360 4	+ 0.004 250 6	+ 0.001 900 2
Uranus	+13.477 909 0	-13.326 472 5	- 6.027 411 7	+ 0.002 866 8	+ 0.002 295 6	+ 0.000 964 7
Neptune	+15.912 991 9	-23.540 387 7	-10.031 419 3	+ 0.002 648 5	+ 0.001 582 4	+ 0.000 581 9
Pluto	-10.912 800 5	-27.573 442 8	- 5.314 488 1	+ 0.002 998 2	- 0.001 229 9	- 0.001 285 5

(b)

$$\begin{bmatrix} \mathbf{A} & \mathbf{B} \\ \mathbf{C} & \mathbf{D} \end{bmatrix}^{-1} = \begin{bmatrix} \mathbf{A}^{-1}+\mathbf{E}\Delta^{-1}\mathbf{F} & -\mathbf{E}\Delta^{-1} \\ -\Delta^{-1}\mathbf{F} & \Delta^{-1} \end{bmatrix} \tag{5.5}$$

where $\Delta=\mathbf{D}-\mathbf{C}\mathbf{A}^{-1}\mathbf{B}$, $\mathbf{E}=\mathbf{A}^{-1}\mathbf{B}$ and $\mathbf{F}=\mathbf{C}\mathbf{A}^{-1}$, see [43], [44], and [45] for additional matrix theory.

One should also be aware that there are four Euler parameters, that is, four angular generalized coordinates per body and there should be no more angular constraint equations per body than there are angular coordinates per body in order to avoid a dimensionally inconsistent system of equations.

Future work may involve including the moons of Mars, Jupiter, Saturn, Uranus, Neptune, and Pluto, larger bodies of the asteroid belt, nutations and librations of the major planets, and a large artificial satellite communication network. Optimal control may be used to obtain better estimates of masses; for example, in order to improve the fitting of the model to any accurate sightings made after $t=0$, using techniques in [46].

6 Conclusions

The principle of virtual work and Lagrange's equations were used to obtain a differential equation representing the spatial dynamics of an orbital multibody system. The inherent constraints involved in this formulation and the additional constraints defining system structure were augmented to the differential equations to form an index 3 DAE. The twice differentiation of the constraint equations allowed the DAE to be cast as the underlying ODE representing the orbital/planetary motion. The numerical computation of the system equations was performed using the software *Multibody System*, which incorporates the variable accuracy integrator LSODAR [20]. The resulting generalized coordinates and their time derivatives form the planetary ephemerides and artificial satellite trajectories and it was shown that accuracy of computation is within a range of three to five significant figures of the data provided by the Astonomical Almanac after simulation times of 200 and 360 days. Tabulated constraint compliance shows that with a relative error tolerance of 10^{-10}, the norm is less than 10^{-6} after 360 days of simulation. Future work may involve increasing the system size, computing nutations and librations of the major planets, and using optimal control to allow better fitting of the system parameters (e.g., masses) of the model to the data.

References

[1] Haug, E. J., ed., 1984, *Computer Aided Analysis and Optimization of Mechanical System Dynamics* (NATO ASI Series, Vol. F9), Springer-Verlag, Berlin.

[2] Nikravesh, P. E., 1988, *Computer Aided Analysis of Mechanical Systems*, Prentice-Hall, Englewood Cliffs, NJ.

[3] Shabana, A. A., 1988, *Dynamics of Multibody Systems*, John Wiley and Sons, New York.

[4] Shabana, A. A., 1994, *Computational Dynamics*, John Wiley and Sons, New York.

[5] Ryan, R. R., 1990, ''ADAMS—Multibody System Analysis Software,'' *Multibody Systems Handbook*, Springer-Verlag, Berlin.

[6] Adams Internet Site, http://www.adams.com/

[7] Smith, R. C., and Haug, E. J., 1990, ''DADS: Dynamic Analysis and Design System,'' *Multibody Systems Handbook*, Springer-Verlag, Berlin.

[8] Lupker, H. A., de Coo, P. J. A., Nieboer, J. J., and Wismans, J., 1991, ''Advances in MADYMO Crash Simulations,'' Internal Report 910879, TNO Road-Vehicles Research Institute Delft, Delft, The Netherlands.

[9] Fox, B., Jennings, L. S., and Zomaya, A. Y., 1999, ''Numerical Computation of Differential-Algebraic Equations for Nonlinear Dynamics of Multibody Systems,'' submitted for publication.

[10] Fox, B., Jennings, L. S., and Zomaya, A. Y., 1999, ''Numerical Computation of Differential-Algebraic Equations for Nonlinear Dynamics of Multibody Android Systems in Automobile Crash Simulation,'' IEEE Trans. Biomed. Eng., **46**, No. 10, pp. 1199–1206.

[11] Simeon, B., Fuhrer, C., and Rentrop, R., 1991, ''Differential-Algebraic Equations in Vehicle System Dynamics,'' *Surveys on Mathematics for Industry*, Springer-Verlag, New York.

[12] Brennan, K. E., Campbell, S. L., and Petzold, L. R., 1989, *Numerical Solution of Initial-Value Problems in Differential-Algebraic Equations*, Elsevier, New York.

[13] Ascher, U. M., and Petzold, L. R., 1992, ''Numerical Methods for Boundary Value Problems in Differential Algebraic Equations,'' *Recent Developments in Numerical Methods and Software for ODEs/DAEs/PDEs*, G. D. Byrn and W. E. Schiesser, eds., World Scientific Publishers, Singapore.

[14] Byrn, G. D., and Schiesser, W. E., 1992, ''An Overview of Recent Develop-

ments in Numerical Methods and Software for ODEs/DAEs/PDEs'' *Recent Developments in Numerical Methods and Software for ODEs/DAEs/PDEs*, G. D. Bryne and W. E. Schiesser, eds., World Scientific Publishers, Singapore.
[15] Gear, C. W., 1991, ''An Introduction to Numerical Methods for ODEs and DAEs,'' *Real Time Integration Methods for Mechanical System Simulation* (NATO, ASI Series, Vol. F69), E. J. Haug, ed., Springer-Verlag, Berlin.
[16] Gear, C. W., and Petzold, L. R., 1984, ''ODE Methods for the Solution of Differential/algebraic Systems,'' SIAM (Soc. Ind. Appl. Math.) J. Numer. Anal., **21**, No. 4. Aug. pp. 716–728.
[17] Petzold, L. R., 1982, ''Differential/Algebraic Equations are not ODEs,'' SIAM J. Sci. Stat. Comput., **3**, No. 3, pp. 367–384.
[18] Petzold, L. R., 1983, ''A Description of DASSL: A Differential/Algebraic System Solver,'' *Scientific Comput.*, R. Stepleman et al., eds., North-Holland, Amsterdam.
[19] Petzold, L. R., 1991, ''Methods and Software for Differential-Algebraic Systems,'' *Real Time Integration Methods for Mechanical System Simulation* (NATO ASI Series, Vol. F69), E. J. Haug, ed., Springer-Verlag, Berlin.
[20] Petzold, L. R., and Hindmarsh, A. E., ''LSODAR,'' Computing and Mathematics Research Division, 1-316 Lawrence Livermore National Laboratory, Livermore, CA.
[21] Petzold, L. R., Ren, Y., and Maly, T., 1997, ''Regularization of Higher-Index Defferential-Algebraic Equations With Rank-Deficient Constraints,'' SIAM J. Sci. Comput. (USA), **18**, No. 3, pp. 753–774.
[22] Yen, J., and Petzold, L. R., 1998, ''An Efficient Newton-Type Iteration for the Numerical Solution of Highly Oscillatory Constrained Multibody Dynamic Systems,'' SIAM J. Sci. Comput. (USA), **19**, No. 5, pp. 1513–1534.
[23] Nakanishi, T., and Shabana, A. A., 1994, ''Contact Forces in the Nonlinear Dynamic Analysis of Tracked Vehicles,'' Int. J. Numer. Comput. Meth. Eng., **37**, pp. 1251–1275.
[24] Nakanishi, T., and Shabana, A. A., 1994, ''On the Numerical Solution of Tracked Vehicle Dynamic Equations,'' Nonlinear Dyn., **6**, pp. 391–417.
[25] Rismantab-Sany, J., and Shabana, A. A., 1989, ''On the Numerical Solution of Differential/Algebraic Equations of Motion of Deformable Mechanical Systems With Nonholonomic Constraints,'' Comput. Struct., **33**, No. 4, pp. 1017–1029.
[26] Sarwar, M. K., Nakanishi, T., and Shabana, A. A., 1995, ''Chain Link Deformation in the Nonlinear Dynamics of Tracked Vehicles,'' J. of Vib. Control, **1**, pp. 201–224.
[27] JPL internet sites: (1) http://www.willbell.com/software/jpl.htm; (2) http://www.nssdc.gsfc.nasa.gov/space/helios/planet.html; (3) http://ssd.jpl.nasa.gov/iau-comm4/
[28] Astronomical Almanac (for the year 1998), 1997, U.S. Government Printing Office, Washington, DC (HMSO London).
[29] Green, R. M., 1985, *Spherical Astronomy*, Cambridge University Press, Cambridge, UK.
[30] Standish, Jr., E. M., 1990, ''The Observational Basis for JPL's DE200: The Planetary Ephermerides of the Astronomical Almanac,'' Astron. Astrophys., **233**, pp. 252–271.
[31] Standish, Jr., E. M., 1990, ''An Approximation to the Outer Planet Ephermeris Errors in JCP's DE200,'' Astron. Astrophys., **233**, pp. 272–274.
[32] Netlib internet site, http://www.netlib.org/
[33] Nikravesh, P. E., 1984, ''Spatial Kinematic and Dynamic Analysis With Euler Parameters,'' *Computer Aided Analysis and Optimization of Mechanical System Dynamics* (NATO ASI Series, Vol. F9), E. J. Haug, ed., Springer-Verlag, Berlin.
[34] Nikravesh, P. E., and Chung, I. S., 1982, ''Application of Euler Parameters to the Dynamic Analysis of Three-Dimensional Constrained Mechanical Systems,'' ASME J. Mech. Des., **104**, pp. 785–791.
[35] Nikravesh, P. E., Wehage, R. A., and Kwon, O. K., 1985, ''Euler Parameters in Computational Kinematics and Dynamics, Part I,'' ASME, J. Mech. Transmission and Automation in Design, **107**, pp. 358–365.
[36] Nikravesh, P. E., Wehage, R. A., and Kwon, O. K., 1985, ''Euler Parameters in Computational Kinematics and Dynamics,'' ASME J. Mech. Transmission and Automation in Design, **107**, pp. 366–369.
[37] Danby, J. M. A., 1992, *Fundamentals of Celestial Mechanics*, 2nd Ed., Willmann-Bell, Richmond, VA.
[38] Carroll, B. W., and Ostlie, D. A., 1996, *An Introduction to Modern Astrophysics*, Addison-Wesley, Reading, MA.
[39] Kibble, T. W. B., 1985, *Classical Mechanics*, 3rd Ed., Longman, New York.
[40] Bressoud, D. M., 1991, *Second Year Calculus: From Celestial Mechanics to Special Relativity* (Undergraduate Texts in Mathematics, Readings in Mathematics), Springer-Verlag, New York.
[41] Shirley, J. H., and Fairbridge, R. W., eds., 1997, *Encyclopedia of Planetary Sciences*, Chapman and Hall, London.
[42] Newhall, X. X., Standish, Jr., E. M., and Williams, J. G., 1983, ''DE 102: A Numerically Integrated Ephemeris of the Moon and Planets Spanning Forty-Four Centuries,'' Astron. Astrophys., **125**, pp. 150–167.
[43] Fisher, M. E., 1989, ''Introductory Numerical Methods With the NAG Software Library,'' Mathematics Department, The University of Western Australia, Perth.
[44] Horn, R. A., and Johnson, L. R., 1991, *Topics in Matrix Analysis*, Cambridge University Press, Cambridge, UK.
[45] Mehta, M. L., 1977, *Elements of Matrix Theory*, Hindustan, Delhi, India.
[46] Jennings, L. S., Fisher, M. E., Teo, K. L., and Goh, C. J., 1991, ''MISER3: Solving Optimal Control Problems: An Update,'' Adv. Eng. Softw., **13**, No. 4, pp. 190–196.

Steady-State Limit of Elastoplastic Trusses for the Plastic Shakedown Region

K. Uetani
Professor,
e-mail: uetani@archi.kyoto-u.ac.jp

Y. Araki
Postdoctoral Fellow,
e-mail: araki@archi.kyoto-u.ac.jp

Graduate School of Engineering,
Kyoto University,
Sakyo, Kyoto 606-8501, Japan

For elastoplastic trusses under quasi-static cyclic loading, a method is presented for finding the steady-state limit that bounds the plastic shakedown and ratchetting regions. In the plastic shakedown region, an assumption employed in the previous approaches for finding the steady-state limit can be invalid in many circumstances. Although strain reversals were assumed to occur only at load reversals, yielding of an element exhibiting plastic shakedown may cause strain reversals in other elements. This difficulty is overcome by relaxing this assumption so that the strain reversals due to yielding are taken into account. Numerical examples showed that the present method can find the steady-state limit even when strong effects of geometrical nonlinearity exist.
[S0021-8936(00)01201-0]

1 Introduction

When a structure is subjected to initial constant loads and subsequent cyclic loading, its response is classified as follows (see, for instance, [1–4]); (1) convergent behavior to the *elastic shakedown* (ESD) or the *classical shakedown*, which is a cyclic and fully elastic response after some histories of plastic deformations; (2) convergent behavior to the *plastic shakedown* (PSD) or the *alternating plasticity*, where a structure behaves cyclically and plastic deformations are included in its steady cycle; and (3) the *ratchetting* or the *incremental collapse*, in which plastic deformations grow with respect to the number of loading cycles. If excessive deformations are induced by the ratchetting, the effect of geometrical nonlinearity becomes significant and total or local buckling may occur [5–8]. Including these cases, as called in our earlier work [9] the phenomenon characterized by the unbounded growth of plastic deformations is referred to as *cyclic instability* (CI) in this paper. Classification of these types of behavior is schematically illustrated in Fig. 1, where ψ and λ_0 indicate, respectively, the amplitude of cyclic loading and the magnitude of constant loads. The regions in which the ESD, PSD, and CI take place are called the ESD region, the PSD region, and the CI region. The boundary between the shakedown regions and the CI region is referred to as the shakedown limit.

To design structures that may suffer plastic deformations under cyclic loading, it is very important to obtain the shakedown limit. For this reason, a number of studies have been conducted on structural responses under quasi-static cyclic loading. The approaches employed in these studies are roughly divided into two categories: one is to trace all loading histories and the other is to find the shakedown limit theoretically without tracing the entire loading history.

A direct approach for investigating elastoplastic responses is to trace all loading histories. For this purpose, experimental, analytical, and numerical methods are available [3]. Tracing the entire loading history allows us to observe the detailed process of deformations and to find the loading condition below which a structure behaves in a stable manner. Nonetheless, generally, analytical methods can be applied only to very simple models. Experimental and numerical approaches require a number of parametric analyses to bound the structural responses. Moreover, it is very difficult to derive a theoretical condition similar to that for the *plastic buckling load* [10] or the *plastic collapse load* [11] from the results of the parametric analyses.

As a theoretical approach, the classical *shakedown theory* (see, e.g., [1,4]) is well known. With the shakedown theory, we can bound the ESD region regardless of loading histories. The classical shakedown theory is extended to the PSD region in several papers [12–15]. In these studies, the effect of geometrical nonlinearity is completely neglected. A few papers [5,16] were published concerning the shakedown limit taking geometrical nonlinearity into account. However, these path-independent shakedown theories are not promising when geometrical nonlinearity has a strong influence on structural responses because the shakedown limit is inherently path-dependent in this case.

To overcome this difficulty, Uetani [17] proposed the *steady-state limit theory* for cantilever beam-columns. Under cyclic bending with continuously increasing amplitude in the presence of a compressive axial force, a beam-column converges to a steady state unless the loading amplitude reaches a certain limit. If the loading amplitude exceeds this limit, the beam-column exhibits the CI. This limit is called the *steady-state limit* (SSL). In the SSL theory, the variation of a steady state with respect to the loading amplitude is regarded as a continuous path, called the *steady-state path*. And the SSL is found as the first limit point of the steady-state path. With the SSL theory, though under a specified loading history, the shakedown limit can be predicted theoretically even if strong effects of geometrical nonlinearity exist. Furthermore, the SSL is found very efficiently because only the variation of a steady state is traced and there is no need for tracing the entire loading history including transient response. Note that the SSL is a specific type of the shakedown limit defined for an idealized cyclic loading program with continuously increasing amplitude.

In our earlier work [9], the SSL theory has been extended to the truss structure, which is one of the simplest discrete structures. In the previous work, however, the discussion was restricted only to the SSL for the ESD region. The reason is stated as follows. In the previous method, similar to the SSL theory for cantilever beam-columns [17], a steady state is represented by a set of the equilibrium states at load reversals in order to trace the steady-state path. This representation is based on the assumption that strain reversals occur only at load reversals. Although this assumption holds in most circumstances in the ESD region, it does not in the PSD

Contributed by the Applied Mechanics Division of THE AMERICAN SOCIETY OF MECHANICAL ENGINEERS for publication in the ASME JOURNAL OF APPLIED MECHANICS. Manuscript received by the ASME Applied Mechanics Division, Aug. 14, 1998; final revision, Apr. 21, 1999. Associate Technical Editor: K. T. Ramesh. Discussion on the paper should be addressed to the Technical Editor, Professor Lewis T. Wheeler, Department of Mechanical Engineering, University of Houston, Houston, TX 77204-4792, and will be accepted until four months after final publication of the paper itself in the ASME JOURNAL OF APPLIED MECHANICS.

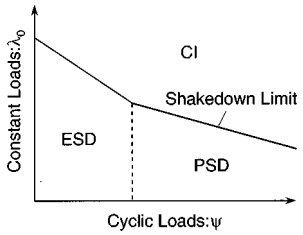

Fig. 1 Classification of the response in a plane of loading combinations

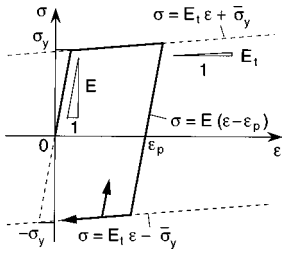

Fig. 3 A bilinear kinematic hardening rule

region. This is because, in the PSD region, not only load reversals but also yielding of the element exhibiting the PSD can cause strain reversals.

The objective of this paper is to present a method for predicting the SSL of elastoplastic trusses that bounds the PSD and CI regions. In this paper, first, governing equations are shown for elastoplastic trusses. Second, the hypothesis in the previous approaches is relaxed so that the strain reversals due to yielding are taken into consideration. Third, based on the relaxed hypothesis, we derive new incremental relations for the variation of a steady state with respect to the loading amplitude. In numerical examples, the validity of the present method is demonstrated by comparing the results of the SSL analysis with those of the response analysis. In the SSL analysis, the SSL is found according to the present method. In the response analysis, on the other hand, the entire loading history is traced using a conventional numerical method [18,19]. Furthermore, we discuss the effects of both geometrical nonlinearity and loading histories on the shakedown limit.

2 Governing Equations

2.1 Analytical Models. Consider a pin-jointed space trusses with M elements and N nodes. Assume large displacements–small strains. In the present truss model, buckling of a single element is ruled out, but that of a global type is taken into account. The total Lagrangian formulation (see, e.g., [18]) is used to measure stresses and strains. As illustrated in Fig. 2, compatibility conditions for an element are given by

$$\varepsilon=\frac{L^2-L_0^2}{2L_0^2}, \tag{1}$$

$$L^2=(x_4-x_1)^2+(x_5-x_2)^2+(x_6-x_3)^2, \tag{2}$$

$$x_i=x_i^0+u_i\,;\quad i=1,\ldots,6, \tag{3}$$

where ε is the Green-Lagrangian strain, L and L_0 are the current and initial lengths of the element, u_i is the nodal displacement, and x_i and x_i^0 indicate the current and initial positions of the nodes at the two ends. For equilibrium, we require

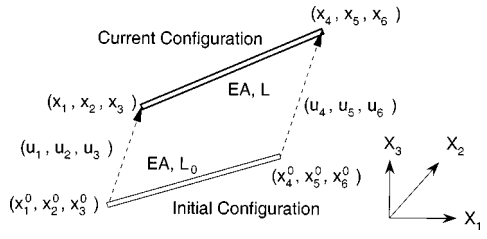

Fig. 2 The positions and the nodal displacements at the two ends of a truss element

$$f_i=AL_0\sigma\frac{\partial\varepsilon}{\partial u_i}, \tag{4}$$

in which f_i is the nodal force, A is the cross-sectional area, and σ is the second Piola-Kirchhoff stress. By assembling the equilibrium equation for the element, we obtain the equilibrium equations for the total system.

As a constitutive model, we employ a bilinear kinematic hardening rule shown in Fig. 3. Let E, E_t, σ_y, and ε_p indicate Young's modulus, the tangent modulus after yielding, the initial yield stress, and the plastic strain, respectively. Then the subsequent yield stresses σ_{yt} and σ_{yc} in tension and compression are expressed as

$$\sigma_{yt}=\frac{EE_t}{E-E_t}\varepsilon_p+\sigma_y\,,\quad \sigma_{yc}=\frac{EE_t}{E-E_t}\varepsilon_p-\sigma_y\,. \tag{5}$$

The stress-strain relations are expressed as follows:

$$\sigma=E(\varepsilon-\varepsilon_p),\quad \text{for } \sigma_{yc}\leqslant\sigma\leqslant\sigma_{yt}\,, \tag{6}$$

$$\sigma=E_t\varepsilon+\overline{\sigma_y}\,,\quad \text{if } \sigma=\sigma_{yt}\,, \tag{7}$$

$$\sigma=E_t\varepsilon-\overline{\sigma_y}\,,\quad \text{if } \sigma=\sigma_{yc}\,, \tag{8}$$

where $\overline{\sigma_y}$ is defined as $\overline{\sigma_y}=(1-E_t/E)\sigma_y$.

2.2 Loading Conditions. The trusses are subjected to initial constant loads $\lambda_0\overline{\mathbf{P}}_0$ and subsequent quasi-static cyclic loading $\lambda_c\overline{\mathbf{P}}_c$. Here, λ and $\overline{\mathbf{P}}$ denote the load factor and the constant vector with $3N$ components, respectively. The subscripts 0 and c indicate the quantities corresponding to the constant loads and the cyclic loading. According to the boundary condition, either the nodal force or the nodal displacement is specified for every component of both $\overline{\mathbf{P}}_0$ and $\overline{\mathbf{P}}_c$.

The load factor λ_c varies between the maximum value $\lambda_c^I=\psi$ and the minimum value $\lambda_c^{II}=-\psi$ in a cycle, where ψ denotes the amplitude of λ_c. Variation of λ_c is defined by a monotonically increasing parameter t, called time or the equilibrium path parameter. The equilibrium states at which $\lambda_c=\lambda_c^I$ and $\lambda_c=\lambda_c^{II}$ are called the Γ^I state and the Γ^{II} state, respectively. The superscripts I and II indicate that state variables, such as stresses, strains, and displacements, refer to Γ^I and Γ^{II}. Though the loading conditions given here are very simple, more complex loading conditions can be treated in the present theory. For example, the absolute values of λ_c^I and λ_c^{II} can be different.

2.3 Cyclic Responses in a Stress-Strain Plane. For later formulation, we classify all possible types of cyclic responses in a stress-strain plane. The classification is schematically illustrated in Fig. 4. The superscripts t and c indicate the quantities belonging to the equilibrium states Γ^t and Γ^c at which the strain takes its maximum and minimum values in a cycle, respectively. Type E is the ESD response whose stress moves within the range $\sigma_{yc}<\sigma<\sigma_{yt}$. If the plastic strain ε_p satisfies $\varepsilon_p=0$, Type E is a purely elastic response, and it is an unloading response otherwise. Type T is the ESD response whose stress reaches σ_{yt}, or $\sigma^t=\sigma_{yt}$. Type C is the ESD response where $\sigma^c=\sigma_{yc}$. Type P is the PSD

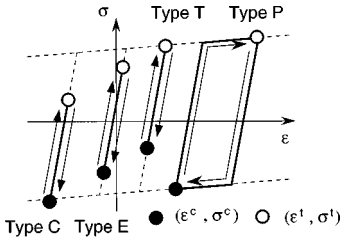

Fig. 4 Classification of all possible types of the cyclic response

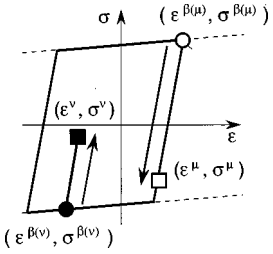

Fig. 5 The equilibrium state $\Gamma^{\beta(\mu)}$ at which the last loading occurs before Γ^{μ}

response. Throughout this paper, the elements exhibiting Types E, C, T, and P are called the E-element, the C-element, the T-element, and the P-element, respectively.

According to this classification, stress-strain relations are formulated for each type of the cyclic response. Let the superscript μ indicate the state variables referring to an arbitrary equilibrium state Γ^{μ} in a steady state. And let the superscript $\beta(\mu)$ indicate the quantities for the equilibrium state at which the last unloading occurs before Γ^{μ} as shown in Fig. 5. Then we can express the stress σ^{μ} in terms of the strains ε^{μ}, ε^{t}, ε^{c}, and $\varepsilon^{\beta(\mu)}$ as follows:

$$\text{Type E: } \sigma^{\mu}=E(\varepsilon^{\mu}-\varepsilon_p^{\mu}), \tag{9}$$

$$\text{Type T: } \sigma^{\mu}=E_t\varepsilon^{\mu}+\overline{\sigma_y}, \quad \text{if } \sigma^{\mu}=\sigma^{t}, \tag{10}$$

$$\sigma^{\mu}=E\varepsilon^{\mu}-(E-E_t)\varepsilon^{t}+\overline{\sigma_y}, \quad \text{if } \sigma^{\mu}\neq\sigma^{t}, \tag{11}$$

$$\text{Type C: } \sigma^{\mu}=E\varepsilon^{\mu}-(E-E_t)\varepsilon^{c}-\overline{\sigma_y}, \quad \text{if } \sigma^{\mu}\neq\sigma^{c}, \tag{12}$$

$$\sigma^{\mu}=E_t\varepsilon^{\mu}-\overline{\sigma_y}, \quad \text{if } \sigma^{\mu}=\sigma^{c}, \tag{13}$$

$$\text{Type P: } \sigma^{\mu}=E_t\varepsilon^{\mu}\pm\overline{\sigma_y}, \quad \text{if } \sigma^{\mu}=\sigma_{yt}^{\mu} \text{ or } \sigma^{\mu}=\sigma_{yc}^{\mu}, \tag{14}$$

$$\sigma^{\mu}=E\varepsilon^{\mu}-(E-E_t)\varepsilon^{\beta(\mu)}\pm\overline{\sigma_y}, \quad \text{if } \sigma_{yc}^{\mu}<\sigma^{\mu}<\sigma_{yt}^{\mu}. \tag{15}$$

Note that plastic strains are eliminated in obtaining Eqs. (11), (12), and (15). Let us show an example of this elimination. The stresses σ^{t} and σ^{μ} are written as

$$\sigma^{t}=E(\varepsilon^{t}-\varepsilon_p^{t}), \quad \sigma^{\mu}=E(\varepsilon^{\mu}-\varepsilon_p^{\mu}), \tag{16}$$

since Hooke's law equation (6) holds in any equilibrium states. From the definition of Type T,

$$\sigma^{t}=E_t\varepsilon^{t}+\overline{\sigma_y}. \tag{17}$$

In an ESD response, ε_p is constant throughout a cycle and we have

$$\varepsilon_p^{t}=\varepsilon_p^{\mu}. \tag{18}$$

Eliminating ε_p^{t} and ε_p^{μ} from Eqs. (16)–(18), we obtain Eq. (11).

3 Fundamental Concepts

In this section, first, we summarize the fundamental concepts and the hypotheses in the previous method of finding the SSL for the ESD region ([9]). Then a general consideration is made on strain reversals. Based on this consideration, the hypotheses are relaxed and the key concepts are shown for finding the SSL for the PSD region.

3.1 The Steady-State Limit (SSL) Theory for the Elastic Shakedown (ESD) Region. The fundamental concepts of the SSL theory are summarized as follows:

1 A steady state is represented by a point in a special space. This space is called the *steady-state space* and is schematically illustrated in Fig. 6.

2 Under an idealized cyclic loading (ICL) program with continuously increasing amplitude, the sequence of these points is regarded as a continuous path, called the steady-sate path.

3 The SSL is found as the first limit point of the steady-state path.

In the ICL program, the loading amplitude ψ varies continuously with respect to the steady-state path parameter τ. The loading cycle is repeated as many times as necessary for a structure to converge to a steady state at each level of ψ as shown in Fig. 7. More rigorous definition of the ICL program was given by Uetani and Araki [9].

In the previous method, the variation of a steady state with respect to τ was formulated in terms of the state variables at load reversals based on the following hypotheses:

(H2*) All the state variables for Γ^{I} and Γ^{II} are continuous and piecewise differentiable functions of τ.

(H3*) For all elements, strain reversals occur only at Γ^{I} or Γ^{II}.

Note that (H3*) is applied not to the transient response but to the steady-state response after convergence.

3.2 The Steady-State Limit (SSL) Theory for the Plastic Shakedown (PSD) Region. In the PSD region, as mentioned in the Introduction, hypothesis (H3*) dose not hold in many circumstances. To deal with this difficulty, let us consider why strain reversals take place in the present truss model. If the relation between strain ε and the equilibrium path parameter t is linear in every element, no strain reversals can occur. On the other hand, strain reversals are possible if the ε-t relation is nonlinear. Obviously, this relation is nonlinear in the present model. The sources

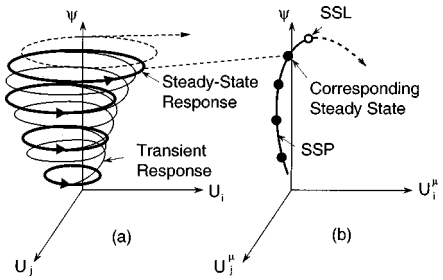

Fig. 6 Fundamental concepts of the SSL theory: (*a*) the equilibrium state space and (*b*) the steady-state space

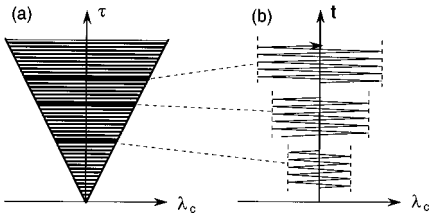

Fig. 7 (*a*) The ICL program and (*b*) the loading process at each amplitude level

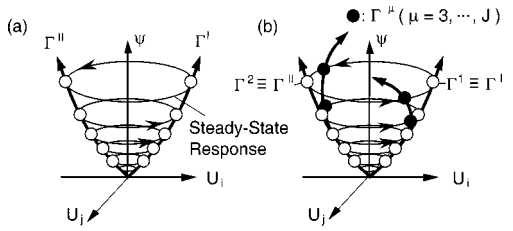

Fig. 8 Key differences between (*a*) the previous method and (*b*) the present method

of this nonlinearity are classified as follows: (1) nonproportional loading or cyclic loading; (2) material nonlinearity, e.g. yielding; and (3) geometrical nonlinearity, or nonlinear strain-displacement relations. In this study, the strain reversals due to geometrical nonlinearity are not considered since they are much less likely to occur than those due to material nonlinearity or nonproportional loading.

Based on the above consideration, (H2*) and (H3*) are relaxed so that the strain reversals due to yielding are taken into consideration:

(H2**) All the state variables for the equilibrium states at which strain reversals occur are continuous and piecewise differentiable functions of τ.

(H3**) For all elements, strain reversals occur only at load reversals or at the yielding of P-elements.

Similar to (H3*),(H3**) is applied not to the transient response but to the steady-state response.

Based on these relaxed hypotheses, a steady state is represented by a set of equilibrium states at which yielding or a load reversal occurs. The key difference between the previous and present methods is shown in Fig. 8. In this paper, the equilibrium state for representing a steady state is called the *representative equilibrium state* or RES. In the RESs, Γ^1 and Γ^2 are defined in such a way that they correspond respectively to the equilibrium states Γ^{I} and Γ^{II}. Once a steady state is represented by a set of the RESs, similar to the previous method, the steady-state path is traced in a step-by-step manner. And the SSL is found as the first limit point of the steady-state path. Note that, in the SSL theory, we trace only the variation of a steady state with respect to the loading amplitude and that no equilibrium paths are traced.

4 Formulation

4.1 Incremental Relations for Variation of a Steady State. Consider a steady state at $\tau=\tau_h$ represented by a set of J RESs Γ^μ $(\mu=1,2,\cdots,J)$. When all the state variables are known in the current steady state at $\tau=\tau_h$, our problem is to find those in the neighboring steady state at $\tau=\tau_{h+1}=\tau_h+\Delta\tau$. Let the dot indicate differentiation with respect to τ. Then, owing to (H2**), the state variables at $\tau=\tau_{h+1}$ are expressed with the Taylor series expansion as

$$\mathbf{U}^\mu(\tau_{h+1})=\mathbf{U}^\mu(\tau_h)+\dot{\mathbf{U}}^\mu(\tau_h)\Delta\tau+\frac{1}{2}\ddot{\mathbf{U}}^\mu(\tau_h)\Delta\tau^2+\cdots, \quad (19)$$

$$\mathbf{F}^\mu(\tau_{h+1})=\mathbf{F}^\mu(\tau_h)+\dot{\mathbf{F}}^\mu(\tau_h)\Delta\tau+\frac{1}{2}\ddot{\mathbf{F}}^\mu(\tau_h)\Delta\tau^2+\cdots, \quad (20)$$

$$\mathbf{E}^\mu(\tau_{h+1})=\mathbf{E}^\mu(\tau_h)+\dot{\mathbf{E}}^\mu(\tau_h)\Delta\tau+\frac{1}{2}\ddot{\mathbf{E}}^\mu(\tau_h)\Delta\tau^2+\cdots, \quad (21)$$

$$\mathbf{E}_p^\mu(\tau_{h+1})=\mathbf{E}_p^\mu(\tau_h)+\dot{\mathbf{E}}_p^\mu(\tau_h)\Delta\tau+\frac{1}{2}\ddot{\mathbf{E}}_p^\mu(\tau_h)\Delta\tau^2+\cdots, \quad (22)$$

$$\mathbf{S}^\mu(\tau_{h+1})=\mathbf{S}^\mu(\tau_h)+\dot{\mathbf{S}}^\mu(\tau_h)\Delta\tau+\frac{1}{2}\ddot{\mathbf{S}}^\mu(\tau_h)\Delta\tau^2+\cdots, \quad (23)$$

where $\mathbf{F}$ and $\mathbf{U}$ are the nodal force vector and the nodal displacement vector with $3N$ components, and $\mathbf{E}$, $\mathbf{E}_p$, and $\mathbf{S}$ denote the strain vector, the plastic strain vector, and the stress vector with M components. Here, recall that M and N are the numbers of the elements and the nodes. To determine the state variables at the neighboring steady state, we must determine the step length $\Delta\tau$ and compute the derivatives of the state variables. In the following subsections, the formulation for obtaining these quantities is shown.

4.2 Rate Forms of Governing Equations. We formulate the rate forms of the governing equations for the total system. Differentiating the compatibility conditions (1)–(3) and the equilibrium condition (4), we have the rate forms of these equations for an element as

$$\dot{\varepsilon}^\mu=\frac{\partial\varepsilon^\mu}{\partial u_i^\mu}\dot{u}_i^\mu, \quad (24)$$

$$\dot{f}_i^\mu=AL_0\left(\dot{\sigma}^\mu\frac{\partial\varepsilon^\mu}{\partial u_i^\mu}+\sigma^\mu\frac{\partial^2\varepsilon^\mu}{\partial u_i^\mu\partial u_j^\mu}\dot{u}_j^\mu\right). \quad (25)$$

Throughout this paper, the summation convention is used only for subscripts i, j, and k that varies from 1 to 6. As shown in Appendix A, the rate forms of the stress-strain relations are expressed as

$$\dot{\sigma}^\mu=\sum_{\nu=1}^{J}D^{\mu\nu}\dot{\varepsilon}^\nu. \quad (26)$$

Substituting Eqs. (24) and (26) into Eq. (25), we obtain the nodal force rate-nodal displacement rate relations for an element as

$$\dot{f}_i^\mu=\sum_{\nu=1}^{J}k_{ij}^{\mu\nu}\dot{u}_j^\nu,$$

$$k_{ij}^{\mu\nu}=AL_0\sum_{\nu=1}^{J}D^{\mu\nu}\frac{\partial\varepsilon^\mu}{\partial u_i^\mu}\frac{\partial\varepsilon^\nu}{\partial u_j^\nu}+AL_0\delta_{\mu\nu}\sigma^\mu\frac{\partial^2\varepsilon^\mu}{\partial u_i^\mu\partial u_j^\mu}, \quad (27)$$

where $\delta_{\mu\nu}$ is Kronecker's delta and $k_{ij}^{\mu\nu}$ is the coefficient relating $\dot{f}_i^\mu$ to $\dot{u}_j^\nu$. By assembling Eq. (27), we obtain the nodal force rate-nodal displacement rate relations for the total system

$$\dot{\mathbf{F}}^\mu=\sum_{\nu=1}^{J}\mathbf{K}^{\mu\nu}\dot{\mathbf{U}}^\nu, \quad (28)$$

where $\mathbf{K}^{\mu\nu}$ is the coefficient matrix of $\dot{\mathbf{U}}^\nu$.

Now we have $J\times 3N$ equations that relate $\dot{\mathbf{F}}^\mu$ to $\dot{\mathbf{U}}^\mu$. Substitute all the components of $\dot{\lambda}_c^\mu\overline{\mathbf{P}}_c$ into Eq. (28) according the boundary condition. Then the number of unknowns becomes $J\times(3N+1)$. Here, it should be noted that $\dot{\lambda}^\mu$ $(\mu=1,\cdots,J)$ are regarded as unknowns as well as the $J\times 3N$ unknown components of the nodal force rates and/or the nodal displacement rates. To determine all these unknowns, additional J equations are needed together with Eq. (28). The additional equations are given by the conditions that characterize the RESs. Since the first two RESs are defined as the equilibrium states at load reversals, the conditions for $\dot{\lambda}_c^1$ and $\dot{\lambda}_c^2$ are written as

$$\dot{\lambda}_c^1=\dot{\psi}, \quad \dot{\lambda}_c^2=-\dot{\psi}. \quad (29)$$

The remaining RESs Γ^μ $(\mu\geqslant 3)$ are characterized by the yielding of P-elements. As shown in Fig. 9, the equilibrium state Γ^μ is characterized by one of the following conditions:

$$\sigma^\mu=\sigma^{\beta(\mu)}, \quad \sigma^\mu=\sigma^{\beta(\mu)}\pm 2\sigma_y. \quad (30)$$

With $\varepsilon_p^\mu=\varepsilon_p^{\beta(\mu)}$ and Hooke's law equation (6), differentiation of every equation in Eq. (30) yields the same rate relation

$$\dot{\varepsilon}^\mu-\dot{\varepsilon}^{\beta(\mu)}=0. \quad (31)$$

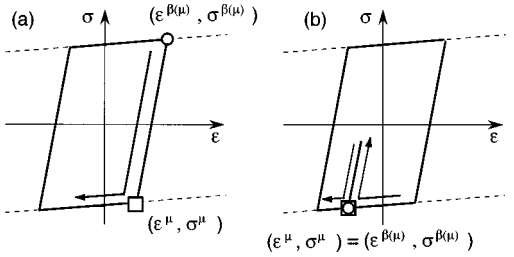

Fig. 9 The yielding conditions (*a*) $\sigma^{\mu}=\sigma^{\beta(\mu)}+2\sigma_y$ and (*b*) $\sigma^{\mu}=\sigma^{\beta(\mu)}$

Table 1 The numbers of equations and unknowns

Derivatives	Number of unknowns	Equation number	Number of equations
$\dot{\mathbf{E}}^{\mu}$, $\dot{\mathbf{U}}^{\mu}$	$J\times 3N$	(28)	$J\times 3N$
$\dot{\lambda}^1$, $\dot{\lambda}^2$	2	(29)	2
$\dot{\lambda}^{\mu}$	$J-2$	(33)	$J-2$
Total	$J(3N+1)$	total	$J(3N+1)$

Condition (31) is expressed in terms of the nodal displacements of an element as

$$\frac{\partial \varepsilon^{\mu}}{\partial u_i^{\mu}}\dot{u}_i^{\mu}-\frac{\partial \varepsilon^{\beta(\mu)}}{\partial u_i^{\beta(\mu)}}\dot{u}_i^{\beta(\mu)}=0. \tag{32}$$

Condition (32) can be rewritten in terms of the nodal displacements for the total system as

$$\mathbf{L}^{\mu}\dot{\mathbf{U}}^{\mu}+\mathbf{L}^{\beta(\mu)}\dot{\mathbf{U}}^{\beta(\mu)}=\mathbf{0}, \tag{33}$$

where $\mathbf{L}$ is the coefficient matrix of $\dot{\mathbf{U}}$, and $\mathbf{0}$ is the zero vector. With these equations together with Eq. (28), the number of the equations becomes identical to that of the unknowns as shown in Table 1. These equations are to be solved by specifying the value of $\dot{\psi}$.

4.3 Termination Conditions for Incremental Steps. In tracing the steady-state path, an incremental step should be terminated at the steady state where the types of stress rate-strain rate relations change. In addition, the step length $\Delta\tau$ should be small enough to prevent an excessive accumulation of truncation errors. Hence $\Delta\tau$ is determined as the smallest value among the values obtained from the following conditions and the specified maximum allowable value $\Delta\bar{\tau}_{\max}$.

For each E-element, $\Delta\tau$ is calculated with the following conditions:

$$\sigma^t(\tau_{h+1})-\sigma_{yt}^t(\tau_{h+1})=0, \quad \text{for E}\rightarrow\text{T}, \tag{34}$$

$$\sigma^c(\tau_{h+1})-\sigma_{yc}^c(\tau_{h+1})=0, \quad \text{for E}\rightarrow\text{C}. \tag{35}$$

Here, in the linear approximation, $\sigma(\tau_{h+1})\approx\sigma(\tau_h)+\dot{\sigma}(\tau_h)\Delta\tau$ and other variables are expressed similarly. Note that $\dot{\sigma}_{yt}^t(\tau_h)=\dot{\sigma}_{yt}^t(\tau_h)=0$ in E-elements. For all E, T, and C-elements, the condition for the transition to Type P is written as

$$\sigma^t(\tau_{h+1})-\sigma^c(\tau_{h+1})-2\sigma_y=0. \tag{36}$$

For P-elements, as illustrated in Fig. 10(*a*), the conditions for the transitions from the elastic range to the strain-hardening range are written as

$$\sigma^{\mu}(\tau_{h+1})-\sigma_{yt}^{\mu}(\tau_{h+1})=0, \quad \sigma^{\mu}(\tau_{h+1})-\sigma_{yc}^{\mu}(\tau_{h+1})=0. \tag{37}$$

The condition for the transition from the straining hardening range to the elastic range shown in Fig. 10(*b*) is given by

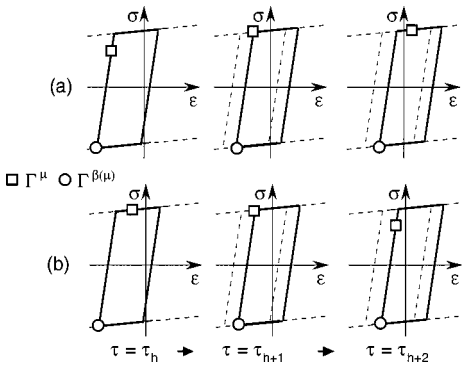

Fig. 10 (*a*) The transition from the elastic range to the strain hardening range and (*b*) the transition from the straining hardening range to the elastic range

$$\varepsilon_p^{\mu}(\tau_{h+1})-\varepsilon_p^{\beta(\mu)}(\tau_{h+1})=0. \tag{38}$$

4.4 Steady-State Limit (SSL) Condition. Substituting the derivatives and the step length into Eqs. (19)–(23), we obtain the state variables at the neighboring steady state. Repeating these procedures, we can trace the steady-state path. As shown in Fig. 6(*b*), the SSL is characterized as the first limit point of the steady-state path with respect to the loading amplitude ψ. The SSL condition is therefore given as

$$\dot{\psi}\leqslant 0. \tag{39}$$

For finding the SSL, a procedure similar to the displacement control schemes [18,19] is employed. More details of the present method are shown in Appendices B, C, and D.

5 Numerical Examples

In this section, the validity of the hypotheses in the present method is discussed. And it is studied how the shakedown limit changes when different types of loading histories are applied. In addition, we examine the effect of geometrical nonlinearity on the shakedown limit. For these purposes, we perform the SSL analysis and a conventional response analysis, in which the entire loading history is traced.

5.1 Steady-State Limit (SSL) Analysis. The present method is applied to the two-bar and ten-bar plane trusses whose ESD boundaries were obtained by Uetani and Araki [19]. Figure 11 shows the initial shapes, the boundary conditions, and the load-

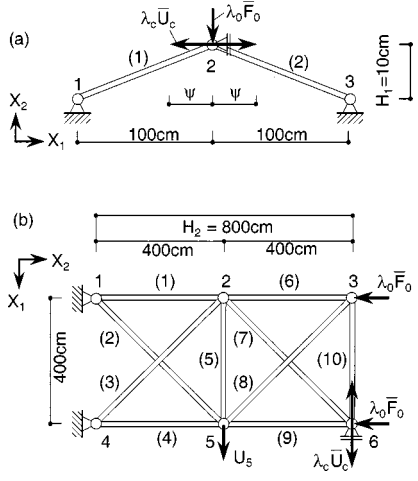

Fig. 11 (*a*) The two-bar truss and (*b*) the ten-bar plane truss

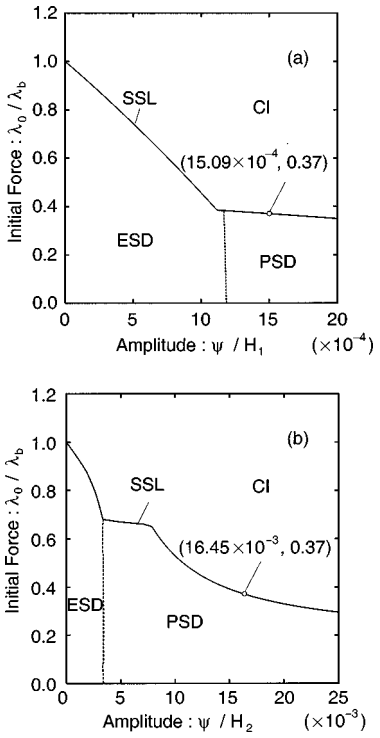

Fig. 12 The SSL for (*a*) the two-bar truss and (*b*) the ten-bar truss

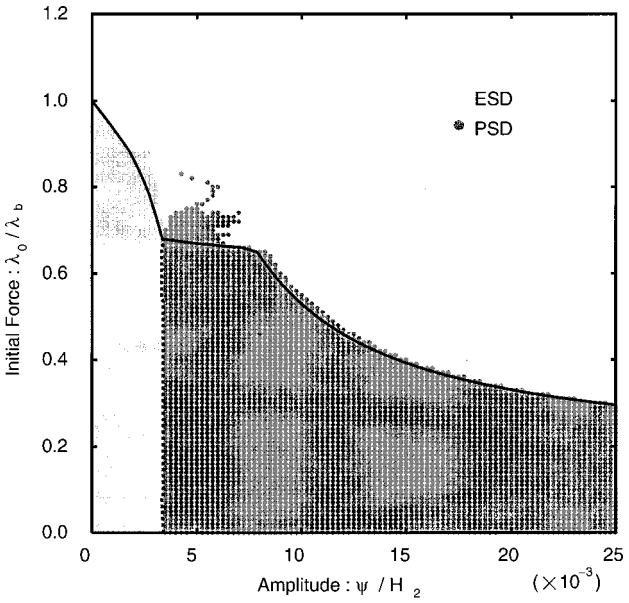

Fig. 14 The SSL and the results of the parametric response analysis

ing conditions of the trusses. When the previous method was applied directly to these trusses, it failed to find the SSL for the PSD region.

The numerical data for these trusses were given as follows. The cross-sectional areas of the two-bar truss were $A_{(1)}=1\ \mathrm{cm}^2$ and $A_{(2)}=2\ \mathrm{cm}^2$. Those of the ten-bar truss were as follows: $A_{(1)}=A_{(4)}=A_{(5)}=11\ \mathrm{cm}^2$, $A_{(2)}=A_{(3)}=1.1\ \mathrm{cm}^2$, $A_{(6)}=A_{(9)}=A_{(10)}=10\ \mathrm{cm}^2$, and $A_{(7)}=A_{(8)}=1\ \mathrm{cm}^2$. For both trusses, material properties were $E=1.961\times10^2$ GPa, $E_t=0.01E$, $\sigma_y=2.942\times10^2$ MPa. When only initial constant loads were applied, buckling loads in the sense of Hill [10] were $\lambda_b=0.7477$ and 40.38 for the two-bar and ten-bar trusses, respectively. Throughout the SSL analysis, higher-order terms were employed up to the second order (see Appendix B). The values of the maximum allowable step length $\Delta\bar{\tau}_{\max}$ were $\Delta\bar{\tau}_{\max}=0.05$ and 0.2 for the two-bar and ten-bar trusses, respectively.

Figures 12(*a*) and (*b*) depict the results of the SSL analysis. In the SSL analysis, the normalized load factor λ_0/λ_b for initial constant loads were changed parametrically between 0 and 1 with the increments of 0.005 and 0.01 for the two-bar and ten-bar trusses. These figures illustrate the value of the loading amplitude ψ_{ssl} at the SSL predicted for each λ_0/λ_b.

5.2 Response Analysis. Entire loading history was traced under two typical cyclic loading programs shown in Fig. 13 ([7]). The STIDAC is a forced displacement program where the amplitude ψ of the forced displacement is increased every half cycle

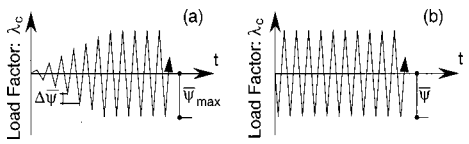

Fig. 13 The cyclic forced displacement programs: (*a*) STIDAC and (*b*) STIDAD

with an increment $\Delta\bar{\psi}$ from zero to a specified value $\bar{\psi}_{\max}$, and then ψ is fixed at $\bar{\psi}_{\max}$ in the following cycles. In the STIDAD program, ψ is fixed at a constant value $\bar{\psi}$ throughout the loading cycles. Note that the loading history of the STIDAC program becomes closer to that of the ICL program as $\Delta\psi$ is made smaller. The details of the solution method for the response analysis and the criteria for convergence are exactly the same as those shown by Uetani and Araki [9].

First, we performed the response analysis for every λ_0/λ_b under the loading conditions $\bar{\psi}_{\max}=(1\pm0.001)\psi_{\mathrm{ssl}}$, $\Delta\bar{\psi}=0.001\psi_{\mathrm{ssl}}$, and $\bar{\psi}=(1\pm0.001)\psi_{\mathrm{ssl}}$. Under the STIDAC program, good agreement was observed between the results of the SSL and the response analyses; convergence was observed in all cases when $\bar{\psi}_{\max}<\psi_{\mathrm{ssl}}$; and divergence was obtained if $\bar{\psi}_{\max}>\psi_{\mathrm{ssl}}$. From these results, it may be stated that the hypotheses in the proposed method are verified. On the other hand, the results of the response analysis under the STIDAD program did not always coincide with the results of the SSL analysis. In the ten-bar truss, convergence was observed in spite of the condition $\bar{\psi}>\psi_{\mathrm{ssl}}$. These results clearly indicate that the shakedown limit for the ten-bar truss is path-dependent.

To study how the shakedown limit changes when different types of loading histories are applied, we carried out a parametric analysis in which not only λ_0 but also $\bar{\psi}$ in the STIDAD program are changed. The load factor λ_0 of the constant load was changed in the same manner as in the SSL analysis. The normalized amplitude $\bar{\psi}/H_2(\times10^{-3})$ was changed from 0 to 25 with the increment of 0.25. Accordingly, we performed the response analysis for 100×100 different combinations of $(\lambda_0,\bar{\psi})$. The result of the parametric analysis is illustrated in Fig. 14. The darker and lighter gray circles indicate the convergence to the PSD and ESD, respectively. It is worth noting in Fig. 14 that the SSL gives the lower bound of the shakedown limit obtained under the STIDAD program.

One might think that the shakedown limit obtained by the conventional shakedown theory, where perfect plasticity and small displacements are assumed, is close to or conservative to the SSL in Fig. 12. Nevertheless these approximations, especially the assumption of small displacements, can lead to a significant error. To show an example of this error we performed the response

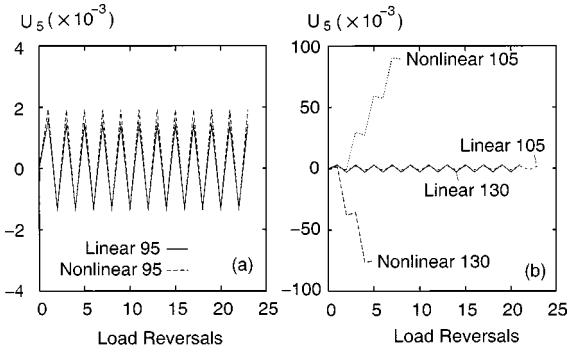

Fig. 15 The relations between U_5 and the number of load reversals for the ten-bar truss under (*a*) $\bar{\psi}<\psi_{ssl}$ and (*b*) $\bar{\psi}>\psi_{ssl}$

analysis based on the assumptions of both large and small displacements. In the assumption of small displacements we used the conventional linear strain-displacement relation. On the other hand, the nonlinear Green-Lagrangian strain shown in Eq. (1) was employed in the assumption of large displacements. The response analysis was conducted for $\bar{\psi}=95$, 105, and 130 percent of ψ_{ssl} under $\lambda_0/\lambda_b=0.37$. Figure 15 shows the results of the response analysis. Noting that the *y* scales are different in Figs. 15(*a*) and (*b*), we can make the following two observations: (1) The error became significant if $\bar{\psi}>\psi_{ssl}$ while it was very small otherwise. (2) The assumption of small displacements did not give a conservative shakedown limit. Similar results were reported for cylindrical shells by Maier et al. [8].

6 Conclusions

For elastoplastic trusses subjected to quasi-static cyclic loading in the presence of constant loads, a new method has been presented for finding the SSL that bounds the PSD region and the CI region. Although strain reversals were assumed to occur only at load reversals in the previous approaches, this assumption can be invalid in many circumstances in the PSD region. In the present theory, therefore, the hypothesis on strain reversals has been relaxed so that the strain reversals due to yielding can be taken into account. Based on the relaxed hypothesis, we have derived new incremental relations for the variation of a steady state with respect to the loading amplitude. With these incremental relations, similar to the previous approaches, the steady-state path is traced in a step-by-step manner and the SSL is found as the first limit point of the steady-state path.

Through numerical examples, the following findings have been made for the two-bar and ten-bar trusses:

1 The results of the SSL analysis agreed very well with those of a conventional response analysis when the loading programs employed in both analyses were close enough. This good agreement shows the validity of the present method.

2 The SSL, defined for the ICL program with continuously increasing amplitude, was conservative or close to the shakedown limit obtained under two typical cyclic loading programs.

3 With the present method, the SSL can be predicted even if strong effects of geometrical nonlinearity exist. The errors due to geometrical nonlinearity were significant if the loading amplitude was larger than the SSL while they were trivial otherwise.

Acknowledgments

This work was supported by JSPS Research Fellowships for Young Scientists and Grant-in-Aid for JSPS Fellows from the Ministry of Education, Science, Sports and Culture of Japan. The authors are grateful to the valuable comments from the reviewers.

Appendix A

Stress Rate-Strain Rate Relations. Consider the stress rate-strain rate relations for the variation of a steady state. Suppose that the following conditions are known during the incremental step defined by $\tau_h \leqq \tau \leqq \tau_{h+1}$:

(C1) The number J of the RESs.

(C2) For every element, the RESs corresponding to the equilibrium states Γ^t and Γ^c, where strain takes its maximum and minimum values in a steady cycle.

(C3) For every P-element, the RESs corresponding to the equilibrium states $\Gamma^{\beta(\mu)}$ ($\mu=1,2,\ldots,J$), where the last unloading occurs before Γ^{μ}.

Then, differentiating Eqs. (9)–(12) with respect to τ, we obtain the stress rate-strain rate relations for the E, T, and C-elements. The rate relations are expressed as

$$\dot{\sigma}^{\mu}=D^{\mu\mu}\dot{\varepsilon}^{\mu}+D^{\mu t}\dot{\varepsilon}^{t}+D^{\mu c}\dot{\varepsilon}^{c}, \tag{40}$$

where $D^{\mu\mu}$, $D^{\mu t}$, and $D^{\mu c}$ are the coefficients that are chosen according to Table 2. For the P-elements, differentiation of Eqs. (14)–(15) leads to

$$\dot{\sigma}^{\mu}=D^{\mu\mu}\dot{\varepsilon}^{\mu}+D^{\mu\beta}\dot{\varepsilon}^{\beta(\mu)}, \tag{41}$$

in which $D^{\mu\mu}$ and $D^{\mu\beta}$ are the coefficients that are selected according to Table 3. With the help of the conditions (C1)–(C3), we can express the rate forms of the stress-strain relations in a general form

$$\dot{\sigma}^{\mu}=\sum_{\nu=1}^{J} D^{\mu\nu}\dot{\varepsilon}^{\nu}, \tag{42}$$

where $D^{\mu\nu}$ is the coefficient of $\dot{\varepsilon}^{\nu}$. Note that, for all T and C-elements, we should choose a set of the coefficients that are consistent with the signs of the resulting strain rates as shown in Table 2. For this purpose, we employ the trial-and-error procedure whose details are shown in our earlier work [9].

Appendix B

Higher-Order Formulation. Though only the formulation with the first-order derivatives is shown in Section 4 for clarity and simplicity of the presentation, it is desirable to use higher-order derivatives for more accurate approximations. For this purpose, a formulation is presented for the SSL analysis with higher-order terms. Though we derive here the derivatives up to the second order, the derivatives higher than the second order can be obtained similarly. Differentiation of the rate forms of governing

Table 2 Stress rate-strain rate relations for an element exhibiting elastic shakedown (ESD)

	E	T			C		
		$\dot{\varepsilon}^t \geqq 0$		$\dot{\varepsilon}^t<0$	$\dot{\varepsilon}^c \leqq 0$		$\dot{\varepsilon}^c>0$
		$\sigma^{\mu}=\sigma^t$	$\sigma^{\mu}\neq\sigma^t$		$\sigma^{\mu}=\sigma^c$	$\sigma^{\mu}\neq\sigma^c$	
$D^{\mu\mu}$	E	E_t	E	E	E_t	E	E
$D^{\mu t}$	0	0	E_t-E	0	0	0	0
$D^{\mu c}$	0	0	0	0	0	E_t-E	0

Table 3 Stress rate-strain rate relations for an element exhibiting plastic shakedown (PSD)

	$\sigma^{\mu}=\sigma^{\mu}_{yt}$	$\sigma^{\mu}=\sigma^{\mu}_{yc}$	$\sigma^{\mu}_{yc}<\sigma^{\mu}<\sigma^{\mu}_{yt}$
$D^{\mu\mu}$	E_t	E_t	E
$D^{\mu\beta}$	0	0	E_t-E

Equations (24)–(32) with respect to the steady-state path parameter τ yields the second-order perturbation equations as follows:

$$\ddot{\varepsilon}^{\mu}=\frac{\partial \varepsilon^{\mu}}{\partial u_i^{\mu}}\ddot{u}_i^{\mu}+\frac{\partial^2 \varepsilon^{\mu}}{\partial u_i^{\mu}\partial u_j^{\mu}}\dot{u}_i^{\mu}\dot{u}_j^{\mu}. \tag{43}$$

$$\ddot{f}_i^{\mu}=AL_0\left(\ddot{\sigma}^{\mu}\frac{\partial \varepsilon^{\mu}}{\partial u_i^{\mu}}+\sigma^{\mu}\frac{\partial^2 \varepsilon^{\mu}}{\partial u_i^{\mu}\partial u_j^{\mu}}\ddot{u}_j^{\mu}+2\dot{\sigma}^{\mu}\frac{\partial^2 \varepsilon^{\mu}}{\partial u_i^{\mu}\partial u_j^{\mu}}\dot{u}_j^{\mu}\right). \tag{44}$$

$$\ddot{\sigma}^{\mu}=\sum_{\nu=1}^{J} D^{\mu\nu}\ddot{\varepsilon}^{\nu}. \tag{45}$$

Note that $\dot{D}^{\mu\mu}=0$ because a bilinear constitutive relation is assumed. Differentiating Eq. (27), we obtain the second-order perturbation equations for each element:

$$\ddot{f}_i^{\mu}=\sum_{\nu=1}^{J} k_{ij}^{\mu\nu}\ddot{u}_j^{\nu}+\hat{f}_i^{\mu}, \tag{46}$$

where the coefficient $k_{ij}^{\mu\nu}$ is identical to that in Eq. (28) and the caret indicates the quantities expressed in terms of the first-order derivatives as

$$\hat{f}_i^{\mu}=2AL_0\dot{\sigma}^{\mu}\frac{\partial^2 \varepsilon^{\mu}}{\partial u_i^{\mu}\partial u_j^{\mu}}\dot{u}_j^{\mu}+AL_0\frac{\partial \varepsilon^{\mu}}{\partial u_i^{\mu}}\sum_{\nu=1}^{J} D^{\nu\nu}\frac{\partial^2 \varepsilon^{\nu}}{\partial u_j^{\nu}\partial u_k^{\nu}}\dot{u}_j^{\nu}\dot{u}_k^{\nu}. \tag{47}$$

Assembling the perturbation equations for an element, we have the second-order perturbation equations for the total system

$$\ddot{\mathbf{F}}^{\mu}=\mathbf{K}^{\mu\nu}\ddot{\mathbf{U}}^{\nu}+\hat{\mathbf{F}}^{\mu}, \tag{48}$$

where the coefficient matrix $\mathbf{K}^{\mu\nu}$ is identical to that in Eq. (28). Differentiation of Eq. (29) and (32) leads to

$$\ddot{\lambda}_c^1-\ddot{\psi}=0, \quad \ddot{\lambda}_c^2+\ddot{\psi}=0, \tag{49}$$

$$\frac{\partial \varepsilon^{\mu}}{\partial u_i^{\mu}}\ddot{u}_i^{\mu}-\frac{\partial \varepsilon^{\beta(\mu)}}{\partial u_i^{\beta(\mu)}}\ddot{u}_i^{\beta(\mu)}+\hat{u}^{\mu\beta}=0, \ (\mu\geqslant 3), \tag{50}$$

where

$$\hat{u}^{\mu\beta}=\frac{\partial^2 \varepsilon^{\mu}}{\partial u_i^{\mu}\partial u_j^{\mu}}\dot{u}_i^{\mu}\dot{u}_j^{\mu}-\frac{\partial^2 \varepsilon^{\beta(\mu)}}{\partial u_i^{\beta(\mu)}\partial u_j^{\beta(\mu)}}\dot{u}_i^{\beta(\mu)}\dot{u}_j^{\beta(\mu)}. \tag{51}$$

Equation (51) can be expressed in terms of nodal displacements for the total system as

$$\mathbf{L}^{\mu}\ddot{\mathbf{U}}^{\mu}+\mathbf{L}^{\beta(\mu)}\ddot{\mathbf{U}}^{\beta(\mu)}+\hat{\mathbf{U}}^{\mu\beta}=\mathbf{0}. \tag{52}$$

By specifying the value of $\ddot{\psi}$, we can solve $J\times(3N+1)$ simultaneous linear Eqs. (48)–(49) and (52). Note that, as stated in our earlier paper [9], the conditions for the transitions T→E and C→E should be considered in determining the step length when we employ the terms higher than or equal to the second order.

Appendix C

Change of the Number of Yielding Points. When the number of yielding points changes, conditions (C1)–(C3) in Appendix A may change. Let us consider a method for determining the change of these conditions. First, we consider when the number of yielding points changes. Suppose that a strain reversal occurs at Γ^{μ} in an element. If Γ^{μ} satisfies Eq. (37), the number of yielding points increases. On the other hand, the number of yielding points decrease if Γ^{μ} satisfies Eq. (38).

Second, when the number of yielding points increases in an element at $\tau=\tau_h$ as illustrated in Fig. 16(*a*), the strain reversal at the new yielding point should be examined in every element as illustrated in Fig. 16(*b*). We examine the strain reversal by using ε'^{-} and ε'^{+}. Here the prime with superscripts − and + indicate partial differentiation with respect to t before and after Γ^{y} in the transient response when the loading amplitude is slightly changed as shown in Fig. 17(*a*). As depicted in Fig. 17(*b*), the strain reversal is judged to occur if $\varepsilon'^{-}\varepsilon'^{+}<0$. Otherwise, strain reversal is judged not to occur. Note that, in the present method, ε'^{+} and ε'^{-} are calculated not for tracing the equilibrium path in the transient response but for examining the strain reversals.

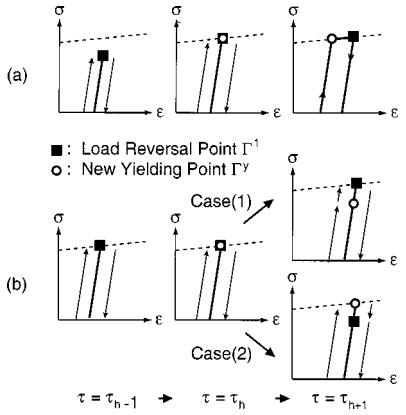

Fig. 16 An example of a new yielding point: (*a*) the transition in an element where the number of yielding point increases and (*b*) the transition in another element

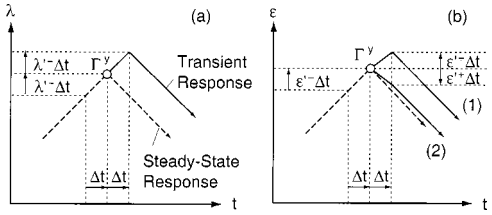

Fig. 17 (*a*) The change of the load factor and (*b*) the examination of strain reversals

To summarize, conditions (C1)–(C3) are changed when one of the following two condition is satisfied: (CE1) the number of yielding points increases and the new yielding point causes strain reversals at least in one element; (CE2) the number of yielding points decreases. For example, in Fig. 16(*b*), the conditions are written as $J=2$ and $\Gamma^{t}=\Gamma^{1}$ for $\tau<\tau_h$. In Case 1, the strain reversal occurs only at the load reversal for $\tau\geqslant\tau_h$ and the conditions $J=2$ and $\Gamma^{t}=\Gamma^{1}$ are kept. In contrast, in Case 2, the strain reversal takes place at Γ^{y}. In this case, the conditions are changed to $J=3$ and $\Gamma^{t}=\Gamma^{3}$.

Appendix D

A Basic Algorithm for the Steady-State Limit (SSL) Analysis.

1 Obtain the equilibrium state under initial constant loads.
2 IF (CE1) or (CE2) is satisfied, change conditions (C1)–(C3).
3 Calculate the derivatives with respect to τ.
4 IF the assumed and resulting signs of strain rates are NOT consistent, change the stress rate-strain rate relations and GO TO Step 3.
5 IF the SSL condition is satisfied, END.
6 Determine the incremental step $\Delta\tau$.
7 Update the variables.
8 IF one of Eqs. (34–37) is satisfied, change the stress rate-strain rate relations. GO TO Step 2.

References

[1] Koiter, W. T., 1960, ''General Theorems for Elastic-Plastic Structures,'' *Progress in Solid Mechanics*, Vol. 1, J. N. Sneddon and R. Hill, eds., North Holland, Amsterdam, pp. 167–221.

[2] Bree, J., 1967, ''Elastic-Plastic Behavior of Thin Tubes Subjected to Internal Pressure and Intermittent High-Heat Fluxes With Application to Fast-Nuclear-Reactor Fuel Elements,'' J. Strain Anal., **6**, pp. 236–249.

[3] Zarka, J., and Casier, J., 1979, ''Elastic-Plastic Response of a Structure to Cyclic Loading: Practical Rules,'' *Mechanics Today*, S. Nemat-Nasser, ed., Pergamon Press, New York, pp. 93–198.

[4] König, J. A., 1987, *Shakedown of Elastic-Plastic Structures*, Elsevier, Amsterdam.

[5] Nguyen, Q. S., Gary, G., and Baylac, G., 1983, ''Interaction Buckling-Progressive Deformation,'' Nucl. Eng. Des., **75**, pp. 235–243.

[6] Siemaszko, A., and König, J. A., 1985, ''Analysis of Stability of Incremental Collapse of Skeletal Structures,'' J. Struct. Mech., **13**, pp. 301–321.

[7] Uetani, K., and Nakamura, T., 1983, ''Symmetry Limit Theory for Cantilever Beam-Columns Subjected to Cyclic Reversed Bending,'' J. Mech. Phys. Solids, **31**, pp. 449–484.

[8] Maier, G., Pan, L. G., and Perego, U., 1993, ''Geometric Effects on Shakedown and Ratchetting of Axisymmetric Cylindrical Shells Subjected to Variable Thermal Loading,'' Eng. Struct., **15**, pp. 453–465.

[9] Uetani, K., and Araki, Y., 1999, ''Steady-State Limit Analysis of Elastoplastic Trusses Under Cyclic Loads,'' Int. J. Solids Struct., **36**, pp. 3051–3071.

[10] Hill, R., 1958, ''A General Theory of Uniqueness and Stability in Elastic-Plastic Solids,'' J. Mech. Phys. Solids, **6**, pp. 236–249.

[11] Drucker, D. C., Prager, W., and Greenberg, H. J., 1952, ''Extended Limit Design Theorems for Continuous Media,'' Quarterly Appl. Math., **9**, pp. 381–389.

[12] Ponter, A. R. S., and Karadeniz, S., 1985, ''An Extended Shakedown Theory for Structures That Suffer Cyclic Thermal Loadings, Part 1: Theory,'' ASME J. Appl. Mech., **52**, pp. 877–882.

[13] Ponter, A. R. S., and Karadeniz, S., 1985, ''An Extended Shakedown Theory for Structures That Suffer Cyclic Thermal Loadings, Part 2: Applications,'' ASME J. Appl. Mech., **52**, pp. 883–889.

[14] Polizzotto, C., 1993, ''A Study on Plastic Shakedown of Structures, Part I: Basic Properties,'' ASME J. Appl. Mech., **60**, pp. 318–323.

[15] Polizzotto, C., 1993, ''A Study on Plastic Shakedown of Structures, Part II: Theorems,'' ASME J. Appl. Mech., **60**, pp. 324–330.

[16] Polizzotto, C., and Borio, G., 1996, ''Shakedown and Steady-State Responses of Elastic-Plastic Solids in Large Displacements,'' Int. J. Solids Struct., **33**, pp. 3415–3437.

[17] Uetani, K., 1984, ''Symmetry Limit Theory and Steady-State Limit Theory for Elastic-Plastic Beam-Columns Subjected to Repeated Alternating Bending,'' Ph.D. thesis, Kyoto University, Kyoto (in Japanese).

[18] Crisfield, M. A., 1991, *Non-linear Finite Element Analysis of Solids and Structures*, Vol. 1, John Wiley and Sons, New York.

[19] Yokoo, Y., Nakamura, T., and Uetani, K., 1976, ''The Incremental Perturbation Method for Large Displacement Analysis of Elastic-Plastic Structures,'' Int. J. Numer. Methods Eng., **10**, pp. 503–525.

R. Sburlati
Dipartimento di Ingegneria
Strutturale e Geotecnica,
Universita' di Genova,
Via Montallegro, 1-16145, Italy

E. Madenci
Mem. ASME

I. Guven

Department of Aerospace
and Mechanical Engineering,
The University of Arizona,
Tucson, AZ 85721

Local Buckling of a Circular Interface Delamination Between a Layer and a Substrate With Finite Thickness

An analytical study investigating the local buckling response of a circular delamination along the interface of an elastic layer and a dissimilar substrate with finite thickness is presented. The solution method utilizes the stability equations of linear theory of elasticity under axisymmetry conditions. In-plane loading and the presence of mixed boundary conditions on the bond-plane result in a homogeneous system of coupled singular integral equations of the second kind with Cauchy-type kernels. Numerical solution of these integral equations leads to the determination of local buckling stress and its sensitivity to geometric parameters and material properties. [S0021-8936(00)01503-8]

1 Introduction

Presence of a delamination in a layered material system such as a thin film over a substrate can reduce the compressive strength to a level that permits premature failure in the form of local buckling. In the experimental investigation conducted by Argon et al. [1] almost all of the delaminations between the thin film (layer) and the substrate had circular boundaries. Also, interface delamination was only observed with thicker films rather than with very thin films. For sufficiently large compressive stresses, the delaminated region buckles out; thus, resulting in blisters. Numerous analytical and or numerical models address the local buckling of a delamination in homogeneous media. As discussed by Madenci [2] these models were based primarily on structural mechanics theories, such as those for plates and beams, and cannot address small ratio of delamination length to thickness, the presence of mixed boundary conditions along the delamination front, and the presence of oscillating stress singularity, near the delamination front, rising from the moduli mismatch between the film and substrate. Madenci and Westmann [3,4] and Madenci [5] addressed the local delamination buckling and growth for homogeneous media within the realm of theory of elasticity in order to impose the appropriate boundary conditions along the delamination front. Only Wang and Takao [6] and Madenci et al. [7] have addressed local buckling of an interface delamination between dissimilar elastic materials.

By considering the stability equations of the theory of elasticity, Wang and Takao [6] and Madenci et al. [7] studied the local buckling response of an interface delamination between a thin layer and a half-space with dissimilar material properties. Under plane-strain assumptions, Wang and Takao provided the buckling stress and the corresponding mode shape for a through-the-width delamination when both the layer and the half-space are subjected to uniform in-plane compressive strain. Madenci et al. provided the stress intensity factors for a circular delamination with a slight initial imperfection when only the delaminated layer bonded to a half-space is subjected to in-plane compressive stress. In these studies, the resulting dual integral equations were reduced to a pair of coupled singular integral equations of the second kind with a Cauchy-type singularity.

Based on the approach described in these previous analyses, this study addresses the local buckling of a circular interface delamination between a layer and a substrate with finite thickness under uniform in-plane compressive strain. The geometry and loading of a partially homogeneous layered medium with a delamination are described in Section 2; the solution method is presented in Section 3; and the numerical method used in the solution of the integral equations is presented in Section 4, along with the numerical results.

2 Problem Statement

The geometry of the layered homogeneous medium with a delamination is described in Fig. 1. A cylindrical coordinate system (r,θ,z) coincides with the center of the circular delamination on the interface plane. The radius of the circular delamination is $a=1$. The thicknesses of the layer and the substrate are denoted by h_l and h_s, respectively. The layer and the substrate materials are isotropic, elastic, and homogeneous, with dissimilar shear moduli, μ_i, and Poisson's ratios, ν_i. The subscripted (or superscripted) i refers to the layer and the substrate of l and s, respectively. In-plane compressive stresses in the layer and the substrate, $\sigma_0^{(l)}$ and $\sigma_0^{(s)}$, respectively, result in a uniform compressive strain, ε_0, which can be expressed as

$$\sigma_0^{(l)}=\frac{2\mu_l(1-\nu_l)}{1-2\nu_l}\varepsilon_0 \quad \text{and} \quad \sigma_0^{(s)}=\frac{\mu_s(1-2\nu_l)}{\mu_l(1-2\nu_s)}\frac{(1-\nu_s)}{(1-\nu_l)}\sigma_0^{(l)}. \tag{1}$$

As given by Flugge [8], the displacement equilibrium equations in cylindrical coordinates under axisymmetric geometric and loading conditions for an elastic medium with spatially constant initial stress, $\sigma_0^{(i)}$, are

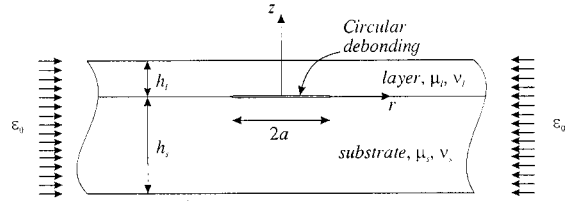

Fig. 1 A circular delamination along the interface of an elastic layer and a dissimilar substrate

Contributed by the Applied Mechanics Division of THE AMERICAN SOCIETY OF MECHANICAL ENGINEERS for publication in the ASME JOURNAL OF APPLIED MECHANICS. Manuscript received by the ASME Applied Mechanics Division, Apr. 21, 1999; final revision, Nov. 7, 1999. Associate Technical Editor: R. C. Benson. Discussion on the paper should be addressed to the Technical Editor, Professor Lewis T. Wheeler, Department of Mechanical Engineering, University of Houston, Houston, TX 77204-4792, and will be accepted until four months after final publication of the paper itself in the ASME JOURNAL OF APPLIED MECHANICS.

$$\left.\begin{aligned}&\frac{2(1-\nu_i)}{1-2\nu_i}\left[\frac{1}{r}(ru_r^{(i)})_{,r}+u_{z,z}^{(i)}\right]_{,r}-(u_{z,r}^{(i)}-u_{r,z}^{(i)})_{,z}-\frac{\sigma_0^{(i)}}{\mu_i}\left[\frac{1}{r}(ru_r^{(i)})_{,r}\right]_{,r}=0\\&\frac{2(1-\nu_i)}{1-2\nu_i}\left[\frac{1}{r}(ru_r^{(i)})_{,r}+u_{z,z}^{(i)}\right]_{,z}+\frac{1}{r}[r(u_{z,r}^{(i)}-u_{r,z}^{(i)})]_{,r}-\frac{\sigma_0^{(i)}}{\mu_i}\frac{1}{r}(ru_{z,r}^{(i)})_{,r}=0\end{aligned}\right\}\ i=l,s \tag{2}$$

in which $u_r^{(i)}$ and $u_z^{(i)}$ are the components of the displacement field.

The boundary conditions associated with the traction-free surfaces of the elastic layer ($z=h_l$) and the substrate ($z=-h_s$) are expressed by

$$\left.\begin{aligned}&\frac{2\mu_i}{1-2\nu_i}\left[(1-\nu_i)u_{z,z}^{(i)}+\nu_i\frac{1}{r}(ru_r^{(i)})_{,r}\right]=0\\&\mu_i(u_{r,z}^{(i)}+u_{z,r}^{(i)})=0\end{aligned}\right\}\ i=l,s\quad r\in[0,\infty). \tag{3}$$

Along the bond line, $z=0$, the continuity of displacement and traction components requires that

$$u_i^{(l)}=u_i^{(s)}\ \text{ with }\ i=r,z\quad r\in(a,\infty) \tag{4a}$$

and

$$\left.\begin{aligned}&\frac{2\mu_l}{1-2\nu_l}\left[(1-\nu_l)u_{z,z}^{(l)}+\nu_l\frac{1}{r}(ru_r^{(l)})_{,r}\right]=\frac{2\mu_s}{1-2\nu_s}\left[(1-\nu_s)u_{z,z}^{(s)}+\nu_s\frac{1}{r}(ru_r^{(s)})_{,r}\right]\\&\mu_l(u_{r,z}^{(l)}+u_{z,r}^{(l)})=\mu_s(u_{r,z}^{(s)}+u_{z,r}^{(s)})\end{aligned}\right\}\ r\in(a,\infty). \tag{4b}$$

Also, traction-free delamination surfaces on the $z=0$ plane require that

$$\left.\begin{aligned}&\frac{2\mu_i}{1-2\nu_i}\left[(1-\nu_i)u_{z,z}^{(i)}+\nu_i\frac{1}{r}(ru_r^{(i)})_{,r}\right]=0\\&\mu_i(u_{r,z}^{(i)}+u_{z,r}^{(i)})=0\end{aligned}\right\}\ i=l,s\quad r\in[0,a). \tag{5}$$

The solution to this instability problem involves the search for compressive uniform strain, ε_0, so that nontrivial solutions of the equilibrium Eqs. (2) exist subject to these boundary conditions.

3 Solution Method

Utilizing the integral representation of the displacement field suggested by Harding and Sneddon [9], $u_r^{(i)}(r,z)$ and $u_z^{(i)}(r,z)$, in the form

$$\left.\begin{aligned}u_r^{(i)}(r,z)&=\int_0^\infty A_i(z,\xi)J_1(r\xi)d\xi\\u_z^{(i)}(r,z)&=\int_0^\infty B_i(z,\xi)J_0(r\xi)d\xi\end{aligned}\right\}\ i=l,s \tag{6}$$

permits the reduction of the displacement equilibrium equations (Eq. (2)) to a pair of ordinary differential equations for $A_i(z,\xi)$ and $B_i(z,\xi)$,

$$\left.\begin{aligned}&A_i''-\frac{2(1-\nu_i)}{1-2\nu_i}\xi^2A_i-\frac{1}{1-2\nu_i}\xi B_i'+\frac{\sigma_0^{(i)}}{\mu_i}\xi^2A_i=0\\&\frac{2(1-\nu_i)}{1-2\nu_i}B_i''-\xi^2B_i+\frac{1}{1-2\nu_i}\xi A_i'+\frac{\sigma_0^{(i)}}{\mu_i}\xi^2B_i=0\end{aligned}\right\}\ i=l,s \tag{7}$$

in which $A_i(z,\xi)$ and $B_i(z,\xi)$ are unknown auxiliary functions and the prime denotes differentiation with respect to the variable z. The general solution to this system of equations can be readily written as

$$\begin{aligned}A_i(z,\xi)&=C_1^{(i)}e^{-\tau_i\xi z}+C_2^{(i)}e^{\tau_i\xi z}+\beta_i[C_4^{(i)}e^{\beta_i\xi z}-C_3^{(i)}e^{\beta_i\xi z}]\\B_i(z,\xi)&=\tau_i[C_1^{(i)}e^{-\tau_i\xi z}-C_2^{(i)}e^{\tau_i\xi z}]+C_3^{(i)}e^{\beta_i\xi z}+C_4^{(i)}e^{-\beta_i\xi z}\end{aligned} \tag{8}$$

where $C_j^{(i)}(\xi)$ $(j=1,\ldots,4)$ are the unknown coefficients to be determined from the boundary conditions and τ_i and β_i are defined as

$$\tau_i=\sqrt{1-\frac{(1-2\nu_i)\sigma_0^{(i)}}{2\mu_i(1-\nu_i)}}\quad\text{and}\quad\beta_i=\sqrt{1-\frac{\sigma_0^{(i)}}{\mu_i}}. \tag{9}$$

Enforcing the traction-free conditions (Eq. (3)) on the surfaces $z=h_l$ and $z=-h_s$ and the continuity of traction components (Eqs. (4)–(5)) along the interface plane $z=0$ permits the determination of $C_1^{(l)}$, $C_2^{(l)}$, and $C_j^{(s)}$ $(j=1,4)$ in terms of $C_3^{(l)}$ and $C_4^{(l)}$. As suggested by Arin and Erdogan [10], expressing these remaining unknowns in terms of two unknown functions, $f_1(r)$ and $f_2(r)$, in the form

$$\begin{aligned}f_1(r)H(a-r)&=[u_z^{(s)}(r,0)-u_z^{(l)}(r,0)]_{,r}\\f_2(r)H(a-r)&=\frac{1}{r}\{r[u_z^{(s)}(r,0)-u_z^{(l)}(r,0)]\}_{,r}\end{aligned} \tag{10}$$

ensures the continuity of displacement components along the interface. As described by Arin and Erdogan, the equations resulting from interpretation of the traction-free conditions on the delamination surfaces can be cast into a homogeneous system of singular integral equations of the form

$$\mathbf{A}\mathbf{f}(r)+\frac{1}{\pi}\int_{-a}^{a}\mathbf{B}\mathbf{f}(t)\frac{dt}{t-r}+\int_{-a}^{a}\mathbf{k}(r,t)\mathbf{f}(t)dt=0,\quad |r|<a \tag{11}$$

with constraints

$$\int_{-a}^{a}f_1(t)dt=0\quad\text{and}\quad\int_{-a}^{a}|t|f_2(t)dt=0. \tag{12}$$

The vector $\mathbf{f}(r)$ contains the unknown functions $f_1(r)$ and $f_2(r)$. Known matrices **A**, **B**, and **k** are given as

$$\mathbf{A}=\begin{bmatrix}0&\overline{a}_1\\\overline{a}_2&0\end{bmatrix},\quad\mathbf{B}=\begin{bmatrix}1&0\\0&1\end{bmatrix},\quad\mathbf{k}(r,t)=\begin{bmatrix}k_{11}(r,t)&k_{12}(r,t)\\k_{21}(r,t)&k_{22}(r,t)\end{bmatrix} \tag{13}$$

where the elements of **k** are expressed as

$$k_{11}(r,t)=\frac{1}{\pi}\frac{m_1(r,t)-1}{t-r}+\frac{1}{2}|t|\int_0^\infty[\overline{b_1}C_{11}(\xi)-1]\times J_0(r\xi)J_1(t\xi)\xi d\xi$$

$$k_{12}(r,t)=\frac{1}{2}|t|\int_0^\infty[\overline{b_1}C_{12}(\xi)-\overline{a_1}]J_0(r\xi)J_0(t\xi)\xi d\xi \tag{14}$$

$$k_{21}(r,t)=\frac{1}{2}|t|\int_0^\infty[\overline{b_2}C_{21}(\xi)-\overline{a_2}]J_1(r\xi)J_1(t\xi)\xi d\xi$$

$$k_{22}(r,t)=-\frac{1}{\pi}\frac{m_2(r,t)-1}{t-r}+\frac{1}{2}|t|\int_0^\infty[\overline{b_2}C_{22}(\xi)-1]\times J_1(r\xi)J_0(t\xi)\xi d\xi.$$

The constants $\overline{a_i}$ and $\overline{b_i}$ $(i=1,2)$ and the explicit expressions for $C_{ij}(\xi)$ $(i,j=1,2)$ are given in Appendix A. The functions m_i $(i=1,2)$ are related to the complete elliptic integrals, K and E, of the first and second kind, respectively, as

$$m_1(r,t)=\begin{cases}\dfrac{t^2-r^2}{|rt|}K\left(\dfrac{t}{r}\right)+\left|\dfrac{r}{t}\right|E\left(\dfrac{t}{r}\right), & |t|<|r|\\ E\left(\dfrac{r}{t}\right), & |t|>|r|\end{cases} \tag{15}$$

and

$$m_2(r,t)=\begin{cases}\left|\dfrac{r}{t}\right|E\left(\dfrac{t}{r}\right), & |t|<|r|\\ \dfrac{t^2}{r^2}E\left(\dfrac{r}{t}\right)-\dfrac{t^2-r^2}{r^2}K\left(\dfrac{r}{t}\right), & |t|>|r|.\end{cases} \tag{16}$$

The dominant part of the system in Eq. (11) is decoupled as

$$\mathbf{g}+\frac{1}{\pi}\int_{-a}^{a}\mathbf{\Lambda g}(t)\frac{dt}{t-r}+\int_{-a}^{a}\mathbf{K}(r,t)\mathbf{g}(t)dt=0 \tag{17}$$

with the constraint conditions

$$\int_{-a}^{a}C(t)\mathbf{g}(t)dt=0 \tag{18}$$

in which $\mathbf{g}=\mathbf{R}^{-1}\mathbf{f}$, $\mathbf{\Lambda}=\mathbf{R}^{-1}\mathbf{DR}$, $\mathbf{K}=\mathbf{R}^{-1}\mathbf{A}^{-1}\mathbf{kR}$, and $\mathbf{C}(t)$ is defined by

$$\mathbf{C}(t)=\begin{bmatrix}1 & 0\\ 0 & |t|\end{bmatrix}\mathbf{R}.$$

The modal matrix of $\mathbf{D}=\mathbf{A}^{-1}\mathbf{B}$ is denoted by $\mathbf{R}$,

$$\mathbf{R}=\begin{bmatrix}\sqrt{\overline{a_1}} & \sqrt{\overline{a_1}}\\ -i\sqrt{\overline{a_2}} & i\sqrt{\overline{a_2}}\end{bmatrix} \tag{19}$$

The elements of the diagonal matrix, $\mathbf{\Lambda}$, are the eigenvalues of the matrix $\mathbf{D}$, i.e., $\Lambda_{11}=i/\sqrt{a_1a_2}$ and $\Lambda_{22}=-i/\sqrt{a_1a_2}$ with $i=\sqrt{-1}$.

Adopting the procedure by Muskhelishvilli [11], the fundamental solutions to the dominant part of this system of equations (Eq. (17)) are of the form

$$w_k(t)=(1-t)^{\alpha_k}(1+t)^{\beta_k},\quad |t|<1$$

in which

$$\alpha_k=\tfrac{1}{2}-i(-1)^k\varepsilon \quad \text{and} \quad \beta_k=\tfrac{1}{2}+i(-1)^k\varepsilon \tag{20}$$

(with $k=1,2$) where

$$\varepsilon=\frac{1}{2\pi}\log\frac{|\sqrt{\overline{a_1a_2}}+1|}{|\sqrt{\overline{a_1a_2}}-1|}.$$

As suggested by Erdogan and Gupta [12], the solution to $\mathbf{g}$ is constructed in terms of an auxiliary function, $\phi_k(t)$, in the form

$$g_k=\frac{\phi_k(t)}{w_k(t)},\quad \text{with } k=1,2. \tag{21}$$

This solution form ensures the proper behavior of $g_k(t)$ at the end points. The unknown auxiliary function, $\phi_k(t)$, is regular on the interval $t\in[-1,1]$.

The complexity of the kernels in Eq. (14) requires that the singular integral equation be solved numerically. The procedure involves the reduction of the integral equation and the constraints to a system of algebraic equations using the collocation technique introduced by Miller and Keer [13] and later extended by Kabir et al. [14]. In this technique, the unknown function, $\phi_k(t)$, is approximated by quadratic Lagrange interpolation polynomials. As a result of this discretization. Equations (11)–(12) can be written as

$$\left.\begin{aligned}&\frac{1}{(1-x_j)^{\alpha_1}(1+x_j)^{\beta_1}}\sum_{m=1}^{3}B_m\phi_{I+m}^{(1)}+\sum_{i=1}^{2N+1}\frac{\Lambda_{11}}{\pi}w_i^{(1)}(x_j)\phi_i^{(1)}+\sum_{i=1}^{2N+1}K_{11}(x_j,t_i)\nu_i^{(1)}\phi_i^{(1)}+K_{12}(x_j,t_i)\nu_i^{(2)}\phi_i^{(2)}=0\\ &\frac{1}{(1-x_j)^{\alpha_2}(1+x_j)^{\beta_2}}\sum_{m=1}^{3}B_m\phi_{I+m}^{(2)}+\sum_{i=1}^{2N+1}\frac{\Lambda_{22}}{\pi}w_i^{(2)}(x_j)\phi_i^{(2)}+\sum_{i=1}^{2N+1}K_{21}(x_j,t_i)\nu_i^{(1)}\phi_i^{(1)}+K_{22}(x_j,t_i)\nu_i^{(2)}\phi_i^{(2)}=0\end{aligned}\right\}\ j=1,2N \tag{22}$$

$$\sum_{i=1}^{2N+1}\nu_i^{(1)}\phi_i^{(1)}+\sum_{i=1}^{2N+1}\nu_i^{(2)}\phi_i^{(2)}=0$$

$$\sum_{i=1}^{2N+1}|t_i|(\nu_i^{(1)}\phi_i^{(1)}+\nu_i^{(2)}\phi_i^{(2)})=0 \tag{23}$$

in which $I=j-1$ or $j-2$ for odd and even values of j, respectively, and N is the number of integration intervals. The singular weight functions, $w_i(x_j)$ and ν_i, and the Lagrange coefficients. B_m, are given by Miller and Keer [13].

4 Numerical Results

In matrix form, Eqs. (22) and (23) can be written as

$$[\mathbf{W}^{(1)}\quad \mathbf{W}^{(2)}]\begin{Bmatrix}\Phi^{(1)}\\ \Phi^{(2)}\end{Bmatrix}=\begin{Bmatrix}\mathbf{0}\\ \mathbf{0}\end{Bmatrix} \tag{24}$$

where $\mathbf{W}^{(1)}$ and $\mathbf{W}^{(2)}$ are the complex coefficient matrix of size $(2N+2\times 2N+2)$ and $\Phi^{(1)}$ and $\Phi^{(2)}$ are the vector of unknown auxiliary functions, $\phi_i^{(1)}$ and $\phi_i^{(2)}$, respectively, evaluated at the collocation points. The components of the coefficient matrix involve the computation of infinite integrals appearing in Eq. (14). The infinite integrals are evaluated by using the modified form of the Filon's numerical integration scheme in order to account for

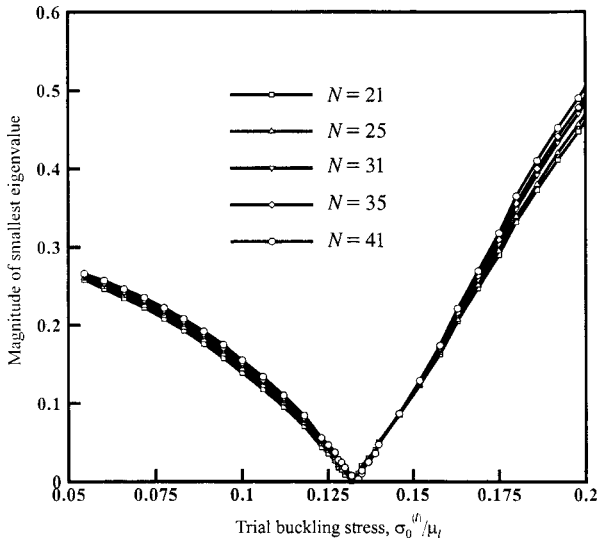

Fig. 2 Search procedure for the buckling stress

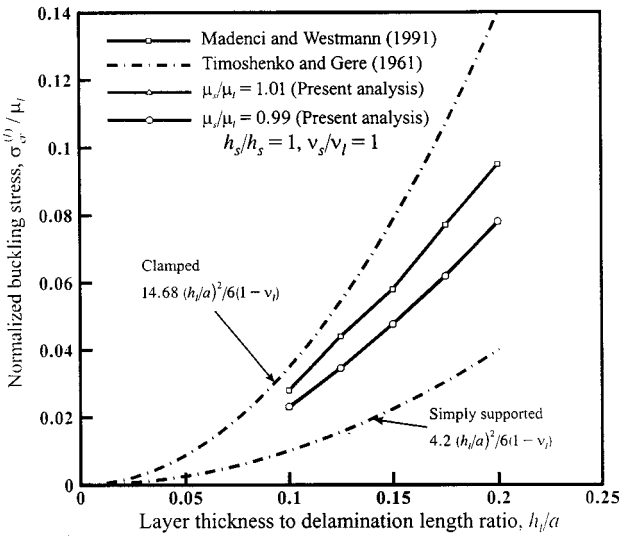

Fig. 3 Effect of delamination length to thickness ratio on buckling stress—similar materials. (Information contained in this figure came from Madenci and Westmann [3] and Timoshenko and Gere [16].)

the oscillations arising from the Bessel functions. This integration scheme is outlined in Appendix B. A nontrivial solution of the homogeneous and coupled system of singular integral equations is achieved by searching for values of buckling strain, ε_0, which causes the magnitude of the smallest complex eigenvalue of the coefficient matrix to vanish. This is equivalent to the determination of a zero eigenvalue for which the determinant of the coefficient matrix becomes zero. The search procedure for finding the local fundamental buckling strain or stress, $\sigma_{cr}^{(l)}$ involves a trial and error procedure. Under a specific geometry and material property configuration, the magnitude of smallest eigenvalue of the coefficient matrix is computed and plotted for several trial buckling stresses, $\sigma_0^{(l)}$. When a change in sign of the slope is observed for the estimates of the trial buckling stresses, an approximate value of the buckling stress is obtained by interpolation. Further trials are conducted around this approximation to refine the value of the buckling stress. This search procedure is illustrated in Fig. 2 for various number of integration intervals, $N=21$, 25, 31, 35 and 41 when $h_l/a=0.15$, $h_s/a=0.45$, $\nu_l=0.3$, $\nu_s=0.2$ and $\mu_s/\mu_l=5$. As shown in Fig. 2, convergence is achieved for the magnitudes of smallest eigenvalues as a function of trial load, $\sigma_0^{(l)}/\mu_l$, with increasing N and that sufficient accuracy is obtained with $N=21$ which is employed throughout this study.

The validity of the present analysis is established by considering a circular delamination in a homogeneous and isotropic plate under in-plane compressive stresses studied by Madenci and Westmann [3]. The geometric configuration and material properties are defined by $h_l/h_s=1$, $\nu_l/\nu_s=1$ and $\mu_l/\mu_s=1$. The variation of the buckling stress as a function of layer thickness to delamination length ratio is presented in Fig. 3. The previous solution to this problem was obtained by solving for the coupled system of Fredholm integral equations of the second kind while taking advantage of the symmetry condition with respect to the mid-plane. In the present analysis, slight differences in shear moduli between the layer and the substrate are introduced as $\mu_s/\mu_l=1.01$ and $\mu_s/\mu_l=0.99$ in order to avoid the breakdown of the present solution method appropriate only for dissimilar materials. The results obtained for both of these ratios coincide with others because of the presence of symmetry. With these ratios, the layer and the substrate exchange places. As shown in this figure, the present analysis results are in acceptable agreement with those of Madenci and Westmann [3]. These results are bounded by the results of the buckling analysis for a clamped and for a simply supported circular plate. As shown in Fig. 3, the plate buckling analysis sets the upper and lower bounds. As expected, the influence of structural approximation on the buckling stress is significant for increasing delamination thickness to length ratio. In the case of a layer thickness to delamination length ratio (h_l/a) of 0.2, the normalized buckling stress, $\sigma_{cr}^{(l)}/\mu_l$ based on the structural buckling analysis with clamped boundary condition is about 0.14. Although still high, this value reduces to 0.08 with the present analysis.

After establishing the validity of the present analysis, the influence of shear modulus ratio, (μ_s/μ_l) and layer thickness to delamination length ratio (h_l/a) on the buckling stress is examined for $h_s/a=0.45$, $\nu_l=0.3$ and $\nu_s=0.2$. Buckling stresses are shown in Fig. 4 as a function of layer thickness to delamination length ratio for various shear modulus ratios. It is apparent that the normalized buckling stress, $\sigma_{cr}^{(l)}/\mu_l$, increases as the layer thickness to delamination length ratio, (h_l/a) increases. However, the effect of shear modulus ratio on the buckling stress becomes less significant for increasing layer thickness to delamination length ratio, (h_l/a) as shown in Fig. 5. It is worth mentioning that the

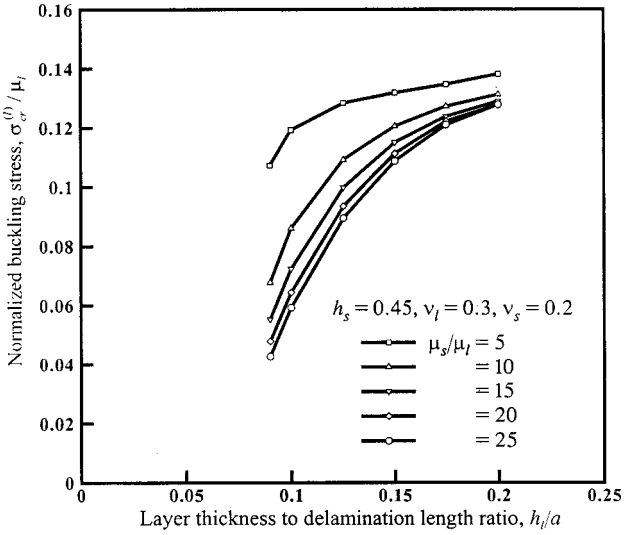

Fig. 4 Effect of delamination length to thickness ratio on buckling stress—dissimilar materials

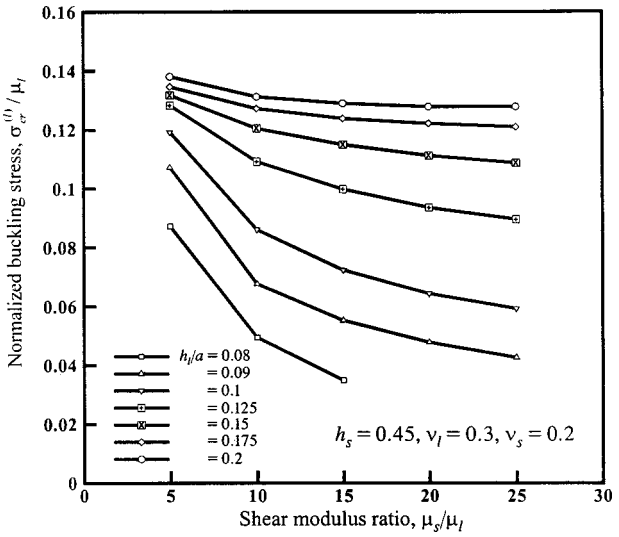

Fig. 5 Effect of modulus ratio on buckling stress—dissimilar materials

results concerning layer thickness to delamination length ratio, (h_l/a) smaller than 0.08 is not presented in Figs. 4 and 5 because of the uncertainty associated with the numerical convergence.

The present analysis provides the solution only to the buckling stress and not the stress field; therefore, the growth of delamination cannot be discussed without a fracture parameter such as the energy release rate. However, as introduced by Madenci [2], an initial imperfection of the delamination can be introduced to alter the nature of the stability problem so that the fracture parameters can be obtained. Also, the buckling stress obtained from the present analysis cannot be compared with the previous solutions such as those given by Evans and Hutchinson [15] based on the plate theory because the previous solutions could not include the effect of the oscillatory nature of the stress field and the mixed boundary conditions along the delamination front.

5 Conclusions

By solving for the stability equations of linear theory of elasticity, this study investigates the local buckling response of a circular delamination between an elastic layer and a substrate with dissimilar material properties. This analysis reveals the sensitivity of the buckling stress to the geometric parameters and material properties. Such knowledge may be useful in controlling the influence of residual stresses arising from the fabrication process involving deposition of thin films. Also, this study provides the bench-mark solutions for related problems addressed by using approximate solution methods.

Appendix A

In Eq. (13), the constants are defined as

$$\bar{a}_1 = \frac{\lim_{\xi\to\infty} C_{12}(\xi)}{\lim_{\xi\to\infty} C_{11}(\xi)}; \quad \bar{a}_2 = \frac{\lim_{\xi\to\infty} C_{21}(\xi)}{\lim_{\xi\to\infty} C_{22}(\xi)};$$

$$\bar{b}_1 = \frac{1}{\lim_{\xi\to\infty} C_{11}(\xi)}; \quad \bar{b}_2 = \frac{1}{\lim_{\xi\to\infty} C_{22}(\xi)}$$

where

$$C_{11}(\xi) = \frac{\Omega_{21}(\xi)}{\Delta(\xi)}; \quad C_{12}(\xi) = \frac{\Omega_{11}(\xi)}{\Delta(\xi)};$$

$$C_{21}(\xi) = \frac{\Omega_{22}(\xi)}{\Delta(\xi)}; \quad C_{22}(\xi) = \frac{\Omega_{12}(\xi)}{\Delta(\xi)}$$

with

$$\Omega_{11}(\xi) = -\tau_1 + \frac{\mu_1\tau_1}{\mu_2} + \frac{(1-2Q_1\tau_1)}{R_1}(4P_1 - b_1 - a_1 - d_1 + c_1) + \frac{\mu_1\tau_1}{\mu_2\tau_2}\frac{(-1+2Q_2\tau_2)}{R_2}(4P_2 - b_2 - a_2 - d_2 + c_2)$$

$$\Omega_{12}(\xi) = \frac{(1-2Q_1\tau_1)}{R_1}(-b_1 + a_1 + d_1 + c_1) + \frac{\mu_1\tau_1 Q_1}{\mu_2\tau_2 Q_2}\frac{(-1+2Q_2\tau_2)}{R_2}(-b_2 + a_2 + d_2 + c_2)$$

$$\Omega_{21}(\xi) = \frac{2P_1 - \beta_1}{R_1}(-b_1 - a_1 + d_1 - c_1) + \frac{\mu_1\tau_1}{\mu_2\tau_2}\frac{\beta_2 - 2P_2}{R_2}(-b_2 - a_2 + d_2 - c_2)$$

$$\Omega_{22}(\xi) = 1 - \frac{\mu_1\tau_1 Q_1}{\mu_2\tau_2 Q_2} + \frac{2P_1 - \beta_1}{R_1}(4Q_1 - b_1 + a_1 - d_1 - c_1) + \frac{\mu_1\tau_1 Q_1}{\mu_2\tau_2 Q_2}\frac{\beta_2 - 2P_2}{R_2}(4Q_2 - b_2 + a_2 - d_2 - c_2)$$

and

$$\Delta(\xi) = \Omega_{11}(\xi)\Omega_{22}(\xi) - \Omega_{12}(\xi)\Omega_{21}(\xi)$$

in which

$$a_1 = (P_1 - Q_1)e^{-(\beta_l+\tau_l)\xi h_l}; \quad a_2 = (P_2 - Q_2)e^{(\beta_s+\tau_s)\xi h_s}$$

$$b_1 = (P_1 + Q_1)e^{-(\beta_l-\tau_l)\xi h_l}; \quad b_2 = (P_2 + Q_2)e^{(\beta_s-\tau_s)\xi h_s}$$

$$c_1 = (Q_1 - P_1)e^{(\beta_l+\tau_l)\xi h_l}; \quad c_2 = (Q_2 - P_2)e^{-(\beta_s+\tau_s)\xi h_s}$$

$$d_1 = (P_1 + Q_1)e^{-(-\beta_l+\tau_l)\xi h_l}; \quad d_2 = (P_2 + Q_2)e^{(-\beta_s+\tau_s)\xi h_s}$$

$$P_1 = \frac{\beta_l}{1+\beta_l^2}; \quad P_2 = \frac{\beta_s}{1+\beta_s^2}$$

$$Q_1 = \frac{1+\beta_l^2}{4\tau_l}; \quad Q_2 = \frac{1+\beta_s^2}{4\tau_s}$$

$$R_1 = -8P_1Q_1 - 2b_1d_1 - 2c_1a_1 + 2Q_1(b_1 + d_1 + a_1 - c_1) + 2P_1(d_1 + c_1 + b_1 - a_1)$$

$$R_2 = -8P_2Q_2 - 2b_2d_2 - 2c_2a_2 + 2Q_2(b_2 + d_2 + a_2 - c_2) + 2P_2(d_2 + c_2 + b_2 - a_2)$$

$$\tau_l = \sqrt{1 - \frac{(1-2\nu_l)\sigma_0^{(l)}}{2(1-\nu_l)\mu_l}}; \quad \tau_s = \sqrt{1 - \frac{(1-2\nu_s)\sigma_0^{(s)}}{2(1-\nu_s)\mu_s}}$$

$$\beta_l = \sqrt{1 - \frac{\sigma_0^{(l)}}{\mu_l}}; \quad \beta_s = \sqrt{1 - \frac{\sigma_0^{(s)}}{\mu_s}}$$

$$\sigma_0^{(s)} = \frac{\mu_s(1-\nu_l)}{\mu_l(1-\nu_s)}\sigma_0^{(l)}.$$

Appendix B

The approximate evaluation of the integral of the type

$$I(r,t;a,b) = \int_a^b f(x)J_p(rx)J_q(tx)dx \qquad (B1)$$

in which $J_p(rx)$ and $J_q(tx)$ are Bessel's functions of the first kind with $p,q=0,1$ and $f(x)$ being smooth in the interval $[a,b]$ can be achieved by

$$I(r,t)=\sum_{j=1,3,5}^{N-1} I_j(r,t;x_{j-1},x_{j+1}) \tag{B2}$$

in which N is the number of integration points in the interval $[a,b]$ leading to equal integration intervals of $(x_{j+1}-x_{j-1})=(b-a)/N$ and I_j is defined as

$$I_j(r,t;x_{j-1},x_{j+1})=\int_{x_{j-1}}^{x_{j+1}} f(x)J_p(rx)J_q(tx)dx. \tag{B3}$$

Over the subinterval $[x_{j-1},x_{j+1}]$, this integral can be approximated as

$$I_j(r,t;x_{j-1},x_{j+1})=w_{j-1}f(x_{j-1})+w_jf(x_j)+w_{j+1}f(x_{j+1}) \tag{B4}$$

in which w_{j-1},w_j,w_{j+1} are the integration weights. They are established by assuming a quadratic variation of the product of the Bessel's functions of the first kind $J_p(rx)J_q(tx)$ in the interval $[x_{j-1},x_{j+1}]$ such that

$$\int_{x_{j-1}}^{x_{j+1}} x^iJ_p(rx)J_q(tx)dx=x_{j-1}^iw_{j-1}+x_j^iw_j+x_{j+1}^iw_{j+1}=R_i$$

$$\text{with } i=0,1,2. \tag{B5}$$

In matrix form, these equations are rewritten as

$$\begin{bmatrix} 1 & 1 & 1 \\ x_{j-1} & x_j & x_{j+1} \\ x_{j-1}^2 & x_j^2 & x_{j+1}^2 \end{bmatrix} \begin{Bmatrix} w_{j-1} \\ w_j \\ w_{j+1} \end{Bmatrix} = \begin{Bmatrix} R_0 \\ R_1 \\ R_2 \end{Bmatrix} \tag{B6}$$

from which the weights are computed after the evaluation of the expressions for $R_i(r,t;x_{j-1},x_{j+1})$. This is achieved by defining the variable $x=Az+B$ with $A=(x_{j+1}-x_{j-1})/2$ and $B=(x_{j+1}+x_{j-1})/2$, and by approximating the Bessel's functions of the first kind, $J_p(rx)$ and $J_q(tx)$ in integrals in Eq. (*B*5) using the Chebychev polynomials of the first kind as

$$J_p[r(Az+B)]=\sum_{m=0}^{M} a_mT_m(z) \tag{B7}$$

and

$$J_q[t(Az+B)]=\sum_{m=0}^{M} b_mT_m(z) \tag{B8}$$

where Σ denotes a finite sum whose first and the last term are to be halved. The coefficients are then given by

$$a_m=\frac{2}{M}\sum_{k=0}^{M} J_p[r(Az_k+B)]\cos(mk\pi/M) \tag{B9}$$

$$b_m=\frac{2}{M}\sum_{k=0}^{M} J_q[t(Az_k+B)]\cos(mk\pi/M) \tag{B10}$$

in which $z_k=\cos(k\pi/M)$. Substitution from Eqs. (*B*7) and (*B*8) into Eq. (*B*5) results in

$$R_i=A\sum_{m=0}^{M}\sum_{n=0}^{N} a_mb_n\int_{-1}^{1}(Az+B)^iT_m(z)T_n(z)dz \quad \text{with } i=0,1,2. \tag{B11}$$

This expression permits the explicit evaluation of R_i with the following identities:

$$\int_{-1}^{1} T_m(z)T_n(z)dz=-\begin{cases} \dfrac{1}{(m+n)^2-1}+\dfrac{1}{(m-n)^2-1}; & m+n=\text{even} \\ 0; & m+n=\text{odd} \end{cases}$$

$$\int_{-1}^{1} zT_m(z)T_n(z)dz=-\begin{cases} \dfrac{1}{(m+n)^2-2^2}+\dfrac{1}{(m-n)^2-2^2}; & m+n=\text{odd} \\ 0; & m+n=\text{even} \end{cases}$$

$$\int_{-1}^{1} z^2T_m(z)T_n(z)dz=-\frac{1}{4}\begin{cases} \dfrac{1}{(m+n)^2-1}+\dfrac{1}{(m-n)^2-1}+\dfrac{3}{(m+n)^2-3^2}+\dfrac{3}{(m-n)^2-3^2}; & m+n=\text{even} \\ 0; & m+n=\text{odd}. \end{cases}$$

Substitution for R_i and numerically inverting the system of Eq. (*B*6) leads to the integration weights. Finally, the approximate value of the integral is calculated from Eq. (*B*11). The accuracy of this integration algorithm is demonstrated by considering the following infinite integral:

$$I=\int_0^{\infty} xe^{-x^2}J_0(x)J_0(x)dx$$

with an exact solution of $I=e^{-1/2}I_0(1/2)/2=0.32252$ in which I_0 is the modified Bessel's function of the second kind. Its numerical evaluation with $N=200$ and $M=4$ for $a=0$ and $b=100$ leads to a value of 0.32259.

References

[1] Argon, A. S., Gupta, V., Landis, H. S., and Cornie, J. A., 1989, ''Intrinsic Toughness of Interfaces Between SiC Coatings and Substrates of Si or C Fibre,'' J. Mater. Sci., **24**, pp. 1207–1218.

[2] Madenci, E., 1987, ''Local Delamination Buckling in Layered Structures,'' Ph.D. thesis, University of California, Los Angeles, CA.

[3] Madenci, E., and Westmann, R. A., 1991, ''Local Delamination Buckling in Layered Systems,'' ASME J. Appl. Mech., **58**, pp. 157–166.

[4] Madenci, E., and Westmann, R. A., 1993, ''Local Delamination Growth in Layered Systems Under Compressive Loads,'' ASME J. Appl. Mech., **60**, pp. 895–902.

[5] Madenci, E., 1991, ''Delamination Growth and Buckling in an Orthotropic Strip,'' Int. J. Solids Struct., **27**, pp. 1773–1788.

[6] Wang, W. X., and Takao, Y., 1995, ''Load Buckling of a Layer Bonded to a Half-Space With an Interface Crack,'' ASME J. Appl. Mech., **62**, pp. 64–70.

[7] Madenci, E., Balkan, H., and Quan, M., 1995, ''Biaxial Comparison of a Thin Layer With a Circular Debonding Over a Substrate,'' Int. J. Solids Struct., **32**, pp. 3465–3477.

[8] Flugge, W., 1972, *Tensor Analysis and Continuum Mechanics*, Springer-Verlag, New York.

[9] Harding, J. W., and Sneddon, I. N., 1945, ''The Elastic Stresses Produced by the Indentation of the Plane Surface of a Semi-Infinite Elastic Body by a Rigid Punch,'' Proc. Cambridge Philos. Soc., **41**, pp. 16–26.
[10] Arin, K., and Erdogan, F., 1971, ''Penny-Shaped Crack in an Elastic Layer Bonded to Dissimilar Half Spaces,'' Int. J. Eng. Sci., **9**, pp. 213–222.
[11] Muskhelishvilli, N. I., 1953, *Singular Integral Equations*, P. Noordhoff, Groningen, The Netherlands.
[12] Erdogan, F., and Gupta, G. D., 1972, ''On the Numerical Solution of Singular Integral Equations,'' Q. Appl. Math., **29**, pp. 525–534.
[13] Miller, G. R., and Keer, L. M., 1985, ''A Numerical Technique for the Solution of Singular Integral Equations of the Second Kind,'' Q. Appl. Math., **43**, pp. 455–465.
[14] Kabir, H., Madenci, E., and Ortega, A., 1998, ''Numerical Solution of Integral Equations With Logarithmic Cauchy and Hadamard Type Singularities,'' Int. J. Numer. Methods Eng., **41**, pp. 617–838.
[15] Evans, A. G., and Hutchinson, J. W., 1984, ''On the Mechanics of Delamination and Spalling in Compressed Films,'' Int. J. Solids Struct., **20**, pp. 455–466.
[16] Timoshenko and Gere, 1961, *Theory of Elastic Stability*, McGraw-Hill, New York.

Antiplane Deformations for Anisotropic Multilayered Media by Using the Coordinate Transform Method

Ru-Li Lin
Graduate Student

Chien-Ching Ma
Professor

Department of Mechanical Engineering,
National Taiwan University,
Taipei, Taiwan 10617 R.O.C.

Green's functions for anisotropic elastic multilayered media subjected to antiplane shear deformation are presented in this study. The antiplane shear deformation due to a concentrated shear force and screw dislocation in an arbitrary layer was investigated in detail. A linear coordinate transformation is introduced in this study to simplify the problem. The linear coordinate transformation reduces the anisotropic multilayered problem to an equivalent isotropic problem without complicating the geometry of the problem. Explicit analytical solutions were derived using the Fourier transform and the series expansion technique. The complete solutions for the multilayered problem consist only of the simplest solutions obtained from an infinite homogeneous medium with concentrated loadings. Numerical results for the full-field stress distribution in multilayered media subjected to a point body force are presented. These numerical results were compared with the solutions obtained by considering the multilayered medium as one layer with effective elastic constants determined from the averaged material constants of the multilayered medium. It is found that the shear stress τ_{yz} of the homogeneous one layer solution is a very good approximation of the result for the multilayered medium; however, the shear stress τ_{xz} in these two solutions has a large discrepancy due to the fact that τ_{xz} is discontinuous at the interfaces of the multilayered medium. [S0021-8936(00)01703-7]

1 Introduction

Antiplane shear deformations are the simplest of two-dimensional deformations that arise in anisotropic or isotropic elastic bodies. For the antiplane shear deformation, the displacement is parallel to the axial coordinate that is normal to the plane and is dependent only on the coordinates in the plane. Such deformation field characterized by a single axial displacement can be regarded as complementary to that of plane-strain deformation (e.g., [1]). The antiplane problem plays a useful role as a pilot problem that reveals simpler aspects of elasticity solutions. The antiplane problem of two dissimilar anisotropic wedges has been considered by Ma [2] and Ma and Hour [3] using the Mellin transform method. They showed that the stress and displacement fields have reduced dependence on the elastic constants. Retting [4] did the antiplane stress analysis of a cracked beam made of orthotropic material. Wu and Chiu [5] discussed interface cracks in anisotropic bimaterials subjected to antiplane shearing. Ting [6] also provided many basic discussions and investigated some fundamental problems for anisotropic antiplane deformations. In addition, considerable attention has been paid to the analysis of antiplane shear deformation in nonlinear elasticity theory for isotropic solids, cf. Jiang and Knowles [7], Polignone and Horgan [8] and the references therein. A comprehensive review of antiplane shear for both linear and nonlinear elasticity is given by Horgan [9].

Analysis of anisotropic elasticity problems is often tedious due to the presence of many elastic constants. It is desirable to reduce the dependence on elastic constants through theoretical considerations in advance of the analysis of a given boundary value problem. For anisotropic elasticity, Lekhnitskii's formulation ([10]) and Stroh's formulation ([11]) are the two widely used methods. The general solutions obtained by these methods showed that the antiplane anisotropic problem can be converted to a corresponding isotropic problem by properly changing the geometry of the original configuration and the tractions on the boundary. In other words, the anisotropic antiplane problem can be simplified to an isotropic problem with the aid of a suitable coordinate transformation. In the isotropic case, the displacement equilibrium equation becomes the Laplace equation which can be solved easily. For the anisotropic problem, however, the governing equilibrium equation is a general second-order partial differential equation with constant coefficients. In particular, a variety of coordinate transformations could be used to convert the general second-order partial differential equation to the Laplace equation. The properties of the coordinate transformations for antiplane deformations have been investigated by Ma [12] and Horgan and Miller [1]. An orthotropic transformation concept was introduced by Yang and Ma [13] to analyze the much complicated and difficult in-plane deformations for planar anisotropic solids.

Because of the rapid expansion in the use of structural components made of laminated materials, predictions of the behavior of multilayered media subjected to arbitrary loads are needed. The stress states at the interfaces of multilayered media are of particular interest because delamination may occur if allowable levels are exceeded. For multilayered anisotropic media, the problem becomes more complicated than that of homogeneous isotropic counterparts. Based on the mixed formulation of elasticity, Bufler [14] and Bahar [15] independently constructed the transfer matrix approach to solve multilayered media problems. A local/global stiffness matrix approach which is similar to the transfer matrix approach was employed by Pindera [16] and Pindera and Lane [17,18] to solve round punch contact problems of arbitrarily lami-

Contributed by the Applied Mechanics Division of THE AMERICAN SOCIETY OF MECHANICAL ENGINEERS for publication in the ASME JOURNAL OF APPLIED MECHANICS. Manuscript received by the ASME Applied Mechanics Division, May 3, 1999; final revision, Nov. 30, 1999. Associate Technical Editor: M.-J. Pindera. Discussion on the paper should be addressed to the Technical Editor, Professor Lewis T. Wheeler, Department of Mechanical Engineering, University of Houston, Houston, TX 77204-4792, and will be accepted until four months after final publication of the paper itself in the ASME JOURNAL OF APPLIED MECHANICS.

nated media. The local/global stiffness matrix method is based on the systematic construction of a global stiffness matrix in terms of local stiffness matrices of the individual layers.

According to the classical Saint-Venant principle, the precise decay factor of the stress with distance from the region of applied load depends on the geometry of the body, the boundary conditions, the applied load and material properties. For layered media, this issue has been examined by Baxter and Horgan [19,20]. They showed that material inhomogeneity significantly affects the practical application of Saint-Venant's principle to sandwich structures. Wu and Chiu [21] have solved the problem of a semi-infinite multilayered monoclinic strip loaded by shear stress at the end by using eigenfunction expansion in conjunction with Betti's reciprocity theorem.

In the current study, an anisotropic elastic multilayered medium with n layers subjected to antiplane loading within an arbitrary layer is investigated. The material properties and the thickness in each layer are different. One of the objectives of this study is to develop an effective analytical methodology to construct the full-field solutions for this complicated problem. A general linear coordinate transformation is introduced in this study to simplify the problem. This linear coordinate transformation will simplify the governing equilibrium equation without complicating the boundary and interface continuity conditions. Based on this transformation, the original anisotropic multilayered problem is converted to an equivalent isotropic multilayered problem. The analytical solutions for the stresses and displacement obtained in this study are exact and are expressed in an explicit closed form. For a numerical example, a multilayered medium with 12 layers is discussed in detail. The stress distribution for the multilayered solution is compared with the homogeneous single layer solution by averaging the material constants of the multilayered medium.

2 Antiplane Shear Deformations of an Anisotropic Elastic Solid

In the absence of body forces, the equilibrium equations for the elastostatic problem are

$$\sigma_{ij,j}=0, \tag{1}$$

where the repeated indices imply summation and a comma stands for differentiation. The generalized Hooke's law for an anisotropic, homogeneous, and linearly elastic solid is given by

$$\sigma_{ij}=C_{ijkl}\varepsilon_{kl}, \tag{2}$$

where $\varepsilon_{kl}=1/2(u_{k,l}+u_{l,k})$ denotes the infinitesimal strain tensor, and C_{ijkl} are the elastic stiffnesses satisfying the usual symmetry conditions. Due to the symmetry of C_{ijkl}, Eq. (2) can be rewritten as

$$\sigma_{ij}=C_{ijkl}u_{k,l}. \tag{3}$$

For a general anisotropic elastic material, an antiplane deformation or a plane deformation in general does not exist. For some special anisotropic materials possessing elastic stiffnesses C_{ijkl} which are written in a contracted notation in the form

$$\mathbf{C}=\begin{bmatrix} C_{11} & C_{12} & C_{13} & 0 & 0 & C_{16} \\ & C_{22} & C_{23} & 0 & 0 & C_{26} \\ & & C_{33} & C_{34} & C_{35} & C_{36} \\ & & & C_{44} & C_{45} & 0 \\ & \text{sym.} & & & C_{55} & 0 \\ & & & & & C_{66} \end{bmatrix}, \tag{4}$$

the plane and antiplane deformations will be uncoupled and such anisotropic elastic materials are capable of an antiplane deformation (see, e.g., Horgan and Miller [1], Ting [6]).

For two-dimensional problems, the Cartesian coordinate system is chosen such that the antiplane deformation is in the z-direction. Let u, v, and w, respectively, represent the displacement components in the x, y, and z-direction of the Cartesian coordinate system. For antiplane shear deformations,

$$u=v=0, \quad w=w(x,y), \tag{5}$$

and the relevant shear stresses are denoted by τ_{yz} and τ_{xz}. If the material constants have the form represented in Eq. (4), then the equilibrium equations in the x and y-directions are automatically satisfied, and the equilibrium equation in the z-direction can be written in terms of the displacement w as

$$C_{55}\frac{\partial^2 w}{\partial x^2}+2C_{45}\frac{\partial^2 w}{\partial x\partial y}+C_{44}\frac{\partial^2 w}{\partial y^2}=0. \tag{6}$$

Equation (6) is the governing equation for an anisotropic antiplane deformation problem, and is a homogeneous second-order partial differential equation for displacement w. The nonzero stresses are related to the displacement as follows:

$$\begin{aligned} \tau_{yz}&=C_{45}\frac{\partial w}{\partial x}+C_{44}\frac{\partial w}{\partial y}, \\ \tau_{xz}&=C_{55}\frac{\partial w}{\partial x}+C_{45}\frac{\partial w}{\partial y}, \\ \sigma_{zz}&=C_{35}\frac{\partial w}{\partial x}+C_{34}\frac{\partial w}{\partial y}. \end{aligned} \tag{7}$$

For monoclinic materials with the plane of symmetry $z=0$, $C_{34}=C_{35}=0$ so that $\sigma_{zz}=0$.

3 Linear Coordinate Transformation

The governing equation expressed in Eq. (6) is a general homogeneous second-order partial differential equation with constant coefficients. Such a linear partial differential equation can be transformed into the Laplace equation by a linear coordinate transformation (see, e.g., Horgan and Miller [1]). A special linear coordinate transformation is introduced as

$$\begin{bmatrix} X \\ Y \end{bmatrix}=\begin{bmatrix} 1 & \alpha \\ 0 & \beta \end{bmatrix}\begin{bmatrix} x \\ y \end{bmatrix}, \tag{8}$$

where $\alpha=-C_{45}/C_{44}$, $\beta=\mu^e/C_{44}$ and $\mu^e=\sqrt{C_{44}C_{55}-C_{45}^2}$. Assume that C_{44} and C_{55} as well as $\sqrt{C_{44}C_{55}-C_{45}^2}$ are all positive. After the coordinate transformation, Eq. (6) can be rewritten as the standard Laplace equation in the (X, Y) coordinate system

$$\mu^e\left(\frac{\partial^2 w}{\partial X^2}+\frac{\partial^2 w}{\partial Y^2}\right)=0. \tag{9}$$

It is interesting to note that the mixed derivative disappears from Eq. (6). The relationships between the shear stresses in the two coordinate systems are given by

$$\begin{aligned} \tau_{yz}(x,y)&=\mu^e\frac{\partial w(X,Y)}{\partial Y}=\tau_{YZ}(X,Y), \\ \tau_{xz}(x,y)&=\beta\mu^e\frac{\partial w(X,Y)}{\partial X}-\alpha\mu^e\frac{\partial w(X,Y)}{\partial Y} \\ &=\beta\tau_{XZ}(X,Y)-\alpha\tau_{YZ}(X,Y). \end{aligned} \tag{10}$$

In a mathematical sense, Eqs. (6) and (7) are transformed to Eqs. (9) and (10) by the linear coordinate transformation expressed in Eq. (8), or in a physical sense, the governing Eq. (6) and the stress displacement relation (7) of an anisotropic antiplane problem are converted into an equivalent isotropic problem by properly changing the geometry of the body using the linear coordinate transformation, Eq. (8). The coordinate transformation in Eq. (8) has the following characteristics: (a) it is linear and continuous, (b) an anisotropic problem is converted to an isotropic problem after the transformation, and (c) there is no stretching and rotation in the

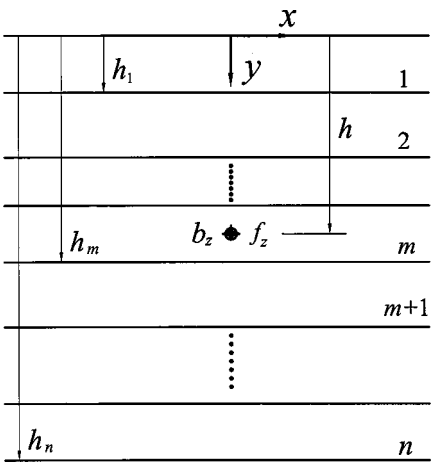

Fig. 1 Configuration and coordinates system of an anisotropic multilayered medium

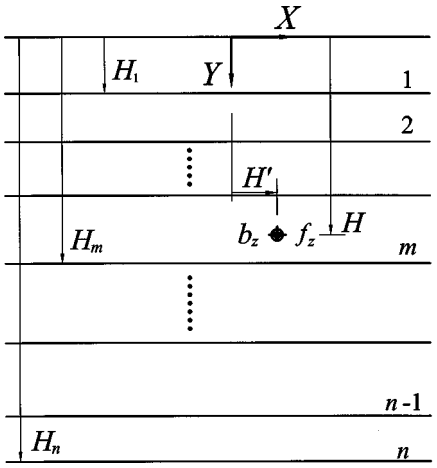

Fig. 2 Configuration and coordinates system for the multilayered medium after the linear coordinate transformation

horizontal direction. These important features offer advantages in dealing with straight boundaries and interfaces in the multilayered system discussed in the present study. The most interesting feature is that a straight line $(x_1,y_0),(x_2,y_0)$ that is parallel to the x-axis will remain a straight line $(X_1,Y_0),(X_2,Y_0)$ parallel to the X-axis after the transformation, and the length of the line will not change, i.e., $X_2-X_1=x_2-x_1$. The relationship between the anisotropic problem and the corresponding isotropic problem in the polar coordinate system and more detailed discussions of this linear coordinate transformation were presented by Ma [12].

The linear coordinate transformation described by Eq. (8) can be used to solve the anisotropic antiplane problem for only a single material. However, for a multilayered anisotropic medium with straight interfaces shown in Fig. 1, a modification of the linear coordinate transformation will be introduced in the following section to transform the multilayered anisotropic problem to an equivalent multilayered isotropic problem.

4 Formulations for Multilayered Media Subjected to Interior Loadings

In the following sections, the Green's function for an anisotropic n-layered medium will be constructed. Consider an anisotropic n-layered medium with n layers subjected to a line of constant force f_z and a screw dislocation of magnitude b_z along the z-axis located in the mth layer. The displacement and shear stresses are independent of the z-axis and so we can consider this problem as a two-dimensional antiplane problem. In other words, the original problem can be simplified as a two-dimensional multilayered medium subjected to a point shear force and a screw dislocation shown in Fig. 1. The displacement equilibrium equation in each layer is expressed as

$$C^j_{55}\frac{\partial^2 w^j}{\partial x^2}+2C^j_{45}\frac{\partial^2 w^j}{\partial x\partial y}+C^j_{44}\frac{\partial^2 w^j}{\partial y^2}=0,\quad j=1,2,\ldots,n. \tag{11}$$

The boundary conditions on the top and bottom surfaces of the layered medium are

$$\tau^1_{yz}(x,0)=0,\quad \tau^n_{yz}(x,h_n)=0. \tag{12}$$

The jump conditions for the shear stress and displacement across the point loads within the mth layer are

$$\begin{aligned}\tau^{m^+}_{yz}(x,h^+)-\tau^{m^-}_{yz}(x,h^-)&=-f_z\delta(x),\\ w^{m^+}(x,h^+)-w^{m^-}(x,h^-)&=-b_zU(x),\end{aligned} \tag{13}$$

where $\delta(\ )$ is the delta function and $U(\ )$ is the heaviside function. In Eq. (13), $\tau^{m^+}_{yz}$ and $\tau^{m^-}_{yz}$ indicate the shear stress above and below the plane of applied loadings in the mth layer; h^+ and h^- denote the position just above and below the applied loadings at $y=h$ (see Fig. 1). Application of the traction and displacement continuity conditions at the interface between the jth and $j+1$th layer, yields

$$\begin{aligned}\tau^j_{yz}(x,h_j)&=\tau^{j+1}_{yz}(x,h_j),\\ w^j(x,h_j)&=w^{j+1}(x,h_j),\end{aligned}\quad j=1,2,\ldots,n-1. \tag{14}$$

In order to maintain the geometry of the layered configuration, the linear coordinate transformation described in Eq. (8) is modified for each layer as follows:

$$\begin{bmatrix}X\\Y\end{bmatrix}=\begin{bmatrix}1&\alpha_j\\0&\beta_j\end{bmatrix}\begin{bmatrix}x\\y\end{bmatrix}+\sum_{k=1}^{j-1}h_k\begin{bmatrix}\alpha_k-\alpha_{k+1}\\ \beta_k-\beta_{k+1}\end{bmatrix},\quad j=1,2,\ldots,n. \tag{15}$$

Comparing with Eq. (8), the first term on the right-hand side of Eq. (15) retains exactly the same form while the second summation term becomes the modified term. The new coordinate transformation possesses the following characteristics: (a) no gaps or overlaps are generated along the interface and (b) no sliding and no mismatches occur along the interface. The geometric configuration in the transformed (X, Y) coordinate is shown in Fig. 2. Note that while the thickness of each layer is changed, the interfaces are parallel to the X-axis. Thus, the new geometric configuration is similar to the original problem.

The equilibrium equations in the transformed coordinate are governed by the standard Laplace equation expressed by

$$\mu^e_j\frac{\partial^2 w^j}{\partial X^2}+\mu^e_j\frac{\partial^2 w^j}{\partial Y^2}=0. \tag{16}$$

The displacement w and the shear stress τ_{YZ} are continuous along the interfaces in the transformed coordinates,

$$\begin{aligned}w^j(X,H_j)=w^{j+1}(X,H_j),\quad \tau^j_{YZ}(X,H_j)=\tau^{j+1}_{YZ}(X,H_j),\\ j=1,2,\ldots,n-1,\end{aligned} \tag{17}$$

where

$$H_j=\beta_jh_j+\sum_{k=1}^{j-1}(\beta_k-\beta_{k+1})h_k.$$

The top and bottom surfaces are traction free and can be expressed as

$$\tau^1_{YZ}(X,0)=0,\quad \tau^n_{YZ}(X,H_n)=0. \tag{18}$$

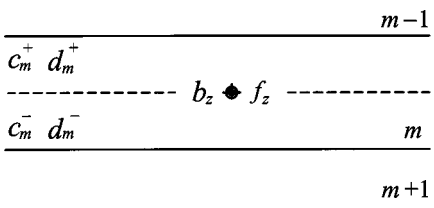

Fig. 3 The jump conditions for applied loadings at the *m*th layer

The jumps within the mth layer caused by the applied antiplane body force and screw dislocation are shown in Fig. 3, and the jump conditions are

$$\begin{aligned} \tau_{YZ}^{m^+}(X,H^+)-\tau_{YZ}^{m^-}(X,H^-)&=-f_z\delta(X-H'),\\ w^{m^+}(X,H^+)-w^{m^-}(X,H^-)&=-b_zU(X-H'), \end{aligned} \tag{19}$$

where

$$H'=\alpha_m h+\sum_{k=1}^{m-1}(\alpha_k-\alpha_{k+1})h_k,$$

$$H=\beta_m h+\sum_{k=1}^{m-1}(\beta_k-\beta_{k+1})h_k.$$

Here $\tau_{YZ}^{m^+}$ and $\tau_{YZ}^{m^-}$ indicate the shear stress above and below the applied loadings, respectively, in the mth layer (see Fig. 3). The location of the applied loadings is shifted by an amount of H' in the horizontal direction. The stress displacement relations expressed in the (X, Y) coordinates within each layer become

$$\begin{aligned} \tau_{XZ}^{j}(X,Y)&=\mu_j^e\frac{\partial w^j(X,Y)}{\partial X},\\ \tau_{YZ}^{j}(X,Y)&=\mu_j^e\frac{\partial w^j(X,Y)}{\partial Y}. \end{aligned} \tag{20}$$

The boundary value problem described by Eqs. (16)–(20) is similar to the multilayered problem for an isotropic material. Hence the linear coordinate transformation presented in Eq. (15) changes the original anisotropic multilayered problem to the corresponding isotropic multilayered problem with a similar geometric configuration and boundary conditions. In the next section, the boundary value problem described by Eqs. (16)–(20) will be solved, and the relationships between the shear stresses in the (x, y) and (X, Y) coordinates established in Eq. (10) will be used to obtain the solutions for the original anisotropic multilayered problem.

5 Fundamental Solutions in the Transformed Domain

The boundary value problem of the previous section can be solved by the integral transform technique. The expressions for the field variables will be found by applying a Fourier transform over the spatial coordinate X with parameter ω. Take the Fourier transform pairs defined as

$$\tilde{g}(\omega,Y)=\int_{-\infty}^{\infty}g(X,Y)e^{-i\omega X}dX,$$

$$g(X,Y)=\frac{1}{2\pi}\int_{-\infty}^{\infty}\tilde{g}(\omega,Y)e^{i\omega X}d\omega,$$

and apply to the governing Eq. (16). Then, Eq. (16) becomes an ordinary differential equation with the following general solution in the Fourier transformed domain:

$$\begin{bmatrix}\tilde{w}^j\\ \tilde{\tau}_{YZ}^{\,j}\end{bmatrix}=\begin{bmatrix}e^{\omega Y} & e^{-\omega Y}\\ \mu_j^e\omega e^{\omega Y} & -\mu_j^e\omega e^{-\omega Y}\end{bmatrix}\begin{bmatrix}c_j\\ d_j\end{bmatrix}. \tag{21}$$

Here c_j and d_j are undetermined coefficients for each layer and can be obtained by applying the boundary, continuity and jump conditions. Substituting the general solution into the continuity conditions at the interfaces, the recurrence relation for the coefficients for each layer can be expressed as

$$\begin{bmatrix}c_{j+1}\\ d_{j+1}\end{bmatrix}=\frac{1}{s_j'}\mathbf{G}^+(j)\begin{bmatrix}c_j\\ d_j\end{bmatrix}, \tag{22}$$

or

$$\begin{bmatrix}c_j\\ d_j\end{bmatrix}=\frac{1}{s_j''}\mathbf{G}^-(j)\begin{bmatrix}c_{j+1}\\ d_{j+1}\end{bmatrix}, \tag{23}$$

where

$$\mathbf{G}^+(j)=\begin{bmatrix}1 & t_je^{-2\omega H_j}\\ t_je^{2\omega H_j} & 1\end{bmatrix},$$

$$\mathbf{G}^-(j)=\begin{bmatrix}1 & -t_je^{-2\omega H_j}\\ -t_je^{2\omega H_j} & 1\end{bmatrix},$$

$$t_j=\frac{\mu_{j+1}^e-\mu_j^e}{\mu_j^e+\mu_{j+1}^e},\quad s_j'=\frac{2\mu_{j+1}^e}{\mu_j^e+\mu_{j+1}^e},\quad s_j''=\frac{2\mu_j^e}{\mu_j^e+\mu_{j+1}^e}.$$

Here t_j is called the reflection coefficient and s_j', s_j'' are the refraction coefficients. By applying the boundary condition for the top layer $\tilde{\tau}_{YZ}^1(\omega,0)=0$, $c_1=d_1$ is obtained, and along with Eq. (22), the coefficients for the mth layer can be related to those of the first layer as follows:

$$\begin{bmatrix}c_m^+\\ d_m^+\end{bmatrix}=\prod_{k=1}^{m-1}\frac{1}{s_k'}\mathbf{G}^+(m-k)\begin{bmatrix}c_1\\ c_1\end{bmatrix}, \tag{24}$$

where

$$\prod_{k=1}^{n}a_k=a_1\cdot a_2\cdots a_n.$$

Similarly, by applying the boundary condition for the bottom layer $\tilde{\tau}_{YZ}^{\,n}(\omega,H_n)=0$, $c_n=d_ne^{-2\omega H_n}$ is obtained, and along with Eq. (23), the coefficients for the mth layer can be represented by

$$\begin{bmatrix}c_m^-\\ d_m^-\end{bmatrix}=\prod_{k=m}^{n-1}\frac{1}{s_k''}\mathbf{G}^-(k)\begin{bmatrix}d_ne^{-2\omega H_n}\\ d_n\end{bmatrix}. \tag{25}$$

Finally, the jump conditions in the mth layer in the transformed domain are employed

$$\begin{aligned} c_m^+e^{\omega H}+d_m^+e^{-\omega H}-c_m^-e^{\omega H}-d_m^-e^{-\omega H}&=\frac{ib_z}{\omega}e^{-i\omega H'},\\ c_m^+e^{\omega H}-d_m^+e^{-\omega H}-c_m^-e^{\omega H}+d_m^-e^{-\omega H}&=\frac{-f_z}{\mu_m^e\omega}e^{-i\omega H'}, \end{aligned} \tag{26}$$

where $i=\sqrt{-1}$ and Eq. (26) can be written in a matrix form as

$$\begin{bmatrix}e^{\omega H} & e^{-\omega H}\\ e^{\omega H} & -e^{-\omega H}\end{bmatrix}\left\{\begin{bmatrix}c_m^+\\ d_m^+\end{bmatrix}-\begin{bmatrix}c_m^-\\ d_m^-\end{bmatrix}\right\}=\begin{bmatrix}\dfrac{ib_z}{\omega}\\ \dfrac{-f_z}{\mu_m^e\omega}\end{bmatrix}e^{-i\omega H'}. \tag{27}$$

For convenience, set $c_m^+=A_1c_1$, $d_m^+=A_2c_1$, $c_m^-=B_1d_n$ and $d_m^-=B_2d_n$, where A_1, A_2, B_1 and B_2 are constants which can be expressed in matrix form as

$$\begin{bmatrix}A_1\\ A_2\end{bmatrix}=\prod_{k=1}^{m-1}\frac{1}{s_k'}\mathbf{G}^+(m-k)\begin{bmatrix}1\\ 1\end{bmatrix},\quad \begin{bmatrix}B_1\\ B_2\end{bmatrix}=\prod_{k=m}^{n-1}\frac{1}{s_k''}\mathbf{G}^-(k)\begin{bmatrix}e^{-2\omega H_n}\\ 1\end{bmatrix}. \tag{28}$$

Therefore, Eq. (27) can be reformulated and coefficients c_1 and d_n are found as follows:

$$\begin{bmatrix} c_1 \\ d_n \end{bmatrix} = \frac{1/2}{A_1B_2 - A_2B_1} \begin{bmatrix} B_2 & -B_1 \\ A_2 & -A_1 \end{bmatrix} \begin{bmatrix} e^{-\omega H} & e^{-\omega H} \\ e^{\omega H} & -e^{\omega H} \end{bmatrix} \times \begin{bmatrix} \dfrac{ib_z}{\omega} \\ \dfrac{-f_z}{\mu_m^e \omega} \end{bmatrix} e^{-i\omega H'}. \tag{29}$$

The undetermined constants c_j and d_j for each layer are obtained with the aid of the recurrence relations given in Eqs. (22) and (23). After substituting the coefficients c_j and d_j into Eq. (21), the full-field solutions for each layer are completely determined in the transformed domain. Omitting the lengthy algebraic derivation, the general solutions for each layer are finally expressed as

$$\begin{bmatrix} \tilde{w}^j \\ \tilde{\tau}^{\,j}_{YZ} \end{bmatrix} = \frac{-e^{-i\omega H'}}{2(A_2B_1 - A_1B_2)\omega\mu_m^e} (B_2 e^{-\omega H}(f_z - i\mu_m^e b_z) + B_1 e^{\omega H}(f_z + i\mu_m^e b_z)) \cdot \begin{bmatrix} e^{\omega Y} & e^{-\omega Y} \\ \mu_j^e \omega e^{\omega Y} & -\mu_j^e \omega e^{-\omega Y} \end{bmatrix} \times \left\{ \prod_{k=1}^{j-1} \frac{1}{s_k'} \begin{bmatrix} 1 & t_{j-k} e^{-2\omega H_{j-k}} \\ t_{j-k} e^{2\omega H_{j-k}} & 1 \end{bmatrix} \right\} \begin{bmatrix} 1 \\ 1 \end{bmatrix}, \tag{30}$$

for $1 \leqslant j \leqslant m$. And for $m \leqslant j \leqslant n$,

$$\begin{bmatrix} \tilde{w}^j \\ \tilde{\tau}^{\,j}_{YZ} \end{bmatrix} = \frac{-e^{-i\omega H'}}{2(A_2B_1 - A_1B_2)\omega\mu_m^e} (A_2 e^{-\omega H}(f_z - i\mu_m^e b_z) + A_1 e^{\omega H}(f_z + i\mu_m^e b_z)) \cdot \begin{bmatrix} e^{\omega Y} & e^{-\omega Y} \\ \mu_j^e \omega e^{\omega Y} & -\mu_j^e \omega e^{-\omega Y} \end{bmatrix} \times \left\{ \prod_{k=j}^{n-1} \frac{1}{s_k''} \begin{bmatrix} 1 & -t_k e^{-2\omega H_k} \\ -t_k e^{2\omega H_k} & 1 \end{bmatrix} \right\} \begin{bmatrix} e^{-2\omega H_n} \\ 1 \end{bmatrix}. \tag{31}$$

6 Full-Field Solutions and Their Physical Meaning

The complete solutions in the Fourier transformed domain for multilayered media have been presented in Eqs. (30) and (31) in the previous section. The solutions are so complicated that it is not easy to obtain the inverse Fourier transform. In order to construct the explicit analytical full-field solution of the *n*-layered medium, the Taylor series expansion is used in this study.

Because of the denominators in Eqs. (29)–(31), it is impossible to invert the Fourier transform directly. By examining the structure of the denominator of Eq. (29), both the numerator and denominator are multiplied by a constant $S = (\Pi_{k=1}^{m-1} s_k')(\Pi_{k=m}^{n-1} s_k'')$.

Then it becomes

$$\begin{bmatrix} c_1 \\ d_n \end{bmatrix} = \frac{S/2}{S(A_1B_2 - A_2B_1)\mu_m^e \omega} \begin{bmatrix} B_2 & -B_1 \\ A_2 & -A_1 \end{bmatrix} \begin{bmatrix} e^{-\omega H} & e^{-\omega H} \\ e^{\omega H} & -e^{\omega H} \end{bmatrix} \times \begin{bmatrix} i\mu_m^e b_z \\ -f_z \end{bmatrix} e^{-i\omega H'}. \tag{32}$$

The denominator in Eq. (32), $S(A_1B_2 - A_2B_1)$, can be decomposed into the form of $(1-p)$ where $p = 1 - S(A_1B_2 - A_2B_1)$. It can be shown that $p < 1$ for $\omega > 0$. By a series expansion, we obtain $1/1 - p = \Sigma_{l=0}^{\infty} p^l$ so that Eq. (32) can be rewritten as

$$\begin{bmatrix} c_1 \\ d_n \end{bmatrix} = \frac{S}{2\omega} \begin{bmatrix} B_2 & -B_1 \\ A_2 & -A_1 \end{bmatrix} \begin{bmatrix} e^{-\omega H} & e^{-\omega H} \\ e^{\omega H} & -e^{\omega H} \end{bmatrix} \begin{bmatrix} ib_z \\ \dfrac{-f_z}{\mu_m^e} \end{bmatrix} e^{-i\omega H'} \cdot \sum_{l=0}^{\infty} p^l. \tag{33}$$

Now, the solutions for c_1 and d_n are linear combinations of exponential functions, i.e., $M_i e^{\pm f(\omega, H_i)}$, and so are c_j and d_j. Note that M_i are constants which denote the magnitude of the exponential function, and $f(\omega, H_i)$ are functions of ω and H_i.

The solutions for the displacement and shear stress in Eqs. (30) and (31) can also be expressed in similar forms. By a complicated algebraic derivation, the explicit expressions for displacement and shear stress in the Fourier transformed domain are obtained as follows:

$$\tilde{w}^j = \sum_{l=0}^{\infty} \sum_{k=1}^{N} \frac{M_k}{\mu_m^e \omega} \begin{bmatrix} -(f_z - i\mu_m^e b_z) e^{\omega(Y - H + F_k^{c'})} - (f_z + i\mu_m^e b_z) e^{\omega(Y + H + F_k^{c''})} \\ -(f_z - i\mu_m^e b_z) e^{-\omega(Y + H - F_k^{d'})} - (f_z + i\mu_m^e b_z) e^{-\omega(Y - H - F_k^{d''})} \end{bmatrix} e^{-i\omega H'}, \tag{34}$$

$$\tilde{\tau}^{\,j}_{YZ} = \sum_{l=0}^{\infty} \sum_{k=1}^{N} \frac{\mu_j^e M_k}{\mu_m^e} \begin{bmatrix} -(f_z - i\mu_m^e b_z) e^{\omega(Y - H + F_k^{c'})} - (f_z + i\mu_m^e b_z) e^{\omega(Y + H + F_k^{c''})} \\ +(f_z - i\mu_m^e b_z) e^{-\omega(Y + H - F_k^{d'})} + (f_z + i\mu_m^e b_z) e^{-\omega(Y - H - F_k^{d''})} \end{bmatrix} e^{-i\omega H'},$$

where

$$\begin{cases} N = 2^{n+j-m-1} \cdot (2^n - 1)^l, & 1 \leqslant j \leqslant m, \\ N = 2^{n+m-j-1} \cdot (2^n - 1)^l, & m \leqslant j \leqslant n. \end{cases}$$

Here n is the number of layers, m denotes the layer that is subjected to the applied loading, and j is the jth layer where the solution is required. The terms M_k, $F_k^{c'}$, $F_k^{c''}$, $F_k^{d'}$, and $F_k^{d''}$ in Eq. (34) are very complicated and difficult to present. The following functions are first defined as

$$\begin{cases} a_1 = 1, f_1^A = 0, \\ a_{i+2^{k-1}} = a_i t_k, & k = 1,2 \cdots m-1, \\ f^{\,A}_{i+2^{k-1}} = -(f_i^A + 2H_k), & i = 1,2 \cdots 2^{k-1}, \end{cases} \tag{35a}$$

$$\begin{cases} b_1 = 1, f_1^{B_1} = -2H_n, f_1^{B_2} = 0, \\ b_{i+2^{k-1}} = -b_i t_{n-k}, & k = 1,2 \cdots n-m, \\ f^{B_1}_{i+2^{k-1}} = -(f_i^{B_1} + 2H_n + 2H_{n-k}), & i = 1,2 \cdots 2^{k-1}, \\ f^{B_2}_{i+2^{k-1}} = -(f_i^{B_2} + 2H_n - 2H_{n-k}), \end{cases} \tag{35b}$$

$$\begin{cases} r^p_{(i-1)\cdot 2^{n-m}+k} = -a_i b_k, & r^p_{2^{n-1}+(i-1)\cdot 2^{m-1}+k} = a_i b_k, \qquad i=1,2,\cdots 2^{m-1}, \\ g^p_{(i-1)\cdot 2^{n-m}+k} = f^A_i + f^{B_2}_k, & g^p_{2^{n-1}+(k-1)\cdot 2^{m-1}+i} = f^{B_1}_k - f^A_i, \quad k=1,2,\cdots 2^{n-m}, \end{cases} \tag{35c}$$

$$\begin{cases} r^l_k = \prod_{0=1}^{l} r^p_{l_0}, \quad i_1, i_2, {}_3, \cdots i_l = 2,3,\cdots 2^n, \\ g^l_k = \sum_{0=1}^{l} g^p_{l_0}, \quad k = \sum_{0=1}^{l-1} (i_0-2)(2^n-1) + (i_l-1), \end{cases} \tag{35d}$$

for $l=0$, $r^0_{i_0}=1$ and $g^0_{i_0}=0$.

For the case of $1 \leqslant j \leqslant m$, the following functions are defined:

$$\begin{cases} f^{c'}_{(i-1)\cdot 2^{n-m}+k} = f^{B_2}_k + f^A_i, \\ f^{c''}_{(i-1)\cdot 2^{n-m}+k} = f^{B_1}_k + f^A_i, \quad i=1,2,\cdots 2^{j-1}, \\ f^{d'}_{(i-1)\cdot 2^{n-m}+k} = f^{B_2}_k - f^A_i, \quad k=1,2,\cdots 2^{n-m}. \\ f^{d''}_{(i-1)\cdot 2^{n-m}+k} = f^{B_1}_k - f^A_i, \end{cases} \tag{35e}$$

Finally, the terms M_k, $F^{c'}_k$, $F^{c''}_k$, $F^{d'}_k$, and $F^{d''}_k$ indicated in Eq. (34) can be expressed explicitly as

$$\begin{cases} M_{(k-1)\cdot 2^{n+j-m-1}+i} = \dfrac{-1}{2}\left(\prod_{0=j}^{m-1} S'_0\right) r^l_k r^p_i, \\ F^{c'}_{(k-1)\cdot 2^{n+j-m-1}+i} = g^l_k + f^{c'}_i, \qquad k=1,2,\cdots (2^n-1)^l, \\ F^{c''}_{(k-1)\cdot 2^{n+j-m-1}+i} = g^l_k + f^{c''}_i, \qquad i=1,2,\cdots 2^{n+j-m-1}. \\ F^{d'}_{(k-1)\cdot 2^{n+j-m-1}+i} = g^l_k + f^{d'}_i, \\ F^{d''}_{(k-1)\cdot 2^{n+j-m-1}+i} = g^l_k + f^{d''}_i, \end{cases} \tag{35f}$$

For the case of $m \leqslant j \leqslant n$, the expressions are

$$\begin{cases} f^{c'}_{(i-1)\cdot 2^{m-1}+k} = f^{B_1}_i + f^A_k, \\ f^{c''}_{(i-1)\cdot 2^{m-1}+k} = f^{B_1}_i + f^A_k, \quad i=1,2,\cdots 2^{n-j}, \\ f^{d'}_{(i-1)\cdot 2^{m-1}+k} = f^{B_2}_i - f^A_k, \quad k=1,2,\cdots 2^{m-1}. \\ f^{d''}_{(i-1)\cdot 2^{m-1}+k} = f^{B_2}_i + f^A_k, \end{cases} \tag{35g}$$

The terms M_k, $F^{c'}_k$, $F^{c''}_k$, $F^{d'}_k$, and $F^{d''}_k$ are presented by

$$\begin{cases} M_{(k-1)\cdot 2^{n-j+m-1}+i} = \dfrac{1}{2}\left(\prod_{0=m}^{j-1} S''_0\right) r^l_k r^p_{2^{n-1}+i}, \\ F^{c'}_{(k-1)\cdot 2^{n-j+m-1}+i} = g^l_k + f^{c'}_i, \qquad k=1,2,\cdots (2^n-1)^l, \\ F^{c''}_{(k-1)\cdot 2^{n-j+m-1}+i} = g^l_k + f^{c''}_i, \qquad i=1,2,\cdots 2^{n+m-j-1}. \\ F^{d'}_{(k-1)\cdot 2^{n-j+m-1}+i} = g^l_k + f^{d'}_i, \\ F^{d''}_{(k-1)\cdot 2^{n-j+m-1}+i} = g^l_k + f^{d''}_i, \end{cases} \tag{35h}$$

The structures of the complete solutions given in Eq. (34) have some interesting characteristics. The solutions are composed of infinite terms, and it is interesting to note that each term represents the solution in the transformed domain for a concentrated loading in an infinite homogeneous medium. The term with $(Y \pm H \pm F_k)$ in the exponential functions indicates the location of the loading. However, $M_k b_z$ and $\mu^e_j/\mu^e_m M_k f_z$ represent the magnitudes of the concentrated dislocation and force, respectively. F_k is dependent on the locations of the interfaces, i.e., H_j, and M_k depends only on the reflection and refraction coefficients, i.e., t_j, s'_j, and s''_j.

Only one term in the infinite series of Eq. (34) represents the applied concentrated force f_z and dislocation b_z in an infinite medium at $Y=H$ and $X=H'$, all the remaining terms are image forces and dislocations that are induced to satisfy the boundary and interface conditions. This method is referred to as the method of images. The advantage of this method is that the solutions of problems with complicated geometric configurations can be constructed by superposing the solution in an infinite medium. The mathematical derivation in this section provides an automatic determination for the locations and magnitudes of all the image forces.

Since the solutions in the transformed domain expressed in Eq.

(34) are exponential functions of ω, only two different inverse Fourier transformations for exponential functions are required, which are

$$\int_{-\infty}^{\infty} e^{-\omega(Y\pm H\pm F_k)}\cdot e^{-i\omega H'}\cdot e^{i\omega X}d\omega = \frac{1}{\pi}\frac{Y\pm H\pm F_k}{(X-H')^2+(Y\pm H\pm F_k)^2},$$

$$\int_{-\infty}^{\infty}\frac{1}{\omega}e^{-\omega(Y\pm H\pm F_k)}\cdot e^{-i\omega H'}\cdot e^{i\omega X}d\omega = \frac{-1}{2\pi}\ln[(X-H')^2+(Y\pm H\pm F_k)^2]. \tag{36}$$

Therefore, the inverse Fourier transformation for Eq. (34) can be easily derived and the results are

$$w^j=\sum_{l=0}^{\infty}\sum_{k=1}^{N}\frac{M_k}{\pi}\left\{\begin{array}{l} b_z\left[\begin{array}{l} -\tan^{-1}\dfrac{Y-H+F_k^{c'}}{X-H'}+\tan^{-1}\dfrac{Y+H+F_k^{c''}}{X-H'} \\ +\tan^{-1}\dfrac{Y+H+F_k^{d'}}{X-H'}-\tan^{-1}\dfrac{Y-H-F_k^{d''}}{X-H'}\end{array}\right] \\ +\dfrac{f_z}{2\mu_m^e}\left[\begin{array}{l}\ln((X-H')^2+(Y-H+F_k^{c'})^2)+\ln((X-H')^2+(Y+H+F_k^{c''})^2) \\ +\ln((X-H')^2+(Y+H-F_k^{d'})^2)+\ln((X-H')^2+(Y-H-F_k^{d''})^2)\end{array}\right]\end{array}\right\}, \tag{37}$$

$$\tau_{YZ}^j=\sum_{l=0}^{\infty}\sum_{k=1}^{N}\frac{\mu_j^e M_k}{\pi}\left\{\begin{array}{l} b_z\left[\begin{array}{l}\dfrac{-(X-H')}{(X-H')^2+(Y-H+F_k^{c'})^2}+\dfrac{(X-H')}{(X-H')^2+(Y+H+F_k^{c''})^2} \\ +\dfrac{(X-H')}{(X-H')^2+(Y+H-F_k^{d'})^2}-\dfrac{(X-H')}{(X-H')^2+(Y-H-F_k^{d''})^2}\end{array}\right] \\ +\dfrac{f_z}{\mu_m^e}\left[\begin{array}{l}\dfrac{Y-H+F_k^{c'}}{(X-H')^2+(Y-H+F_k^{c'})^2}+\dfrac{Y+H+F_k^{c'}}{(X-H')^2+(Y+H+F_k^{c''})^2} \\ \dfrac{Y+H-F_k^{d'}}{(X-H')^2+(Y+H-F_k^{d'})^2}+\dfrac{Y-H-F_k^{d''}}{(X-H')^2+(Y-H-F_k^{d''})^2}\end{array}\right]\end{array}\right\}. \tag{37}$$

Finally, by substituting X and Y defined in Eq. (15) into Eq. (37), and using the displacement and stress relations in Eq. (10), the complete solutions for the original problem of the anisotropic multilayered medium can be obtained. Equation (37) is the explicit expression of the Green's function for the multilayered medium subjected to the antiplane shear deformation.

7 Numerical Examples and Discussions

The full-field analysis of shear stresses in a layered medium consisting of 12 layers subjected to interior forces is presented in this section. In the analysis of a nonhomogeneous multilayered medium, it is sometimes the practice to treat the multilayered medium as a single homogeneous layer with effective or homogenized stiffness constants. The differences in the stress distributions between layered medium with 12 layers and one homogeneous layer with the effective material constants obtained from the averaged material properties of 12 layers will be discussed in detail. The effective stiffness constants of one homogeneous layer, $\tilde{C}_{ij}$, are obtained from the homogenized weighted properties of the 12 layers using the formula

$$\tilde{C}_{ij}=\frac{\sum_{k=2}^{n}C_{ij}^k(h_k-h_{k-1})+C_{ij}^1h_1}{h_n}. \tag{38}$$

As indicated in Eq. (38), the effective stiffness constants are obtained by averaging the stiffness constants over the thickness of each layer. The complete explicit expressions for the displacement and shear stress given in Eqs. (35) and (37) are used to construct the program for numerical calculations. For the 12-layered medium, the thickness of each layer is the same and equal to 1, and the elastic stiffness constants for each layer are listed as follows:

$$\begin{aligned}&[C_{44}^1,C_{45}^1,C_{55}^1;C_{44}^2,C_{45}^2,C_{55}^2;\ldots;C_{44}^{12},C_{45}^{12},C_{55}^{12}]\\ &=[3960,0,7170;7170,1220,3960;3960,\\ &\quad -1220,7170;3585,610,3960;3960,\\ &\quad -610,3585;4430,0,0,4430;1980;0,1980;7170,1220,3585;\\ &\quad 5158,-610,3585;3585,0,5185;3960,0,3960;6160,\\ &\quad -2440,3330]\text{GPa}.\end{aligned}$$

The effective elastic constants for one homogeneous layer obtained from Eq. (38) are

$$[\tilde{C}_{44},\tilde{C}_{45},\tilde{C}_{55}]=[4347,-169,4131]\text{GPa}.$$

An antiplane body force f_z is applied within the seventh layer at $x=0$ and $y=6.5$. The distributions of the shear stress τ_{yz} along the y-axis at $x=0$ and $x=2$ are shown in Figs. 4 and 5, respectively. In addition, the τ_{xz} stress distributions along the y-axis at $x=0$ and $x=2$ are displayed in Figs. 6 and 7, respectively. To generate the shear stress distributions, the series solution is truncated if the numerical calculation is within the accuracy of 0.1 percent.

As shown in Figs. 4 and 5, the multilayered solution for τ_{yz} is continuous at the interfaces and approaches zero at the top and bottom boundaries. The results of τ_{yz} for multilayered solutions and one homogeneous layer solution are closely related at $x=0$, and only a small difference appears at $x=2$. This implies that the

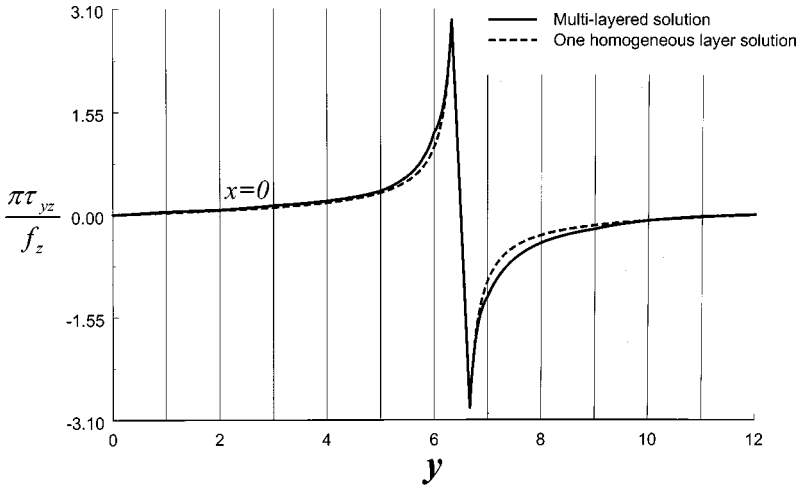

Fig. 4 Distribution of τ_{yz} at $x=0$ along y-axis for the 12-layered medium and one homogeneous layer

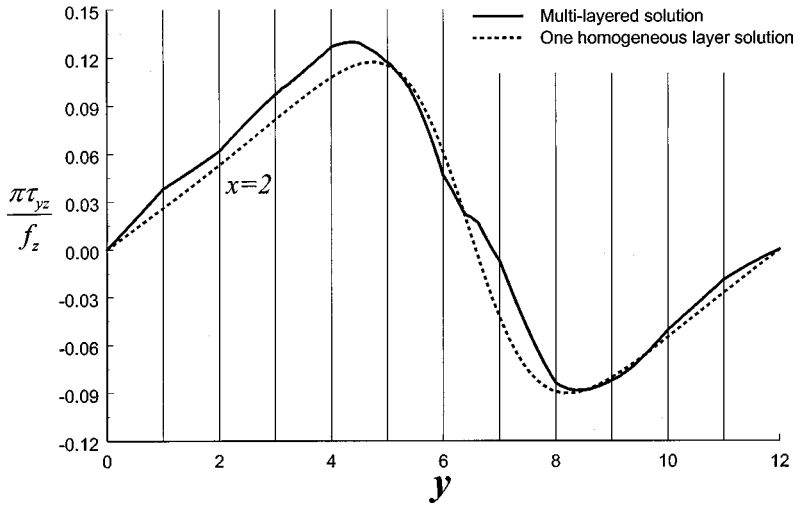

Fig. 5 Distribution of τ_{yz} at $x=2$ along y-axis for the 12-layered medium and one homogeneous layer

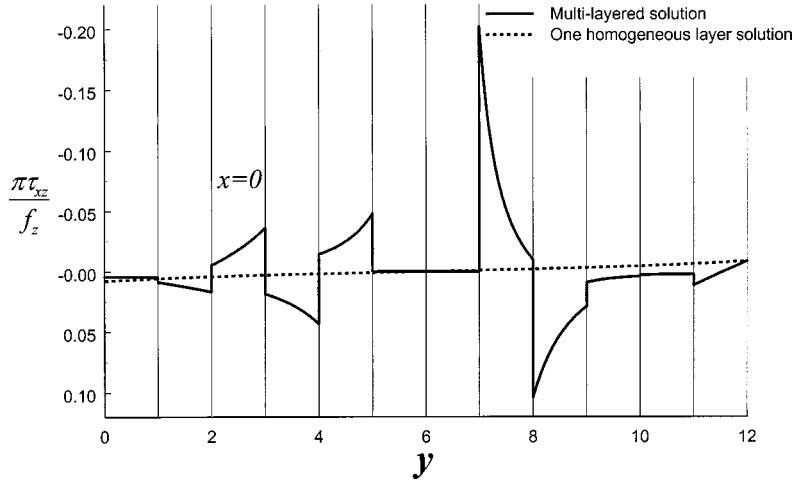

Fig. 6 Distribution of τ_{xz} at $x=0$ along y-axis for the 12-layered medium and one homogeneous layer

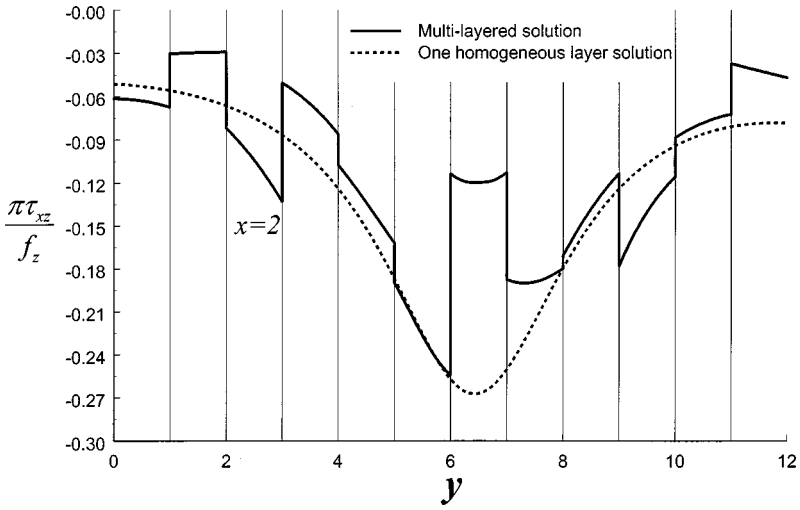

Fig. 7 Distribution of τ_{xz} at $x=2$ along y-axis for the 12-layered medium and one homogeneous layer

shear stress τ_{yz} of the multilayered problem can be obtained with good approximation from the result of a much simpler one homogeneous layer solution. As indicated in Figs. 6 and 7, since τ_{xz} is discontinuous at the interfaces for the multilayered solution, the results for multilayered solution and one homogeneous layer solution differ substantially. This indicates that it is not suitable to use the single homogeneous layer solution to simulate the multilayered problem for the shear stress τ_{xz}.

8 Concluding Remarks

An analytical investigation of multilayered anisotropic media subjected to concentrated forces and screw dislocations has been provided in this study. A general linear coordinate transformation for multilayered media was introduced to simplify the governing equilibrium equation without complicating the boundary and interface continuity conditions. With this linear coordinate transformation, the original anisotropic multilayered problem can be reduced to an equivalent isotropic multilayered problem. The linear coordinate transformation introduced in this study substantially reduces the dependence on elastic constants in the antiplane anisotropic multilayered media. By using the Fourier transform technique and a series expansion, analytical solutions for displacement and stresses are presented in an explicit form. The complete solutions for this complicated problem consist only of very simple solutions obtained from an infinite homogeneous medium with concentrated loadings. Except for the original applied loading, the remaining terms in the infinite series are image forces which are induced to satisfy the boundary and interface conditions. The mathematical approach introduced in this study provides an automatic determination for the locations and magnitudes of all the image forces. A computational program for numerical calculation of the full-field analysis is easily constructed by using the explicit formulation of the solutions. In order to simplify the problem, the nonhomogeneous multilayered medium is sometimes treated as a single homogeneous layer with effective material constants. Hence the numerical results for the multilayered problem were compared with the solutions obtained by considering the multilayered medium as a single homogeneous layer with effective material constants.

Acknowledgments

The financial support of the authors from the National Science Council, Republic of China, through Grant NSC 87-2218-E002-022 to National Taiwan University is gratefully acknowledged. The authors also wish to express their great appreciation to the Associate Editor and reviewers for their valuable suggestions.

References

[1] Horgan, C. O., and Miller, K. L., 1994, ''Antiplane Shear Deformations for Homogeneous and Inhomogeneous Anisotropic Linearly Elastic Solids,'' ASME J. Appl. Mech., **61**, pp. 23–29.
[2] Ma, C. C., 1992, ''Antiplane Problems of Monoclinic Material,'' ASCE J. Eng. Mech., **118**, pp. 1765–1782.
[3] Ma, C. C., and Hour, B. L., 1989, ''Analysis of Dissimilar Anisotropic Wedges Subjected to Antiplane Shear Deformation,'' Int. J. Solids Struct., **25**, pp. 1295–1309.
[4] Retting, G., 1986, ''Anti-plane Stress Analysis of a Cracked Rectangular Orthotropic Beam,'' Eng. Fract. Mech., **23**, pp. 441–454.
[5] Wu, K. C., and Chiu, Y. T., 1991, ''Antiplane Shear Interface Cracks in Anisotropic Bimaterials,'' ASME J. Appl. Mech., **58**, pp. 399–403.
[6] Ting, T. C. T., 1996, *Anisotropic Elasticity*, Oxford University Press, New York.
[7] Jiang, Q., and Knowles, J. K., 1991, ''A Class of Compressible Elastic Materials Capable of Sustaining Finite Anti-plane Shear,'' J. Elast., **25**, pp. 193–201.
[8] Polignone, D. A., and Horgan, C. O., 1992, ''Axisymmetric Finite Anti-plane Shear of Compressible Nonlinearly Elastic Circular Tubes,'' Q. Appl. Math., **50**, pp. 323–341.
[9] Horgan, C. O., 1995, ''Anti-Plane Shear Deformations in Linear and Nonlinear Solid Mechanics,'' SIAM Rev., **37**, pp. 53–81.
[10] Lekhnitskii, S. G., 1963, *Theory of Elasticity of an Anisotropic Body*, Holden-Day, San Francisco, CA.
[11] Stroh, A. N., 1958, ''Dislocations and Cracks in Anisotropic Elasticity,'' Philos. Mag., **7**, pp. 625–646.
[12] Ma, C. C., 1996, ''Relationship of Anisotropic and Isotropic Materials for Antiplane Problems,'' AIAA J., **34**, pp. 2453–2456.
[13] Yang, W., and Ma, C. C., 1998, ''Orthotropic Transform for Planar Anisotropic Elasticity and Reduced Dependence of Elastic Constants,'' Proc. R. Soc. London, Ser. A, **A454**, pp. 1843–1855.
[14] Bufler, H., 1971, ''Theory of Elasticity of a Multilayered Medium,'' J. Elast., **1**, pp. 125–143.
[15] Bahar, L. Y., 1972, ''Transfer Matrix Approach to Layered Systems,'' J. Eng. Mech. Div., **98**, pp. 1159–1172.
[16] Pindera, M.-J., 1991, ''Local/Global Stiffness Matrix Formulation for Composite Materials and Structures,'' Composites Eng., **1**, pp. 69–83.
[17] Pindera, M.-J., and Lane, M. S., 1993, ''Frictionless Contact of Layered Half-Planes, Part I: Analysis,'' ASME J. Appl. Mech., **60**, pp. 633–639.
[18] Pindera, M.-J., and Lane, M. S., 1993, ''Frictionless Contact of Layered Half-Planes, Part II: Numerical Results,'' ASME J. Appl. Mech., **60**, pp. 640–645.
[19] Baxter, S. C., and Horgan, C. O., 1995, ''End Effects for Anti-Plane Shear Deformations of Sandwich Structures,'' J. Elast., **40**, pp. 123–164.
[20] Baxter, S. C., and Horgan, C. O., 1997, ''Anti-Plane Shear Deformations of Anisotropic Sandwich Structures: End Effect,'' Int. J. Solids Struct., **34**, pp. 79–98.
[21] Wu, K. C., and Chiu, Y. T., 1996, ''Antiplane Shear Analysis of a Semi-infinite Multi-layered Monoclinic Strip,'' Acta Mech., **117**, pp. 205–214.

Elastodynamic Fracture Analysis of Multiple Cracks by Laplace Finite Element Alternating Method

W.-H. Chen
Professor,
Mem. ASME

C.-L. Chang[1]

C.-H. Tsai[2]

Department of Power Mechanical Engineering,
National Tsing Hua University,
Hsinchu, Taiwan 30043, R.O.C.

The Laplace finite element alternating method, which combines the Laplace transform technique and the finite element alternating method, is developed to deal with the elastodynamic analysis of a finite plate with multiple cracks. By the Laplace transform technique, the complicated elastodynamic fracture problem is first transformed into an equivalent static fracture problem in the Laplace transform domain and then solved by the finite element alternating method developed. To do this, an analytical solution by Tsai and Ma for an infinite plate with a semi-infinite crack subjected to exponentially distributed loadings on crack surfaces in the Laplace transform domain is adopted. Finally, the real-time response can be computed by a numerical Laplace inversion algorithm. The technique established is applicable to the calculation of dynamic stress intensity factors of a finite plate with arbitrarily distributed edge cracks or symmetrically distributed central cracks. Only a simple finite element mesh with very limited number of regular elements is necessary. Since the solutions are independent of the size of time increment taken, the dynamic stress intensity factors at any specific instant can even be computed by a single time-step instead of step-by-step computations. The interaction among the cracks and finite geometrical boundaries on the dynamic stress intensity factors is also discussed in detail. [S0021-8936(00)02103-6]

1 Introduction

When a stress wave is disturbed by the presence of cracks, some of the waves are reflected and others are refracted. Therewithal, the singular behavior in the elastodynamic stress field ([1]) is found around the crack tip. In general, the time-dependent dynamic stress intensity factor has a peak value higher than the corresponding static value. These phenomena of scattering and singularity have received much attention in seismology, as well as in some material testing techniques. Hence, the study of elastodynamic response with the events of scattering and singularity of existing cracks under dynamic loadings becomes increasingly important.

In general, the elastodynamic response for a finite cracked body subjected to dynamic loadings is difficult to obtain analytically. The analytical solutions for such problems are limited to simplified cases with infinite or semi-infinite domains. Sih and Loeber [1,2] made a detailed study of a finite crack in an infinite plane-strain plate subjected to plane harmonic compressive and shear waves by an integral transform method. Mal [3] used a Fredholm integral equation to yield the near-field as well as far-field stresses of Sih's problem under a harmonic compressive wave. Thau and Lu [4,5] investigated the mode I and mode II dynamic stress intensity factors of a finite crack in an infinite plane-strain plate subjected to plane dilatational and horizontal shear waves incident on the crack surface by a generalized Wiener-Hopf technique ([6]). It was found that the elastodynamic responses could be up to 30 percent higher than the static values depending on Poisson's ratio.

An analytical approach which combined the Laplace transform method and Wiener-Hopf technique was developed by Freund [7] to deal with an elastic plate containing a semi-infinite crack subjected to a concentrated tensile impact loading on the crack surfaces. Brock [8] took the Freund's solution as the Green's function to solve the problem with the impact loading distributed on the semi-infinite crack arbitrarily. Since multiple integrals involved in the formulation, only the dynamic stress intensity factors are computed. Tsai and Ma [9] used the Freund's method ([7]) to evaluate not only the dynamic stress intensity factors but also the stress response of the same cracked plate, but with the impact loading distributed on the crack surfaces exponentially.

It is noted that all those analytical solutions as mentioned above were valid only for the problems with a crack in infinite or semi-infinite domains. However, many of practical problems are a finite domain containing multiple cracks under complex dynamic loadings. Generally, they are difficult or nearly impossible to tackle analytically.

Numerical methods have been proven to be efficient tools in the determination of dynamic stress intensity factors for general geometry as well as complex dynamic loadings. Among the numerical methods, finite difference method ([10]), finite element method ([11–13]), and boundary element method ([14,15]) have been adopted to analyze the elastodynamic fracture problems. But, numerical experiments indicate that the accuracy of the dynamic stress intensity factors computed by these methods is strongly mesh dependent. In addition, to the author's best knowledge, very little work has been done for the elastodynamic analysis of multiple cracks.

The present Laplace finite element alternating method, which combines the advantages of the Laplace transform technique and the finite element alternating procedure, is thus proposed to deal with the elastodynamic analysis of a finite plate with multiple cracks. By the Laplace transform technique, the governing partial

[1]Currently, Engineer, Opto-Electronics & Systems Laboratories, Industrial Technology Research Institute.

[2]Currently, Associate Professor, Hua Fan University.

Contributed by the Applied Mechanics Division of THE AMERICAN SOCIETY OF MECHANICAL ENGINEERS for publication in the ASME JOURNAL OF APPLIED MECHANICS. Manuscript received by the ASME Applied Mechanics Division, June 7, 1999; final revision, Dec. 26, 1999. Associate Technical Editor: A. K. Mal. Discussion on the paper should be addressed to the Technical Editor, Professor Lewis T. Wheeler, Department of Mechanical Engineering, University of Houston, Houston, TX 77204-4792, and will be accepted until four months after final publication of the paper itself in the ASME JOURNAL OF APPLIED MECHANICS.

differential equations as well as the corresponding time-dependent boundary conditions can be transformed an equivalent static problem in Laplace transform domain. Thereafter, the solutions in the Laplace transform domain can be solved easily by the finite element alternating method ([16]). The so-called finite element alternating method which is the combination of the conventional finite element procedure and the Schwarz-Neumann alternating technique has been successfully developed for two-dimensional ([16,17]), three-dimensional ([18–20]), and plate bending ([21]) static fracture problems with multiple cracks. The real-time responses are then computed by the numerical Laplace inversion algorithm of Honig and Hirdes [22].

When carrying out the finite element alternating procedure in the Laplace domain, the Laplace domain analytical solution of an infinite plate with a semi-infinite crack subjected to an appropriately distributed loading is necessary. However, the analytical solution of Brock [8] is difficult to be applied for the present technique because multiple integrals are involved in the formulation. Also, the limitation of the Laplace parameter used in Tsai and Ma's solution ([9]) restricts its direct application and necessary modification is done in the present analysis.

The studies of the work include: (1) the computation of the dynamic stress intensity factors for a finite plate with arbitrarily distributed multiple edge cracks or symmetrically distributed multiple central cracks under impact loadings, and (2) the effect of the cracks and finite geometric boundaries on the dynamic stress intensity factors. Only a simple Laplace finite element model with very limited number of regular elements is required. Besides, since the size of time increment can be taken arbitrary, the dynamic stress intensity factors at any specific instant can even be determined by a single time increment. The present technique established will be helpful for the development of seismology or nondestructive testing technique to detect the presence of cracks in material.

2 Tsai and Ma's Solution ([9])

During the operation of the finite element alternating procedures in the Laplace domain, to simulate the traction-free condition on the crack surfaces, it is necessary to release the stresses at the location of fictitious cracks in an uncracked plate. Although Tsai and Ma's solution ([9]) can provide relevant stress field at the fictitious crack, the solution cannot be applied to the present technique directly because the Laplace parameter p is constrained as real and positive.

For clarity, the Tsai and Ma's solution is first briefly stated as follows. In the Laplace transform domain, as seen in Fig. 1, consider an infinite plate containing a semi-infinite crack subjected to an exponentially distributed normal traction $e^{p\eta_N x_1}$ and shear traction $e^{p\eta_S x_1}$ on the crack surfaces ($-\infty<x_1<0$). These tractions are transformed from real-time tractions by one-sided Laplace transform with respect to time. The one-sided Laplace variable $p=v+iw$ is a complex with its real and imaginary parts, v and w. η_N and η_S are complex numbers for describing the prescribed tractions. Since such a mixed boundary value problem is exceedingly difficult to solve in the Laplace domain, Tsai and Ma [9] used two-sided Laplace transform with respect to x_1 in conjunction with the application of the Wiener-Hopf technique under the assumption that the variable p is real and positive, say, $p=v(v>0)$.

Based on the displacement $\tilde{u}_i(x_1,x_2,v)$ and stress field $\tilde{\sigma}_{ij}(x_1,x_2,v)$ in the Laplace transform domain derived by Tsai and Ma [9], the Laplace domain solution for the problem with distributed loading applied on the semi-infinite crack can then be superposed from them. To obtain the real-time response, the Cagniard-de Hoop's method ([23]) is employed, but is valid only for the problem with infinite domain ([9]). However, for the real-time response of the elastodynamic fracture problems with finite geometric boundary, it is very difficult to obtain analytically. Hence, to solve such complicated problems, a numerical Laplace

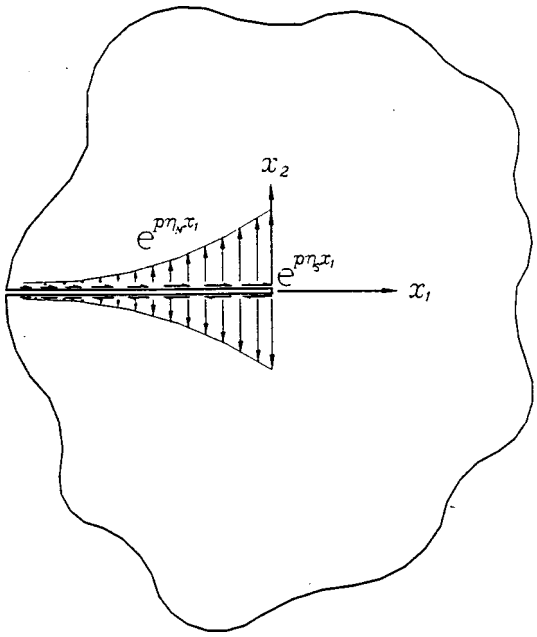

Fig. 1 An infinite plate with a semi-infinite crack subjected to exponential normal and shear tractions in the Laplace domain

inversion algorithm ([22]) is adopted in this work. By this method, a sequence of selected complex Laplace parameters $p_k=v+iw_k$ ($k=1,2,\ldots N$) instead of the real and positive Laplace parameter $p=v$, as taken in Tsai and Ma's work ([9]), need to be adopted to obtain the real-time response at a specific instant (see the Appendix).

To confirm the Laplace parameter p to be a complex number, the Tsai and Ma's Solution ([9]) is rewritten as

$$\tilde{u}_i(x_1,x_2,p)=\frac{1}{2\pi i\mu}\int_{\zeta_1-i\infty}^{\zeta_1+i\infty}[U_i^1(p,\eta_N,\eta_S,\zeta)e^{-\alpha x_2+\zeta x_1}+U_i^2(p,\eta_N,\eta_S,\zeta)e^{-\beta x_2+\zeta x_1}]d\zeta \tag{1}$$

and

$$\tilde{\sigma}_{ij}(x_1,x_2,p)=\frac{1}{2\pi i}\int_{\zeta_1-i\infty}^{\zeta_1+i\infty}[S_{ij}^1(p,\eta_N,\eta_S,\zeta)e^{-\alpha x_2+\zeta x_1}+S_{ij}^2(p,\eta_N,\eta_S,\zeta)e^{-\beta x_2+\zeta x_1}]d\zeta \tag{2}$$

where

$$\begin{aligned}
S_{11}^1&=(b^2p^2-2\zeta^2)(b^2p^2-2\alpha^2)\alpha_+(p\eta_N)F(p\eta_N,\zeta)/\alpha_+(\zeta)\\
&\quad-2\beta_-(\zeta)\zeta(b^2p^2-2\alpha^2)\beta_+(p\eta_S)F(p\eta_S,\zeta),\\
S_{11}^2&=-4\alpha_-(\zeta)\beta(\zeta)\alpha_+(p\eta_N)\zeta^2F(p\eta_N,\zeta)\\
&\quad-2\beta_-(\zeta)\zeta(b^2p^2-2\zeta^2)\beta_+(p\eta_S)F(p\eta_S,\zeta),\\
S_{12}^1&=-2\alpha_-(\zeta)\alpha_+(p\eta_N)\zeta(b^2p^2-2\zeta^2)F(p\eta_N,\zeta)\\
&\quad+4\alpha\beta_-(\zeta)\beta_+(p\eta_S)\zeta^2F(p\eta_S,\zeta),\\
S_{12}^2&=2\alpha_-(\zeta)\alpha_+(p\eta_N)\zeta(b^2p^2-2\zeta^2)F(p\eta_N,\zeta)\\
&\quad+(b^2p^2-2\zeta^2)^2\beta_+(p\eta_S)F(p\eta_S,\zeta)/\beta_+(\zeta),\\
S_{22}^1&=(b^2p^2-2\zeta^2)^2\alpha_+(p\eta_N)F(p\eta_N,\zeta)/\alpha_+(\zeta)\\
&\quad-2\zeta(b^2p^2-2\zeta^2)\beta_-(\zeta)\beta_+(p\eta_S)F(p\eta_S,\zeta),\\
S_{22}^2&=4\zeta^2\alpha_-(\zeta)\beta(\zeta)\alpha_+(p\eta_N)F(p\eta_N,\zeta)\\
&\quad+2\zeta(b^2p^2-2\zeta^2)\beta_-(\zeta)\beta_+(p\eta_S)F(p\eta_S,\zeta),
\end{aligned}$$

$$U_1^1=\zeta(b^2p^2-2\zeta^2)\alpha_+(p\eta_N)F(p\eta_N,\zeta)/\alpha_+(\zeta)$$
$$-2\zeta^2\beta_-(\zeta)\beta_+(p\eta_S)F(p\eta_S,\zeta),$$
$$U_1^2=-2\alpha_-(\zeta)\alpha_+(p\eta_N)\beta(\zeta)\zeta F(p\eta_N,\zeta)$$
$$-(b^2p^2-2\zeta^2)\beta_-(\zeta)\beta_+(p\eta_S)F(p\eta_S,\zeta),$$
$$U_2^1=-\alpha_-(\zeta)\alpha_+(p\eta_N)(b^2p^2-2\zeta^2)F(p\eta_N,\zeta)$$
$$+2\zeta\alpha\beta_-(\zeta)\beta_+(p\eta_S)F(p\eta_S,\zeta),$$

and

$$U_2^2=-2\alpha_-(\zeta)\alpha_+(p\eta_N)\zeta^2F(p\eta_N,\zeta)$$
$$-\zeta(b^2p^2-2\zeta^2)\beta_+(p\eta_S)F(p\eta_S,\zeta)/\beta_+(\zeta).$$

In the above,

$$F(p\eta,\zeta)=1/[2(b^2p^2-a^2p^2)(p\eta-\zeta)(cp-\zeta)(cp+p\eta)$$
$$\times S_-(\zeta)S_+(p\eta)],$$
$$S_\pm(\zeta)=\exp\left\{-\frac{1}{\pi}\right.$$
$$\left.\times\int_{ap}^{bp}\tan^{-1}\left[\frac{4\xi^2(\xi^2-a^2p^2)^{1/2}(b^2p^2-\xi^2)^{1/2}}{(b^2p^2-2\xi^2)^2}\right]\frac{d\xi}{\xi\pm\zeta}\right\}$$
$$\alpha(\zeta)=(a^2p^2-\zeta^2)^{1/2},\quad \alpha_+(\zeta)=(ap+\zeta)^{1/2},\quad \alpha_-(\zeta)=(ap-\zeta)^{1/2},$$
$$\beta(\zeta)=(b^2p^2-\zeta^2)^{1/2},$$
$$\beta_+(\zeta)=(bp+\zeta)^{1/2}\ \text{ and }\ \beta_-(\zeta)=(bp-\zeta)^{1/2},$$

and ζ is the variable of the two-sided Laplace transform. a, b, and c denote the slowness of the longitudinal, shear, and Rayleigh waves, respectively.

In the Laplace transform domain, since the piecewise continuous normal and tangential tractions on the crack surfaces can be superposed by a series of exponential loadings $e^{p\eta_N x_1}$ and $e^{p\eta_S x_1}$, the complete analytical solutions of the displacement and stress can be thus superposed from Eqs. (1) and (2), respectively.

The mode I and mode II stress intensity factors in the Laplace transform domain $\tilde{K}_{\mathrm{I}}(p)$ and $\tilde{K}_{\mathrm{II}}(p)$ are thus found as

$$\tilde{K}_{\mathrm{I}}(p)=-\sqrt{2}\,\frac{\alpha_+(p\eta_N)}{p(c+\eta_N)S_+(p\eta_N)},\tag{3}$$

and

$$\tilde{K}_{\mathrm{II}}(p)=-\sqrt{2}\,\frac{\beta_+(p\eta_S)}{p(c+\eta_S)S_+(p\eta_S)}.\tag{4}$$

To demonstrate the validity of the analytical solution, the normal traction $e^{p\eta_N x_1}(p=1+i,\eta_N=1)$ is applied on the crack surfaces. The stress $\tilde{\sigma}_{22}(-1,0,1+i)$ and the displacement $\tilde{u}_2(1,0,1+i)$ computed are found as $0.1986-0.3095i$, and 0. There are in good agreement with the normal traction e^{-1-i} $(=0.1988-0.3096i)$ at $(-1, 0)$ and the displacement $\tilde{u}_2(1,0,1+i)=0$ due to symmetry.

3 Laplace Finite Element Formulation

As a complicated elastodynamic fracture problem is first transformed into an equivalent static fracture problem by the Laplace transform technique, the finite element alternating procedure developed here is performed to obtain the solution of the equivalent static fracture problem using a successive, iterative superposition of sequences of solution. The sequences of solutions are constructed by some simpler uncracked and cracked problems. The former uncracked solutions in the Laplace domain can be computed by the Laplace finite element model as stated below. The latter cracked solutions can be determined by substituting the coordinates of the same finite geometric boundary as the equivalent static fracture problems into the analytical solutions (1) and (2). (The detailed procedures are referred to Chen and Chang [16].)

Consider a real-time two-dimensional isotropic uncracked plate with prescribed traction $\overline{t_i}(t)$ over the boundary S_σ and displacement $\overline{u_i}(t)$ over the boundary S_u. Neglecting the body force, the functional which governs the elastodynamic response of the plate can be described by the Hamilton's principle in finite element approximation as

$$\Pi(u_i(t))=\int_{t_1}^{t_2}\sum_m\left[\int_{A_m}\left(\frac{1}{2}E_{ijkl}\epsilon_{ij}(t)\epsilon_{kl}(t)-\frac{1}{2}\rho\dot{u}_i(t)\dot{u}_i(t)\right)dA\right.$$
$$\left.-\int_{S_{\sigma_m}}\overline{t_i}(t)u_i(t)dS\right]dt,\tag{5}$$

where A_m is the area of element m, S_{σ_m} is the boundary of element m where the traction $\overline{t_i}(t)$ is prescribed, and E_{ijkl} is the elastic tensor. $u_i(t)$ and $\dot{u}_i(t)$ denote the element interior displacement and velocity, respectively. $\epsilon_{ij}(t)=1/2(u_{i,j}(t)+u_{j,i}(t))$ is the strain tensor and ρ is the density of the isotropic material.

The element interior displacement $u_i(t)$, velocity $\dot{u}_i(t)$ and strain $\epsilon_{ij}(t)$ can be approximated in terms of element nodal displacement $q(t)$ and velocity $\dot{q}(t)$ as (in matrix form)

$$\{u_i\}=[N]\{q\},\tag{6}$$
$$\{\dot{u}_i\}=[N]\{\dot{q}\},\tag{7}$$

and

$$\{\epsilon_{ij}\}=[B]\{q\},\tag{8}$$

where the matrix $[B]$ is the spatial derivative of the interpolation function $[N]$. Substituting Eqs. (6)–(8) into Eq. (5), following the general finite element formulation procedures, the simultaneous ordinary differential equations are obtained as

$$[M^*]\{\ddot{q}^*(t)\}+[K^*]\{q^*(t)\}=\{F^*(t)\},\tag{9}$$

where

$$[M^*]=\sum_m\int_{A_m}\rho[N]^T[N]dA,$$
$$[K^*]=\sum_m\int_{A_m}[B]^T[E_{ijkl}][B]dA$$

and

$$[F^*(t)]=\sum_m\int_{S_{\sigma_m}}[N]^T\{\overline{t_i}(t)\}dS.$$

$\{q^*(t)\}$ and $\{\ddot{q}^*(t)\}$ represent the global nodal displacement and acceleration vectors.

To transform the simultaneous ordinary differential equations to a set of linear algebraic equations in Laplace domain, the one-sided Laplace transform $\tilde{f}(x_1,x_2,p)$ of a real-time response $f(x_1,x_2,t)$ is defined by

$$\tilde{f}(x_1,x_2,p)=\int_0^\infty f(x_1,x_2,t)e^{-pt}dt,\tag{10}$$

where p is the one-sided Laplace parameter, which is a complex as mentioned in the previous section.

After taking the one-sided Laplace transform on Eq. (9) under zero initial conditions $\{q^*(0)\}=\{\dot{q}^*(0)\}=\{0\}$, Eq. (9) becomes

$$[\mathbf{K}^*(p)]\{\tilde{q}^*(p)\}=\{\tilde{F}^*(p)\},\tag{11}$$

where

$$[\mathbf{K}^*(p)]=p^2[M^*]+[K^*]$$

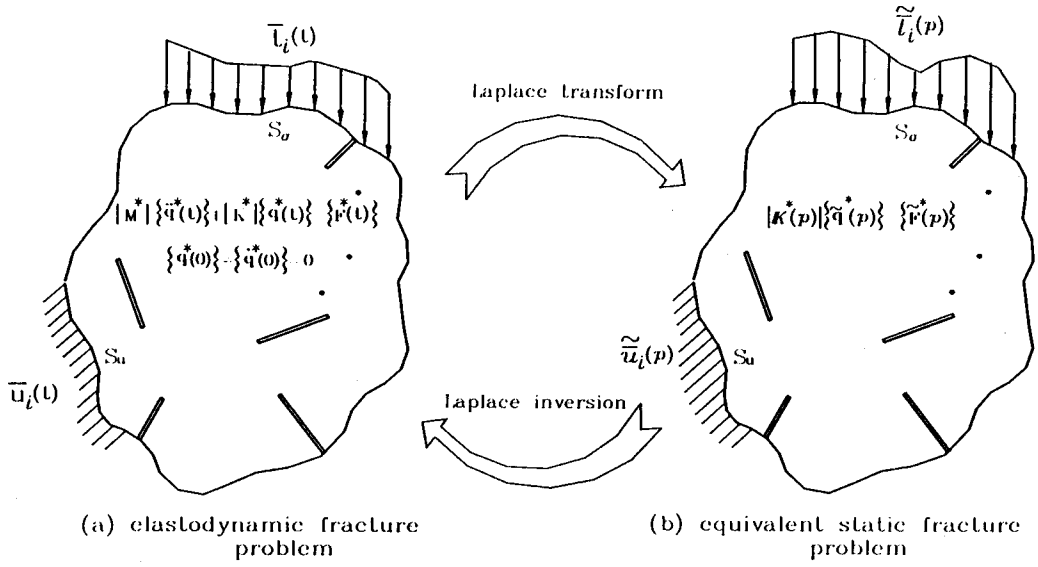

Fig. 2 Analysis of the elastodynamic fracture problem

and

$$[\tilde{F}^*(p)]=\sum_m \int_{S_{\sigma_m}} [N]^T\{\tilde{t}_i(p)\}dS.$$

By dividing the complex quantities of Eq. (11) into their real and imaginary parts, a set of linear algebraic equations are formed as

$$\begin{bmatrix}[\mathbf{K}_R^*(p)] & -[\mathbf{K}_I^*(p)]\\ [\mathbf{K}_I^*(p)] & [\mathbf{K}_R^*(p)]\end{bmatrix}\begin{Bmatrix}\{\tilde{q}_R^*(p)\}\\ \{\tilde{q}_I^*(p)\}\end{Bmatrix}=\begin{Bmatrix}\{\tilde{F}_R^*(p)\}\\ \{\tilde{F}_I^*(p)\}\end{Bmatrix} \quad (12)$$

where

$$[\mathbf{K}^*(p)]=[\mathbf{K}_R^*(p)]+i[\mathbf{K}_I^*(p)],$$

$$\{\tilde{q}^*(p)\}=\{\tilde{q}_R^*(p)\}+i\{\tilde{q}_I^*(p)\},$$

and

$$\{\tilde{F}^*(p)\}=\{\tilde{F}_R^*(p)\}+i\{\tilde{F}_I^*(p)\}.$$

The transformed displacement vectors $\{\tilde{q}_R^*(p)\}$ and $\{\tilde{q}_I^*(p)\}$ can be evaluated numerically by the Gauss-Jordan method for a sequence of selected Laplace parameters $p_k=v+w_k(k=1,2,\ldots,N)$. Finally, the numerical inversion scheme to inverse the Laplace domain solutions for all the selected Laplace parameters p to those of the real-time response at any specific instant can be carried out by Honig and Hirdes [22].

4 Laplace Finite Element Alternating Procedures

The Laplace finite element alternating method, which combines the merits of the Laplace transform technique, finite element alternating procedure, and the Laplace inversion algorithm, is established to analyze the elastodynamic fracture problems with multiple cracks and explained here. Consider a two-dimensional finite domain containing multiple cracks subjected to dynamic loadings as shown in Fig. 2(*a*). By the Laplace transform technique, the complicated elastodynamic fracture problem is first transformed into an equivalent static fracture problem in the Laplace transform domain as shown in Fig. 2(*b*). The finite element alternating method can be used to obtain the solution of the Laplace transform domain equivalent static fracture problem using a successive, iterative superposition of sequences of solutions. The sequences of solutions are constructed by some known simpler solutions of the problems with specific boundary conditions, which are computed by a conventional finite element procedure and/or available analytical solution. Finally, the real-time response can be achieved by using the numerical Laplace inversion algorithm ([22]). For completeness, several main steps are stated below:

1 For a selected instant t_I, an optimal parameter v_I can be chosen by the method of Honig and Hirdes [22] (see the Appendix) and a sequence of Laplace parameters $p_k=v_I+ik\pi/\tau(k=1,2,\ldots,N)$ are determined.

2 For each of the Laplace parameters $p_k(k=1,2,\ldots,N)$, the governing equation (Eq. (13)) and boundary conditions (see Fig. 2(*b*)) of the equivalent static fracture problem in the Laplace transform domain are obtained.

3 Based on the finite element alternating procedure as described in detail in Chen and Chang [16], the Laplace transform displacement, stress, and stress intensity factors for the selected Laplace parameter p_k are computed.

4 Once the Laplace transform domain solutions of all the Laplace parameters p_k are solved, the corresponding real-time response of the elastodynamic fracture problem at the selected instant t_I can then be obtained by Eq. (*A*4) as stated in the Appendix.

5 For the elastodynamic response of another instant, repeat steps (1) to (4).

6 Repeat steps (1) to (5) until the desired time history is performed.

It is worthwhile to mention that the choice of the sequence of the Laplace parameters p_k depends on the selected instant only. Hence, the real-time response of any instant can be solved directly without computing the response of other instants. For the same reason, the accuracy of the solutions obtained by the present technique is independent of the size of the time increment taken.

5 Results and Discussions

To evaluate the accuracy and versatility of the Laplace finite element alternating procedure developed, several elastodynamic fracture problems with multiple edge and central cracks under transient loadings are analyzed. The phenomena of the overshoots of the dynamic stress intensity factors and the interactions of the stress waves between cracks and boundaries are also considered.

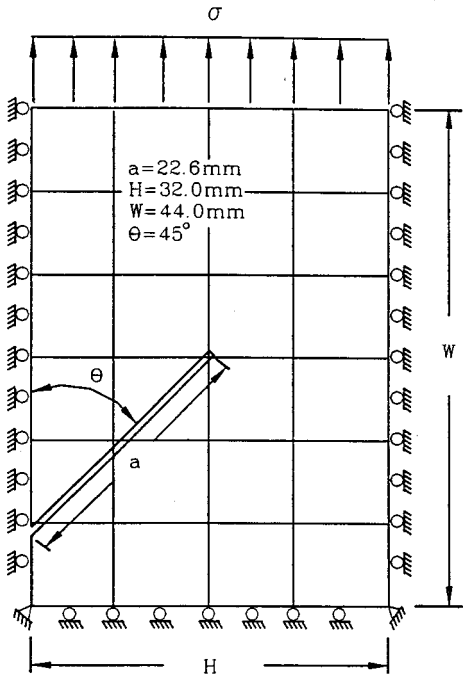

Fig. 3 A rectangular plate with an inclined edge crack under uniform Heaviside loading

Example 1: A Rectangular Plate With an Inclined Edge Crack. A finite plate with an inclined edge crack under uniform Heaviside tension $\sigma N/m^2$ is first analyzed as shown in Fig. 3. Twenty-four eight-node isoparametric quadratic finite elements are taken in the Laplace transform domain. Since the equivalent static fracture problem is solved in the Laplace transform domain, the constraints of the size and shape of elements for elastodynamic problem are not necessary. The problem was also studied by Dominguze and Gallego [15] by a boundary element method with time increment $\Delta t = 0.4\,\mu$s. The material properties are: shear modulus $\mu = 29.4$ GPa, Poisson's ratio $\nu = 0.286$, and density $\rho = 2.45\times 10^3$ Kg/m^3 and the longitudinal wave speed $c_p = 4.60\times 10^3$ m/s. Figure 4 shows the variations of the mode I and mode II dynamic stress intensity factors normalized by $\sigma\sqrt{\pi a}$. Two different calculations by the time increments of $\Delta t = 1\,\mu$s (20 time increments) and $\Delta t = 5\,\mu$s (four time increments) are made and both are in good agreement with the reference solution. It is noted that the dynamic stress intensity factors remain zero until the longitudinal wave arrives at the crack tip ($\sim$3.48 μs).

Example 2: A Rectangular Plate With Four Inclined Edge Cracks. To estimate the interation effect among cracks and the finite geometrical boundaries on the dynamic stress intensity factors, a plate containing four inclined edge cracks subjected to uniform time-dependent Heaviside loadings at the top and bottom surfaces is considered. The material properties are: the Young's modulus is 68.95 GPa, the Poisson's ratio is 0.333, the mass density is 2.76×10^3 Kg/m^3 and the longitudinal wave speed $c_p = 6.12\times 10^3$ m/s. Due to symmetry, only one half of the problem is solved as shown in Fig. 5. Forty-five Laplace eight-node isoparametric finite elements in a Laplace domain are used. The normalized dynamic stress intensity factors at crack tips *A* and *B* with changing distances $e/L = 0.2$, 0.4 and 0.6 are plotted in Figs. 6 and 7, respectively. It is noted that the *P*-wave from the loaded edge that impinges on the crack *A* generates a reflected wave and a scattering wave so that the stress wave on crack *B* becomes more complex. The times of arrival at crack tips *A* and *B* of the *P*-wave

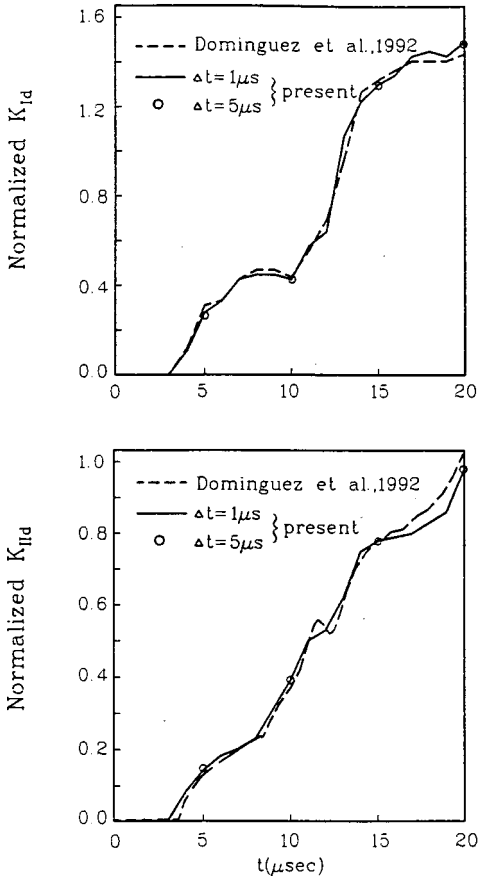

Fig. 4 The normalized dynamic stress intensity factors of the problem with an inclined edge crack

generated by the loaded edges are at different times, and the dynamic stress intensity factors of crack *B* are less than the values of crack *A* due to the resistance of the stress wave by the crack *A*. It also shows that the dynamic stress intensity factors of crack *A* increase due to increasing e/L. The dynamic stress intensity fac-

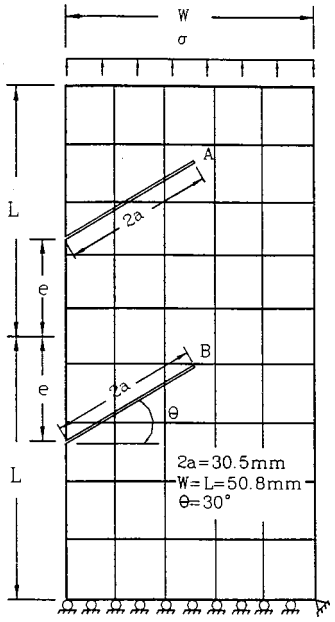

Fig. 5 A rectangular plate with four inclined edge cracks under a Heaviside loading

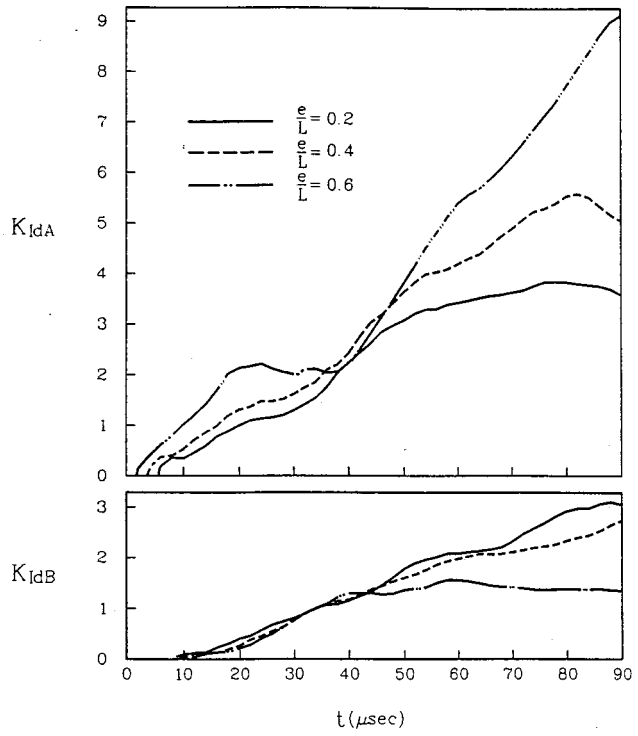

Fig. 6 The mode I dynamic stress intensity factors of the four inclined edge cracks for the cases of $e/L=0.2$, 0.4, and 0.6

tors of crack *A* are enhanced by the propagation and scattering of stress waves between boundaries of the plate and crack *A*.

Example 3: A Rectangular Plate With a Central Crack Subjected to Heaviside Loading. To demonstrate the applicability of the present technique to the analysis of the symmetrically distributed central cracks, a rectangular plate with a central crack subjected to Heaviside loadings at the top and bottom boundaries of the plate as shown in Fig. 8 is analyzed. Due to symmetry, only one quarter of the problem is solved. Hence, the problems with symmetric central cracks can be treated as the problems with edge cracks. Twenty-four Laplace eight-node isoparametric quadratic elements are used. The material properties are as follows: the shear modulus $\mu=76.9$ GPa, the Poisson's ratio $v=0.3$, and the density $\rho=5.\times10^3$ Kg/m^3. In Fig. 9, the normalized dynamic stress intensity factors for different crack lengths $a/W=0.25$, 0.5, and 0.75 are plotted, and good agreement is found for the case of $a/W=0.25$ with available results obtained by Li [24] using the Gurtin variational Principle. In Fig. 9, the symbol P_1 denotes the time required for the incident *P*-wave from the loaded edges to the crack tip, which can be computed as $L/c_p=2.73$ μs. The P_1 value of the present computed response is 2.60~2.65 μs as compared with 2.30 μs obtained by Li [24]. R_1 is the time required for the first Rayleigh wave to arrive at the crack tip considered. ($P_1^s-P_1$) and ($S_1^s-P_1$) mean the times of the scattered *P*-wave and *S*-wave to travel from the crack tip to the nearest boundary and back. P_2 is the time for the incident *P*-wave reflected from the opposite boundary surface, and return back to the crack. R_2, P_2^s, and S_2^s caused by the secondary excited wave are introduced in a manner analogous to R_1, P_1^s, and S_1^s, respectively. The dynamic stress intensity factors of the three cases remain zero until the *P*-wave has arrived (P_1) from the loaded edges. Although the peak values of the dynamic stress intensity factors of the three cases take place at different times and possess different values, the character is the same. That is, the dynamic stress intensity factors reach a peak value higher than the corresponding static value and the peak value which happenes during the first and second Rayleigh wave arriving the crack tip. The corresponding static stress intensity factors are 1.05, 1.20, and 1.62 for the cases of $a/W=0.25$, 0.5, and 0.75, respectively. From the one-step solution obtained, it is concluded that the size of the time increments taken

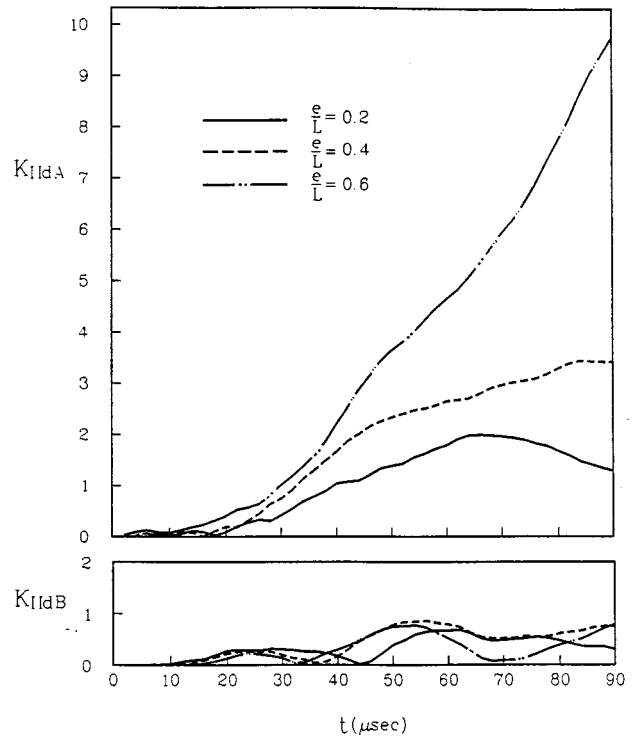

Fig. 7 The mode II dynamic stress intensity factors of the four inclined edge cracks for the cases of $e/L=0.2$, 0.4, and 0.6

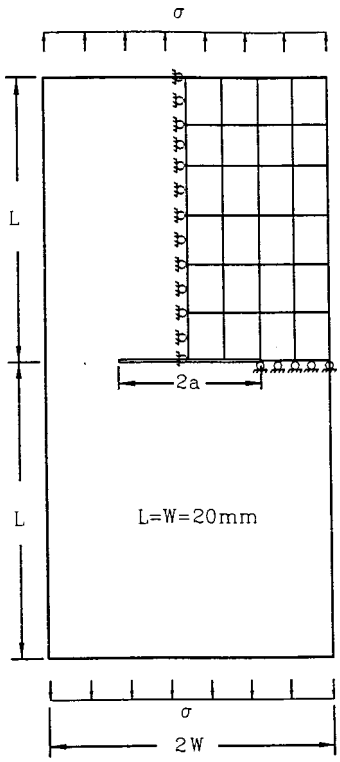

Fig. 8 The Laplace finite element mesh of the finite plate with a central crack

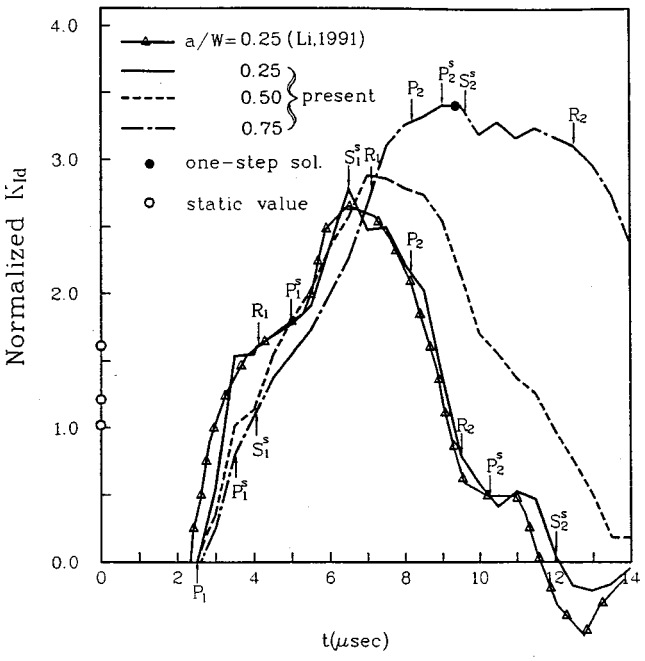

Fig. 9 The normalized dynamic stress intensity factors of the finite plate with a central crack for the cases of $a/W=0.25$, 0.50, and 0.75

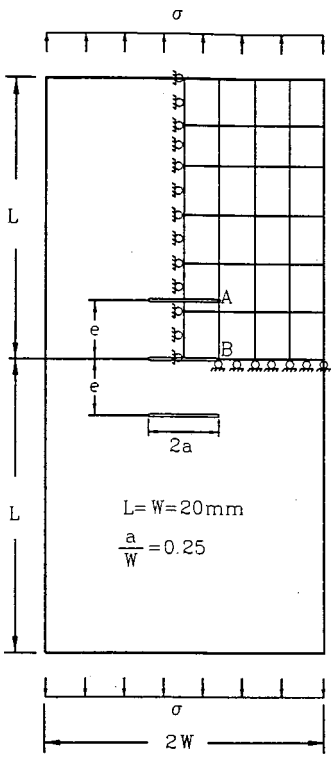

Fig. 10 The Laplace finite element mesh of a finite plate with parallel triple cracks

in the present technique can be arbitrary. It is mentioned that, as seen in Fig. 9, some negative dynamic stress intensity factors are observed due to the lack of accounting for the dynamic contact on the crack surfaces. However, to the principal authors' experience ([13]), as far as the peak dynamic stress intensity factors are concerned, the mathematical crack surface interpenetration can be ignored.

Example 4: A Rectangular Plate With Parallel Triple Central Cracks. In order to estimate the wave propagation among cracks, a finite plate with parallel triple cracks subjected to Heaviside loadings on the opposite sides of the plate as shown in Fig. 10 is analyzed. Twenty-four Laplace eight-node isoparametric quadratic elements are used. The normalized dynamic stress intensity factors of the crack tip A for different distances $e/L=0.1$, 0.2, and 0.5 and $a/W=0.25$ are plotted in Fig. 11. The symbols t_1, t_2, and t_3 on the time axis denote the different times for the incident P-wave arriving at the crack tip A from the loaded edges for the cases $e/L=0.5$, 0.2, and 0.1, respectively. It is worth noting that the crack tip A exists a mode II dynamic stress intensity factor due to the scattered P-wave traveling from the crack tip B, and the values are enhanced when the upper crack gets closer. t_4, t_5, and t_6 denote the time of arrival at the crack tip A of the scattered P-wave from the crack tip B of the cases $e/L=0.1$, 0.2, and 0.5, respectively. In Fig. 12, the peak value of the normalized mode I dynamic stress intensity factors of the crack tip B increase due to the increasing distance e. As the distance e is large enough, the peak value of the normalized dynamic stress intensity factors of B converges to the value of a single crack as shown in Fig. 9 (for the case of $a/W=0.25$). It is noted that the upper crack can be considered as a barrier to reduce the dynamic stress intensity factors of the middle crack. The CPU time for computing a single time instant by 586 PC (Pentium 200) is about 48.4 seconds.

Example 5: A Rectangular Plate With Different Distributions of Triple Cracks. Based on the previous example, obviously there exists an unexpected fracture mode due to the interaction of cracks. To further estimate the influence of different distributions of cracks on the dynamic stress intensity factors, the problems with different distributions of triple cracks subjected to Heaviside loadings are analyzed. They include H-type (case (*a*)) and collinear (case (*b*)) permutations of cracks. However, as seen in Fig. 13, the same Laplace eight-node isoparametric finite element mesh is used. The normalized mode I dynamic stress intensity factors of the crack tip A for different permutations of cracks

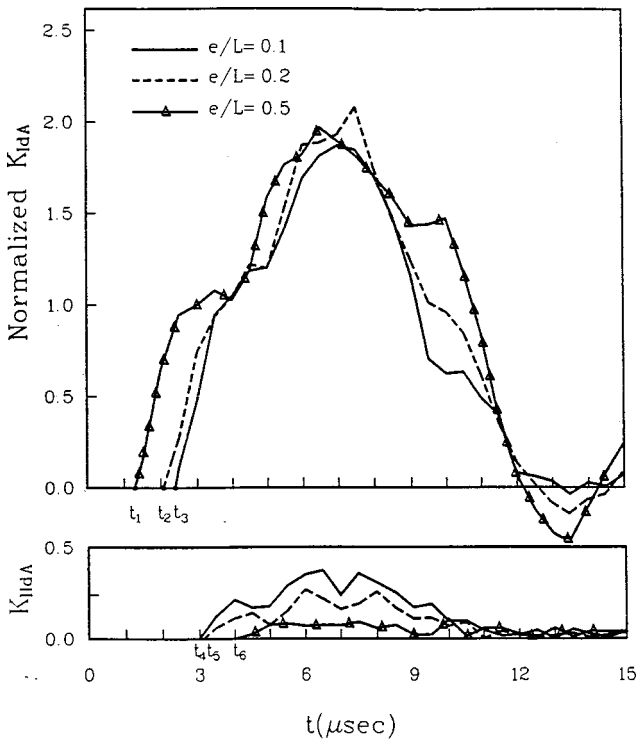

Fig. 11 The normalized dynamic stress intensity factors of crack tip *A* of the finite plate with parallel triple cracks

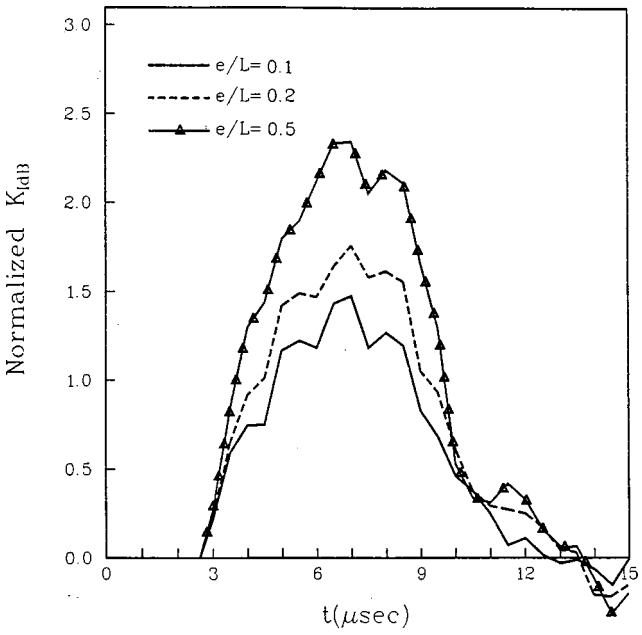

Fig. 12 The normalized dynamic stress intensity factors of crack tip *B* of the finite plate with parallel triple cracks

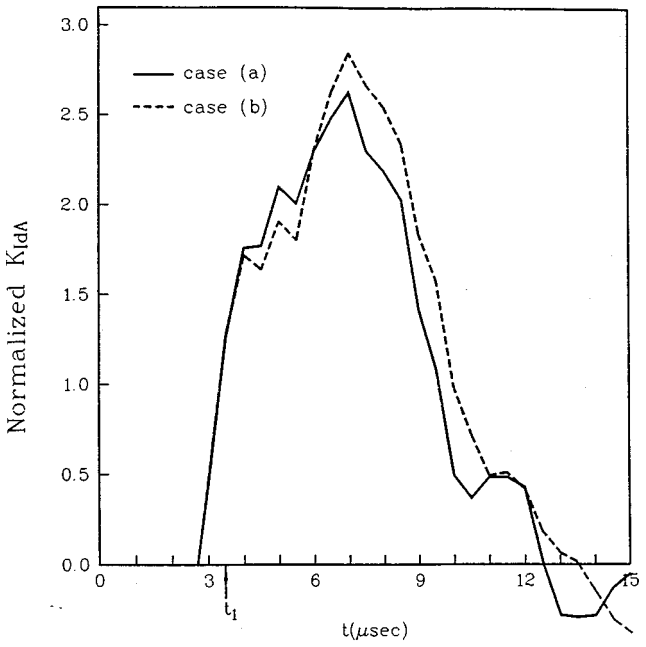

Fig. 14 The normalized dynamic stress intensity factors of the crack tip *A* for different permutation cracks

are compared in Fig. 14. The normalized mode I dynamic stress intensity factors of the crack 1 for the case (*a*) are consistent with those of the case (*b*) until the time (t_1) of arrival at the crack tip *A* of the reflected *P*-wave from crack 2. The peak value of the crack tip *A* for the case (*a*) is lower than that of the case (*b*) because the crack 2 resists the reflected waves from the right boundary. There are two unexpected fracture modes on the crack 2 due to the scattered wave which arrived from the crack 1. The normalized dynamic stress intensity factors of the crack 2 as well as crack 3 are plotted in Fig. 15. The symbols t_2 and t_3 on the time axis denote the time of the incident *P*-wave to arrive at crack tip *C* (case (*b*)) and that of the scattered *P*-wave from the crack tip *A* to the crack tip *B* (case (*a*)), respectively. It is found that the peak value of the normalized dynamic stress intensity factors is dependent on the plate configuration as well as crack permutation.

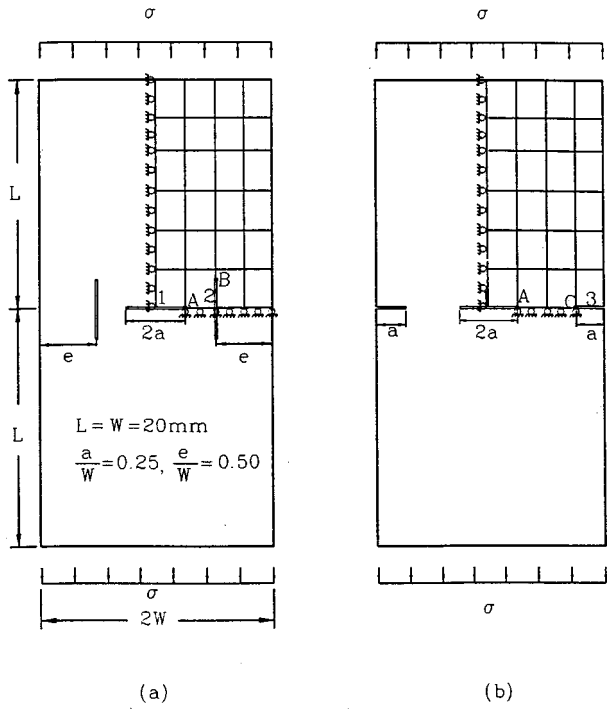

Fig. 13 The Laplace finite element mesh of the finite plate with different permutation triple cracks

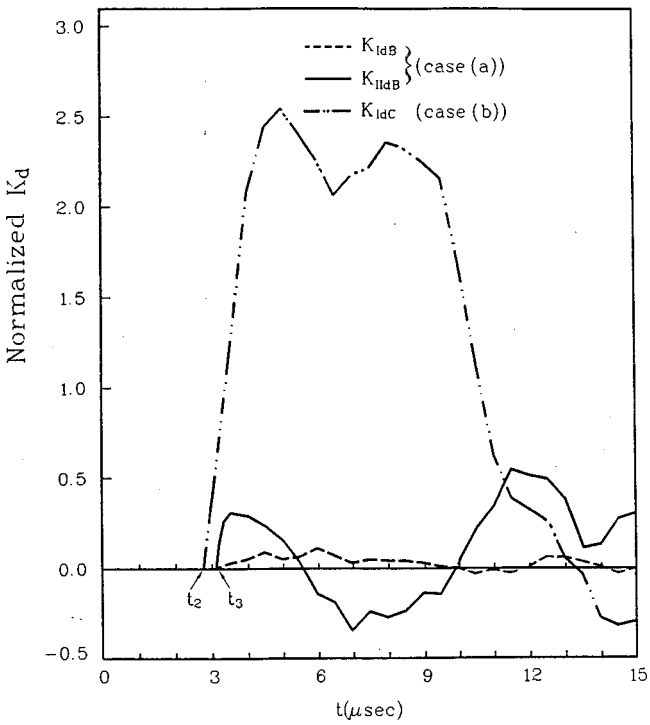

Fig. 15 The normalized dynamic stress intensity factors of the crack tip *B* and *C* for different permutation cracks

6 Conclusions and Recommendations

Based on the present Laplace finite element alternating procedures established, the calculation of the dynamic stress intensity factors in a finite plate with arbitrary number/distribution of edge cracks or symmetrically distributed central cracks has been successfully performed with a limited number of regular elements. The solution is independent of the size of the time increment taken and one can even determine the dynamic stress intensity factors at any instant by a single time-step instead of step-by-step computations. The influences of the scattering waves on the dynamic stress intensity factors for several representative examples are studied in detail.

According to results obtained, it is found that the dynamic stress intensity factors computed exhibit the similar characteristics. They remain zero until the time of arrival at the crack tip of the incident wave, and reach the peak values higher than the corresponding static values, then fluctuate about the static values with a decreasing amplitude. In addition to the length, number, and distribution of cracks, the peak values of the dynamic stress intensity factors are also dependent on the finite geometric boundaries significantly. They may exist an unexpected fracture mode due to the complicated wave propagation.

To widen the applicability of the technique, once an analytical solution for an infinite plate with a central crack subjected to arbitrarily distributed loading on the crack surfaces in the Laplace domain is achieved, an extension to arbitrarily distributed central cracks would be recommended. Moreover, this technique can be extended to the possible application to the NDT technique to predict the presence, length, position, and orientation of cracks by studying the wave patterns in cracked bodies.

Acknowledgment

The authors are grateful to the National Science Council of the Republic of China for financial support through grants NSC 85-2212-E-007-041 and NSC 89-2212-E-007-023.

Appendix

Numerical Laplace Inversion Algorithm. In many engineering applications, the Laplace transform domain responses are too difficult to be inverted analytically. There are many numerical Laplace inversion algorithms which have been developed. An accurate and efficient method proposed by Honig and Hirdes [22], which is based on the Fourier series expansion developed by Durbine [25], can efficiently compute the result at a selected instant by the optimal value of the parameter v, say, the real part of the Laplace parameters $p_k = v + iw_k (k = 1,2,\ldots,N)$.

The Laplace inversion formula for a function $f(t)$ whose transform is $\tilde{f}(p)$ can be established by both finite Fourier cosine and sine transforms as follows:

$$f(t) = \frac{e^{vt}}{\tau}\left\{ -\frac{1}{2}\mathrm{Re}\{\tilde{f}(v)\} + \sum_{k=0}^{N} [\mathrm{Re}\{\tilde{f}(p_k)\}\cos w_k t - \mathrm{Im}\{\tilde{f}(p_k)\}\sin w_k t]\right\} - F_d(v,t,\tau) + F_t(N,v,t,\tau) \quad \text{for } 0 < t < 2\tau \tag{A1}$$

where τ is the half period of $f(t)$ and $w_k = k\pi/\tau$. The discretization error $F_d(v,t,\tau)$ and truncation error $F_t(N,v,t,\tau)$ are given as

$$F_d(v,t,\tau) = \sum_{k=1}^{\infty} e^{-2kv\tau} f(2k\tau + t) \tag{A2}$$

and

$$F_t(N,v,t,\tau) = \frac{e^{vt}}{\tau}\left[\sum_{k=N+1}^{\infty} \{\mathrm{Re}\{\tilde{f}(p_k)\}\cos w_k t - \mathrm{Im}\{\tilde{f}(p_k)\}\sin w_k t\}\right]. \tag{A3}$$

Hence, the approximate value $f_N(t)$ becomes

$$f_N(t) = \frac{e^{vt}}{\tau}\left[-\frac{1}{2}\mathrm{Re}\{\tilde{f}(v)\} + \sum_{k=0}^{N} [\mathrm{Re}\{\tilde{f}(p_k)\}\cos w_k t - \mathrm{Im}\{\tilde{f}(p_k)\}\sin w_k t]\right]. \tag{A4}$$

The discretization error $F_d(v,t,\tau)$ as shown in Eq. (*A*2) can be made arbitrarily small if the product $v\tau$ is sufficiently large. However, the truncation error $F_t(N,v,t,\tau)$ as seen in Eq. (*A*3) may be divergent for a large $v\tau$. An appropriate choice of parameter N and $v\tau$ is very important not only for the accuracy but also for the convergent rate of an inverted solution. The Honing method allows a reduction of the discretization error without enlarging the truncation error by an optimal choice of the parameter v. There are two methods proposed to determine the optimal v for a fixed N and τ. The method *A* is to make the absolute values of discretization error $F_d(v,t,\tau)$ and truncation error $F_t(N,v,t,\tau)$ equal. The method *B* is to make the sum of the absolute values of discretization and truncation error minimal. Further, according to the numerical experiments of this work, sufficient accuracy can be achieved at any time instant as $N = 60 \sim 100$ for an optimal choice of the parameter v.

References

[1] Sih, G. C., 1968, ''Some Elastodynamic Problems of Crack,'' Int. J. Fract. Mech., **4**, pp. 51–68.

[2] Sih, G. C., and Loeber, J. F., 1969, ''Wave Propagation in an Elastic Solid With a Line of Discontinuity or Finite Crack,'' Q. J. Mech. Appl. Math., **27**, pp. 193–213.

[3] Mal, A. K., 1970, ''Interaction of Elastic Waves With a Griffith Crack,'' Int. J. Eng. Sci., **8**, pp. 763–776.

[4] Thau, S. A., and Lu, T. H., 1970, ''Diffraction of Transient Horizontal Shear Waves by a Finite Crack and a Finite Rigid Ribbon,'' Int. J. Eng. Sci., **8**, pp. 857–874.

[5] Thau, S. A., and Lu, T. H., 1971, ''Transient Stress Intensity Factors for a Finite Crack in an Elastic Solid Caused by a Dilatational Wave,'' Int. J. Solids Struct., **7**, pp. 731–750.

[6] Noble, B., 1958, *The Wiener-Hopf Technique*, Vol. 17, Pergamon Press, New York, pp. 247–268.

[7] Freund, L. B., 1974, ''The Stress Intensity Factor due to Normal Impact Loading of the Faces of a Crack,'' Int. J. Eng. Sci., **12**, pp. 179–189.

[8] Brock, L. M., 1985, ''The Dynamic 2D Analysis of a Concentrated Force Near a Semi-Infinite Crack,'' Q. Appl. Math., **43**, pp. 201–210.

[9] Tsai, C. H., and Ma, C. C., 1992, ''Transient Analysis of a Semi-Infinite Crack Subjected to Dynamic Concentrated Forces,'' ASME J. Appl. Mech., **59**, pp. 804–811.

[10] Chen, Y. M., 1975, ''Numerical Computation of Dynamic Stress Intensity Factors by a Lagrangian Finite-Difference Method (the HEMP Code),'' Eng. Fract. Mech., **7**, pp. 653–660.

[11] Kelley, J. W., and Sun, C. T., 1979, ''A Singular Finite Element for Computing Time Dependent Stress Intensity Factors,'' Eng. Fract. Mech., **12**, pp. 13–22.

[12] Kishimoto, K., Aoki, S., and Sakata, M., 1980, ''Dynamic Stress Intensity Factors Using J-Integral and Finite Element Method,'' Eng. Fract. Mech., **13**, pp. 387–394.

[13] Chen, W. H., and Wu, C. W., 1981, ''On Elastodynamic Fracture Mechanics Analysis of Bi-material Structures Using Finite Element Method,'' Eng. Fract. Mech., **15**, pp. 155–168.

[14] Murti, V., and Valliappan, S., 1986, ''The Use of Quarter Point Element in Dynamic Crack Analysis,'' Eng. Fract. Mech., **23**, pp. 585–614.

[15] Dominguez, J., and Gallego, R., 1992, ''Time Domain Boundary Element Method for Dynamic Stress Intensity Factor Computations,'' Int. J. Numer. Methods Eng., **33**, pp. 635–649.

[16] Chen, W. H., and Chang, C. L., 1994, ''Heat Conduction Analysis of a Finite Plate With Multiple Insulated Cracks by Finite Element Alternating Method,'' Int. J. Solids Struct., **31**, pp. 1343–1355.

[17] Chen, W. H., and Chang, C. S., 1989, ''Analysis of Two-Dimensional Mixed Mode Crack Problems by Finite Element Alternating Method,'' Comput. Struct., **33**, pp. 1451–1458.

[18] Nishioka, T., and Atluri, S. N., 1983, ''Analytical Solution for Embedded

Elliptical Cracks, and Finite Element Alternating Method for Elliptical Surface Crack Subjected to Arbitrary Loading,'' Comput. Struct., **17**, pp. 247–268.
[19] O'donoghue, P. E., Nishioka, T., and Atluri, S. N., 1984, ''Multiple Surface Cracks in Pressure Vessels,'' Eng. Fract. Mech., **20**, pp. 545–560.
[20] Simon, H. L., O'donoghue, P. F., and Atluri, S. N., 1987, ''A Finite Element Alternating Technique for Evaluating Mixed Mode Stress Intensity Factors for Part-Elliptical Surface Flaw,'' Int. J. Numer. Methods Eng., **24**, pp. 689–709.
[21] Chen, W. H., and Shen, C. M., 1993, ''A Finite Element Alternating Approach for the Thin Plate in Bending Containing Mixed Mode Cracks,'' Int. J. Solids Struct., **30**, pp. 2261–2276.
[22] Honig, G., and Hirdes, U., 1984, ''A Method for the Numerical Inversion of Laplace Transforms,'' J. Comput. Appl. Math., **10**, pp. 113–132.
[23] De Hoop, A. T., 1958, ''Representation Theorem for the Displacement in an Elastic Solid and Their Application to Elastodynamic Diffraction Theory,'' Doctoral Dissertation, Technische Hoegschool, Delft.
[24] Li, Yuechuan, 1991, ''The Application of the Gurtin Variational Principle in the Computation of Dynamic Stress Intensity Factors,'' Eng. Fract. Mech., **39**, pp. 469–476.
[25] Durbine, F., 1973, ''Numerical Inversion of the Laplace Transforms: An Effective Improvement of Durbner and Abate's Method,'' Comput. J., **17**, pp. 371–376.

Journal of Applied Mechanics

Brief Notes

A Brief Note is a short paper that presents a specific solution of technical interest in mechanics but which does not necessarily contain new general methods or results. A Brief Note should not exceed 1500 words *or equivalent* (a typical one-column figure or table is equivalent to 250 words; a one line equation to 30 words). Brief Notes will be subject to the usual review procedures prior to publication. After approval such Notes will be published as soon as possible. The Notes should be submitted to the Technical Editor of the JOURNAL OF APPLIED MECHANICS. Discussions on the Brief Notes should be addressed to the Editorial Department, ASME, United Engineering Center, Three Park Avenue, New York, NY 10016-5990, or to the Technical Editor of the JOURNAL OF APPLIED MECHANICS. Discussions on Brief Notes appearing in this issue will be accepted until two months after publication. Readers who need more time to prepare a Discussion should request an extension of the deadline from the Editorial Department.

The Top With a Blunted Vertex Slipping With Light Friction at a High Rate of Spin

P. C. Paris, L. Zhang, and H. Tada
School of Engineering and Applied Science, Washington University, St. Louis, MO 63130-4899

The problem of determining the motion of a top is a classic example of a complex analysis in analytical dynamics. Adding a blunt tip to the top and setting it spinning on a surface with sliding friction might be thought to render it intractable for simple analysis. However, if it is set in motion with a high rate of spin it is possible to find a simple approximate solution for the case of approximate steady precession. For this pseudo-steady motion it will be noted that the rate of diminution of the nutation will also be almost constant. Further, the ratio of these rates (latter over former) will be equal to the negative of the coefficient of friction for the top slipping on the surface. As a consequence the mass center of the top will tend to proceed around a steady circle above the plane. These results will first be observed by writing the full Lagrange's equations for the problem and reducing them prior to integration by observing appropriate approximations by deleting relatively smaller terms. The above results will then follow directly. Further, the full Lagrange's equations will be numerically integrated to show that the analytically developed approximate results are appropriate. Once these results are known, it is observed that a subsequent intuitive analysis based on time rate of change of angular momentum leads to the same results, if only the angular momentum about the spin axis is considered with other relevant assumptions. [S0021-8936(00)00203-8]

The motion of a top with a slightly blunted vertex in contact with a horizontal surface with continuous frictional slipping due to a high rate of axial rotation, compared to precession and nutation rates, is a tractable problem. There are few examples where frictional slipping allows a direct solution for the main behavior with the use of Lagrange's equations. This example is offered here to encourage attempts of analysis of such problems, which might look implausible at first glance, but which yield a solution upon careful consideration. Such a top is shown in Fig. 1, with a truncated vertex of radius, a. The top is assumed to be axially symmetric with axial and transverse centroidal moments of inertia, I_A and I_T, respectively. The stem length, l, of the top from the centroid to the truncated vertex is assumed to be large compared to the vertex radius, a. It is further assumed that the top is spinning rapidly enough that the friction force, F, will be perpendicular to the axis of the top. The position of the point directly below the mass center is denoted, Y, Z, and the contact point is a distance, d, away. This distance and the height, h, of the mass center above the plane of contact are

$$d = l\sin\theta - a\cos\theta$$
$$h = l\cos\theta + a\sin\theta. \tag{1}$$

Taking the differential of the latter expression gives

$$\delta h = -l(\sin\theta)\,\delta\theta + a(\cos\theta)\,\delta\theta \quad \text{or} \quad \dot{h} = -l\dot{\theta}\sin\theta + a\dot{\theta}\cos\theta.$$

The other two perpendicular components of velocity of the mass center are $\dot{Y}$ and $\dot{Z}$. The angular velocity components of the body may be expressed as (with the y-axis remaining horizontal)

$$\omega_x = \dot{\psi} + \dot{\phi}\cos\theta$$
$$\omega_y = \dot{\theta} \tag{2}$$
$$\omega_z = \dot{\phi}\sin\theta.$$

The kinetic energy may then be written in the form

$$T = \frac{1}{2}m[(-l\sin\theta + a\cos\theta)^2\dot{\theta}^2 + \dot{Y}^2 + \dot{Z}^2]$$
$$+ \frac{I_A}{2}(\dot{\psi} + \dot{\phi}\cos\theta)^2 + \frac{I_T}{2}(\dot{\theta}^2 + \dot{\phi}^2\sin^2\theta). \tag{3}$$

The generalized forces, from the work rates of independent instantaneous variations of each coordinate, are found to be

$$Q_\theta = \frac{-mg\,\delta h}{\delta\theta} = +mg(l\sin\theta - a\cos\theta)$$
$$Q_\phi = \frac{Fd\,\delta\phi}{\delta\phi} = \mu mg(l\sin\theta - a\cos\theta)$$
$$Q_\psi = \frac{-Fa\,\delta\psi}{\delta\psi} = -\mu mga \tag{4}$$

Contributed by the Applied Mechanics Division of THE AMERICAN SOCIETY OF MECHANICAL ENGINEERS for publication in the ASME JOURNAL OF APPLIED MECHANICS. Manuscript received by the ASME Applied Mechanics Division, Aug. 17, 1999; final revision, Dec. 5, 1999. Associate Technical Editor: N. C. Perkins.

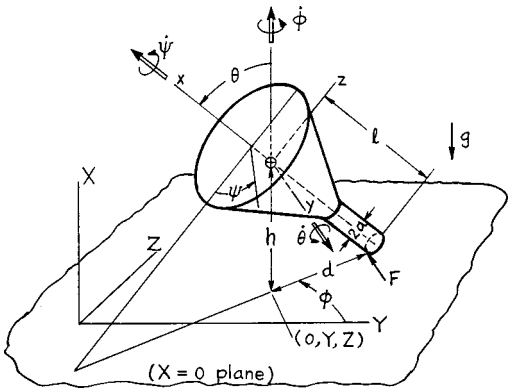

Fig. 1

$$Q_Y = \frac{F_Y \delta Y}{\delta Y} = -\mu mg \sin\phi$$

$$Q_Z = \frac{F_Z \delta Z}{\delta Z} = \mu mg \cos\phi$$

assuming the vertical acceleration is very small and μ is the friction coefficient. From these forms, Eqs. (3) and (4), the ingredients for the basic form of the Lagrange's equations are available and may be employed. Recall that this form of Lagrange's equations is ([1])

$$\frac{d}{dt}\left(\frac{\partial T}{\partial \dot{q}_r}\right) - \frac{\partial T}{\partial q_r} = Q_r \quad \text{for} \quad (q_r = \theta, \phi, \psi, Y, Z). \tag{5}$$

The five resulting Lagrange's equations follow:

$$\frac{d}{dt}[I_T\dot{\theta} + m(-l\sin\theta + a\cos\theta)^2\dot{\theta}] + I_A(\dot{\psi} + \dot{\phi}\cos\theta)\dot{\phi}\sin\theta$$

$$-I_T\dot{\phi}^2\sin\theta\cos\theta + m(-l\sin\theta + a\cos\theta)$$

$$\times(l\cos\theta + a\sin\theta)\dot{\theta}^2 = mg(l\sin\theta - a\cos\theta) \tag{6a}$$

$$\frac{d}{dt}[I_A(\dot{\psi} + \dot{\phi}\cos\theta)\cos\theta + I_T\dot{\phi}\sin^2\theta] = \mu mg(l\sin\theta - a\cos\theta) \tag{6b}$$

$$\frac{d}{dt}[I_A(\dot{\psi} + \dot{\phi}\cos\theta)] = -\mu mga \tag{6c}$$

$$\frac{d}{dt}[m\dot{Y}] = -\mu mg\sin\phi \tag{6d}$$

$$\frac{d}{dt}[m\dot{Z}] = \mu mg\cos\phi. \tag{6e}$$

Now these equations of motion appear to be quite formidable, and not at all attractive for solution. However, it is observed from the motion of tops that if a high spin rate, $\dot{\psi} \cong \Omega_o$, is induced initially, then by comparison the precession and nutation rates, $\dot{\phi}$ and $\dot{\theta}$, will be relatively small. That is

$$\dot{\psi} \cong \Omega_o >> \dot{\phi}, \dot{\theta}.$$

In addition it is noted that

$$l >> a.$$

Armed with these relative sizes, Eqs. (6) may be reconsidered. Notice that the first three equations of motion 6(*a*), 6(*b*), and 6(*c*) do not involve *Y* or *Z* and stand separately for the solution for

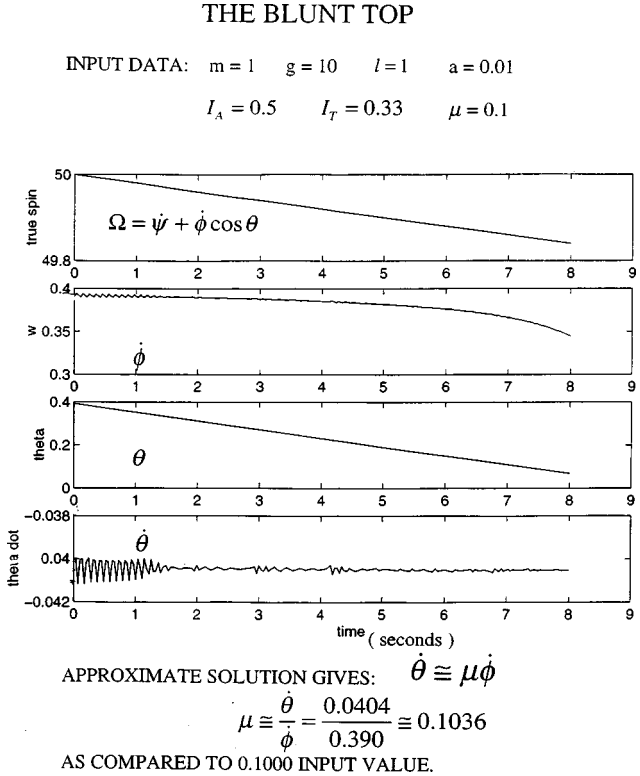

Fig. 2

θ, ϕ, ψ as functions of time. Once that is done 6(*d*) and 6(*e*) are easy to attack. Consider first the second equation, 6(*b*), in light of the above inequalities, and it becomes

$$\frac{d}{dt}[I_A\Omega_o\cos\theta] \cong \mu mgl\sin\theta.$$

Differentiating as indicated and canceling sin θ gives

$$I_A\Omega_0\dot{\theta} = -\mu mgl. \tag{7}$$

Integrating this expression gives

$$\theta = \theta_o - \frac{\mu mgl}{I_A\Omega_o}t. \tag{8}$$

Equation (8) shows that, starting from its initial value θ_o, θ will diminish approximately linearly with time until the top is standing straight up. The predicted time for this behavior from Eq. (8) is

$$t_F = \frac{I_a\Omega_o\theta_o}{\mu mgl}. \tag{9}$$

Substituting this approximately constant value of $\dot{\theta}$ from Eq. (7) into the first full equation of motion, (1), and also neglecting terms which are relatively small according to the above inequalities leads to

$$\dot{\phi} \cong \frac{mgl}{I_A\Omega_o}. \tag{10}$$

As observed from Eqs. (7) and (10), the precession and nutation rates obey the simple relation:

$$\dot{\theta} \cong -\mu\dot{\phi}. \tag{11}$$

It is further noticed that the radius of the blunt vertex is not found in these relationships. This fact implies that an arbitrarily rounded vertex will have the same effects as long as the coefficient of

friction, μ, remains relatively constant and slip continues to occur as the motion progresses. Indeed tops generally exhibit this behavior pattern for high rates of spin! Further putting these results into the last two equations of motion, (4) and (5), implies that the vertical projection of the mass center on the Y-Z plane will describe a circle.

Numerical Verification of Results

The full Lagrange's equations, (6), were programmed into Matlab without consideration of the inequalities following Eqs. (6). Numerical evaluation of the coordinates as functions of time for a typically proportioned top were then performed, where initial conditions for $\dot{\theta}$ and $\dot{\phi}$ were chosen as proportionally related by μ in the approximate results (Eq. (8)). Figure 2 shows that the behavior with time is closely predicted by the approximate solution (Eqs. (7)–(11)). These results strongly support the concept that approximate solutions may be developed from rather difficult looking Lagrange's equations (in this case five nonlinear coupled second-order differential equations) to give simple and relevant results for certain physical systems.

Physical Intuitive Method of Analysis

Once the approximate solution is known or observed, it suggests that perhaps a simpler solution may be gained by methods less complex than the full Lagrangian method. Indeed, rephrasing the problem in terms of time rates of changes of momenta ([2]), is a possible approach. In order to do that in a reasonably simple way, it is first important to observe that the angular momentum about the spin axis (x-axis) is assumed to be very large compared to those about the other principal axes of the body. Neglecting those smaller angular momenta leads to

$$[\mathbf{H}] \cong H_x = I_A(\dot{\psi} + \dot{\phi}\cos\theta) \cong I_A\Omega. \tag{12}$$

Equating the applied moments about each of the axes to the time rates of change of this approximate angular momentum, Eq. (12), due to the angular rates, $\dot{\theta}$, $\dot{\phi}$, and $\dot{\Omega}$, leads to

$$\begin{aligned} M_z &= \dot{H}_z \cong -I_A\Omega\dot{\theta} \cong \mu mgl \\ M_y &= \dot{H}_y \cong I_A\,\Omega\sin\theta\dot{\phi} \cong mgl\sin\theta \\ M_x &= \dot{H}_x \cong I_A\dot{\Omega} = -\mu mga. \end{aligned} \tag{13}$$

Note that in the far right-hand terms of Eqs. (13) additional terms of the order of a as compared to l have also been neglected. Now it is seen that these results lead directly to Eqs. (7)–(11) without having to write and reduce the original Lagrange's equations. However, it is doubted that one would find or have confidence in the correctness of this more intuitive method without already having known that a simple solution is possible as demonstrated by the Lagrangian method.

Acknowledgment

John L. Berneron first suggested this problem to the authors.

References

[1] Whittaker, E. T., 1937, *A Treatise on the Analytical Dynamics of Particles and Rigid Bodies*, 4th Ed., Cambridge University Press, Cambridge, UK.

[2] Bwer, F. P., and Johnston, E. R., 1977, *Vector Mechanics for Engineers*, 6th Ed., McGraw-Hill, New York, Chapter 18.

Nonsingular Boundary Integral Equations for Two-Dimensional Anisotropic Elasticity

K.-C. Wu

Professor, Institute of Applied Mechanics, National Taiwan University, Taipei, Taiwan, R.O.C.

Nonsingular boundary integral equations for two-dimensional anisotropic elasticity problems are developed. The integral equations can be solved numerically by Gaussian quadratures. A numerical example is given to illustrate the effectiveness of the integral equations. [S0021-8936(00)00303-2]

1 Introduction

The currently popular boundary element method is based on displacement boundary integral equations in linear elastic solid mechanics. The strain field is computed by differentiating the displacements analytically and the stresses are obtained from the strains through Hooke's law. This method works well in the interior of the body, but at the boundary it gives rise to hypersingular integrals which cannot be evaluated accurately without special treatment. For two-dimensional problems, Wu et al. [1] proposed a new formulation of boundary integral equations using Stroh's formalism for anisotropic elasticity ([2]). The new formulation is expressed in terms of the tractions and displacement gradients, which can be used to calculate the boundary stresses or strains directly.

The formulation of Wu et al. provides dual sets of boundary integral equations that are linearly dependent. In principle either set can be used for numerical implementation. Both sets, however, contain singular integrals of Cauchy's type so that principal values must be evaluated. In this paper, the sets of boundary integral equations are transformed such that the integrals associated with the unknown boundary data are regularized. The transformation is done by employing certain eigenrelations in Stroh's formalism. The integral equations can be solved using Gaussian-type integration formulas directly without dividing the boundary into discrete elements. This is particularly useful for problems with infinite boundaries. An example of an infinite anisotropic plate subjected to collinear compressive line forces is provided to illustrate the effectiveness of the numerical scheme.

2 Nonsingular Boundary Integral Equations

For two-dimensional anisotropic elasticity problems, Wu et al. [1] derived the following dual sets of boundary integral equations:

$$\frac{1}{2}\mathbf{d}(\mathbf{x}) = \int_C [-\hat{\mathbf{W}}(\mathbf{x},\mathbf{x}';\hat{\mathbf{x}}_C)\mathbf{d}(\mathbf{x}') + \hat{\mathbf{U}}(\mathbf{x},\mathbf{x}';\hat{\mathbf{x}}_C)\mathbf{t}(\mathbf{x}')]ds', \tag{1}$$

$$\frac{1}{2}\mathbf{t}(\mathbf{x}) = \int_C [\hat{\mathbf{V}}(\mathbf{x},\mathbf{x}';\hat{\mathbf{x}}_C)\mathbf{d}(\mathbf{x}') - \hat{\mathbf{W}}(\mathbf{x},\mathbf{x}';\hat{\mathbf{x}}_C)^T\mathbf{t}(\mathbf{x}')]ds', \tag{2}$$

where C is a smooth contour parametrized by the arc length s, $\mathbf{d} = \partial\mathbf{u}/\partial s$ is the gradient of the displacement $\mathbf{u}$, $\mathbf{t}$ is the traction on C, $\mathbf{x}(s) = (x_1(s), x_2(s))$ is a generic point on C, $\hat{\mathbf{x}}_C = (\hat{x}_1(s), \hat{x}_2(s)) = \partial\mathbf{x}(s)/\partial s$ is the unit vector tangent to C at $\mathbf{x}, \mathbf{x}'$ is an integration point, and

Contributed by the Applied Mechanics Division of THE AMERICAN SOCIETY OF MECHANICAL ENGINEERS for publication in the ASME JOURNAL OF APPLIED MECHANICS. Manuscript received by the ASME Applied Mechanics Division, Sept. 15, 1999; final revision Jan. 14, 2000. Associate Technical Editor: J. R. Barber.

$$\hat{\mathbf{W}}(\mathbf{x},\mathbf{x}';\hat{\mathbf{x}}_C)=-\frac{1}{\pi}\mathrm{Im}\left[\mathbf{A}\left\langle\frac{\hat{z}_*(s)}{z'_*(s')-z_*(s)}\right\rangle\mathbf{B}^T\right], \tag{3}$$

$$\hat{\mathbf{U}}(\mathbf{x},\mathbf{x}';\hat{\mathbf{x}}_C)=-\frac{1}{\pi}\mathrm{Im}\left[\mathbf{A}\left\langle\frac{\hat{z}_*(s)}{z'_*(s')-z_*(s)}\right\rangle\mathbf{A}^T\right], \tag{4}$$

$$\hat{\mathbf{V}}(\mathbf{x},\mathbf{x}';\hat{\mathbf{x}}_C)=-\frac{1}{\pi}\mathrm{Im}\left[\mathbf{B}\left\langle\frac{\hat{z}_*(s)}{z'_*(s')-z_*(s)}\right\rangle\mathbf{B}^T\right]. \tag{5}$$

The direction of increasing s is such that when describing a circuit around the contour, the domain of interest is to the left. In Eqs. (3), (4), and (5), Im denotes the imaginary part, $\mathbf{A}=(\mathbf{a}_1,\mathbf{a}_2,\mathbf{a}_3)$, $\mathbf{B}=(\mathbf{b}_1,\mathbf{b}_2,\mathbf{b}_3)$, and $\langle\hat{z}_*(s)/z'_*(s')-z_*(s)\rangle$ represents the diagonal matrix given by

$$\left\langle\frac{\hat{z}_*(s)}{z'_*(s')-z_*(s)}\right\rangle = \begin{pmatrix} \dfrac{\hat{z}_1(s)}{z'_1(s')-z_1(s)} & 0 & 0 \\ 0 & \dfrac{\hat{z}_2(s)}{x'_2(s')-z_2(s)} & 0 \\ 0 & 0 & \dfrac{\hat{z}_3(s)}{z'_3(s')-z_3(s)} \end{pmatrix}$$

with $z_k(s)=x_1(s)+p_kx_2(s)$ and $\hat{z}_k(s)=\partial z_k(s)/\partial s=\hat{x}_1(s)+p_k\hat{x}_2(s)$, $k=1,2,3$, and $\mathrm{Im}[p_k]>0$. The complex vectors $\mathbf{a}_k,\mathbf{b}_k$ and scalars p_k are determined by the following eigenvalue problem:

$$\begin{pmatrix}\mathbf{N}_1 & \mathbf{N}_1\\ \mathbf{N}_3 & \mathbf{N}_1^T\end{pmatrix}\begin{pmatrix}\mathbf{a}_k\\ \mathbf{b}_k\end{pmatrix}=p_k\begin{pmatrix}\mathbf{a}_k\\ \mathbf{b}_k\end{pmatrix} \tag{6}$$

where

$$\mathbf{N}_1=-\mathbf{T}^{-1}\mathbf{R}^T,\quad \mathbf{N}_2=\mathbf{T}^{-1},\quad \mathbf{N}_1=\mathbf{R}\mathbf{T}^{-1}\mathbf{R}^T-\mathbf{Q},$$

$$Q_{ik}=C_{i1k1},\quad R_{ik}=C_{i1k2},\quad T_{ik}=C_{i2k2}$$

and C_{ijkl} is the elasticity tensor. Equations (1) and (2) are not independent. In principle, either set of equations can be used to solve for either the unknown boundary displacement gradients or the tractions from the special field boundary data. Once the unknown boundary quantities are determined, the boundary stresses and strains can be calculated directly from **d** and **t** by Hooke's law. The displacement gradients along an arbitrary direction $\hat{\mathbf{x}}_\Gamma$ and the tractions based on the normal obtained by rotating $\hat{\mathbf{x}}_\Gamma$ by $\pi/2$ clockwise at a generic point **x** in the body can be evaluated by

$$\mathbf{d}(\mathbf{x};\hat{\mathbf{x}}_\Gamma)=\int_C[-\hat{\mathbf{W}}(\mathbf{x}',\mathbf{x};\hat{\mathbf{x}}_\Gamma)\mathbf{d}(\mathbf{x}')+\hat{\mathbf{U}}(\mathbf{x}',\mathbf{x};\hat{\mathbf{x}}_\Gamma)\mathbf{t}(\mathbf{x}')]ds', \tag{7}$$

$$\mathbf{t}(\mathbf{x};\hat{\mathbf{x}}_\Gamma)=\int_C[\hat{\mathbf{V}}(\mathbf{x}',\mathbf{x};\hat{\mathbf{x}}_\Gamma)\mathbf{d}(\mathbf{x}')-\hat{\mathbf{W}}(\mathbf{x}',\mathbf{x};\hat{\mathbf{x}}_\Gamma)^T\mathbf{t}(\mathbf{x}')]ds'. \tag{8}$$

Either Eq. (1) or Eq. (2) contains singular integrals related to **d** as well as **t**. This fact precludes the direct use of many convenient numerical integration schemes such as Gaussian quadratures in seeking numerical solutions.

We can transform Eqs. (1) and (2) into expressions that involve singular integrals of either **d** or **t** only. The transformation is based on the following identity ([3]):

$$\begin{pmatrix}\mathbf{S} & \mathbf{H}\\ -\mathbf{L} & \mathbf{S}^T\end{pmatrix}\begin{pmatrix}\mathbf{A}\\ \mathbf{B}\end{pmatrix}=i\begin{pmatrix}\mathbf{A}\\ \mathbf{B}\end{pmatrix}, \tag{9}$$

where **S**, **H**, and **L** are the Barnett-Lothe tensors ([4]) defined as

$$\mathbf{S}=i(2\mathbf{A}\mathbf{B}^T-I),\quad \mathbf{H}=2i\mathbf{A}\mathbf{A}^T,\quad \mathbf{L}=-2i\mathbf{B}\mathbf{B}^T. \tag{10}$$

Here $i=\sqrt{-1}$, and **I** is the identity matrix. The Barnett-Lothe tensors are real. Moreover, **H** and **L** are symmetric and positive-definite. With Eqs. (9), Eqs. (1) and (2) can be combined to give

$$\frac{1}{2}[\mathbf{S}\mathbf{d}(\mathbf{x})-\mathbf{H}\mathbf{t}(\mathbf{x})]=\int_C(-\hat{\mathbf{W}}^*(\mathbf{x},\mathbf{x}';\hat{\mathbf{x}}_C)\mathbf{d}(\mathbf{x}')+\hat{\mathbf{U}}^*(\mathbf{x},\mathbf{x}';\hat{\mathbf{x}}_C)\mathbf{t}(\mathbf{x}'))ds', \tag{11}$$

$$\frac{1}{2}[\mathbf{L}\mathbf{d}(\mathbf{x})+\mathbf{S}^T\mathbf{t}(\mathbf{x})]=\int_C(-\hat{\mathbf{V}}^*(\mathbf{x},\mathbf{x}';\hat{\mathbf{x}}_C)\mathbf{d}(\mathbf{x}')-\hat{\mathbf{W}}^*(\mathbf{x},\mathbf{x}';\hat{\mathbf{x}}_C)^T\mathbf{t}(\mathbf{x}'))ds', \tag{12}$$

where

$$\hat{\mathbf{W}}^*(\mathbf{x},\mathbf{x}';\hat{\mathbf{x}}_C)=-\frac{1}{\pi}\mathrm{Re}\left[\mathbf{A}\left\langle\frac{\hat{z}_*(s)}{z'_*(s')-z_*(s)}\right\rangle\mathbf{B}^T\right], \tag{13}$$

$$\hat{\mathbf{U}}^*(\mathbf{x},\mathbf{x}';\hat{\mathbf{x}}_C)=-\frac{1}{\pi}\mathrm{Re}\left[\mathbf{A}\left\langle\frac{\hat{z}_*(s)}{z'_*(s')-z_*(s)}\right\rangle\mathbf{A}^T\right], \tag{14}$$

$$\hat{\mathbf{V}}^*(\mathbf{x},\mathbf{x}';\hat{\mathbf{x}}_C)=-\frac{1}{\pi}\mathrm{Re}\left[\mathbf{B}\left\langle\frac{\hat{z}_*(s)}{z'_*(s')-z_*(s)}\right\rangle\mathbf{B}^T\right], \tag{15}$$

and Re denotes the real part. By expressing $z'_*(s')$ as a Taylor's series about $s'=s$, it can be shown that as $s'\to s$,

$$\lim_{s'\to s}\frac{\hat{z}_*}{z'_*-z_*}=\frac{1}{(s'-s)}-\frac{1}{2\bar{z}_*}\frac{\partial^2 z_*}{\partial s^2}. \tag{16}$$

Substitution of Eq. (16) into Eqs. (13), (14), and (15) yields

$$\lim_{\mathbf{x}'\to\mathbf{x}}\hat{\mathbf{W}}^*(\mathbf{x},\mathbf{x}';\hat{\mathbf{x}}_C)=-\frac{1}{2\pi(s'-s)}\mathbf{I}, \tag{17}$$

$$\lim_{\mathbf{x}'\to\mathbf{x}}\hat{\mathbf{U}}^*(\mathbf{x},\mathbf{x}';\hat{\mathbf{x}}_C)=\frac{1}{2\pi}\mathrm{Re}\left[\mathbf{A}\left\langle\frac{1}{\hat{z}_*(s)}\frac{\partial^2 z_*(s)}{\partial s^2}\right\rangle\mathbf{A}^T\right], \tag{18}$$

$$\lim_{\mathbf{x}'\to\mathbf{x}}\hat{\mathbf{V}}^*(\mathbf{x},\mathbf{x}';\hat{\mathbf{x}}_C)=\frac{1}{2\pi}\mathrm{Re}\left[\mathbf{B}\left\langle\frac{1}{\hat{z}_*(s)}\frac{\partial^2 z_*(s)}{\partial s^2}\right\rangle\mathbf{B}^T\right], \tag{19}$$

where Eq. (10) has been used. Equations (18) and (19) clearly show that $\hat{\mathbf{U}}^*(\mathbf{x},\mathbf{x};\hat{\mathbf{x}}_C)$ and $\hat{\mathbf{V}}^*(\mathbf{x},\mathbf{x}';\hat{\mathbf{x}}_C)$ are nonsingular at $s'=s$. For the displacement problem where **d** is specified at the boundary, Eq. (11) is a set of nonsingular integral equations for **t**. On the other hand, for the traction problem where **t** is specified on the boundary, Eq. (12) is a set of nonsingular integral equations for **d**.

3 Numerical Example

As an illustration, Eq. (12) is applied numerically to solve the problem of an infinite plate subjected to a pair of collinear compressive line forces as shown in Fig. 1. The (x_1,x_3) plane is taken

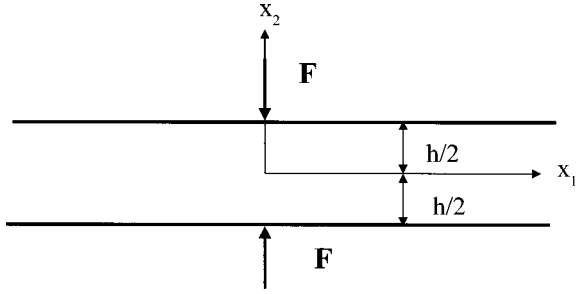

Fig. 1 An infinite plate subjected to a pair of collinear compressive line forces

to coincide with the midplane of the plate. The top and bottom surfaces are at $x_2=h/2$ and $x_2=-h/2$, respectively, h being the thickness of the plate. The compressive forces $\mathbf{F}=F\mathbf{e}_2$ and $-\mathbf{F}$ are applied, respectively, at $\mathbf{y}^{(1)}=(0,-h/2)$ and $\mathbf{y}^{(2)}=(0,h/2)$, where $\mathbf{e}_2$ is the unit vector in the x_2-direction. This problem has been studied using integral transform techniques by Filon [5] for isotropic materials and by Chiu and Wu [6] for anisotropic materials.

For the problem considered, Eq. (12) becomes

$$\frac{1}{2}[\mathbf{L}\mathbf{d}(\mathbf{x}^{(1)})+\delta(x_1)\delta(x_2+h/2)\mathbf{S}^T\mathbf{F}] = -\frac{1}{2\pi x_1}\mathbf{F}+\hat{\mathbf{W}}^*(\mathbf{x}^{(1)},\mathbf{y}^{(2)};\mathbf{e}_1)^T\mathbf{F} + \int_{-\infty}^{\infty}\hat{\mathbf{V}}^*(\mathbf{x}^{(1)},\mathbf{x}^{(2)\prime};\mathbf{e}_1)\mathbf{d}(\mathbf{x}^{(2)\prime})dx_1' \tag{20}$$

$$\frac{1}{2}[\mathbf{L}\mathbf{d}(\mathbf{x}^{(2)})-\delta(x_1)\delta(x_2-h/2)\mathbf{S}^T\mathbf{F}] = -\frac{1}{2\pi x_1}\mathbf{F}+\hat{\mathbf{W}}^*(\mathbf{x}^{(2)},\mathbf{y}^{(1)};\mathbf{e}_1)^T\mathbf{F} - \int_{-\infty}^{\infty}\hat{\mathbf{V}}^*(\mathbf{x}^{(2)},\mathbf{x}^{(1)\prime};\mathbf{e}_1)\mathbf{d}(\mathbf{x}^{(1)\prime})dx_1' \tag{21}$$

where $\delta(x_1)$ is the Dirac delta distribution, $\mathbf{e}_1$ is the unit vector in the x_1 direction, $\mathbf{x}^{(1)}=x_1\mathbf{e}_1-h/2\mathbf{e}_2$ and $\mathbf{x}^{(2)}=x_1\mathbf{e}_1+h/2\mathbf{e}_2$. To avoid appearance of $\delta(x_1)$ in Eqs. (20) and (21), we introduce $\mathbf{q}(\mathbf{x})$ defined as

$$\mathbf{q}(\mathbf{x}^{(1)})=\mathbf{d}(\mathbf{x}^{(1)})+\delta(x_1)\delta(x_2+h/2)\mathbf{L}^{-1}\mathbf{S}^T\mathbf{F}, \tag{22}$$

$$\mathbf{q}(\mathbf{x}^{(2)})=\mathbf{d}(\mathbf{x}^{(2)})-\delta(x_1)\delta(x_2-h/2)\mathbf{L}^{-1}\mathbf{S}^T\mathbf{F}. \tag{23}$$

Equations (20) and (21) can then be expressed in terms of $\mathbf{q}(\mathbf{x})$ as

$$\frac{1}{2}\mathbf{L}\mathbf{q}(\mathbf{x}^{(1)})=\mathbf{f}(\mathbf{x}^{(1)},\mathbf{y}^{(2)})+\int_{-\infty}^{\infty}\hat{\mathbf{V}}^*(\mathbf{x}^{(1)},\mathbf{x}^{(2)\prime};\mathbf{e}_1)\mathbf{q}(\mathbf{x}^{(2)\prime})dx_1', \tag{24}$$

$$\frac{1}{2}\mathbf{L}\mathbf{q}(\mathbf{x}^{(2)})=\mathbf{f}(\mathbf{x}^{(2)},\mathbf{y}^{(1)})-\int_{-\infty}^{\infty}\hat{\mathbf{V}}^*(\mathbf{x}^{(2)},\mathbf{x}^{(1)\prime};\mathbf{e}_1)\mathbf{q}(\mathbf{x}^{(1)\prime})dx_1' \tag{25}$$

where

$$\mathbf{f}(\mathbf{x},\mathbf{y})=-\frac{1}{2\pi x_1}\mathbf{F}+\hat{\mathbf{W}}^*(\mathbf{x},\mathbf{y};\mathbf{e}_1)^T\mathbf{F}+\hat{\mathbf{V}}^*(\mathbf{x},\mathbf{y};\mathbf{e}_1)\mathbf{L}^{-1}\mathbf{S}^T\mathbf{F}.$$

Table 1 $\bar{\sigma}_{22}=-\pi h\sigma_{22}/4F$ **as a function of** $\bar{x}_1=2x_1/h$ **for** $n=6, 12, 18$ **by the present method and by the integral transform method**

$\bar{x}_1$	$n=6$	$n=12$	$n=18$	Ref. [6]
0	1.3932	1.3990	1.3990	1.3947
0.2	1.2444	1.2397	1.2397	1.2403
0.4	0.8997	0.8961	0.8960	0.8985
0.6	0.5521	0.5670	0.5670	0.5646
0.8	0.3112	0.3285	0.3292	0.3292
1.0	0.1722	0.1782	0.1776	0.1791
1.2	0.0941	0.0885	0.0869	0.0860
1.4	0.0460	0.0354	0.0352	0.0347
1.6	0.0136	0.0067	0.0076	0.0086
1.8	−0.0063	−0.0066	−0.0064	−0.0065
2.0	−0.0144	−0.0122	−0.0125	−0.0135

In solving Eqs. (24) and (25), it is expedient to make a change of variable $x=\tan(\pi\phi/2)$ so that the range of integrations is from -1 to 1. The transformed integrals in terms of ϕ can be approximated by the Gaussian integration formula

$$\int_{-1}^{1}f(\phi)d\phi\simeq\sum_{j=1}^{n}w_jf(\phi_j)$$

where ϕ_j and w_j are, respectively, the integration point and the corresponding weight and n is the number of integration points. A system of algebraic equations can be obtained by enforcing Eqs. (24) and (25) at $\mathbf{x}^{(\alpha)}(\phi_i)$, $\alpha=1,2$ and $i=1,2\ldots n$. The result is

$$\frac{1}{2}\mathbf{L}\mathbf{q}_i^{(1)}-\sum_{j=1}^{n}\mathbf{C}_{ij}^{(12)}\mathbf{q}_j^{(2)}=\mathbf{f}_i^{(1)}, \tag{26}$$

$$\sum_{j=1}^{n}\mathbf{C}_{ij}^{(21)}\mathbf{q}_j^{(1)}+\frac{1}{2}\mathbf{L}\mathbf{q}_i^{(2)}=\mathbf{f}_i^{(2)} \tag{27}$$

where

$$\mathbf{q}_i^{(\alpha)}=\mathbf{q}(\mathbf{x}^{(\alpha)}(\phi_i)),\quad \mathbf{f}_i^{(\alpha)}=\mathbf{f}(\mathbf{x}^{(\alpha)}(\phi_i),\mathbf{y}^{(3-\alpha)}),$$

$$\mathbf{C}_{ij}^{(\alpha\beta)}=\frac{\pi w_j}{2\cos^2(\pi\phi_j/2)}\hat{\mathbf{V}}^*(\mathbf{x}^{(\alpha)}(\phi_i),\mathbf{x}^{(\beta)}(\phi_j);\mathbf{e}_1),\quad \beta=3-\alpha.$$

Once $\mathbf{q}_i^{(\alpha)}$ are solved from Eqs. (24) and (25), $\mathbf{d}(\mathbf{x}^{(\alpha)}(\phi_i))$ can be determined by Eqs. (22) and (23). The stresses in the plate can be calculated using Eq. (8) with the Gaussian integration formula. In particular, the stress σ_{22} at $x_2=0$ was computed for a vinyl ester reinforced by unidirectional glass fibers with the following properties:

$$E_1=24.4\text{ GPa},\quad E_2=6.89\text{ GPa},$$

$$G_{12}=2.85\text{ GPa},\quad \nu_{12}=\nu_{12}=.325.$$

Table 1 displays the result of $\bar{\sigma}_{22}=-\pi h\sigma_{22}/4F$ as a function of $\bar{x}_1=2x_1/h$ for $n=6$, 12, and 18. For comparison purposes, the values obtained using the integral transform method ([6]) are also shown. For a fixed value of $\bar{x}_1$, the value of $\bar{\sigma}_{22}$ converges very rapidly with increasing n. Indeed the values for $n=12$ are essentially the same as those for $n=18$, which are in close agreement with the results obtained using the integral transform method. The result is quite satisfactory even for $n=6$.

4 Conclusion

Nonsingular boundary integral equations for two-dimensional anisotropic elasticity have been developed. The integral equations can be treated numerically using Gaussian quadratures rather than by dividing the boundary into discrete elements. This is especially convenient for problems with infinite boundaries. An example of an infinite plate subjected to a pair of compressive forces is given to illustrate the effectiveness of the numerical scheme. It is shown that very accurate results could be obtained with few integration points.

Acknowledgments

The research was supported by the National Science Council of Taiwan under grant No. NSC 87-2212-E-002-033.

References

[1] Wu, K.-C., Chiu, Y.-T., and Hwu, Z.-H., 1992, ''A New Boundary Integral Equation Formulation for Linear Elastic Solids,'' ASME J. Appl. Mech., **9**, pp. 344–348.
[2] Stroh, A. N., 1958, ''Dislocations and Cracks in Anisotropic Elasticity,'' Philos. Mag., **3**, pp. 625–646.
[3] Ting, T. C. T., 1996, *Anisotropic Elasticity—Theory and Application*, Oxford University Press, New York.
[4] Barnett, D. M., and Lothe, J., 1973, ''Synthesis of the Sextic and the Integral Formalism for Dislocations, Green's Function and Surface Waves in Anisotropic Elastic Solids,'' Phys. Norv., **7**, pp. 13–19.

[5] Filon, L. N. G., 1903, ''On an Approximate Solution for the Bending of a Beam of Rectangular Cross-Section Under Any System of Load, With Special Reference to Points of Concentrated or Discontinuous Loading,'' Philosophical Transaction of the Royal Society of London, **A201**, pp. 63–155.
[6] Chiu, Y.-T., and Wu, K.-C., 1998, ''Analysis for Elastic Strips Under Concentrated Loads,'' ASME J. Appl. Mech., **65**, pp. 626–634.

The Nonlinear Response of a Simply Supported Rectangular Metallic Plate to Transverse Harmonic Excitation

O. Elbeyli and G. Anlas
Department of Mechanical Engineering, Bogazici University, 80815 Bebek, Istanbul, Turkey

In this study, the nonlinear response of a simply supported metallic rectangular plate subject to transverse harmonic excitations is analyzed using the method of multiple scales. Stability of solutions, critical points, types of bifurcations in the presence of a one-to-one internal resonance, together with primary resonance, are determined. [S0021-8936(00)00603-6]

Introduction

In an early work, the nonlinear response of a metallic square plate was investigated by Chu and Herrmann [1] who used Von Karman strains, and obtained the in-plane deformation fields by double Fourier series. Later, Yang and Sethna studied nonlinear vibrations of near square metallic plates subjected to parametric ([2]), and external ([3]) excitations in the presence of a one-to-one internal resonance. They studied the interaction of two antisymmetric modes. Chang et al. [4] analyzed the nonlinear vibration of rectangular plates in the presence of a one-to-one internal resonance. They used the method of averaging starting from the equations of motion that are in terms of transverse deflection and stress function.

In this study, the nonlinear response of a simply supported metallic rectangular plate subject to transverse harmonic excitations is analyzed using the method of multiple scales. For a rectangular metallic plate, antisymmetric modes cannot be forced to have the same natural frequencies unlike the case of a square plate ([3]). As a result, two arbitrary modes represented by modal amplitudes T_{mn} and T_{rs} with same natural frequencies are studied where m, n, r, and s are the mode numbers. Stability of solutions, critical points, types of bifurcations in the presence of a one-to-one internal resonance together with primary resonance are determined. In contrast to the study of Yang and Sethna [2], the parameters used in this analysis are closely related to physical quantities. To measure the nearness of the frequencies of the two interacting modes, one of the system parameters is assigned to tune the aspect ratio of the rectangular plate. In-plane stretching forces that are used by Chang et al. [4] are not present here. The geometry of the problem and the loading are shown in Fig. 1.

Plate Equations

Using $\varepsilon = h^2/a^2$ as a small dimensionless parameter and $x = x_0/a$, $y = y_0/b$, $z = z_0/a$, $u = u_0/\varepsilon^2 a$, $v = v_0/\varepsilon^2 a$, $w = w_0/\varepsilon a$, $\lambda^2 = k + \varepsilon\gamma/2$, $\overline{c} = c_p c \varepsilon^2 \rho/\sqrt{3}$, and $F = 12a(1-\nu^2)\overline{F}/\varepsilon^3 Eh$ with $\lambda = a/b$, the nondimensional equations of motion in x, y, and z-directions are obtained ([5]):

$$\frac{\partial^2 u}{\partial x^2} + \frac{\partial w}{\partial x}\frac{\partial^2 w}{\partial x^2} + (1+\nu)/2\left(\frac{a}{b}\frac{\partial^2 v}{\partial x \partial y} + \frac{a^2}{b^2}\frac{\partial w}{\partial y}\frac{\partial^2 w}{\partial x \partial y}\right) + (1-\nu)/2\left(\frac{a^2}{b^2}\frac{\partial^2 u}{\partial y^2} + \frac{a^2}{b^2}\frac{\partial w}{\partial x}\frac{\partial^2 w}{\partial y^2}\right) = \ddot{u}\frac{\varepsilon}{12}, \tag{1}$$

$$\frac{\partial^2 v}{\partial y^2} + \frac{a}{b}\frac{\partial w}{\partial y}\frac{\partial^2 w}{\partial y^2} + (1+\nu)/2\left(\frac{b}{a}\frac{\partial u}{\partial x \partial y} + \frac{b}{a}\frac{\partial w}{\partial x}\frac{\partial^2 w}{\partial x \partial y}\right) + (1-\nu)/2\left(\frac{b^2}{a^2}\frac{\partial^2 v}{\partial x^2} + \frac{b}{a}\frac{\partial w}{\partial y}\frac{\partial^2 w}{\partial x^2}\right) = \ddot{v}\frac{\varepsilon}{12}\frac{b^2}{a^2}, \tag{2}$$

$$\begin{aligned}&\frac{\partial^4 w}{\partial x^4} + 2k\frac{\partial^4 w}{\partial x^2 \partial y^2} + k^2\frac{\partial^4 w}{\partial y^4} + \frac{\partial^2 w}{\partial t'^2} + \varepsilon\left\{2c\frac{\partial w}{\partial t'} + k\gamma\frac{\partial^4 w}{\partial x^2 \partial y^2}\right.\\ &+ k\gamma\frac{\partial^4 w}{\partial y^4} - 12\frac{\partial u}{\partial x}\frac{\partial^2 w}{\partial x^2} - 6\left(\frac{\partial w}{\partial x}\right)^2\frac{\partial^2 w}{\partial x^2}\\ &- 12\nu\left(\frac{a}{b}\frac{\partial v}{\partial y}\frac{\partial^2 w}{\partial x^2} + \frac{1}{2}k\left(\frac{\partial w}{\partial y}\right)^2\frac{\partial^2 w}{\partial x^2}\right) - 12\frac{a}{b}k\frac{\partial v}{\partial y}\frac{\partial^2 w}{\partial y^2}\\ &- 6k^2\left(\frac{\partial w}{\partial y}\right)^2\frac{\partial^2 w}{\partial y^2} - 12\nu\left(k\frac{\partial u}{\partial x}\frac{\partial^2 w}{\partial y^2} + \frac{1}{2}k\left(\frac{\partial w}{\partial x}\right)^2\frac{\partial^2 w}{\partial y^2}\right)\\ &\left.- 12(1-\nu)\left(k\frac{\partial u}{\partial y}\frac{\partial^2 w}{\partial x \partial y} + \frac{a}{b}\frac{\partial v}{\partial x}\frac{\partial^2 w}{\partial x \partial y} + k\frac{\partial w}{\partial x}\frac{\partial w}{\partial y}\frac{\partial^2 w}{\partial x \partial y}\right)\right\}\\ &= \varepsilon F(x,y,t) + O(\varepsilon^2).\end{aligned} \tag{3}$$

Note that a and b are the dimensions of the plate, h is the thickness, u_0, v_0, and w_0 are the midplane displacements in the x, y and z-directions, respectively, ρ is the density, E is the elastic modulus, ν is Poisson's ratio, $\overline{F}$ is the external force per unit area, $\overline{c}$ is the transverse viscous damping per unit area, c is the dimensionless damping coefficient, and $k = a^2/b^2$ and $c_p^2 = E/\rho(1-\nu^2)$. Parameters related to plate geometry are shown in Fig. 1. Dots indicate differentiation with respect to dimensionless time $t = \sqrt{\varepsilon/12}c_p/at'$.

The plate is simply supported on all four sides and the nondimensional boundary conditions are

$$\text{at } x = 0,1: \quad w = \frac{\partial^2 w}{\partial x^2} = u = 0, \quad \text{at } y = 0,1: \quad w = \frac{\partial^2 w}{\partial y^2} = v = 0. \tag{4}$$

Note that in the case of Chang et al. [4], the boundary conditions are satisfied on the average.

Solution. It is assumed that two modes are interacting with each other through a one-to-one internal resonance. Because there is damping, the modes that are not excited directly by an external excitation or through an internal resonance will die out in a finite time, and only two modes will dominate the transverse motion of the plate. As a result w may be expressed as follows:

$$w(x,y,t) = T_{mn}(t)\sin(m\pi x)\sin(n\pi y) + T_{rs}(t)\sin(r\pi x)\sin(s\pi y) + O(\varepsilon). \tag{5}$$

The terms $T_{mn}(t)$ and $T_{rs}(t)$ represent the time-dependent modal amplitudes of the two interacting modes. The above transverse motion assumption is more general than the one assumed by Yang and Sethna [2,3] who used antisymmetric modes T_{mn} and T_{nm}.

The right hand sides of Eqs. (1) and (2) can be neglected because it is assumed that in-plane displacements are small as compared to the out-of-plane displacement. The left-hand sides of Eqs. (1) and (2) do not contain nonlinear terms in u and v. Therefore, after substituting Eq. (5) into (1) and (2), u and v can be

Contributed by the Applied Mechanics Division of THE AMERICAN SOCIETY OF MECHANICAL ENGINEERS for publication in the ASME JOURNAL OF APPLIED MECHANICS. Manuscript received by the ASME Applied Mechanics Division, Feb. 24, 1999; final revision, May 2, 2000. Associate Technical Editor: A. A. Ferri.

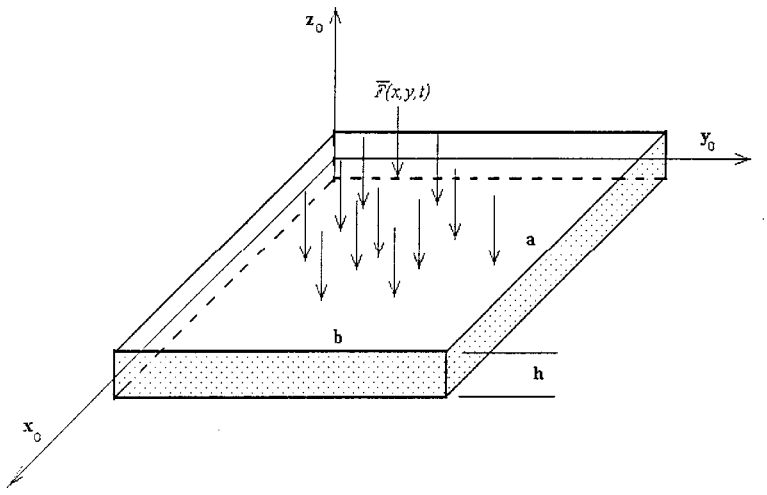

Fig. 1 The geometry of the problem

calculated by expressing them as linear combinations of *sine* terms and using the method of undetermined coefficients. Once u and v are calculated, substituting them and w into Eq. (3), multiplying by $\sin(m\pi x)\sin(n\pi y)$ and by $\sin(r\pi x)\sin(s\pi y)$, and integrating over the plate, the governing equation in the $-z$ direction will yield the following equations in terms of T_{mn} and T_{rs}:

$$\frac{d^2T_{mn}}{dt^2}+2c\varepsilon\frac{dT_{mn}}{dt}+\omega_1^2T_{mn}+(k-1)\varepsilon\gamma m^2n^2\pi^4T_{mn}+\varepsilon BT_{mn}T_{rs}^2+\varepsilon DT_{mn}^3=\varepsilon F_1, \tag{6}$$

$$\frac{d^2T_{rs}}{dt^2}+2c\varepsilon\frac{dT_{rs}}{dt}+\omega_2^2T_{rs}+(k-1)\varepsilon\gamma s^2r^2\pi^4T_{rs}+\varepsilon HT_{rs}T_{mn}^2+\varepsilon GT_{rs}^3=\varepsilon F_2, \tag{7}$$

where the natural frequencies ω_1 and ω_2 of the two interacting modes are

$$\omega_1=\left(m^2+\left(k+\frac{\varepsilon\gamma}{2}\right)n^2\right)\pi^2 \quad \text{and} \quad \omega_2=\left(r^2+\left(k+\frac{\varepsilon\gamma}{2}\right)s^2\right)\pi^2. \tag{8}$$

B, D, G, and H are constants involving m, n, r, s and geometric and material properties of the plate, and $[F_1;F_2]=\int_0^1\int_0^1F(x,y,t)[\sin(m\pi x)\sin(n\pi y);\sin(r\pi x)\sin(s\pi y)]dxdy+O(\varepsilon^2)$ ([5]). It turns out that in the case analyzed here $B=H$, and $D=G$. The modal amplitudes are governed by nonlinear Eqs. (6) and (7), they are solved using the method of multiple scales ([6]). To determine a first-order approximation, T_{mn} and T_{rs} can be expressed in the following form:

$$T_{mn}(t,\varepsilon)=X_0(T_0,T_1)+\varepsilon X_1(T_0,T_1)+O(\varepsilon^2) \tag{9}$$

$$T_{rs}(t,\varepsilon)=Y_0(T_0,T_1)+\varepsilon Y_1(T_0,T_1)+O(\varepsilon^2) \tag{10}$$

where $T_i=\varepsilon^i t$ are the time scales and ε is a small parameter introduced earlier. Substituting (9) and (10) into (6) and (7), and collecting coefficients of like powers of ε we get differential equations governing X_0, X_1, Y_0, and Y_1. The equations from ε^1 order, governing X_1 and Y_1 are as follows, where primes indicate derivatives with respect to time scale T_1 and Ω is the external excitation frequency:

$$\begin{aligned}\frac{\partial^2X_1}{\partial T_0^2}+\omega_1^2X_1=&\frac{1}{2}e^{i\Omega T_0}F_1+\frac{1}{2}e^{-i\Omega T_0}F_1-A_x\gamma km^2n^2\pi^4e^{i\omega_1T_0}+A_x\gamma n^2m^2\pi^4e^{i\omega_1T_0}-2iA_x\omega_1ce^{i\omega_1T_0}-\overline{A}_x\gamma km^2n^2\pi^4e^{-i\omega_1T_0}\\&+\overline{A}_x\gamma m^2n^2\pi^4e^{-i\omega_1T_0}+2i\overline{A}_x\omega_1ce^{-i\omega_1T_0}-3A_x^2\overline{A}_xDe^{i\omega_1T_0}-3A_x\overline{A}_x^2De^{-i\omega_1T_0}-D\overline{A}_x^3e^{-3i\omega_1T_0}+2i\overline{A}_x'\omega_1e^{-i\omega_1T_0}\\&-2iA_x'\omega_1e^{i\omega_1T_0}-B\overline{A}_xA_y^2e^{i(2\omega_2-\omega_1)T_0}-BA_x\overline{A}_y^2e^{i(\omega_1-2\omega_2)T_0}-B\overline{A_x\overline{A}_y^2}e^{i(-\omega_1-2\omega_2)T_0}-2BA_xA_y\overline{A}_ye^{i\omega_1T_0}\\&-2B\overline{A}_xA_y\overline{A}_ye^{-i\omega_1T_0}-DA_x^3e^{3i\omega_1T_0}-BA_xA_y^2e^{i(\omega_1+2\omega_2)T_0}\end{aligned} \tag{11}$$

and

$$\begin{aligned}\frac{\partial^2Y_1}{\partial T_0^2}+\omega_2^2Y_1=&\frac{1}{2}e^{i\Omega T_0}F_2+\frac{1}{2}e^{-i\Omega T_0}F_2-A_y\gamma kr^2s^2\pi^4e^{i\omega_2T_0}+A_y\gamma r^2s^2\pi^4e^{i\omega_2T_0}-2iA_y\omega_2ce^{i\omega_2T_0}-DA_y^3e^{3i\omega_2T_0}-\overline{A}_y\gamma kr^2s^2\pi^4e^{-i\omega_2T_0}\\&+\overline{A}_y\gamma r^2s^2\pi^4e^{-i\omega_2T_0}+2i\overline{A}_y\omega_2ce^{-i\omega_2T_0}-3A_y^2\overline{A}_yDe^{i\omega_2T_0}-D\overline{A}_y^3e^{-3i\omega_2T_0}+2i\overline{A}_y'\omega_2e^{-i\omega_2T_0}-2iA_y'\omega_2e^{i\omega_2T_0}\\&-B\overline{A}_yA_x^2e^{i(2\omega_1-\omega_2)T_0}-BA_y\overline{A}_x^2e^{i(\omega_2-2\omega_1)T_0}-BA_yA_x^2e^{i(2\omega_1+\omega_2)T_0}-B\overline{A_y\overline{A}_x^2}e^{i(-2\omega_1-\omega_2)T_0}-2BA_yA_x\overline{A}_xe^{i\omega_2T_0}\\&-2B\overline{A}_yA_x\overline{A}_xe^{-i\omega_2T_0}-3A_y\overline{A}_y^2De^{-i\omega_2T_0}.\end{aligned} \tag{12}$$

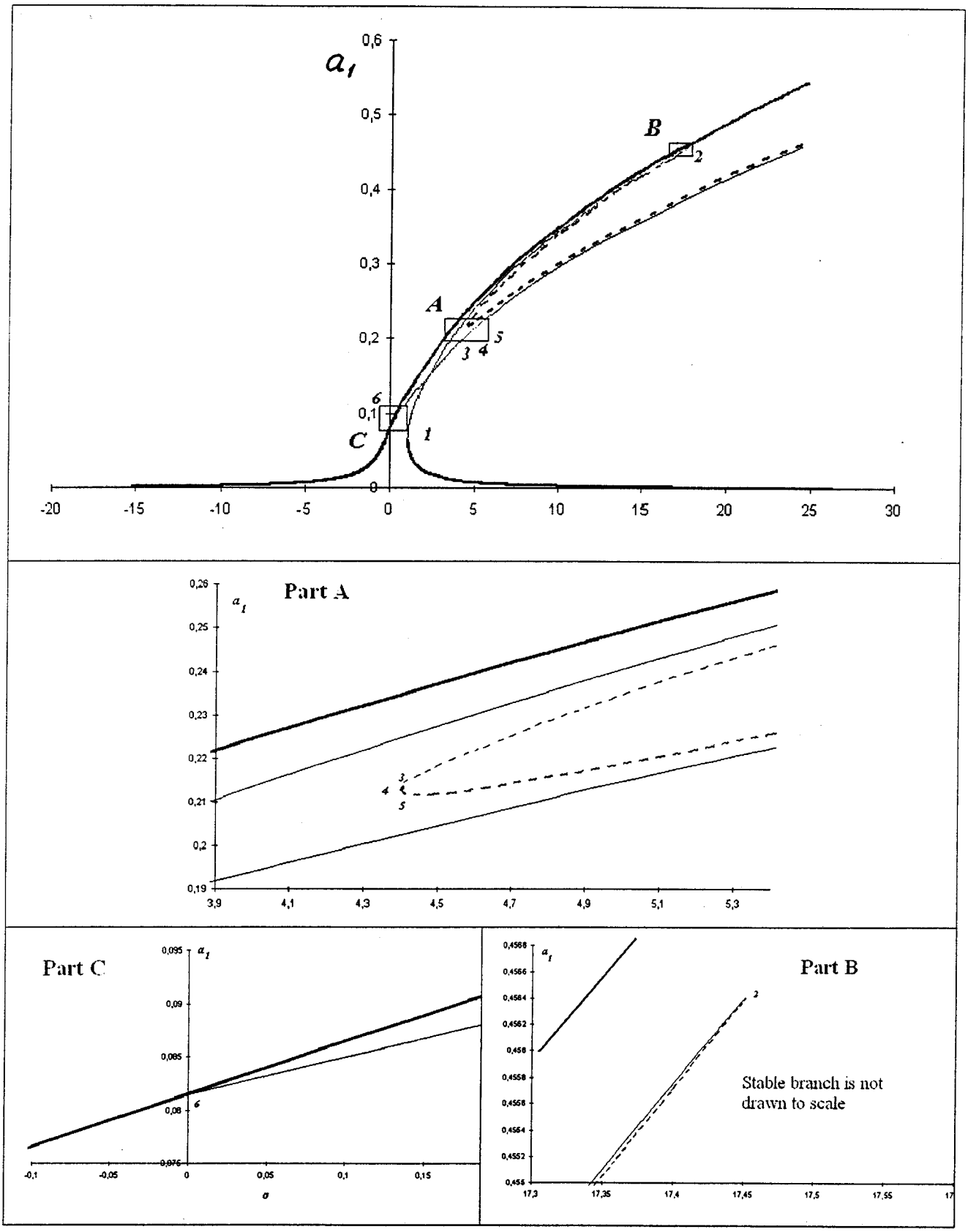

Fig. 2 External resonance detuning parameter, σ versus the first-mode amplitude a_1, in the presence of one-to-one internal resonance. $a=0.5$, $b=1$, $m=1$, $n=8$, $s=2$, $r=4$, $k=1/4$, $\gamma=0.0005$, and $c=0.03$, $B=13571.6$, $D=37281.6$, $F_2=0$, $\omega_{1,2}=167.78$.

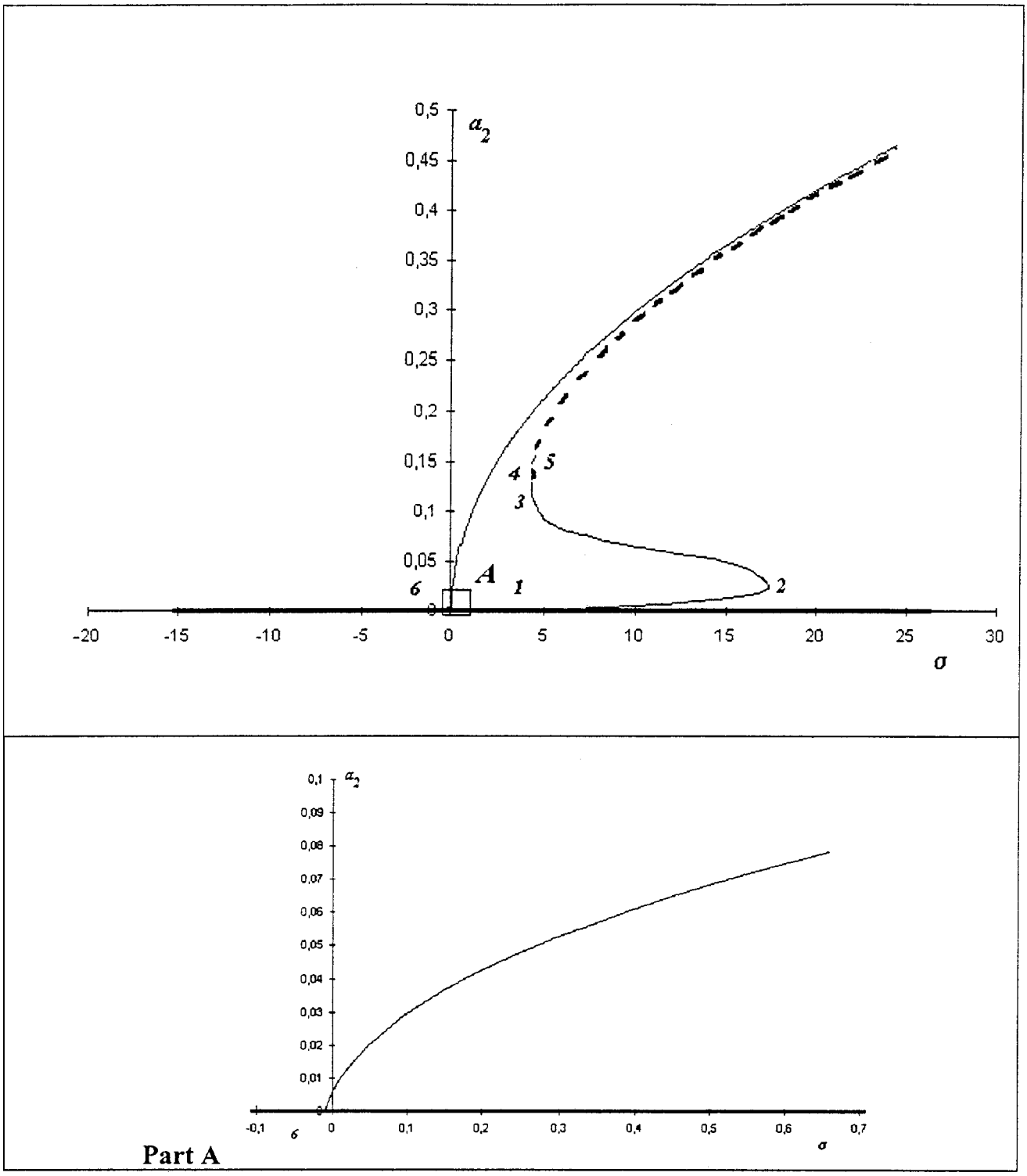

Fig. 3 External resonance detuning parameter, σ versus the second-mode amplitude a_2, in the presence of one-to-one internal resonance. $a=0.5$, $b=1$, $m=1$, $n=8$, $s=2$, $r=4$, $k=1/4$, $\gamma=0.0005$, and $c=0.03$, $B=13571.6$, $D=37281.6$, $F_2=0$, $\omega_{1,2}=167.78$.

In the presence of a one-to-one internal resonance, $\omega_1 \approx \omega_2$, $\omega_1 = \omega_2 + \varepsilon\Delta$ where $\Delta = (\gamma(n^2-s^2)\pi^2)/2$, (the mode numbers must satisfy $m^2+kn^2=r^2+ks^2$); together with primary resonance, $\Omega \approx \omega_1$, $\Omega = \omega_1 + \varepsilon\sigma$ (note that the nearness of the excitation frequency Ω to any of the natural frequencies ω_1 or ω_2 of the plate is expressed by using the detuning parameter σ), the particular solutions of Eqs. (11) and (12) contain secular terms, depending on the resonance condition of the system. The solvability conditions are obtained by equating the secular terms to zero as shown below:

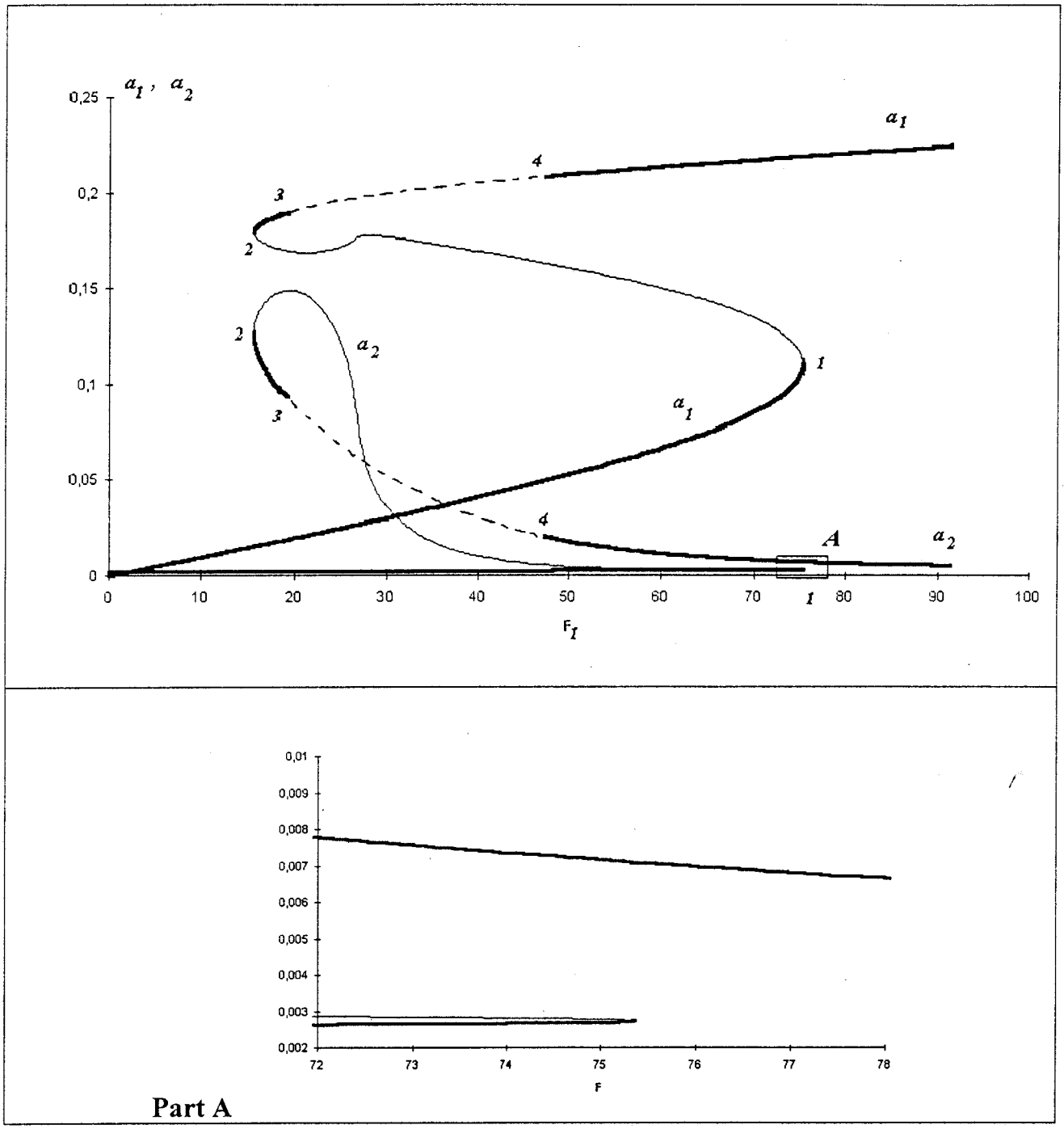

Fig. 4 Force-response curve, F_1 versus a_1 and a_2. $c=0.3$, $\gamma=0.02$, $\sigma=3$, $k=1/4$, $a=0.5$, $b=1$, $m=1$, $n=8$, $s=2$, and $r=4$, $B=13571.6$, $D=37281.6$, $F_2=3$, $\omega_{1,2}=167.78$.

$$\frac{1}{2}e^{i\Omega T_0}F_1-A_x k\gamma m^2n^2\pi^4e^{i\omega_1T_0}+A_x\gamma m^2n^2\pi^4e^{i\omega_1T_0}$$
$$-2iA_x\omega_1ce^{i\omega_1T_0}-3A_x^2\overline{A}_xDe^{i\omega_1T_0}-2iA_x'\omega_1e^{i\omega_1T_0}$$
$$-B\overline{A}_xA_y^2e^{i(2\omega_2-\omega_1)T_0}-2BA_xA_y\overline{A}_ye^{i\omega_1T_0}=0, \qquad (13)$$

and

$$\frac{1}{2}e^{i\Omega T_0}F_2-A_y\gamma kr^2s^2\pi^4e^{i\omega_2T_0}+A_y\gamma r^2s^2\pi^4e^{i\omega_2T_0}$$
$$-2iA_y\omega_2ce^{i\omega_2T_0}-3A_y^2\overline{A}_yDe^{i\omega_2T_0}-2iA_y'\omega_2e^{i\omega_2T_0}$$
$$-B\overline{A}_yA_x^2e^{i(2\omega_1-\omega_2)T_0}-2BA_yA_x\overline{A}_xe^{i\omega_2T_0}=0. \qquad (14)$$

Let $A_x=1/2(p_1-iq_1)e^{i\lambda_1}$ and $A_y=1/2(p_2-iq_2)e^{i\lambda_2}$ where p_i,

q_i and λ_i are real functions of T_1 ([7]). Substituting A_x and A_y in (13)–(14) we get

$$p_1' = -\frac{2\omega_1 c p_1}{B} + \frac{(k-1)\gamma m^2 n^2 \pi^4 q_1}{B} + \frac{3D(p_1^2 q_1 + q_1^3)}{4B} - q_1\lambda_1' + \frac{3q_1 q_2^2 + p_2^2 q_1 + 2p_1 p_2 q_2}{4}, \tag{15}$$

$$q_1' = \frac{F_1}{B} + \frac{(1-k)\gamma m^2 n^2 \pi^4 p_1}{B} - \frac{3D(p_1^3 + p_1 q_1^2)}{4B} + p_1\lambda_1' - \frac{3p_1 p_2^2 + p_1 q_2^2 + 2p_2 q_1 q_2}{4} - \frac{2\omega_1 c q_1}{B}, \tag{16}$$

$$p_2' = \frac{2p_1 p_2 q_1 + 3q_1^2 q_2 + p_1^2 q_2}{4} - \frac{2\omega_1 c p_2}{B} - q_2\lambda_2' + \frac{(k-1)\gamma r^2 s^2 \pi^4 q_2}{B} + \frac{3D(p_2^2 q_2 + q_2^3)}{4B}, \tag{17}$$

$$q_2' = \frac{-3p_1^2 p_2 + p_2 q_1^2 + 2p_1 q_1 q_2}{4} + \frac{(1-k)\gamma r^2 s^2 \pi^4 p_2}{B} - \frac{2\omega_2 c q_2}{B} - \frac{3D(p_2 q_2^2 + p_2^3)}{4B} + p_2\lambda_2' + \frac{F_2}{B} \tag{18}$$

where $\lambda_1 = 2M\pi + \sigma T_1$, $\lambda_2 = \Delta T_1 + \sigma T_1 - 2N\pi$ and M, N are integers.

The stability analysis is done using the pseudo arc length approach suggested by Nayfeh and Balachandran [8], because the algebra is very tedious, Mathematica is used extensively to find the equilibrium points. For further information, the reader is recommended to refer to Nayfeh and Balachandran [8] where the methods applicable to such problems are discussed in detail. Note that in the stability analysis $a_i = (p_i^2 + q_i^2)^{1/2}$.

Results of General Two-Mode Solution for a Rectangular Plate, With $k = 1/4$

In Fig. 2, thick solid lines represent stable equilibrium, and all other lines represent the unstable equilibrium. The solution loses stability at point 1 through a saddle node bifurcation, where $\sigma = 1.03228$, and jumps to the upper stable branch. In the unstable portion, from point 1 to point 2, one eigenvalue of the Jacobian matrix has a positive real part. At point 2, where $\sigma = 17.4508$, two eigenvalues start having positive real parts, (see enlarged portion *B*), which concludes that the solution is again unstable. The location of points 3, 4, and 5 is presented in detail in enlarged portion *A*. Point 3 is where one can observe a Hopf bifurcation with $\sigma = 4.40351$. After point 3, the equilibrium points assume a stable solution until point 4 is reached with $\sigma = 4.40016$. At point 4, due to a saddle-node bifurcation, the equilibrium points again lose stability and a jump occurs to the lower branch. At point 5, where $\sigma = 4.40339$ the number of eigenvalues that have positive real parts increases to three which means that it is a Hopf bifurcation point. In enlarged portion *C*, at point 6, due to a Pitchfork bifurcation the system loses stability. The unstable branch has one eigenvalue with a positive real part. The external resonance detuning parameter, σ, is -0.05085. Although in Fig. 2 only first mode's amplitude, a_1, is drawn, the picture will be complete if it is evaluated with Fig. 3, where the frequency response curve of the second mode is given. Note that equally numbered points correspond to each other.

The stability of the equilibrium points versus excitation amplitude is presented for a rectangular geometry in Fig. 4. The excitation of the second mode is not zero. At point 1, where $F_1 = 75.3654$, system loses stability through a saddle-node bifurcation and jumps to the upper branch. On the stable branch, after point 1, one of the eigenvalues of the Jacobian matrix assumes a positive real part. As the excitation amplitude decreases to $F_1 = 15.7078$, where point 2 is met, the system again assumes a stable solution through a saddle-node bifurcation. At point 3, with $F_1 = 19.5179$, a Hopf bifurcation is observed. Between points 3 and 4 there exist two eigenvalues with positive real parts. When point 4 is reached, again due to a Hopf bifurcation the equilibrium points are stable. At point 4, the excitation amplitude F_1 assumes a value of 47.3177. A detailed figure for the critical points is given in enlarged portion *A*.

Acknowledgments

Funding for this research has been provided by Bogazici University Research Fund Grant No: 98A601 and National Science Foundation. The authors would like to thank Dr. A. H. Nayfeh and Dr. C. M. Chin for their helpful suggestions.

References

[1] Chu, H., and Herrmann, G., 1956, ''Influence of Large Amplitudes on Free Flexural Vibrations of Rectangular Elastic Plates,'' ASME J. Appl. Mech., **23**, pp. 532–540.

[2] Yang, X. L., and Sethna, P. R., 1991, ''Local and Global Bifurcations in Parametrically Excited Vibrations of Nearly Square Plates,'' Int. J. Non-Linear Mech., **26**, No. 2, pp. 199–220.

[3] Yang, X. L., and Sethna, P. R., 1992, ''Non-linear Phenomena in Forced Vibrations of a Nearly Square Plate: Antisymmetric Case,'' J. Sound Vib., **155**, No. 3, pp. 413–441.

[4] Chang, S. I., Bajaj, A. K., and Krousgrill, C. M., 1993, ''Nonlinear Vibrations and Chaos in Harmonically Excited Rectangular Plates With One-to-One Internal Resonance,'' Nonlinear Dyn., **4**, pp. 433–460.

[5] Elbeyli, O., 1998, ''The Nonlinear Response of Simply Supported Rectangular Metallic Plate to Transverse Harmonic Excitations,'' M.S. thesis, Bogazici University, Istanbul.

[6] Nayfeh, A. H., and Mook, D. T., 1993, *Nonlinear Oscillations*, John Wiley and Sons, New York.

[7] Anlas, G., 1999, ''Effect of Two-to-One Internal Resonance in a Nonlinearly Restrained Fluid Valve,'' ASME J. Vibr. Acoust., **121**, No. 1, pp. 59–63.

[8] Nayfeh, A. H., and Balachandran, B. 1995, *Applied Nonlinear Dynamics*, John Wiley and Sons, New York.

Capillary Instability of a Cylindrical Jet With an Elastic Shroud: A Model for the Breakup of an Oxidized Metal Jet

H. Haj-Hariri
Professor, Department of Mechanical and Aerospace Engineering, University of Virginia, Charlottesville, VA 22903

D. Poulikakos
Professor, Fellow ASME, Institute of Energy Technology, Swiss Federal Institute of Technology, ETH-Zentrum, CH-8092 Zurich, Switzerland

Stability of an inviscid axisymmetric jet of uniform surface tension and flexural rigidity is investigated. It is shown that for large enough values of flexural rigidity the capillary instabilities are suppressed. The result corroborates the observed stabilization

Contributed by the Applied Mechanics Division of THE AMERICAN SOCIETY OF MECHANICAL ENGINEERS for publication in the ASME JOURNAL OF APPLIED MECHANICS. Manuscript received and accepted by the ASME Applied Mechanics Division, June 30, 1999; final revision, May 5, 2000. Associate Technical Editor: R. C. Benson.

and possible non-breakup of solder jets in the presence of atmospheric oxygen, which causes the appearance of a layer of oxides on the interface. The work is timely because of its direct relevance to a host of emerging technologies exemplified by solder jetting in the manufacturing of microelectronic components.
[S0021-8936(00)01203-4]

1 Motivation and Introduction

Physical phenomena involving droplet generation and transport mechanisms are of central importance in today's science and technology. Examples of today's leading technologies in this area range from chemical and pharmaceutical, to power/energy and environmental technologies. Examples of emerging novel technologies are manufacturing and cooling of electronics and microelectronics, the processing of new materials with advanced properties, biotechnologies, and micro and nanoscale technologies. The present work investigates an unexplored aspect of the basic problem of monodispersed droplet generation by oscillation and breakup of a liquid jet. It is an aspect relevant to surface oxidation of liquid metal jets, and directly applicable to a novel micromanufacturing process referred to as solder jetting. This process targets to dispense picoliter quantities (droplets) of solder at high generation rates for the mounting of micro-electronic components (Hayes and Wallace [1]). With this process, molten droplets are applied directly to the bonding pads of a semiconductor die (or chip) using a technique similar to ink-jet printing. Solidified droplets after impact are then used to bond the die to a substrate or circuit board. Another relevant technology is metal spray and droplet deposition in micro-casting and advanced coating processes. The state of the art in this technology was recently reviewed by Poulikakos and Waldvogel [2].

From the point of view of fluid dynamics, the problem of interest in this work is the dynamics of a molten-solder jet, or molten-metal jet, whose capillary breakup creates the desired droplets. Even when shrouded by a sheath of inert gas, the jet is susceptible to surface oxidation. The inert gas environment can at best only limit the oxidation process. Such oxidation leads to a new morphology of the interface. One dynamic aspect of the oxidized interface, which is the focus of the present contribution, is the added elasticity and the attendant flexural stiffness of the interface. This very aspect is the central point of the present work. It is our goal to develop an understanding of the role of these effects on the capillary breakup characteristics of the jet. Thus we investigate the stability of an inviscid axisymmetric jet of uniform surface tension and flexural rigidity. It is shown that for large enough values of flexural rigidity the capillary instabilities are suppressed. The result corroborates the observed stabilization and possible non-breakup of solder jets in the presence of atmospheric oxygen, which causes the appearance of a layer of oxides on the interface.

It should be noted that we are aware of only one other (semi-)analytical study which attempts to investigate the role of oxidation on the instability of a molten-metal jet (Artemev and Kochetov [3]). While that study mostly focuses on the development of a model for the oxidation process, its treatment of the surface rigidity is rather primitive, and amounts to retaining only the last term on the left-hand side of Eq. (3) below in order to capture the elastic effects; thus missing a major portion of the contribution of the flexural stiffness to the stabilization.

Whereas the algebraic manipulations below follow closely Rayleigh's original derivations, the main contribution is the particular form of the dynamic boundary condition in Eq. (3) below, as well as noting the relevance, and hence the need for a quantitative understanding, of this physical problem.

This problem constitutes the first step in modeling the influence of surface oxidation on the capillary breakup of a jet of molten metal. The work is timely because of its direct relevance to a host of emerging technologies exemplified by solder jetting in the manufacturing of microelectronic components.

2 Problem Definition

The problem to be studied is now defined. Consider the capillary instability of a cylindrical jet of an ideal fluid having a surface tension, γ, and a surface rigidity, D, described further below. The radius of the jet is a. In what follows, both γ and D are assumed to be uniform in the azimuthal direction, θ. Furthermore, they are taken as uniform in the axial direction, x, as well, in order to simplify the analysis. Physically, the assumption of axial uniformity is justified based on the observations of the phenomenon. In the case of solder, a monolayer of tin oxide forms very rapidly (practically immediately) after the exit from the orifice. The mechanism of the monolayer formation is oxygen adsorption. Thereafter, the oxidation slows down and diffusion assumes an important role, hence the thickness of the shell does not vary very much, and the axial uniformity assumption holds (Ricci, Castello, and Passerone [4]). The assumption of azimuthal uniformity of γ and D follows from the observation that such distributions result in the least stable behavior of the jet.

It is expected that viscous effects do not play a primary role in the breakup dynamics of thin molten-metal jets, due to the high Reynolds number of the flow which is due in turn to the high speed of the flow and the low kinematic viscosity of the material. Therefore, the jet flow is assumed to be an ideal flow in the current analysis.

3 Base-State Solution

In the frame moving at the uniform speed of the slug jet profile the basic-state pressure and velocity for the incompressible, ideal flow, are respectively,

$$P=\frac{\gamma}{a},\quad \mathbf{U}=0.$$

4 Perturbed-State Governing Equations

Small, linear perturbations to the above basic state are governed by the following restrictions of the Euler and continuity equations:

$$\rho\frac{\partial\mathbf{u}}{\partial t}=-\nabla p,\quad \nabla\cdot\mathbf{u}=0,$$

wherein ρ, $\mathbf{u}(x,r,\theta,t)$, and $p(x,r,\theta,t)$ denote the constant density, and the perturbation to the velocity and pressure, while r and t denote the radial coordinate and time, respectively. Combining the above equations yields

$$\nabla^2 p=0,$$

i.e., p is harmonic.

Interfacial conditions (linearized) are needed on $r=a$ in order to complete the formulation. The kinematic condition for this ideal flow is simply

$$\frac{\partial u_r}{\partial t}=\zeta,$$

where subscript r denotes the radial component, and ζ $(=\zeta(x,\theta,t))$ is the local perturbation to the shape of the jet. The second and final condition is the dynamic condition on the interface, which requires that the pressure perturbation, p, of the jet, just below the interface, be balanced solely by the surface tension and rigidity of the interface.

In the absence of surface-tension (membrane) effects, shape perturbations of a pressurized elastic cylindrical shell of radius a are governed by

$$D\nabla^4\left(\frac{1}{a^2}+\nabla^2\right)^2\zeta+\frac{Eh}{a^2}\zeta''''=\nabla^4 p, \tag{1}$$

where E is the Young's modulus, h is the uniform shell thickness, and D is the so-called flexural rigidity, defined as

$$D \equiv \frac{Eh^3}{12(1-\nu^2)},$$

with ν denoting the Poisson's ratio of the shell. Equation (1) is the isotropic limit of the general case which was studied in Simmonds [5]. On the other hand, in the absence of elastic effects, if solely the capillary effects are considered, a simple analysis shows (cf. Drazin and Reid [6])

$$-\gamma\left(\frac{\zeta}{a^2}+\nabla^2\zeta\right)=p. \tag{2}$$

Given the linearity of the analysis, Eqs. (1) and (2) can be combined in the leading order as follows:

$$\underline{-\gamma\nabla^4\left(\frac{\zeta}{a^2}+\nabla^2\zeta\right)}+D\nabla^4\left(\frac{1}{a^2}+\nabla^2\right)^2\zeta+\frac{Eh}{a^2}\zeta'''=\nabla^4 p. \tag{3}$$

The form of the underlined term is selected so as to ensure the correct form of the dispersion relation in the linear limit. The operator ∇^4 is added in front of the underlined term in order to cancel the same in front of p in the right-hand side, in the limit $E=0$. As an aside, the origin of the a^{-2} term is the curvature of the unperturbed interface.

5 Perturbed-State Governing Solution

Modal expansions are assumed for all quantities as follows:

$$(\mathbf{u},p,\zeta)=(\hat{\mathbf{u}}(r),\hat{p}(r),\hat{\zeta})e^{st+\iota(kx+n\theta)}.$$

Subsequently dropping the carets, the solutions to the Euler and continuity equations are given as

$$p(r)=AI_n(kr),$$

$$\mathbf{u}(r)=\frac{A}{\rho s}\left[\iota kI_n(kr),kI_n'(kr),\frac{\iota n}{r}I_n(kr)\right],$$

where I_n denotes the modified Bessel function of order n of the first kind.

Using the above forms for p and u_r, the kinematic and dynamic boundary conditions read, respectively, as

$$-\frac{AkI_n'(ak)}{\rho s}=s\zeta,$$

$$\left\{-\gamma\left[\left(-k^2-\frac{n^2}{a^2}\right)^2\left(\frac{1}{a^2}-k^2-\frac{n^2}{a^2}\right)\right]+D\left(-k^2-\frac{n^2}{a^2}\right)^2\left(\frac{1}{a^2}-k^2-\frac{n^2}{a^2}\right)^2+\frac{Eh}{a^2}k^4\right\}\zeta=\left(-k^2-\frac{n^2}{a^2}\right)^2 AI_n(ka).$$

Eliminating ζ between the above two equations and dividing the result by a^4 (and defining the dimensionless wave number, α $(\equiv ak)$), one obtains the following dispersion relation for the temporal growth rate, s, of the disturbances:

$$\left[-\frac{\gamma}{a^2}(\alpha^2+n^2)^2(1-\alpha^2-n^2)+\frac{D}{a^4}(\alpha^2+n^2)^2(1-\alpha^2-n^2)^2+\frac{Eh}{a^2}\alpha^4\right]\left(-\frac{\alpha I_n'(\alpha)}{\rho a s^2}\right)=(\alpha^2+n^2)^2 I_n(\alpha).$$

Solving for the growth rate, s, and rearranging to cast the result in dimensionless form, one obtains

$$\frac{s^2}{\gamma/(\rho a^3)}=\left[\frac{\alpha I_n'(\alpha)}{I_n(\alpha)}(1-\alpha^2-n^2)\right]-\frac{Ea}{\gamma}\left[\frac{h}{a}\frac{\alpha I_n'(\alpha)}{I_n(\alpha)}\times\left[\frac{(h/a)^2}{12(1-\nu^2)}(1-\alpha^2-n^2)^2+\frac{\alpha^4}{(\alpha^2+n^2)^2}\right]\right]. \tag{4}$$

6 Discussion

Instability results if there exists a root of s which possesses a positive real part. In the classic limit of $Ea/\gamma=0$ it is seen clearly that the growth rate is given by Rayleigh's original expression:

$$s^2=\gamma\left[\frac{1}{a^3\rho}\frac{\alpha I_n'(\alpha)}{I_n(\alpha)}(1-\alpha^2-n^2)\right].$$

Thus, in the absence of surface rigidity $(E=0)$ all long-wave axisymmetric modes $(n=0)$ with dimensionless wave number, α, less than unity are unstable. The introduction of rigidity $(E\neq 0)$ reduces the growth rate and will eventually render the problem fully damped, even for the long-wave disturbances. The stabilization follows from the positivity of the coefficient of E in Eq. (4). Therefore, a molten-metal jet whose oxidized interface builds up rapidly enough in the downstream direction will become stable to capillary breakup.

Acknowledgments

HHH acknowledges support of the NASA Microgravity Fluid Physics Program.

References

[1] Hayes, D. J., and Wallace, D. B., 1998, ''Solder Jet Printing: Wafer Bumping and CSP Applications,'' Chip Scale Review, **2**, pp. 75–80.

[2] Poulikakos, D., and Waldvogel, J. M., 1996, ''Heat Transfer and Fluid Dynamics in the Process of Spray Deposition,'' Adv. Heat Transfer, **28**, pp. 1–73.

[3] Artemev, B. V., and Kochetov, S. G., 1991, ''Capillary Breakup of a Liquid-Metal Jet in an Oxidizing Medium,'' J. Eng. Phys., **60**, pp. 425–429.

[4] Ricci, E., Castello, P., and Passerone, A., 1994, ''Liquid Metal Surface Tension Measurements: A Kinetic-Fluodynamic Model of Surface Oxygen Availability,'' Mater. Sci. Eng., **A178**, pp. 99–104.

[5] Simmonds, J. G., 1966, ''A Set of Simple, Accurate Equations for Circular Cylindrical Elastic Shells,'' Int. J. Solids Struct., **2**, pp. 525–541.

[6] Drazin, P. G., and Reid, W. H., 1981, *Hydrodynamic Stability*, Cambridge University Press, Cambridge, UK.

Love's Stress Function for Torsionless Axisymmetric Deformation of Elastically Isotropic Bodies With Body Forces

J. G. Simmonds

Fellow ASME, Department of Civil Engineering, University of Virginia, Charlottesville, VA 22903

This note shows that the axisymmetric deformation of an elastically isotropic solid of revolution, subject to both axial and radial body forces, may be described in terms of Love's stress function, provided certain simple terms are added to the displacement-stress function relations. [S0021-8936(00)01003-5]

Contributed by the Applied Mechanics Division of THE AMERICAN SOCIETY OF MECHANICAL ENGINEERS for publication in the ASME JOURNAL OF APPLIED MECHANICS. Manuscript received by the ASME Applied Mechanics Division, Nov. 19, 1999; final revision, May 5, 2000. Associate Technical Editor: J. R. Barber.

Let (r, θ, z) denote the standard set of polar cylindrical coordinates. This note was inspired by the statement on p. 197 of Fung [1] that, in the linear theory of elastically isotropic axisymmetric bodies under axisymmetric loads, a body force p_z in the z-direction is ... ''the only non-vanishing component that can be treated by [Love's stress] function.''[1] This statement is based on the observation that the z-component of the Galerkin vector satisfies the inhomogeneous biharmonic equation

$$(1-\nu)\nabla^4 F_z = -p_z \tag{1}$$

and that the auxiliary equations for the physical components (σ_r, σ_θ, σ_z, τ) of the axisymmetric stress tensor have the same form as those given by Love [2] on p. 276 in terms of a stress function χ. In (1), $\nabla^2 = \partial^2/\partial r^2 + r^{-1}\partial/\partial r + \partial^2/\partial z^2$ is the axisymmetric Laplacian and ν is Poisson's ratio. Fung's remark might suggest that the only way to treat an axisymmetric radial body force p_r is to introduce the radial component F_r of the Galerkin vector. This, in turn, would lead to an additional nonhomogeneous biharmonic equation to solve.

The present note gives a simpler alternative for treating radial body forces. I show that the introduction of a *radial load potential*

$$\Theta = \int\int p_r dr dz, \tag{2}$$

and a slight modification of the expressions given by Love for the radial and axial displacement components u and w lead to the nonhomogeneous biharmonic equation

$$(1-\nu)\nabla^4 \chi = -p_z + (1-2\nu)\nabla^2\Theta + \Theta_{,zz}, \tag{3}$$

where a comma followed by a subscript denotes differentiation with respect to that subscript . If p_r (and hence Θ) vanish, (3) reduces to (1).

The key step in accommodating radial as well as axial body forces is to modify the second of the two equations (66) on p. 276 of Love [2] by adding a certain load term. Thus, I set

$$\begin{aligned} Eu &= -(1+\nu)\chi_{,rz}, \\ Ew &= (1+\nu)[2(1-\nu)\nabla^2\chi - \chi_{,zz} - 2(1-2\nu)\Theta], \end{aligned} \tag{4}$$

where E is Young's modulus. From these equations, the strain-displacement relations,

$$e_r = u_{,r}, \quad e_\theta = r^{-1}u, \quad e_z = w_{,z}, \quad \gamma = u_{,z} + w_{,r}, \tag{5}$$

and the stress-strain relations,

$$\begin{aligned} (1+\nu)\begin{Bmatrix} \sigma_r \\ \sigma_\theta \\ \sigma_z \end{Bmatrix} &= \frac{\nu E}{1-2\nu}(e_r + e_\theta + e_z) + E\begin{Bmatrix} e_r \\ e_\theta \\ e_z \end{Bmatrix}, \\ 2(1+\nu)\tau &= E\gamma, \end{aligned} \tag{6}$$

([3], p. 11) follow the stress-stress function representations

$$\sigma_r = (\nu\nabla^2\chi - \chi_{,rr} - 2\nu\Theta)_{,z} \tag{7}$$

$$\sigma_\theta = (\nu\nabla^2\chi - r^{-1}\chi_{,r} - 2\nu\Theta)_{,z} \tag{8}$$

$$\sigma_z = [(2-\nu)\nabla^2\chi - \chi_{,zz} - 2(1-\nu)\Theta]_{,z} \tag{9}$$

$$\tau = [(1-\nu)\nabla^2\chi - \chi_{,zz} - (1-2\nu)\Theta]_{,r}. \tag{10}$$

Of course, these expressions reduce to Love's if the body forces vanish.

All that remains is to satisfy the two equilibrium equations in the radial and axial directions:

$$\sigma_{r,r} + \tau_{,z} + r^{-1}(\sigma_r - \sigma_\theta) + p_r = 0, \quad \tau_{,r} + \sigma_{z,z} + r^{-1}\tau + p_z = 0. \tag{11}$$

[1]Fung calls this a ''strain'' function.

It is readily verified using (7–11) that $(11)_1$ is satisfied identically, whereas $(11)_2$ reduces to (3).

References

[1] Fung, Y. C., 1965, *Foundations of Solid Mechanics*, Prentice-Hall, Englewood Cliffs, NJ.
[2] Love, A. E. H., 1944, *A Treatise on the Mathematical Theory of Elasticity*, Dover, New York.
[3] Timoshenko, S. P., and Goodier, J. N., 1970, *Theory of Elasticity*, 3rd Ed., McGraw-Hill, New York.

Proper Boundary Conditions for Infinitely Layered Orthotropic Media

E. L. Bonnaud
Graduate Student

J. M. Neumeister
Associate Professor

Department of Solid Mechanics, Royal Institute of Technology, S-100 44 Stockholm, Sweden

A stress analysis of a plane infinitely layered medium subjected to surface loadings is performed using Airy stress functions, integral transforms, and a revised transfer matrix approach. Proper boundary conditions at infinity are for the first time established, which reduces the problem size by one half. Methods and approximations are also presented to enable numerical treatment and to overcome difficulties inherent to such formulations.
[S0021-8936(00)01103-X]

1 Introduction

Layered media, and their analysis are important in many technical applications: e.g., microelectronic components, sandwich structures, structural composite materials, or soil layers. Laminated composites consist of different elastic layers, often individually orthotropic, but can from a structural mechanics point of view be sufficiently well described with homogenized elastic properties ([1,2]). However, detailed stress fields in individual layers close to highly loaded regions are still necessary for, e.g., failure analysis. For a fair picture of elastic responses, standard finite element methods are sufficient but for a large number of layers, for high stress gradients and singularities, etc., analytical and semi-analytical methods still have advantages. Generally, integral transforms render layerwise four coefficients and thus systems with p layers require determination of $4p$ unknowns. The stiffness or flexibility matrix approach uses layer strains or stresses as state variables giving a system of $2p$ simultaneously linear equations ([3–5]). Another method, the transfer matrix approach, step by step eliminates the unknowns for intermediate layers. Final equations to be solved involve only layers with boundary conditions prescribed ([6–8]).

In previous work, semi-infinite systems are modeled as a finite number of layers on semi-infinite half-planes which, using the transfer matrix method, leads to a linear system of eight equations. Here, proper far-field boundary conditions for periodic infinitely

Contributed by the Applied Mechanics Division of THE AMERICAN SOCIETY OF MECHANICAL ENGINEERS for publication in the JOURNAL OF APPLIED MECHANICS. Manuscript received by the ASME Applied Mechanics Division, Nov. 16, 1999; final revision, Apr. 21, 2000. Associate Technical Editor: J. R. Barber.

layered systems are presented based on the transfer matrix approach, which reduces the number of equations to four. More details of the analysis can be found elsewhere ([9]).

2 Airy Stress Functions and One-Dimensional Fourier Transform

Solutions to plane boundary value problems are readily expressed with the Airy stress function $\varphi(x,y)$ fulfilling a fourth-order PDE. With boundaries and axes of orthotropy (1 and 2) coinciding with x and y-coordinates (Fig. 1), a one-dimensional Fourier transform (with respect to x) results in an ODE (in y) for the transformed stress function $\Phi(\xi,y)$, the solution to which is ([1])

$$\Phi_{\text{ortho}}(\xi,y)=a(\xi)e^{-\alpha|\xi|y}+b(\xi)e^{-\beta|\xi|y}+c(\xi)e^{\alpha|\xi|y}+d(\xi)e^{\beta|\xi|y} \tag{1a}$$

$$\Phi_{\text{iso}}(\xi,y)=[a(\xi)+b(\xi)y]e^{-|\xi|y}+[c(\xi)+d(\xi)y]e^{|\xi|y}. \tag{1b}$$

Only for the orthotropic case, the solution depends on elastic constants through α and β (see Eqs. (*A*1)). The coefficients $a(\xi)$, $b(\xi)$, $c(\xi)$, $d(\xi)$ are functions of the transform variable ξ; they are determined by transformed boundary conditions imposed on transformed stresses $\Sigma_y(\xi,y)$, $\Sigma_{xy}(\xi,y)$ (but not $\Sigma_x(\xi,y)$) or on transformed displacements $U(\xi,y)$ and $V(\xi,y)$ (see Eqs. (*A*2)).

3 Continuity, Boundary, and Infinity Conditions

A local coordinate system (x,y) is used in each layer where the y-coordinate always measures the distance from each respective layer top (see Fig. 1). Continuity between layer i and $i+1$ implies that real, and thus transformed, values of both stresses with y-components and displacements remain unchanged over a bonded interface. With these collected in a vector state $S_i(\xi,y)=[\Sigma_y(\xi,y),\Sigma_{xy}(\xi,y),U(\xi,y),V(\xi,y)]_i^T$ continuity reads

$$S_i(\xi,y=t_i)=S_{i+1}(\xi,y=0), \tag{2}$$

where t_i is the thickness of layer i. Collecting the sought for coefficients in a vector $K_i(\xi)=[a(\xi),b(\xi),c(\xi),d(\xi)]_i^T$, $S_i(\xi,y)$ is rewritten as $S_i(\xi,y)=\mathbf{Q}_i(\xi,y)K_i(\xi)$ (see Eqs. (*A*5), (*A*6) and (*A*7) for explicit expressions for $\mathbf{Q}_i(\xi,y)$). After solving for $K_{i+1}(\xi)$ in Eq. (2), the continuity condition reads

$$K_{i+1}(\xi)=\mathbf{Q}_{i+1}^{-1}(\xi,y=0)\mathbf{Q}_i(\xi,y=t_i)K_i(\xi)\equiv\mathbf{M}_i(\xi)K_i(\xi). \tag{3}$$

Equation (3) defines the transfer matrix $\mathbf{M}_i(\xi)$ used here, which is slightly different compared to previous work ([6–8]). With the choice of local coordinates, all transfer matrices depend on only layer properties and not of layer position which is essential here. For any other layer $i+p$, repetitive use of Eq. (3) leads to

$$K_{i+p}(\xi)=[\mathbf{M}_{i+p-1}(\xi)\ \ldots\ \mathbf{M}_i(\xi)]K_i(\xi). \tag{4}$$

These four equations and eight unknowns together with four boundary conditions need only to be solved for finite stackings. For semi-infinite layered media, boundary conditions at both the surface and infinity can be expressed involving only the first layer set of coefficients which reduces the size of the system to four.

Two boundary conditions are prescribed at the top layer surface, expressing Fourier transforms of applied tensile and shear stresses $\Sigma_y(\xi,y=0)=\Sigma_y^s(\xi)$ and $\Sigma_{xy}(\xi,y=0)=\Sigma_{xy}^s(\xi)$.

In semi-infinite periodic layered media (repetitive units with q layers, see Fig. 1) the coefficients in layers 1 and $1+mq$ can be related to each other through repetitive use of Eq. (4). After diagonalization of the multiple layer transfer matrix $[\mathbf{M}_q(\xi)\ \ldots\ \mathbf{M}_1(\xi)]$, this gives

$$\begin{aligned}K_{1+mq}(\xi)&=[\mathbf{M}_q(\xi)\ \ldots\ \mathbf{M}_1(\xi)]^mK_1(\xi)\\&=\mathbf{P}_1(\xi)\mathbf{D}_1^m(\xi)\mathbf{P}_1^{-1}(\xi)K_1(\xi).\end{aligned} \tag{5}$$

This $[\mathbf{M}_q(\xi)\ \ldots\ \mathbf{M}_1(\xi)]$ matrix has unity determinant ([8]). Its four eigenvalues λ_i, positive and reciprocal in pairs, are collected in descending order in the diagonalized matrix $\mathbf{D}_1(\xi)$ so that $\lambda_1>\lambda_2>1/\lambda_2>1/\lambda_1$. In subsurface layers stresses must be limited (as m increases) and thus the corresponding set of coefficients $K_{1+mq}(\xi)$ must be bounded since $\Phi_{1+mq}(\xi,y)$ is expressed in local coordinates, cf. Eqs. (1),(2). This implies that all terms involving λ_1 and λ_2 must vanish since λ^m increases indefinitely with m for $\lambda>1$. This, in turn, gives the sought for conditions for the top layer coefficients K_1 expressing infinity condition for a layered half-plane: The first two components in the vector $\mathbf{P}_1^{-1}(\xi)K_1(\xi)$ of Eq. (5) must be zero. With $L_1(\xi)$ and $L_2(\xi)$ being the first two lines in $\mathbf{P}_1^{-1}(\xi)$, these conditions read

$$L_1(\xi)K_1(\xi)=0 \tag{6a}$$

$$L_2(\xi)K_1(\xi)=0. \tag{6b}$$

With l additional layers on top of a repetitive unit, $K_{l+1}(\xi)$ is first related to $K_1(\xi)$ through Eq. (4) and replaced in Eqs. (6*a*,*b*) which again poses the appropriate conditions only on $K_1(\xi)$. Also for nonperiodic stackings or media of finite thickness, the previous method is still applicable: $L_1(\xi)$ and $L_2(\xi)$ tend towards a limit as q increases since the influence of the far-field conditions on the state of the first layer diminishes with increasing q (Saint Venant's principle). Truncating at finite q corresponds to approximating the medium with an infinite sequence of q-sized unities.

With $K_1(\xi)$ known, all others $K_i(\xi)$ are determined through Eq. (4); insertion in appropriate expressions and inverse Fourier transform then gives stresses and displacements.

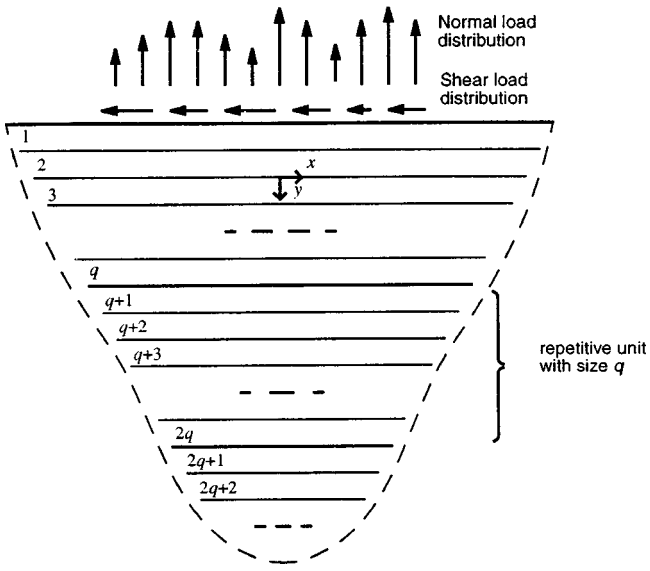

Fig. 1 Multilayered half-plane with repetitive unit of *q* layers (local coordinates (*x*,*y*) for every layer)

4 Solution and Numerical Procedure

The analysis presented above generally requires numerical treatment, which involves difficulties while extracting eigenvalues and eigenvectors due to ill-conditioned matrices ([7,10,11]). Reliable $a(\xi), b(\xi), c(\xi), d(\xi)$ values can only be obtained up to a certain limit $\xi_{\lim}$ ($\xi_{\lim}$ depends only on laminate properties) while the inverse Fourier transform requires accuracy for high ξ particularly for small x and y-values.

For small y, far from the loaded region, accuracy is not a major concern since stresses approach zero. On the other hand, accuracy becomes essential for concentrated or singular (e.g. line) loads, when also the x-distance is sufficiently small. There, in the close vicinity of a highly loaded region, the influence of the lamina thickness disappears and the solution asymptotically approaches the one of a loaded homogeneous half-plane. Such solutions are available in closed form ([12]: isotropic; [2]: orthotropic) and can additionally be integrated from $\xi_{\lim}$ up to infinity thereby avoiding truncation errors in the inverse Fourier transform. The approximation is inaccurate (in a relative sense) in regions of low significance, i.e., with low stress magnitudes while the agreement is excellent where it matters. Improved accuracy by one order of magnitude over the entire ξ-domain can further be achieved by numerically evaluating the difference between the homogeneous half-plane (hhp) and multilayered half-plane (mhp) solutions. $\Sigma^{\text{mhp}}(\xi,y)e^{-ix\xi}$ and $\Sigma^{\text{hhp}}(\xi,y)e^{-ix\xi}$ are harmonics of the real stress functions $\sigma^{\text{mhp}}(x,y)$ and $\sigma^{\text{hhp}}(x,y)$ ([6]) and both describe the same material, submitted to the same load but with different boundary conditions at $y=t_1$. The shorter the wavelength (i.e., the higher ξ), the less significant is the influence from the boundaries, i.e., the first interface. Thus, the two functions tend toward one another as ξ approaches infinity. With inverse Fourier transform F^{-1}, real stress becomes

$$\sigma^{\text{mhp}}(x,y)=\sigma^{\text{hhp}}(x,y)+F^{-1}[\Sigma^{\text{mhp}}(\xi,y)-\Sigma^{\text{hhp}}(\xi,y)]. \quad (7)$$

Stresses $\sigma^{\text{hhp}}(x,y)$ and hhp-coefficients to be inserted in $\Sigma^{\text{hhp}}(\xi,y)$ are given in Eqs. (*A*3), (*A*4).

5 Conclusion

A simple and straightforward method to formally establish the full stress solution for infinitely layered media with generally orthotropic constituents is devised. Both boundary and infinity conditions are posed on the top layer solution; hereby the size of the system to be solved reduces to four. In regions where numerical difficulties due to ill-conditioned matrices arise, they are circumvented with the aid of existing asymptotically correct homogeneous half-planes solutions. As an example, the detailed stress analysis of a cross-ply laminate subjected to tensile and tangential line loads is presented in an extended report by [9].

Acknowledgment

This project is financed by faculty funding from the Royal Institute of Technology, Sweden. The authors would like to express their sincere gratitude to Prof. Peter Gudmundson for many valuable ideas and comments.

Appendix

Orthotropic constitutive equation and coefficients:

$$\begin{bmatrix}\varepsilon_x\\ \varepsilon_y\\ 2\varepsilon_{xy}\end{bmatrix}=\begin{bmatrix}s_{11}&s_{12}&0\\ s_{21}&s_{22}&0\\ 0&0&s_{66}\end{bmatrix}\begin{bmatrix}\sigma_x\\ \sigma_y\\ \tau_{xy}\end{bmatrix} \quad (A1)$$

$$\alpha,\beta=\sqrt{\frac{s_{66}+2s_{12}}{2s_{11}}\pm\sqrt{\left(\frac{s_{66}+2s_{12}}{2s_{11}}\right)^2-\frac{s_{22}}{s_{11}}}}$$

Real and transformed stresses and displacements:

$$\begin{cases}\sigma_x(x,y)=\dfrac{\partial^2\phi}{\partial y^2}(x,y) & \Sigma_x(\xi,y)=\dfrac{d^2\Phi}{dy^2}(\xi,y)\\ \sigma_y(x,y)=\dfrac{\partial^2\phi}{\partial x^2}(x,y) & \Sigma_y(\xi,y)=-\xi^2\Phi(\xi,y)\\ \tau_{xy}(x,y)=\dfrac{\partial^2\phi}{\partial x\partial y}(x,y) & \Sigma_{xy}(\xi,y)=-i\xi\dfrac{d\Phi}{dy}(\xi,y)\\ U(\xi,y)=-i\left(\dfrac{s_{11}}{\xi}\dfrac{d^2\Phi}{dy^2}(\xi,y)-s_{11}\xi\Phi(\xi,y)\right)\\ V(\xi,y)=\dfrac{s_{11}}{\xi^2}\dfrac{d^3\Phi}{dy^3}(\xi,y)-(s_{66}+s_{12})\dfrac{d\Phi}{dy}(\xi,y)\end{cases} \quad (A2)$$

Homogeneous half-plane stresses (with $\sigma_y^s(s)$ and $\tau_{xy}^s(s)$ prescribed surface stresses):

$$\begin{cases}\sigma_x^{\text{hhp}}(x,y)=\dfrac{\alpha+\beta}{\pi}\displaystyle\int_{-\infty}^{\infty}\frac{[\alpha\beta y\sigma_y^s(s)+(x-s)\tau_{xy}^s(s)](x-s)^2}{[(\alpha y)^2+(x-s)^2][(\alpha y)^2+(x-s)^2]}ds\\ \sigma_y^{\text{hhp}}(x,y)=\dfrac{\alpha+\beta}{\pi}y^2\displaystyle\int_{-\infty}^{\infty}\frac{\alpha\beta y\sigma_y^s(s)+(x-s)\tau_{xy}^s(s)}{[(\alpha y)^2+(x-s)^2][(\alpha y)^2+(x-s)^2]}ds\\ \tau_{xy}^{\text{hhp}}(x,y)=\dfrac{\alpha+\beta}{\pi}y\displaystyle\int_{-\infty}^{\infty}\frac{[\alpha\beta y\sigma_y^s(s)+(x-s)\tau_{xy}^s(s)](x-s)}{[(\alpha y)^2+(x-s)^2][(\alpha y)^2+(x-s)^2]}ds\end{cases} \quad (A3)$$

Coefficients for a homogeneous half-plane:

$$a^{\text{hhp}}(\xi)=\frac{\beta\Sigma_y^s(\xi)-i\,\text{sgn}(\xi)\Sigma_{xy}^s(\xi)}{(\beta-\alpha)\xi^2}\quad b^{\text{hhp}}(\xi)=\frac{\alpha\Sigma_y^s(\xi)-i\,\text{sgn}(\xi)\Sigma_{xy}^s(\xi)}{(\beta-\alpha)\xi^2}\quad c^{\text{hhp}}(\xi)=d^{\text{hhp}}(\xi)=0 \quad (A4)$$

Matrix relating state vector S_i to coefficient vector K_i:

$$\mathbf{Q}_i(\xi,y)=\mathbf{C}_i(\xi,y)\mathbf{D}_i(\xi,y)\mathbf{E}_i(\xi,y) \quad (A5)$$

Orthotropic case:

$$\begin{cases} \mathbf{C}_i(\xi)=\mathrm{diag}(-\xi^2, i\xi|\xi|, -i\xi, -|\xi|) & \mathbf{E}_i(\xi,y)=\mathrm{diag}(e^{-\alpha|\xi|y}, e^{-\beta|\xi|y}, e^{\alpha|\xi|y}, e^{\beta|\xi|y}) \\ \mathbf{D}_i=\begin{bmatrix} 1 & 1 & 1 & 1 \\ \alpha & \beta & -\alpha & -\beta \\ f_1(\alpha) & f_1(\beta) & f_1(\alpha) & f_1(\beta) \\ g_1(\alpha) & g_1(\beta) & -g_1(\alpha) & -g_1(\beta) \end{bmatrix} & \begin{array}{l} f_1(\gamma)=s_{11}\gamma^2-s_{12} \\ g_1(\gamma)=s_{11}\gamma^3-(s_{12}+s_{66})\gamma \\ (\gamma\in\{\alpha,\beta\}) \end{array} \end{cases} \tag{A6}$$

Isotropic case:

$$\begin{cases} \mathbf{C}_i(\xi,y)=\mathrm{diag}(-|\xi|, i\xi, -i\,\mathrm{sgn}(\xi), -1) & \mathbf{E}_i(\xi,y)=\mathrm{diag}(e^{-\alpha|\xi|y}, e^{-\beta|\xi|y}, e^{\alpha|\xi|y}, e^{\beta|\xi|y}) \\ \mathbf{D}_i(\xi,y)=\begin{bmatrix} 1 & |\xi|y & 1 & |\xi|y \\ 1 & f_2(y) & -1 & f_2(-y) \\ k_2 & g_2(y) & k_2 & -g_2(-y) \\ l_2 & h_2(y) & -l_2 & h_2(-y) \end{bmatrix} & \begin{array}{l} k_2=s_{11}-s_{12} \\ l_2=s_{11}-(s_{12}+s_{66}) \\ f_2(y)=|\xi|y-1 \\ g_2(y)=(s_{11}-s_{12})|\xi|y-2s_{11} \\ h_2(y)=s_{11}(|\xi|y-3)-(s_{12}+s_{66})(|\xi|y-1) \end{array} \end{cases} \tag{A7}$$

References

[1] Lekhnitsky, S. G., 1968, *Anisotropic Plates*, Gordon and Breach, New York (English translation by S. W. Tsai and T. Cheron).
[2] Bjarnehed, H. L., 1991, ''Rigid Punch on Stressed Orthotropic Half-Plane With Partial Slip,'' ASME J. Appl. Mech., **58**, No. 1, pp. 128–133; Erratum, *ibid.*, 1991, **58**, No. 2, p. 565.
[3] Choi, H. J., and Thangjitham, S., 1991, ''Micro- and Macromechanical Stress and Failure Analyses of Laminated Composites,'' Compos. Sci. Technol., **40**, pp. 289–305.
[4] Choi, H. J., and Thangjitham, S., 1991, ''Stress Analysis of Multilayered Anisotropic Elastic Media,'' ASME J. Appl. Mech., **58**, pp. 382–387.
[5] Small, J. C., and Booker, J. R., 1984, ''Finite Layer Analysis of Layered Elastic Materials Using a Flexibility Approach, Part 1—Strip Loadings,'' Int. J. Numer. Methods Eng., **20**, pp. 1025–1037.
[6] Bufler, H., 1971, ''Theory of Elasticity of a Multilayered Medium,'' J. Elast., **1**, pp. 125–143.
[7] Bahar, L. Y., 1972, ''Transfer Matrix Approach to Layererd Systems,'' J. Eng. Mech., **98**, No. EM5, pp. 1159–1172.
[8] Bahar, L. Y., 1975, ''A State Space Approach to Elasticity,'' J. Franklin Inst., **229**, pp. 34–41.
[9] Bonnaud, E. L., and Neumeister, J. M., 1999, ''Stress Analysis of General Orthotropic Multilayered Systems Subjected to Surface Loading,'' Report 238. Department of Solid Mechanics, Royal Institute of Technology, Stockholm, Sweden.
[10] Chen, W. T., 1971, ''Computation of Stresses and Displacements in a Layered Elastic Medium,'' Int. J. Eng. Sci., **9**, pp. 775–800.
[11] Yue, 1995, ''On Generalized Kelvin Solutions in a Multilayered Elastic Medium,'' J. Elast., **40**, pp. 1–43.
[12] Johnson, K. L., 1985, *Contact Mechanics*, Cambridge University Press, Cambridge, UK.

Chain Reaction From Impact on Coaxial Multibody Systems

W. J. Stronge
Department of Engineering, University of Cambridge, Cambridge CB2 1PZ, UK. Mem. ASME

In a mechanism or system of ''rigid'' bodies that are joined or connected by compliant points of contact, an external impact at one point in the system generates a pulse of reaction force that propagates outward successively through neighboring joints or connections. At each point of contact between adjacent bodies, this wave of reaction force is just sufficient to change the relative velocities so that interpenetration of the bodies is prevented; i.e., the reactions enforce the displacement constraints. Each connection has a local wave speed that depends on the contact compliance and the mass of the adjacent bodies. Where the local wave speed is decreasing with ''distance'' from the external impact, the reaction impulses at neighboring contacts occur sequentially whereas if the local wave speed is increasing substantially with distance, the impulses at neighboring contacts occur simultaneously. Between these limits, the dynamics of impact of multibody systems with compliant contacts depends on coupling between time-dependent contact forces rather than some assumed timing of the resultant impulses. [S0021-8936(00)00903-X]

Contributed by the Applied Mechanics Division of THE AMERICAN SOCIETY OF MECHANICAL ENGINEERS for publication in the JOURNAL OF APPLIED MECHANICS. Manuscript received by the ASME Applied Mechanics Division, September 1, 1999; final revision, May 2, 2000. Associate Technical Editor: A. A. Ferri.

For hard bodies with nonconforming contact surfaces, impact results in very rapid changes in relative velocity of the colliding bodies as a result of large interaction forces that act in a small area of contact during a brief period of collision. When the bodies are part of a kinematic chain or mechanism, the velocity changes induce small relative displacements at other points where the colliding bodies are supported or connected to adjacent bodies; the reaction forces developed as a consequence of these small relative displacements at secondary contacts are the means of transmitting the impact process through the mechanism.

To analyze effects of impact in a multibody system of ''rigid'' bodies, some previous authors assume that impulsive reactions occur simultaneously at all points of contact; e.g., [1–3]; essentially, this is the method of rigid-body dynamics (Pars [4]). Other authors assume that in multibody dynamics the reaction impulses at points of contact occur sequentially; e.g., [5–8]. A third approach was employed by Cundall and Strack [9] and Chatterjee [10]; they used discrete element modeling of the local compliance at each contact point. With this more detailed, time-dependent analytical approach, Stronge [11,13] has shown that in a periodic system, a collision between two elements in a kinematic chain generates a wave of compression that propagates away from the impact point. This is a dispersive wave that travels at a speed which depends on the local compliance at each contact point and the inertia properties of neighboring bodies. In this periodic system the compression pulse propagating away from an impact necessarily envelopes two or more contact points at any time; i.e., pulse components with small wavelength do not propagate. To analyze these more detailed results of impact on a system of ''rigid'' bodies connected by compliant unilateral displacement constraints, it is necessary to consider two distinct scales of relative displacement. Very small relative displacements must be considered in order to obtain the time-dependent interaction forces that change the relative velocities—these displacements must be sufficiently small, however, so that they have negligible effect on inertia properties of the system. This note investigates the range of

applicability of various analytical assumptions regarding timing of reactions in an elastic multibody system where the inertia and contact compliance properties vary smoothly.

Dynamics of Chain of Rigid Bodies Connected by Compliant Contacts

Consider a collinear system of three elastic spheres B_1, B_2, B_3 such as that shown in Fig. 1; the spheres have masses M_1, M_2, M_3, respectively. At any time t the spheres are located at coordinates $X_i(t)$ and they have speeds $\dot{X}_i(t)$, $i=1,2,3$ in the axial direction. This system has kinetic energy T where

$$2T=\sum_{i=1}^{3} M_i\dot{X}_i^2. \tag{1}$$

When any pair of bodies are compressed together, contact forces act between the bodies at the points of contact $j=1,2$. These forces prevent overlap or interpenetration; if the bodies are nonconforming and have small compliance of each contact region, the forces arise from internal deformations that decrease rapidly with radial distance from the contact area between each pair of touching bodies. Because these deformations remain local to the small area of contact where a pair of nonconforming bodies touch, they cause only a very small displacement or indentation of the surface. The normal component of relative displacement or indentation at the jth contact point δ_j, which is the sum of the surface indentations of both bodies, is given by

$$\delta_j=X_{j+1}-X_j, \quad j=1,2. \tag{2}$$

If the system has no active external forces acting during the collision period, momentum is conserved and the center of mass has speed $\hat{V}=M^{-1}\Sigma_{i=1}^{3}M_i\dot{X}_i(0)$, $M=M_1+M_2+M_3$. For this system where momentum is conserved the kinetic energy can be separated into part that is invariant during the collision process and a partial kinetic energy of relative motion $T_{\rm rel}$; i.e., $T=T_{\rm rel}+0.5M\hat{V}^2$. The kinetic energy of normal relative motion $T_{\rm rel}$ is defined as

$$2T_{\rm rel}(t)\equiv\sum_{i=1}^{3} M_i[\dot{X}_i(t)-\hat{V}]^2. \tag{3}$$

At any point of contact, a part of the initial kinetic energy of normal relative motion $T_{\rm rel}(0)$ is transformed during compression into strain energy of internal deformation.

Conservation of translational momentum relative to the center of mass $0=\Sigma_{i=1}^{3}M_i(\dot{X}_i-\hat{V})$, together with (1) and (2) give

$$\begin{aligned}2T_{\rm rel}&=M^{-1}[M_1(M_2+M_3)\dot{\delta}_1^2+2M_1M_2\dot{\delta}_1\dot{\delta}_2+M_3(M_1+M_2)\dot{\delta}_2^2]\\&=\dot{z}_1^2+2\dot{z}_1\dot{z}_2\cos\alpha+\dot{z}_2^2\end{aligned} \tag{4}$$

where

$$z_1=\delta_1[M^{-1}M_1(M_2+M_3)]^{1/2}, \quad z_2=\delta_2[M^{-1}M_3(M_1+M_2)]^{1/2}. \tag{5}$$

These nondimensional variables which symmetrize the equations were suggested by Ivanov and Larina [12].

The normal contact forces F_j, $j=1,2$ which cause these relative displacements are solely compressive and they depend on the geometry of the contact region. The normal contact forces at contacts C_1 and C_2 can be expressed as

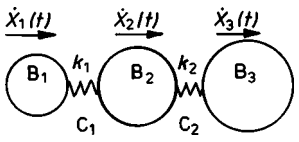

Fig. 1 Collinear system of three spheres with small local compliance at contact points

$$F_j=f(\delta_j)H(\delta_j) \quad \text{where} \quad H(\delta_j)\equiv\begin{cases}1, & \delta_j\geqslant 0\\ 0, & \delta_j<0\end{cases} \tag{6}$$

The contact force-displacement relation $f(\delta_j)$ for any contact depends on the geometry of the contact region and the contact pressure. If the bodies are elastic and contacting surfaces are spherical, the stress field is three dimensional and Hertz contact theory gives $f(\delta_j)=k_{sj}\delta_j^{3/2}$ while if the contacting surfaces are cylindrical with parallel axes, the stress field is two dimensional and $f(\delta_j)=k_{cj}\delta_j$. Here k_{sj} and k_{cj} are the stiffness coefficients at the jth contact for spherical and cylindrical contacts, respectively. These interaction forces can be derived from potential functions for either spherical contact U_s or cylindrical contact U_c.

$$(5/2)U_s=k_{s1}\delta_1^{5/2}H(\delta_1)+k_{s2}\delta_2^{5/2}H(\delta_2) \tag{7a}$$

or

$$2U_c=k_{c1}\delta_1^2H(\delta_1)+k_{c2}\delta_2^2H(\delta_2). \tag{7b}$$

The three-body system is conservative if the stresses remain elastic. Assuming that there are no changes in configuration during contact because the contact period is very small (but at the same time acknowledging that contact forces are generated by very small relative displacements), the equations of relative motion for cylindrical contacts can be obtained from (4), (5) and (7*b*) together with Lagrange's equation;

$$\begin{Bmatrix}0\\0\end{Bmatrix}=\begin{bmatrix}1 & \cos\alpha\\ \cos\alpha & 1\end{bmatrix}\begin{Bmatrix}d^2z_1/d\tau^2\\ d^2z_2/d\tau^2\end{Bmatrix}+\sin^2\alpha\begin{Bmatrix}z_1H(z_1)\\ \gamma^2z_2H(z_2)\end{Bmatrix} \tag{8}$$

where a nondimensional time τ and ratio of stiffness to mass gradients γ^2 are obtained as

$$\omega_0^2=k_1/M_2 \qquad \tau=\omega_0 t\sqrt{1+M_2/M_1}.$$

$$\cos\alpha=\sqrt{\frac{M_1M_3}{(M_1+M_2)(M_2+M_3)}}, \quad \gamma^2=\frac{k_2}{k_1}\frac{M_1(M_2+M_3)}{M_3(M_1+M_2)}. \tag{9}$$

This paper is concerned with identifying necessary conditions for multibody dynamics where accurate calculations can be obtained on the basis of an assumed order of impulsive reactions at multiple contacts; namely that reactions can be assumed to occur either sequentially or simultaneously. For this purpose, consider a system that has a smooth gradation of properties where η is the gradient of mass and κ is the gradient of stiffness; e.g., let masses $M_1=\eta^{-1}M_2$, M_2, $M_3=\eta M_2$ and stiffnesses $k_2/k_1=\kappa$. These inertia and stiffness gradients give

$$\cos\alpha=\frac{1}{1+\eta}, \quad \gamma^2=\frac{\kappa}{\eta} \tag{10}$$

where $\gamma-1$ is the gradient of wave speed and a characteristic frequency ω_0 is given by $\omega_0^2=k_1/M_2$.

In this coupled system, the question of whether reaction impulses at C_1 and C_2 are simultaneous or sequential is a manifestation of the difference in phase of response at contacts. The eigenvalues that give nondimensional frequencies of modes are

$$\frac{\omega_i^2}{\omega_0^2}=\frac{(1+\eta)(1+\gamma^2)}{2}\left\{1\pm\sqrt{1-\frac{1+\eta+\eta^2}{(1+\eta)^2}\frac{4\gamma^2}{(1+\gamma^2)^2}}\right\}. \tag{11}$$

To retrieve the velocities in an inertial frame from the nondimensional relative velocities $dz_i/d\tau$, the following relations are obtained:

$$\begin{Bmatrix}\dot{X}_1\\ \dot{X}_2\\ \dot{X}_3\end{Bmatrix}=\begin{Bmatrix}\hat{V}\\ \hat{V}\\ \hat{V}\end{Bmatrix}+\frac{1}{\sqrt{(1+\eta)(1+\eta+\eta^2)}}\begin{bmatrix}\eta(1+\eta) & \eta^{3/2}\\ -1 & \eta^{3/2}\\ -1 & -\eta^{-1/2}(1+\eta^2)\end{bmatrix}\times\begin{Bmatrix}dz_1/d\tau\\ dz_2/d\tau\end{Bmatrix}. \tag{12}$$

Equations (8) are solved numerically by means of a Runge-Kutta method of first order. For a system of initially unstressed bodies, $\delta_1 = \delta_2 = 0$. A distribution of initial velocities that represents direct collinear impact between a single body B_1 and the remainder of the chain is considered; i.e., $\dot{X}_1 = V_0$, $\dot{X}_2 = \dot{X}_3 = 0$ or $\dot{\delta}_1 / V_0 = 1$, $\dot{\delta}_2 / V_0 = 0$.

Effect of Property Gradients on Terminal Velocity Distribution

In Fig. 2 the distribution of final velocities in a three ball chain has been plotted as a function of γ^2 at two different values of the mass gradient η. Essentially, if $\gamma < 1$ the results asymptotically approach those for sequential collisions whereas if $\gamma \gg 1$ the results asymptotically approach those for simultaneous collisions. With a pair of nondimensional parameters that characterize the system γ and η, the magnitude of final velocities depend on the gradient of masses but the distribution of final velocities is not affected by the mass gradient η. The results for both cylindrical and spherical contacts converge to the same asymptotic limits; convergence is slightly faster for cylindrical contacts but the behavior is qualitatively the same.

The timing of reactions at the different contact points depends on only one parameter—the gradient of wave speed $\gamma - 1$ in the system. Figure 3 shows that if $\gamma < 1$, after impact within the system the maximum compression at the second point of contact C_2 occurs substantially later than that at C_1; i.e., the local wave speed decreases with increasing distance from the impact point. On the other hand, if $\gamma \gg 1$ maximum compression occurs almost simultaneously at C_1 and C_2. For linear compliance, maximum compression occurs simultaneously if $\gamma \cong 6.7$, and larger values of the gradient of wave speed $\gamma - 1$ result in maximum compression at the more distant contact point C_2 before maximum compression at C_1. With very large γ this occurs because the natural period of oscillation at C_2 is small in comparison with the natural period at C_1; i.e., the rapidly increasing rate of oscillation for successive contact forces in the direction of propagation is the cause of premature separation and a subsequent secondary impact at C_2.

In a collinear system of compact hard bodies with nonconforming contacts that are initially touching, impact results in a wave of compression that travels away from the point of impact. This wave travels at a speed that depends on the compliance of local deformation at each contact and the inertia of the adjacent bodies. For a periodic chain of spherical bodies composed of material with density ρ, this speed of propagation through the chain is of the order of $c \approx \sqrt{Y/\rho}$ where Y is the uniaxial yield stress.[1] This speed typically is of the order of 0.1 of the speed of propagation $\sqrt{E/\rho}$ through a continuum composed of the same material. If the system has smoothly varying properties, the only factor affecting simultaneity of reactions at the contact points is the gradient of wave speed $\gamma - 1$. If $\gamma \gg 1$ the reactions are almost simultaneous and may involve secondary impacts whereas if $\gamma < 1$ the reactions are almost sequential and they occur in order of increasing distance from the point of impact. The reactions that develop at initially quiescent contacts are the result of very small deforma-

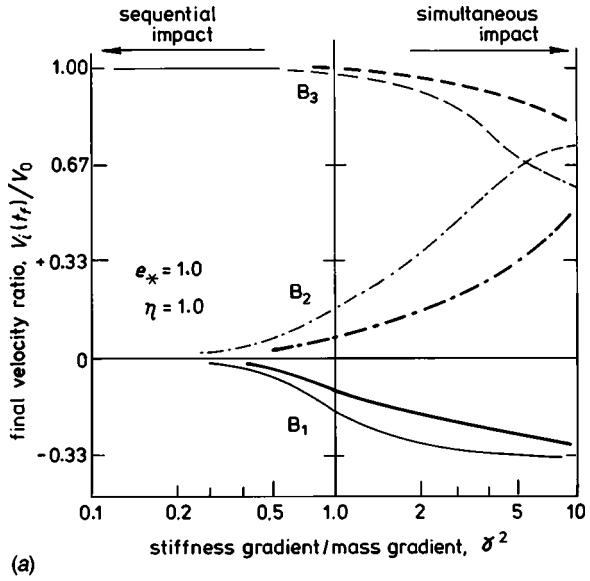

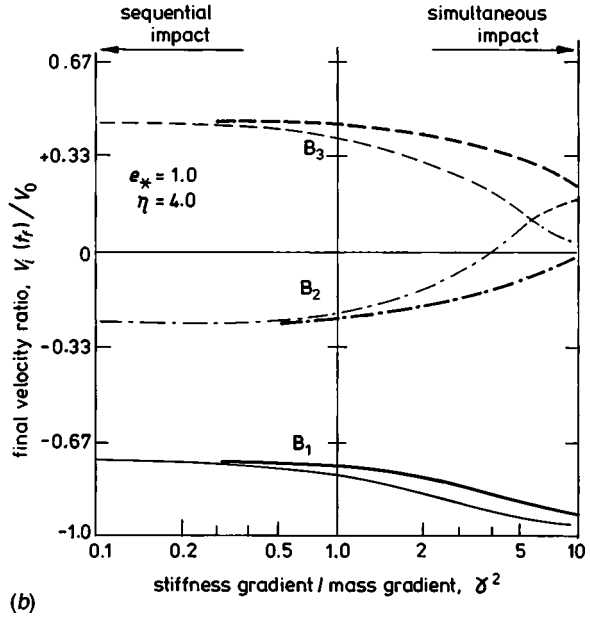

Fig. 2 Effect of gradient of wave speed $\gamma - 1$ on terminal velocities of balls B_1, B_2, and B_3 in three-sphere chain with mass gradient (*a*) $\eta = 1$ and (*b*) $\eta = 4$. Calculations assume elastic impact ($e_* = 1$) and either linear compliance (light lines) or Hertz compliance (heavy lines).

[1]Linear contact stiffness $k_c = 2.76 Y R_*$ is energetically equivalent at the force for initial yield to nonlinear Hertzian contact stiffness.

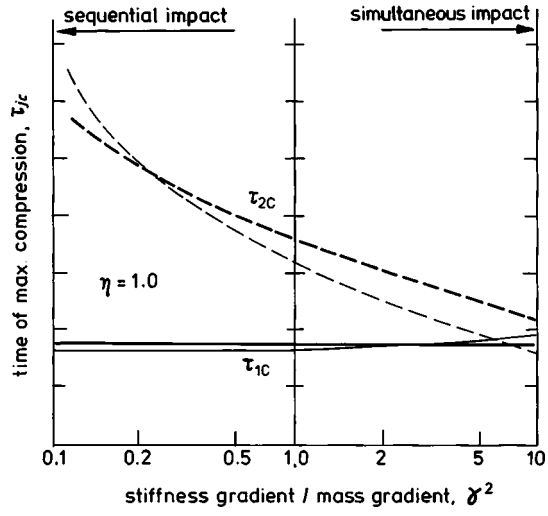

Fig. 3 Nondimensional time of maximum compression τ_{jc} at first and second contact points as function of gradient of wave speed $\gamma - 1$. Calculations assume elastic impact ($e_* = 1$) and either linear compliance (light lines) or Hertz compliance (heavy lines).

tions that arise during the contact period. In analyses of multibody impact dynamics, these time-dependent reactions can be replaced by reaction impulses at points of secondary contact only if either $\gamma \ll 1$ or $\gamma \gg 1$.

References

[1] Wittenburg, J., 1977, *Dynamics of Systems of Rigid Bodies*, B. G. Teubner, Stuttgart.

[2] Glocker, Ch., and Pfeiffer, F., 1995, ''Multiple Impacts With Friction in Rigid Multibody Systems,'' *Advances in Nonlinear Dynamics*, A. K. Bajaj and S. W. Shaw, eds., Kluwer, Dordrecht, The Netherlands.

[3] Pereira, M. S., and Nikravesh, P., 1996, ''Impact Dynamics of Multibody Systems With Frictional Contact Using Joint Coordinates and Canonical Equations of Motion,'' Nonlinear Dyn., **9**, pp. 53–71.

[4] Pars, L. A., 1966, *Treatise on Analytical Dynamics*, Oxbow Press, Oakville, CT.

[5] Johnson, W., 1976, '''Simple' Linear Impact,'' Int J. Mech. Engng. Ed. **4**, pp. 167–181.

[6] Hurmuzlu, Y., and Marghitu, D. B., 1994, ''Rigid Body Collisions of Planar Kinematic Chains With Multiple Contact Points,'' Int. J. Robot. Res., **13**, pp. 82–92.

[7] Ivanov, A. P., 1995, ''On multiple impact,'' Prikl. Mat. Mekh., **59**, No. 6, pp. 887–902.

[8] Adams, G., 1997, ''Imperfectly Constrained Planar Impact—A Coefficient of Restitution model,'' Int. J. Impact Eng., **19**, No. 8, pp. 693–701.

[9] Cundall, P. A., and Strack, O. D. L., 1979, ''A Discrete Numerical Model for Granular Assemblies,'' Geotechnique, **29**, pp. 47–65.

[10] Chatterjee, A., 1999, ''Asymptotic Solution for Solitary Waves in a Chain of Elastic Spheres,'' Phys. Rev. E, **59**, No. 5, pp. 5912–5919.

[11] Stronge, W. J., 1998, ''Mechanics of Impact for Compliant Multi-Body Systems,'' *IUTAM Symp. on Unilateral Multibody Dynamics*, Ch. Glocker and F. Pfeiffer, eds., Kluwer, Dordrecht, The Netherlands.

[12] Ivanov, A. P., and Larina, T. V., 1999, ''On the Problem of Collinear Triple Collision,'' *Proceedings of EUROMECH 397*, Grenoble, Springer-Verlag, New York.

[13] Stronge, W. J., 2000, *Impact Mechanics*, Cambridge University Press, New York.

Journal of Applied Mechanics

Discussions

Discussion: ''Response Bounds for Linear Damped Systems'' (Hu, B. and Eberhard, P., 1999, ASME J. Appl. Mech., 66, pp. 997–1003)

S. M. Shahruz
Berkeley Engineering Research Institute, P.O. Box 9984, Berkeley, CA 94709
e-mail: shahruz@robotics.eecs.berkeley.edu

In a recent paper, the authors consider the dynamics of an n-degree-of-freedom linear system represented by

$$M\ddot{y}(t)+D\dot{y}(t)+Ky(t)=f(t),\quad y(0)=y_0,\quad \dot{y}(0)=\dot{y}_0, \tag{1}$$

for all $t\geqslant 0$, where the vector of displacements $y(t)\in\mathbb{R}^n$ and the vector of applied forces $f(t)\in\mathbb{R}^n$. They obtain upper bounds on the norms of responses of the system (1) for the cases of free and forced vibration.

The authors obtain an upper bound on $\|y(t)\|:=[y(t)^Ty(t)]^{1/2}$ for all $t\geqslant 0$. Although, it is useful to know the time evolution of an upper bound on the function $t\mapsto\|y(t)\|$, it is more important to have a tight upper bound on

$$\|y\|:=\max_{t\geqslant 0}\|y(t)\|, \tag{2}$$

which is an indication of the largest displacement (strain) of the system (1). A tight bound upper bound on $\|y\|$, which is desirable for the worst-case scenario studies, results in less conservative designs.

The authors write that [1] ''In comparison to the response bounds available in the literature, the ones presented here are not only closer to the exact responses, but are also simpler to compute.'' This statement is evaluated in the following discussion.

According to [1], an upper bound on $\|y\|$ for the case of free vibration is obtained as follows:

(i) Compute

$$D^*=M^{-1/2}DM^{-1/2},\quad K^*=M^{-1/2}KM^{-1/2}. \tag{3}$$

(ii) Compute

$$\mu=\begin{cases}\lambda_{\min}(D^*)/2, & \text{for } \lambda^2_{\max}(D^*)\leqslant 4\lambda_{\min}(K^*),\\ \min\left\{\dfrac{1}{2}(\lambda_{\max}(D^*)-\sqrt{\lambda^2_{\max}(D^*)-4\lambda_{\min}(K^*)}),\right. & \\ \left.\quad\dfrac{1}{2}\lambda_{\min}(D^*)\right\} & \text{otherwise.}\end{cases} \tag{4}$$

(iii) Compute

$$D'=D-2\mu M,\quad K'=K-\mu D+\mu^2M, \tag{5}$$

$$E_0=\frac{1}{2}\dot{y}_0^TM\dot{y}_0+\frac{1}{2}y_0^TKy_0, \tag{6a}$$

$$E_0^*=E_0+\mu^2y_0^TMy_0+\mu y_0^TM\dot{y}_0-\mu y_0^TDy_0/2. \tag{6b}$$

(iv) An upper bound on $\|y\|$ is

$$\|y\|\leqslant\min\{\sqrt{2\lambda^{-1}_{\min}(K)E_0},\sqrt{2\lambda^{-1}_{\min}(K')E_0^*}\}. \tag{7}$$

The computation of the upper bound in (7) via steps (i)–(iv) is not as easy as that of some bounds in the literature. For instance, according to Shahruz and Mahavamana [2] an upper bound on $\|y\|$, when the matrix $DM^{-1}K+KM^{-1}D$ is positive definite (such as in classically damped systems), is

$$\|y\|\leqslant([\lambda_{\max}(M)/\lambda_{\min}(M)](y_0^Ty_0+\dot{y}_0^T\dot{y}_0/\omega_1^2))^{1/2}, \tag{8}$$

where ω_1 is the smallest undamped natural frequency of the system (1). It is evident that the computation of the upper bound in (8) is much simpler than that in (7) via steps (i)–(iv).

Now, it is determined how conservative the upper bounds in (7) and (8) are. In [1], the system (1) with the following coefficient matrices is considered:

$$M=\begin{bmatrix}1&0\\0&1\end{bmatrix},\quad K=\begin{bmatrix}5&-1\\-1&1\end{bmatrix},\quad D=(M+K)/2. \tag{9}$$

For different initial conditions the following upper bounds are obtained:

(B1) $y_1(0)=1$, $y_2(0)=0$, $\dot{y}_1(0)=\dot{y}_2(0)=0$:

$$\text{From numerical simulation:}\quad \|y\|=1, \tag{10a}$$
$$\text{According to (7):}\quad \|y\|\leqslant 2.51, \tag{10b}$$
$$\text{According to (8):}\quad \|y\|\leqslant 1. \tag{10c}$$

(B2) $y_1(0)=0$, $y_2(0)=1$, $\dot{y}_1(0)=\dot{y}_2(0)=0$:

$$\text{From numerical simulation:}\quad \|y\|=1, \tag{11a}$$
$$\text{According to (7):}\quad \|y\|\leqslant 1.15, \tag{11b}$$
$$\text{According to (8):}\quad \|y\|\leqslant 1. \tag{11c}$$

Results in (10) and (11) show that the upper bounds computed by (7) are *much more* conservative than those obtained by (8).

Next, upper bounds are computed for another system whose coefficient matrices are given in (92) of [1]. For the coefficient $\xi=0.1$ (see [1] for details), $y_0=[0\ 0\ 0\ 0]^T$, and $\dot{y}_0=[1\ 1\ 1\ 1]^T$, it is concluded that

$$\text{From numerical simulation:}\quad \|y\|=1.64, \tag{12a}$$
$$\text{According to (7):}\quad \|y\|\leqslant 4.14, \tag{12b}$$
$$\text{According to (8):}\quad \|y\|\leqslant 4.11. \tag{12c}$$

This example shows that both (7) and (8) yield conservative upper bounds on $\|y\|$, even though (8) resulted in a tight bound for the system whose coefficients matrices are given in (9).

In summary, it is shown that the upper bounds on responses of the system (1) derived in [1] are neither easily computable nor are tight, as it is evident from (10) and (11). Also, it is shown that no upper bound can be expected to be tight for all systems, as it is apparent from (12).

References

[1] Hu, B., and Eberhard, P., 1999, ''Response Bounds for Linear Damped Systems,'' ASME J. Appl. Mech., **66**, pp. 997–1003.
[2] Shahruz, S. M., and Mahavamana, P. A., 1998, ''An Upper Bound on Responses of Non-Classically Damped Linear Systems,'' J. Sound Vib., **218**, pp. 883–891.

Closure to ''Discussion of 'Response Bounds for Linear Damped Systems''' (2000, ASME J. Appl. Mech., 67, p. 636)

Bin Hu
e-mail: hbi@mechb.uni-stuttgart.de

Peter Eberhard

Institute B of Mechanics, University of Stuttgart,
Pfaffenwaldring 9, D-70550 Stuttgart, Germany

We thank Mr. S. Shahruz for his interest in our paper and welcome his comment. In our paper we consider a response bound as a bound with time evolution. Instead of Eq. (7) in Mr. Shahruz's discussion, our original response bound (Eq. (49) in [1]) reads

$$\|\mathbf{y}(t)\| \leq \min\{\sqrt{2\lambda_m^{-1}(\mathbf{K})E_0},\ e^{-ut}\sqrt{2\lambda_m^{-1}(\mathbf{K}')E_0^*}\}. \qquad (1)$$

The term e^{-ut} appearing in this response bound plays an important role. For the maximum amplitude of the response $\max_t\|\mathbf{y}(t)\|$, we prefer to call it amplitude bound. S. Shahruz and P. Mahavamana's results in paper ([2]) and some results from W. Schiehlen and the first author of this closure in papers ([3,4]) are for the amplitude bounds. Here we would like to point out that the procedure listed in S. Shahruz's discussion should be to compute our response bound given in Eq. (1) above. It may not be meaningful for the amplitude bounds. In Eq. (29) of our paper, we gave an amplitude bound

$$\max_t\|\mathbf{y}(t)\| \leq \sqrt{2\lambda_m^{-1}(\mathbf{K})E_0} \qquad (2)$$

which also follows directly from Eq. (1) in this closure. We can see that for the computation of this amplitude bound, most operations in the procedure listed in S. Shahruz's discussion are not necessary. Compared with Mr. Shahruz and Mr. Mahavamana's amplitude bound given in Eq. (8) of Mr. Shahruz's discussion, we have the opinion that our amplitude bound is not harder to compute since either the computation of the smallest undamped frequency ω_1 or the determination whether the matrix $\mathbf{D}\mathbf{M}^{-1}\mathbf{K}+\mathbf{K}\mathbf{M}^{-1}\mathbf{D}$ is positive semi-definite costs extra time. Though he showed their amplitude bounds are tighter than ours for two examples, we do not think this conclusion holds in general. Let us choose a simple example to explain this point. If we change the mass matrix in Eq. (9) of Mr. Shahruz's discussion to

$$\mathbf{M}=\begin{bmatrix}10 & 0\\ 0 & 1\end{bmatrix} \quad \text{or} \quad \mathbf{M}=\begin{bmatrix}0.1 & 0\\ 0 & 1\end{bmatrix} \qquad (3)$$

and the numerical values of the damping matrix and the stiffness matrix remain unchanged, then Mr. Shahruz and Mr. Mahavamana's amplitude bounds for both cases B1 and B2 become 10. However, our amplitude bounds remain unchanged. They are still 2.51 for the case B1 and 1.15 for the case B2. It is not difficult to find examples which show neither method to be superior.

Besides, we would like to state that although Mr. Shahruz and Mr. Mahavamana's paper about amplitude bounds for some nonclassically damped systems was published in December 1998 in the *Journal of Sound and Vibration*, their results were not known to the authors since our paper was received by the ASME Applied Mechanics Division on Aug. 24, 1998 and the final revision of the paper was received on Jan. 19, 1999. Therefore, a comparison with their results was not possible (and maybe not even reasonable since in our paper we discussed mainly response bounds with time evolution and not amplitude bounds).

In conclusion, we agree with Mr. Shahruz that no upper bound can be expected to be tight for all systems. In fact, in our paper we also stated that K. Yae and D. Inman's response bounds given in paper ([5]) are in some cases better than ours. But in contrary to Mr. Shahruz we think that improvements on the *response bounds* are meaningful and do not consider only the *amplitude bounds* to be important. Mr. Shahruz stated that our response bounds are neither easily computable nor are tight. We hope that we have been able to contribute to this interesting field of research and that in the future more easily computable and tighter response bounds will be developed.

References

[1] Hu, B., and Eberhard, P., 1999, ''Response Bounds for Linear Damped Systems,'' ASME J. Appl. Mech., **66**, pp. 997–1003.
[2] Shahruz, S. M., and Mahavamana, P. A., 1998, ''An Upper Bound on Responses of Non-Classically Damped Linear System,'' J. Sound Vib., **218**, pp. 883–891.
[3] Hu, B., and Schiehlen, W., 1996, ''Amplitude Bounds of Linear Forced Vibrations,'' Arch. Appl. Mech., **66**, pp. 357–368.
[4] Schiehlen, W., and Hu, B., 1995, ''Amplitude Bounds of Linear Free Vibrations,'' ASME J. Appl. Mech., **62**, pp. 231–233.
[5] Yae, K. H., and Inman, D. J., 1987, ''Response Bounds for Linear Underdamped Systems,'' ASME J. Appl. Mech., **54**, pp. 419–423.

Discussion: ''An Energy Method for Analyzing Magnetoelastic Buckling and Bending of Ferromagnetic Plates in Static Magnetic Fields'' (Yang, W., Pan, H., Zheng, D., and Cai, Z., 1999, ASME J. Appl. Mech., 66, pp. 913–917)

You-He Zhou
Professor, Department of Mechanics, Lanzhou University,
Gansu 730000, P. R. China

The authors gave an energy method to analyze the magnetoelastic buckling and bending of ferromagnetic plates in different static magnetic fields. The elastic strain energy of Eq. (2) employed in this paper is for the bending of the beam-type plate. And in the derivation of magnetic energy of Eq. (5), the effect of end edges on magnetic fields is not taken into account. After the longitudinal and transverse demagnetizing factor N_l and N_h are calculated by Eqs. (12)–(13), respectively, the expressions of critical field B_{cr} and bending deformation δ at free end are formulated by Eqs. (14) and (17), respectively. In this approach, the effect of width, denoted by w here, is considered only in the demagnetizing factors but not in the deformation. If a rectangular ferromagnetic plate under consideration is constrained by simple or clamped supports along the edges normal to the direction of width, it is possible that the same results for the magnetoelastic interaction will be obtained since N_l and N_h are independent on the boundary conditions. In other words, the results given in this paper are independent upon the support conditions of the edges along the longitudinal direction, which is obviously in contradiction to the practical problems. When the width of a rectangular plate increases to infinite, from the theory of plates, we know that the deflection of the plate approaches to that of a correspondingbeam-

type plate. When χ is very large, e.g., 10^3 order in Moon and Pao [1] to this case, the condition $1/\chi \ll N_l = 1$ is satisfied ($N_l = 1$ may be got by Eq. (12) when $w \to \infty$). According to Eq. (14*a*), however, it is found that the critical magnetic field $\overline{B}_{cr}$ for this case of cantilevered plates in transverse magnetic fields approaches to infinite. This results in contradiction to the finite critical magnetic fields given in literature to the same problem, e.g., Moon and Pao [1], Zhou et al. [2], and Zhou and Zheng [3] which are in agreement with the experimental data ([1,4]). For the prediction of bending of the plate in this paper, it is found by Eq. (17) and Fig. 3 that the incident angle α of the magnetic field does not influence the critical magnetic field B_{cr} of the magnetoelastic instability. This result is also in contradiction to the conclusion given in the literature using the imperfect sensitive analysis in Popelar [5] and the numerical analysis in Zhou et al. [2]. In fact, both the experimental measurement ([1,6]) and theoretical research display a fact that the critical magnetic field of a cantilevered ferromagnetic plate in transverse magnetic field is sensitive to the imperfect of incident angle of misalignment or oblique magnetic field. That is one of reasons why the theoretical predictions for the perfect case of the cantilevered plate in transverse magnetic field ([1,3,7] for example) are almost higher than their experimental data ([2]). For the case of a ferromagnetic plate in longitudinal magnetic field, the authors gave a differential Eq. (20) which indicates that there is neither bend nor buckle. The authors did not give a comparison of their theoretical prediction and the experimental data to the increasing of natural frequency of the considered plate ([8]). Zhou and Miya [9] successfully gave a theoretical prediction of this problem. For the general model of magnetoelastic interaction for ferromagnetic plate structures and bodies in arbitrary magnetic fields, by which the experimental phenomena of magnetoelastic buckling, bending and increasing of natural frequency can be described, it can be found in Zhou and Zheng [10,11]. It is obvious that these recent researches of magnetoelastic interaction do not support the opinion of authors: ''It seems that no further progress has been made in theoretical analysis since the Moon-Pao theory was presented.''

References

[1] Moon, F. C., and Pao, Y. H., 1968, ''Magnetoelastic Buckling of a Thin Plate,'' ASME J. Appl. Mech., **35**, pp. 53–58.

[2] Zhou, Y. H., Zheng, X. J., and Miya, K., 1995, ''Magnetoelastic Bending and Snapping of Ferromagnetic Plates in Oblique Magnetic Fields,'' Fusion Eng. Des., **30**, pp. 325–337.

[3] Zhou, Y. H., and Zheng, X. J., 1996, ''A Theoretical Model of Magnetoelastic Buckling for Soft Ferromagnetic Thin Plates,'' Acta Mech. Sin., **12**, pp. 213–224.

[4] Miya, K., Hara, K., and Someya, K., 1978, ''Experimental and Theoretical Study on Magnetoelastic Buckling of a Ferromagnetic Cantilevered Beam-Plate,'' ASME J. Appl. Mech., **45**, pp. 355–360.

[5] Popelar, C. H., 1972, ''Postbuckling Analysis of a Magnetoelastic Beam,'' ASME J. Appl. Mech., **39**, pp. 207–211.

[6] Popelar, C. H., and Bast, C. O., 1972, ''An Experimental Study of the Magnetoelastic Postbuckling Behavior of a Beam,'' Exp. Mech., **12**, pp. 537–542.

[7] Pao, Y. H., and Yeh, C. S., 1973, ''A Linear Theory for Soft Ferromagnetic Elastic Solids,'' Int. J. Eng. Sci., **11**, No. 4, pp. 415–436.

[8] Tagaki, T., Tani, J., Matsubara, Y., and Mogi, T., 1995, ''Dynamic Behavior of Fusion Structural Components Under Strong Magnetic Fields,'' Fusion Eng. Des., **27**, pp. 481–489.

[9] Zhou, Y. H., and Miya, K., 1998, ''A Theoretical Prediction of Natural Frequency of a Ferromagnetic Beam-Plate With Low Susceptibility in In-Plane Magnetic Field,'' ASME J. Appl. Mech., **65**, pp. 121–126.

[10] Zhou, Y. H., and Zheng, X. J., 1997, ''A General Expression of Magnetic Force for Soft Ferromagnetic Plates in Complex Magnetic Fields,'' Int. J. Eng. Sci., **35**, No. 15, pp. 1405–1417.

[11] Zhou, Y. H., and Zheng, X. J., 1999, ''A Generalized Variational Principle and Theoretical Model for Magnetoelastic Interaction of Ferromagnetic Bodies,'' Sci. China, Ser. A: Math., Phys., Astron. Technol. Sci., **42**, pp. 618–626.